Forward & Inverse Modeling for Synthetic Aperture Radar Observables in Bistatic Configuration. Applications in Forest Remote Sensing

Ludovic Villard

THÈSE

En vue de l'obtention du

DOCTORAT DE L'UNIVERSITÉ DE TOULOUSE

Délivré par **l'Institut Supérieur de l'Aéronautique et de l'Espace**
Spécialité : Micro-ondes, électromagnétisme et optoélectronique

---

Présentée et soutenue par **Ludovic VILLARD**
le 21 décembre 2009

Modélisation directe et inverse des observables radar à synthèse d'ouverture en configuration bistatique. Applications à la télédétection des milieux forestiers

Forward and Inverse Modelling for Synthetic Aperture Radar Observables in the Bistatic Configuration. Forest Remote Sensing Applications

---

JURY

M. Hervé Aubert, président
M. Pierre Borderies, directeur de thèse
M. Nicolas Floury
Mme Irena Hajnsek
M. Thuy Le Toan
M. Carlos López-Martínez, rapporteur
M. Alberto Moreira, rapporteur
M. Joseph Saillard, rapporteur

École doctorale : **Génie électrique, électronique et télécommunications**

Unité de recherche : **Équipe d'accueil ISAE-ONERA OLIMPES**

Directeur de thèse : **M. Pierre Borderies**

Foreword & Acknowledgments

The main part of this work has been undertaken at ONERA (The French Aerospace Lab) within DEMR –ElectroMagnetism and Radar Department– of Toulouse headed by Mr Florent Christophe, to whom I would like to express my first acknowledgements for his support throughout this period.

Besides, an agreement with DLR – German Aerospace Center – gave me the opportunity to achieve a fifteen months exchange at the HR institute (Hochfrequenztechnik und Radarsysteme) located in Oberpffafenhofen (Bavaria) so that I would like to thank as well Professor Alberto Moreira for his specific interest towards my work.

The cooperation between ONERA and DLR, both members of the EREA, comes with the European willingness to gather skills and facilities between the various national establishments. These combined efforts can be illustrated through common symposium like ODAS which foster the exchange of guest scientists but also with common projects in various fields of research. Prominent among them, aeronautics, acoustic, propulsion technologies are concerned but also radar systems, which can be illustrated more specifically with the achievement of a joint bistatic campaign in 2002, all the more meaningful as a matter of cooperation that it has been made possible using the RAMSES and E-SAR sensors, the respective airborne radar facilities at ONERA and DLR.

This brings us actually to the topic of this thesis. Beyond the technological challenges which have risen this campaign – the first of this kind – to a great milestone in the history of bistatic experiments, the physical potential of the new observables (ensued from the bistatic geometry) is rather concerned throughout this thesis. Indeed, the question of how these new observables can improve the retrieval of land parameters of interest – within the context of forest remote sensing – turned out to be widely opened so that it prompted Pierre Borderies – my supervisor at ONERA – to engage this thesis. Beyond this nice prospective idea, I really would like to thank him for his open mind and our friendly relationship. Thank you also Pierre for this voracious appetite for new ideas, sometimes truly courageous regarding pressing deadlines with dispersive PhD students ! Meanwhile, I'm also grateful for his wiseness which bring us to share this somehow 'risky' thesis subject with one of the leading team regarding SAR remote sensing, that is the Pol-InSAR group leaded by Irena Hajnsek.This was indeed a great opportunity and I would like to pronounce due thanks to Irena for her time, laying aside surface backscattering for some brainstormings about forest scattering in bistatic. I'm also very thankful for her her open-mindedness and availability, even to arrange administrative issues despite more than tight schedules ! Special thanks also on that matter to her best delegates (namely Thomas & Mr Beautiful !) for their very friendly helping hand, especially to make a German beginner discover both beautiful and somehow impenetrable Bavarian voices. Besides, the time I spent in DLR was besides all the more interesting that it was a quite intense period regarding bistatic activities. Indeed, on top of possibilities for opportunistic acquisitions offered by the successful launch of TerraSAR-X (on June 15, 2007), the reiterating project of a bistatic airborne campaign using RAMSES and E-SAR gave birth to very interesting idea concerning advanced type of configurations. Even if that plan didn't come out, the engaged working sessions were very fruitful, especially to realise the constrains brought by system requirements, to which I wasn't really confronted with EM modeling...A special appreciation is de facto due to Gerhard Krieger's team, for their motivation and expertise, together with the very friendly brainstorming sessions and discussions with Marc. More generally, together with the very great welcome from all the various HR working teams, I've really appreciated the very dynamic atmosphere, especially thanks to the many scientist guests but also to the many post-docs and PhD students. On the one hand it is – scientifically-wise

– really fruitful and on the second hand, it comes with a very nice cosmopolitan atmosphere. I already apologize for the ambassadors I may forget, and starting from the farthest, I would like to express my friendly greetings towards Koichi, Seung-Kok & Jun Su for the Asian side, my office mate Jayanti, Rapha-ldo & Georges from the quasi-opposite longitude, Noora & Kais for the more or less Middle East, el equipo Español with Marc, Pao, Jaime and of course the essential Italian scuderia (at DLR as in other nice places !) with Francesco, Luca, Matteo and Mickaele. Closest but not least many friendly thanks to the local "gemütlich mannschaft" : mister beautiful Helmut (sorry quasi-local !), the "Konig des Waldes" Florian and both Northern and Bavarian (FC !) Thomas. Besides, this world trip brings me to acknowledge people at ONERA's Toulouse center which really ease the conditions of this exchange and especially the involvement of Mr Boutry (director of DEMR). My staying at DLR and especially the working from a distance with Pierre have been indeed really facilitated by several round trips (from which I could truly experiment by myself the advantages of bistatic links !) and it also helped me to keep an eye on the DEMR news. Among its permanent orchestra, I would like first to acknowledge Danielle, Corrine and Bas, Cédric D & M, José, Thibault and Xavier for their kind interest on the 'green' side of radars. Also essential to the DEMR lively ambiance, very friendly thanks to my PhD mates with from A to Z : Arnaud, Bertille, Clément, Janus, Julien, the Jazz performers Maxime-Nico-Stéph & Thomas, Laura, Laurent, Nadia, Simon and once more Z ! Together with the nice ambiance, I'm also really thankful for the great working conditions, with of course the computing facilities (special due to F. Malecki's team)

Together with the nice ambiance, I'm also really thankful for the great working conditions, including of course the computing facilities (special thanks for P. Malecki's team) and especially the widening to other research groups, whether in the framework of wide cooperations (such as with DLR), contracts (e.g with ESA) or internal research projects like ENVIRO bringing together several ONERA's departments, which gives me the opportunity to thank Pascale and her team at ONERA Salon de Provence center. These various exchanges are always fruitful, especially to get familiar with the who's who in radar remote sensing. In particular I had the chance to meet my future jury members : Nicolas Floury, Irena Hajnsek, Carlos López-Martínez, Alberto Moreira, Joseph Saillard and Thuy Le Toan to whom I would like to address my sincere acknowledgements, not only for their relevant proofreading but also for their understanding during the finalization of the manuscript. Beyond to that favourable working environment, I would like finally to express due thanks to my family and friends, definitively essential to step back and get some fresh air.As a matter of fresh & great air – and by the way to experiment slope effects – very special thanks to my mountain team mates, beyond all (for being there !) the Pyrennees and its famous mountaineering spots we enjoy with Baptiste, Benj, Clara, Gauthier, Fréde & Marion, Wannes....& co, i.e all the topo masters from the SCUAPS and of 'course' (or on courses) its maestro Sergio ! To continue on high altitudes, a special wink to the CVVR's gliding team, definitively the best place for fancy & friendly flights and perhaps to get initiated to the future of flying formation ! Even higher (but powered...energy sources not reported), a big-up to all the ENAC crews for unforgettable tours, especially to Alex, Tiboat (& co from the 'àP'club) and of course to our unique p'tit Prés & super Chinese (alias Raphy & Hoang) for these great times within and out of the collocation...big thank Hoang for the logistic too ! As a matter of resourcing times, special thanks to Sandrine & Quyen (the best ambassador of IC & Vn cooking), Alexandra & François for downtown tours, Mélissa for the first year inspiration, the Vertigo group (esp Dania, Jo & Tarik) and beyond all Sarah for the overall orient delices.

Last but not least, my deepest acknowledgments are due to my family, for so much and simply for being there (merci Papy !). A special wink to my big band of cousins for all these funny tours, to my sisters Anne-Aude-Véro for having paved the way (especially with my two sweet

goddaughters Lou & Marie and Nina-Yann-Zoé), naturally to my parents for so many things and particularly for their sharp sense of geometry, to Madé (for taking care...esp of the rice in crucial moments !), to my great mother and uncle Adrien for their benevolent and smart eye.

Finally, not to ruffle anyone, my last acknowledgments (and apologizes) are due to all the people which haven't found their word, especially those who stop for a while for overall discussions on the specificity of the bistatic configuration, though it is a bit frustrating to realise that its interest was obvious for most people (let's say it's rather common in science that core but non demonstrated ideas become principles...) To conclude that long and somehow hazardous exercise, I would like to reassure the reader : his bistatic position should – under the heart of the thesis – ease his understanding of what is going on...

Abstract

Forest observation worldwide is paramount in many fields of study, not only regarding environment applications – whether at a global or local scale (carbon cycle and climate stakes, ecosystems health) – but also towards anthropogenic activities (forestry, detection related to military or rescue purposes). Though vast – with about one third of earth's land surface – its importance lies rather in its highly sensitive nature versus climate or human pressure, which thereby strengthen the need of observation and monitoring. Within this scope, remote sensing technique can't be overlooked and takes truly part in a better understanding of Earth System Science. Prominent among these, radar is favored by supplying its own illumination (as a active system) and by the all-whether as well as medium penetration capabilities of microwaves. Radar remote sensing is thereby particularly relevant to probe forest structure, especially with the Pol-InSAR acquisition which enables to localize the polarimetric information about the medium scattering nature, on top of the imaging capacity. As testified by the fertile number of campaigns and theoretical studies, one can truly assert the golden age of SAR use, among which the bistatic configuration could bring major improvements. Although revisited several times, its potential for forest remote sensing hasn't been assessed so far. The current resurgence for bistatic, fostered by noticeable technical advances (e.g on synchronization) and well illustrated by recent successful airborne and hybrid spaceborne campaigns, makes the well known geometrical, opportunistic and discretion advantages of a receive only sensor more and more attractive. Nonetheless, such acquisition haven't been achieved yet for forest remote sensing (e.g at P or L band), our investigation will be thus based forward electromagnetic simulation. The latter finds indeed a great importance to understand and foresee the scattering behaviour. For that purpose, MIPERS – Multistatic Interferometric and Polarimetric model for Remote Sensing – based on a coherent and discrete formulation, has been developed to cope not only with the multistatic geometry (and the subsequent imaging constrains) but also with possible complex scenarios of forest, including man-made structures by means of an original multi-zone approach. Theoretical validations but also confrontations with experimental monostatic data have been performed and emphasize through a sensitivity analysis the importance of specific ground truth elements. Moreover, simulations have been achieved in order to set forth specific scattering behaviour intrinsic to a given bistatic geometry. On top of symmetry properties and polarization effects which turn out to be relevant to discriminate coherent and distributed targets (especially for detection applications), the sensitivity of the scattering mechanisms towards the possible bistatic configurations has been analysed to extend the current retrieval methods in monostatic based on the P-HV or on the Pol-InSAR approach. For the latter, an ad-hoc inversion scheme has been developed to cope not only with the extension to bistatic but also with an improved description of the forest model, particularly for what concerns the structured medium and the coupling terms between volume and ground scatterers. Whether for this quantitative inversion approach involving descriptive parameters or for biomass retrieval directly based on polarimetric intensities, optimal bistatic configurations have been set forth in the light of simulations analysis, coming thereby with the planning of innovative campaigns as further prospects.

Keywords: Forward & Inverse EM Modeling – Bistatic Pol-InSAR – Forest Radar Remote Sensing

Résumé

Essentielles au sein de la biosphère ainsi que pour la régulation climatique (cycle de l'eau, du carbone), les forêts sont aussi caractérisées par une forte sensibilité aux activités anthropiques à l'origine de changements manifestes, rendant leur surveillance d'autant plus pertinente. Dans ce contexte, le SAR constitue un moyen de télédétection unique, fort des propriétés micro-ondes de sensibilité et de pénétration du couvert végétal ainsi que d'atouts opérationnels majeurs (auto-illumination, couverture, résolution spatiale et temporelle). Néanmoins, l'interprétation de la sensibilité des mesures SAR aux variables d'intérêts de terrain n'est pas triviale et constitue de multiples axes de recherche dont l'étude de la configuration bistatique, définie par une séparation entre émetteur et récepteur d'une distance significative par rapport à la scène considérée. Bénéficiant de progrès significatifs concernant les précisions de synchronisation/localisation, la période actuelle atteste d'une certaine résurgence pour le bistatique, comme en témoigne le succès de récentes campagnes aéroportées (e.g acquisition conjointe ONERA-DLR en 2002) ou mixte spatioportées (acquisition d'opportunité via TerraSAR-X). Principalement mis en avant pour des considérations systèmes et stratégiques, la question du potentiel physique des observables bistatiques reste peu traitée, d'autant moins dans le cas de la caractérisation des milieux forestiers. Cette thèse s'inscrit donc dans cet objectif, avec pour méthodologie l'exploration de configurations bistatiques optimales au sens d'une amélioration de l'inversion des paramètres d'intérêts tout en considérant leur faisabilité. Dans ce cadre, la modélisation électromagnétique constitue un outil fondamental, illustrée ici par le développement spécifique du simulateur MIPERS – Multistatic Interferometric and Polarimetric model for Remote Sensing – dont les originalités par rapport aux modèles existants ont montré toute leur importance pour la compréhension du comportement des nouvelles observables. L'extension des approches d'inversion en monostatique à partir de l'intensité SAR ou d'acquisitions Pol-InSAR – visant à estimer la biomasse ou des paramètres descriptifs de modèles de forêts (dont la présence de cibles artificielles) – est alors développée, à l'issue d'analyses théoriques mais aussi phénoménologiques, découlant des résultats de simulations. Outre de futures campagnes expérimentales bistatiques, sont aussi mises en avant des perspectives innovantes de configurations multistatiques, notamment via des signaux d'opportunités de type SAR ou GNSS-R.

Mots-clés: Modélisation électromagnétique directe et inverse – Pol-InSAR Bistatique – Télédétection des forêts

Zusammenfassung

Von großer Bedeutung innerhalb der Biosphäre sowie im Rahmen der Klimaregelurierung, sind die Wälder gleichzeitig sehr sensitiv gegenüber menschlichen Aktivitäten und Eingriffen, was ihr Monitoring umso relevanter macht. In diesem Zusammenhang bildet der SAR ein einzigartiges Mittel zur Fernerkundung, welches die vorteilhaften physikalischen Eigenschaften der Mikrowellen mit den operationalen Vorteilen der Hauptsysteme vereint (selbständige Erhellung, Abdeckung, räumliche und zeitliche Auflösung). Dennoch ist die Interpretation von SAR-Maßnahmen nicht trivial und bringt viele Forschungsgebiete hervor, darunter das der bistatischen Konfiguration, welches durch eine Trennung zwischen Sender und Empfänger defininiert ist. Bedeutende Fortschritte bezüglich der Synchronisation und Lokalisierung führten zu einem gewissen Wiederaufleben der bistatischen Konfiguration, wie beispielsweise durch die neuen Airbornes (z.B. die gemeinsame ONERA-DLR Kampagne), oder die gemischten Spaceborne-Kampagnen (opportunistische Anschaffungen von TerraSAR-X) bezeugt wird. Obwohl hervorgehoben wegen System und strategischen Vorteilen, bleibt das physikalische Potenzial von bistatic observables schlecht erforscht umso mehr vor dem Hintergrund der bewaldeten Landcharakterisierung. Basierend auf dieser Frage, hat diese Dissertation zum Ziel, die optimalen bistatischen Konfigurationen zu untersuchen, um die Wiederauffindung zu erleichtern, und dabei die Umsetzbarkeit in Betracht zu ziehen. In diesem Rahmen ist das EM Modellieren von größter Bedeutung, wie hier mit der Entwicklung des Simulators MIPERS gezeigt. Dessen Vorteile im Vergleich zu vorhandenen Modellen zeigen seine große Bedeuting für das Verständnis des neuen sich zerstreuenden Verhaltens. Beruhend auf diesen theoretischen und phänomenologischen Ergebnissen, folgte aus unseren Simulationen, innovative Verlängerungen der zwei Hauptwiederauffindungsannäherungen in monostatisch sind hervor gesetzt worden, entweder Biomasse-Bewertung mittels Intensitätsniveaus oder allgemein beschreibendere Waldmusterrahmen (einschließlich der möglichen Anwesenheit künstlicher Elemente) betrachtend. Abgesehen von experimentellen Vorhaben die von dieser Arbeit inspiriert wurden, tragen unsere Ergebnisse zur Untersuchung von viel versprechender Aussichten von multistatischen Beschaffungen bei, besonders hinsichtlich opportunistischer Signale (SAR oder GNSS).

Schlüsselworte: Vorwärts und inverse Elektromagnetisches Modellierung – Bistatische SAR – Wald-Monitoring

Contents

List of Figures

List of Tables

Introduction

Concerns about Earth's health have never been so high since we realize its living dimension in the sense that the planet resources and tolerance towards pollutions are limited. This feeling is scientifically supported by the major environmental organizations such as the IPCC (Intergovernmental Panel on Climate Change) or its European counterpart the EEA (European Environment Agency). Indeed, all agree to impute the different records, not only about global temperature increment but also concerning matter changes involved in the hydrological, nitrogen, phosphorus, sulphur and carbon cycle to anthropogenic activities, which effects are now well distinguished from the long term solar illumination and Earth orbit cycle ones (prominent during ice ages). In addition to human living conditions damages conveyed by these various pollutions, severe threats on biodiversity and thereby on ecosystems resilience are likely. The pressure on climate, especially through global warming, come also with strengthened climatic crisis and in a general way, will contribute to reinforce inequalities throughout the world. Besides, with one-sixth of the global population suffering from hunger, agriculture is becoming one of the greatest stake for the century as testified also by the last year (2008) major food crisis. Though intensified by economic and speculation dumping, the current international run for arable lands reveals much more than immediate interests. Thereby, these worries rise the problem of resources and geohazards management which goes hand by hand with a better understanding of the Earth processes dynamic. Indeed its inherent complexity lies in the interlinked and feedback nature of a network involving at different spatial and temporal scale, the atmosphere, the solid Earth, the hydrosphere, the cryosphere, the biosphere and last but not least the anthroposphere.

Consistent with this view as a collection of systems ("the Earth System Science"), remote sensing turns out to be fundamental in the sense that its technique enable to characterize the latter, whether through radiative variables (infrared radiation, emissivity, scattering coefficient) or state variables concerning surface/structure intrinsic properties (humidity, chlorophyll content, height, biomass) and acting as boundary limit conditions. What is more, this can be mostly performed from the land scale to the global one and via non intrusive measurements. Indeed, with a tremendous range of applications concerning Earth science -too numerous to be enumerated- and supported by an extensive number of campaigns during the past twenty years, spaceborne and airborne remote sensing techniques have demonstrated their versatility but such complex and various means need a specific policy and strategy for an efficient operational use. ESA (European Space Agency) is working on it especially through the future science challenges (cf. the ESAC – Earth Science Advisory Committee – guidelines formulation) and the resulting major priorities for remote sensing in coordination with the various national working prospective groups (e.g the PNTS and TOSCA in France). Without being exhaustive, the major requirements and points at issue lie in temporal and spatial resolution as well as coverage, continuity (with the follow-on mission concept) and interdisciplinarity to encourage exchanges between communities and ease thereby the data access. Fostered by the European commission, the GMES – Global Monitoring for the Environment and Security – initiative conducted at ESA have been made for that purpose. Likewise, on the global scale and still within this scope of interoperability and effectiveness, the GEOSS – Global Earth Observation System of System – have been created, gathering more than 77 countries through their spatial agencies (such as ESA, NASA, JAXA to name only a few).

Beyond these different expectations and plans, prospective researches on new algorithms and systems can't be of course overlooked. To this respect, as far as active radar remote sensing is hereafter concerned, the innovative point at issue lies in the bistatic configuration that is when the receiver is separated from the transmitter, by a distance large enough to be comparable to the one with the scattering surface. Though long-standing is the concept -the bistatic radar configuration has been indeed revisited several times since the monostatic one took the leadership- several

points remain worthwhile to investigate, fostered furthermore by an innovative join campaign conducted in 2003 at ONERA and DLR. As a matter of fact, for about 10 years, a new resurgence seems to occur as testified by various demonstrative bistatic image acquisitions involving airborne and even hybrid spaceborne campaigns. Concerning measurements and commonly in mono or bistatic configuration, images are ensued from successive radar acquisitions forming the synthetic aperture, hence the Synthetic Aperture Radar (SAR) designation. Then, the pixels complex values carrying the information depend on how the signal is scattered onto the surface and towards the receiver. On top of different polarimetric channels sensitive to the type of scattering event, Pol-SAR images are enriched with the interferometric measure providing an information about the vertical localization of the target. The cornerstone of the monostatic Pol-InSAR (Polarimetric and Interferometric SAR) success story lies in this combination of informations. Indeed, joined with the penetration capabilities of radar waves not only regarding atmospheric propagation but also through the media structure of interest, the Pol-InSAR acquisition has proven its great interest and particularly for forest remote sensing. Within the environmental stakes context mentioned previously and considering about 3.9 billion hectares worldwide, forest monitoring is of the greatest importance whether for land use, biodiversity, local or global climate issue through its carbon sink role. Beyond that, such important Earth coverage rises also the interest for detection through the vegetation cover, concerning camouflaged targets for military applications or lost ones for search and rescue. With these specificities, such acquisition is truly remarkable and unique in remote sening as long as image acquisitions from LIDAR, although very promising to characterize forest structure, are at the moment not operational. Yet, before putting Pol-InSAR into space, several improvements are under investigation especially to cope with the inversion algorithm robustness in order to retrieve quantitatively forest descriptive parameters such as vegetation height. Research is also in progress concerning the operational part to improve image processing – signal to noise ratio (SNR), motion compensation (MoC), interferometric frange quality – and recently many innovative modes have been demonstrated to cope with classical SAR limitations (for instance the trade-off between wide swath and high resolution). In this prospective framework, the bistatic configuration and precisely the potential of the subsequent new SAR observables to characterize the region of interest deserve a specific investigation. On top of the well known concept advantages reminded afterwards, we'll focus particularly on the observables potential to ease the previously mentioned inversion algorithm, inferred in the light of our understanding of forest bistatic scattering. For that purpose and since -to our knowledge- biPol-InSAR acquisitions at suitable frequencies (i.e P to C band) haven't been achieved yet, we will naturally head for electromagnetic forward models. Indeed, within the objective of predicting the SAR observables behaviour in new configurations, forward models bring a paramount support to our understanding of scattering mechanisms and ease thereby the qualitative and quantitative data inversion. As sophisticated as they can be, their ability to model exactly the electromagnetic process is naturally utopian but in a general way, in the light of validation and confrontation with experimental data in given configurations (mostly monostatic), derivations from this reference point are physically reasonable.

In view of these considerations, the thesis outlines can be drawn as follows :

- The **first chapter** is dedicated to the specificities of forests as a natural medium and to the specificities of radar as a remote sensor. One the one hand, the need of forest monitoring is explained mainly in the light of current environmental issues which brings us the parameters of interest to be studied within the remote sensing scope. On the other hand, radar and especially SAR capabilities are emphasized, in comparison with passive remote sensing whether within the microwave or the optical domain. The various observables ensued

from these techniques are presented in a qualitative and quantitative way.The potential of these approaches in forest remote sensing is then emphasized on account of their overall sensitivity, regarding variables of interest but also perturbing factors. The status of bistatic radars is also introduced especially for what concerns interests at the origin of its latest resurgence.

- In the **second chapter**, forward electromagnetic modeling is concerned with the presentation of the developed simulator **MIPERS** – Multistatic Interferometric and Polarimetric model for Remote Sensing – from which our investigation of the bistatic radar potential will be conducted. Consistent with the currently more advanced acquisition type in monostatic – the Pol-InSAR one – the coherent approach and discrete formulation will be detailed as well as more original elements with respect to the current state of the art. Indeed, on top of the multi-static capabilities among which the monostatic configuration is a particular case, the possibility of considering not only homogeneous or sparse forests but also man made structure inside the vegetation cover using an ad-hoc multi-zone description will be pointed out. Besides, within the paramount requirement of modeling processed SAR observables as faithfully as possible, we'll get onto operational points commonly omitted in monostatic but which can be severely impacted by the bistatic geometry. Then, the presentation of various confrontations with experimental monostatic SAR data illustrates the modeling process – including the ground truth use – and lead us to a sensitivity analysis to emphasize the most relevant parameters impacting the observables, ensued from the scattering mechanisms decomposition. Detection capabilities in bistatic will be also presented in a specific example with a vehicle (truck) under a temperate forest like Nezer.

- Specific properties of bistatic scattering are investigated in **chapter 3** with the aim of a better understanding of the observables behaviour. Such analysis will then be of the greatest interest for the retrieval strategies conducted in the following applications chapters, especially to set forth optimal configurations which are moslty determined by the continuity of a scattering favourable phenomenon whatever the forest type. For that purpose, theoretical considerations especially concerning polarimetry and symmetry are pointed out. This brings us also to the paramount distinction between coherent (point-like scatterer) or distributed target so that the chapter ends with specific bistatic advantages concering detection applications.

- **Chapter 4** is focused on the potential of the bistatic configuration to retrieve forest biomass directly from polarimetric scattering coefficient intensities (σ^0_{qp}). This approach, based ideally on the bijective dynamic between backscattering and the biomass level has been successfully used in monostatic but turns out to be limited by its robustness towards the various possible kind of forests, among which the ones of highest biomass are not tractable in view of the saturation phenomenon. Hence the motivations to transpose that approach in bistatic, with the search for optimal configurations regarding these challenging issues.

- Prominent among the monostatic retrieval methods is also the quantitative inversion of Pol-InSAR coherences based on the analytical formulation of the volume decorrelation. Likewise, we propose in **chapter 5** to investigate the extension of this approach in the bistatic case. On top of the theoretical work concerning an improved description of the forest model with structure effects and coupling terms between volume and ground, a more advanced and general inversion scheme has been proposed which enables to assess the inversion feasibility in multiple configurations of forest model complexity and radar

acquisitions simulated with MIPERS, restricted to nearly the same bistatic angle with possibly several baselines. Based on this analysis, optimal configurations can then be set forth on account of the trade-off between the interest in additional descriptive parameters and the required number of measures to ensure the inversion success.

Finally, the major conclusions will be drawn mainly on account of the potential of specific bistatic configurations set forth through the simulation analysis whereas a discussion concerning the general method and the proposed improvements originate research topics for further campaign prospects and further investigations.

Notations

	Notations & Symbols	Definitions
Mathematics	j	standard imaginary unit ($j^2 = -1$)
	$\|\mathbf{x}\|$	standard norm ($\|\cdot\|_2$) generalized to scalars, vectors or matrices)
	$\hat{x}$	unitary vector
	$(\hat{x}, \hat{y}, \hat{z})$	canonical Cartesian basis
	$\vec{x}$	arbitrary vector
	$[\,\cdot\,]$	arbitrary matrix
	A^t	transpose matrix ($A^t = A^{-1}$ for A orthogonal)
	$A^\dagger$	adjoint matrix ($A^\dagger = A^{-1}$ with A unitary)
	' . '	standard scalar product (between scalars or real vectors), inner scalar product between complex vectors or ordinary matrix product
	'$\wedge$'	standard cross product between vectors
	'$\odot$', '$\otimes$'	Hadamard and Kronecker product for vectors or matrices
	$\mathrm{diag}(\,\cdot\,)$	Operator turning a square matrix A into the vector $a = [A_{ii}]^t$
Geometrical parameters	$\vec{r}_{\mathrm{T}}$	vector from 0 (origin reference point) to T : $\vec{r}_{\mathrm{T}} = \overrightarrow{OT}$
	$\widehat{(\vec{r}_1, \vec{r}_2)}$	oriented angle between $\vec{r}_1$ and $\vec{r}_2$
	β	bistatic angle : $\beta = \widehat{(\vec{r}_{\mathrm{R}}, \vec{r}_{\mathrm{T}})}$
	ψ_{az}, ψ_{ins}, ψ_{int}	orientation angles for branches (see p189)
Electromagnetics	c, f, λ	celerity of light, frequency and wavelength
	k_0, w_0	free space wave number/pulsation at center frequency
	ε_r, μ_r	relative dielectric and permeability constants ($= \frac{\varepsilon}{\varepsilon_0}, \frac{\mu}{\mu_0}$)
	$\vec{E}_{\hat{t}}(\vec{r}, T)$	em field at $\vec{r}$ due to transmission in polarization $\hat{t}$ from T
	$[c_{pp}]_{p\in[v,h]}$	vector $[c_{vv}, c_{hh}]^t$
	$[c_{qp}]_{(q,p)\in[v,h]}$	matrix $\begin{bmatrix} c_{vv} & c_{vh} \\ c_{hv} & c_{hh} \end{bmatrix}$
	$\mu_{qp}^{(\mathrm{dg})}$, $\mu_{qp}^{(\mathrm{Tsg})}$, $\mu_{qp}^{(\mathrm{Rsg})}$	polarimetric (qp) ratios of scattered intensity resp. for direct and specular ground contributions (cf. p199,207)
	$\widehat{\iota}$	angle related to the equivalent ground point (cf. p204)

Chapter 1

Forest Radar Remote Sensing

Contents

1.1 The Remote Sensing Approach

A concise definition of *'remote sensing'* is the field of study related to information extraction about an object or a phenomenon without coming into physical contact with it (cf. [Colwell, 1983; Campbell, 1987; Robin, 2001] among others). At a first sight, this definition has a broad meaning and indeed encompasses a wide range of applications from planetary and earth observation to more common ones, in medical imaging for instance or simply with human vision. However, the term *'remote sensing'* has become implicitly more restrictive with the ERTS-1 NASA project in the sixties (Landsat-1, launched in 1972), which besides matches the period when it was coined by Evelyn Pruit. As a matter of fact, as emphasizes by [Colwell, 1983], this breakthrough stands out from previous approaches such as conventional photography (in the visible domain) in optics in the way that it demonstrates the huge quantity of information brought by the multispectral and by the spaceborne acquisition at the global scale.

This approach truly gives the primacy to indirect methods, as opposed to direct ones (cf. [Campbell and Norman, 1987]). The latter relies on direct estimation procedures and statistical summarization with descriptive variables of the natural medium (for instance tree density or height in the forest case) simplified sometimes with the knowledge of allometric relations. Such procedures can go as far as harvesting, felling and weighing. This labour intensive and time consuming approach presents thereby severe practical limitations for large or inhomogeneous areas. On the other hand, indirect methods with a much faster data acquisition process is much more promising regarding earth observation challenges but needs to focus the work on on appropriate sensors and theoretical analysis. Besides, at the local scale, direct methods are of great importance not

only for specific ecosystem studies but also for the purpose of indirect methods calibration and validation, particularly as far as modeling will be herein concerned, for which an accurate land description is needed to feed forward simulators.

As far as forest remote sensing is concerned, the following part (section 1.2) will be dedicated in the first place to forest monitoring stakes and then in a second place to how this medium can be characterized, that is which quantitative state variables are relevant regarding the observation need.

Once the medium has been defined, the further point at issue will concern the radiative variables which sensitivity encompass the state parameters, namely the information vector. Among the different remote sensing approaches, the RADAR specificity as a remote sensor will be emphasized as well as its capabilities, still in the light of forest monitoring.

1.2 Forested Land Surfaces : Stakes and Characteristics

Among the five spheres encompassed by earth science, biosphere presents a singular complexity, and even within this scope restricted to vegetated land surfaces. Indeed, due to its high spatial heterogeneity and temporal variability, a consequent wide set of parameters are required to characterize the concerned media. This issue will be discussed in the second paragraph, before the emphasis of its high importance regarding many pregnant stakes at the moment.

1.2.1 Forest Monitoring Stakes

In the first place, one can relay this outstanding fact from the United Nation FAO (Forest and Agriculture Organization, Roma) :

Forests worldwide has shrunk by some 20 % since the beginning of the twentieth century, 40 % since agriculture began 11000 years ago, covering nowadays about one third of the earth land surfaces with roughly 3.9 billion hectares. What is more, this trend goes on at a sustained rate so that we do not need to go back very far in time to appreciate the changes, as testified by figures in table 1.1.

World Forest Cover : 1990–2005

Dates / Continents	1990	2000	2005
Africa	699	656	635
Asia	574	567	572
Europe	989	998	1,001
North and Central America	711	708	706
Oceania	213	208	206
South America	891	853	832
TOTAL WORLD	**4,007**	**3,989**	**3,952**

(Million Hectares)

Figure 1.1: Forest repartition around the world and evolution since 1990, from FAO statistics, cf. [Food and of the United Nations, 2009] and http://www.fao.org

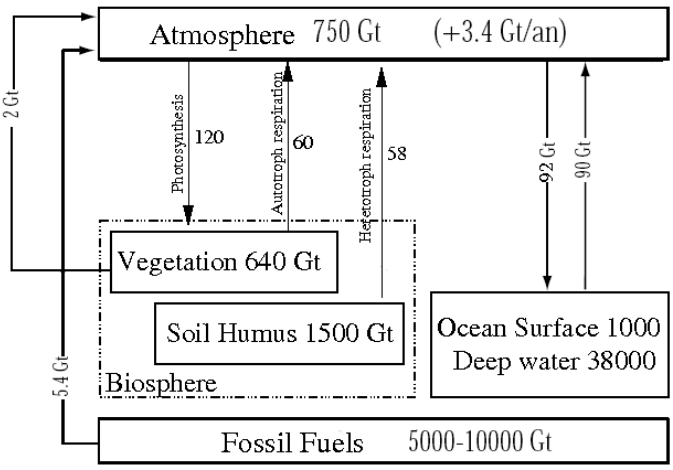

Figure 1.2: Global carbon budget with its different actors from the IPCC organization, cf. [IPCC, 2007], stocks and fluxes are respectively represented by boxes in billion tons and arrows in billion tons per year.

This loss affects mainly tropical and subtropical forests and fortunately is slowed down by planting or natural reforestation of temperate/boreal ones (cf. [GFC, 2006] report). These data are geographically more or less difficult to collect and analyse but in a general way, the reasons for this drop lie essentially in the growing demand of forest products (fuel, lumber and paper) as well as in the need of arable lands. Far beyond goods that forest supplies, its role is also paramount environmentally-wise whether for climate regulation, soil and biodiversity conservation, flood control and generally the water cycle or nutrient storage and recycling. Though less manifest, these considerations all together are of the greatest value regarding living conditions on earth (cf. [Costanza et al., 1997]). What is more, these phenomenons are generally involved in a unstable and pernicious feedback loop which tends to intensify the deforestation process when it starts, leading up to desertification. For instance, at the local scale of an ecosystem, this concerns the water cycle for which forest surface albedo is fundamental to regulate and take advantage of the precipitations (cf. [Charney et al., 1975]).

Besides, that retro-action effect holds also at the global scale and captivates currently many studies and prospects, such as in [Chabin, 2005; Robert and Saugier, 2003] regarding forest health and behaviour towards the coupled increase of both global temperature and atmospheric carbon dioxide, for which besides the anthropogenic impact makes from now on no doubts (independently from the solar illumination large-scale time factor, cf. [Berger, 1992]). As a matter of fact, whereas temperature has risen over the twentieth century by about 0.6 ^{o}C ($\pm$ 0.2 ^{o}C), atmospheric carbon dioxide rate has increased by roughly 30 % to reach in 2002 372 ppmv (parts per million by volume) according to [Keeling and Whorf, 2004]. In addition, according to the IPCC organization, annual emission rate are estimated to 5.4 GtC (Giga tonnes of Carbon, also often expressed in PgC for Peta grammes of Carbon) due to fossil fuel combustion and 2 Gt due to deforestation, resulting in an annual growth of 3.4 GtC (1.5 ppm volume). The remaining 4 Gt are half stocked by ocean and half by biosphere, as summarized in the synopsis 1.2. Prominent among these annual carbon fluxes are the forest ones.

Although relatively modest regarding ocean or soil carbon stocks and even neutral if deforestation is taken into account, the exchanged quantities between forests and the atmosphere are

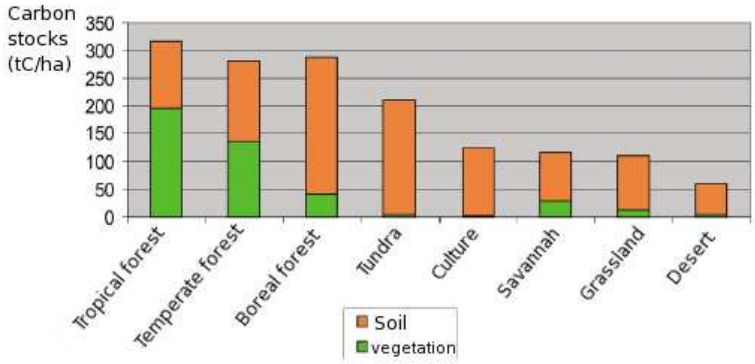

Figure 1.3: Renewable carbon stocks repartition between soil and vegetation for the major kind of land surfaces, taken from [Post et al., 1982].

indeed really significant. If we bear in mind the reasonable time factor of the planting and deforestation process as well as human manifest influence, forests present truly an unique capacity of carbon storage (cf. [Cox et al., 2000],[Betts et al., 1997]). An efficient policy could thereby be really significant for the global carbon budget, whether stimulating a sustainable agriculture (cf. [Brown et al., 2002]) and generally a better global forest management. This rises the problem of a better identification and understanding of the different carbon sequestration ecosystems. As a matter of fact, the carbon repartition between soil and vegetation is relatively well quantified, provided the type of land surface is known, as shown in figure 1.3 from [Post et al., 1982]. Yet, the spatial distribution of forest biomass is known very roughly at the globe scale. At this stage, the term 'forest biomass' can be specified as the quantity of woody aerial dry matter per surface unit, referred to as AGB (Above Ground Biomass) and mostly quantified in tons per hectare (ton/ha), which also represents the renewable carbon mass : a ton of dry wood corresponds to about 400/500 kg of carbon. Indeed, figure 1.4 is ensued from various data types and sources (GIS approach, from remote and non remote sensors and collected by the FAO) which accuracy has to be improved and confirmed (cf. [Kindermann et al., 2008]), even more with the upcoming carbon issue as a great geopolitical stake.

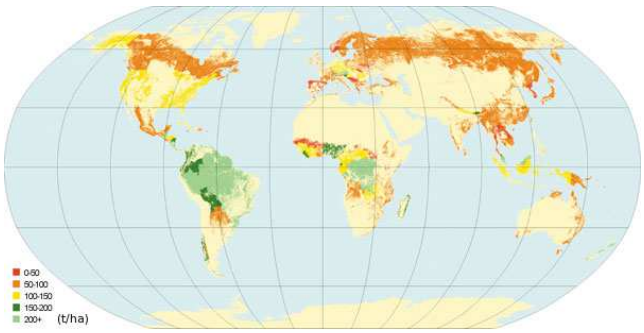

Figure 1.4: Spatial distribution assessment of forest biomass throughout the world, sources from the FRA – Forest Resources Assessment and cf. [Kindermann et al., 2008]

The estimation of biomass at the global scale is thus a a core research topic, whether from optic or radar remote sensing techniques and has been therefore particularly emphasized. Notwithstanding, the other stakes listed before, related to environmental issues or not, plea just as much for efficient forest monitoring means. Besides, that is the case for what concerns the field of search and rescue (SAR). Indeed, with one third of Earth land surfaces covered, these applications, civilian or military, are very likely to involve high capability forest remote sensors to detect, identify, recognize or analyse man-made structures under vegetation. In view of the microwave ability to penetrate through the cover – by comparison to optic remote sensing techniques – this aspect will be also discussed in the following.

1.2.2 Forested Media Characterization, Variables of Interest

As mentioned beforehand, forest is a quite complex medium characterized by an high macroscopic heterogeneity (in comparison with the ocean or the cryosphere for instance), whether at the spatial or temporal level with phenological changes and its description requires thereby a large set of parameters. Different taxonomic approaches can be used, according to structure stand elements such as leaves, twigs, branches, shrubs, trunks or stems, the soil nature (bare or covered with grass, undergrowth, flooded or not in the mangrove case...) and their respective physical composition (chemical, dry or fresh matter, dead or living parts) or function (e.g photosynthetic elements or not).

Though natural, one can easily figures out that an exhaustive and faithful description is on the one hand intractable and on the other hand not necessarily required since a focus on specific variables of interest, related to a given topic, is mostly more efficient. For instance and as far as forward theoretical models will be concerned afterwards, the description can be restricted to parameters which presence is noticeable regarding the electromagnetic interaction. A common approach is thus to define various clusters or groups of elements pieced together according to their geometrical properties (statistical angular, position or size distributions, density...) from which spatial homogeneous subparts/regions can be emphasized, whether horizontally (separated by gaps, clearings...) or vertically with various layers. Associated to this statistical approach, allometric, fractal relations and its derivative approach L(Lindenmayer)-Systems enable to link geometrical properties between different kind of elements and are really powerful when applied to given species, vegetation architecture (and especially plants rather than trees) being particularly well suited to such description models (cf. [Prusinkiewicz and Lindenmayer, 1996; Prusinkiewicz, 2004]). However, they are limited naturally to specific species and are not always available or applicable. Many different models of canopy architecture can be found in the literature, more or less versatile regarding the possible species and the user subsequent applications. Within the scope of optical geometrical models, one can refer to [Li and Strahler, 1992; Franklin and Strahler, 1988], Concerning the ones used for microwaves forward simulation, this point will be considered afterwards but examples of allometric studies are given in [Champion et al., 2001; Saleh et al., 2007] among others and the use of fractal descriptions in [Lin and Sarabandi, 1999]. Prominent among them is also the AMAP software, an architectural tree growth model (cf. [Fourcoud et al., 2003]), also used for microwaves applications (cf. [Castel et al., 2001; Fourcoud et al., 2003]).

Jointly to the geometrical description is the physical composition one. Likewise, descriptive variables must be adapted regarding the relevance of these components and their ability to be properly sensed. Among the eighteen nutrients essential for trees composition and growth (cf. [Smil, 2008]), carbon, hydrogen and oxygen represent about 90 % of plant mass tissues and come from water, CO2 and O2 fluxes with soil and atmosphere. Then, nitrogen but also sulfur cycle are also relevant but since their correlation regarding microwave interaction is hard to emphasize, we'll focus hereafter exclusively on water cycle and carbon.

For that concern vegetation and the water cycle, the exchanges lie mainly in the absorption and evapo-transpiration process respectively from the soil and through the foliage. The dielectric constant (also called relative permittivity) of a given (dielectric) medium is the macroscopic variable describing its electromagnetic response. For an heterogeneous one, that is a medium made of several constituents, mixing laws, based on each known permittivity, are commonly used. As a matter of fact, the water dielectric permittivity is really different from the others vegetation constituents (mainly xylem/wood, phloem) so that we can qualitatively get that humidity changes impact significantly electromagnetic interaction. Yet, if this sensibility is not questioned, this parameter turns out to be quite challenging in modeling since it is liable to

rapid temporal and spatial variations, regarding diurnal meterological or phenological changes (cf. [Franchois et al., 1998; Salas et al., 1994]). As a result, within a validation scope, direct measurements -whether based on oven-dried or portable dielectic probe methods- require an extensive and long-time work, considering the quick significant variations, possibly within the order of an hour and between each type of canopy elements. The same problem holds also for the soil, radar measurements are also really sensitive but with the same difficulty to cope with the water content gradient, whether temporal (depending also on diurnal temperature variation, meterological conditions...) or vertical which lower boundary is assessed regarding the penetration depth of microwaves. To bear in mind the water content order of magnitude, water, xylem and soil are about 80, 10 and 5 (cf. [Zimmermann et al., 1995; Peplinski et al., 1995]).

As mentioned beforehand, carbon is the other major component whether concerning stocks or fluxes. Indeed, wood (xylem) is essentially made of organic mater (mainly cellulose + lignin) that is of carbon produced by the plants themselves. As far as the renewable carbon cycle is concerned, the primary production is a paramount variable of interest which is commonly used to assess the amount of carbon captured by vegetation. Expressed in tons of dry matter per hectare and per year for the productivity, it thereby characterizes the spatial and temporal production, namely the ecosystem dynamic. To consider quantitatively the different process involved that is (photo and respiration), different concept are distinguished : the gross primary productivity ($t \cdot ha^{-1} \cdot \text{year}^{-1}$) represents whereas the net primary productivity (NPP) and the net ecosystem productivity (NEP) takes into account the autotroph and heterotroph respiration (R_a and R_h), as detailed below :

$$\begin{aligned} NPP &= GPP - R_a \\ NEP &= GPP - R_a - R_h \\ &= \Delta B \end{aligned} \tag{1.1}$$

with ΔB being the ecosystem budget that is the biomass variation. This study of forest carbon budget is particularly interesting versus forest age, especially during the first growth stage where the ecosystem acts truly as a carbon sink (cf. [Ramade, 1984]). Besides, more specific notions can be found in the literature, to emphasize foliage, ligneous, aerial or underground biomass as well as possibly more relevant temporal indicators such as peak biomass, P/B ratio or turn over (cf. [Cronk and Fennessy, 2001]). Again, allometric relations, providing simple link between the different vegetation constituents, may bring significant simplification among these various quantities which can mostly be deduced by the geometrical description discussed beforehand. Indeed, an extensive number of allometric models have been developed, for instance one can refer to 'gap model' concerning forest growth (cf. [Botkin et al., 1972]) or to the public domain *BIOPACK* software (cf.[Means et al., 1994]) providing an exhaustive set of relations. More than that, specific relations related to possible retrieved variables from remote sensor are also very interesting. Prominent among them are relations giving the biomass versus canopy height (cf.[Mette et al., 2004]), DBH (Diameter at Breast height), volume (cf. [Brown and Lugo, 1984]), LAI (cf. [Bartelink, 1997]) or LAD (cf. [Toda et al., 2009; Treuhaft et al., 2003]). The two latter being the leaf area index and density, that is respectively the total one sided green leaf area per unit ground surface area (thus dimensionless) and the total one sided area per unit volume in the canopy (m^2/m^3,cf. [Myneni et al., 1989]).

This point about dedicated relations between biomass and retrieved variables rise the question of the different sensor sensitivity. It introduces thereby the following part in which the SAR specificity will be emphasized, essentially versus optical and passive microwave remote sensing.

1.3 Radar as a Remote Sensor

On top of the medium of interest, characterized in the previous section, the point now at issue concerns the radiative quantities to be measured and constituting the information vector, the cornerstone of remote sensing. It also rises the captor's capabilities question which sensitivity to the medium descriptive parameters is naturally paramount for a remote characterization, taking also into account the possible perturbations coming with atmospheric propagation, as far as surface remote sensing is herein concerned. For the purpose of emphasizing the radar specificities within this general scope, the following two parts will be dedicated first to a qualitative overview of the microwave remote sensing assets and then to a more quantitative approach of the measures content.

1.3.1 Qualitative Overview of Radar Specificities

As emphasized previously, the cornerstone of remote sensing lies in the interaction between electromagnetic wave and matter. Considering first the theoretical case of a single scatterer, three physical phenomenons can be distinguished : scattering, absorption and emission. Depending on the radiation wavelength, these three phenomenons are more or less related to the object attributes that is geometrical features, physical composition and temperature. For instance, the scattered power varies with λ^{-4} in the Rayleigh region for particle (typically air particle interaction with sun light, at the origin of the blue sky), as opposed to the non selective one (also called optics region in the radar community), for which all wavelength are similarly scattered. Between both – for particle size roughly equals to the wavelength – is the resonant region characterized by an oscillating behaviour, well illustrated by the Mie series solution for a perfectly conducting sphere (hence the often used term 'Mie scattering', though distinct from the theoretical solution, also valid in the Rayleigh region). Likewise, absorption is closely dependant to the wavelength and quantifies the interaction elasticity, that is the loss of electromagnetic radiation converted into calorific or chemical energy whereas emission which characterized the particle intrinsic radiation (its spectral signature) is in addition dependent on its physical temperature (and generally compared to the black body reference). As specified in the next paragraph, under the elasticity and thermal equilibrium assumptions, scattering, absorption and emission are closely related.

Considering now the whole medium, the way these three phenomenons affect the intensity propagation is given by the radiative transfer equation, reminded hereafter :

$$\frac{dI_\nu(s)}{ds} = -(k_a + k_s)I_\nu(s) + \rho e + \iint \mathbf{P}(\Sigma, \nu)I_\nu d\nu d\sigma \tag{1.2}$$

which traduces the radiation losses during propagation by absorption and scattering – corresponding actually to extinction – jointly to energy gain represented by the two last right hand-side terms respectively for emission (ρe) and scattering from the surrounding particles (averaged coefficient).

Although simple in the formulation, the resolution of this equation becomes generally tough to solve especially when dealing with non canonical media, often heterogeneous and encompassing scattering particles which phase matrix is not straightforward. Fortunately, as pointed out previously, some assumptions can be made on account of the working frequency and the resulting media sensitivity. As a typical example, a paramount advantage of the microwave domain (typically from $\lambda = 1$ mm to 1 m) is the quasi transparency of atmosphere as reminded in figure 1.5. However, heavy precipitations are liable to affect frequencies already beyond the X-band, hence

the cloud mapping capabilities of Ku radars. Alternatively, propagation at low frequencies (below L-band) may be strongly affected by the ionosphere (atmospheric region roughly between 50 and 2000 km), which also finds applications with trans-horizon radars and propagation beyond the line of sight, commonly called HFSWR (High Frequency Surface Wave Radar). From the physical point of view, the solar X and UV radiations are at the origin of the medium ionization which can be characterized by a number of electrons per volume unit N_e. This phenomenon can be accounted for within Maxwell's equations by means of a conduction current which leads to a modified equivalent refraction index, reminded below :

$$n^2 = 1 - \frac{N_e e^2}{\varepsilon_0 m w^2}$$

with e and m the electron's electric charge and mass. The w^{-2} dependence is at the origin of the waveguide-like structure between Earth's surface and the ionosphere for low frequencies. As an example, the coverage is about 500-600 km for Nostradamus (6-30 MHz ONERA radar). To derive the previous index expression, the Earth's magnetic field have been neglected. Yet, it can be demonstrated that on top of being dispersive – with a frequency-dependent index – the medium becomes birefringent with two intrinsic propagation modes (cf. ordinary and extraordinary waves) resulting in the so called Faraday rotation. As a matter of fact, the latter constitutes a serious drawback for linear polarization radars, especially during high solar activity cycle. The following formula :

$$\Omega = \frac{108}{f_{GHz}^2}\left(\frac{TEC}{10^{17}}\right)$$

expresses clearly that a linear polarized wave is 108^o rotated at 1 GHz with a TEC (Total Electron Content) of 10^{17} electrons per square meter – the TEC is obtained by integrating N_e over the propagation path for a 1 m^2 cross section area and depends thereby on the incident angle. The TEC ranges typically from $10^{16} m^{-2}$ during the night and up to $10^{19} m^{-2}$ during high solar activity cycle and for grazing incidence. Among a abundant literature on the impact of these specific effects, concerning also group phase delay and amplitude scintillations, one can refer to the quite exhaustive survey presented in [Z.W.Xu et al., 2004] but in a general way to be more specific with the frequency domain considered afterwards, if these constraints must be taken account at P-band for high solar activity cycle, the problem can be left aside at L-band.

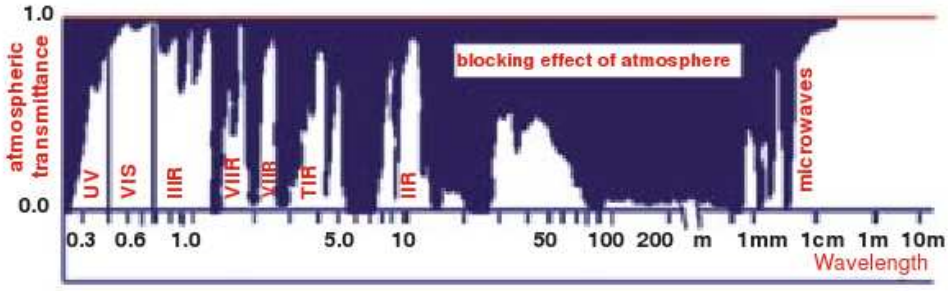

Figure 1.5: Atmospheric windows for the electromagnetic spectrum

On the contrary, as recalled in figure 1.5, the atmospheric windows are much more stringent in the optic region. Among the main atmospheric gases involved, ozone and dioxygen ($0_3, 0_2$) enable the protection against very high energy/radiation and absorb most of the em scattering

up to short wavelength portions of UV ($\lambda < 0.24$) whereas H_20, CO_2 but also NO_2 absorption rays are spread throughout the mid and far infrared (as an example, CO_2 strongly absorbs the 13-17.5 μm region whereas the bands 5.5-7 μm and above 27 μm are important regions of water vapour absorption.

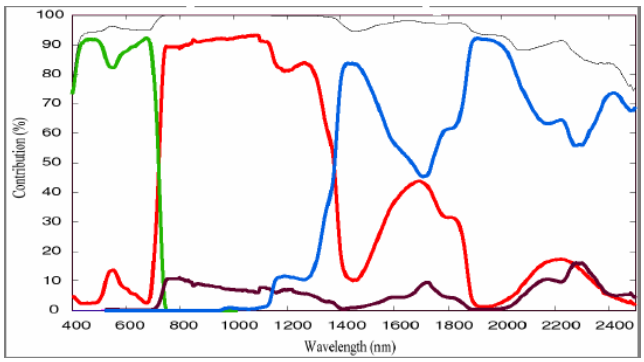

Figure 1.6: Contribution to the reflectance spectrum of green vegetation for VIS (visible), NIR (Near Infrared Region) and MIR (Middle Infrared Region) wavelengths (black pigments not accounted for). For visible wavelengths, the reflectance is clearly dominated by green pigments, in comparison to red pigments and the relative reflectance of water and dry matter (respectively in blue and violet).

Conjointly to propagation, the sensitivity towards frequency also holds naturally for the scattering and emission phenomenons. Likewise, specific regions can be emphasized which, as it will be shown, simplify considerably the data interpretation. Indeed, apart from the intermediate band between 3 to 5.5 μm where both reflection and self-emission hold, the 8 to 14 portion corresponding also to a atmospheric window is known as the thermal emission from earth's surface, whereas within the 0.3 to 3 μm region the radiation comes from reflection of solar energy. The fractional amplitude of the reflected em field is known as the reflectivity, while its magnitude square, the reflectance, refers to the fraction of incident power reflected at an interface. The spectral reflectance, as opposed to the albedo, refers to that ratio but for a given part of the em spectrum.These quantities rise thereby the resolutions criteria from which three types of optical images can be distinguished between the **panchromatic** ones characterized by a very high spatial resolution but a poor spectral one (in the visible domain, 0.4-0.7 μm) and the multispectral (MS) or the hyperspectral (HS) images able respectively to record simultaneously about 3-8 bands or up to 200 for the latter with a spectral bandwidth close to the nanometer. With the aim of optimizing such trade-off, the fusion between these different kind of images is an important field of study in the optical community and is referred as the 'pansharpening' process between panchromatic and MS images, while HS-MS fusion has been more recently achieved (cf. for instance [Winter et al., 2007]). As current examples among an extensive number of missions initiated by the Landsat ones, the spatial resolution is 30 m for the HYPERION hyperspectral sensor covering the 0.4 to 2.5 μm spectrum with about 220 bands, in comparison with the IKONOS Or QUICKBIRD 4 meter with 4 bands about 0.1 μm width in the visible domain, 0.8 m in panchromatic mode. The swath and the related temporal resolution is also to be considered, which have been more favoured than the spatial resolution for multispectral radiometers such as AHVRR, SPOT vegetation, MODIS, MSG SEVIRI with possible daily revisit periods.

The paramount interest of optical sensors stem from this very high spectral discrimination capacity which for instance potentially gives an information about the physical state and the

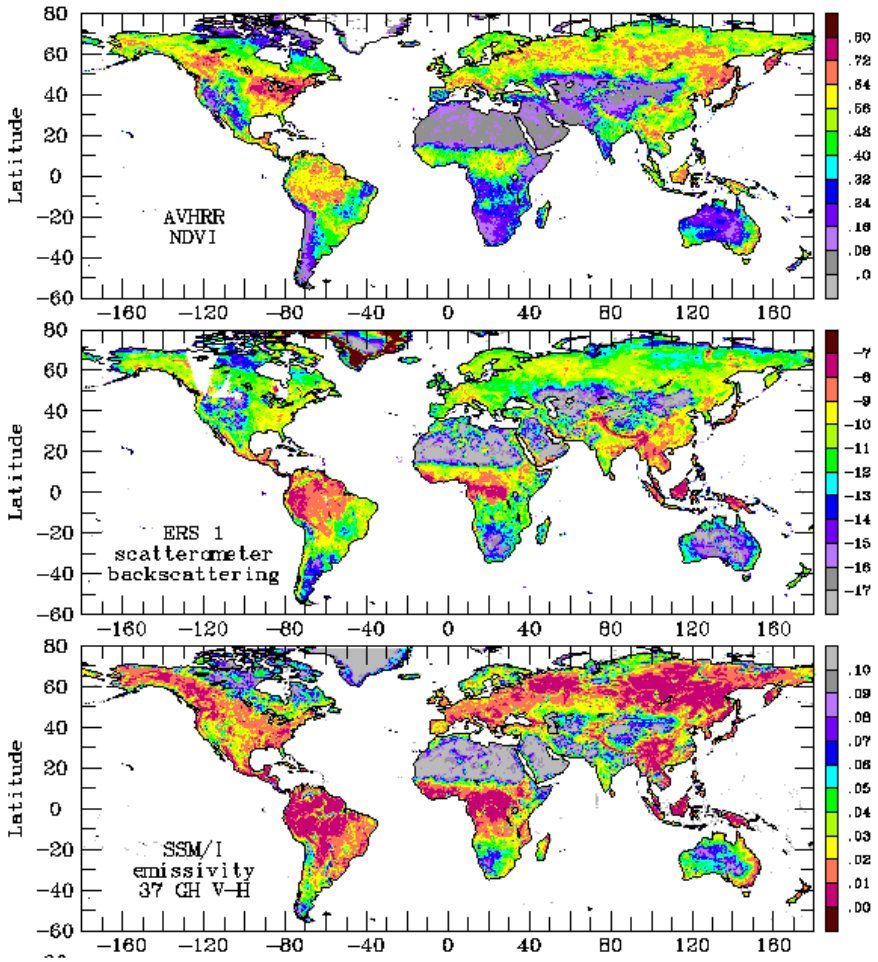

Figure 1.7: Sensitivity of various remote sensing sensors, compiled by [Prigent et al., 2005, 2006] with data available to the community.

chemical composition of soil or vegetation, as shown with the typical relative reflectances for green vegetation (cf. figure 1.6), among which the one due to plant pigments (chlorophyll) are naturally more favourable to green wavelengths reflection and referred to as the FPAR (Fraction of Photosythetically Active Radiation absorbed by vegetation). In a general way, the associated retrieval methods are base on multivariate analysis from specific indexes, making an optimal use of the spectral reflectances. Typical indexes are built from a combination of shortwave infrared reflectances (SWIR) with near infrared ones (NIR), according to ratios like

$$\frac{\rho_X - \rho_Y}{\rho_X + \rho_Y}$$

The bands choice (X and Y) depends on the variable of interest and originates different indexes such as the NDII, NDVI, NDWI standing respectively for the Normalized Difference Infrared, Vegetation or Water Indexes. Prominent also among these indexes are the TVDI (Temperature Vegetation Dryness Index) which accounts for the water stress of the vegetation or the ones

related to the composition such as the CAI (Cellulose Absorption Index) or the ND[LN]I for Lignin and Nitrogen. As far as vegetation water content will be particularly concerned afterwards, a current method (cf. [Yilmaz et al., 2008] consists in estimating the EWT (Equivalent Water Thickness) of leaves well correlated to the NDII and then deduce the whole canopy water content from the relation VWC=EWT*LAI in which we remind that the LAI (Leaf Area Index) is the one-sided green leaf area per unit ground area for broadleaf canopies and half the total needle surface area for coniferous ones.

In comparison with what holds for the optical domain, the spectral discrimination in the radar field is far from the above-cited values, on account of both natural surfaces sensitivity and system capabilities for carrier frequencies around one GHz. Notwithstanding, the radar measurements are sensitive towards the whole or a least a much more important part of the medium with volume scattering, made possible by the stronger penetration. As an illustration in figure 1.7, comparisons over the global map are given with the sensitivity resulting from of the three major types of remote sensing sensors that is on the one hand the passive ones in the optical domain or the microwave radiometers and on the second hand active radars, providing their own source of illumination. Though essential – as for any field in physics –, such relationships rise then the question of their use within a retrieval scope, which actually turns out to be more challenging in radar, mainly in view of mixed contributions from the medium, as opposed to the filtered ones in optics with the higher spectral resolution. With the aim of a better understanding of the radar sensitivity, electromagnetic modeling provides fundamental tools from which retrieval strategies can be set forth – all of that being precisely the subject of the following chapters with the bistatic configuration. In a general way, it has been shown (jointly with experimental validations) that the radar measurements are sensitive towards the target permittivity, its geometrical attributes and besides for distributed ones towards structure. As pointed out in § 1.2.2, the sensitivity towards permittivity stems mainly from the media water content, on account on the large difference between water and the others natural elements permittivity usually encountered in natural media, whether concerning the soil (organic or mineral composition) or vegetation (cellulose, lignin as the main constituents of xylem). For what concerns geometrical attributes, the dimensions and shape importance is driven by their relative value compared to the wavelength as stressed previously and likewise, it is a paramount criteria for the impact of roughness. Typically, a surface can be considered smooth according respectively to the Rayleigh or to the Fraunhofer criteria as long as :

$$\Delta h < \lambda/(8\cos\theta) \text{ or } \Delta h < \lambda/(32\cos\theta)$$

with Δh being the maximum height between points surface (coming with a resulting phase difference lower than $\pi/2$ or $\pi/32$). Together with possible heterogeneous permittivity within the scatterer, these characteristics originate the complexity of em scattering for which analytical derivations become quickly difficult for fine modeling description and require mostly approximations, as shown in the next chapter. In addition, for distributed targets, structure – that is the spatial arrangement of scatterers – is also important to consider. As a typical example, periodic media originate important structure effects and for natural surfaces can be encountered over the sea, with the well-known Bragg backscattering phenomenon – occurring for $\lambda_s = \lambda/2\pi$ with λ_s the surface period (e.g sea surface wavelength).

On account of these various sensitivity origins, the complexity of radar measurements interpretation can easily be figured out and holds all the more with coherent radar such as imaging ones (i.e SAR) coming with an important speckle (due to the coherent superposition of all the scattering contributions). For that reason, SAR systems are not optimal for objects characterization in comparison with scatterometers (non imaging active radar), particularly for those

transmitting broad band signals (referred originally as 'panchromatic and polypanchromatic' radars, cf. [Moore et al., 1969]). Notwithstanding, the need of spatial resolution coming with finite extend region of interest (ROI), especially as far as land remote sensing is concerned – unlike for instance to sea monitoring – justifies the relevance of radar images. Though structural and permanent, the speckle hindrance may be limited from various approaches, starting from the use of appropriate observables (cf. next §) to more sophisticated filtering techniques (i.a [Lee, 1986a,b; López-Martínez and Fàbregas, 2002]). Besides, the texture information –that is statistical spatial interaction with a given pixel and its neighbour ones – can be used to partly recover the lost information by speckle (cf. [Grandi et al., 2003]).

In addition to imaging capabilities, 3D information can potentially be derived from imaging radar technique. Indeed, simply the SLR (Side Looking Radar, that is a real or synthetic aperture) provides relief enhancement (with shadowing, layover of foreshortening effects, cf. chapter 2), though not always advantageously. 3D reconstruction is also made possible with stereoscopic configurations (referred as mosaic SAR imagery and radargrammetry), performed with the acquisitions from different point of view as for instance in its most sophisticated version with 3D circular SAR (cf. [for FOPEN using flashlight mode images along circular trajectories, 2007]) Tomography has been also achieved from multibaseline acquisitions (cf. [Reigber and Moreira, 2000]).

Furthermore, concerning information and retrieval potential, the Pol-InSAR measures turn out to be the most complete ones with an unique capacity to combine the interferometric information to the fully polarimetric one (detailed afterwards), both being intractable in the optical domain, limited at the moment to incoherent acquisition.

In a general way, the trade-off between additional measures and additional sensor complexity and subsequent cost is well touched with these different acquisitions so that one can realise that the presented sensors represent the optimal ones in that sense, for instance among sonar, spectrometers, magnetometers and also LIDAR. The latter, as another active remote sensing technique using NIR (1-1.5 μm) emitting source have not yet been presented, since up to now such system were mostly used as range finder, rather than for media physical characterization. Notwithstanding, the full waveform technique being now mature enough (involving a larger footprint than with discrete return acquisition, see for instance airborne experiments with the systems SLICER or LVIS), so that the potential of LIDAR has truly to be considered, on account of its easy characterization of the whole forest structure – at least for relatively sparse forests – well demonstrated by a long experience as a ground truth device. Besides, synergy with SAR acquisition is also very attractive – both techniques being very complementary – as pushed by the NASA DESDnyl mission proposal.

Finally, beyond the various type of instrument presented, another paramount element to be considered lies in the vector choice carrying the captors, for instance to cite the most common ones spaceborne, airborne vectors but also Unmanned Aerial Vehicle (UAV), zeppelin or balloons. Its nature must be naturally closely linked to the captor requirements and constraints, the orbit or flight characteristics being fundamental concerning spatial and temporal resolution. With that respect, the radar offer a much larger versatility since for instance it does not require an off-nadir acquisition and more, it is neither dependent on solar illumination nor on weather conditions. These points constitute indeed stringent constraints for optical systems which implies mostly the use of heliosynchronous orbit with an high revisit period, to cope with the likely overcast conditions.

1.3.2 Quantitative Radar Measures

Similarly to every field in remote sensing, the fundamental radar measures lie on radiometry which aims at assessing quantitatively the received power for a given captor. Whether in radar or optics, the various radiometric measurements definitions are thereby closely linked, though very contrasting at a first sight, in view of the prolific vocabulary used by the respective communities. As a matter of fact, these definitions are marked by the involved captors technique, hence antenna and power budget concepts for what concerns active radar radiometry and historically detection. Indeed, the definition of the radar cross section comes naturally in order to derive the radar one and two way equations :

$$\sigma = \frac{P_s^{\Theta}}{\Pi_i(\theta_i, \varphi_i)} \tag{1.3}$$

with P_s^{Θ} being the omnidirectional scattered power and $\Pi_i(\theta_i, \varphi_i)$ the incident power density which corresponds to the time average of the Poynting vector (hence the notation in which the time average brackets, implicit hereafter, will be left aside). Π_i can also be expressed according to the system parameters (P_t, G_t) as the transmitted power and antenna gain, all of that along the direction of arrival (DOA) given by (θ_i, φ_i) :

$$\Pi_i(\theta_i, \varphi_i) = \frac{G_t P_t}{4\pi r_1^2}$$

so that the power density at the receiving antenna is $\frac{P_s^{\Theta}}{4\pi r_2^2}$. With an effective aperture noted A_w (the real aperture times the efficiency) linked classically to the antenna gain by :

$$G_r = \frac{4\pi A_w}{\lambda^2}$$

the received power at that end will be :

$$P_r = P_s^{\Theta} * \frac{A_w}{4\pi r_2^2}$$

Combined with equation 1.3, the latter leads to the bistatic radar power equation :

$$P_r = \frac{\lambda^2 G_r G_e P_t \sigma}{4\pi)^3 r_2^2 r_1^2} \tag{1.4}$$

To derive the previous expression, the hypothesis of a single, localized and coherent scatterer has been implicitly assumed. However, as far as distributed target is considered, that is a collection of scatterers which extent is larger than the resolution cell, it is more consistent to express the received power with the differential area ds of cross section per unit area σ^0 :

$$P_r \iint_{A_0} \frac{\lambda^2 G_r G_e P_t \sigma^0(x,y)}{4\pi)^3 r_2^2 r_1^2} ds$$

If we further assume a collection of statistically identical scatterers throughout the pixel, the integration is simplified and leads to the '*sigma nought*' scattering coefficient :

$$\sigma^0 = \frac{\langle \sigma \rangle}{A_0} = \frac{4\pi R^2}{A_0} \frac{\langle |E^s(\theta_s, \varphi_s)|^2 \rangle}{\langle |E^i(\theta_i, \varphi_i)|^2 \rangle} \tag{1.5}$$

Notwithstanding, the previous derivation requires to know the ground illuminated area which supposes implicitly also the surface slopes. Indeed, without this information, the ground resolution can not be deduced from the radar slant one (noted Δs), as evinced in the simple case shown figure 1.8 for a tilted surface angle within the scattering plane $(\hat{k_i}, \hat{k_s})$ for which :

$$A_0 = \frac{\Delta s \Delta az}{\sin \theta_i} = \frac{\Delta s \Delta az}{\sin(\theta_e - \psi_g)}$$

Δaz stands for the azimuthal slant or ground resolution, identical for this equivalent two dimensional problem in the difference between incident and elevation angles (θ_i, θ_e) have been also pointed out. In view of these geometric considerations, the only normalization which does not require the surface slopes knowledge is the slant direction one, hence the recommendation to use β^0 –the radar brightness – for that cases (cf. [Raney et al., 1994]). Its definition is thus :

$$\beta^0 = \frac{\langle \sigma \rangle}{\Delta s \Delta az} \tag{1.6}$$

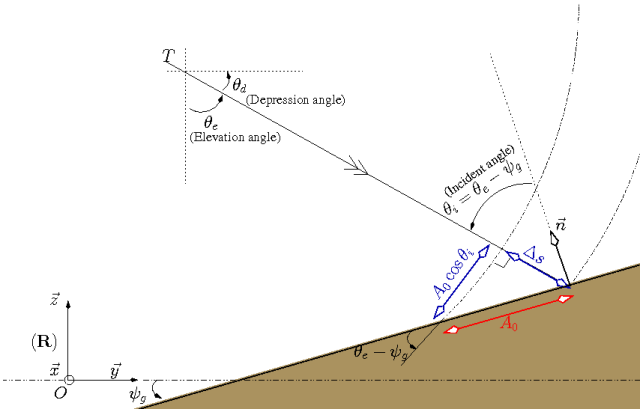

Figure 1.8: Radar side looking geometry effects along slant, ground and beam directions for a titled surface.

Besides, alternatively to σ^0, another relevant radiometric measure when dealing likewise with known local surface slopes is the gamma nought scattering coefficient (γ^0), often call in the literature the bistatic scattering coefficient and defined with the remaining direction in figure 1.8 by :

$$\gamma^0 = \frac{\langle \sigma \rangle}{A_0 \cos(\theta_i)} \tag{1.7}$$

which thereby corresponds to the incident beam or wave front normalization. The appellation 'gamma nought scattering coefficient' instead of 'bistatic scattering coefficient' is hereafter preferred since, within the scope of our study, the coefficient σ^0 will be also used in bistatic. The traditional name comes from the fact that bistatic configuration is more common in optics so far, and most of the surfaces exhibit a Lambertian scattering behaviour which makes the γ^0 use consistent. Indeed, according to that property of isotropic scattering, the scattered power depends only on surface attributes and on the incident power, that is $P_s \propto A_0 cos\theta_i$, hence the normalization to reach direclty the information of interest about the surface state itself. The

Lambertian behaviour originates in the random characteristic of scattering events upon the surface which resulting scattering is not favoured by any direction. As far as microwave is concerned, the scattering from a random volume is Lambertian (cf. section 3 in chapter 3 about bistatic scattering properties and the spherical diagram of the span) as well as the incoherent contribution of a surface, beyond a certain roughness. γ^0 is thus preferred instead of σ^0 when dealing with experimental datasets entailing various incident angles and with the aim of characterizing the medium itself (for instance the forest biomass with the cross polarization, as explained in the section about radar sensitivity change with bistatic).

In addition, since these quantities result directly from incident and scattered fields, their definition can be extended to vectorial scattering coefficients. Indeed, a powerful intrinsic property of active radar remote sensing is the ability to transmit in a chosen polarization ($\hat{p}$) and receive the scattered field onto another one projection ($\hat{q}$).

The arbitrary polarizations state $\hat{q}$ and $\hat{p}$ are usually defined within the vertical and horizontal canonical basis, in which the scattering matrix is defined to link the scattered field to the incident one as follows :

$$E^s_{\hat{q}}(\theta_s,\varphi_s) = |E^s(\theta_s,\varphi_s)| \begin{bmatrix} \hat{q}\cdot\hat{v_s} \\ \hat{q}\cdot\hat{h_s} \end{bmatrix} = e^{-j\hat{k}_s\cdot\vec{r}_2}\frac{1}{r_2^2}\cdot\begin{bmatrix} s_{v_sv_i} & s_{v_sh_i} \\ s_{h_sv_i} & s_{h_sh_i} \end{bmatrix}\cdot|E^i(\theta_i,\varphi_i)|\begin{bmatrix} \hat{p}\cdot\hat{v_i} \\ \hat{p}\cdot\hat{h_i} \end{bmatrix} \quad (1.8)$$

hence an often more convenient expression for the polarimetric scattering coefficients, for instance with σ^0_{qp} :

$$\sigma^0_{qp} = \frac{4\pi}{A_0}\langle|s_{qp}(\theta_s,\varphi_s)|^2\rangle \quad (1.9)$$

and likewise for γ^0_{qp} and β^0_{qp}.

Besides, the difference between the just defined radar brightness (β^0) and brightness can be stressed for the sake of clarity. Indeed, the brightness along a direction (θ_i,φ_i) at a distance R of the differential area ds is defined by the ratio between the differential power density emitted per unit solid angle ($W.m^{-2}.sr^{-1}$), the latter being subtended by ds viewed from the captor :

$$B(\theta,\varphi) = \frac{d\Pi(\theta,\varphi)}{ds\cos\theta/R^2} = \frac{d\Pi(\theta,\varphi)}{d\Omega} \quad (1.10)$$

Though different and ambiguously called, these quantities are nevertheless related under the thermal equilibrium hypothesis with as a result, the Kirchhoff's law which states the equality $P_a = P_e$ between the absorbed and emitted power for a given surface at a constant temperature. Plus, according to the energy conservation principle, the fractions of absorbed and scattered power to the incident one are related by : $P_a/P_i = 1 - P_s/P_i$ Through a given surface, the fractional absorbed power is thus equal to the fractional emitted power density, that is the ratio between the emitted power density to the incident one. Invoking again the thermal equilibrium condition, the incident power density is furthermore equal to the emitted one by the equivalent blackbody at the same temperature. Hence the following equalities :

$$P_e/P_i = \frac{d\Pi_e/d\Omega}{d\Pi_i/d\Omega} = \frac{d\Pi_e/d\Omega}{d\Pi_{bb}/d\Omega} = B/B_{bb}$$

which is precisely the emissivity definition of a surface (which times its real temperature gives the surface brightness temperature T_B according to the Rayleigh-Jeans approximation). Consequently, the link between emissivity and the fractional scattered power is now straightforward :

$$e = P_a/P_i = 1 - P_s/P_i$$

which can be made explicit by means of the scattered and incident fields within their respective polarizations states as follows :

$$P_s^{\Theta} = \int_0^{2\pi} \int_0^{\pi/2} \frac{|E_{pp}^s|^2 + |E_{qp}^s|^2}{\eta_0} R^2 sin\theta_s d\varphi_s d\theta_s$$
$$P_i(\theta_i, \varphi_i, \hat{p}) = \frac{|E_p^i|^2}{\eta_0} A \cos\theta_i \tag{1.11}$$

with η_0 being the impedance of air ($\eta_0 = \sqrt{\frac{\mu_0}{\varepsilon_0}}$),

Finally, these derivations bring us to the fundamental relation between emissivity and bistatic scattering, given in equation 1.12 with for instance the gamma nought scattering coefficient (but equivalently with σ^0 or β^0). This relation entails indeed the potential synergy between passive and active bistatic microwave remote sensing (especially with the current SMOS mission, the first spaceborne radiometer at L band and thereby likely suitable with opportunistic multistatic acquisitions, providing by interpolation the integral detailed below).

$$e_p(\theta, \varphi) = 1 - \frac{1}{4\pi} \int_0^{2\pi} \int_0^{\pi/2} \gamma_{pp}^0(\theta_s, \varphi_s, \theta, \varphi) + \gamma_{qp}^0(\theta_s, \varphi_s, \theta, \varphi) sin\theta_s d\varphi_s d\theta_s \tag{1.12}$$

Furthermore, to bring closer the various radiometric measures in remote sensing, the identity between the brightness afore-mentioned and radiance can be stressed, the latter being usually defined by :

$$\mathcal{R} = \frac{d^2 P_s}{dA d\Omega(A_c, C) \cos\theta}$$

expressed in $W.m^{-2}.sr^{-1}$ and with d^2P_s the elementary radiant flux through dA and within $d\Omega(A_c, C)$, the solid angle subtended by the surface A_c of the receiving captor R and viewed from the scattering point C. This expression differs at a first sight from equation 1.10, but it just comes from the embedded solid angles, as detailed below :

$$\begin{aligned}
\mathcal{R} &= \frac{d^2 P_s}{\cos\theta dA d\Omega(A_c, C)} \\
&= \frac{d^2 P_s}{\cos\theta dA A_c \cos\theta / R^2} \\
&= \frac{d^2 P_s}{\cos\theta A_c} \cdot \frac{1}{dA \cos\theta / R^2} \\
&= \frac{d\Pi_s}{d\Omega(dA, R)} \\
&= B
\end{aligned} \tag{1.13}$$

The ratio between the surface radiance to the irradiance $\mathcal{R}$ ($W.m^{-2}$) – the time average of the Poynting vector perpendicular to the surface – gives the BRDF, the bidirectional reflectance

distribution function noted $\mathcal{F}$ (sr^{-1}) :

$$\begin{aligned}\mathcal{F}(\theta_s,\varphi_s,\theta_i,\varphi_i) &= \frac{\mathcal{L}(\theta_s,\varphi_s,\theta_i,\varphi_i)}{\mathcal{R}(\theta_i,\varphi_i)} \\ &= \frac{d^2P_s/(dA\cos\theta_s d\Omega(A_c,C)}{\Pi_i\cos\theta_i} \\ &= \frac{d^2P_s/d\Omega(A_c,C)}{dA\cos\theta_s\Pi_i\cos\theta_i} \\ &= \frac{R^2dP_s/(dA_c\cos\theta_s)}{dA\cos\theta_s\Pi_i\cos\theta_i} \\ &= \frac{1}{4\pi\cos\theta_s}\cdot\frac{4\pi R^2 d\Pi_s}{dA\cos\theta_i\Pi_i}\end{aligned} \tag{1.14}$$

which introduces the link with the radar scattering coefficients γ^0 or σ^0 :

$$\begin{aligned}[\mathcal{F}] &= \frac{\gamma^0}{4\pi\cos\theta_s} \\ &= \frac{\sigma^0}{4\pi\cos\theta_s\cos\theta_i}\end{aligned} \tag{1.15}$$

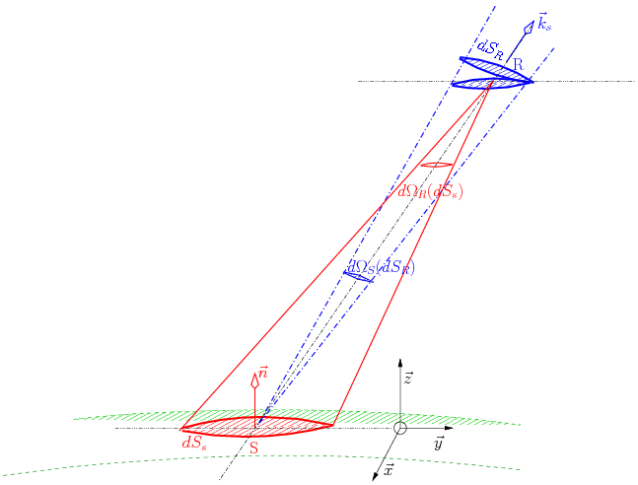

Figure 1.9: Illustration of the notations used for solid angle, with for instance $d\Omega_R(dS_s)$ the solid angle defined from the intercepted surface $d\vec{S}_s = dS_s\vec{n}$ from the receiver location R.

In LIDAR applications, the radiometric measurable quantity instead of the BRDF is the biconical reflectance ρ, defined by the fraction of scattered to incident radiant flux within their respective solid angles :

$$\rho(\Omega_s,\Omega_i) = \frac{P_s(\theta_s,\varphi_s,\Omega_s)}{P_i(\theta_i,\varphi_i,\Omega_i)} \tag{1.16}$$

which can also be deduced from $\mathcal{F}$ after integration of the radiant and incident flux over their respective solid angles, giving within the small solid angles assumption :

$$\rho(\Omega_s,\Omega_i) = [\mathcal{F}(\theta_s,\varphi_s,\theta_i,\varphi_i)]\cdot\Omega_s\cos\theta_s \tag{1.17}$$

hence the subsequent relations with radar radiometric coefficients :

$$\begin{aligned}\rho(\Omega_s, \Omega_i) &= \frac{\Omega_s}{4\pi}\gamma^0 \\ &= \frac{\Omega_s}{4\pi\cos\theta_i}\sigma^0\end{aligned} \tag{1.18}$$

In view of these derivations and the resulting equations 1.15,1.17, 1.18, we can establish that the radiometric measures commonly used in radar or optical remote sensing are actually closely related, though disparate at first sight. These differences originate in the corresponding captor specificities which justifies the preference between either the scattered power throughout the all space (for σ^0), for a fraction of it (in ρ thanks to LIDAR capacity to handle with a given solid angle) or per unit solid angle (within $\mathcal{F}$). The link with emissivity is less straightforward since it is ensued from passive sensor and thereby do not used the incident power normalization. However, under the Kirchhoff's law, the link with bistatic active radars has been reminded and constitutes a very promising possibility of remote sensing techniques fusion.

On top of the similarities between these radiometric quantities, the polarimetric use has been also stressed with the possibility of dual-polarization acquisition for passive systems and plus, quad-pol for active ones. Moreover, a specificity of active radars is the capability to handle with the received signal phase which carries a fundamental information whether for classification or interferometric applications as detailed afterwards. Indeed, a simple spatial average between adjacent pixel (multilook process, not always optimal though, as stressed in the next chapter) results generally in a coherence magnitude sufficiently high to estimate correctly its phase (it naturally holds only for homogeneous pixels). This spatial average is also implicitly based on the SAR systems asset, that is the imaging capability. This spatial mean ($< . >$ symbol) instead of a more general and rigorous pixel-by-pixel expectation – noted E(.) – provides a simple estimator of the polarimetric coherences which is expressed as follows with the scattering matrix terms 's_{qp}' (given in equation 3.7) :

$$\begin{aligned}\gamma_{qpmn} &= \frac{E\big(s_{qp}s_{mn}\big)}{\sqrt{E\big(|s_{qp}|^2\big)E\big(|s_{mn}|^2\big)}} \\ \hat{\gamma}_{qpmn} &= \frac{\langle s_{qp}\cdot\, s^*_{mn}\rangle}{\langle|s_{qp}|^2\rangle\langle|s_{mn}|^2\rangle}\end{aligned} \tag{1.19}$$

In the case of an homogeneous scene, $\hat{\gamma}_{qpmn}$ is also known as the maximum likelihood estimator (MLE, cf. [Touzi et al., 1999]). Besides, this expression justifies also the often used appellation 'correlation coefficient' (implicitly linear according to the Bravais-Pearson's definition) although the 'coherence' is more rigorous as its range is between 0 and 1 rather than [-1:1] and plus, since the coherence function deals generally in the statistical field with spectral quantities, similarly to the frequency domain s_{qp} terms. From the retrieval point of view and on top of being a phase quality indicator, the coherence provides a measure of the degree of linear correlation between the polarimetric radar returns. The use of a generalized coherence operator (involving appropriated basis functions to compute the expectation function of equation 1.19) could be of the greatest interest as an inversion technique but hasn't been successfully achieved yet to our best knowledge. To come back to the state of art concerning the problem of coherence estimators, many studies have been performed to cope typically with the twofold objective : preserving resolution which is the main drawback of the multi-look method as well as limiting the estimation bias. The estimator assessment is naturally eased when its analytical expression can be derived, hence the

use of various speckle models to characterize the scatterers statistical behaviour. The Gaussian and stationary assumption is commonly used, its fruitful consequences on SAR speckle analysis and optimal filters development (cf. [Lee, 1986a,b; López-Martínez and Fàbregas, 2002]) will be discussed afterwards, in the next chapter. That speckle, which is in a way a drawback of SAR or coherent radar (cf. previous §) justifies the preferable use of order two or higher moments than the mean values ensued from the Sinclair matrix, null as far as distributed targets are considered (typically partially random media as vegetated lands). Apart from the seldom cases where the scatterers behaviour is precisely known, higher statistical moment than order two are not really worthwhile. The latter are usually merged into the covariance matrix, which in its general form can be expressed as follows :

$$\begin{aligned} \mathbf{C} &= E\big(\vec{k}\cdot\vec{k}^{\dagger}\big) \\ \text{with } \vec{k} &= [s_1, s_2, ..., s_m]^t \end{aligned} \tag{1.20}$$

where k is the target vector defined according to the various considered radar measurements s_p. For instance, in the case of a quad-pol acquisition, m = 4 and using the so-called lexicographic basis, the target vector becomes $\vec{k}_L = [s_{hh}, s_{hv}, s_{vh}, s_{vv}]^t$. The resulting covariance matrix is 4*4, filled actually with the non normalized coherence terms $< s_{qp}s^*_{mn} >$. The latter can be also enriched with interferometry (cf. [Bamler and Hartl, 1998]) and for a two baselines acquisition (superscripts 1,2) : $\vec{k}_L = \Big[[s^1_{qp}], [s^2_{qp}]\Big]^t$, (m=8). As detailed in chapter 5, the extension to Pol-InSAR coherences, considered as the culmination of radar information, brings indeed a considerable improvement for retrieval with on top of the scattering mechanism characterization by polarimetry, an associated height. As far as scattering mechanisms are concerned, a convenient way widely used in the literature to express the target vector lies on its decomposition onto the Pauli matrices. Alternatively to the lexicographic basis and its resulting covariance matrix, this decomposition leads to the coherence matrix T defined likewise by :

$$\mathbf{T} = \langle \vec{k}_P \cdot \vec{k}_P^{\dagger} \rangle, \text{with } : \vec{k}_P = \frac{1}{\sqrt{2}} \begin{bmatrix} s_{hh} + s_{vv} \\ s_{hh} - s_{vv} \\ s_{hv} + s_{vh} \\ j(s_{hv} - s_{vh}) \end{bmatrix}$$

and thereby well adapted to described the major scattering mechanisms occurring in forested land, with odd or even interactions (cf. chapter 3). Prominent in polarimetry, the target decomposition theory is precisely dedicated to the characterization of these scattering mechanisms and will be detailed in chapter 3, especially regarding the bistatic specificities. In a few words, three approaches can be distinguished among target decomposition theorems : the Huynen type decomposition, the eigenvector one of the previously mentioned coherence or covariance matrix and unlike the latter, coherent decomposition theory. The origin of target decomposition has been indeed mainly initiated by Huynen, which proposed the extraction of a single characteristic scattering behaviour from the Kennaugh matrix (or equivalently Mueller in the FSA convention) relating the scattered and incident Stokes vectors. Apart from the use of the coherence/covariance matrix instead of the Kennaugh/Mueller one which are actually all closely related (cf. chapter 3), the main difference with the eigenvector decomposition lies in the summation of the averaged data onto several statistically independent type of scattering mechanisms. This method is thereby particularly adapted to describe forest scattering with its mixed contribution and has been extensively used for radar classification. However, Huynen type decomposition entails directly the information about the wave degree of polarization, which retrieval potential could be

more often considered (cf. [Souyris and Tison, 2007]). In addition, the Freeman decomposition can also be mentioned (cf. [Freeman and Durden, 1998]), which can be considered as an hybrid method between Huynen and eigenvector decomposition since it considers the separation between the three scattering mechanisms directly from a weighted sum representation of the coherence matrix, without eigenvector decomposition, hence some limitations regarding the mathematical existence of such representation.

Last, the coherent decomposition approach is on the contrary based on the coherently averaged Sinclair matrix representation into a weighted sum of canonical scattering matrices. For the latter, the Pauli basis is often used – with sphere, straight and $\pi/4$ titled dihedral components – alternatively to the Krogager decomposition between the sphere, the diplane and the helix scattering matrices, better adapted when dealing with circular polarizations, though disadvantageously not orthogonal. As mentioned previously, such averaged matrices (order 1) are not appropriated when dealing with the generally high speckle of SAR data. Nevertheless, this decomposition can be achieved in the case of a dominant scatterer within the resolution cell, which can also concerned natural scenes (for instance at high resolution, the double bounce return from a trunk near forest clearings may behave as a coherent scatterer, cf. chapter 3).

1.3.3 Bistatic Radars

The overall radar specificities as a remote sensor has been presented in the previous subsection, among microwave and optical techniques. To that end, also pointed out has been the difference between active and passive remote sensing, to which actually semi-active radar systems can be added, involving a (non-natural) transmitter and a single or multiple receivers. The resulting possibility to separate the emitter and receiver's location brings us thus to the bistatic radar configuration – actually in the same way as an optical receiver in the reflectivity domain of sun energy.

This subsection is dedicated to bistatic radars, however with the modest ambition to point out only the overall concepts and besides, to precise definitions and specific terms used afterwards as well as to realize the reasons which originate the current resurgence for bistatic. Indeed, the subject being well documented in the literature, the interested reader can refer to [David, 1969; Willis and Griffiths, 2007; Blanchard, 2004; Cherniakov et al., 2008] for an exhaustive overview, especially concerning the radar history which came with the last century events.

To date, bistatic configurations started in the early age of radar since about 20 years after the Hülsmeyer's telemobilskop in 1904, one can refer to the experiment of US Navy Lab engineers (Dr. Taylor and Young) which noticed the possible detection wooden steamers using a transmitter and receiver that were physically separated of a few miles. Fostered by the detection and the localization military purpose urged by the historical context, various demonstrations of bistatic experiments were carried out at about the same time in U.S, England, France, Germany, Italy and Japon. Prominent among these early examples, one can cite the bistatic fence initiated by P. David and referred as the "electromagnetic barrier", using a CW radar and the Doppler variation due to targets passing through the emitter and receivers. An other famous illustration of achievement taking profit of bistatic was the German 'Klein Heidelberg' system which used the British Chain Home radars as illuminators of opportunity and warned the approaching Allied Bombers while they were still over the English Channel.

As illustrated with these few examples, the bistatic configuration offers a versatility at the origin of several concepts. First of all, the basic definition of bistatic system can be reminded, as *a configuration involving a physically separated transmitter and receiver with a significant fraction of the distance to the target*, as opposed to the deployment of different but close emitting and receiving antennas. The pioneer bistatic experiments were ground based but their airborne or spaceborne counterparts can be naturally envisioned – combined configurations likewise. In addition, the term hybrid bistatic configuration is used for configuration involving a transmitter which is also receiving. As far as the emitting source is concerned, important is the concept of transmitter of opportunity whether cooperative (friendly) or non-cooperative (neutral or hostile sources). The following specificities can be also stressed : in the case of a monostatic radar transmitter, the receiver is called a hitchhiker whereas one refers as Passive Bistatic Radar (PBR) or Passive Coherent Location (PCL) when the source is from commercial broadcast, communications signals and last but not least the **GNSS-R** (Global Navigation Satellite Systems - Reflectometry) concept with radionavigation signals. Besides, a configuration which centralized acquisitions involving several emitting or receiving sites is called multistatic, though possibly made only of monostatic radars forming radar net coverage. On top of the higher geometrical versatility and the possibly low cost acquisitions, an obvious advantage of passive receiver is the discretion with respect to emitting source detectability, in a military context. Besides, one can also add the counter-stealth capability of bistatic radars, since the target shape is usually designed to minimize its monostatic RCS and the bistatic one is unlikely to be reduced as well.

Yet, bistatic systems has been left aside after World War II, especially because of specific op-

erational progress achieved for monostatic radars, such as the developments of pulsed waveforms (which rise the problem of an accurate synchronization to be transposed in bistatic) and the duplexer, offering from now on the possibility to use a single transmitting and receiver antenna. Since then, the monostatic mindset has been implicitly added to the disadvantages of bistatic radars which has thus been revisited only in the framework of niche applications. Nevertheless, in view of the relatively recent GNSS deployment fostering also the progress on time oscillators, the resulting spatial and temporal level of accuracy possibly obtained eases considerably the pregnant synchronization issue coming with bistatic systems.

As a great illustration, SAR processing has been recently performed whether in the stationary or non stationary cases (cf. chapter 2). Rather, BGMTI (Bistatic Ground Moving Target Indicator) applications are currently designed for which development of specific STAP (Space-Time Adaptative Processing) and DBF (Digital Beam Forming) techniques are an important research topic. One can refer to the airborne bistatic ONERA-DLR campaign conducted with their respective RAMSES and ESAR radars or combined experiments involving the TerraSAR-X satellite with the airborne radar FSAR (DLR) or PAMIR (FGAN).

Besides, these campaigns make also profit from scientific results ensued from experiments of proximity, particularly for what concerns overall scattering characterization (σ or σ^0) whether for physical applications related to remote sensing or for the purpose of calibration study, being also more innovative in bistatic (cf.[Kahny et al., 1992; Bradley et al., 2005a,b]). For instance, one can refer to experiments conducted in the EMSL (European Microwave Signature Laboratory) at JRC, in the Michigan University or in the DLR's Bistatic Measurement Facility (BMF, cf. [Roo and Ulaby, 1994; Khadhra, 2008]) but also to on site experiments with network analysers (cf. [Guern et al., 2004]).

Also important within this scope of the current bistatic resurgence, configurations of opportunity are becoming much more realistic with the nowadays huge number of various possible microwave sources. As mentioned above, the transmitter of opportunity can be divided into three types, for the following specificities can be pointed out.

With a monostatic radar as transmitter, the hitchhiker acquisition is potentially the easiest configuration from the operational point of view, depending obviously on the source's disposition to cooperate. Among the important criteria concerning the emitted signal, its power, waveform, continuity (time-wise) and origin localization are naturally paramount for the resulting SNR, spatial and temporal resolution. As an examples, the previously cited demonstrations with TerraSAR-X satellite and airborne receivers were the first of that type, whereas the design of future missions such as BISSAT (Bistatic Interferometric SAR SATellite, cf. [D'Errico and Moccia, 2003; D'Errico and Fasano, 2008]) has been prepared with the ambitious aim of several LEO satellites using ENVISAT or COSMO-Skymed emitter and involved in a cartwheel or pendulum configuration (cf. [Massonnet, 2001; Krieger et al., 2003]) – hence the possible along or across-track interferometric acquisition.

Alternatively, with the use of broadcast or communications signals – such as DVB-[STH] for Digital Video Broadcast (Satellite, Terrestrial, Handheld), FM radio and TV or GSM –, PCL or PBR are more commonly envisioned with ground based bistatic receivers for the purpose of detection and localization ([Tan et al., 2005], rather remote sensing imaging. Indeed, though potentially possible (e.g for land or sea surface characterization) remote sensing applications are liable to suffer from the use of linear polarization, basic modulation coding and frequencies either too high (Ku-band) or too low (VHF for FM radio or TV transmissions), in spite of an expected SNR acceptable, all the more if we consider the time continuity of the signal.

Initiated by promising remote sensing studies and experiments for sea surface height determination (cf. [Martin-Neira, 1993; Martin-Neira et al., 2001]) or characterization (cf. [Zavorotny

and Voronovich, 2000]), the GNSS-R (Reflectometry) presents several assets as a bistatic configuration of opportunity from radionavigation signals. Prominent among them are the long lifetime of GNSS constellations, a global coverage, an high temporal resolution, an accurate localization and signal modulation coding, also continuous in time with a frequency (L-band) and circular polarization well-suited to remote sensing applications.

In addition, relevant studies concerning imaging capabilities with the D2M – Delay-Doppler Map – generation (cf. [Elfouhaily et al., 2002; et al., 2005; D'Addio and Buck, 2008]) are also promising as well as research about retrieval method from hybrid polarization (right circular emission, linear H,V on receive) observables – for instance the POPI (Polarimetric Phase Interferometry) technique, cf. [Cardellach et al., 2006]) – or to cope with the very low incident power density onto the ground, being the main drawback of GNSS-R. Indeed, the possible long integration time and the preferable use of specular scattering direction which could improve the SNR is actually limited by the varying geometry. Within this research area about GNSS-R, we can finally also mention experiments conducted at ESA about soil moisture retrieval (cf. [Buck and D'Addio, 2007]) and also the acquisition of sea reflected GPS signals with the polar-LEO satellites belonging to the United Kingdom's Disaster Monitoring Constellation (UK-DMC, cf. [Clarizia, 2008]).

Conclusion

A general presentation of forest remote sensing from radar measurements has been exposed in this first chapter with an overview of both specificities, forests as media of interest and radar as remote sensor. The paramount importance of forests throughout the world has been stressed, especially regarding environmental issue. Hence a pregnant need of efficient monitoring worldwide, all the more that forested media change rapidly, on account of their close sensitivity to anthropogenic activities. Among the various remote sensing techniques, the active radar's specificities has been pointed out in comparison with passive radar or optical ones. Prominent among them are the full polarimetric and interferometric acquisitions which constitute the culmination of radar information with unique capabilities. The interpretation of these measurements however is not straightforward, especially more complex than the use of single channel radar or optic radiometry, which similarities have been also emphasized, actually all the more closer with the bistatic radar configuration. Within a retrieval scope, Pol-InSAR measurements exhibit a paramount sensitivity towards target geometrical attributes – especially with size and orientation characteristics – as well as physical ones with the scatterers intrinsic permittivity and rather, towards structure and particle arrangement. Although necessary, this sensitivity is not sufficient yet as far as inverse problem is concerned. Advanced theoretical studies are thus required to understand the measures dynamic, especially for an efficient use of radar parameters, among which frequency and plus in our framework the bistatic geometry can be set forth to ease the retrieval. The status of bistatic radar has been indeed also presented, with the aim of pointing out the overall reasons at the origin of its current resurgence and mainly from the operational point of view. This brings us to the underlying question about the interest in bistatic observables, liable indeed to come with an higher retrieval potential within the scope of forest remote sensing which is precisely the topic of the following chapters, concerning first of all forward electromagnetic modeling as the core of the subsequent analysis of these new configurations.

Bibliography

R. Bamler and P. Hartl. Synthetic aperture radar interferometry. *Inverse Problems*, 14, 1998.

H.H. Bartelink. Allometric relationships for biomass and leaf area of beech (fagus sylvatica l). *Annals of Forest Science*, 54:39–50, 1997.

A. Berger. *Le climat de la Terre*. De Boeck Université, Bruxelles, 1992. 479 pages.

R.A. Betts, P. M. Cox, S.E. Lee, and F.I. Woodward. Contrasting physiological and structural vegetation feedbacks in climate change simulations. *Nature*, 387:796–799, 1997.

Yves Blanchard. *Le radar - 1904-2004 - Histoire d'un siècle d'innovations techniques et opérationnelles*. Ellipses, Mars 2004.

D.B. Botkin, J.F. Janak, and J.R. Wallis. Some ecological consequences of a computer model of forest growth. *Journal of Ecology*, 60, 1972.

C.J. Bradley, P.J. Collins, J. Fortuny-Guasch, M.L. Hastriter, G. Nesti, A.J. Terzuoli, and K.S. Wilson. An investigation of bistatic calibration objects. *IEEE Transactions on Geoscience and Remote Sensing*, 43:2177–2184, Oct. 2005a.

C.J. Bradley, P.J. Collins, J. Fortuny-Guasch, M.L. Hastriter, G. Nesti, A.J. Terzuoli, and K.S. Wilson. An investigation of bistatic calibration objects. *IEEE Transactions on Geoscience and Remote Sensing*, 43:2185–2191, Oct. 2005b.

Lester R. Brown, Janet Larsen, and Bernie Fischlowitz-Roberts. *The earth policy reader*. W.W. Norton, 2002.

S. Brown and A.E. Lugo. Biomass of tropical forests: a new estimate based on forest volume. *Science*, 223:1290–1293, 1984.

C. Buck and S. D'Addio. Status and perspectives of gnss-r at esa. In *Geoscience and Remote Sensing Symposium (IGARSS), Barcelona (Spain)*. IEEE, 2007.

G.S. Campbell and J.M. Norman. *The description and measurement of plant canopy structure*. Soc. Exp. Biol., Seminar Series 31. Cambridge University Press, russell et al., plant canopies: their growth, form and function edition, 1987.

J.B. Campbell. *Introduction to remote sensing*. Guilford, 1987.

E. Cardellach, S. Ribo, and A. Rius. Technical note on polarimetric phase interferometry (popi). *arXiv Physics*, 2006.

T. Castel, A. Beaudoin, N. Floury, T. Le Toan, Y. Caraglio, and J.-F. Barczi. Deriving forest canopy parameters for backscatter models using the amap architectural plant model. *IEEE Transactions on Geoscience and Remote Sensing*, 39:571–583, 2001.

J-P. Chabin. *La forêt dans tous ses états: de la prhistoire à nos jours*. Annales Littéraires. Presses Universitaires De Franche-Comté, Décembre 2005. 409 pages.

I. Champion, A. Porté, D. Bert, D. Loustau, and M. Guedon. Tree architecture in remote sensing analytical models : The bray experiment. *International Journal of Remote Sensing*, 22:1827–1843, 2001.

J. Charney, P. H. Stone, and W.J. Quirk. Drought in sahara - biogeophysical feedback mechanism. *Science*, 187(4175):434–435, February 1975.

M. Cherniakov, Antonio Moccia, Alberto Moreira, Gerhard Krieger, and Marco D'Errico. *Bistatic Radars : Emerging Technology*. John Wiley & Sons., 2008.

M.P. Clarizia. Global navigation satellite system-reflectometry (gnss-r) from the uk-dmc satellite for remote sensing of the ocean surface. In *Geoscience and Remote Sensing Symposium (IGARSS), Boston (Massachusetts-USA)*. IEEE, 2008.

Robert N. Colwell. *Manual of Remote Sensing*. American society of Photogrammetry, 1983. 2 volumes.

R. Costanza, R. D'Arge, and R.D. Groot. The value of the world's ecosystem services and natural capital. *Nature*, 387(6630):253–260, 1997.

P. M. Cox, R. A. Betts, C. D. Jones, S. A. Spall, and I. J. Totterdell. Acceleration of global warming due to carbon-cycle feedbacks in a coupled climate model. *Nature*, 409:184–187, 2000.

J.K. Cronk and M.S. Fennessy. *Wetland Plants: Biology and Ecology*. CRC Press/Lewis Publishers, 2001. 440 pages.

S. D'Addio and C. Buck. Performance assessment of gnss-r space based scatterometry by means of delay-doppler map. In *Geoscience and Remote Sensing Symposium (IGARSS), Boston (Massachusetts-USA)*. IEEE, 2008.

P. David. *Le Radar*, volume 381. PUF, coll. Que sais-je ?, editions des presses universitaires de france edition, 1969.

M. D'Errico and G. Fasano. Design of interferometric and bistatic mission phases of cosmo/skymed constellation. *Acta Astronautica*, 62 (2-3):97–111, 2008.

M. D'Errico and A. Moccia. Attitude and antenna pointing design of bistatic radar formations. *IEEE Transactions on Geoscience and Remote Sensing*, 39:949–960, July 2003.

T. Elfouhaily, D.R. Thompson, and L. Linstrom. Delay-doppler analysis of bistatically reflected signals from theocean surface: theory and application. *IEEE Transactions on Geoscience and Remote Sensing*, Mar 2002.

S. Gleason et al. Detection and processing of bistatically reflected gps signals from low earth orbit for the purpose of ocean remote sensing. *IEEE Transactions on Geoscience and Remote Sensing*, 2005.

Food and Agriculture Organization of the United Nations. *State of the World's Forests 2009 (SOFO)*. State of the World's Forests. 2009. Also available at www.fao.org/docrep/011/i0350e/i0350e00.html.

POLINSAR for FOPEN using flashlight mode images along circular trajectories. H. cantalloube and e.k. colin. In *International Geoscience and Remote Sensing Symposium (IGARSS)*, pages 1139–1142. IEEE, 2007.

T. Fourcoud, F. Blaise, P. Lac, P. Castera, and P. De Reffye. Numerical modelling of shape regulation and growth stresses in trees ii. implementation in the amap para software and simulation of tree growth. *Trees - Structure and Function*, 17:31–39, 2003.

A. Franchois, Y. Pineiro, and R.H. Lang. Microwave permittivity measurements of two conifers. *IEEE Transactions on Geoscience and Remote Sensing*, 36:1384–1395, Sept. 1998.

J. Franklin and A.H. Strahler. Invertible canopy reflectance modeling of vegetation structure in semi-arid woodland. *IEEE Transactions on Geoscience and Remote Sensing*, 26:809–825, November 1988.

A. Freeman and S.L. Durden. A three-component scattering model for polarimetric sar data. *IEEE Transactions on Geoscience and Remote Sensing*, 36(3):963–973, May 1998.

GFC. *Report on Independent Monitoring of the Implementation of Article 4.1 (d) of the Unites Nations Framework Convention on Climate Change*. March 2006. Also available at http://www.globalforestcoalition.org.

G. De Grandi, J.S. Lee, D. Schuler, and E. Nezry. Texture and speckle statistics in polarimetric sar synthesized images. *IEEE Transactions on Geoscience and Remote Sensing*, 9:2070–2088, 2003.

R. Guern, M. Lesturgie, J. Derosch, P. Borderies, L.C. Tai, HL Chan, H.W. Seah, Y.L. Lu, and W.X. Liu. Benefits of ultra wide band for radar imaging through the forest: examples from a boom-sar experimentation. In *International Geoscience and Remote Sensing Symposium (IGARSS)*. IEEE, 2004.

IPCC. *Climate Change 2007: Synthesis Report. Contribution of Working Groups I, II and III to the Fourth Assessment Report of the Intergovernmental Panel on Climate Change [Core Writing Team, Pachauri, R.K and Reisinger, A. (eds.)]*. Academic Press, November 2007.

D. Kahny, K. Schmitt, and W. Wiesbeck. Calibration of bistatic polarimetric radar systems. *IEEE Transactions on Geoscience and Remote Sensing*, 30:847–852, Sept. 1992.

C.D. Keeling and T.P. Whorf. *Atmospheric CO2 records from sites in the SIO air sampling network (1957-2002)*. Trends: A Compendium of Data on Global Change. Carbon Dioxide Information Analysis Center (CDIAC), 2004.

K. Ben Khadhra. *Surface Parameter Estimation using Bistatic Polarimetric X-band Measurements*. Dissertation, Technischen Universitt Chemnitz, Fakultät für Elektrotechnik und Informationstechnik — Deutsches Zentrum für Luft und Raumfahrt (DLR) in der Helmholtz-Gemeinschaf, 2008.

G.E. Kindermann, I. McCallum, S. Fritz, and M. Obersteiner. A global forest growing stock biomass and carbon map based on fao statistics. *Silva Fennica (International journal of forest science)*, 42:387–396, 2008.

G. Krieger, H. Fiedler, J. Mittermayer, K. Papathanassiou, and A. Moreira. Analysis of multistatic configurations for spaceborne sar interferometry. In *Radar, Sonar and Navigation*, volume 150 (3), pages 87–96. IEE, 2003.

J.-S. Lee. Speckle analysis and smoothing of synthetic aperture radar images. *Computer Graphics and Image Processing*, 17:24–32, May 1986a.

J.-S. Lee. Speckle suppression and analysis for synthetic aperture radar images. *Optical Engineering*, 25:636–643, May 1986b.

X. Li and A.H. Strahler. Geometric-optical bidirectional reflectance modeling of the discrete crown vegetation canopy: effect of crown shape and mutual shadowing. *IEEE Transactions on Geoscience and Remote Sensing*, 30:276–292, March 1992.

Yi-Cheng Lin and K. Sarabandi. A monte carlo coherent scattering model for forest canopies using fractal-generated trees. *IEEE Transactions on Geoscience and Remote Sensing*, 37: 440–451, Jan. 1999.

C. López-Martínez and X. Fàbregas. Modelling and reduction of sar interferometric phase noise in the wavelet domain. *IEEE Transactions on Geoscience and Remote Sensing*, 40:2553–2566, Dec. 2002.

M. Martin-Neira. A passive reflectometry and interferometry system (paris): application to ocean altimetry. *ESA journal*, pages 331–355, 1993.

M. Martin-Neira, M. Caparrini, and J. Font-Rosselo. The paris concept: An experimental demonstration of sea surface altimetry using gps reflected signals. *IEEE Transactions on Geoscience and Remote Sensing*, 39:142–150, 2001.

D. Massonnet. Capabilities and limitations of the interferometric cartwheel. *IEEE Transactions on Geoscience and Remote Sensing*, 39:506–520, 2001.

J.E. Means, H.A. Hansen, G.J. Koerper, P.B. Alaback, and M.W. Klopsh. *Software for computing plant biomass BIOPAK users guide*. Technical Report PNW-GTR-340. U.S. Department of. Agriculture, Forest Service, 1994.

T. Mette, K. Papathanassiou, I. Hajnsek, H. Pretzsch, and P. Biber. Applying a common allometric equation to convert forest height from pol-insar data to forest biomass. In *Geoscience and Remote Sensing Symposium (IGARSS), Anchorage (Alaska)*, volume 20-24. IEEE, 2004.

R.K. Moore, W.P. Waite, and J.W Rouse. Panchromatic and polypanchromatic radar. In *Proceedings of the IEEE*, volume 57, pages 590–593, 1969.

R.B. Myneni, J. Ross, and G. Asrar. A review on the theory of photon transport in leaf canopies. *Agricultural and Forest Meteorology*, 45, 1989.

N.R. Peplinski, F.T. Uaby, and M.C. Dobson. Dielectric properties of soils in the 0.3-1.3-ghz range. *IEEE Transactions on Geoscience and Remote Sensing*, 33:803–807, May 1995.

W.M. Post, W.R. Emanuel, P.J. Zinke, and A.G. Stangenberger. Soil carbon pools and world life zones. *Nature*, 298:156–159, 1982.

C. Prigent, I. Tegen, F. Aires, B. Marticorena, and M. Zribi. Estimation of the aerodynamic roughness length in arid and semi-arid regions over the globe with ers scatterometer. *Journal of Geophysical Research*, 110, 2005.

C. Prigent, F. Aires, and W.B. Rossow. Land surface microwave emissivities over the globe for a decade. *American Meteorological Society*, 110:1573–1584, May 2006.

P. Prusinkiewicz. Self-similarity in plants: Integrating mathematical and biological perspectives. *In M. Novak (ed.), Thinking in Patterns: Fractals and Related Phenomena in Nature*, pages 103–118, 2004.

Przemyslaw Prusinkiewicz and Aristid Lindenmayer. *The algorithmic beauty of plants Purchase this Book*. Springer-Verlag, 1996. Univ. of Regina, Canada.

F. Ramade. *Ecologie Fondamentale*. Ediscience International, MacGraw-Hill, 1984. 302p.

R.K. Raney, T. Freeman, R.W. Hawkins, and R. Bamler. A plea for radar brightness. In *International Geoscience and Remote Sensing Symposium (IGARSS)*, volume 2, pages 1090–1092. IEEE, 1994.

A. Reigber and A. Moreira. First demonstration of airborne sar tomography using multibaseline l-band data. *IEEE Transactions on Geoscience and Remote Sensing*, 38:2142–2152, Sept. 2000.

M. Robert and B. Saugier. Contribution of terrestrial ecosystems to carbon sequestration. *Comptes Rendus - Geoscience*, 335 (6-7):577–595, 2003.

Marc Robin. *La télédétection: des satellites aux systèmes d'information géographiques*. Nathan Universite, second edition edition, 2001. 320p.

R.D. De Roo and F.T. Ulaby. Bistatic specular scattering from rough dielectric surfaces. *IEEE Transactions on Antennas and Propagation*, 42:220–231, 1994.

W.A. Salas, J.K. Ranson, B.N. Rock, and K.T. Smith. Temporal and spatial variations in dielectric constant and water status of dominant forest species from new england. *Remote Sensing of Environment*, 47:109–119, 1994.

K. Saleh, A. Porte, D. Guyon ans P. Ferrazzoli, and J.P. Wigneron. A forest geometric description of a maritime pine forest suitable for discrete microwave models. *Geoscience and Remote Sensing, IEEE Transactions on*, 43:2024–2035, Sept. 2007.

Vaclav Smil. *Energy In Nature And Society: General Energetics Of Complex Systems*. Mit Press Ltd, 2008.

J.C. Souyris and C. Tison. Polarimetric analysis of bistatic sar images from polar decomposition : A quaternion approach. *IEEE Transactions on Geoscience and Remote Sensing*, 45(9): 2701–2714, Sept. 2007.

D.K.P. Tan, H. Sun, Y. Lu, M. Lesturgie, and H.L. Chan. Passive radar using global system for mobile communication signal: theory, implementation and measurements. *Radar, Sonar and Navigation, IEE Proceedings*, 152:116–122, June 2005.

M. Toda, M. Yokozawa, A. Sumida, T. Watanabe, and T. Hara. Foliage profiles of individual trees determine competition, self-thinning, biomass and npp of a cryptomeria japonica forest. *IEEE Transactions on Geoscience and Remote Sensing*, 220, September 2009.

R. Touzi, A. Lopés, J. Bruniquel, and P.W. Vachon. Coherence estimation of sar imagery. *IEEE Transactions on Geoscience and Remote Sensing*, 37:135–149, 1999.

R.N. Treuhaft, G.P. Asner, and B.E. Law. Structure-based forest biomass from fusion of radar and hyperspectral observations. *Geophysical Research Letters*, 30(9), 2003.

Nicholas J. Willis and Hugh D. Griffiths. *Advances in Bistatic Radar*. SciTech Publishing, 2007.

M.E. Winter, S.G. Beaven, and A.J. Ratkowski. Hyperspectral image sharpening using multispectral data. In *Aerospace Conference*, pages 1–9. IEEE, 2007.

M.T. Yilmaz, E.R. Hunt, and T.J. Jackson. Remote sensing of vegetation water content from equivalent water thickness using satellite imagery. *Remote Sensing of Environment*, 112:2514–2522, 2008.

V.U. Zavorotny and A.G. Voronovich. Scattering of gps signals from the ocean with wind remote sensing application. *IEEE Transactions on Geoscience and Remote Sensing*, Mar 2000.

R. Zimmermann, K. McDonald, R. Oren, and J. Way. Xylem dielectric constant, water status, and transpiration of young jack pine (pinus banksiana lamb.) in the southern boreal zone of canada. In *Geoscience and Remote Sensing Symposium (IGARSS)*, volume 2, pages 1006–1008. IEEE, 1995.

Z.W.Xu, J. Wu, and Z-S.Wu. A survey of ionospheric effects on space-based radar. *Waves in Random media*, 14:189–273, 2004.

Chapter 2

Forward Modeling

Contents

2.1 Electromagnetic Modeling in Forest Scattering

2.1.1 The Coherent and Discrete Approach

Within the scope of forest scattering modeling, the interaction between em waves and scatterers from the vegetation cover rises the twofold problem of transmission (propagation) and scattering (reflective part), referred as the two fundamental phenomenons in active radar remote sensing, as presented in the previous introduction chapter, as well as the forest media complexity (cf. section 1.2.2). Hence, on account of the multiple kind of attributes characterizing the individual scatterers, whether geometric (various shapes, sizes) or physical (resulting in a given dielectric constant, reminded to be mainly driven by the water content regarding the whole chemical composition) the discrete approach is particularly well adapted.

Besides, in view of its relatively moderate volume fraction (typically lower than 5 %, apart for dense tropical forests), the **DBWA** (Distorted Born Wave Approximation) holds and can be used actually for the two afore-mentioned scattering physical phenomenons (cf. [Tsang et al., 1985]). This order one assumption considers that the field at a given location can be expressed as the incident one plus the contribution resulting from the individual simple and independent interactions due to the other scatterers encompassed in the media.

For the propagation phenomenon, the **DBWA** leads to the Foldy's approximation, also referred as the **EFA** (Effective field approximation) since derived with the Forward Scattering Theorem, itself ensued from the application of the stationary phase one (cf. [Ishimaru, 1978]), as detailed in section 5.3 (chapter 5). It can be indeed demonstrated under these assumptions that the em field verifies :

$$\begin{aligned} \frac{d\langle E_v\rangle}{dr} &= j\big(k_0 - \frac{\sigma_{vv}}{2}\big)\langle E_v\rangle - j\frac{\sigma_{vh}}{2}\langle E_h\rangle \\ \frac{d\langle E_h\rangle}{dr} &= -j\frac{\sigma_{hv}}{2}\langle E_v\rangle + j\big(k_0 - \frac{\sigma_{hh}}{2}\big)\langle E_h\rangle \end{aligned} \tag{2.1}$$

where r is the radial distance variable along the propagation direction (k_0 the free space wave vector and j the unit imaginary number). σ_q is herein defined as the power extinction cross section, a real function of the direction of arrival angles (θ, ϕ) so that in the most general case :

$$\sigma_{qp}(\theta,\phi) = \frac{4\pi n_0}{k_0}\langle Im(S_{qp}(\theta,\phi))\rangle_{p,o,s} \tag{2.2}$$

where the brackets $\langle\cdot\rangle_{p,o,s}$ denote the statistical mean over the type of constituent p (detailed in the newt §) of density n_0, orientation o and size s, S_{qp} being the scattering coefficient in the forward direction (hence the 'Forward Scattering Theorem' reference).

As a case of great importance, for media exhibiting an azimuthal symmetry with respect to the horizontal reference plane (defined by the vertical vector $\hat{z}$), it can be demonstrated that only the average for the co-polarizations and only the site angle dependence $\langle Im(S_{qq}(\theta))\rangle_{p,o,s}$ remain. This condition holds for most of the natural media, apart from tilted surfaces (cf. subsection 2.2.1), so that the EFA can be simplified into :

$$\frac{d\langle E_q\rangle}{dr} = j\big(k - \frac{\sigma_q}{2}\big)\langle E_q\rangle, \qquad q \in [v,h] \tag{2.3}$$

Likewise, the scattered field is derived according to the **DBWA** and the case where the phase is preserved within the summation leads to the so-called coherent models, as opposed to the incoherent ones which on the one hand considered only the mean amplitude field but on the other hand are better suited to cope with an higher level of scattering interaction (plus the intrinsic emissivity) thanks to the radiative transfer equation (reminded chapter 1, equation 2).

Furthermore, it can be also stressed that the phase preservation may also impact the intensity, typically in the case of the backscattering enhancement for coupling terms between volume scatterers and the ground (i.a [Saatchi and McDonald, 1997]), generalized herein to specific bistatic cases, as shown afterwards in chapter 3 section 4. This coherent effect is thereby not accounted for within the original incoherent formulation, though possibly added by corrective approaches (cf. [Durden et al., 1989; Dahon et al., 2006]). For the purpose of modeling interferometric radar observables, the coherent approach has been naturally chosen.

As far as scattering mechanisms are concerned, single interaction and coupling terms between the volume and the ground are typically taken into account within coherent models :

- Single interaction scattering mechanism concerns the direct contribution from the volume as well as the ground one. According to the afore-mentioned DBWA assumptions, the scattered field $\mathbf{E}_s(\vec{r}_{\mathrm{R}};\vec{r}_{\mathrm{T}})$ at location $\vec{r}_{\mathrm{R}}$ due to an incident one coming from the transmitter T at $\vec{r}_{\mathrm{T}}$) can thus be expressed as the coherent summation over the contribution of each scatterer P at $\vec{r}_{\mathrm{P}}$, taking into account the extinction for the down coming direction $\vec{k}_i =$

$\vec{r}_{\mathrm{P}} - \vec{r}_{\mathrm{T}}$ and upcoming signal $\vec{k}_s = \vec{r}_{\mathrm{R}} - \vec{r}_{\mathrm{P}}$.

$$\begin{aligned}\mathbf{E}_s(\vec{r}_{\mathrm{R}};\vec{r}_{\mathrm{T}}) = \Big(\sum_p e^{-j\varphi_p^{\mathrm{ds}}}[t_p(\hat{k}_s)]\cdot\big[S_p(\hat{k}_i,\hat{k}_s)\big] \\ \cdot[t_p(\hat{k}_i)]\Big)\cdot\mathbf{E}_i(\hat{k}_i)\end{aligned} \tag{2.4}$$

with $\big[S_p\big]$ as the scattering matrix (cf. next §) of each element p, $\big[S_p\big]$ as the transmissivity matrix reaching p for the direction $\hat{k}_s$ or $\hat{k}_s$ and with $e^{-j\varphi_p^{\mathrm{ds}}}$ as the phase propagation term which – in the case of direct scattering 'ds' mechanism – is simply :

$$\varphi_p^{\mathrm{ds}} = k_0\big(|\vec{r}_{\mathrm{P}} - \vec{r}_{\mathrm{T}}| + |\vec{r}_{\mathrm{R}} - \vec{r}_{\mathrm{P}}|\big)$$

- the coupling terms between volume scatterers and the ground are also referred as double bounce or specular ground mechanism since – as shown in chapter 5 section 2.4 – it involves the interaction with a volume element and the specular Fresnel reflection onto the ground point – G^T or G^R – determined whether with the transmitter or the receiver's mirror image, as depicted in figure 5.2. The subsequent analysis (i.a sections 5.3.2, 5.4.3) will show that this twofold aspect of the double bounce mechanism is a paramount difference from the monostatic to the bistatic configuration.

  Following the same formalism than for the direct scattering contribution, the scattered for the specular ground terms can be expressed as :

$$\begin{aligned}\mathbf{E}_s^{T,RsG}(\vec{r}_{\mathrm{R}}) &= \big[\mathcal{S}^{\mathrm{T,RsG}}(\hat{k}_i,\hat{k}_s)\big]\cdot\mathbf{E}_i(\vec{r}_{\mathrm{T}}) \\ \big[\mathcal{S}^{\mathrm{TsG}}(\hat{k}_i,\hat{k}_s)\big] &= \sum_p [t_p(\vec{r}_{\mathrm{R}} - \vec{r}_{\mathrm{P}})]\cdot\big[S_p(\hat{\aleph}_i^p,\hat{k}_s^p)\big] \\ &\qquad \cdot[t_p(\vec{r}_{\mathrm{P}} - \vec{r}_{\mathrm{GT}})]\cdot[\mathcal{R}(\theta_i^p)]\cdot[t_p(\vec{r}_{\mathrm{GT}} - \vec{r}_{\mathrm{T}})] \\ \big[\mathcal{S}^{\mathrm{RsG}}(\hat{k}_i,\hat{k}_s)\big] &= \sum_p [t_p(\vec{r}_{\mathrm{R}} - \vec{r}_{\mathrm{GR}})]\cdot[\mathcal{R}(\theta_s^p)]\cdot[t_p(\vec{r}_{\mathrm{GR}} - \vec{r}_{\mathrm{P}})] \\ &\qquad \cdot\big[S_p(\hat{k}_i^p,\hat{\aleph}_s^p,)\big]\cdot[t_p(\vec{r}_{\mathrm{P}} - \vec{r}_{\mathrm{T}})]\end{aligned} \tag{2.5}$$

  where is the unitary vector $\hat{\aleph}_i$ or $\hat{\aleph}_s$ are defined by :

$$\aleph_{i,s} = \hat{k}_{i,s} - 2(\hat{k}_{i,s}\cdot\hat{z})\hat{z}$$

  as shown in figure 5.2, as well as the specular ground points G^T and G^R. Also used are the modified Fresnel coefficients $(\mathcal{R}_v, \mathcal{R}_h)$ since this mechanism involves the specular ground contribution for each path, that is either transmitter (T) $\rightarrow$ scatterer (P) $\rightarrow G^R \rightarrow$ receiver (R) or T $\rightarrow G^T \rightarrow$ P $\rightarrow$ R (cf. [Villard et al., 2007]). Their role is of the greatest importance for the resulting whole double bounce mechanism, as emphasized in the last chapter (e.g figure 5.41 and 5.42).

Furthermore, the coupling terms involving twice the specular ground points are herein neglected, though reported in many coherent models (i.a [Marliani et al., 2002]), we found this contribution significant only in the case of strong dihedral effect, which concerns thereby more urban areas than forest ones. On the other hand, a triple bounce mechanism is currently under investigation, since preliminary results have shown its possible manifest impact in specific bistatic configurations.

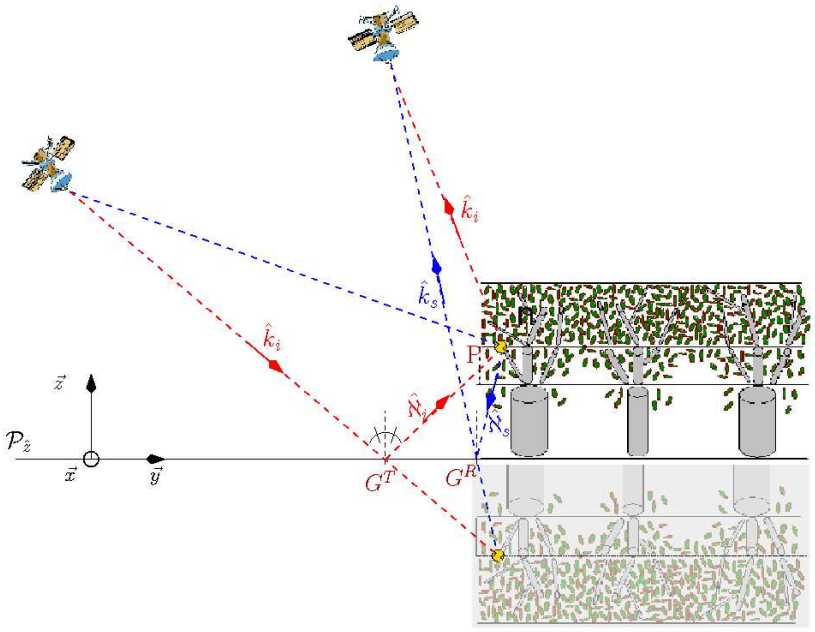

Figure 2.1: Bistatic specular ground terms with respect to the transmitter or to the receiver.

Besides, as far as multiple interaction is concerned, the case of dense media can be commented. For such cases, the afore-mentioned fundamental hypothesis of independence doesn't hold anymore and multiple interaction effects must be accounted for. By means of an appropriate pair distribution function (characterizing the correlation between particles), the Quasi Crystalline Approximation (**QCA**) is an analytical approach as well as the **EFA** but using second order terms within the Foldy-Lax multiple scattering equation (cf. [Tsang and Kong, 2000b]). This method, also derived with the **QCA-CP)** (with Coherent Potentiali) has demonstrated its great potential and enlarge the fractional volume range up to 30 % (cf. [Tsang et al., 2007; Guo et al., 2002]), coming thereby with successful applications, as for instance in snow scattering modeling (cf. [Chen et al., 2003]). For such cases, the fact that the extinction coefficients do not saturate (cf. chapter 4, section 4.2.1) Actually, collective scattering effects may be also encountered for temperate forests, typically in the case of dense pack of needles for which **EFA** can not be applied. Nevertheless, as presented in [Wang and Sarabandi, 2007], an alternative approach consists in considering each dense pack as a individual bulk scatterer with its own scattering matrix (which can be derived from numerical methods, FDTD for instance cf. section 2.2.2.

2.1.2 The Model Components : Standard & Improved Elements

In the previous subsection, the overall principle of the coherent model has been presented, assuming the knowledge of the bistatic scattering matrix for each element. In the framework of em scattering models for forests, ground scatterers are commonly simulated using rough dielectric surfaces whereas volume scatterers are simulated using basic geometrical shapes. Standard scattering models currently used in the literature will be presented in the two next paragraphs, respectively for ground and volume scatterers whereas improved shapes for the later will be put forward in § 2.1.2.

Standard Modeling of Ground Scattering

In many fields of applications and particularly for land remote sensing, em wave scattering from rough surfaces is an important issue and thus has been extensively covered in the literature. Typically in em theoretical problems, two approaches can be distinguished : on the one hand, numerical methods – such as the MoM (Methods of Moments) or the FDTD presented with the hybridization in § 2.2.2 – which aims at resolving Maxwell equations by a discretization of the problem and on the second hand analytical approximate models which cope with the drawback of the former, being mostly intractable for realistic three dimensional and dielectric surfaces regarding the computing time. Exhaustive reviews of the major numerical methods can be found for instance in [Saillard and Sentenac, 2001; Warnick and Chew, 2001].

Concerning analytical approximate models, two standard approaches paved the way to the subsequent improvements, namely the *Small Perturbation Method (SPM)* and the *Kirchhoff Approximation (KA)*. Whereas the former holds for slightly rough surfaces, the latter is on the contrary valid for surfaces with large curvature radii. The ground surface is mostly described statistically as the realization of a random Gaussian or exponential process, characterized by its root mean square height (standard deviation) noted h_{rms} and its correlation length (l_c), the length beyond which the surface autocorrelation function is divided by e^1). The rms slope can then be deduced and for a given h_{rms}, it follows typically an opposite trend to the correlation length.

When both h_{rms} and l_c are smaller than the wavelength, the SPM can be formulated from a perturbative Taylor-Volterra expansion of the scattering amplitude with respect to height. Using the Fourier transform of the height function, analytical calculations can be conducted until the second order, resulting in the so-called SPM1 and SPM2 versions. Therefore, as long as that small height condition is fulfilled, SPM uses a rigorous mathematical formulation and turns out to be a standard for any approximate model in the low $k \cdot h_{rms}$ domain.

Alternatively, in the framework of the Kirchhoff approximation, the field on the surface is taken as the one which would be produced by a tangent plane at the same point. As a result, it relies only on the Fresnel reflection coefficient at the local incident angle and does not consider the surface curvature or non local effects which comes with multiple scattering. Nonetheless, these simplifications of the field on the surface make possible the use of integral analytical expressions of the scattering field as in the Stratton-Chu formulas (cf. a.o [Stogryn, 1967]). Depending of the surface complexity, the calculation of such integral expressions requires further assumptions. Prominent among them is the *high frequency approximation (KA-HF)* which performs the integral thanks to the *Stationary Phase Theorem (SPT)* and leads to the famous *Physical Optics (PO)* method. Furthermore, when that high frequency approximation reduces the integral to the probability density function of the surface distribution at the specular points, the *Specular Point Theory* well-known as the *Geometrical Optics (GO)* limit is reached.

The validity domain of both SPM and KA approaches being mostly too restrictive in radar ground remote sensing, unifying methods turn out to be a wide research subject and has originated many methods, as reviewed for instance by [Elfouhaily and Guérin, 2004].

Among them, the *Integral Equation Method (IEM)* which has been implemented in MIPERS (cf. 2.2) is one of the most widely used analytical model, providing indeed good predictions not only in backward, forward scattering but also in the general bistatic case. Its range of validity includes $k \cdot h_{rms}$ and $k \cdot l_c$ until respectively about 1 and 6. The IEM is based on the iterative solution of the integral equations for the tangential components of the electric and magnetic fields, as formulated by Poggio and Miller. It then consists in a decomposition between the Kirchhoff field and a complementary term, accounting for non-local effects (multiplicative effects). The drawbacks of the method lies in the calculation of this integral formulation, which implies some simplifications such as the approximation for the cross polarization of the Fresnel coefficient by $(R_{//} - R_{\perp})/2$, the removal of the spatial dependence of the Fresnel coefficient (either along the backscattering or the specular direction) and also the approximation of the phase terms (unsigned) within the surface Green's function and within its gradient. Furthermore, is can be stressed that the two latter approximations has been corrected with the *Advanced Integral Equation Method (AIEM)* (cf. [Chen et al., 2003]), extended the range of validity to about 2.5 and 8 for $k \cdot h_{rms}$ and $k \cdot l_c$ respectively. Another improvement to account for edge-diffraction terms has been proposed by [Du, 2007] using the correction of shadowing effects. Though significant for the simulation of bare soils, our modeling of the underlying ground in the case of forest scattering, for instance without litter, makes the approximations used in the standard IEM version relavant.

Besides, the ground being modeled as a rough dielectric surface, the question of its permittivity is obviously risen, especially to account for soil moisture variation at a given frequency. The standard approach uses a semi-empirical model (cf. [Dobson et al., 1985; Hallikainen et al., 1985]), providing an analytical expression of the real and the imaginary part of the dielectric constant. This model is based on a mixing law (as for the vegetation further presented), considering indeed with four components : air, soil solid particles, free and bound water. Whereas the dielectric constant of free water is well accounted for by the Debye dispersion equation, the one for the bound water is not well understood. Indeed, the proportion of free and bound water within the total volume fraction is governed by the so-called *specific area* (m^2/g) which is closely dependent on the soil mixture. As a result, most of the models requires a particular care for their generalization to other type of soil than those for which it has been validated. In MIPERS (cf. 2.2), the version detailed in [Peplinski et al., 1995] has been implemented since it permits an extension of the afore-mentioned semi-empirical model from 0.3 to 1.3 GHz. As a further improvement, a more recent approach can be found in [Mironov et al., 2004] which proposes an alternative method to estimate the free and bound water dielectric constant.

Canonical Shapes for Volume Scatterers

The leaves, branches and trunks are typically simulated by canonical elements, such as ellipsoids or cylinders. Indeed, on the one hand these shapes are particularly well adapted to match of the natural scatterers mostly encountered in forest modeling. On the other hand, their scattering matrix can be derived analytically and has been extensively detailed in the literature, to which the reader is invited to refer :

Concerning the dielectric ellipsoids, the RCS calculations are performed using the generalized Rayleigh-Gans approximation (cf. [Karam and Fung, 1989]), which consider the internal field equals to the incident one, provided the twofold fact that at least one dimension of the ellipsoids is a small fraction of the wavelength (Rayleigh's approximation) and that the dielectic constant

(Gans's condition) is relatively close to the host medium one.

In the case of cylindric shapes, the calculations are conducted using the plane to cylindrical em wave series expansion, so that the approximation in the case of infinite cylinder relies only on the series truncation (cf. [Tsang and Kong, 2000a]). Though related to numerical inaccuracies within the hypergeometric series involved, a particular care in practice must be considered regarding the series convergence for small radius, as reported also in [Lin and Sarabandi, 1995]. For thin cylinders (i.e $r \ll h$), the cylinder edges can be neglected so that the currents matching the infinite case can be employed to perform the scattered field. For that purpose, two approaches can be followed, using whether the volume integral as in [Karam and Fung, 1988; Sarabandi and Nashashibi, 1996] or the surface one, detailed in [Tsang et al., 1992].

On top of the vegetation scatterers' shape, the dielectric constant takes on a great importance. Its value is derived commonly from a mixing law between the permittivities of the vegetation material, the free and the bound water as expressed below with their respective volume fraction (V_v, V_f, V_b) :

$$\varepsilon = V_v\varepsilon_v + V_f\varepsilon_f + V_b\varepsilon_b$$

Whereas the permittivity of the bulk vegetation material can be assumed non dispersive :

$$1.5 \leq \varepsilon' \leq 2.0, \quad 1.5 \leq \varepsilon'' \leq 0.1$$

the ones of free and bound water can be formulated respectively according to Debye and Cole-Cole relaxation terms, as very well detailed in [El-Rayes and Ulaby, 1987; Ulaby and El-Rayes, 1987]. Indeed, based on theoretical and phenomenological considerations, a particular emphasis of the bound water behaviour is given, being the most difficult component to assess on account of its dependence on the host medium and on its inability (by definition) to be isolated. To improve these models, more advanced mixing laws have been developed as reported in [Shrestha et al., 2007], especially with the PL (Power Law) Model, with the modified Debye Cole-Cole Model including a conductivity depending on the volume fraction of free saline water or with Bruggeman Models. Indeed, especially for low frequencies (below 300 MHz), the behaviour of the conductivity could be improved since most models overestimate the dielectric loss (imaginary part of the permittivity).

As already mentioned in the first chapter, the high sensitivity of microwave towards humidity can be understood in view of this mixture law, involving a relatively weak value of the vegetation material permittivity in comparison with the water one. Hence the noticeable permittivity spatial and temporal gradients, according to the water content changes for instance between heartwood and sapwood within trunks or between upper or bottom parts of the canopy (cf. [Franchois et al., 1998]), along with temporal effects regarding seasonal as well as diurnal cycles (cf. [Gates, 1991]).

Improved Shapes with Curvature Effects

Commonly in forest scattering models, branches are represented by straight homogeneous cylinders. According to the category of tree, this assumption may be reasonable or unduly exaggerated according to the way branches are curved. In the last case, exists the solution of cutting a long, curved branch into smaller straight ones, but the electromagnetic computation may be affected by this way of representation. The present section treats these points, first numerically, and later proposing a new analytical solution to account for these curvature effects.

Numerical simulations: In this part are considered typical branches ; radius 2 cm, length 1.41 m, moisture content 50 %. The straight one, which is the chord of the curved ones, binds

the origin M1(x1=1,y1=0,z1=0) to the extremity M2(x2=0,y2=1,z2=0) : it is in the plane xOy, perpendicular to the line (D) y=x. Later, this branch is curved in shape of a circle arc with keeping the same extremities and moving the centre of curvature on (D) with x<0 thereby attributing to this circle arc a variable radius of curvature R and a variable curvature C=1/R. The scattering diagram of such a branch with varying curvature C at P band is plotted on figure 2.2 with incident plane wave orthogonal to the chord. Incident wavevector is on the xOy plane ($\theta_i = 90^o, \varphi_i = 45^o$) so that incident plane wave hits concavity of the curved branch. The diagram is plotted in the incidence plane perpendicular to the chord as a function of tetas ($\theta_s = 90^o$ represents the backscattering) for $\varphi_s = \varphi_i + \pi$ in HH polarization which is the most sensitive one due to the configuration and the geometry. When C tends to 0, the branch tends to be straight and diagram is nearly uniform with θ_s. It can be seen that with increasing curvature, diagram also bends with a stronger decrease in the backscattering direction than in the other ones. Down to approximately C=0.2 change remains less than 0.5 dB, however beyond this value it increases abruptly. This result is quite normal : until curvature induces an 'aperture ' phase variation smaller than 90 degrees change in scattering is weak, but becomes important for higher values. This interpretation may be corroborated by examination of which shows the variation of phase along the typical branch we are dealing with in this part. It can be seen here that accounting correctly for curvature is fundamental for P band scattering of forest since backscattering volume is directly impacted. In the convex side (b) this change is more abrupt.

Forward scattering is poorly impacted by curvature : only C=1 yield a significant effect, both in concave and convex sides, and this effect remains in the order of 0.5 dB – see case (c). At last, cross polarization remains extremely weak in the backscattering direction and over all the diagram insignificant with respect to the co-polarization : even for curved branches, cross polarization is thus generated by geometrical considerations like for straight branches. The consequences are the following :

- classical computation of forward scattering should be performed with the chord of a curved branch, with some weighting for very high curvatures.
- cross-polarization for curved branches should be computed as usual
- backscattering computation (and specular scattering one) introduce the need of an 'effective length' to represent the curved branches. If the phase variation along the curved branch is less than 90^o, then the real length is the effective one. However, in the opposite case, it is the corresponding chord : it means that long, curved branches should be cut in effective ones depending on the frequency of work, with the corresponding probabilities of orientation : in this case, the description of the canopy should be matched to the frequency.

However, in MIPERS, a new category of scatterers 'curved cylinders' is introduced and computed with the original technique proposed in next subsection.

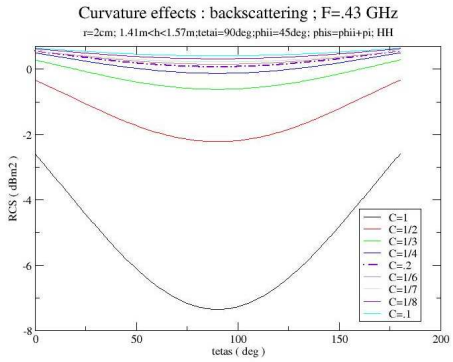

(a) $\varphi_i = 45^o$

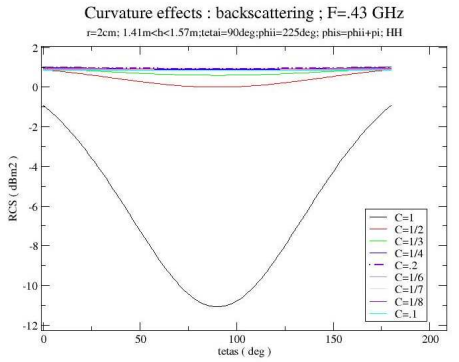

(b) $\varphi_i = 225^o$, (convex curved branch)

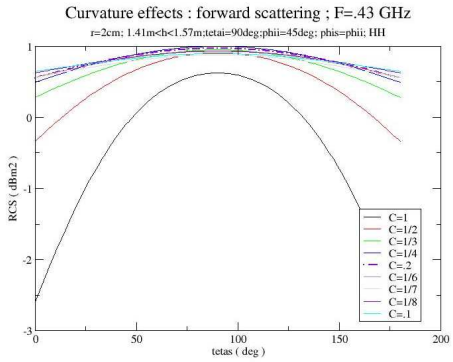

(c) forward scattering plane

Figure 2.2: Scattering diagram of a branch with varying curvature C at P band; incident plane wave is orthogonal to the chord; curved branch and incident wave vector are on the xOy plane ($\theta_i = 90^o, \varphi_i = 45^o$) so that incident plane wave hits concavity; diagram is plotted in the incidence plane perpendicular to the chord as a function of θ_s ($\theta_s = 90^o$ represents the backscattering) for $\varphi_s = \varphi_i + \pi$; only HH polarization is figured.

Analytical approach : In this section is proposed an approach to treat analytically the curved branches and which is new to our best knowledge: this approach is first presented and further validated with comparisons with FDTD. The idea underlying this approach is the following : since analytical computation of finite length cylinders rests on physical optics integration of currents or fields starting from infinite cylinder approximation, then subdividing it in short cylinders and coherently summing the complex scattered fields do not change the total scattered field. This statement has been verified by subdividing a typical straight branch in shorter ones do not change the scattered field. Then, when the real geometry gently departs from the straight one, this subdivision should remain a fair approximation of it and this concept is applied here. In the follow-up, this method of subdivision and coherent summation will be referred to as CSA (coherent summation approximation).

It is expected that CSA gives accurate results as long as curvature remain reasonable, and to see how long this approximation holds a reference solution for curved cylinders is computed with FDTD, but it is to keep in mind the discrepancy will incorporate both curvature effects and end effects. At P band, end effects are important since typical branches are in the order of a few wavelength : one can consider that when the whole error is in the order of the error between CSA and FDTD for straight branch then CSA accounts accurately for the curvature effect. It can be seen on figure 2.3 that beyond R=3 it is the case.

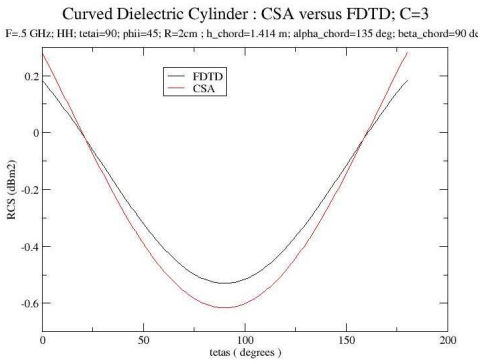

Figure 2.3: Geometry of figure 2.2 (a); comparison of FDTD and CSA for R=3.

It can be checked on figure 2.3 (a) the overall agreement between methods is rather good at P band : relatively significant differences at large curvatures correspond to relatively small echos. Figure 2.4 (b) shows that this agreement is even better at L band, certainly since end effects are much less on such typical branch and interact les with curvature effects.

Conclusion The 'brick' improvements shown in this section have been integrated in MIPERS. However, they come with more complex ground truth datasets which did not appear to be prominent in the theoretical studies which are to be carried on in the following chapters. Then, the choice of representing the curved branches by realistic effective length ones has been done, as well as representing the real multilayer branches and trunks by effective homogeneous ones. Actually these bricks will become more necessary when the ground truth will be known more deeply than in the forests and campaigns we had to treat.

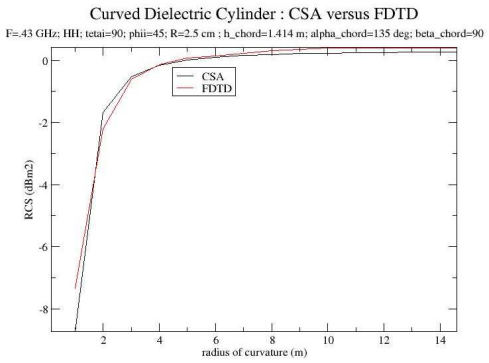

(a) P-band

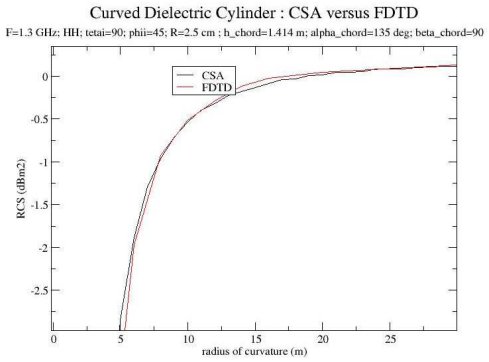

(b) L-band

Figure 2.4: Comparison of backscattering coefficient between FDTD and CSA as a function of radius of curvature in the P and L-band cases

2.2 MIPERS Features

MIPERS – Multistatic Interferometric and Polarimetric model for Remote Sensing – is based on a discrete description of the medium, using the various shapes afore-detailed (see subsection 2.1.2) as brick elements. The em scattering of such medium is calculated according to the DBWA theory, resulting in the Foldy' approximation for the propagation phenomenon, as presented before in subsection 2.1.1. It can be also stressed that our modeling is coherent which makes interferometric simulations possible in the sense that the propagation phase is conserved – as opposed to incoherent models based on the radiative transfer (see e.g [Ulaby et al., 1986, 1990; Ferrazzoli and Guerriero, 1996; Liang et al., 2005]).

Among the other coherent models presented in the literature, our modeling approach can be compared to those used in [Marliani et al., 2002; Williams and Harris, 2003; Thirion et al., 2006]). Apart from the improved shapes detailed in subsection 2.1.2, the originality of MIPERS lies in various modes of scene generation, described in the next subsection and making possible an easy hybridization with ancillary data as it will be presented in 2.2.2.

2.2.1 A Versatile Scene Generation

The Original Layer Description

The original medium description (commonly used in the first coherent models) lies on the concept of infinite and superimposed layers. Geometrically, these layers are defined by a bottom and top infinite horizontal planes. This description suits a twofold objective : on the one hand it enables a discrete generation of the scattering elements according to their vertical position and on the second hand it makes possible a continuous description for the attenuation factor calculation. Indeed, considering a homogeneous forest, the main axis of variation regarding the kind of scattering elements is vertical so that a layered medium is particularly well adapted. Based on in-situ measurements, these scatterers are merged according to various types (e.g classes of trunks, branches) depending on their specific shape, concentration (fractional volume) and statistical geometrical parameters for their size and their 3D orientation. A layer is thus also defined by its composition with these various types. Given that composition with the matching statistical distributions, formula (2.2) can then be applied. The resulting extinction coefficients can then be used together with the associated travelling distance within each layer in order to get the attenuation factor, formalized as follows with the transmissivity matrix :

$$[t(\vec{r})] = \begin{bmatrix} \prod_l e^{-\sigma_v^l(\hat{k})d_l/2} & 0 \\ 0 & \prod_l e^{-\sigma_h^l(\hat{k})d_l/2} \end{bmatrix} \tag{2.6}$$

where the product covers the various layers (index l) with $\theta = (\widehat{-\hat{z}, \vec{r}})$, N as the layer number and d_l, $\sigma_q^l(\theta)$ the respective running distance and extinction coefficient for the direction $\hat{k}$ through the layer l in the polarization q (vertical or horizontal). To compute efficiently this product, the ray tracing proces requires a dynamic association between a given scatterer and the matching number of crossed layers and is performed using a linked list.

To determine the most appropriated number of layers, the resulting extinction coefficient from formula (2.2) has to be accounted for since trade-off must be found to avoid important discontinuities between the various layers (which would create a refractive index) but keeping a sufficient discretization to make the integral average relevant and representative of the layer specificity. In forest scattering modeling, this number is typically between two and four. Concerning the statistical distributions for the geometrical sizes, Gaussian pdf characterized by their average and their standard deviation are mostly considered, as well as for their radio-electric properties. Regarding the 3D orientation of the scattering elements, more specific laws are needed using the three Euler angles ψ_{az}, ψ_{ins} and ψ_{int}, defined with the following sequel of rotations :

$$[\hat{z}, \psi_{az}],\ [\hat{y}', \psi_{ins}],\ [\hat{x}'', \psi_{int}]$$

where superscript $'$ denotes the axis resulting from one rotation transform, as displayed in figure 3.2 (chapter 3).

As far as symmetry of revolution objects (SRO) are concerned (e.g with cylinders and ellipsoids) the last attitude angle – called the intrinsic angle ψ_{int}) – can be left aside since it doesn't add more freedom degree. Concerning the azimuthal angle ψ_{az}, its distribution is assumed uniform since natural elements exhibit mostly an azimuthal symmetry (i.e invariance through a arbitrary rotation around the vertical $\hat{z}$ axis. Last but not least is attitude angle ψ_{ins} called the branch insertion angle within our forest modeling framework. A specific focus on this angle can be given since it characterizes the scatterer orientation and their impact on the resulting radar observables. Considering a spherical space, its distribution is typically uniform that is with an

equal probability to find the element into the elementary surface dS throughout the possible loci S, delineated by a specific angular sector $[\psi_{min}, \psi_{max}]$. In a Cartesian representation, such pdf takes the following form :

$$\begin{aligned} p(\psi_{ins}) &= \frac{dS}{S} \\ &= \frac{\sin\psi_{ins}}{\int_{\psi_{min}}^{\psi_{max}} \sin\psi d\psi} \\ &= \frac{\sin\psi_{ins}}{\cos\psi_{ins}^{\min} - \cos\psi_{ins}^{\min}} \ , \ \psi_{ins} \in \left[\psi_{ins}^{\min}, \psi_{ins}^{\max}\right] \end{aligned} \tag{2.7}$$

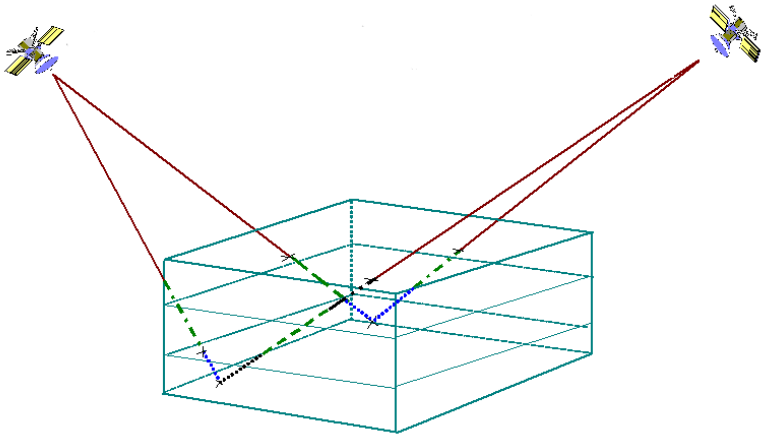

Figure 2.5: Travelling wave pathes through the various layers which, together with the matching extinction coefficients give the resulting attenuation on a given scatterer. Also emphasized are the side effects on the attenuation in this case of a finite region.

Improved Generation Modes & Generalized Layer Concept

Using the original infinite layers description, only vertical heterogeneities can be simulated. Nonetheless, in order to model side effects, finite regions can be considered, using the same layered description but not infinite anymore, as shown in figure 2.5. This capability has been used in order to simulate the effects of forest clearings, as detailed in the subsection 2.3.1. This concept of finite layer comes also with the introduction of a local geometry characterized by the following intrinsic parameters : $(0_i, \alpha_i, w_i, l_i)$ standing respectively for the origin, the tilted angle, the width and the length of the region, as shown in figure 2.6. In MIPERS, all the scattering elements are generated in the local geometry of the region, their coordinates in the global coordinate system is further deduced using a similitude transformation of translation $\overrightarrow{OO_i}$ and rotation α_i. These coordinates can then be used for the imaging process, according to these global coordinates or the range towards the transmitter and the receiver (cf. subsection 2.2.3), also localized in the

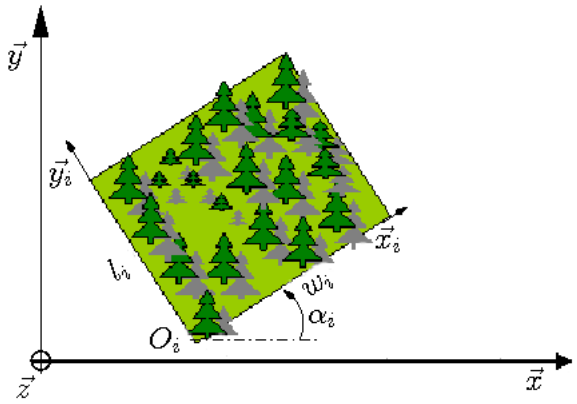

Figure 2.6: Geometrical parameters $(0_i, \alpha_i, w_i, l_i)$ defining the local geometry of a region of interest.

main coordinate system. Apart from the simulation of side effects, this concept of finite layer can be also used to generate several regions, which enables to model much more complex scene. A case of importance is the simulation of sparse forests (see figure 2.8) for which this multi-regions approach can model more accurately the horizontal heterogeneities, especially for that concerns the clearings which really impact the wave attenuation.

Til this point, the same layer concept – whether finite or infinite – has been used for both the scene generation and the calculation of extinction coefficients. Another improvement developed in MIPERS is the capability of individual trees according to the specific architecture of a given specie. The main difference in comparison with the layer description lies in the fact that the various sections of the trunks and the branches are pieced together (see figure 2.7). Nonetheless, the discrete elements forming such tree models are still merged into layers, according to the same considerations detailed previously (cf. the trade-off between a sufficient number of layers and the refractive index constrain). In addition, between these two capabilities to model the forest medium is a mixed approach, using a 2 part tree models made of a trunk plus a crown. The trunk is formed by a sequel of decreasing radius cylinder and the crown by a conical or an ellipsoid volume, as shown in figure 2.9. For that mode, the layers are delineated in each crown by horizontal planes. Such capability has been developed to match the case of dense tropical forest, characterized by their larger spatial variability due to a number of species much more important than in the case of temperate or boreal forests (for instance, the presence of emergent trees would be difficult to simulate accurately without this two-part tree model). Furthermore, another advantage of the two last generation modes is the simulation of an underlying topography, which in the case of a layer description is on the one hand more complex since it requires a sequel of coordinate system change (since each scatterer within a layer is generated in the local flat geometry) and on the second hand less realistic in the case of varying slopes (since the top surface of the layers follows the underlying topography).

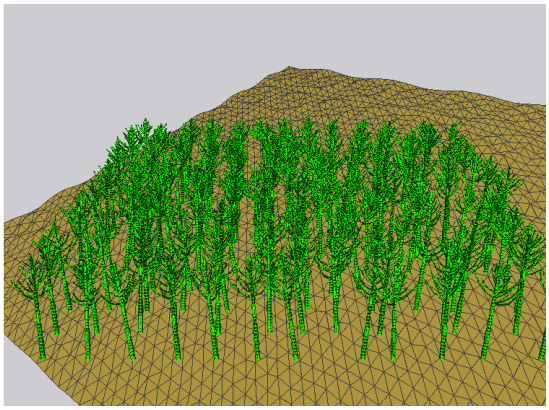

Figure 2.7: Scene generation according to the 'growth model' mode.

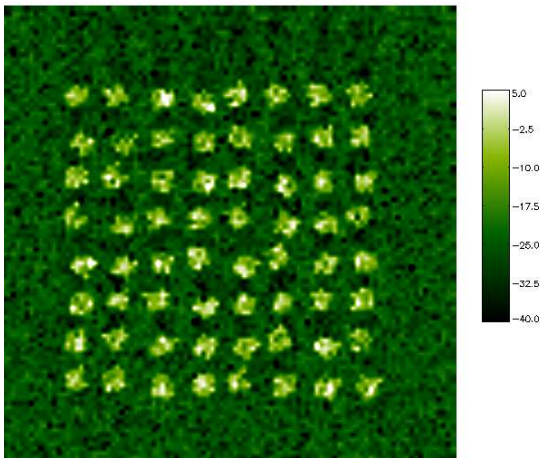

Figure 2.8: Simulation of a sparse forest using the multi-region concept. Each tree is indeed encompassed within a superimposed sequel of parallelepiped layers. Specular and direct ground are thereby less attenuated than in the infinite layer case.

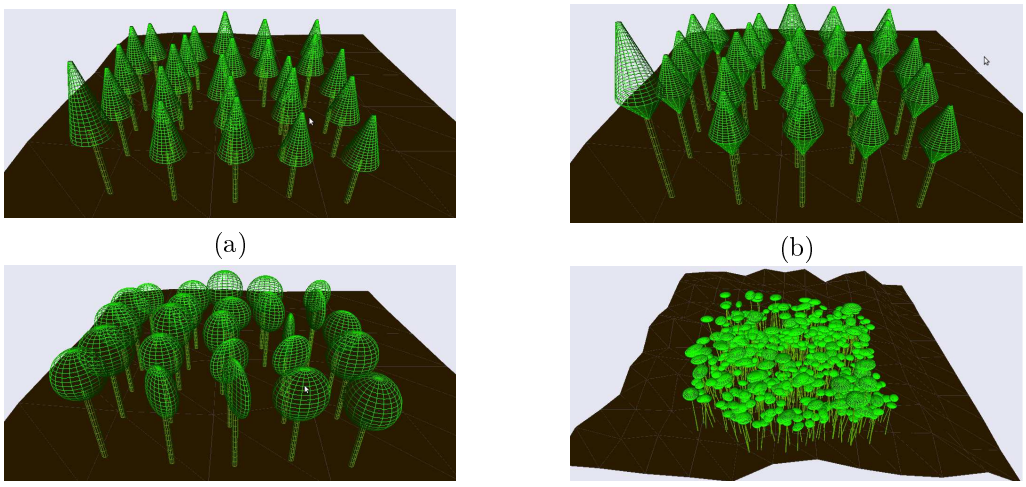

(a) (b) (c) (d)

Figure 2.9: Illustration of various type of two-part tree models, using conic or spherical crowns respectively in (a), (b) or (c). In (d), the case of a tropical forest is simulated using ellipsoid crowns.

2.2.2 Hybridization with Numerical Methods

To simulate the em wave scattering of more complex structures than those encountered with the natural scatterers – approximated by basic geometrical shapes – a single order hybridization has been developed using the Finite-Difference Time Domain (FDTD). As proposed by Yee (cf. [Yee, 1966]), FDTD performs an iterative algorithm to solve Maxwell's equations, using a join spatial and temporal discretization of both electric and magnetic fields. Typically during such algorithms, stability (to ensure the finite nature of the fields) as well as numerical dispersion are two fundamental criteria to be controlled. In addition, since the numerical resolution of such problems requires a finite space, boundary conditions must be introduced to simulate an infinite space in order to cope with open problems. This issue is the main challenge of the FDTD and many theoretical studies are still going on. Among the standard approaches, the one relying only on the inbound fields proposed by [Mur, 1981] can be distinguished by the mathematically more efficient method introduced by Berenger (cf. [Berenger, 1994, 1996; Fang and Wu, 1999]) and using well known *Perfectly Matched Layers (PML)*.

The example of a truck shown in figure 2.10 has been chosen, since experimental validations (ONERA's bistatic measurement facility) have been jointly conducted.

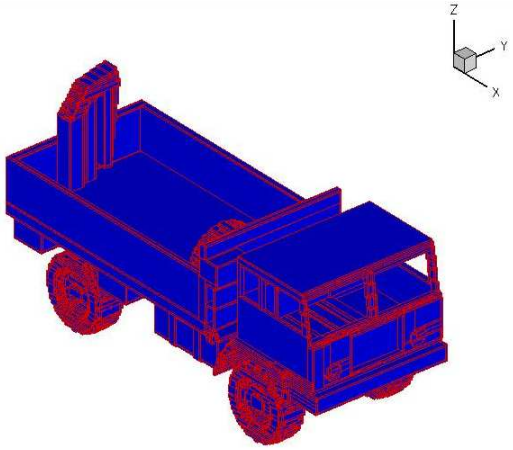

Figure 2.10: Chosen target which scattering data – that is the scattering matrix for all the incident and scattered directions (i.e $[S](\theta_i, \theta_s)$) – has been performed with the FDTD method.

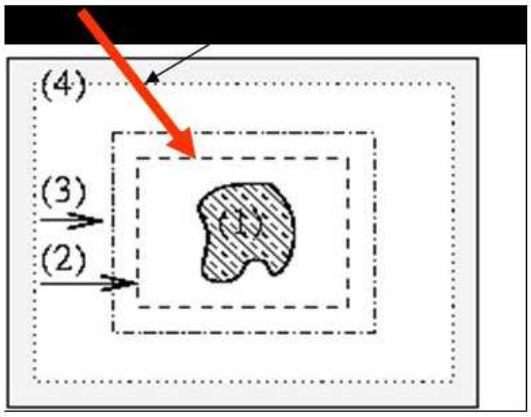

Figure 2.11: Processing volume made with : (1) target volume, (2) injection surface, (3) scattering surface and (4) PML layers.

2.2.3 Simulations of SAR Images : Bistatic Constraints

Range and Doppler Gated Process and Image Generation

All the scattered signals (whatever the interaction order) are recorded according to their running distance (cf. [Villard et al., 2007]) and then discriminated along the SAR "long-time" direction thanks to their own Doppler (what we call range/Doppler gated process). The interest of the following method lies in several points : First, severe image distortion (especially non linear ones which are spatially dependent) are liable to occur, that's why for radiometric purpose the pixel area involved in the bistatic scattering coefficient (σ_0) must be known for each position. Assuming ergodicity property, the effect of different volume resolution cell corresponding to one pixel (voxel) can be neglected excepted near border zone where we retrieve the time dependency (layover) between the different mechanisms (which is all the more relevant in bistatic as for example double bounce will be not anymore projected on the ground). In addition, for interferometric applications, in order to reproduce as faithfully as possible the phase sensibility, the voxel curvature is also essential as related to the ambiguity height. Then, once one scatterer is generated, its contribution is recorded according to the time and Doppler frequency associated to its position (cf. respective definition of these sets). In this way, as long as the configuration keeps stationary (i.e when iso-range and Doppler associated to each acquisition during the "long time" can be assumed parallel) resolution distortion as well as layover effects can be reproduced. From this process, a grid of iso-range/Doppler can be built. This array can then be used to defined pixels which vertices are established by intersection between range loci at R and R+δR and Doppler one at f_d, $f_d + \delta f_d$. To do so, a quasi-Newton method can be used to minimized the function :

$$\|rng_{R0}(x, y, 0) - (2.c_a)\|^2 + \|f_D(x, y, 0) - c_D\|^2 \tag{2.8}$$

where c_a and c_d refer respectively to the current range and Doppler on one point of the scene, the subscript "$_{R0}$" refers to the main coordinate system as both range and Doppler loci should naturally be expressed with respect to the same coordinates system. This implies the coordinates transformation for the range loci, from R_0 to R_I obtained after two Euler rotations around $\overrightarrow{z}$ and $\overrightarrow{y'}$ (superscript points out the resulting axis after one transformation) with respective angle $\langle \overrightarrow{x}, \overrightarrow{\overrightarrow{ER} - \overrightarrow{ER} \cdot \overrightarrow{z}} \rangle$ and $\langle \overrightarrow{\overrightarrow{ER}, \overrightarrow{x'}} \rangle$ followed by the translation along $\overrightarrow{OI}$ towards the new origin I. Then, provided the fact that there is a domain (which should match to the region of interest) without range or Doppler ambiguities (i.e isomorphism from the range/Doppler space U onto V, the scene coordinates space) each couple (n,p) will be associated to a unique (x,y).

$$(n, p) \overset{U \subset \mathbb{R}^2 \to V \subset \mathbb{R}^2}{\longmapsto} (x, y) = RD(n, p)$$

Our image can then be defined for each pixel (x,y) as follows :

$$f(x, y) = RD[g^{-1}(x, y)] \tag{2.9}$$

Iso-range and Doppler curves are established by the following :

- The set made of points situated in the same range gate is defined by :
  $\{M \subset \mathbb{R}^3 / ME + MR = 2 \cdot a\}$ which can be also expressed in the coordinate system R_I :
  $\{M \subset \mathbb{R}^3 / MF = \frac{c}{a} \cdot MH\}$, with H the projected point on the directrix (D) : $x'' = a^2/c$ defining an ellipsoid of exentricity $e = \frac{c}{a}$ with Emitter and receiver as foci and demi axes : a and $\sqrt{a^2 - c^2}$. With P standing for the 2 rotations transform (use of quaternion can

reduce 3 consecutive rotations into one 3*3 real matrix) ($\overrightarrow{OM} = P \cdot \overrightarrow{OM'}$), this set becomes in the main coordinate system :

$$\begin{aligned} &\{M(x,y,z) \subset \mathbb{R}^3 / \\ &\frac{[(P^{-1} \cdot \overrightarrow{OM'})_x]^2}{a^2} + \frac{[(P^{-1} \cdot \overrightarrow{OM'})_y]^2}{b^2} + \\ &\frac{[(P^{-1} \cdot \overrightarrow{OM'})_z]^2}{b^2} = 1 \text{ with } \overrightarrow{OM'} = \overrightarrow{OM} - \overrightarrow{0I}\} \end{aligned} \tag{2.10}$$

(deduced by R_0 from 2 rotations origin in I middle of [ER])

- The Doppler shift result from the combined effect of the emitter and receiver velocities and within the non relativist approximation, we obtained for a monochromatic signal of wavelength λ emitted by E and receiving by R after reflection on the target C :

$$f_D = \frac{1}{\lambda} \cdot [\overrightarrow{v_E} \cdot \frac{\overrightarrow{EC}}{\|\overrightarrow{EC}\|} + \overrightarrow{v_R} \cdot \frac{\overrightarrow{RC}}{\|\overrightarrow{RC}\|}] \tag{2.11}$$

Making this equation explicit with respect to Cartesian coordinates, we come up with higher order curves than the monostatic iso-Doppler hyperboloid. For this latter case in the classical strip map mode and in the far range approximation, we retrieve the linear Doppler variation with respect to the acquisition time (t_{acq}):

$$f_D = 2 \cdot \frac{1}{\lambda} \cdot \frac{v_{Ex} \cdot x}{r_0} = 2 \cdot \frac{1}{\lambda} \cdot \frac{v_{Ex}^2 \cdot t_{acq}}{r_0} \tag{2.12}$$

From the analytical point of view, range and Doppler resolution can be found from differentiation of (3) and (4) (cf. [Krieger and Moreira, 2006]):

$$df = \overrightarrow{grad} f(x,y,z) \cdot \overrightarrow{dM} \tag{2.13}$$

which shows that the gradient is orthogonal to our iso-range/Doppler ($df = 0 \rightarrow \overrightarrow{grad} f \perp \overrightarrow{dM}$), therefore an infinitesimal displacement (i.e the projected resolution onto ground) in the gradient direction leads to : $\|dM_{ground}\| = \frac{df}{\|\overrightarrow{grad} f(x,y,h)\|}$ where df is by the radar capacity to discriminate those variations (directly linked for range or Doppler to their respective chirp bandwidth). As an example, with an emitter and receiver respectively located at $[50, -5.10^3, 5.10^3]$ and $[10^3, 50, 10^3]$ as displayed in fig. 2.12. Image figure 2.13 is obtained the gated process. Then applying the transformation to match with iso-range/Doppler (displayed in fig. 2.14) we come up with fig. 2.15.

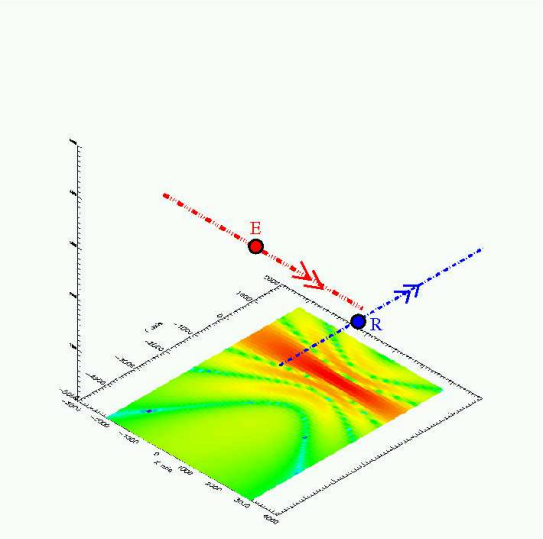

Figure 2.12: Combined footprint resulting from the emitter E and receiver R antenna pattern, flying respectively along the red and the blue lines.

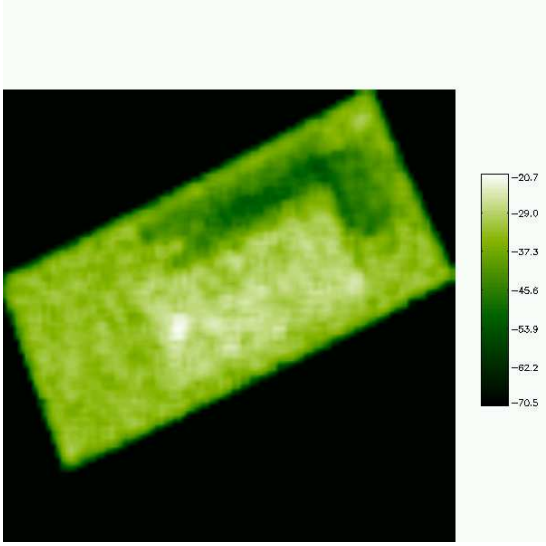

Figure 2.13: Example of range and Doppler gated image in VV polarisation with associated scattering level σ_0 in dBm^2/m^2.

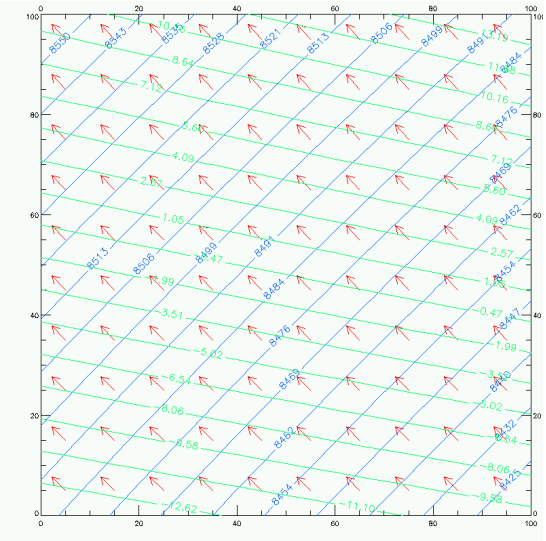

Figure 2.14: Iso-Doppler lines (green), iso-range ones (blue) and gradients (red arrows).

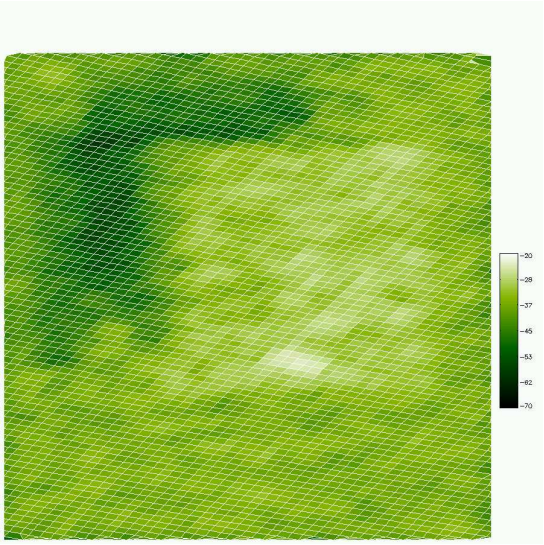

Figure 2.15: Image resulting from the transformation from the range and Doppler space towards the reference coordinates one. The iso-range and Doppler are represented with the white lines superimposed on the image. The plot is delineated by the red polygon.

2.3 Model Exploitation & Confrontations with Experimental Data

2.3.1 Effects of Forest Clearings on SAR Images

Sparse Forests : a Case of Importance

To predict and analyse such potential, electromagnetic modeling is of great interest, (for instance to evaluate retrieval algorithms (quantitative inversion or based on classification indicators). Em models (among others [Lin and Sarabandi, 1999; Pottier et al., 2005; Lucas et al., 2006; Roo et al., 2002]) have proven their ability to account for most SAR observables, at least at the phenomenological level, concerning forests of relatively large areas as long as ground truth is well documented. Most of them assume forest of infinite extent, that is without taking into account possible border effects caused by forest clearings. Nevertheless, the effect of sparse forests are often manifest in SAR images, especially with the nowadays trend for high resolution systems. For instance, one can refer to the Indrex campaign, carried out in 1996 over the Indonesian region of Kalimantan :

(a)

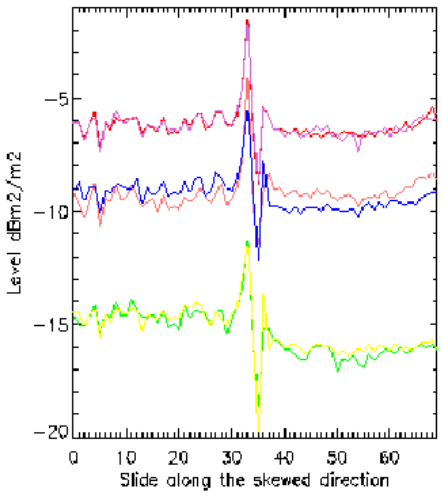

(b)

Figure 2.16: Indrex experimental results

The effects on radar intensities in both monostatic and bistatic configurations have been presented in previous studies (see [Villard and Borderies, 2007],[Villard et al., 2007]). Whereas the shadowing zones sensitivity towards geometry and attenuation is quite straightforward even in bistatic, the reinforcement ones deserve a particular attention especially with layover effects. What is more, even though double bounce is not the major contribution in the 'quiet' region (far from the edges), it turns out in the monostatic case to be mainly responsible for the border reinforcement. In the next subsection (cf. 2.3.1), we will go back over this point with additional theoretical elements followed by a comparison with experimental airborne SAR data where such phenomenon are manifest. Other studies report the importance of edge effects, especially those based on classification process (cf. [of full polarimetric SAR-data using artificialneural networks

Table 2.1: Winter (without leaves) and summer ground truth parameters

	elements	length♣	diameter	density	angles♢	wc♠
Top $(3m)^\sharp$	Leaves	7.5e-3	4.76e-3	×/1230	0,90	×/54
	Twigs	7.5e-3	4e-3	27.2	0-90	46
Middle (5.5)	Twigs	7.5e-3	4e-3	27.2	0-90	46 / 46
	Sec. Branches	2.5	1.5e-2	0.2	0-90	46/46
	Pr. Branches	2.5	1.5e-2	0.3	0-90	46/46
	Trunks	5.5	3.8e-2	0.05	0-90	46|46
Bottom (6)	Trunks	6	8e-2	0.05	0-20	46 / 46

(♣) Dimensions are given in meters
(♯) Layer height
(♢) Angles in degrees
(♠) Water content in percents

and fuzzy algorithms, 1999]) when dealing with fragmented regions due to urbanisation or deforestation (cf. [Demaze et al., 2001; Zakharov et al., 2003]), Indeed, within Land Cover and Land Use -LCLU- applications, one may be interested in delineating as faithfully as different regions giving much importance to borders ([Benz and Pottier, 2001]). Besides, biologically wise, these edge effects referred as ecotones are under many investigations especially about flora properties and competition between species (cf. [Didham and Lawton, 1999]). In addition to the impact on polarimetry -mostly used by the cited classification approach- interferometric observables are also subject to strong variations near the border zones resulting in bias for the corresponding height retrieval (cf. [Woodhouse et al., 2006]). Thus, even for Pol-InSAR acquisition and the derived detection algorithms (e.g [Cloude et al., 2004]), the contrast between the target and the surrounding media is liable to strong variations. This is all the more consistent that both target contrast and edge effects are emphasized with high resolution. Consequently, the transposition of this issue to the bistatic configuration may deserve interest, especially as far as the different scattering mechanisms radiometry is concerned.

Case of the Fontainebleau Forest

As a example of simulations to analyse the border effects, the case of the Fontainebleau forest is chosen, since ERS data are also available. The ground truth is given in the following tables :

As previously stated, figure 2.6 gives the basic geometry under study : a right parallelepiped rectangular forest volume rests on a rectangular flat area of larger extent which is the total imaged zone. The forest area is horizontally skewed of an arbitrary angle α and radar coordinates are given with respect to the drawn axis on the figure. It is decided here to perform this study with a forest which ground truth description has been well documented over large periods of time, and for this purpose the multi temporal data issued from [Proisy, 1999] over Fontainebleau forest are considered. By way of an example, a typical image obtained is reported on figure 2.17 which corresponds to a surface of 40*40 meters square forest zone over an imaged zone of 100*100 meters in summer and in VV polarization.

For each pixel, after an 9*9 average filter in order to avoid speckle effect in the presented images, the backscattering coefficient (σ_0) is displayed. The ground resolution is of one meter, the same as the azimuth one. This longitudinal resolution corresponds to the interception of the

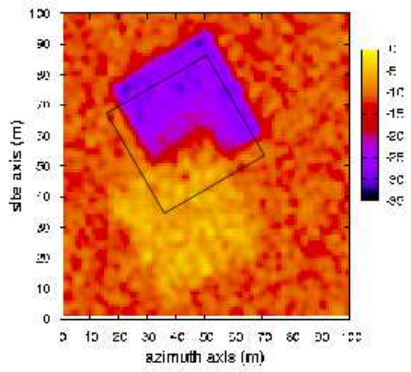

Figure 2.17: Intensity at C-band (in dBm^2/m^2), VV polarization at 23^o incidence, Winter season

flat ground by the range gate. In the following, this longitudinal resolution will be maintained constant, whatever the angle of incidence, which will imply a implicit change of the radar impulsion duration. Moreover, it will ensure to consider the same voxel volume for every different geometry configurations, which is required to make unbiased comparisons. The origin of the forest zone is at coordinates (35,35,0), $\alpha = 30^o$ and the radar at $(50, -330.10^3, 785.10^3)$, which corresponds to an incident angle of 23 degrees. The reinforcements and shadowing effects are present as expected, just like the migration effect for any element above the ground (the plotted square represents the real contour of the parcel) If we plot the same in HV polarization (cf. figure. 2.17), we can check that the contour of the forest image is much more similar to the contour of the forest zone (apart from the migration effect) : this can be interpreted as due to the fact that while co-polarized backscattering involve all the scattering mechanisms, cross-polarized backscattering one is mainly sensitive to volume scattering and thus reproduces more faithfully the volume projection.

Moreover, it seems that several superimposed layers may be distinguished. It is due to the height localization of strong and weak scattering mechanisms which overlap and emphasize the layover effect. By the way, it is all the more clear for simulations in P-band for which when penetration is higher. Indeed, an additional layer, fitting perfectly to the real contour, can be observed which probably tallies with the double bounce. This layer effect will be revisited in the subsequent analysis. So, these border effects are dependent on many parameters which range from the forest descriptive parameters, some of them subject to temporal variation, the size and orientation of the forest zone and of course the radar configuration ones. The model proposed here permits simulating the influence of all these parameters on the polarimetric and interferometric observables and to stick to any given real scenario.

Introduction to 2D plot : To restrict the number of parameters in the analysis, we will maintain in the sequel the same inner forest description as in the previous section and first extend the area sizes to 50*160 m^2. To make easier the display of the results and their analysis, it will also chosen to deal with $\alpha = 0^o$ degrees, which enables a 2D representation. The analysis will be restricted to the intensity and the radar parameters will be ERS ones (i.e. C Band, 23^o of incidence and location $(50, -330.10^3, 785.10^3)$) except the resolution. Such an image is

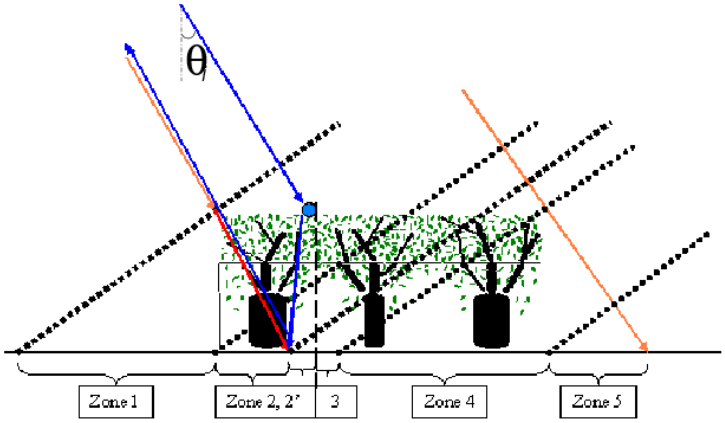

Figure 2.18: Gated Process

plotted in figure 2.17 while the corresponding 2D plot, The corresponding 2D plot is shown in figure 2.19, as a function of y (site axis) and enables to emphasize all partial contributions. For every contribution, the average over all the pixels (belonging to the forest parcel) in the azimuth direction have been performed. To analyze these different contributions, let us refer to figure 2.18 which decomposes the total zone of forest interaction with the incident wave into several zones corresponding to changes in the composition of the backscattered signal, (with the assumption of order one scattering) with respectively direct soil, volume and double bounce contributions associated with all layers inside the forest zone. It is to note that, due to range effects, for any given scatterer, its contribution to direct volume scattering is advanced with respect to its position along Oy, whereas its contribution to double bounce scattering is exactly on the projection of the phase center of this scatterer on Oy. In other words, in a range cell i, there is the contribution of the corresponding direct soil [yi, yi+dy], the double bounce of the scatterers which are located in the volume [yi, yi+dy] and the direct volume scattering of the scatterers which are located in the range interval [r(yi), r(yi+dy)]. This translation effect becomes important when considering borders with high range resolution. At the beginning (zone 1) backscattered signal is made of the contribution of the soil exterior to the forest parcel summed with direct volume scattering with successive layers, characterized by growing average attenuation and growing intercepted volume as abscissa increases, which are phenomena of opposite effect which tend to cancel each other. This zone terminates at the front edge of the forest parcel. At that line, outer soil is substituted with inner one and double bounce is initiated, higher scatterers interacting with the outer soil tending to decrease and lower scatterers with the inner soil tending to increase. This line initiates the zone (2) where the volume participating in the direct volume scattering begins to be constant in each range cell, the attenuations for double bounce and direct soil are growing. Zone (2) is an enhanced one when comparing with infinite forests. In the following zone (2'), range cells contain constant volume inside each layer and all mechanisms except the double bounce suffer from the same linear attenuation. Indeed, the double bounce still benefit from less attenuation than in the infinite forest. Then in zone (3) everything behaves as in horizontally infinite forests, we can define a kind of 'quiet zone' in the parcel.

By the way, ERS measured levels can be retrieved on the total field (cf. [Ruiz and Borderies, 2005]). Next, in zone 4, a process reverse to the process of zone 1 takes place : direct inner soil is constant, direct volume is progressively decreased due to the fact that the number of scatterers involved decreases whereas the linear attenuation is constant : this is a shadow region. At last,

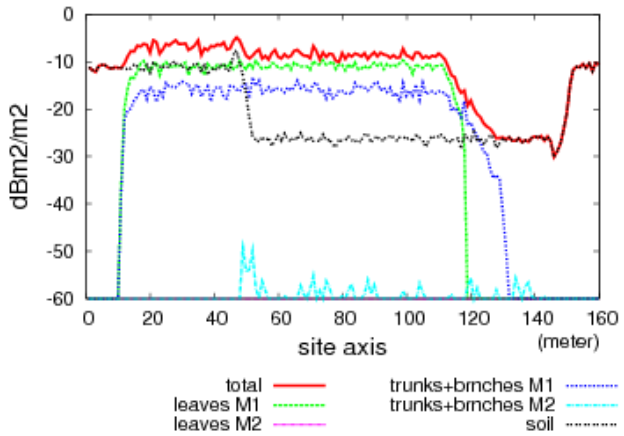

Figure 2.19: Backscattering profile $\sigma_0(dBm^2/m^2)$, C-Band, 23^o incidence, Summer season

in zone 5 remains only the outer direct soil with a decreasing attenuation : this is a second shadow region. Then, these considerations enable identifying geometrical effects which will be modulated by the electromagnetic properties. Note that such effects have been also reported in [Lopez-Sanchez et al., 2006] with wide band indoor real data.

In view of these considerations, let's come back to figure 2.19 where the mechanism of direct contribution and interaction with the soil are respectively mentioned as M1 and M2. In the follow up, $\sigma_{branchesM1}$, $\sigma_{branchesM2}$ denotes respectively the backscattering coefficient for the branches in direct scattering and in interaction with soil (same notation for the leaves).

It can be noticed that double bounce plot delineates the forest zone and extend over the above named zones 2, 2' and 3. However it is negligible when compared with the other contributors : it is a combined effect of incidence angle and strong cover attenuation at this frequency. The zone (3) permits retrieving the experimental results which were obtained with ERS measurements (cf. [Proisy, 1999]), thereby validating the approach (at least in this configuration). In zone (1), direct soil scattering is constant at level of outer soil, then presents a jump at the beginning of zone 2, which corresponds to soil under cover without attenuation, and progressively decays until reaching its infinite forest value. Entering zone 5, it first retrieves the outer soil value will full attenuation and progressively return to the outer value. It will then give a quite fine estimation of the extinction in the case where signal to noise ratio is sufficient. Direct soil is a major contributor in zones 1, 2 and 5, whereas it is rather secondary in zone 3. Its contribution makes total backscattering stronger in zone 2 than in zone 3, and gives rise to a peak at limit of zone 2. Leaves volume scattering presents roughly a constant value over a parcel translated from the forest one, which is not surprising since leaves are described in the modeling as all pertaining to the upper layer. On the contrary, direct scattering of branches and trunks spread over zones 2, 3 and 4. As the only difference with ERS configuration is the resolution, it is interesting to look at its influence on the results. The equivalent of table 2.1 with coarser resolution (3m) is displayed in figure 2.19. We can observe that we still retrieve the ERS results in zone 3 which thereby validates our approach. Nevertheless, the border effects are smoothed due to averaging on larger pixels.

To proceed on the analysis on influence of season, frequency and incidence angle (denoted in the following θ_i), we are going to consider 2 states of the forest given by table 2.1 for the summer and winter seasons. As zone 3 represents poor interest in this border analysis, we will limit the

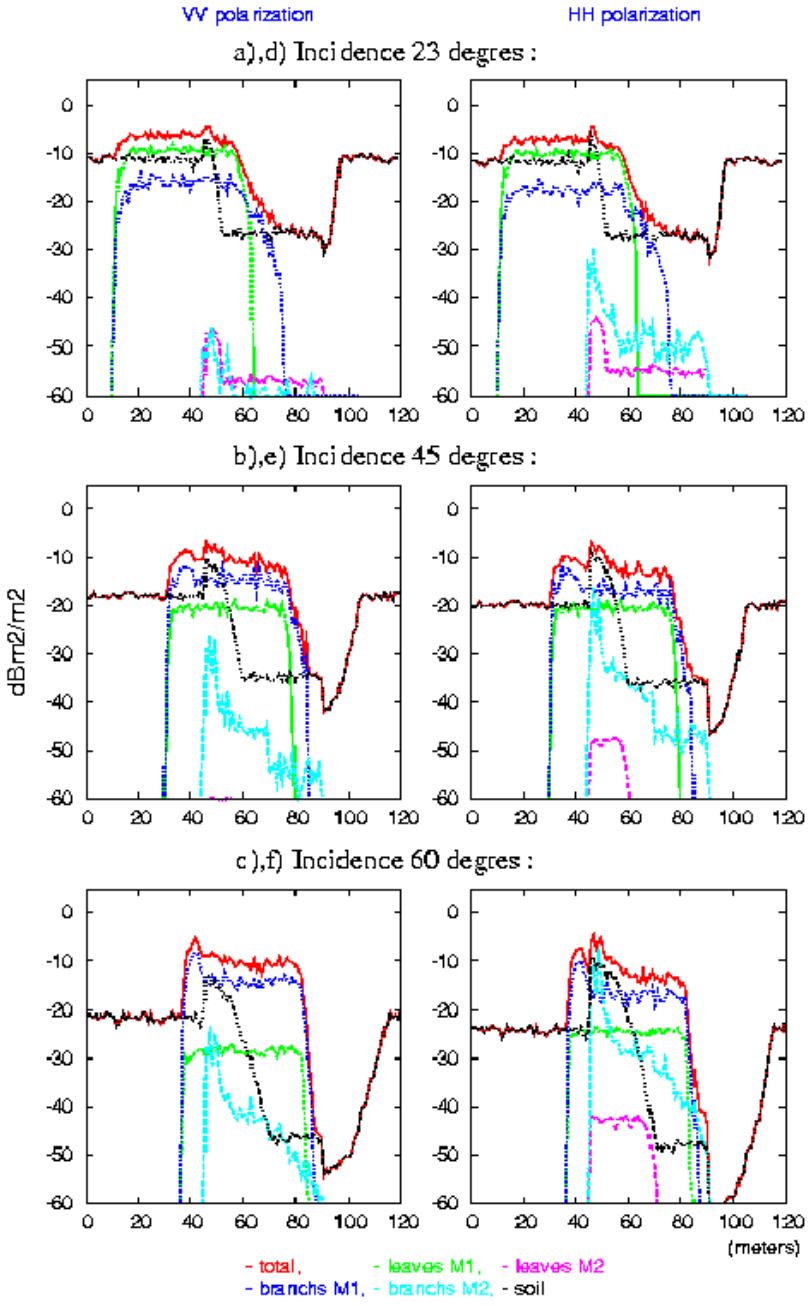

Figure 2.20: σ_0 for different incidences for both VV (a.,b.,c.) and HH (e.,f.,g.) polarizations at C Band in Summer

length of the parcel studied to 45 m (still with 50 meters wide in azimuth direction). Indeed in the quiet zone, the different levels for the backscattering coefficient σ_0 show the same trends as those of the infinite forest (e.g. those due to the correlated effects between the scattering and extinction sensibility as a function of incidence, frequency and polarization particularly as volume is not entirely uniformly random).

C Band Results : Whatever θ_i in Summer (cf. VV polarization plots in figure 2.20 (a-b-c)), most characteristics described in the previous section occur with a variable impact. Whereas the overall σ_0 remains of the same order of magnitude for the total field, the zones dimensions and the different contributions are strongly dependent on the incidence angle.
First, geometrical properties can be emphasised as the migration effect which truly changes the curves look at 23^o of incidence. In the shadow region (zone 5), the dip is also all the more marked as the running distance through the layers is higher due to the increment of the incidence angle. Moreover, as zone 2 becomes wider with the incidence angle, the peak width due to the inner soil increases and the double bounce enhancement extent (zone 2') follows the same trend, reducing thereby the 'quiet zone' which disappear at 60^o of incidence for such small forest parcels. On the contrary, zone 1 decreases for higher incidence so that the first radar range gates contain more and more scatterers close to the border, that's why a peak from the volume contribution can be seen before the inner soil one. At the back of the parcel (end of zone 4), the total backscattering coefficient is only due to the soil (as the double bounce is negligible). The size of this region is also very dependent on the incidence. Note that all these geometrical features are also present for the HH polarization (cf. figure 2.20 (d-e-f)).
In addition, classical properties of infinite forests can be retrieved. For example, as the leaves are not uniformly oriented, their backscattering coefficient is strongly dependent on θ_i as on polarization. They are for the 23^o configuration the main contribution whereas for the two other incidences $\sigma_{branchesM1}$ is higher. Their contribution in the extinction is also function of θ_i as it can be shown in comparison with the HH polarization. Indeed, as the upper branches (i.e. the randomly oriented scatterers) are predominant in C-Band in the $\sigma_{branchesM1}$, they should have an independent backscattering coefficient for both polarizations versus θ_i. Nevertheless, $\sigma_{VV,branchesM1}$ slightly increases with θ_i whereas $\sigma_{HH,branchesM1}$ remains constant. In the same way, the shadow effect upon the soil is also sensitive to the different extinction with polarization. Besides, the double bounce is also truly dependent on θ_i and on polarization. It remains a relatively weak contributor except at beginning of zone 1 where it contributes, particularly in the horizontal polarization, to the overshoot. For the latter, the contribution can be negligible (cf. figure 2.20 (a)) to predominant (cf. figure 2.20 (f)). So, these different properties related to the infinite forest enable analysing the total backscattering coefficient composition in the border zones before the parcel as well as at the back. In view of these considerations, we can now more easily interpret figure 2.17. Indeed, in this skewed configuration, the total σ_0 is made of several contributions so that there is a superposition effect, due to the spread of scattering mechanism phase center in height.

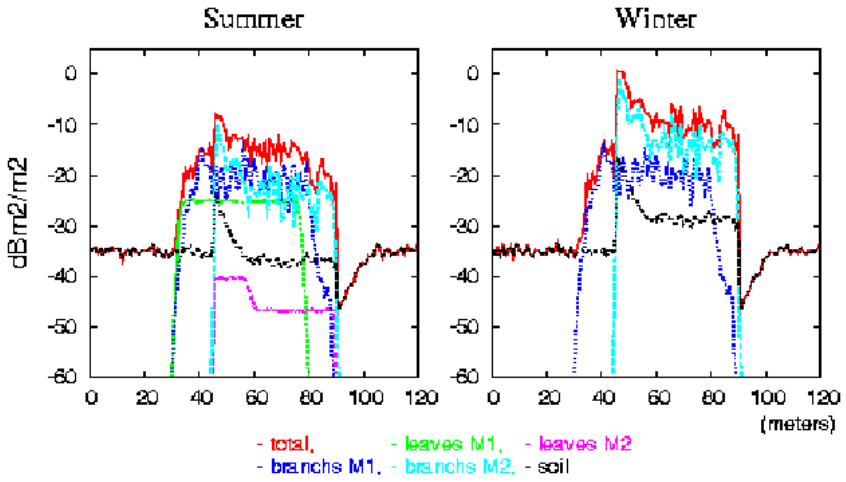

Figure 2.21: σ_0 for VV polarization at 45^o incidence, P-Band for both seasons.

P Band Results : As it can be seen on figure 2.21, major contributions mainly find their origin in branches and trunks direct scattering and above all in double bounce. The parcel is here easy to localize between the first peak and the shadowing zone. In winter, the double bounce is predominant by itself when present, impressing the look of the total field. Indeed, double bounce benefits from the combined effect of less attenuation, (due to absence of leaves), and change in soil properties (there is more moisture content). Moreover, it is interesting to note that simply with the total σ_0, we can identify by means of border effects, different contributions. Indeed, as the double bounce is still important at the back of the parcel, we can extrapolate its inside value by means of geometric considerations and therefore access to the volume contribution by difference. This request can of course be achieved by the use of circular polarization to identify the double bounce, in so far as such radar is available. Besides, this contribution from double bounce could be very interesting in the framework of land area contour detection context. By the way, we can imagine that the backscattering level will be very sensitive to the size of the oriented elements nearby the zenith direction, that is trunks and the first category of branches (see table 2.1). As an example, if making vary their diameter and length from -10 % to 20 % as shown in figure 2.22, a maximum gap of 4 dBm^2/m^2 can be reached. In the particular case treated here, we can notice that the higher level is not obtained for the largest scatterers as we are in the resonant zone for the cylinders representing the trunks.

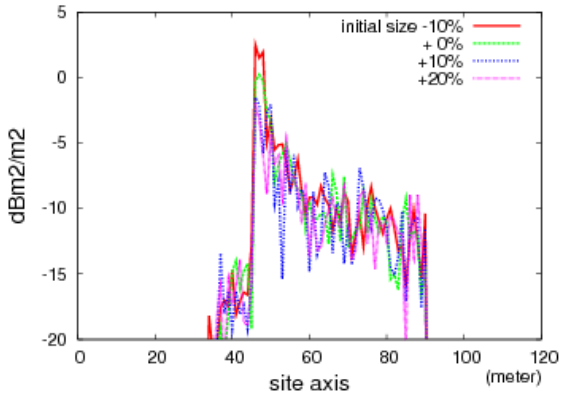

Figure 2.22: Backscatter sensitivity to the size of the oriented scatterers.

Theoretical modeling of an isotropic volume : Let a random volume composed of identical scatterers of density n_o, of average backscattering coefficient σ_0 and extinction coefficient α for a plane wave incidence angle θ_i, as depicted in figure 2.23.

For $0 \leq r \leq r_f (= H \cdot \cos\theta_i)$:

$$\sigma^u(r) = \int_{u=0}^{u=l^{T^u}(r)=\frac{r}{\tan\theta_i}} n_o \cdot \exp(-2\alpha \cdot \tan\theta_i (l^{T^u}(r) - u))du \tag{2.14}$$

$$\sigma^d(r) = \int_{u=0}^{u=l^{T^d}(r)=r\cdot tan\theta_i} n_o \cdot \exp(-2\alpha \cdot \frac{1}{\tan\theta_i}(l^{T^d}(r) - u))du \tag{2.15}$$

$$\begin{aligned} \sigma(r)|_{0\leq r\leq r_f} &= \frac{n_o}{2\alpha} \cdot \Phi_\theta (1 - \exp(-2\alpha r)) \\ \text{with : } \Phi_\theta &= \tan\theta_i + \frac{1}{\tan\theta_i} \end{aligned} \tag{2.16}$$

For $r_f \leq r \leq r_s = (\frac{H}{\cos\theta_i})$: σ^d is changed into

$$\begin{aligned} \sigma^d(r) &= \int_{u=0}^{u=l^{T^d}(r)=\frac{r_s-r}{\tan\theta_i}} n_o \cdot \exp(-\frac{-2\alpha}{\tan\theta_i} \cdot (l^{T^d}(r) - u))du \\ &= \frac{n_o i \tan\theta_i}{2\alpha}(1 - \exp(-\frac{2\alpha}{\tan^2\theta_i}(r_s - r))) \end{aligned} \tag{2.17}$$

$$\begin{aligned} \sigma(r)|_{r_f\leq r\leq r_s} = \frac{n_o}{2\alpha} \cdot [&\tan\theta_i \cdot (1 - \exp(-\frac{2\alpha}{\tan^2\theta_i (r_s - r)})) \\ &+ \frac{1}{\tan\theta_i} \cdot (1 - \exp(-2\alpha r))] \end{aligned} \tag{2.18}$$

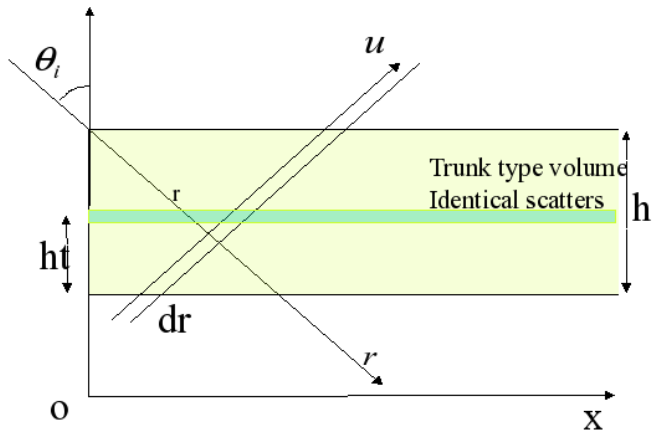

Figure 2.23: Illustration of the varying volume of scatterers along with the radar slant direction.

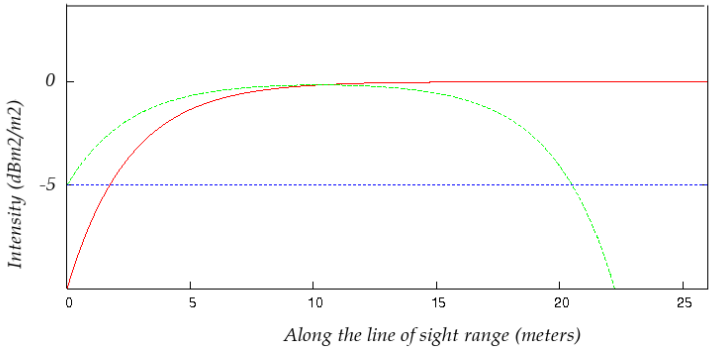

Figure 2.24: Backscatter variation considering a theoretical isotropic media.

Then once the stable region ($r \geq r_s$) is reached, σ^d is nul and σ^u becomes :

$$\begin{aligned}\sigma(r) &= \sigma^u(r) \\ &= \int_{u=l^{T_1^u}=\frac{r-r_s}{\tan\theta_i}}^{u=l^{T_2^u}(r)=\frac{r}{\tan\theta_i}} n_o \cdot \exp(-2\alpha \tan\theta_i \cdot (l^{T_2^u}(r) - u))du \\ &= \frac{n_o}{2\alpha \tan\theta_i} \cdot (1 - \exp(\frac{-2\alpha H}{\cos\theta_i}))\end{aligned} \tag{2.19}$$

2.3.2 Confrontation with Experimental Data : the HOMSAR campaign

The monostatic **HOMSAR** campaign over the Ebersberg forest took place during 2005. Quad-pol and multipass interferometric measurements were conducted with the DLR's **E-SAR** sensor with a center frequency at 1.3 GHz, range and azimuthal resolution respectively of 2 and 4.5 m at about 3000 m altitude with a chosen incidence angle of 45^o. The multipass acquisitions were carried out with several baseline (around 10-20 m) and gave satisfactory results for height retrieval. Nevertheless, we will in this paper first focus on radiometric ones. Indeed, the significant aspect of this investigation is that we have a detailed ground measurements of the forest, which is in many case a tricky point. Indeed, relevant studies about the Ebersberg forest have been undertaken (notably in [Pretzsch and Kahn, 1998] and [Seifert, 2003]) and we went directly on site to carry out several measures. The next part will be thus devoted to the description of this ground measurements, then the comparisons with **MIPERS** will be discussed.

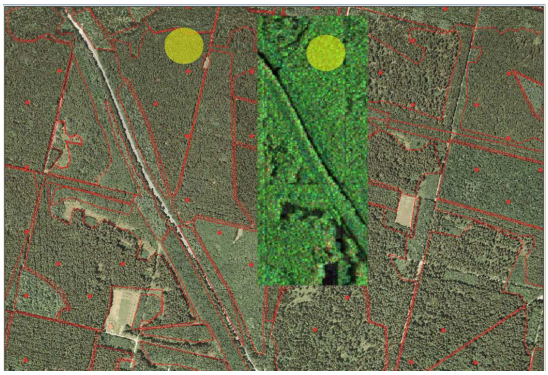

Figure 2.25: Optical Image in background and RGB composite ([HH,$\sqrt{2}$HV,VV]) SAR one. The homogeneous stand of interest is marked by the yellow circle.

Case of the Ebersberg Forest

The Ebersberg forest is mainly composed of spruce and beech stand sometimes mixed up. This heterogeneity can be easily seen on the optical image (cf. the background of figure 2.25 but also retrieved with differences of texture in the SAR one (cf. the composite [HH,$\sqrt{2}$HV,VV] image on figure 2.25) especially for the stand along and just above the road. As a result, criteria to select the sample to model were its homogeneity and also its apparent conformity to theoretical models (in the sense of allometric relations) detailed in [Pretzsch and Kahn, 1998] and [Seifert, 2003]. Nevertheless, even with a one hectare parcel large, specific factors (other than phenology) due to the environment are liable to bring out atypical behavior, we thus went on site to set up a ground measurements as detailed as possible. We processed as follows : first 3 plots of 10*10 square meter among the selected homogeneous parcel were chosen, then in each we have collected the DBH (diameter at breast height), the total height, the crown base height and the crown diameter (in 4 azimuthal directions) for each tree. These results are displayed and show a very good agreement to allometric relations between DBH, crown height and width (cf. [Pretzsch and Kahn, 1998] pp 205-206). Then knowing the age of this stand (about 40 years old) and the growth curve the number of shoots (i.e the number of branches in a given vertical plane) can be deduced. In the azimuth direction assumed symmetrical, allometric relations (cf. [Seifert,

2003] pp 156) gives us the branches number, as well as their radius from their length (cf. Seifert [2003] pp 141). Finally, knowing the shape of the crown (cf. Pretzsch and Kahn [1998] pp 204) the volume fraction can be deduced. Therefore, this set of parameters gives us a quite accurate description of the media summarized in table 2.2. On the other hand, one element which remains still under investigation is the angle distribution of the branches as an ideal representation would be curved branches. This will be discussed in the next part.

Concerning the soil, we haven't got at the moment thorough description but as it will be shown of slightest importance for the direct contribution (i.e except through the double bounce) we will be content with an analogy with the Fontainebleau forest that is 39%, $h_{rms} = 0.01m$ and $L_c = \lambda$ respectively for the water content, roughness and the correlation length. Besides, studies also done by the Chair of Forest Yield Science department from Munich University of Technology enables us to set the water content to 50 %.

Quad-Pol radiometric results

Once the ground measurements stage is done and converted into table 2.2 providing the convenient inputs for the model, a scene of one hectare is generated with barely the same resolution (for simplicity) than the experimental campaign i.e 2 and 4 m respectively in range and azimuth. This approximation (4 instead of 4.5) doesn't bring about significant effects as it has been established close to the same one by one meter resolution (within one dB). The needle presence is also neglected as their modeling by thin ellipsoids have been shown of slightest importance (remind L-Band). As mentioned previously, freedom parameters remains inside the upper layers (3 & 4) concerning the angle distribution of the branches. Indeed, we have noticed that single primary branches (larger than those written in table 2.2 which length would fit the gap between the trunk and the limit of the crown) with an orientation close to the normal of the trunks leads to improvable results. This comes from the curved shape of the branches, that's why we separate them into two shorter cylinders with different dimensions and orientations, which will give good results -in average less than 0.5 dB for HH and within 1 and 2 dB for VV and HV. In-situ parameters have thus been adapted to match modeling possibilities but still with reasonable values and according the considerations found in [Seifert, 2003]). In any case, this gives a referee point from which other configurations can be derived (e.g. structural or pheno-

Table 2.2: In-situ measurements :

	Type	f_v	Length♣	Radius	Angles♢
Top layer (5.5)♯	twigs	2.5E-5	1.3E-1	3E-3	11-70
	Pr. branches	1.9E-4	6.3E-1	5E-3	55-70
Middle l.(1.5)	Sec. branches	1E-4	3.3E-1	6.63E-3	70-90
	Pr. branches	9E-4	1.	1E-2	70-90
Shadow l. (3.)	Pr. branches	4.2E-3	9E-1	1E-2	40-90
	trunks	4.2E-3	3.	1E-1	0-8.5
Bottom l. (12.)	trunks	4.2E-3	3.	1E-1	0-8.5

(♯) Layer height
(♣) All dimensions in meters
(♢) Angles in degrees

Figure 2.26: Typical area through the Ebersberg (Germany) forest.

logical ones, in different frequency bands and also bistatic). To adjust these parameters, layers were generated one by one (cf. figure 2.27) and we have checked the backscattering for all the contributions (as a tomography study would do but without the need of correct the offset due to the attenuation of the upper layers). It has been then possible to see where the discrepancy with the experimental results came from. The experimental forest response can be characterized by a HH major contribution (cf. figure 2.28), around 2 dB higher than VV and more specifically a cross polar one very high (around 14-15 dB).

From our simulations with the final modeling, we can establish (cf. figure 2.27) that the difference between HH and VV comes mainly from the stem layer double bounce (higher in HH due to Fresnel coefficients). Then the shadow crown and above all the middle layer will bring about a strong attenuation in comparison to the other ones and tend to level HH and VV. In our first trials, our problems came from this over-attenuation due to larger cylinders. Finally the top layer gives the importance to the volume and enable to reach the specific high cross polar level due to the branches orientation. Besides and still due to oriented volume, the gap between co polarization increases until 3 dB. In this way, our simulated results match with the experimental ones with a quite good agreement, also for the standard deviation brought about by speckle.

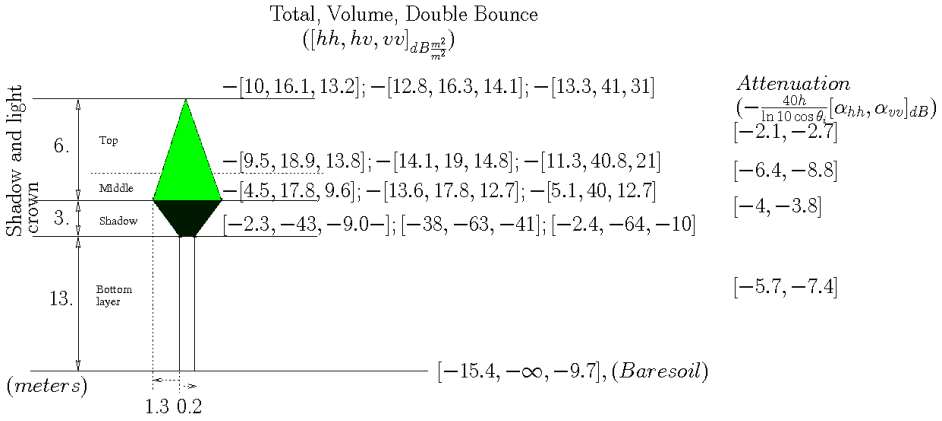

Figure 2.27: Forest structure, associated backscattering levels and attenuation for each layers

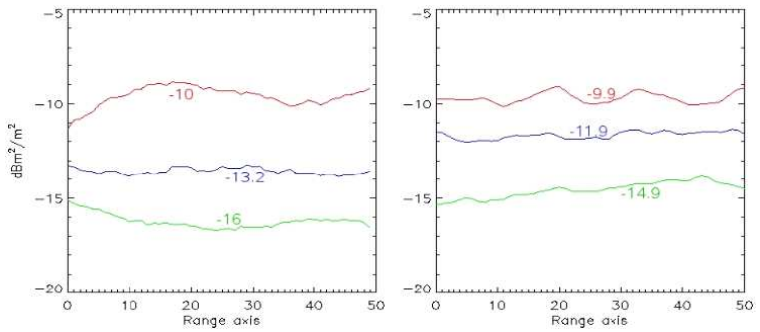

Figure 2.28: Experimental (left handside) and MIPERS simulated backscattering coefficients ($dB\frac{m^2}{m^2}$) in the HH, HV and VV respectively in red, green and blue (numbers in colour indicate the mean values).

2.3.3 Sensitivity towards Biomass : case of the Nezer Forest

Forest Modeling for Nezer

For studying biomass influence on SAR observables for a complete forest, there is the need of a reliable description of how evolve the descriptive parameters of the forest with age and to subsequently evaluate their correlation with biomass. Actually, these parameters, which constitute a large part of the ground truth, are statistical parameters describing the sizes, orientations and concentrations of the discrete components of the considered forest (stems, branches and leaves which constitute the forests). Then, modeling of interaction of electromagnetic waves is always difficult since this ground truth acquisition requires lot of in situ measurements (see for example) for a specific forest, and make more difficult to study a forest versus its age and subsequently its biomass. Actually, focus is done here on *Les Landes* forest since it is a site over which exist both a large variety of airborne experimental data, acquired in 1989, 2001 and 2004, over parcels of varying age, and over which extensive ground truth measurements have been performed. However, one must realize that this extensive ground truth has been done in 'similar' parcels, of same age, and that they are not the really measured ones by the Radar.

In the sequel, we are going to compare the experimental results with those obtained with MIPERS. For this, we first try to derive a simplified physical model which represents the ground truth as a function of age whatever the year of measurement. It is to note that cultural practices and forest height may have evolved within such relatively large intervals of time : this point is not considered in the following, it is supposed that geometric features do not change between dates of acquisition, and that only the variable features like moisture do so according to for example.

Let us recall that our model is based on the description of trees as a set of homogeneous cylinders for trunks and branches (needles are assumed insignificant at P band), and then the input descriptive parameters specific to forest geometry which are required are :

- The number of layers and the height of each layer
- inside each layer :
  - the number of cylinders categories
  - length and radius, for each category, in average and in distribution
  - orientation law distribution, for each category. Assuming azimuthally symmetry, only Euler angle ψ_{ins} is considered.

The other parameters for which information is required concern the soil characteristics (here assumed to be flat), i.e. the r.m.s. height and the correlation length, and the moisture content inside both soil and vegetation. To derive a model suitable to show the evolution of these parameters, we have relied on the works described in two next paragraphs :

Model 1 (Saleh's description) : The descriptive input data are given in [Champion et al., 2001; Saleh et al., 2007]. Extensive measurements of descriptive parameters of *Les Landes* forest were done and related to the age for three ages: 5, 26 and 32 years old. Then, there is the possibility of interpolating these data to other ages, which is done in the paper through fit formulas or remained to be done by interpolation. It assumes 3 layers, layer 1 possessing only trunks. Referring to [Saleh et al., 2007], the following steps are followed as a function of age:

- diameter at breast height (DBH) as a function of age (eq. 5) diameter versus height z (eq. 14 + table VI) (with particularity for low ages)

- total height as a function of DBH (eq. 7)
- layers thickness as a function of height and DBH (eq. 8)
- trunks number density for the 3 ages (table I), which also permit deriving trunks biomass knowing the density of wood
- branches biomass (eq. 9) as a function of age and DBH, and its repartition for each branch order according to the ramification order with table III
- branches diameter for order 1 (primary) ones from table IV, from which volume of these branches is deduced from (eq. 10) and later length is derived;
- also from biomass of primary branches, volume and density can be deduced the concentration in primary branches for each upper layer.
- steps 6 and 7 may be repeated for each ramification, with including a supplementary parameter which is a fractal order binding each order greater than 1 to the previous one
- branches orientation is deduced from the branch diameter with (eq. 12).

Tables I, III and IV were linearly interpolated. Following this model, some descriptive data may be directly deduced from the age, but for other interpolations must be done.

Other geometrical models : The previous model is actually a very interesting one since it gives through the way of analytical formulas or interpolation an evolution of the statistical geometrical ground truth with age. However, this model has been built up with only 3 ages and does not pretend to have been checked with extra ages. In particular, for ages older than 32 one must be very prudent with the results. It is why some other global descriptions have been considered. The first one addresses the same trees population (maritime pines), with a ground truth more limited (only about trunks) but extended to more ages. The second one addresses other conifers but includes also branch biomass.

Model 2 : based on T. Le Toan and Beaudoin' description Data are extracted from [Le Toan et al., 1992], in which the above parameters directly as a function of age are given :

- DBH as a function of age
- height as a function of age
- number density of trunks as a function of age
- trunk biomass as a function of age

We can see that this model does not give information on branches sizes and orientations, nor on branches biomass.

Model 3 : based on Fung's description (cf. [Fung, 1994]) In this paper, ground truth is presented every 8 years of age with a detailed description of branches at these ages. Based on these data we could compute again the branches biomass.

Models illustration The above models present most of time a coincident gross behaviour but are slightly different in some parts, which may have a strong electromagnetic impact. As examples:

- DBH (diameter at breast height) behave somehow differently with models 1 and 2 as shows figure 2.29 (a) : the divergence for low values infers very strong differences for small ages
- Figure 2.29 (b) shows that both models are coincident for the concentration of trees versus age, and that the analytical fit of model 2 is well confirmed by model 1
- Figure 2.29 (c) shows a nice agreement between both models for the total height, however only model 1 gives the thickness of each layer among the three ones describing the forest canopy.
- Figure 2.29 (d) shows the biomass of trunks with model 1 but according to DBH versus age computed with model 2; branches' biomass is displayed for model 3 which shows a branches biomass of about 14% the trunk's one, which is coincident with for conifers and with model 1 in intermediate ages.

The model which was retained for the follow up study, further named as model 4, mixes some of the above relations starting from general relations of model 1, but incorporating :

- DBH versus age of model 2
- branches biomass of model 3

The fact of following the chain of incorporating other models helped in maintaining the consistency of the various ones. Note that the biomass tends to saturate at large ages, due to the associated spacing between trees.

Polarimetric Results in 2001

Figure 2.30 shows the experimental results which were obtained on Nezer forest in 2001 together with the simulations done with the ground truth at an incidence angle of 40 degrees following model 1. On this data set, HH and VV are of the same level. In most reported observations like , in P band, double bounce contribution is important and drives the HH total scattering since due to Fresnel coefficients HH double bounce is usually higher than VV one. To be in agreement with experimental data, one has to consider high moisture content in the branches, which may makes sense as we will see in the next sections. It is to note that for young trees, the model underestimates the experimental values: obviously model 1 does not reflect the observations for low biomass. This discrepancy also is reflected in the polarimetric coherence between HH and VV at low biomasses which is unity with the model and around 0.5 (natural value) experimentally. Note that this effect is amplified by the fact that DBH for small trees is particular since it is very close to the top of the trees. It is also visible that for large ages the saturation appears too early when comparing with experimental results. Figure 2.31 displays the intensity as a function of incidence angle for an age of 25 years. Agreement is satisfactory, which confirms that for this class of ages model 1 is correct.

Now following model 4 the results of figure 2.32 for age and figure 2.33 for biomass are displayed. We can check that now the agreement covers all classes of age. Also polarimetric coherence HH-VV is in agreement. One can see that :

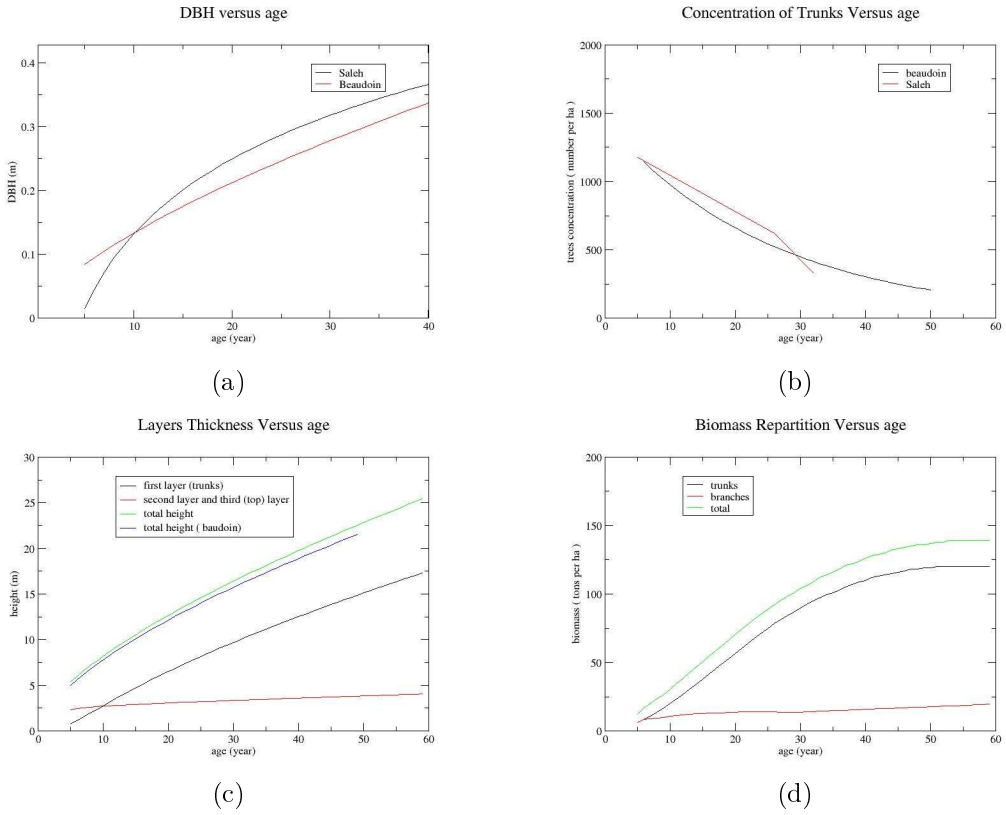

Figure 2.29: (a) Comparison of models 1 and 2 for DBH versus age, (b) Comparison of models 1 and 2 for trees concentration versus age, (c) Comparison of models 1 and 2 for layer thickness (d) biomass repartition evolution versus age (model 4).

- HH is originated by the double bounce very predominantly, and it exhibits a growing with age and biomass
- VV finds its repartition between double bounce and volume for young trees, and is purely originated by volume for large trees, so it presents a 'flat' evolution
- HV finds its origin in volume only, and is slightly underestimated in the model. Influence of moisture content is noticeable : one can see the change of VV versus HH behaviour, still staying within reasonable values when comparing with experimental data.

Polarimetric Results in Dry Conditions

Using the geometric values of the previous paragraph with less moisture content inside the soil and inside the vegetation (trunks and branches), simulation results with model 4 are compared with experimental results published in [Fung, 1994]. Note that these results, corresponding to measurements done by AIRSAR in 1989 during summer, are much less detailed than the previous ones corresponding to RAMSES measures. One can observe a good agreement, but obviously introducing moisture content in vegetation, increasing with decreasing ages since it seems that young trees withdraw from the soil and convey more water than the old ones, would

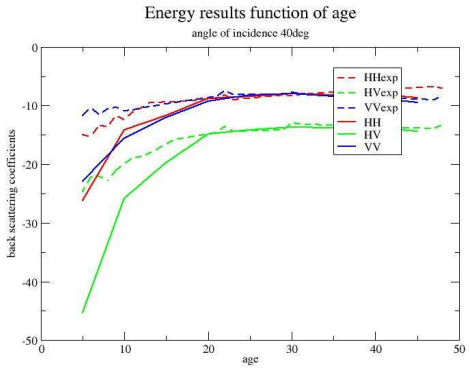

Figure 2.30: Radiometic results in dry conditions: experimental ones in interrupted line; full line : model 1

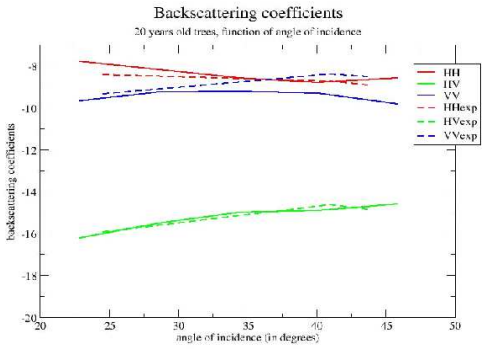

Figure 2.31: Same as in figure 2.30 with radiometry as a function of incidence angle.

improve the agreement. Comparing with 2001, one can note that now HH finds its origin not only in double bounce but in volume also. These results show the importance of ground truth at P band, and the need of the sensitivity study which is followed in the follow up.

Through the previous results, both the physical model and MIPERS are validated versus experiments in full polarimetry, over a large range of biomass and in distinct moisture conditions. The main interest of such modeling is to be able now to go towards other configurations and applications, like the derivation of the influence of the various descriptive parameters on the observables and the subsequent retrieval (cf. [contract 20449 ESA]), FOPEN studies or bistatic configuration. However, it is to note that even if MIPERS would match any forest type, the physical model used here is limited to the Maritime Pine, and that the development done here has to be renew if another kind of forest has to be considered. Nevertheless, use of generic forests may be done like for example in chapter 4 where larger values of forest biomass are needed.

2.3.4 FOPEN Study : Case of a Camoufled Vehicle

Forest Bistatic Scattering at Low Frequencies

Before going through the FOPEN problem, it is interesting to study how forest scattering behaves versus frequency, for a range adapted to penetration through the forest and thus to

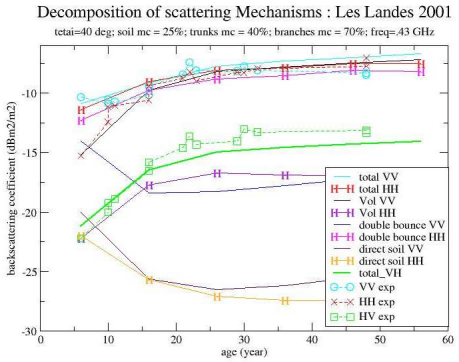

Figure 2.32: Backscattering coefficient as a function of age for the total, the volume, the double bounce and the direct soil for VV, HH and HV; the plots for HH incorporate specific symbols.

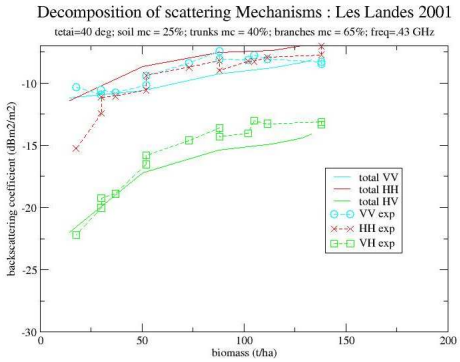

Figure 2.33: Intensity as a function of biomass; Les Landes 2001, model 4.

target detection. For frequencies at and above P band, forest scattering will be analyzed in chapter 3 and 4. However, monostatic or bistatic detection of targets under foliage may be envisioned at much lower frequencies, that is below VHF frequency band. One can refer to figure 2.36 where a frequency of 100 MHz has been chosen to show the forest bistatic scattering behaviour.

Figure 2.36 gives the scattering diagrams of the forest considered which the same as in section 2.3.3 for ages of 25 years in HH, VH, VH et VV. One may observe first that HV and VH are similar but not identical, with peaks in directions around the plane orthogonal to the plane of incidence. In VV, one may observe a crown for which the maximum is at the backscattering direction. This crown is located at site angles close to the site of the incidence angle. On the contrary, in HH, this crown is initiated close to the incident direction but vanishes around perpendicular azimuth. Figure 2.37 shows this plot again for the double bounce only and for HH and VV : it can be checked that the total scattering diagram is totally impressed by the double bounce. At this frequency, the only significant interaction is from the trunks, and mainly through the double bounce process, whatever the radiation directions.

Then, these diagrams may be interpreted as follows. The double bounce is driven by the scattering diagram of the homogeneous cylinder, which at low frequencies is azimuthally symmetric

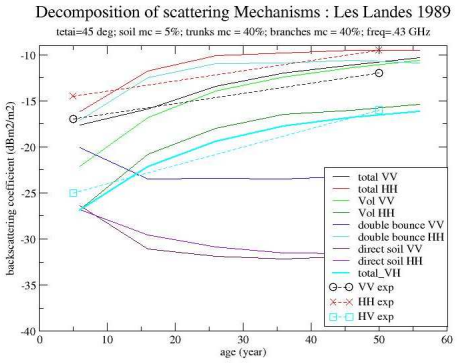

Figure 2.34: Backscattering coefficient as a function of age for the total, the volume, the double bounce and the direct soil for VV, HH and HV.

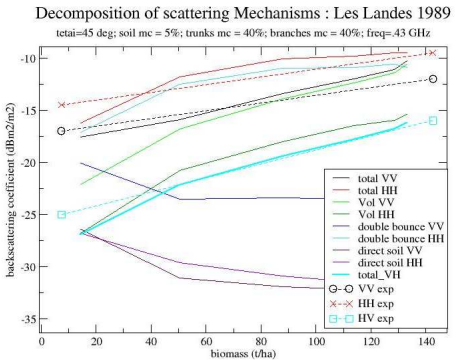

Figure 2.35: Backscattering coefficient as a function of biomass for the total, the volume, the double bounce and the direct soil for VV, HH and HV.

in VV but present a null in the perpendicular direction in HH, hence the different diagrams. At higher frequencies, this trend remains but as the volume contribution significantly increases scattering diagrams become more complicated to analyse.

Actually, figure 2.38 shows the evolution with frequency of the forest scattered intensity, as a function of azimuth angle and for 2 site angles : on the top, at same site angles as the angle of incidence and on the bottom at a smaller one. One can note the predominance of VV below approximately 100 MHz, and a relative stability of the results above 400 MHz.

Scattering from the Camouflaged Target

The target under consideration is a truck as presented in paragraph 2.2.2. The scattering matrix computation has been achieved using the FDTD method, over the same frequency bands than the forest. The scattering diagram of the target alone is represented in figure 2.39. Using MIPERS and its FDTD hybridization, the order 1 scattering is straightforward, since in this case the target is a scatterer like the others as described in section 2.2.2. The target scattering in the presence of the ground (considering a soil moisture equals to 20%) is plotted in figure 2.39 (a) and (b). Its straight position has been chosen and this diagram results from MIPERS simulations

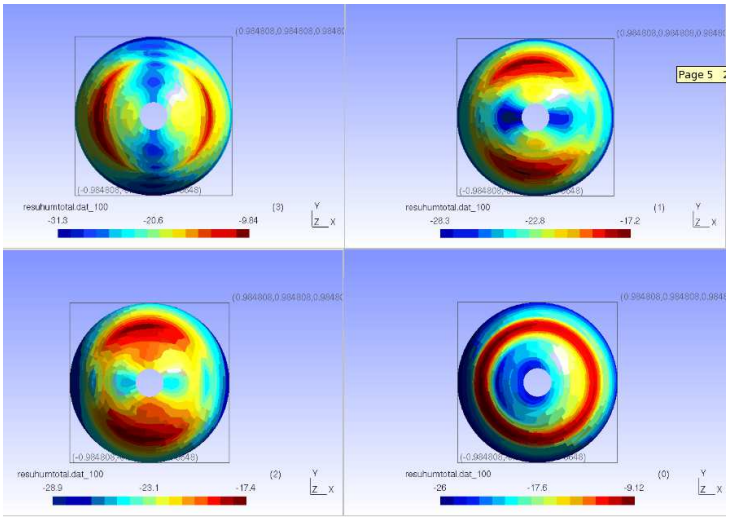

Figure 2.36: VHF (100 MHz) scattering diagram for the forest with a constant transmitter at $\theta^{\mathrm{T}} = 30^o, \varphi^{\mathrm{T}} = 0^o$ and a receiver covering the all hemispherical space. From the top left to the right bottom : $\sigma^0_{hh}, \sigma^0_{hv}, \sigma^0_{vh}, \sigma^0_{vv}$.

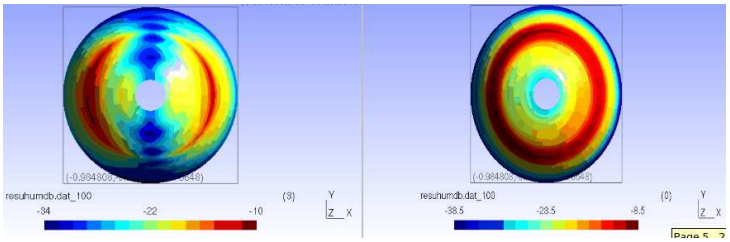

Figure 2.37: VHF (100 MHz) hemispherical scattering diagram for the forest double bounce contribution with $\theta^{\mathrm{T}} = 30^o, \varphi^{\mathrm{T}} = 0^o$ and for the like polarizations (HH on the left).

without forest scatterers. Coupling with the ground is shown separately in (c), from which its importance can be stressed.

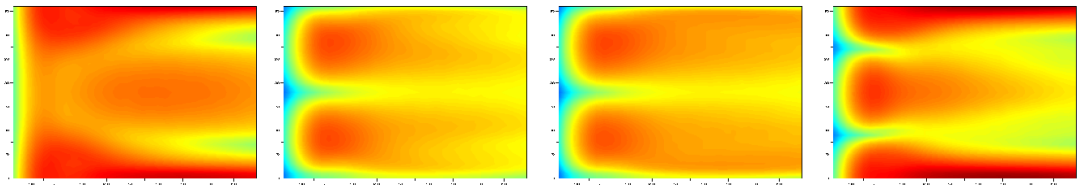

(a)

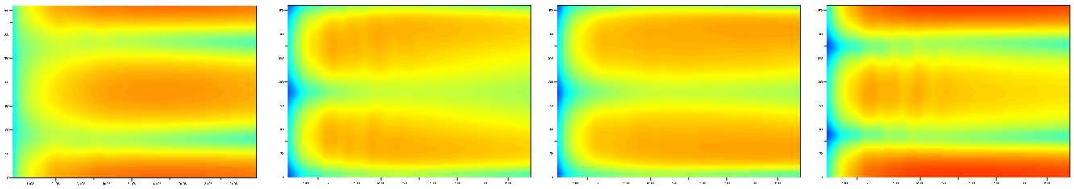

(b)

Figure 2.38: From the left to the right, scattering coefficients $\sigma^0_{vv}, \sigma^0_{hv}, \sigma^0_{vh}, \sigma^0_{hh}$ for the forest total contribution. For (a) : $\theta^{\mathrm{T}} = 30^o, \theta^{\mathrm{R}} = 30^o$ and for (b) : $\theta^{\mathrm{T}} = 30^o, \theta^{\mathrm{R}} = 15^o$.

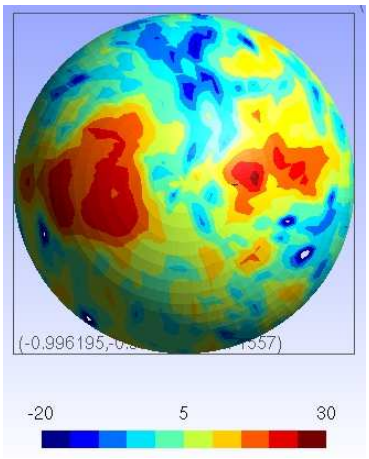

(a)

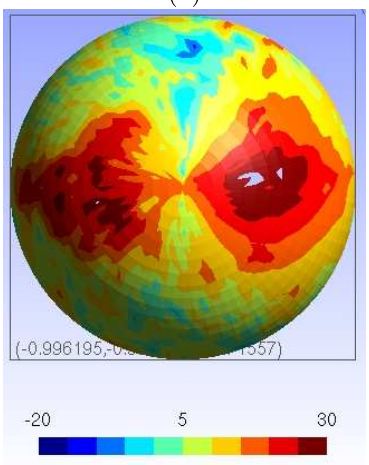

(b)

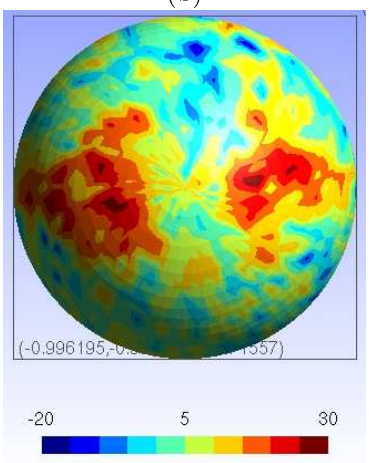

(c)

Figure 2.39: P-band (430 MHz) hemispherical scattering diagram with $\theta^{\mathrm{T}} = 30^o, \varphi^{\mathrm{T}} = 0^o$. (a) Lonely target, straight position; (b) target plus coupling effect with the ground (wc = 20 %) ; (c) coupling terms contribution only.

Applications

Figure 2.40 gives the images obtained in the case of the target inserted inside a forest patch, of small size, with a fine resolution of 1 m : target presence is clearly visible whatever the polarization. One can note on these synthetic images the presence of shadowing and reinforcement effects due to borders. On figure 2.41 which corresponds to a coarser and more realistic resolution (2 m) one can see that even if the target is still visible it is very poorly detectable due to the large number of false alarms which have appeared because of the borders reinforcements. This phenomenon is countered for specific bistatic configurations, within the incident scattering plane (figure 2.42) or for more general ones (combining also a azimuth variation, as shown in figure 2.43).

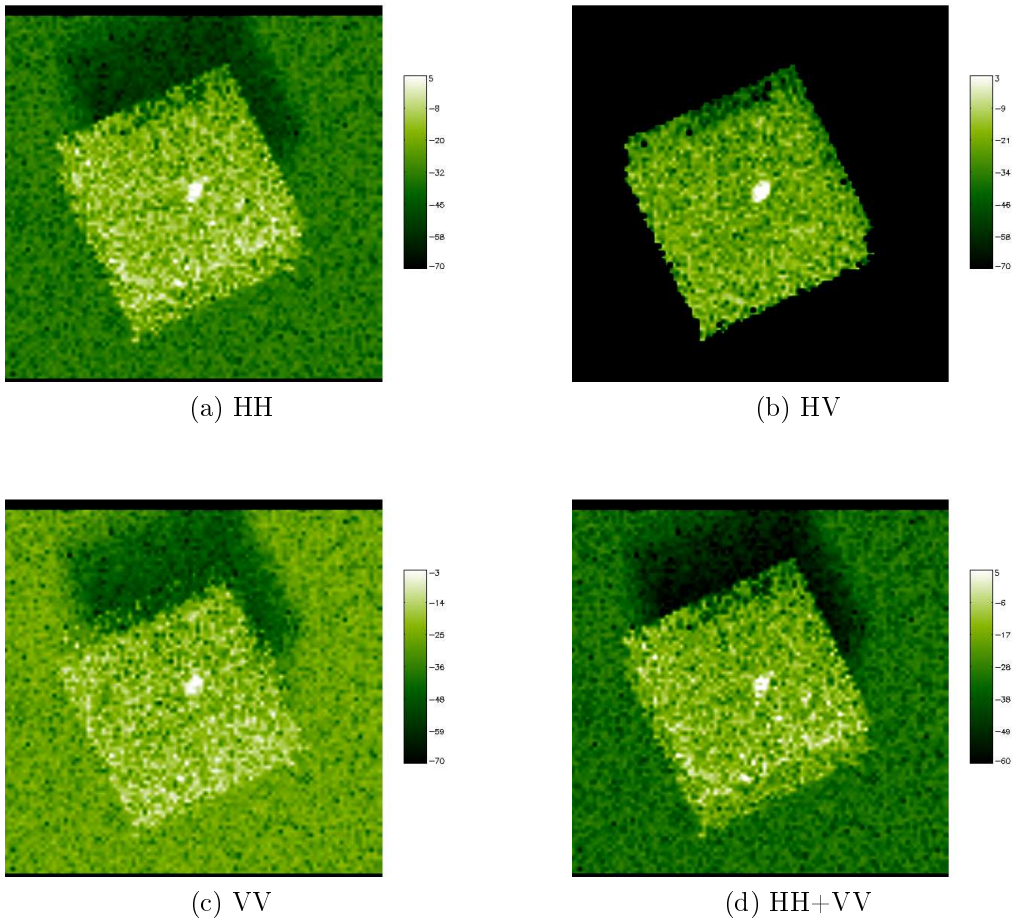

(a) HH (b) HV

(c) VV (d) HH+VV

Figure 2.40: P-band (430 MHz) simulation, monostatic, 1 m^2 resolution, $\theta^{\mathrm{T}} = 60^o$.

In this section, the capacity of MIPERS to cope with muti-regions scenes has been illustrated, with an inner region encompassing the target and an surrounding region. Plus, monostatic as well as bistatic synthetic images have been generated with a truck like target under the foliage. The simulation of such complex scenes illustrates the versatility of the simulator MIPERS and the efficiency of such possibilities to achieve sensitivity studies. As a example, the

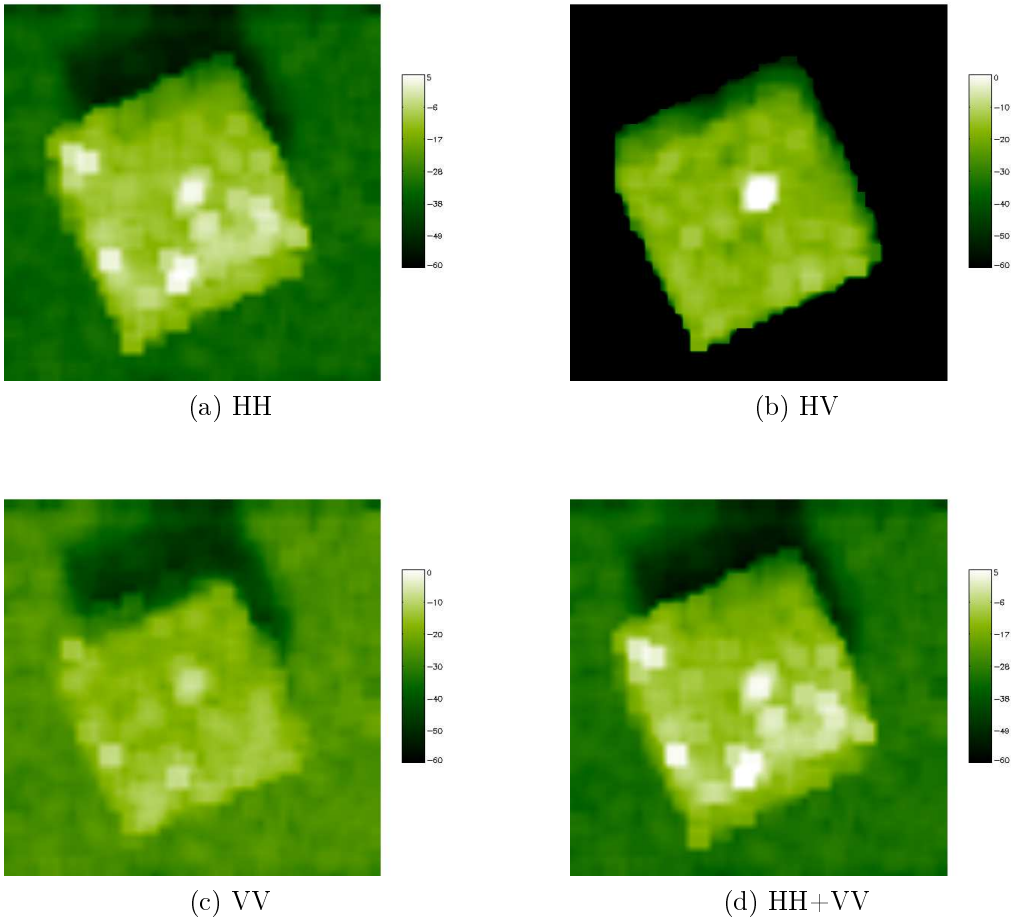

(a) HH (b) HV

(c) VV (d) HH+VV

Figure 2.41: P-band (430 MHz) simulation, monostatic, 2 m^2 resolution, $\theta^{\mathrm{T}} = 60^o$.

reader is invited to see the fourth chapter and the subsection 3.4.2.

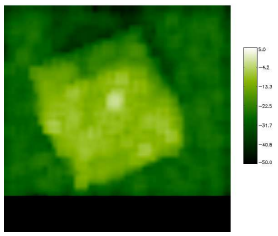

(a) HH

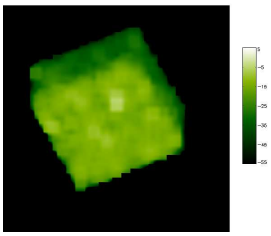

(b) HV

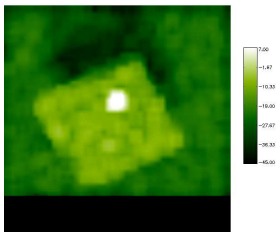

(c) VV

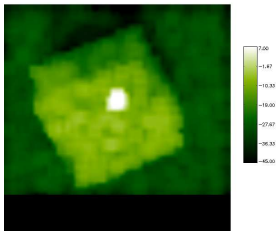

(d) HH+VV

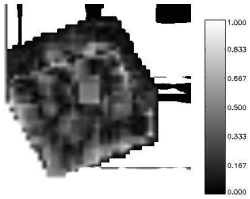

(e) $|\gamma_{vvvh}|$

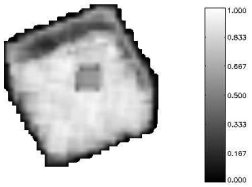

(f) H

Figure 2.42: P-band (430 MHz) simulation, site bistatic $\theta^{\mathrm{T}} = 60^o, \theta^{\mathrm{R}} = 30^o$.

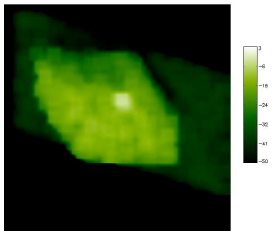

(a) HH

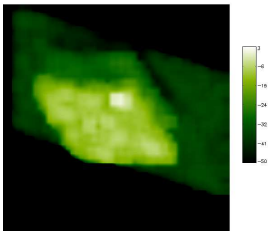

(b) HV

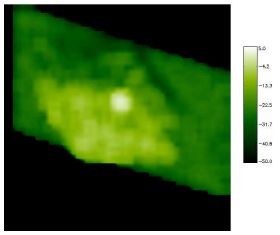

(c) VV

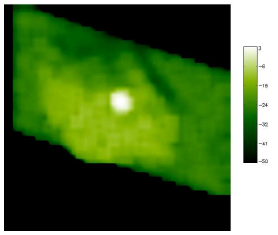

(d) HH-VV

(e) $\varphi\big(\gamma_{hhhv}\big)$

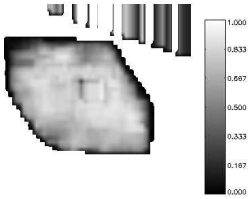

(f) H

Figure 2.43: P-band (430 MHz) simulation, site bistatic $\theta^{\mathrm{T}} = 60^o, \theta^{\mathrm{R}} = 30^o, \Delta\varphi = 90^o$.

Bibliography

U. Benz and E. Pottier. Object based analysis of polarimetric sar data in alpha-entropy-anisotropy decompositionusing fuzzy classification by ecognition. In *International Geoscience and Remote Sensing Symposium (IGARSS)*. IEEE, 2001.

J.P Berenger. A perfectly matched layer for the absorption of electromagnetics waves. *Journal of computational physics*, 114:185–200, 1994.

J.P Berenger. Three-dimensional perfectly matched layer for the absorption of electromagnetics waves. *Journal of computational physics*, 127:363–379, 1996.

I. Champion, A. Porté, D. Bert, D. Loustau, and M. Guedon. Tree architecture in remote sensing analytical models : The bray experiment. *International Journal of Remote Sensing*, 22:1827–1843, 2001.

K.S. Chen, Tzong-Dar Wu, Leung Tsang, Qin Li, Jiancheng Shi, and A.K. Fung. Emission of rough surfaces calculated by the integral equation method with comparison to three-dimensional moment method simulations. *Geoscience and Remote Sensing, IEEE Transactions on*, 41(1):90 – 101, jan 2003.

S.R. Cloude, D.G. Corr, and M.L. Williams. Target detection beneath foliage using polarimetric sar interferometry. *Waves in Random Media*, 14:393–414, 2004.

contract 20449 ESA. *Rigorous numeric techniques applied to microwave interaction with natural targets : volume scattering*, volume volume 2.

C. Dahon, L. Ferro-Famil, C. Titin-Schnaider, and E. Pottier. Computing the double-bounce reflection coherent effect in an incoherent electromagnetic scattering model. *IEEE Geoscience and Remote Sensing Letters*, 3:241–245, April 2006.

M. Tsayem Demaze, L. Polidori, and J.M. Fotsing. Caractérisation multi-échelle et multi-capteur de la déforestation tropicale amazonienne. In *Bulletin de la Société Franéaise de Photogrammétrie et Télédétection*, volume 161, pages 74–84, 2001.

R. K. Didham and J. H. Lawton. Edge structure determines the magnitude of changes in microclimate and vegetation structure in tropical forest fragments. *Biotropica*, 31, 1999.

M.C. Dobson, F.T. Ulaby, M.T. Hallikainen, and M.A. El-Rayes. Microwave dielectric behavior of wet soil-part ii: Dielectric mixing models. *Geoscience and Remote Sensing, IEEE Transactions on*, GE-23(1):35 –46, jan. 1985.

S.L. Durden, J.J. Van Zyl, and H.A. Zebker. Modeling and observation of the radar polarization signature of forested areas. *IEEE Transactions on Geoscience and Remote Sensing*, 27:290–301, May 1989.

M.A. El-Rayes and F.T. Ulaby. Microwave dielectric spectrum of vegetation-part i: Experimental observations. *Geoscience and Remote Sensing, IEEE Transactions on*, GE-25(5):541–549, Sept. 1987.

T. Elfouhaily and C-A. Guérin. A critical survey of approximate scattering wave theories from random rough surfaces. *journal Waves in Random and Complex Media*, 14:R1–R40, Oct. 2004.

Jiayuan Fang and Zhonghua Wu. Generalized perfectly matched layer – an extension of berenger's perfectly matched layer boundary condition. *IEEE microwave and guided wave letters*, 30: 4583–4588, 1999.

P. Ferrazzoli and L. Guerriero. Passive microwave remote sensing of forests: a model investigation. *IEEE Transactions on Geoscience and Remote Sensing*, 34:433–443, March 1996.

A. Franchois, Y. Pineiro, and R.H. Lang. Microwave permittivity measurements of two conifers. *IEEE Transactions on Geoscience and Remote Sensing*, 36:1384–1395, Sept. 1998.

Adrian K. Fung. *Microwave Scattering and Emission Models and Their Applications*. Artech House, 1994.

D.M. Gates. Water relations of forest trees. *IEEE Transactions on Geoscience and Remote Sensing*, 29:836–842, 1991.

Jianjun Guo, Leung Tsang, Kung-Hau Ding, A.T.C. Chang, and Chi-Te Chen. Frequency dependence of scattering by dense media of small particles based on monte carlo simulation of maxwell equations. *Geoscience and Remote Sensing, IEEE Transactions on*, 40(1):153–161, Jan 2002. ISSN 0196-2892. doi: 10.1109/36.981357.

M.T. Hallikainen, F.T. Ulaby, M.C. Dobson, M.A. El-Rayes, and Lil-Kun Wu. Microwave dielectric behavior of wet soil-part 1: Empirical models and experimental observations. *Geoscience and Remote Sensing, IEEE Transactions on*, GE-23(1):25 –34, jan. 1985.

A. Ishimaru. *Wave propagation and scattering in random media*, volume 2. Academic Press, 1978.

M.A. Karam and A.K. Fung. Electromagnetic scattering from a layer of finite randomly oriented, circular cylinders over a rough interface with application to vegetation. *Int. Journal of Remote Sensing*, 9:1109–1134, 1988.

M.A. Karam and A.K. Fung. Leaf-shape effects in electromagnetic wave scattering from vegetation. *IEEE Transactions on Geoscience and Remote Sensing*, 9:687–697, 1989.

G. Krieger and A. Moreira. Spaceborne bi- and multistatic sar : potential and challenge. In *Radar, Sonar and Navigation, Proceedings*, volume 153, pages 184–198, 2006.

T. Le Toan, A. Beaudoin, J. Riom, and D. Guyon. Relating forest biomass to sar data. *IEEE Transactions on Geoscience and Remote Sensing*, 30:403–411, March 1992.

P. Liang, L.E. Pierce, and M. Moghaddam. Radiative transfer model for microwave bistatic scattering from forest canopies. *IEEE Transactions on Geoscience and Remote Sensing*, 43: 2470–2483, Nov. 2005.

Yi-Cheng Lin and K. Sarabandi. Electromagnetic scattering model for a tree trunk above a tilted ground plane. *IEEE Transactions on Geoscience and Remote Sensing*, 33:1063–1070, July 1995.

Yi-Cheng Lin and K. Sarabandi. A monte carlo coherent scattering model for forest canopies using fractal-generated trees. *IEEE Transactions on Geoscience and Remote Sensing*, 37: 440–451, Jan. 1999.

J.M. Lopez-Sanchez, J.D. Ballester-Berman, and J. Fortuny-Guasch. Indoor wide-band polarimetric measurements on maize plants: a study of the differential extinction coefficient. *IEEE Transactions on Geoscience and Remote Sensing*, 44:758–767, 2006.

R.M. Lucas, A.C. Lee, and M.L. Williams. Enhanced simulation of radar backscatter from forests using lidar and optical data. *IEEE Transactions on Geoscience and Remote Sensing*, 44:2736–2754, Oct. 2006.

F. Marliani, S. Paloscia, P. Pampaloni, and J.A. Kong. Simulating coherent backscattering from crops during the growing cycle. *IEEE Transactions on Geoscience and Remote Sensing*, 40, 2002.

V.L. Mironov, M.C. Dobson, V.H. Kaupp, S.A. Komarov, and V.N. Kleshchenko. Generalized refractive mixing dielectric model for moist soils. *IEEE Transactions on Geoscience and Remote Sensing*, 42:773–785, April 2004.

G. Mur. Absorbing boundary condition for the finie-difference approxima- tion of the time-domain electromagnetics-field equations. *IEEE Transaction on electromagnetic compatibility*, 23:377–382, November 1981.

Classification of full polarimetric SAR-data using artificialneural networks and fuzzy algorithms. M. hellmann and g. jager and e. kratzschmar and m. habermeyer. In *International Geoscience and Remote Sensing Symposium (IGARSS)*, volume 4, pages 1995–1997. IEEE, 1999.

N.R. Peplinski, F.T. Uaby, and M.C. Dobson. Dielectric properties of soils in the 0.3-1.3-ghz range. *IEEE Transactions on Geoscience and Remote Sensing*, 33:803–807, May 1995.

E. Pottier, S. Cloude, I. Hajnsek, and T. Pearson. Polsarpro v2.0: the polarimetric sar data processing and educational toolbox. In *Geoscience and Remote Sensing Symposium (IGARSS)*, volume 5, pages 3173–3176. IEEE, 2005.

H. Pretzsch and M. Kahn. *Konzeption und Konstruktion von Wuchs- und Prognosemodellen für Mischbestnde in Bayern*. Chair of Forest Yield Science, Technische Universität München, 1998.

C. Proisy. *Apport des données radar à synthèse d'ouverture pour l'étude de la dynamique des écosystèmes forestiers*. Phd dissertation, Université Paul Sabatier Toulouse III — CESBIO, mars 1999.

R.D. De Roo, L. Munn, L.E. Pierce, A.Y. Nashashibi, F.T. Ulaby, and G.S. Samples. Spri: simulator of polarimetric radar images. *IEEE Transactions on Geoscience and Remote Sensing*, 38:252–261, Jan 2002.

C. Ruiz and P. Borderies. Sensitivity analysis for forest interferometric, polarimetric observables estimation. In *Proceeding of Polinsar 2005*. ESA, 2005.

S.S. Saatchi and K.C. McDonald. Coherent effects in microwave backscattering models for forest canopies. *IEEE Transactions on Geoscience and Remote Sensing*, 35:1032–1044, July 1997.

M. Saillard and A. Sentenac. Rigorous solutions for electromagnetic scattering from rough surfaces. *Waves Random Media*, 11:03–37, 2001.

K. Saleh, A. Porte, D. Guyon ans P. Ferrazzoli, and J.P. Wigneron. A forest geometric description of a maritime pine forest suitable for discrete microwave models. *Geoscience and Remote Sensing, IEEE Transactions on*, 43:2024–2035, Sept. 2007.

K. Sarabandi and A. Nashashibi. A novel bistatic scattering matrix measurement technique using a monostatic radar. *IEEE Transactions on Antennas and Propagation*, 44:41–50, Jan. 1996.

T. Seifert. *Integration of wood quality, grading and bucking in forest growth models sensitive to silvicultural treatment.* Phd dissertation, Munich University of Technology (TUM), 2003.

B.L. Shrestha, H.C. Wood, and S. Sokhansanj. Modeling of vegetation permittivity at microwave frequencies. *Geoscience and Remote Sensing, IEEE Transactions on*, 45(2):342 –348, feb. 2007.

A Stogryn. Electromagnetic scattering from rough finitely conducting surfaces. *Radio Science*, 2(9):415–428, 1967.

L. Thirion, E. Colin, and C. Dahon. Capabilities of a forest coherent scattering model applied to radiometry, interferometry, and polarimetry at p- and l-band. *IEEE Transactions on Geoscience and Remote Sensing*, 44:849–862, April 2006.

L. Tsang and J.A. Kong. *Scattering of Electromagnetic Waves*, volume Theories and applications of *Remote Sensing and Digital Image Processing.* Wiley Series, 2000a.

L. Tsang and J.A. Kong. *Scattering of Electromagnetic Waves*, volume Advanced Topics. Wiley Series, 2000b.

L. Tsang, J.A. Kong, and R. Shin. *Theory of Microwave remote sensing.* Wiley Interscience, 1985.

L. Tsang, C.H. Chan, J.A. Kong, and J. Joseph. Polarimetric signatures of a canopy of dielectric cylinders based on first and second order vector radiative transfer theory. *Journal of Electromagnetic Waves and Applications*, 6:19–51, 1992.

Leung Tsang, Jin Pan, Ding Liang, Zhongxin Li, D.W. Cline, and Yunhua Tan. Modeling active microwave remote sensing of snow using dense media radiative transfer (dmrt) theory with multiple-scattering effects. *Geoscience and Remote Sensing, IEEE Transactions on*, 45(4): 990–1004, April 2007. ISSN 0196-2892. doi: 10.1109/TGRS.2006.888854.

F.T. Ulaby and M.A. El-Rayes. Microwave dielectric spectrum of vegetation - part ii: Dual-dispersion model. *Geoscience and Remote Sensing, IEEE Transactions on*, GE-25(5):550–557, Sept. 1987.

F.T. Ulaby, R.K. Moore, and A.K. Fung. *Microwave Remote Sensing: Active and Passive*, volume III, Volume Scattering and Emission Theory of *Advanced Systems and Applications.* Artech House, 1986.

F.T. Ulaby, K. Sarabandi, K. McDonald, M. Whitt, and M.C. Dobson. Microwave canopy scattering model. *International Journal of Remote Sensing*, 11:1223–1254, 1990.

L. Villard and P. Borderies. Backscattering border effects for forests at C-band. *PIERS Online (Progress in Electromagnetics Research Journal)*, 3:731–735, 2007.

L. Villard, P. Borderies, P. Dubois Fernandez, and J.F. Nouvel. Bistatic border effects modelling in forest scattering. In *International Geoscience and Remote Sensing Symposium (IGARSS).* IEEE, 2007.

Feinian Wang and K. Sarabandi. A physics-based statistical model for wave propagation through foliage. *Antennas and Propagation, IEEE Transactions on*, 55(3):958–968, March 2007. ISSN 0018-926X. doi: 10.1109/TAP.2007.891841.

K.F. Warnick and W.C. Chew. Numerical simulation methods for rough surface scattering. *Waves Random Media*, 11:1–30, 2001.

M.L. Williams and N. Harris. Demonstration of reduced false alarm rates using simulated l-band polarimetric sar imagery of concealed targets. In *Proceedings of the International Radar Conference*, pages 535–540. IEEE, 2003.

I.H. Woodhouse, I. Wallington, and E.D. Turner. Edge effects on tree height retrieval using x-band interferometry. *Geoscience and Remote Sensing, IEEE Letters*, 3, July 2006.

K.S. Yee. Numerical solution of initial boundary value problems involving maxwell¿s equations in isotropic media. *IEEE Transactions Antennas and Propagation*, 14:302–307, 1966.

A. I. Zakharov, L. Zakharova, V. P. Sinilo, and M. V. Sorochinsky. Monitoring of the forest state in the chernobyl area using radar. In *International Geoscience and Remote Sensing Symposium (IGARSS)*, volume 4, pages 2472–2476. IEEE, 2003.

Chapter 3

Remarkable Properties of Bistatic Scattering

Contents

Introduction

With the aim of a better understanding and rather for a better use of forest scattering behaviour – naturally in the framework of its characterization from radar measurements – the present chapter is dedicated to explain and set forth remarkable properties brought by the bistatic geometry. This study comes thus before the following chapters about detection applications, the radar intensity sensitivity to forest biomass and bistatic vectorial interferometry. As mentioned previously, a extensive number of studies about forest scattering in monostatic can be found in the literature whereas the investigation of many points remains in bistatic, and all the more when dealing with coherent models. Concerning the most recent works on the topic, our approach can be compared to the simulations proposed by [Thirion et al., 2006; Thirion-Lefevre and Colin-Koeniguer, 2008] whereas studies in [Ferrazzoli and Guerriero, 1996; Liang et al., 2005] are based on incoherent ones.

Within this scope of scattering analysis, the first point at issue concerns the observables at our disposal. As presented in the first chapter, the search for the most relevant representation of the measures set brings us to distinguish the so called points like scatterers from distributed targets for which the second order statistics (i.e covariance, coherence matrices) are more appropriated than the simple scattering matrix. As far as forest scattering is concerned, the observables ensued from the latter approach will be naturally preferred, although it will be shown that specific scattering properties stem from the intrinsic behaviour of non isotropic SRO (Symmetry of Revolution Object), especially with orientation effects. In this connection, many questions remain about the impacts of a structured and/or oriented medium on bistatic observables and the subsequent potential use of these properties within a retrieval scheme. As a basis statement, we can naturally refer to the monostatic configuration and the standard approach consisting in the association of an orientation angle to every scatterer for which a polarization basis enables to cancel the cross polarization term. Since most of the natural scatterers verify this property, this technique is quite versatile although limited by the retrieval of an angle defined within the incident wave plane which do not correspond to the 'true' target orientation (i.e independently from the radar coordinate system, for instance with Euler angles). As an example, the single retrieved angle resulting from a titled surface (i.a [Schuler et al., 1996]) naturally does not enable to provide the two Euler angles required to characterize completely the three dimensional problem. Apart from surfaces study, another stringent assumption lies also in a point like scatterer behaviour, which is far from obvious in SAR images. Indeed, the retrieval angle technique mostly consists first in a detection approach of the so-called CS – Coherent Scatterer – as described in [Souyris et al., 2003; Schneider et al., 2006] which are based on the use of spectral sub-look within the azimuthal compression process (to minimize the distributed targets contribution which will vanish with a reconstructed Doppler spectrum, unlike shinning point like scatterer) This approach however can be omitted with nowadays high resolution system which are more favourable to dominant scatterer within the pixel, mostly due to a strong backscattering enhancement stemming from vertical structures, widely present over urban area (cf. [Iribe and Sato, 2007]) but also with trunks near clearings.

This brings us to the extended approach to bistatic and rise the question of the matching between the polarization basis rotations – associated to a specific **[S]** matrix and the target orientation. The additional complexity can be already established since two polarization basis are involved – with respect to the transmitter and receiver positions – and since the scattering matrix have one more freedom degree, with two possibly different cross polarization terms, leading to singular rather than eigenvalue decomposition.

Notwithstanding, an extensive work has been achieved concerning the generalization of polarization theory to the bistatic configuration. This generalization has come also with a thorough mathematical formulation, which is quite fruitful in algebra, especially concerning Lie groups theory. For a complete survey, one can refer to [Cloude, 1986], also well synthesize in [Kostinski and Boerner, 1986] concerning the most fundamental applications in the radar field. In addition, this extension brought closer the theoretical aspects of radar and optical polarimetry, the bistatic configuration being actually usual for the latter. This link has been emphasized in [Hubbert, 1994] introducing various concepts to clarify the different approaches such as OPT (Optical Polarization Theory) and the SNPT (Specular Null Polarization theory), closer to TPT (Transmission Polarization Theory) for forward scattering, alternatively to the commonly used KPT (Kennaugh Polarization Theory) for the backscattering case. Although subject to various polemics (see for instance [Lüneburg and Hubbert, 1997]), the problem's cornerstone lies essentially in the change introduced with the afore-mentioned FSA or BSA conventions (beyond the rotation basis, the time reversal should also be considered), the former being natural for an

observer following the electromagnetic wave, whereas the latter using sensor coordinates brings convenient simplifications.

As far as conventions matters, the bistatic geometry rises also the question of the cross polarization definition, which originates also different point of view. Actually, if the basic definition (according to I3E standards) considered the cross polarization to be the receiving polar state orthogonal to a reference one, the latter is still subject to various possible choice, especially within a bistatic geometry – transmitting or receiving sensor type of coordinates, rectangular, spherical or linked to antennas pattern. This issue has indeed been particularly tackled in the field of radar antennas, with the use of the various Ludwig's polarizations (cf. [Ludwig, 1973; Roy and Shafai, 2001]) which main interest lies in the minimization of geometrical effects only, in aids of electromagnetic ones. Though different but within the same purpose, this aspect will be stressed in the following section (3.2.3), especially regarding symmetry properties biased by the bistatic geometry, set forth in [Nashashibi and Ulaby, 2007] and for which the authors coined the term 'polarization artefacts'.

Prominent in the applications of radar polarization theory, the use of the optimal polarization basis with the aim of characterizing a region/target of interest is particularly efficient and makes the quad pol acquisition. The optimization criteria consists in minimizing a given contribution (and acts actually like a filter) or alternatively in maximizing specific radar measures, typically for detection with the power of a given target over the vegetation clutter ratio but also (more recently) with Pol or Pol-InSAR coherences (cf. [Colin et al., 2006; Pascal et al., 2002]). Concerning the basis of power polarimetric optimization, one can refer to forerunner works in [Huynen, 1970] conveniently associated to the successful Poincaré sphere representation, in order to emphasize the various polarization states. Characteristic points upon the sphere have been also set forth in the bistatic configurations, still in order to represent efficiently specific polarizations states and the resulting power (cf. [Davidovitz and Boerner, 1986; Czyz, 1991; Germond et al., 1997]). The underlying algebra principles at the origin of this representation will be briefly reminded in the following section about the various type of radar observables, thorough details can be founded in [Germond, 1999]. More recently, a more exhaustive generalization of the Huynen theory has been given in [Titin-Schnaider, 2008] to characterize the coherent scattering mechanisms in bistatic and exhibit their canonical **[S]** matrices. The cornerstone of this extension consists in the singular value decomposition to diagonalize the scattering matrix, non symmetric anymore – and leads with two different unitary transforms to different optimal transmitting and receiving polarizations states. For incoherent (i.e random) mechanisms, the power optimization in the general bistatic case is more difficult to achieve and analytical solutions can be derived only with additional constraints on the transmitted and received polarizations as shown in [Titin-Schnaider, 2007] – partly based on the monostatic approach given by [Lüneburg et al., 1991]). Indeed, as stressed previously, distributed targets imply to work on second order statistics matrices (Kennaugh, Muller, covariance or coherency), hence a mathematical formulation more complex coming with the matrix dimension increase. Notwithstanding, as far as natural media are hereafter concerned, the spatial azimuthal and reflection symmetries impact – jointly to the temporal one – on the just mentioned second order matrices will be stressed in § 3.1.2, after the first subsection (3.1.1) reminding the fundamental definitions and conventions used afterwards (particularly important for polarizations basis change). It will be shown also that these simplifications ease also the generalization of the widely used Cloude-Pottier classification in bistatic (cf. [Cloude, 2005]). Besides, a alternative and recent method proposed in [Souyris and Tison, 2007] will be only briefly detailed since its exploitation at that time hasn't been finalized, though potentially promising as a classification method in bistatic.

Next, on account of these theoretical considerations, the scattering behaviour analysis will be

assessed with the aim of setting forth remarkable properties entailed by the bistatic configuration, liable to be permanently encountered with forest media. Hence the study of generic cases such as a volume filled with cylindric-shape scatterers. The resulting direct scattering will be studied in section 3.2 whereas the coupling terms in 3.3, according for both cases a particular importance to the scatterers orientation effects.

The emphasized properties will then be useful not only to interpret recurrent phenomenons in bistatic through the following chapters but also to take advantage of these specific behaviours for retrieval strategies.

3.1 Bistatic Observables : Theoretical Aspects

3.1.1 Polarization Theory : Intrinsic Specificities of Bistatic

Within the scope of studying the radar polarimetric intensities in the bistatic case, this subsection aims at clarifying basic considerations – quite common in monostatic – concerning polarization theory. As mentioned in the introduction, the overall monostatic mindset in the radar community introduces many specific definitions which may be confusing and not well-adapted to the more general bistatic case.

First of all, the framework of monochromatic plane waves will be considered, so that a em field solution of the free-space wave equation can be expressed as :

$$\vec{E}(r,t) = E_{0q}\cos(wt - kr + \delta_q)\hat{q} + E_{0p}\cos(wt - kr + \delta_p)\hat{p} \tag{3.1}$$

with $\hat{r} = \hat{q} \times \hat{p}$ has the propagation direction and $(\hat{p}, \hat{q})$ the equi-phase plane, which can be transposed to the complex notation :

$$\vec{E}(r,t) = Re\{e^{j\delta_q}e^{j(wt-kr)}\begin{bmatrix} E_{0q} \\ E_{0p}e^{j\delta} \end{bmatrix}\} = Re\{e^{j\delta_q}e^{j(wt-kr)}[\ E(r=r_0)]\} \tag{3.2}$$

where the proper and relative phase are emphasized respectively with δ_p and $\delta = \delta_p - \delta_q$ (the latter being also commonly called the polarimetric phase difference).

The extremity of the field vector $\vec{E}(r,t)$ describes while t varies the so-called polarization ellipse within a given plane at $r = r_0$. Without loss of generality, the wave propagation terms concerning r and t can be left aside which bring us to the Jones vector :

$$\vec{E} = e^{j\delta_q}\begin{bmatrix} E_q \\ E_p e^{j\delta} \end{bmatrix} = \begin{bmatrix} \mathcal{J}_q \\ \mathcal{J}_p \end{bmatrix} \tag{3.3}$$

The polarization ellipse is characterized by its orientation noted χ, its ellipticity τ, proper phase δ_q, phase difference δ and amplitude $A^2 = E_q^2 + E_p^2$. These geometrical parameters can then be used to expressed more explicitly the Jones vector :

$$\vec{E} = Ae^{j\delta_q}\begin{bmatrix} \cos\chi & -\sin\chi \\ \sin\chi & \cos\chi \end{bmatrix}\begin{bmatrix} \cos\tau \\ j\sin\tau \end{bmatrix} \tag{3.4}$$

which can be also written as :

$$\vec{E} = A\begin{bmatrix} \cos\chi & -\sin\chi \\ \sin\chi & \cos\chi \end{bmatrix}\begin{bmatrix} \cos\tau & j\sin\tau \\ j\sin\tau & \cos\tau \end{bmatrix}\begin{bmatrix} e^{-j\delta_q} & 0 \\ 0 & e^{j\delta_q} \end{bmatrix}\begin{bmatrix} 1 \\ 0 \end{bmatrix} \tag{3.5}$$

This latter expression enables to introduce the special unitary group (**SU(2)**) of the Pauli matrices, reminded below :

$$\sigma_0 = \begin{bmatrix} 1 & 0 \\ 0 & 1 \end{bmatrix}, \quad \sigma_1 = \begin{bmatrix} 1 & 0 \\ 0 & -1 \end{bmatrix}, \quad \sigma_2 = \begin{bmatrix} 0 & 1 \\ 1 & 0 \end{bmatrix}, \quad \sigma_3 = \begin{bmatrix} 0 & -j \\ j & 0 \end{bmatrix}, \tag{3.6}$$

SU(2) is built from the unitary matrices by means of the matrix exponential function as follows :

$$e^{j\nu[\sigma_p]} =_{0\leq p\leq 3} \cos\nu[\sigma_0] + j\sin\nu[\sigma_p\ ]$$

Hence the Jones vector expression in equation 3.5 can be simplified into the form :

$$\vec{E} = Ae^{-j\chi[\sigma_3]}e^{j\tau[\sigma_2]}e^{-j\delta_q[\sigma_1]}\hat{q}$$

Also simplified is the paramount relation concerning polarization basis change. Indeed, the general transformation from a given orthogonal polarization basis (p_a, p_b) to another one (p_c, p_d) that is (for contravariant components) :

$$[p_a, p_b]^t = \mathcal{U}_{(a,b)}^{(c,d)} \cdot [p_c, p_d]^t$$

can be viewed as the one from (p_a, p_b) to the canonical one, then from the canonical one to (p_a, p_b), hence :

$$\mathcal{U}_{(a,b)}^{(c,d)} = e^{-j\chi_a[\sigma_3]}e^{j\tau_a[\sigma_2]}e^{-j\delta_{qa}[\sigma_1]} \cdot e^{j\delta_{qc}[\sigma_3]}e^{-j\tau_c[\sigma_2]}e^{+j\chi_c[\sigma_3]}$$

We insist on the fact that $\mathcal{U}$ is thereby unitary.

In the case of distributed target, we've seen in the first chapter that second order statistics are more relevant to interpret the speckled received field so that the following wave coherency matrix can be build from the Jones vector $\vec{\mathcal{J}}$:

$$\mathcal{C} = \langle \vec{math}calJ \cdot \vec{math}calJ^{\dagger} \rangle$$

The decomposition of $\mathcal{C}$ onto the Pauli matrices leads to the so-called Stokes vector which can thus be expressed as :

$$\vec{\mathcal{G}} = \begin{bmatrix} g_0 \\ g_1 \\ g_2 \\ g_3 \end{bmatrix} = \begin{bmatrix} \langle |E_q|^2 \rangle + \langle |E_p|^2 \rangle \\ \langle |E_q|^2 \rangle - \langle |E_p|^2 \rangle \\ 2\langle 2Re\{E_q E_p^*\} \rangle \\ \text{-}2\langle Im\{E_q E_p^*\} \rangle \end{bmatrix}$$

which can be also expressed using the polarization ellipse parameters or the polarization ratio ($\rho = \mathcal{J}_p/\mathcal{J}_q$) : or the polarization ellipse parameters :

$$\vec{\mathcal{G}} == \begin{bmatrix} A^2 \\ A^2\cos 2\chi\cos 2\tau \\ A^2\sin 2\chi\cos 2\tau \\ A^2\sin 2\tau \end{bmatrix} = \begin{bmatrix} 1+|\rho|^2 \\ 1-|\rho|^2 \\ 2Re(\rho) \\ 2Im(\rho) \end{bmatrix}$$

Prominent among these radar observables for distributed target, the degree of wave coherency can be also defined :

For fully polarized wave, this degree equals so that $\mathcal{C}$ is not invertible which implies also :

$$g_0^2 - (g_1^2 + g_2^2 + g_3^2) = \det(\mathcal{C}) = 0$$

On top of providing an efficient formalism, the use of the Pauli matrices group enables also to transpose the characterization of polarization state from the complex domain to the real three dimensional one. Indeed, thanks to the homomorphism between SU(2) and O(3) – the group of orthogonal rotation –, any combination of the Pauli matrices (that is any polarization state) can be represented by an unique combination of orthogonal rotation in $\Re^3$. Hence the famous geometrical representation of the polarization state onto the Poincaré sphere (of radius g_0 and position according to $2\chi, 2\tau$ as the classical spherical angles, sometimes also turn into the Deschamps parameters), particularly efficient to emphasize specific relations between different polarization basis (such as the Huynen Fork). As mentioned in the introduction, theoretical studies about the extension in bistatic of the polarization state characterization onto the Poicaré sphere can be found in [Davidovitz and Boerner, 1986; Czyz, 1991; Germond, 1999]. Besides, on can refer to [Cloude, 1986] concerning other very well emphasized relevant applications of Pauli groups or Lie algebra in electromagnetism.

Furthermore, in active and full polarimetric radar remote sensing, the complex 2*2 scattering matrix is mostly used since it synthesizes efficiently the 7 independent measures – 8 minus the reference phase (and 5 in monostatic) – as reminded below :

$$\vec{E}^s_{\hat{q}}(\theta_s,\varphi_s) = |\vec{E}^s(\theta_s,\varphi_s)| \begin{bmatrix} \hat{q}\cdot\hat{v_s} \\ \hat{q}\cdot\hat{h_s} \end{bmatrix} = \frac{1}{r_2^2}\cdot \begin{bmatrix} s_{v_sv_i} & s_{v_sh_i} \\ s_{h_sv_i} & s_{h_sh_i} \end{bmatrix} \cdot |\vec{E}^i(\theta_i,\varphi_i)| \begin{bmatrix} \hat{p}\cdot\hat{v_i} \\ \hat{p}\cdot\hat{h_i} \end{bmatrix} \tag{3.7}$$

by means of the canonical linear horizontal and vertical polarization basis, which nevertheless can be defined according to several conventions, among which the FSA (Forward Scattering Alignment) or the SSA (Specular Scattering Alignment) are generally preferred in bistatic to the BSA (Backscattering) one defined to match the monostatic case. The FSA or the SSA convention will be thus widely used in this study and are reminded in figure 3.1. The BSA convention (see [Ulaby et al., 1981]) can defined from the FSA using a time reversal operation and an horizontal coordinate change, since their respective scattering vectors $\hat{k}_s$ and $\hat{h}_s$ are opposite, that is :

$$[S]_{FSA} = \begin{bmatrix} 1 & 0 \\ 0 & -1 \end{bmatrix} \cdot [S]^*_{BSA} \tag{3.8}$$

In addition, since the FSA is defined according to the wave coordinates, the scattering matrices corresponding to two different polarization basis are logically †equivalent, that is :

$$S_{(c_i,d_i),(c_s,d_s)} = \mathcal{U}^{(c_s,d_s)}_{(a_s,b_s)})^\dagger \cdot S_{(a_i,b_i),(a_i,b_i)} \cdot \mathcal{U}^{(c_i,d_i)}_{(a_i,b_i)}$$

whereas they are ^{t}equivalent in BSA. Indeed, as a paramount verification, the received voltage (V_r) must be invariant by basis change. In FSA :

$$\begin{aligned} V_r^c &= \mathcal{J}_r^c)^\dagger E_s^c \\ &= (\mathcal{U}^\dagger \mathcal{J}_r)^\dagger (\mathcal{U}^\dagger E_r) \\ &= \mathcal{J}_r^\dagger \mathcal{U}\mathcal{U}^\dagger E_s \\ &= V_r \end{aligned} \tag{3.9}$$

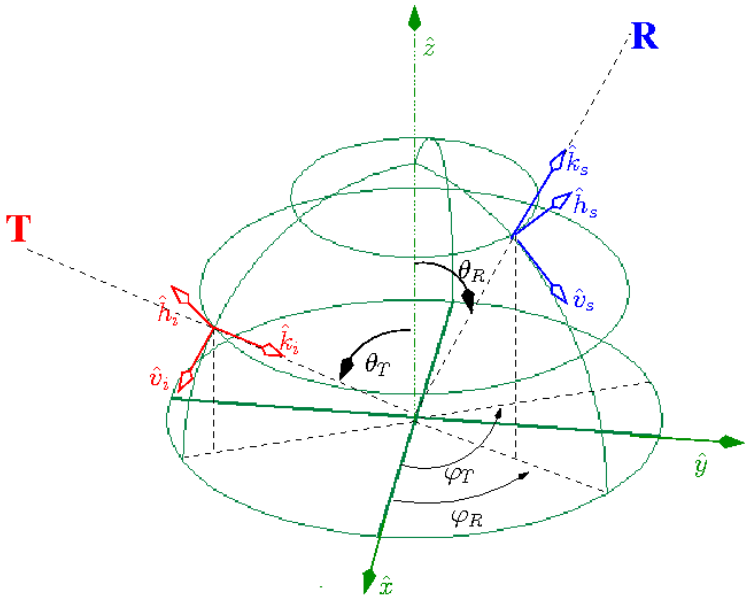

Figure 3.1: Transmit $(\hat{k}_i, \hat{v}_i, \hat{h}_i)$ and receive $(\hat{k}_s, \hat{v}_s, \hat{h}_s)$ polarization bases according to the FSA convention from which the SSA one differs only from $\theta_{\mathrm{T}}^{\mathrm{SSA}} = \pi - \theta_{\mathrm{T}}^{\mathrm{FSA}}$.

In BSA :

$$\begin{aligned} V_r^c &= \mathcal{J}_r^c)^{\dagger *} E_s^c \\ &= \left(\mathcal{U}^t \mathcal{J}_r\right)^t \left(\mathcal{U}^t E_r\right) \\ &= \mathcal{J}_r^t \mathcal{U}^* \mathcal{U}^t E_s \\ &= \mathcal{J}_r^t \mathcal{U}^* \left(\mathcal{U}^*\right)^{-1} E_s \\ &= V_r \end{aligned} \tag{3.10}$$

In the case of distributed targets, the link between the incident and the scattered Stokes vector is given by the so-called Muller (M) or Kennaugh (K) matrices, according respectively to the FSA or to the BSA convention. The polarization basis transformation can be conducted through the scattering matrix – expressed in the new basis – since both Muller and Kennaugh matrices can be derived from S as follows :

$$[M] = [\Lambda] \cdot \left([S_{\mathrm{FSA}}] \otimes [S_{\mathrm{FSA}}^*]\right)[\Lambda] \tag{3.11}$$

with $\otimes$ as the Kronecker product for matrices and :

$$[\Lambda] = \frac{1}{\sqrt{2}} \begin{bmatrix} 1 & 0 & 0 & 0 \\ 0 & 0 & 1 & -j \\ 0 & 0 & 1 & j \\ 1 & -1 & 0 & 0 \end{bmatrix}$$

Likewise for the Kennaugh matrix :

$$[K] = [\Lambda] \cdot \left([S_{\mathrm{BSA}}] \otimes [S_{\mathrm{BSA}}^*]\right)[\Lambda] \tag{3.12}$$

Whether in the case of the Muller or the Kennaugh matrix, the 4*4 real matrix coefficients naturally do not represent an additional information in comparison with the 7 independent parameters within the Sinclair matrix. As a result, 9 (16-7) independent equations can be written between the Muller or Kennaugh coefficients which are known as the target equations and used for the study of desoriented targets with the Huynen parameters (cf. [Huynen, 1970]).

Still for the purpose of distributed targets characterization, S. Cloude (cf. [Cloude, 2001]) introduced the covariance [C] or the coherency [T] matrices which by construction, present the paramount advantage of being Hermitian, definite semi-positive. Indeed :

$$T = \langle k_{4\mathrm{P}}, k_{4\mathrm{P}}^{\dagger} \rangle \tag{3.13}$$

or :

$$C = \langle k_{4\mathrm{L}}, k_{4\mathrm{L}}^{\dagger} \rangle \tag{3.14}$$

in which $k_{4\mathrm{L}}$, $k_{4\mathrm{P}}$ correspond to the decomposition of the scattering matrix respectively according to the lexicographic basis or to the Pauli one, that is in the BSA convention :

$$k_{4\mathrm{L}} = [s_{hh}, s_{hv}, s_{vh}, s_{vv}]^t \tag{3.15}$$

$$k_{4\mathrm{P}} =_{\mathrm{sensor}} [s_{hh} + s_{vv}, s_{hh} - s_{vv}, s_{hv} + s_{vh}, j(s_{hv} - s_{vh})]^t \tag{3.16}$$

Though equivalent, especially after the Hermitian product, the scattering vector $k_{4\mathrm{P}}$ is mostly used since it corresponds already to a physical decomposition between common scattering mechanism, that is the iso-surface one, the iso-dihedral, the 45^o-titled iso-dihedral and the iso cross-polarizer (cf. [Cloude, 2001]).

These scattering vectors can naturally be derived with respect to the FSA convention :

$$k_{4\mathrm{P}} =_{\mathrm{wave}} [s_{hh} - s_{vv}, s_{hh} + s_{vv}, s_{hv} - s_{vh}, j(s_{hv} + s_{vh})]^t \tag{3.17}$$

which respective component correspond still to the same mechanisms since the phase distribution between horizontal and vertical polarization are also opposite. Indeed, as stated in chapter 2, the phase distribution of $\langle s_{qq} s_{qp}^* \rangle$ or $\langle s_{qp} s_{pq}^* \rangle$ are centered on π for odd interaction and on 0 for even ones in FSA and conversely in BSA, hence the maximization of these mechanisms with such combination of polarization.

Also useful in the following, the matrices [T] or [C] expression in a new polarization basis can be derived naturally through the intermediate of the new Sinclair matrix. For the covariance matrix, a more direct relation can be derived using the $vect_l(\,)$ operator (for which we stress the difference with k_{4L}) :

$$vect_l([S]) = [s_{hh}, s_{vh}, s_{hv}, s_{vv}]^t$$

and the relation :

$$\begin{aligned} [S^c] &= \mathcal{U}_s^{\dagger} \cdot [S_a] \cdot \mathcal{U}_i \\ \Rightarrow vect_l([S^c]) &= \left(\mathcal{U}_i^t \otimes \mathcal{U}_s^{\dagger} \right) \cdot vect_l([S^a]) \end{aligned} \tag{3.18}$$

As proposed in [Cloude, 2005], the extension of the Cloude-Pottier decomposition to the bistatic case does not rise any difficulty (at least from the mathematical point of view). As mentioned above, the bistatic coherency matrix – being Hermitian positive semi-definite – can be advantageously diagonalized, which brings us to the following decomposition :

$$[T] = \mathcal{U}_4 \cdot \begin{bmatrix} \lambda_1 & 0 & 0 \\ 0 & \lambda_2 & 0 \\ 0 & 0 & \lambda_3 \end{bmatrix} \cdot \mathcal{U}_4^{\dagger} = \sum_{i=0}^{4} \lambda_i \hat{e}_i \hat{e}_i^{\dagger} \tag{3.19}$$

with the positive eigenvalues $\lambda_1, \lambda_2, \lambda_3, \lambda_4$ associated to the orthogonal eigenvectors $\hat{e}_1, \hat{e}_2, \hat{e}_3, \hat{e}_4$. The latter can be also expressed with the 7 following independent parameters :

$$\hat{e}_i = \begin{bmatrix} \cos\alpha_i e^{j\Phi_1} \\ \sin\alpha_i \cos\beta_i e^{j\Phi_2} \\ \sin\alpha_i \sin\beta_i \cos\gamma_i e^{j\Phi_3} \\ \sin\alpha_i \sin\beta_i \sin\gamma_i e^{j\Phi_4} \end{bmatrix} \tag{3.20}$$

Considering a Bernoulli process for the realization of these mechanisms, the following classification indicators can finally be built :

$$\begin{aligned} p_i &= \frac{\lambda_i}{\sum_{s=0}^{4} \lambda_s} \\ \bar{\alpha} &= \sum_{i=0}^{4} p_i \alpha_i \\ \bar{\beta} &= \sum_{i=0}^{4} p_i \beta_i \\ \bar{\gamma} &= \sum_{i=0}^{4} p_i \gamma_i \end{aligned} \tag{3.21}$$

together with the entropy H and anisotropy A :

$$\begin{aligned} H &= -\sum_{i=0}^{4} p_i log_4 p_i \\ A &= \frac{\lambda_2 - \lambda_3}{\lambda_2 + \lambda_3} = \frac{p_2 - p_3}{p_2 + p_3} \end{aligned} \tag{3.22}$$

from which the 'H/A/α' algorithm – widely used in monostatic for polarimetric classification – is based (cf. Cloude and Pottier [1996]).

3.1.2 Fundamental Relations Ensued from the Medium Symmetries

The purpose of this subsection is to point out the impact of the various symmetries characterizing the medium on the various radar observables, reminded in previous §. This is indeed particularly relevant since forest lands as well as most of natural media exhibit important symmetry properties. Although spatial or temporal symmetries can be distinguished, their link is actually very close in the case of reciprocal medium, as it will be pointed out below. For the sake of clarity, geometrical definitions often used afterwards will be detailed. First, the employed notation $\mathcal{P}_{\hat{\eta}}$ refers to the plane being normal to the unitary vector $\hat{\eta}$. The other notation $\mathcal{P}_{\perp}^{\varphi}$ corresponds to a plane orthogonal to the reference horizontal one $(\hat{x}, \hat{y})$ and will be more precisely defined in section 3.2.

The following unitary vectors are also introduced as well as the resulting planes :

$$\begin{aligned}
&\hat{\beta} = \frac{\hat{k}_s - \hat{k}_i}{|\hat{k}_s - \hat{k}_i|} \text{ the bisectrix vector and} \\
&\quad \mathcal{P}_{\hat{\beta}} \text{ the ellipsoid or equirange tangential plane} \\
&\hat{\alpha} = \frac{\hat{k}_i \times \hat{k}_s}{|\hat{k}_i \times \hat{k}_s|} \text{ and } \mathcal{P}_{\hat{\alpha}} \text{ the bistatic or the scattering plane} \\
&\hat{\delta} = \hat{\beta} \times \hat{\alpha} \text{ and } \mathcal{P}_{\hat{\delta}} \text{ the bisectrix plane}
\end{aligned} \tag{3.23}$$

As shown in [Hulst, 1981], three specific geometrical transformations can be pointed out for which the resulting scattering matrix can be expressed simply with the coefficients of the original one :

- the transformation which consists in the orthogonal rotation of π around the bisectrix $\hat{\beta}$ so that the incident scattering vectors $\hat{k}_i$ and $\hat{k}_s$ are exchanged respectively into $-\hat{k}_s$ and $-\hat{k}_i$, hence the obtained 'reciprocal position'.
- the transformation which mirrors the problem with respect to the scattering/bistatic plane $\mathcal{P}_{\hat{\alpha}}$.
- the mirror transformation with respect to the bisectrix plane $\mathcal{P}_{\hat{\delta}}$.

Considering now the following scattering matrix of original problem :

$$[S] = \begin{bmatrix} s_1 & s_2 \\ s_3 & s_4 \end{bmatrix} \tag{3.24}$$

the point at issue is thus to derive the ones matching the transformed problem, noted S_{π}, $S_{\hat{\alpha}}$, $S_{\hat{\delta}}$.

In the case of the former one, the reciprocal transformation, the reciprocity theorem for vector waves will be naturally used. Among its various expressions resulting from several possible demonstrations – see for instance [Morse and Feshback, 1953] as a well application of the variational principle in electromagnetism – its formulation derived from the antennas field of study gives :

$$\iiint_{(V)} I_A^t \cdot E_s^B - I_B^t \cdot E_s^A \; dV = 0 \tag{3.25}$$

in which $E_s^A(\vec{r}_{\mathrm{B}})$ is the scattered field due to the current I_A at $\vec{r}_{\mathrm{A}}$ and similarly for E_s^B and I_B. Considering Dirac distributions for the currents and the scattering matrix formalism with respect to sensor coordinates (BSA), we can write :

$$\begin{aligned} I_B^t \cdot E_s^A &= I_A^t \cdot E_s^B \\ I_B^t \cdot S(\hat{k}_i, \hat{k}_s) &= I_A^t \cdot S(-\hat{k}_s, -\hat{k}_i) \\ &= V \end{aligned} \tag{3.26}$$

Theses quantities (voltage V) being scalar, $V = V^t$ brings us to :

$$S(\hat{k}_i, \hat{k}_s) = S^t(-\hat{k}_s, -\hat{k}_i) \tag{3.27}$$

and the famous result in monostatic :

$$\begin{aligned} s_{vh}(\hat{k}_i, \hat{k}_s) &= s_{hv}(-\hat{k}_s, -\hat{k}_i) \\ &= s_{hv}(\hat{k}_i, \hat{k}_s) \end{aligned} \tag{3.28}$$

Equation 3.27 can be also expressed with respect to the FSA convention :

$$\begin{bmatrix} 1 & 0 \\ 0 & -1 \end{bmatrix} \cdot S(\hat{k}_i, \hat{k}_s) = \begin{bmatrix} 1 & 0 \\ 0 & -1 \end{bmatrix} \cdot S^t(-\hat{k}_s, -\hat{k}_i) \tag{3.29}$$

hence the reciprocity relation for scattering matrix according to wave coordinates :

$$S(\hat{k}_i, \hat{k}_s) = -S^t(-\hat{k}_s, -\hat{k}_i) \tag{3.30}$$

and the resulting form for S_π :

$$[S_\pi] = \begin{bmatrix} s_1 & -s_3 \\ -s_2 & s_4 \end{bmatrix} \tag{3.31}$$

With the second transformation, we have to consider the mirrored target with respect to the, the scattering problem is thus the same for the co-polarizations whereas for the cross ones, only the direction of the horizontal polarizations is reversed, hence :

$$[S_{\hat{\alpha}}] = \begin{bmatrix} s_1 & -s_2 \\ -s_3 & s_4 \end{bmatrix} \tag{3.32}$$

Finally, it can be judiciously noted that the latter transformation results from the applications of both former reciprocal and reflection ones that :

$$[S_{\hat{\delta}}] = \begin{bmatrix} s_1 & s_3 \\ s_2 & s_4 \end{bmatrix} \tag{3.33}$$

Knowing from now on the scattering matrix expressions resulting from the geometrical transformations, it is straightforward to derive the relations corresponding to the others radar observables (T, C, M, K), on account of their possible derivations from [S].

As a example of importance, the coherency matrix T for a reciprocal media can be written as the superposition of its two states : the one corresponding to the original targets and the one

to their reciprocal position. Considering then T_o and T_π deduced respectively from S_o and S_π it turns out that :

$$[T] = [T_o] + [T_\pi] = \begin{bmatrix} t_{11} & t_{21}^* & t_{31}^* & 0 \\ t_{21} & t_{22} & t_{32}^* & 0 \\ t_{31} & t_{32} & t_{33} & 0 \\ 0 & 0 & 0 & t_{44} \end{bmatrix}$$

hence the 3 important relations for such media :

$$\begin{aligned} \langle j(s_{hv} + s_{vh})(s_{hh} - s_{vv})^* \rangle &= 0 \\ \langle j(s_{hv} + s_{vh})(s_{hh} + s_{vv})^* \rangle &= 0 \\ \langle j(s_{hv} + s_{vh})(s_{hv} - s_{vh})^* \rangle &= 0 \end{aligned} \tag{3.34}$$

Similarly, the coherency matrix T for a media verifying the reflection symmetry – with respect to the bistatic plane – can be written as the superposition of its original state and its mirror image one. With T_o and $T_{\hat{\alpha}}$ deduced respectively from S_o and $S_{\hat{\alpha}}$ it turns out that :

$$[T] = [T_o] + [T_{\hat{\alpha}}] = \begin{bmatrix} t_{11} & t_{21}^* & 0 & 0 \\ t_{21} & t_{22} & 0 & 0 \\ 0 & 0 & t_{33} & t_{43}^* \\ 0 & 0 & t_{43} & t_{44} \end{bmatrix}$$

hence the important relations for such media :

$$\begin{aligned} \langle (s_{hv} - s_{vh})(s_{hh} - s_{vv})^* \rangle &= 0 \\ \langle (s_{hv} - s_{vh})(s_{hh} + s_{vv})^* \rangle &= 0 \\ \langle j(s_{hv} + s_{vh})(s_{hh} - s_{vv})^* \rangle &= 0 \\ \langle j(s_{hv} + s_{vh})(s_{hh} + s_{vv})^* \rangle &= 0 \end{aligned} \tag{3.35}$$

Finally, for media exhibiting the reflection symmetry with respect to the plane $\mathcal{P}_{\hat{\delta}}$, the decomposition of the coherency matrix between likewise original targets and their symmetric counterpart brings us to :

$$[T] = [T_o] + [T_{\hat{\delta}}] = \begin{bmatrix} t_{11} & t_{21}^* & 0 & t_{41}^* \\ t_{21} & t_{22} & 0 & t_{42}^* \\ 0 & 0 & t_{33} & 0 \\ t_{41} & t_{42} & 0 & t_{44} \end{bmatrix}$$

hence the relations :

$$\begin{aligned} \langle (s_{hv} - s_{vh})(s_{hh} - s_{vv})^* \rangle &= 0 \\ \langle (s_{hv} - s_{vh})(s_{hh} + s_{vv})^* \rangle &= 0 \\ \langle j(s_{hv} + s_{vh})(s_{hv} - s_{vh})^* \rangle &= 0 \end{aligned} \tag{3.36}$$

More explicitly, the latter gives :

$$\begin{aligned} |s_{hv}| &= |s_{vh}| \\ Im\big(s_{hv} s_{vh}^*\big) &= 0 \end{aligned} \tag{3.37}$$

Naturally, these relations hold in monostatic as a specific bistatic case with however an additional specificity concerning the latter transformation about the mirror plane $\mathcal{P}_{\hat{\delta}}$. Indeed, in monostatic $\hat{\delta}$ is actually undefined (cf. definitions 3.23), as well as the bisectrix plane which

could correspond to any plane perpendicular to the equi-phase one $(\hat{h}_i, \hat{v}_i)$. A more stringent symmetry state can be thereby introduced, that is the invariance by orthogonal rotation with respect to the line of sight ($\hat{k}_i$) for which it can be demonstrated – considering the Cloude-Pottier decomposition (cf. [Cloude, 2001]) – that :

$$\begin{gathered} t_{22} = t_{33} \\ \text{that is in BSA :} \\ |s_{hh} - s_{vv}|^2 = |s_{hv}|^2 \end{gathered} \tag{3.38}$$

Furthermore, the bistatic coherency matrix of media verifying the reflection symmetry with respect to $\mathcal{P}_{\hat{\alpha}}$ and either the π one or the of the will have the simplified following form :

$$[T_{\hat{\alpha},\hat{\delta}}] = \begin{bmatrix} t_{11} & t_{12}^* & 0 & 0 \\ t_{12}^* & t_{22} & 0 & 0 \\ 0 & 0 & t_{33} & 0 \\ 0 & 0 & 0 & t_{44} \end{bmatrix}$$

providing thereby 5 classification indicators for such media.

3.2 Specificities of Volume Scattering in Bistatic

Subsequent to the theoretical aspects detailed in the previous section, especially concerning symmetries, the point now at issue lies in the simulations analysis of volume bistatic scattering. As presented in the chapter's introduction, the purpose of the following simulations is to emphasize specific properties concerning the bistatic configuration but generic ones with regards to forested media. Hence the focus on basic frequently encountered forest descriptions such as a volume filled with cylinders, which are quite versatile to model most of the natural scatterers – being SRO. Their orientation distribution will be also pointed out, restricted to the branch insertion angle (cf. figure 3.2. Concerning electromagnetic interactions, volume scattering is hereafter analysed whereas coupling terms are left for the next section (3.3). Although the study of higher interactions has revealed significant effects in specific forest cases, they are herein left aside to be consistent with the search of general properties.

The volume composition is detailed in the following table (3.1), corresponding in the first place only to the indicated upper layer. For the latter, a random distribution concerning the branch insertion angle is considered. The notation RV standing for Random Volume can be reminded, as opposed to the OψV model for an Oriented Volume). For the sake of simplicity, ψ matches the branches insertion angle ψ_{ins} which is used when the situation is ambiguous with its counterparts ψ_{az} and ψ_{int}, standing respectively for the azimuthal and the intrinsic branches orientation angles (defined in figure 3.2).

To start with a general point of view, the volume scattering contribution through the whole bistatic space is firstly envisioned. For that purpose, the scattering coefficient is performed considering a given transmitter and a receiver's position sweeping over the whole upper hemisphere. The resulting diagrams are displayed in figures 3.3 and 3.4 respectively at P and L band (it can be reminded that in such representations, the spherical coordinates are used for the angles defining the position of the transmitter, as shown for instance in figure 4.5). This study will be also restricted to these two frequency domains, as justified previously by their optimal status in forest remote sensing, concerning together penetration capabilities and embedded system constrains.

Although within the Rayleigh scattering region (on account of the radius dimensions ranging from 1 to 5 cm), the frequency dependence of the whole volume is quite moderate. An higher

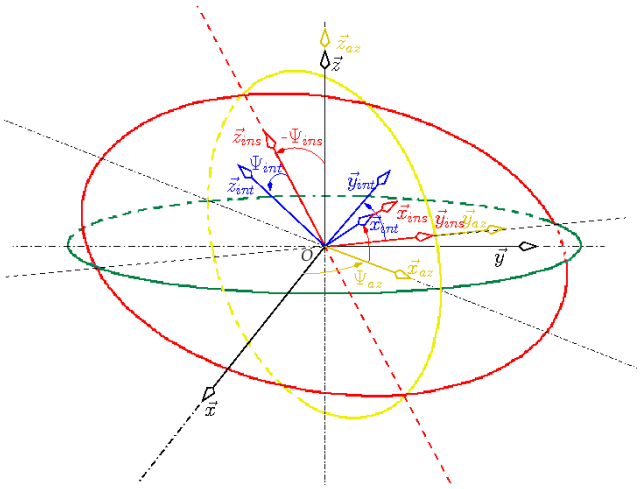

Figure 3.2: Definition of the rotations angles sequence $\psi_{az} - -\psi_{ins} - -\psi_{int}$ to characterize the scatterer orientation according to the two lines of node matching the green, yellow and red great circle.

	f_v	height (m)	radius (m)	$\psi^{\mathrm{R,O}\psi\mathrm{V}}{}_{\updownarrow(\min,\max)}$
Trunk layer	$2.2 * 10^{-3}$	9.9	0.1	0.,0.10
Upper layer[1]	$0.4 * 10^{-4}$	0.6	0.01	$0., \frac{\pi}{2} \updownarrow \frac{2\pi}{5}, \frac{\pi}{2}$
	$0.3 * 10^{-3}$	0.8	0.02	
	$0.5 * 10^{-3}$	1.0	0.03	
	$1.6 * 10^{-3}$	1.2	0.04	

Table 3.1: Description of the various simulated models, the dimensions are given in meter, a default value for the vegetation water content of $wc_v = 50\%$ has been also chosen.

dynamic and contrast can be established in L-band, which essentially stems from the more accentuated trough values but the general diagrams shapes are similar. For both frequency domains, the HH and the cross polarizations' diagrams are quite complementary, which lets suggest a much more homogeneous diagram for the SPAN (the total power $s_{hh}^2 + s_{hv}^2 + s_{vh}^2 + s_{vv}^2$). Notwithstanding, the scattering behaviour is more complex than a surface Lambertian one as it will be shown afterwards and also as already exhibited by the VV's diagram, less intuitive to interpret with for instance a forward scattering not really favoured in comparison to the backward direction. These diagrams deserve thus a deeper analysis which can be achieved within different slices – that is perpendicular planes of constant azimuthal value. With that aim, it turns out that the information entailed in each diagram can be well characterized with only two planes $\mathcal{P}_0^{\perp}$ and $\mathcal{P}_{90}^{\perp}$ respectively defined by $\left(\hat{k}_i, \hat{v}_i\right)$ and $\left(\hat{k}_s, \hat{v}_s\right)\big|_{\varphi_s - \varphi_i = \pi/2}$. Indeed, the whole diagram can then be recovered by means of an azimuthal rotation of these two planes, with the additional knowledge of the azimuthal angle making the transition between both and defining in a way the aperture of the lobes. Besides, this property could be interestingly used within the scope of multistatic acquisitions aiming at retrieving the emissivity from the scattering diagram integration over an interpolated upper hemisphere (cf. Kirchhoff formula).

Consequently, the next two subsections will be dedicated to the scattering behaviour within these two planes, starting with $\mathcal{P}_0^{\perp}$, also called hereafter the normal bistatic plane – since given

by $\left(\hat{k}_i, \hat{v}_i\right)$ – thereby orthogonal to the reference plane (xOy).

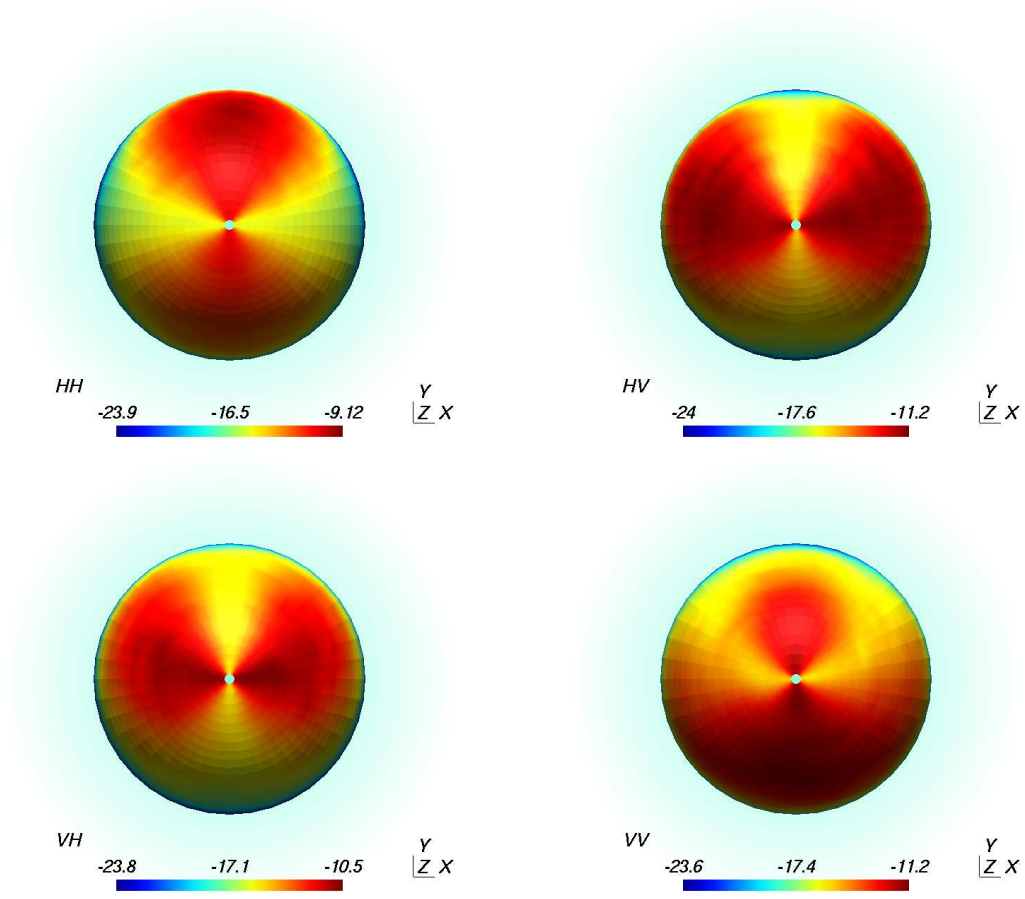

Figure 3.3: P-band (430 MHz) scattering diagram representing the bistatic scattering coefficient σ^0_{qp} for the volume contribution in the random orientation case. The transmitter's location is given by ($\theta_{\mathrm{T}} = 45^o$, $\varphi_{\mathrm{T}} = -\pi/2$) whereas the receiver's positions sweep over the whole upper hemisphere. The (v,h) linear polarizations have been used as indicated above.

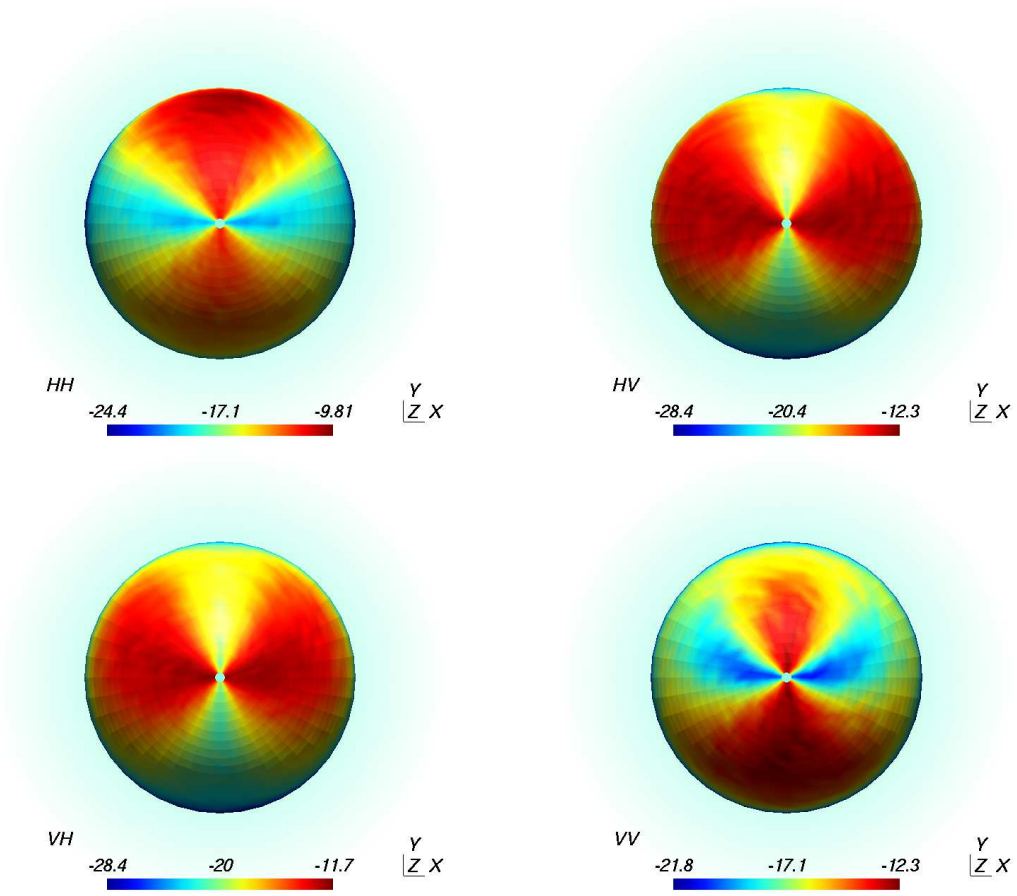

Figure 3.4: L-band (1.27 GHz) scattering diagram representing the bistatic scattering coefficient σ^0_{qp} for the volume contribution in the random orientation case. The transmitter's location is given by ($\theta_{\mathrm{T}} = 45^o$, $\varphi_{\mathrm{T}} = -\pi/2$) whereas the receiver's positions sweep over the whole upper hemisphere. The (v,h) linear polarizations have been used as indicated above.

3.2.1 Case of the Normal Bistatic Plane

As introduced previously, this subsection is dedicated to the study of the bistatic scattering diagram restricted to the plane ($\mathcal{P}_0^{\perp}$). The simulations have been also achieved for the P and L-band considering the randomly oriented volume afore-detailed. In addition to the previous simulations, three incident angles are considered in order to assess the scattering dependence towards β, the bistatic angle but also towards the incident or scattering angles, $(\theta_{\mathrm{T}}, \theta_{\mathrm{R}})$ defined according to the transmitter and receiver's positions. As shown with figures 3.5 and 3.6, the like polarizations dependence towards β is clearly manifest and is higher than expected at first sight, on account of a randomly oriented volume. Notwithstanding, if we keep in mind that the volume is filled with non isotropic scatterers, we can figure out that the sensitivity towards β stems from the fact that for each configurations, all the possible realizations – given β plus the drawn positioning angles of the cylinder – are not similar. In order to illustrate the importance of the realization of these specific configurations, the scattering diagram of a single cylinder have been considered. For instance if we considered the HH polarization, the higher specular return for larger incidence angle shown for the whole volume in figure 3.5 stems mainly from the increasing scattering amplitude coming with the bistatic angle for a single vertical cylinder, as shown in figure 3.8, case a). This favourable configuration (vertical cylinder) and large bistatic angle can indeed not be retrieved with a possible equivalent combination between β and another set of angles for the cylinder. The trend is also similar for the lying cylinder configuration – case b) – with a smaller impact though. Likewise, the difference between the like polarizations comes also from the realizations of more or less favourable configurations. As long as the cylinder lies in the scattering plane $(\hat{k}_i, \hat{k}_s)$, the cross polarizations are quasi null and the VV return is mostly higher than HH. Notwithstanding, in view of the 3D possible orientations, these realizations represent a small port of all the possible ones for which actually HH dominates. Indeed, on account of the random distribution considered for the insertion angle – which do not concerned directly ψ_{ins} but an equal number of drawn cylinder per unit spherical sector, as detailed in chapter 2 – there are actually much more cylinders rather horizontally oriented. Since the latter are equivalent to the previous situation within the scattering plane but switching VV to HH, it turns out that the resulting total contribution in the horizontal polarization is favoured. This effect can be also illustrated with a single cylinder in the configurations presented in figure 3.9. The incident and scattering angles have been set to a constant position whereas the intrinsic orientation angle (ψ_{int}) varies. The sheaf of curves have then be obtained for various insertion angle (ψ_{ins}) as a parameter study. It can be noticed that the configuration where VV dominates are much more seldom and concerns indeed $\psi_{int} = 0$ or π corresponding to the cylinder attitude within the scattering plane. The maximum gap is logically obtained for $\psi_{int} = \pi/2$ where the cylinder is lying on the contrary along the horizontal direction. In addition this situation emphasizes also the case where even within the scattering plane, VV does not dominate. Indeed, it happens in the grazing positions ($\psi_{int} = \pi/4 = \theta_{\mathrm{R}}$) but rather, as reminded in figure 3.8 with the configurations close to the Brewster angle, which sensitivity towards the refraction index have been stressed with various water content value and thereby various permittivity. Besides, a Brewster-like behaviour can be set forth with such volume scattering. Indeed, as shown in figure 3.7 in which all the specular angles have been simulated ($\theta_{\mathrm{T}} = \theta_{\mathrm{R}} = \beta/2$), a trough value can be obtained. Although the medium does not transmit all the transverse magnetic (TM) mode – vertical polarization herein –, the trough varying position with the individual permittivity shows that an equivalent one could be found, on account of the mixing law.

On top of the scattering dependency towards β, the incidence angle importance is also clearly manifest as testified by the simulated total power (SPAN) in figure 3.6 with θ_{T} as parameter for

a varying bistatic angle. It can be again noticed that the scattering is far from a Lambertian one (only dependent to the incident power which would give a constant SPAN after normalization by $\cos\theta_{\mathrm{T}}$) and it turns out that the strong variation, especially for grazing scattering angles whether in the backward or in the forward directions are actually due to a typical volume effect, that is the attenuation. Indeed, though moderate in P or L-band, the propagation length within the media varying with $\frac{H-z}{\cos\theta}$ becomes truly important for grazing viewing angles, naturally on account of the em plane wave and Foldy's approximation. As it will be pointed out in subsection 3.4.2, the attenuation impact is really specific in bistatic and the induced shadowing effects may be interestingly used for detection, whether in the infinite forest case or in the finite one with the presence of clearings. Without this attenuation, it has been checked that the SPAN is a only a function of the bistatic angle, which is consistent with symmetry rules for a randomly oriented volume. As far as symmetry is concerned, an interesting combination of temporal and spatial symmetries can be also emphasized. Indeed, on the one hand invoking the reciprocity principle, θ_{T} and θ_{R} can be switched but on the second hand, an azimuthal rotation of π should be also invariant for scattering. That's actually the reason why each of the three curves, still in figure 3.6, exhibits two intersection points. To be more explicit, the example with $(\theta_{\mathrm{T}} = 66^o, \theta_{\mathrm{R}} = 19^o)$ is reciprocal with $(\theta_{\mathrm{T}} = 19^o, \theta_{\mathrm{R}} = 66^o)$ which corresponds – after the π azimuthal rotation – to a point on the plotted $\theta_{\mathrm{T}} = 19^o$ curve, hence an intersection for the bistatic angle $\beta = 85^o$. Likewise, whether in the P or L-band cases displayed, the other intersection points can be verified for $\beta = 66+45 = 111^o$ or $\beta = 45+19 = 64^o$. This could have been naturally noticed in figure 3.5 but the identical levels are not emphasized by intersection points since the plots are versus θ_{R} rather than β.

Besides, such property could be also used within a detection framework, provided the fact that the man-made structure does not exhibit the 'π azimuthal symmetry' invariance. Although cost effective from the system constraints point of view since it requires naturally two bistatic acquisitions, such method will be assessed afterwards in the subsection 3.4.1 and at first sight could be more interesting than usual algorithm which can not work with single look complex image and are thereby limited by averaging process.

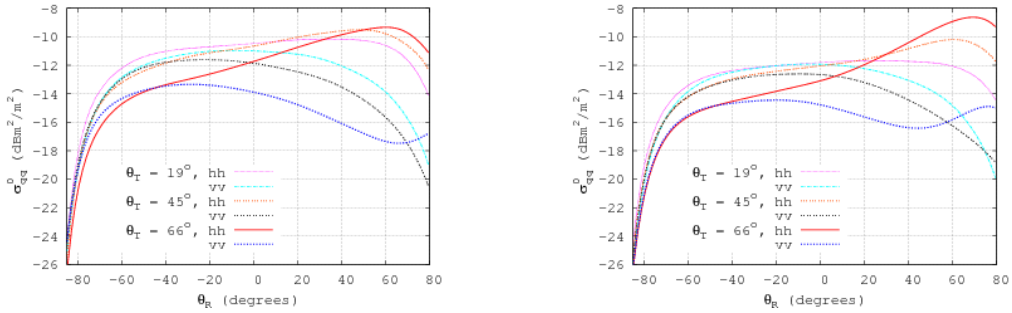

(a) P-band (b) L-band

Figure 3.5: σ^0_{qq} for the volume contribution versus the bistatic angle within the plane $\mathcal{P}_0^{\perp}$ in the random volume case. Three different incident angles (θ_{T}) are also considered, as indicated above.

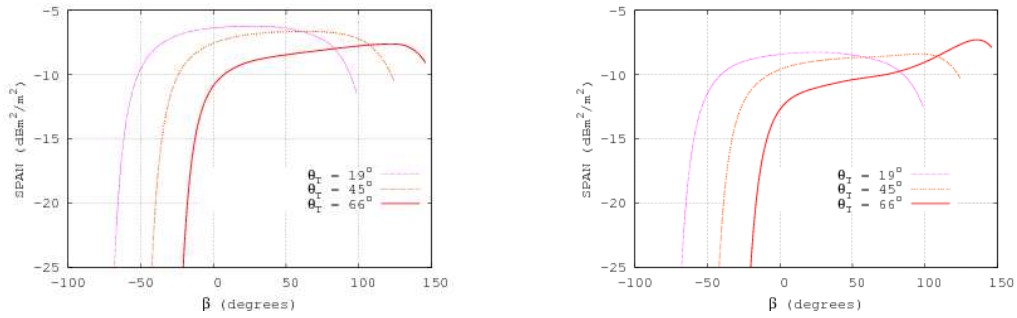

(a) P-band (b) L-band

Figure 3.6: SPAN of the volume contribution versus the bistatic angle within the plane $\mathcal{P}_0^{\perp}$ in the random volume case. Three different incident angles (θ_{T}) are also considered, as indicated above.

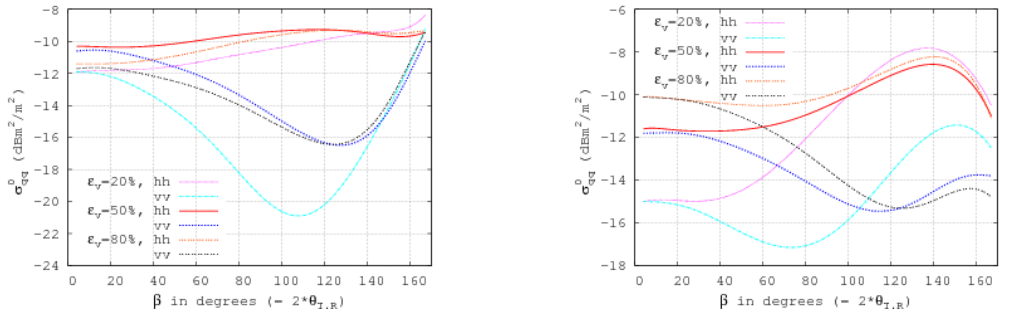

(a) P-band (b) L-band

Figure 3.7: σ^0_{qq} of the volume contribution versus the specular bistatic angle (so that $\theta_{\mathrm{T}} = \theta_{\mathrm{R}} = \beta/2$) within the plane $\mathcal{P}_0^{\perp}$ in the random volume case. The 3 different incident angles indicated above are also considered.

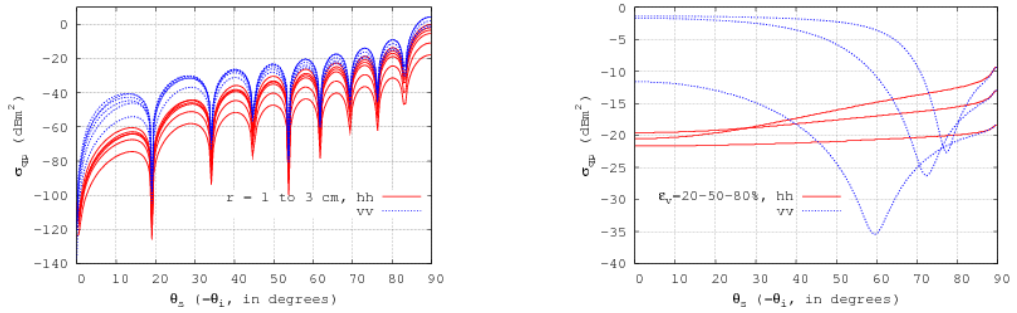

(a) Radius as parameter (b) vs eps

Figure 3.8: RCS of a vertical (a) or an horizontal (b) cylinder versus the specular scattering angle $\theta_{\mathrm{R}} = |_{SSA}\theta_{\mathrm{T}}$ ($\varphi_{\mathrm{R}} = |_{SSA}\varphi_{\mathrm{T}}$ with respectively the radius or the water content as study parameter at L-band (1.27 GHz) with h=1m and r=1cm

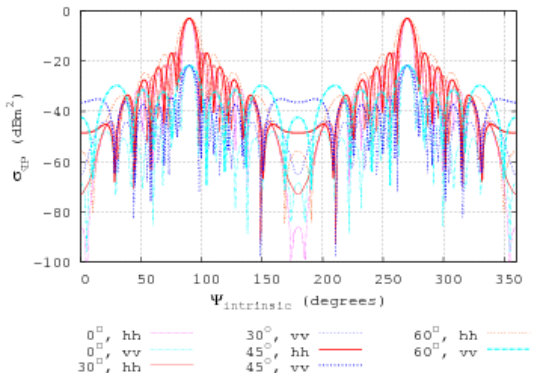

(a) $\theta_{\mathrm{R}} = 20^o$

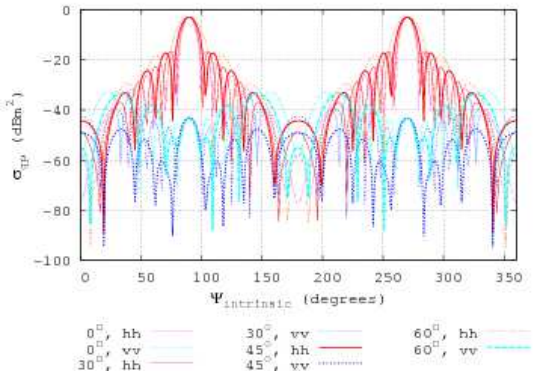

(b) $\theta_{\mathrm{R}} = 45^o$

Figure 3.9: RCS of a cylinder versus the intrinsic rotation angle ψ_{int} for a constant incident and scattering directions positions given in the SSA convention by $\varphi_{\mathrm{T}} = \varphi_{\mathrm{R}} = 90^o$ and $\theta_{\mathrm{T}} = \theta_{\mathrm{R}} = 20^o$ in (a) or 45^o in (b). The sheaf of curves is obtained for various insertion angles Ψ_{ins} as study parameter, ranging from 0^o to 60^o as indicated above knowing also that $\psi_{az} = \pi/2$. In addition, f=1.27 GHz, h=1m and r=1cm.

3.2.2 Characterization of Oriented Scatterers

The importance of the afore-mentioned specific statistical realizations involving the bistatic and the scatterer attitude angles can be also pointed out with the oriented volume case. We remind that for all this study, the azimuthal symmetry is always verified and the orientation distribution applies for the insertion angle only. Consistent with the previously discussed assertions, the different scattering behaviour between like polarizations goes hand in hand with rather horizontal or vertical orientation distribution, as shown with figure 3.10 in which ψ_{ins} has been restricted to specific angular sectors, in comparison with the random case also reminded.

Moreover, these specific orientations rise the question of the cross polarizations interpretation, since in bistatic both may differ and their discrepancy is likely to be well correlated towards the scatterer attitude angles. Still in figure 3.10, the cross polarizations behaviour towards β is also given and one can indeed notice that whereas both are roughly equal for the random case, they are slightly different for the horizontal orientation and really different for the rather vertical one in the steep scattering angles region. Besides, the absolute levels between the three kinds of orientation are also really different. As a reference, for the random volume and in the monostatic case, the gap between co and cross polarizations is about 7 dB, which can be compared to the 4.77 dB ($s_{qp}^2 = s_{qq}^2/3$) for the theoretical case of a random volume made of dipole scatterers. This difference stems naturally from the fact that cylinders are considered instead of dipoles for which the HH polarization is not zero in the canonical position (vertical) and is going up together with the radius (in the Rayleigh region), as reminded in figure 3.11. Also illustrated is the importance of the permittivity value in this dipole-like behaviour since for dielectric media, it is more relevant to compare the equivalent radius, defined as the geometrical one divided by the medium index. On account of these non trivial relations between the like polarizations ratio and the cylinder modeling parameters, a theoretical level with the cross polarizations can not derived in a simple way from the orientation angle pdf only. Besides, the statistical convergence within our simulations as well as the results interpolation between scattering angles brings also slight biases, as it can be noticed still with the discrepancy between co polarizations, theoretically equal for the monostatic case.

Furthermore, a more thorough analysis has been achieved and it emerges that for a single scatterer – being an SRO – the difference between the cross polarizations is related to the relative position of the bistatic vector with $\hat{c}_\beta$, being the projection of cylinder axis ($\hat{c}$) onto the bistatic plane $\mathcal{P}_{\hat{\beta}}$, which can be formalized mathematically by :

$$\begin{aligned} \vec{c}_\beta &= \hat{c} - (\hat{c}\cdot\hat{\alpha})\hat{\alpha} \\ \vec{\alpha} &= \hat{k}_i \times \hat{k}_s \\ \sigma_{hv} - \sigma_{vh} &= f\left[\ \left(\hat{c}_\beta \times \hat{\beta}\right)\cdot\hat{x}\ \right] \end{aligned} \tag{3.39}$$

where f is an increasing continuous function verifying plus f(0)=0 and sign(f(x)) = sign(x). In addition, it turns out that additional parameters (e.g equivalent radius, length) are actually also involved and make difficult the derivation of an analytical expression for the f function. Although a quantitative retrieval can thereby not be achieved without such expression, it gives the relative localization of $\hat{c}_\beta$ that is within the angular sector given by $\left(\hat{\beta}, -\hat{\beta}+2\hat{\beta}\cdot\hat{z}\right)$ for which $\sigma_{hv} - \sigma_{vh} > 0$. or within $\left(-\hat{k}_i, -\hat{x}\right)$ and $\left(\hat{y}, \hat{k}_i + 2\hat{k}_i\cdot\hat{z}\right)$ for which conversely $\sigma_{hv} - \sigma_{vh} < 0$.. These properties are well emphasized if we look at the cross pol RCS of a cylinder for which $\mathcal{P}_\beta(\hat{c})$ keeps a constant direction within the specific angular sectors, as simulated in figure 3.12. For that purpose, the intrinsic orientation angle is variable and depending on the insertion angle – which corresponds directly to the direction along $\mathcal{P}_\beta(\hat{c})$ since $\psi_{az} = \pi/2$ – the VH level is either

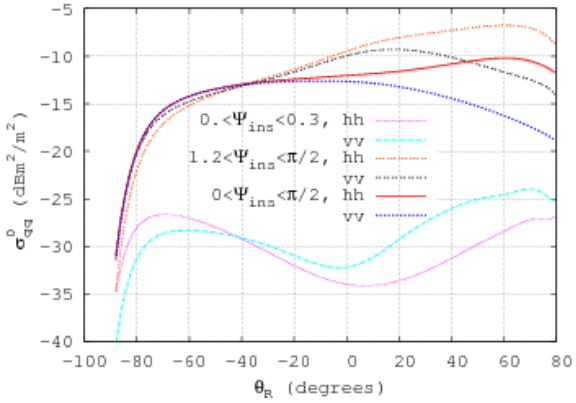

(a) like polarizations

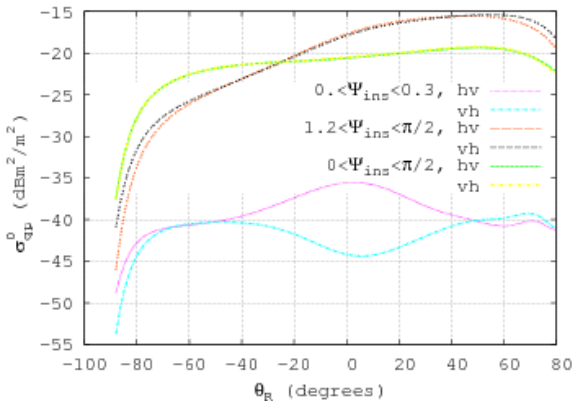

(b) cross pol.

Figure 3.10: L-band σ^0_{qp} of the volume contribution versus the scattering angle θ_{R} in the oriented volume case concerning the insertion angle ψ_{ins}, limited to a specific range, as indicated above. The incident angle is $\theta_{\mathrm{T}} = 45^o$.

upper, equal or lower to HV, all of that whatever ψ_{int}.

Consequently, the results given in figure 3.10 can now be interpreted : the rather vertically oriented volume exhibit the largest gap between the cross polarizations levels since for such cylinders, $\hat{c}_\beta$ will be always within the same angular sector while the remaining freedom angle ψ_{az} varies. Then, the amplitude of this difference is directly driven by the bistatic angle from which these angular sectors are defined. On the contrary, for the rather horizontally oriented cylinders, this projected vector will cover, for each azimuthal orientation angle, all the angular sectors within the bistatic plane so that the orientation effect will be sometimes more favourable to VH, sometimes to HV, hence a resulting impact negligible. In advance with the subsequent analysis at § 3.2.3, this discrepancy between cross polarizations in the case of rather vertically oriented scatterers will also be very sensitive to the bistatic angle with an arbitrary azimuthal component, as shown with the hemispherical scattering diagram shown in figure 3.16.

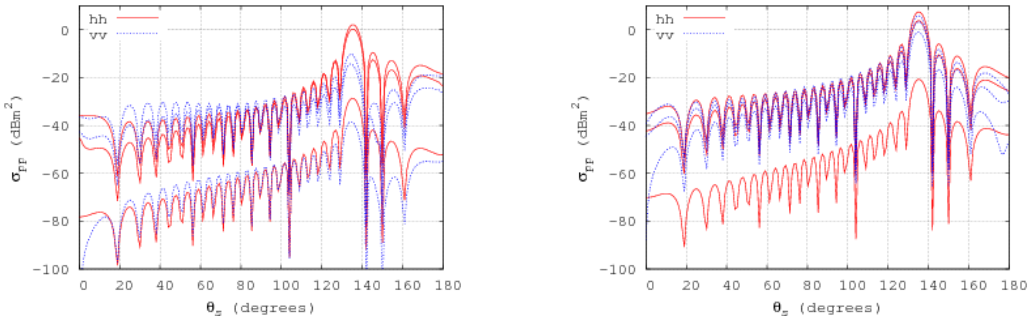

(a) wc = 10 % (b) wc = 70 %

Figure 3.11: L-band RCS (dBm^2) for a vertical cylinder (h=3m) versus θ_s, expressed in the SSA convention as well as $\theta_i = 45^o$ and $\varphi_s = \varphi_i$. The sheaf of lines is obtained with the radius as study parameter, which levels follow the increasing radius values 0.5, 2.75 and 5 cm.

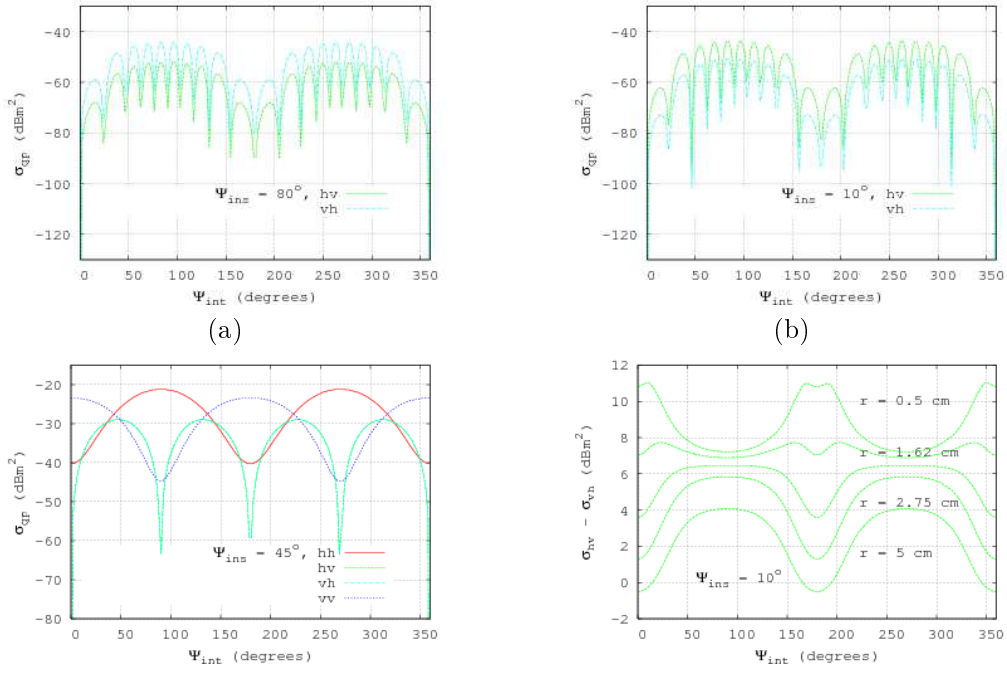

(a) (b)

(c) (d)

Figure 3.12: Polarimetric RCS variations of a single cylinder versus the intrinsic orientation angle (ψ_{int}) with for various insertion angles (ψ_{int}), as indicated in (a), (b), (c) and knowing that the initial rotation $\psi_{az} = \pi/2$ as been done first. In the latter case (d), the cross polarizations RCS difference is plotted also for a given ψ_{ins} and versus ψ_{int} but with the cylinder radius as study parameter. The cylinder height and radius are 3 m and 5 cm and its RCS has been computed at P-band, in the bistatic configuration given by $[\theta_{\mathrm{T}} = 71.5^o, \theta_{\mathrm{R}} = 18.5^o, \varphi_{\mathrm{T}} = \varphi_{\mathrm{R}}]_{SSA}$.

With the aim of retrieving the scatterers orientation angle, a study of scattering matrix shape can be also envisioned, alternatively to the afore-mentioned approach. Indeed, based on the difference between the cross polarization levels, the latter has been demonstrated interesting as an orientation indicator but not thorough enough – even in the coherent scatterer case – to perform a quantitative inversion, all the more for what concerns a three dimensional problem with Euler's angles. As presented in the introduction, methods based on the scattering matrix form and using thereby optimal polarization states have proven their capabilities in monostatic for that purpose, though limited to the retrieval of a one dimensional angle. This angle corresponds indeed to the one between the standard vertical polarization vector and the projected vector of the scatterer main axis onto the plane orthogonal to $\hat{k}_i$, noted $\mathcal{P}_{\hat{k}_i}$. Such method – at least in its usual application, cf. [Huynen, 1970] – relies also on the fact that there exists a specific polarization basis (the canonical one) for which the cross polarization term is null or minimum, like for the typical cases of natural surfaces which fulfill the reflection symmetry property or coherent SRO.

In its typical form, linear polarizations are considered and the retrieval algorithm consists in finding a polarization basis for which the vertical and horizontal states enable to recover the reflection symmetry that is for instance when the vertical polarization vector lines up with the projection onto $\mathcal{P}_{\hat{k}_i}$ of the surface normal in the case of a tilted land or with the scatterer revolution axis in the SRO case (referred beforehand to as $\hat{c}$). To be more explicit, it can be expressed by :

$$\vec{v}' \propto \left[\hat{c} - (\hat{c} \cdot \hat{k}_i)\hat{k}_i\right]$$

which normalization leads to :

$$\hat{v}' = \frac{1}{\sin(\widehat{\hat{c}, \hat{k}_i})}\left[\hat{c} - (\hat{c} \cdot \hat{k}_i)\hat{k}_i\right]$$

For the sake of simplicity, the radar geometry given by $(\theta_i, \varphi_i = -\pi/2)$ is chosen as a generic example so that :

$$\hat{v} = \begin{bmatrix} 0 \\ \cos\theta_i \\ \sin\theta_i \end{bmatrix}, \hat{h} = \begin{bmatrix} 1 \\ 0 \\ 0 \end{bmatrix}, \hat{c} = \begin{bmatrix} c_x \\ c_y \\ c_z \end{bmatrix}$$

and the sought orientation angle ψ_r^{mn} can be expressed as follows :

$$\cos\psi_r^{\text{mn}} = \frac{n_y \cos\theta_i + n_z \sin\theta_i}{\sin(\widehat{\hat{c}, \hat{k}_i})} \tag{3.40}$$

Since the direction $\vec{x}$ is invariant with the projection onto the plane $\mathcal{P}_{\hat{k}_i}$, also important is the relation :

$$\sin\psi_r^{\text{mn}} = \frac{-n_x}{\sin(\widehat{\hat{c}, \hat{k}_i})}$$

so that ψ_r^{mn} can be related to the azimuthal and LoS (Line of Sight) slope angles – noted respectively ζ_{az} and ζ_s – by :

$$\begin{aligned} \tan\psi_r^{\text{mn}} &= \frac{-c_x/c_z}{\frac{n_y}{n_z}\cos\theta_i + \sin\theta_i} \\ &= \frac{-\tan\zeta_{az}}{-\tan\zeta_s \cos\theta_i + \sin\theta_i} \end{aligned} \tag{3.41}$$

which points out the remaining ambiguity between the orientation angles ζ_{az} and ζ_s from the knowledge of $\psi_r^{\rm mn}$ only.

The point at issue in bistatic lies thus in the search for a canonical form of the scattering matrix reached with a particular polarization state which can be associated to a physical angle – geometrically-wise – characteristic of the scatterer attitude. can be derived. From the mathematical point of view and more precisely invoking linear algebra factorization theorems, the scattering matrix – in its general bistatic from – can be diagonalized according to the singular value decomposition (SVD). Nevertheless, the interpretation of the various rotation angles corresponding to the new emitting and receiving polarization basis ensued from the unitary transforms hasn't been conclusive.

As a first investigation, the search for specific polarization states has thus be limited to the ones deduced by rotations (orthogonal transforms) from linear polarizations. Consistently with less freedom parameters, we head for less stringent canonical scattering matrix froms with anti-symmetric ones. Yet, in the case of two dimensional matrices, it can be demonstrated that an arbitray complex matrix can not be put under the anti-symmetric shape (without residuals), whether using similar or different orthogonal transforms $(\Theta_{\rm T}, \Theta_{\rm R})$. Besides, though possibly achieved in the real case, such restriction is too important as far as EM scattering matrices are concerned. On the other hand, these matrices are naturally not representative either of arbitrary ones in $\mathcal{M}_{2,2}(\mathbb{C})$, particularly since for SRO like cylinders or ellipsoids the off-diagonal terms stems essentially from rotations to leave the canonical geometry. Indeed, an extensive number of scattering configuration have been tested according to various shapes of revolution (cylinders, ellipsoids), dimensions, attitude angles as well as various radar configurations still limited to the normal bistatic plane $\mathcal{P}_{\perp}^{\varphi 0}$ though. In view of these simulations, it turns out that for each case, a unique rotation angle concerning the polarization basis (hence $\Theta_{\rm R} = \Theta_{\rm T}$) could be found in order to transform the original scattering matrix into an anti-symmetric one. More interestingly, it has been also found that for a given bistatic geometry, this angle does depend only on the SRO attitude angles, that is whatever the frequency or the scatterer description (dimensions, dielectric constant). Consequently, if the cylinder orientation can be characterized by a single angle, it is possible to build a look-up table which associates this angle – coming thereby with the introduction of its specific plane – to the one obtained from the optimal polarization basis rotation. In order to find a relevant specific plane, the join monostatic acquisition corresponding to the transmitter's position is anew considered from which naturally the orientation angle $\psi_r^{\rm mn}$ can be derived, as explained above. Therefore, the sought SRO axis $\hat{c}$ is from now on restricted to the plane $\mathcal{P}_{\hat{h}'}$ which will be chosen as the afore-mentioned specific plane. Finally, $\hat{c}$ can be completely characterized with the additional angle $\widehat{(\hat{c}, \hat{k}_i)} = {\rm LUT}(\psi_r^{\rm bi})$ deduced from the inversion based on the look-up table (LUT) and the optimal polarization state of the bistatic configuration. Besides, it implicitely supposes a bijective LUT which excludes the case when $\mathcal{P}_{\perp}^{\varphi 0}$ and $\mathcal{P}_{\hat{h}'}$ coincide, for which the scattering matrix off diagonal terms are quasi null, hence anti-symmetric whatever the angle $\psi_r^{\rm bi}$. In addition, we looked also towards the possible link, more intuitive, between the polarization basis rotation and the projection of $\hat{c}$ onto the bisectrix plane $\mathcal{P}_{\hat{\delta}}$ but it appeared limited by the non unicity of the solution angles, at least within our own framework.

To illustrate the proposed method by means of a concrete example, the case of a cylinder is considered with an arbitrary orientation defined by the angles $\psi_{az} = 0.2$ and $\psi_{ins} = 1.0$, being the object of the proposed retrieval. In the first place, the monostatic acquisition is considered – herein with $[\theta_{\rm T} = 45^o, \varphi_{\rm T} = 90^o]_{\rm SSA}$ – which brings us to the angle $\psi_r^{\rm mn} = 58.76^o$, as shown in figure 3.13 (a) with the functional variation. For that purpose, the minimization of the off

diagonal terms has been achieved, considering all the possible polarization basis rotation and the functional $\mathcal{F} = |s_{qp}|$. With ψ_r^{mn} and thereby $\hat{h}'$, the plane $\mathcal{P}_{\hat{h}'}$ can be deduced from which the look-up table (LUT) corresponding to the bistatic acquisition $[\theta_{\text{T}} = 18.43^o, \varphi_{\text{T}} = -90^o]_{\text{SSA}}$ can be set up. In our case, we obtain $\text{LUT}(17.18^o) = 74.7^o$. Then, the determination of $\hat{c}$ is straightforward with

$$\vec{c} \propto \sin\left[\text{LUT}(17.18^o)\hat{v}'\right] - \cos\left[\text{LUT}(17.18^o)\right]\hat{k}_i$$

which thus characterizes completely the cylinder's main axis.

Besides, it can be also noticed that the retrieval of the attitude angles for SRO can be also performed with two monostatic acquisitions. Indeed, the aboved method can be independently achieved for both configurations, leading to the two planes $\mathcal{P}_{\hat{h^1}'}$, $\mathcal{P}_{\hat{h^2}'}$ which intersection turns out to line up with $\hat{c}$, providing naturally the fact that the latters are not identical (ensured by $\varphi_{\text{T}}^1 \neq \varphi_{\text{T}}^2, \varphi_{\text{T}}^2 + \pi$). Notwithstanding, the join acquisition enables to save one transmitting source, among other advantages of passive receivers (cf. chapter 1).

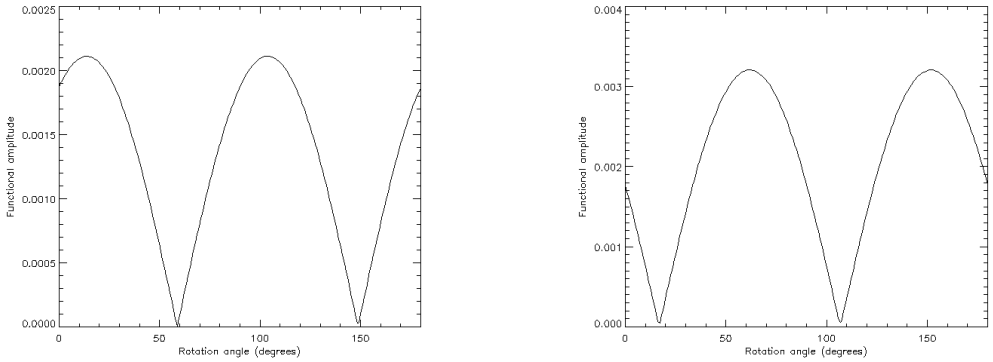

(a) monostatic functional (b) bistatic functional

Figure 3.13: Minimums of the monostatic (a) and bistatic (b) functionals (defined in the text body) for the whole coverage of the possible rotation angle from which the new polarization state is obtained, considering in both cases $\Theta_{\text{R}} = \Theta_{\text{T}}$. For that purpose, a 2 m heigh cylinder of radius 1/2 cm at P-band has been simulated which position has been set according to the attitude angles : $\psi_{az} = 0.2$, $\psi_{ins} = 1.0$ and $\psi_{int} = 0.$. The join monostatic plus bistatic acquisition are given by : $[\theta_{\text{T}} = 45^o, \varphi_{\text{T}} = 90^o]_{\text{SSA}}$, $[\theta_{\text{R}} = 18.4^o, \varphi_{\text{R}} = -90^o]_{\text{SSA}}$.

3.2.3 General Configuration : Case of the Tilted Bistatic Plane

The point now at issue concerns general bistatic configurations, that is with an arbitrary bistatic plane $\mathcal{P}_\beta$ (defined previously by $[\hat{k}_i, \hat{k}_s] \equiv \mathcal{P}_{\hat{\alpha}}$) as opposed to $\mathcal{P}_\perp^{\varphi 0}$ referred to as the normal bistatic plane since it is perpendicular to the reference horizontal one $(\hat{x}, \hat{y})$, on top of being also the incidence plane $(\hat{k}_i, \hat{z})$.

Whether at P or L-band, a relatively strong dependency towards scattering directions have been noticed with the hemispherical scattering diagrams shown in figures 3.3 and 3.4, though simulated for an uniform volume. The sensitivity versus β within $\mathcal{P}_\perp^{\varphi 0}$, has been explained in the previous section but much greater variations concern the azimuthal sector around $\mathcal{P}_\perp^{\varphi 90}$.

On account of considerations about symmetry, it turns out that the definition of the reflection symmetry is not straightforward using the classical polarization basis (BSA, FSA, SSA conventions). Inspired for the work published in [Hulst, 1981], the use of the bistatic plane as the reference one is actually much more adapted, and can be used to define the transmitted and received polarizations and the reflection symmetry plane. This has been recently explicitly proposed in [Nashashibi and Ulaby, 2007] with a polarization bases defined within the common plane $\mathcal{P}_\beta$ instead of $\mathcal{P}_\perp^{\varphi_T}$ and $\mathcal{P}_\perp^{\varphi_R}$ so that the new polarizations horizontal vectors noted $\hat{h}_i^\beta$ and $\hat{h}_s$ will be again parallel, both being perpendicular to $\mathcal{P}_\beta$. These new polarization bases with respect to the incident and scattered directions will be referred to as the 'β' polarization bases and noted :

$$(\hat{k}_i^\beta, \hat{v}_i^\beta, \hat{h}_i^\beta) \text{ and } (\hat{k}_s^\beta, \hat{v}_s^\beta, \hat{h}_s^\beta)$$

Considering the classical polarization bases $(\hat{k}_i, \hat{v}_i, \hat{h}_i)$ and $(\hat{k}_s, \hat{v}_s, \hat{h}_s)$ according to the FSA convention, the β bases are defined as follows :

$$\begin{aligned}
\hat{k}_i^\beta &= \hat{k}_i \\
\hat{k}_s^\beta &= \hat{k}_s \\
\hat{h}_i^\beta &= \frac{\hat{k}_i^\beta \times \hat{\beta}}{|\hat{k}_i^\beta \times \hat{\beta}|} \\
\hat{h}_s^\beta &= \frac{\hat{k}_s^\beta \times \hat{\beta}}{|\hat{k}_s^\beta \times \hat{\beta}|} \\
\hat{v}_i^\beta &= \hat{h}_i^\beta \times \hat{k}_i^\beta \\
\hat{v}_s^\beta &= \hat{h}_s^\beta \times \hat{k}_s^\beta
\end{aligned} \tag{3.42}$$

This transformation is illustrated in figure 3.14. Consequently, the scattering matrix can thus be derived according to this new polarizations basis. For that purpose, the following unitary and rather orthogonal transformation matrices are employed, which brings us to the relations :

$$\mathcal{O}_{a\to n}^i = \begin{bmatrix} \hat{h}_i^\beta \cdot \hat{h}_i & \hat{v}_i^\beta \cdot \hat{h}_i \\ \hat{h}_i^\beta \cdot \hat{v}_i & \hat{v}_i^\beta \cdot \hat{v}_i \end{bmatrix}$$

$$\mathcal{O}_{a\to n}^s = \begin{bmatrix} \hat{h}_s^\beta \cdot \hat{h}_s & \hat{v}_s^\beta \cdot \hat{h}_s \\ \hat{h}_s^\beta \cdot \hat{v}_s & \hat{v}_s^\beta \cdot \hat{v}_s \end{bmatrix}$$

$$[S_n] = [\mathcal{O}_{a\to n}^s]^{-1} \cdot [S_a] \cdot [\mathcal{O}_{a\to n}^i]$$

On account of the similarity transform (norm conservation), it can be stressed that the SPAN is unchanged. From this new scattering matrix $[S_n]$, the second order statistical moments within

the matrices [T], [C], [M] or [K] can be obtained using the transformations detailed in subsection 3.1.1). Considering for instance natural media, the reflection symmetry property can be emphasized within these matrices, especially with null correlation between co and cross polarizations, as shown in subsection 3.1.2 (one can also refer to [Nashashibi and Ulaby, 2007]).

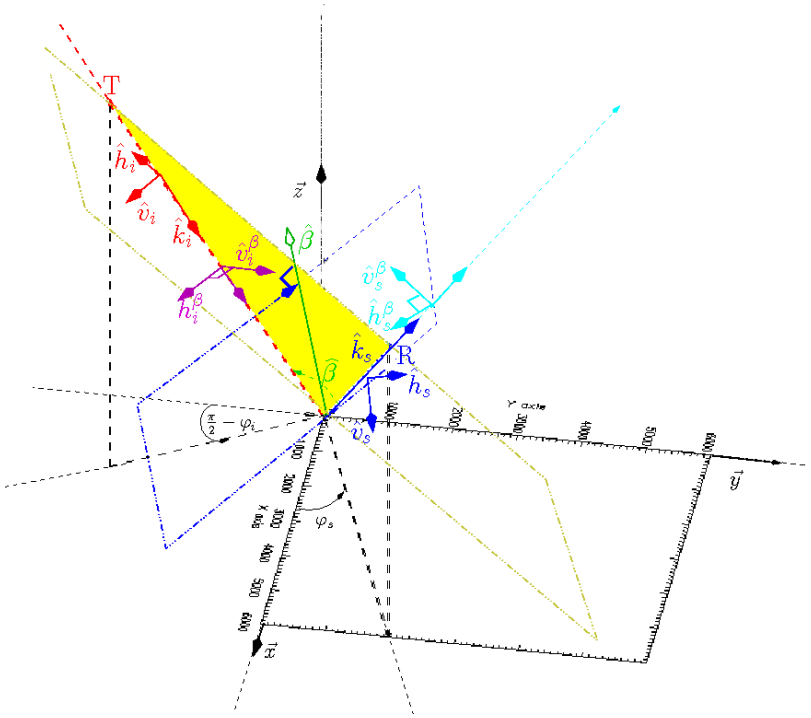

Figure 3.14: Polarization basis β, defined from the transmitter and receiver FSA polarization basis $(\hat{k}_i, \hat{v}_i, \hat{h}_i)$ and $(\hat{k}_i, \hat{v}_i, \hat{h}_i)$ respectively to $(\hat{k}_i, \hat{v}_i^\beta, \hat{h}_i^\beta)$ and $(\hat{k}_s, \hat{v}_s^\beta, \hat{h}_s^\beta)$.

This basis transformation has thus been applied, as seen for instance with the resulting hemispherical scattering diagrams in figures 3.15 and 3.17 respectively for the uniform or the oriented cases. In the former, the degree of azimuthal dependence is now much lower, the total azimuth invariance can naturally not be obtained on account of the importance of the transmitter location, from which the backward and forward regions are defined (i.e respectively $-\pi/2\delta\varphi < \pi/2$ or $\pi/2\delta\varphi < 3\pi/2$). With the β polarization basis, every scattering direction is characterized only by the incident (θ_T) and the bistatic (β) angles, whatever $\hat{\alpha}$, hence similar values throughout the diagram. On the contrary, with the standard polarization basis an additional freedom parameter φ_R is needed.

Likewise, in the oriented volume case, the scattering diagrams can be interpreted using the β polarization basis and considering the equivalent problem with scatterers orientation characterized according to the bistatic plane. The previous results concerning the link between the orientation and the difference between cross-polarizations (cf. subsection 3.2.2) can thus be anew applied.

Before giving the example of the plane $\mathcal{P}_\perp^{\varphi 90}$, it can be pointed out that in spite of the different color scale, the same variation is obtained within the plane $\mathcal{P}_\perp^{\varphi 0}$ whether in the β or in the standard polarization basis. The variations within the plane $\mathcal{P}_\perp^{\varphi 90}$ can be emphasized with slice curves as in figure 3.18, for a constant incidence direction given by $\theta_\mathrm{T} = 45^o$ and $\varphi_\mathrm{T} = -\pi/2$,

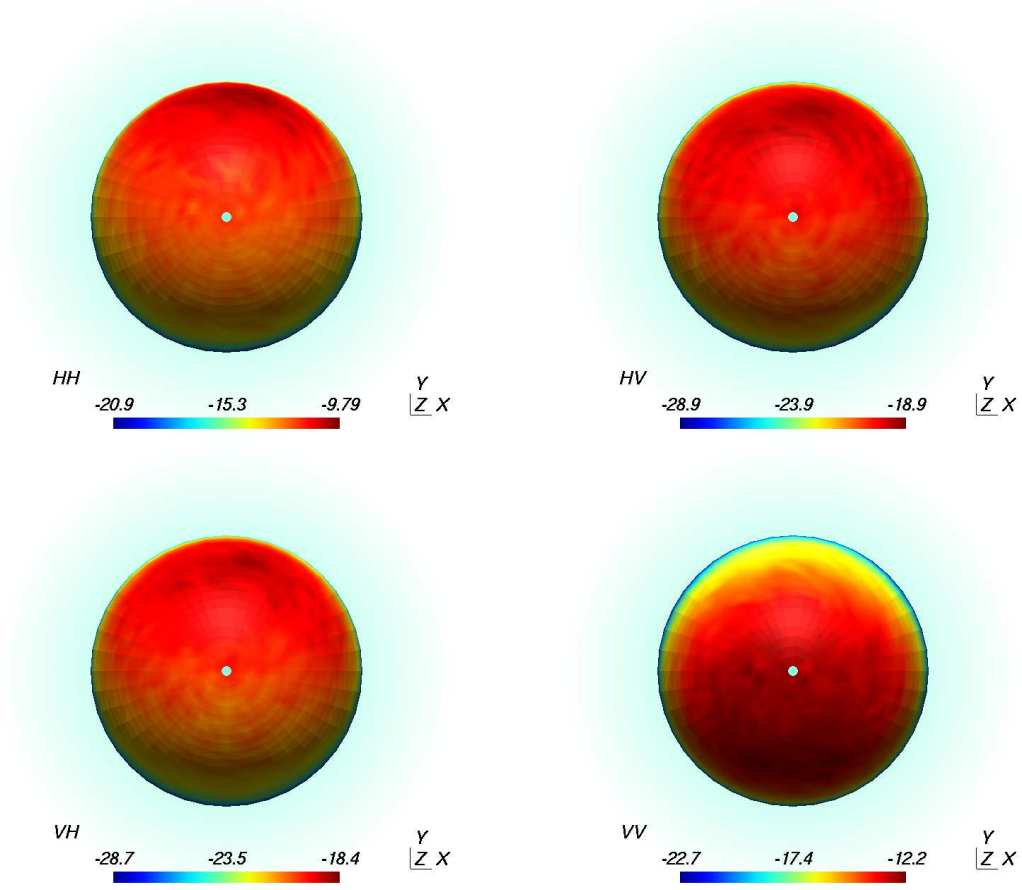

Figure 3.15: L-band (1.27 GHz) scattering diagram representing the bistatic scattering coefficient σ^0_{qp} for the volume contribution in the random orientation case. The linear polarizations indicated above do correspond to the ones within the β polarization basis. The transmitter's location is still given by ($\theta_{\mathrm{T}} = 45^o$, $\varphi_{\mathrm{T}} = -\pi/2$) whereas the receiver's positions sweep over the whole upper hemisphere.

with a varying receiver from both part of the $\hat{x}$ axis, hence the symmetry between the negative and positive values of θ_{R}.

In the uniform volume case first, it can be noticed that the co-polarizations retrieve typical higher values than the cross ones with a switch between both for the off-nadir singularity. On the contrary to the standard polarization basis case for which the cross-pol scattering levels are clearly different – excepted for $\theta_{\mathrm{R}} = 45^o$ corresponding to the reciprocal symmetry – the cross-polarizations retrieve nearly the same values with the β basis, whatever the scattering angle θ_{R}. These results can be also compared to the behaviour shown previously within $\mathcal{P}^{\varphi 0}_{\perp}$ (see figure 3.10). The slight discrepancy is actually due to the reflection symmetry with is not rigorously verified on account of the attenuation, naturally higher on the upper side. Besides, it has been verified that without the attenuation losses, the scattering levels match the ones within $\mathcal{P}^{\varphi 0}_{\perp}$ using the equivalent incident and bistatic angles.

On the contrary, the equivalent situation within $\mathcal{P}^{\varphi 0}_{\perp}$ is more tricky to find for the oriented volume case (see figures 3.18 c and d) since the equivalent branch insertion angles (ψ_{ins}) with

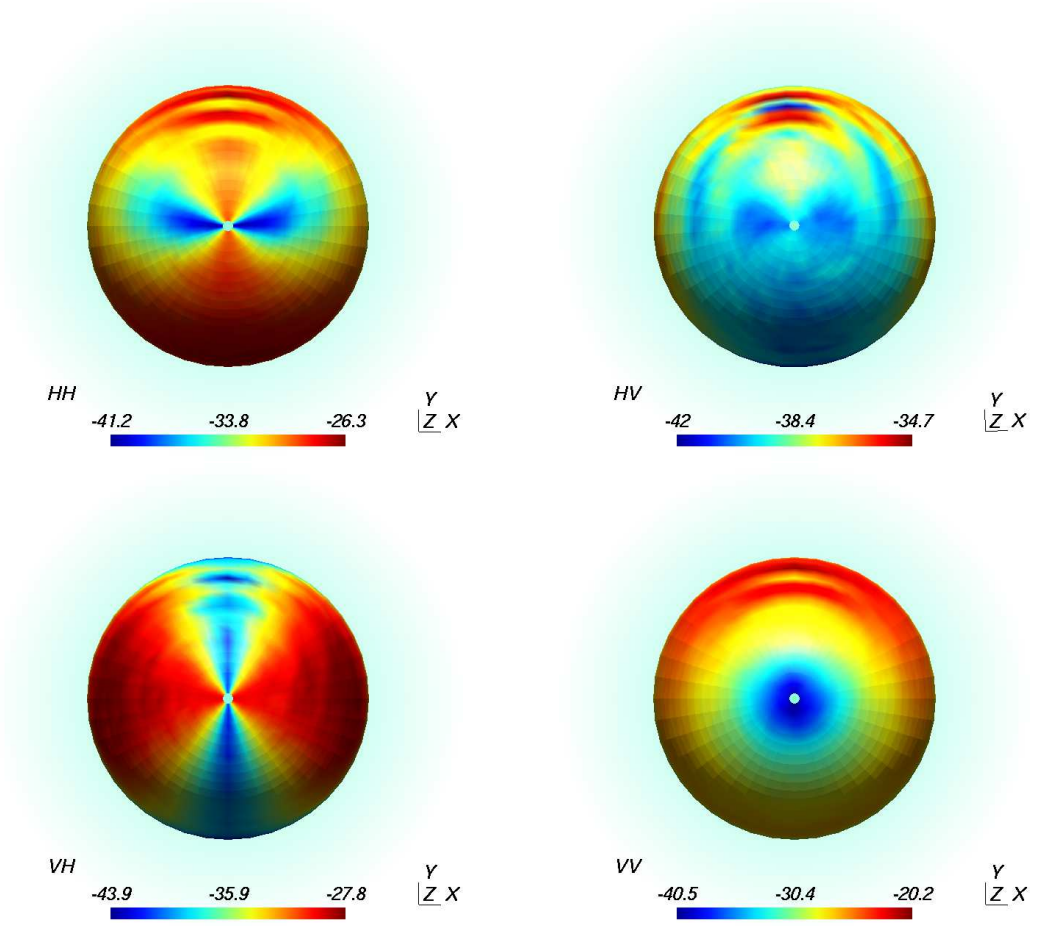

Figure 3.16: L-band (1.27 GHz) scattering diagram representing the bistatic scattering coefficient σ^0_{qp} for the volume contribution in the oriented volume case with ψ_{ins} restricted to $[0., 17.2^o]$. The transmitter's location is given by ($\theta_{\mathrm{T}} = 45^o$, $\varphi_{\mathrm{T}} = -\pi/2$) whereas the receiver's positions sweep over the whole upper hemisphere. The standard (v,h) linear polarizations have been used as indicated above.

respect to the bistatic plane are different. For instance for $\theta_{\mathrm{R}} = 45^o$, the equivalent orientation would correspond to rather horizontal scatterers so that VH is greater and not equal to HV. Nevertheless, the general link between the branches orientation and the gap between cross-pol is still valid using the bistatic plane. As another example, for the steep scattering angles, the orientation can still be considered rather vertical so that HV is clearly greater than VH, as opposed to the situation with standard polarizations basis (see graph c still in figure 3.18).

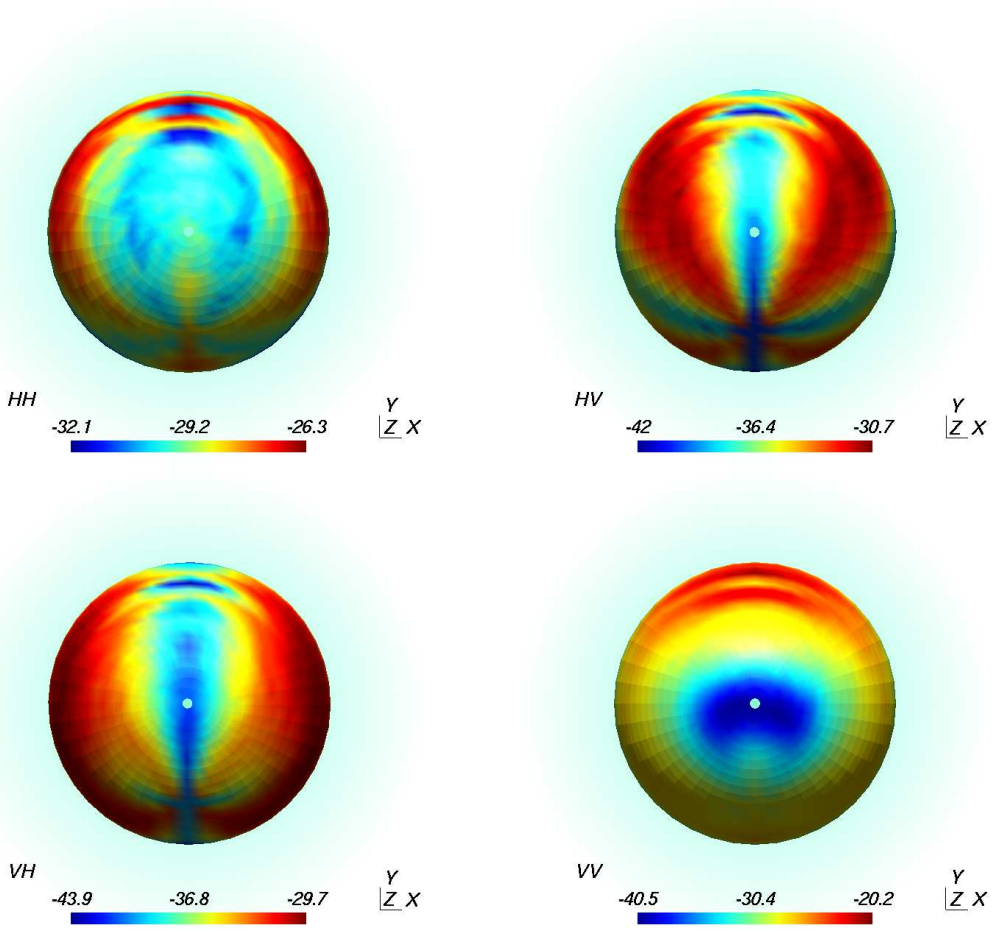

Figure 3.17: L-band (1.27 GHz) scattering diagram representing the bistatic scattering coefficient σ^0_{qp} for the volume contribution in the oriented volume case with ψ_{ins} restricted to $[0., 17.2^o]$. The linear polarizations indicated above do correspond to the ones within the β polarization basis. The transmitter's location is still given by ($\theta_{\mathrm{T}} = 45^o$, $\varphi_{\mathrm{T}} = -\pi/2$) whereas the receiver's positions sweep over the whole upper hemisphere.

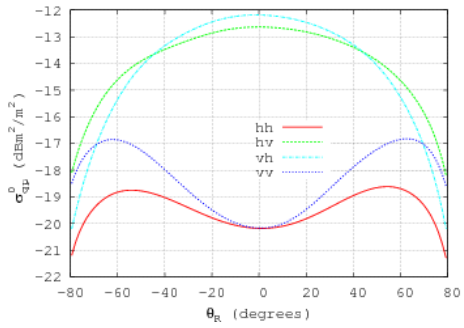

(a) RV

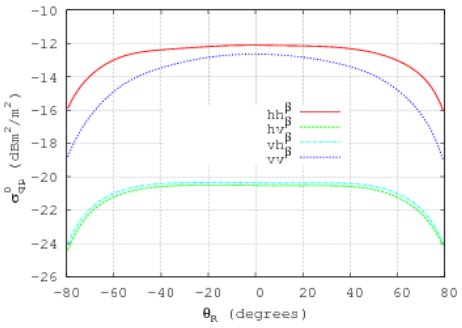

(b) RV, β pol

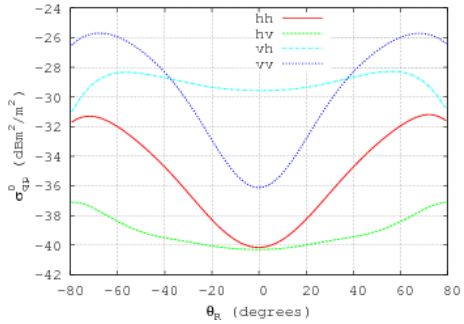

(c) ψV

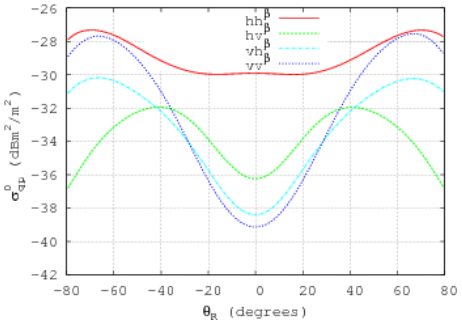

(d) ψV, β pol

Figure 3.18: L-band (1.27 MHz) σ^0_{qp} of the volume contribution versus the scattering angle θ_{R} within the plane $\mathcal{P}_{\perp}^{\varphi 90}$ with a transmitter position given by $\theta_{\mathrm{T}} = 45^o, \varphi_{\mathrm{T}} = -\pi/2$. The randomly oriented volume case (a)-(b) or oriented one with ψ_{ins} restricted to $[0., 17.2^o]$ in (c)-(d) are considered according to either the standard vertical, horizontal linear polarizations or to the ones defined in the β polarization basis.

3.3 Typical Behaviour of Coupling Terms in Bistatic

3.3.1 Status of the Scattering Enhancement

The point now at issue concerns the scattering behaviour of the coupling terms, which will be focused though on generic characteristics since a more thorough sensitivity analysis with various incidence angles and ground types (for roughness and soil water content) will be conducted in chapter 4 and 5.

As conducted previously for the analysis of the volume scattering only, the normal bistatic plane will be studied first, before the whole hemispherical scattering diagrams. The case of the uniform or oriented volume can be considered likewise, so that the same volume layers as in section 3.2 (cf. table 3.1) have been simulated considering this time the double bounce contribution, as shown in figure 3.19 with the resulting polarimetric scattering coefficients versus θ_{R}. Whether oriented or not, a characteristic phenomenon can be noticed with the two peak and trough values respectively for the co and cross polarizations and in the monostatic and specular configurations. As explained in the second chapter, we remind that the overall scattered field due to the coupling contribution is made with two terms : the double bounce – also referred as the specular ground – with respect to the transmitter or to the receiver. This twofold composition is actually at the origin of this kind of singularities and is well-known in monostatic for the like polarizations as the backscattering enhancement. Indeed, from the geometrical point of view, it turns out that for both monostatic or bistatic configurations, the propagation phase is identical for the two specular ground terms. Concerning the scattering amplitude involved at the level of the volume element, both configurations are also specific.

To clarify this behaviour, these contributions can be made explicit using the scattering matrix formalism. Indeed, on account of the involved matrix product (cf. chapter 2, formula 2.5), the specular ground terms can be expressed as follows :

$$\begin{aligned} S_{qp}^{\mathrm{Tsg}} &= \overset{-}{t}{}_q^i \;\; s_{qp}(\hat{\aleph}_i, \hat{k}_s)\; e^{-jk\mathcal{L}_{\mathrm{Tsg}}}\; \mathcal{R}_p \;\; \overset{+}{t}{}_q^i \\ S_{qp}^{\mathrm{Rsg}} &= \overset{+}{t}{}_q^i \;\; s_{qp}(\hat{k}_i, \hat{\aleph}_s)\; e^{-jk\mathcal{L}_{\mathrm{Rsg}}}\; \mathcal{R}_q \;\; \overset{-}{t}{}_q^i \end{aligned} \tag{3.43}$$

in which the indices q,p stand either for v or h, $\mathcal{R}_q$ for the polarimetric modified Fresnel coefficients and with the transmittivity terms :

$$\begin{aligned} \overset{-}{t}{}_q^i &= \exp\big[-\frac{\sigma_{q,p}(h-z)}{\cos\theta_{s,i}}\big] \\ \overset{+}{t}{}_q^i &= \exp\big[-\frac{\sigma_{q,p}(h+z)}{\cos\theta_{s,i}}\big] \end{aligned} \tag{3.44}$$

We remind also invoking the far field approximation that the unitary vector $\aleph_{i,s}$ can be expressed as :

$$\aleph_{i,s} = \hat{k}_{i,s} - 2(\hat{k}_{i,s}\cdot\hat{z})\hat{z}$$

A mentioned previously, the scattered field corresponding to the specular ground terms can be expressed in its complex scalar from as :

$$E_s^{\mathrm{sg}} = E_s^{\mathrm{Tsg}} + E_s^{\mathrm{Rsg}}$$

giving for the scattering coefficient :

$$\begin{aligned} \sigma^{0,\mathrm{sg}} \propto \langle E_s^{\mathrm{sg}}, \overset{*}{E}{}_s^{\mathrm{sg}}\rangle &= \langle E_s^{\mathrm{Tsg}} + E_s^{\mathrm{Rsg}}, (E_s^{\mathrm{Tsg}} + E_s^{\mathrm{Rsg}})^*\rangle \\ &= |E_s^{\mathrm{Tsg}}|^2 + |E_s^{\mathrm{Rsg}}|^2 + 2Re\big(\langle E_s^{\mathrm{Tsg}}, \overset{*}{E}{}_s^{\mathrm{Rsg}}\rangle\big) \end{aligned} \tag{3.45}$$

In monostatic first and for the like polarization, the reciprocity theorem naturally holds so that $E_s^{\mathrm{Tsg}} = E_s^{\mathrm{Rsg}}$. In comparison with a non-specular bistatic configurations, the right hand side correlation term in equation 3.45 is not zero, we have :

$$\left[E_s^{\mathrm{sg}}(\beta = 0)\right]^2 = 4\left[E_s^{\mathrm{Tsg}}(\beta = 0)\right]^2 = 2\left[E_s^{\mathrm{sg}}(\beta \neq 0)\right]^2$$

hence the 3 dB gain for $\sigma^{0,\mathrm{sg}}$ which can be retrieved in figure 3.19.

Still in monostatic but this time for the cross polarizations, the propagation phase term are naturally still identical between E_s^{Tsg} and E_s^{Rsg} but the specificity comes from the following product :

$$\begin{aligned}\langle E_s^{\mathrm{Tsg}}, \overset{*}{E_s^{\mathrm{Rsg}}} \rangle &\propto \langle \mathcal{R}_p s_{qp}(\hat{\aleph}_i, \hat{k}_s) \cdot \mathcal{R}_q s_{qp}(\hat{k}_i, \hat{\aleph}_s) \rangle \\ &= \langle \mathcal{R}_p \mathcal{R}_q s_{qp}(\hat{\aleph}_i, -\hat{k}_i) s_{qp}(\hat{k}_i, -\hat{\aleph}_i) \rangle \\ &= -\langle \mathcal{R}_p \mathcal{R}_q s_{qp}(\hat{\aleph}_i, -\hat{k}_i) s_{pq}(\hat{\aleph}_i, -\hat{k}_i) \rangle\end{aligned} \tag{3.46}$$

for which the reciprocity theorem has been applied between the two last lines. From this expression and especially from its negative sign (since both individual product between Fresnel or scattering terms are negative), we can get the origin of the trough value for the cross polarizations. The drop amplitude is however non constant and depends on the modeled ground truth values (especially for those involved within the Fresnel coefficients). It can be particularly interesting on order to minimize the double bounce term for studies concerning the volume dependence towards cross polarization, as detailed in chapter 4 about biomass retrieval.

Concerning the specular bistatic peak and trough values, another important coherent effect occurs. Indeed, from the geometrical point of view, we demonstrate in chapter 5 that the involved path for both specular mechanism is equivalent to a simple scattering interaction onto a specific ground point, determined from the angle $\iota = (\theta_{\mathrm{T}} - \theta_{\mathrm{R}})/2$. It is all the more clear in the specular configuration for which $\iota = \theta_{\mathrm{T,R}}$. In addition, in the specular configuration, the tangential vector to the iso-range ellipsoid is parallel to the horizontal reference so that every ground scatterers in this region will have about the same geometrical phase (the well-know resolution singularity for imaging, cf chapter 2). Considering these two facts – the equivalent ground point as well as the iso-range loci – the very strong enhancement can be clarified since every specular ground contribution from the various scatterers adds coherently. Furthermore, for cross-polarizations, an amplitude decrease can be noticed in the case of the oriented volume. In this case indeed, the correlation between E_s^{Tsg} and E_s^{Rsg} is non null and rather, brings a negative term as explained in monostatic. This effect concerns only vertical cylinder (or nearly vertical in view of the relatively large side lobes in P-band and such heigh of cylinders) for which :

$$s_{qp}(\hat{\aleph}_i, \hat{k}_s) = s_{qp}(\hat{k}_i, \hat{\aleph}_s)$$

in view of the mirroring symmetry with respect to the plane $(\hat{x}, \hat{y})$. Hence the trough is all the more manifest than the volume is vertically oriented, as confirmed also with the scattering diagram for a trunk layer, displayed in figure 3.22.

As far as the whole bistatic space is concerned, the hemispherical scattering diagram of the previous random volume is shown in figure 3.19. On account of the geometrical phase involved in the double bounce mechanism, it turns out that the enhancement due to the coherent effect holds also for bistatic configurations as long as the azimuthal invariance of the traveling paths remains. As a result, a characteristic crown-like ridge is mostly present in the scattering diagrams. The gap is also roughly of 3 dB but not rigorously since the amplitude for E_s^{Tsg} and E_s^{Rsg} are different,

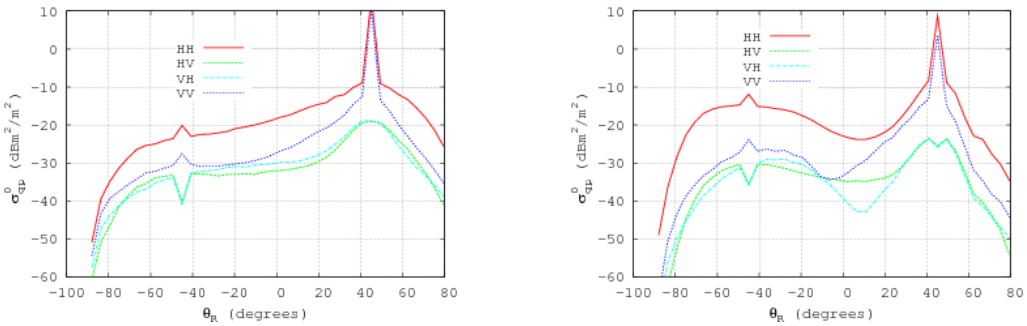

(a) RV (b) ψV

Figure 3.19: L-band (1.27 GHz) σ^0_{qp} of the volume contribution versus the scattering angle θ_{R} within the plane $\mathcal{P}^{\varphi 0}_{\perp}$ with a transmitter position given by $\theta_{\mathrm{T}} = 45^o, \varphi_{\mathrm{T}} = -\pi/2$. The randomly oriented volume case (a) or oriented one with ψ_{ins} restricted to $[0., 17.2^o]$ in (b) are considered according to the the standard vertical, horizontal linear polarizations

as shown in figure 3.23 with the RCS of a single cylinder in such configuration with for instance an azimuthal difference of 45^o. Conversely the trough values for cross polarizations concern essentially the monostatic configuration and with a smaller impact the specular ones since for the others general configurations the inter-mechanisms correlation is null.

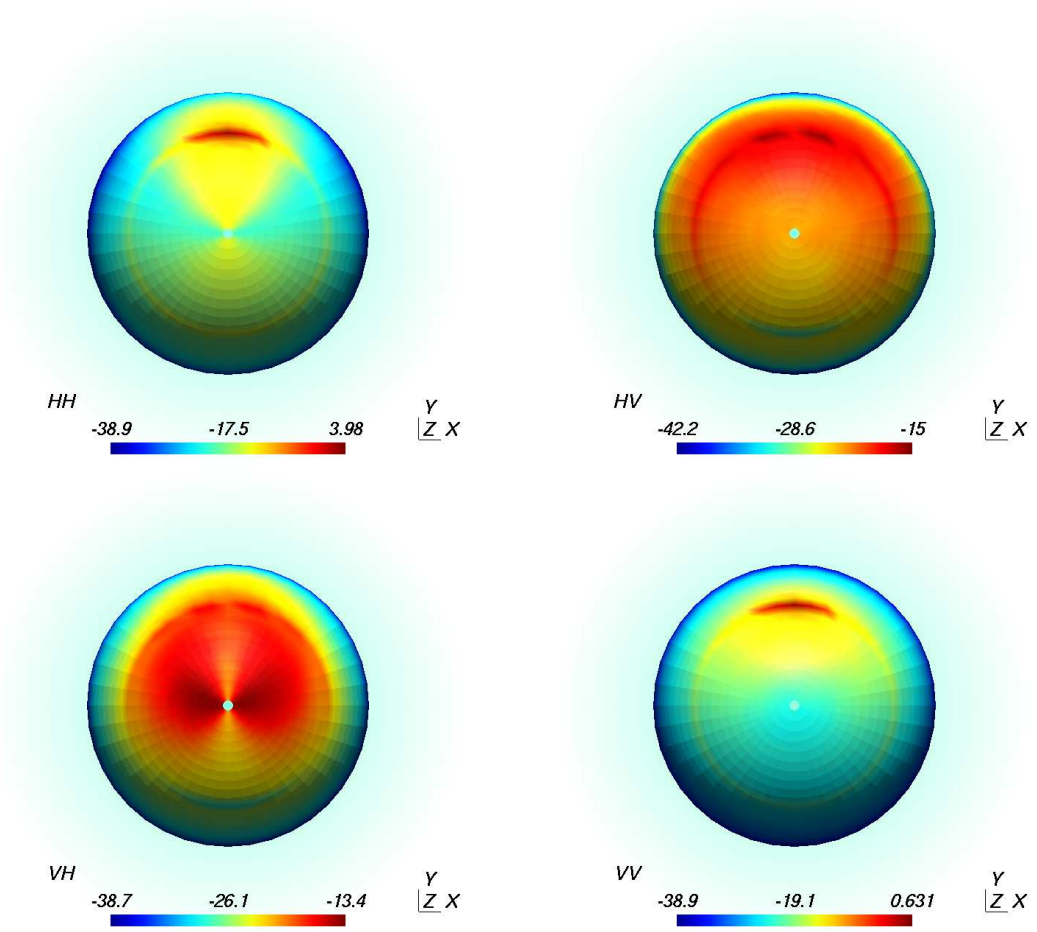

Figure 3.20: P-band (430 MHz) scattering diagram representing the bistatic scattering coefficient σ^0_{qp} for the double bounce contribution in the random volume case. The standard (v,h) linear polarizations have been used as indicated above. The transmitter's location is still given by ($\theta_{\mathrm{T}} = 45^o$, $\varphi_{\mathrm{T}} = -\pi/2$) whereas the receiver's positions sweep over the whole upper hemisphere.

3.3.2 Effects of a Vertical Structure

Apart the coherent effects presented before, the threefold origin of the double bounce scattering sensitivity towards directions can be pointed out. First of all, attenuation has to be considered, particularly as far as the incidence is increasing, as well as for the volume which may strengthen the difference between E_s^{Tsg} and E_s^{Rsg} in the case of an oriented or structure volume, as shown with the C2SORVoG and C2SOψVoG models employed in chapter 5. Double bounce specificities concerning attenuation have been also presented in chapter 2 in the case of sparse forests with clearings and will be also pointed out regarding detection applications in the next section.

Secondly, the Fresnel specular reflection has also a great impact with the varying incidence angle and originates also important difference between like polarizations, especially as far as the Brewster region in VV is concerned. The analysis of the resulting sensitivity towards soil humidity, incidence angle and its subsequent optical ground roughness will be used in chapter 5 (see for instance figures 5.41 and 5.42).

Finally, the scattering interaction with the volume element takes naturally a great part and is particularly emphasized by the difference between the uniform or oriented volume and rather with the difference between the oriented branches or trunks-like scatterers, shown with the hemispherical diagrams in figures 3.21 and 3.22. To analyse this sensitivity towards scattering directions, we can refer to the RCS of a single cylinder, for the configurations likely to be involved such as in figure 3.23 which would correspond directly to scattering directions encompassed for E_s^{Rsg}. Indeed, apart from $\Delta\varphi$ which gives – cases (a) to (f) – the scattering plane $\mathcal{P}_{\perp}^{\varphi}$ after interaction onto the cylinder, the highest values for θ_s correspond to steep viewing angle (i.e close to the nadir) for the receiver and conversely. Notwithstanding, the double bounce with respect to the transmitter (E_s^{Tsg}) can be also analysed with these plots invoking the mirroring symmetry – regarding the horizontal plane $(\hat{x}, \hat{y})$ which holds for vertical cylinder. Besides, on the contrary E_s^{Rsg}, the sensitivity of E_s^{Tsg} towards scattering directions do not depend on the varying Fresnel coefficient with the specular angle, which has to be kept in mind for the following comparisons (with directions involving different site angles).

Concerning first the HH polarization, a trough region is clearly manifest On the contrary to scattering diagrams for the volume contribution and these low values within $\mathcal{P}_{\perp}^{\varphi 90}$ likewise, the polarization artefacts are not concerned since it depends on the scatterer attributes. For instance, apart from the nadir region, such minimums are not present with trunks-like scatterers in figure 3.22. It can be explained actually from the cylinder RCS behaviour : indeed concerning the nadir region, that is θ_s higher than 150^o, it can be noticed that for $\varphi \sim 80, 90^o$ the level suddenly decreases whereas it is roughly equal between other azimuth angles. This drop is besides all the more important that the radius is small (as an example with (a) and (d) around -10 and -50 dBm^2 respectively for r=5 and 0.5 cm). Notwithstanding, if we look this time at larger incidence angle for the receiver (i.e θ_s around 120^o), it turns out that the decrease for azimuth angles close to 90^o concerns only the small radius : still between (a) and (d), the gap is around -50 dBm^2 for r=0.5 cm and only a few dBm^2 for r =5 cm). Besides, even restricted to the nadir region in the case of trunk-like scatterers, a weak double bounce in HH can be used as an interesting bistatic property, for the purpose of maximizing the volume contribution, typically as used for biomass retrieval methods (cf. chapter 4).

For the VV polarization, the most noticeable difference concerns the trough region which is manifest in the backward off-nadir region (cf. figure 3.22) for trunks and not present at all in figure 3.21). This comes likewise from the cylinder RCS in this configuration : for instance, in the small case radius, the level remains constant ($\sim -35 dBm^2$ for $\theta_s = 150^o$) whatever the

azimuthal case from (a) to (f) in 3.23. Hence in figure 3.21 the quite homogeneous scattering diagram regarding the azimuth variation, in which the cylinder RCS's lobes are also visible. On the contrary, for larger radius, the scattering level it goes up together with the azimuthal angle, from about -10 to 0 dBm^2.

In addition, the cross-polarizations are also sensitive to the scatterer geometrical attributes, especially towards orientation. Indeed, the difference between the uniform or oriented cases (figures 3.20 and 3.21) shows truly this sensitivity, whereas the difference between oriented branches and trunks (3.21 and 3.22) do not change significantly the diagram shape. As detailed in the previous section, it results directly from the oriented volume scattering sensitivity towards the bistatic angle, so that about the same behaviour for the cross-polarizations between volume and double bounce can be emphasized, particularly with the relations between the orientations and the HV-VH difference. For instance, it is clearly manifest around the off-nadir region with the rather vertically oriented scatterers, as shown in figure 3.19 and 3.10 respectively for coupling and direct volume contributions.

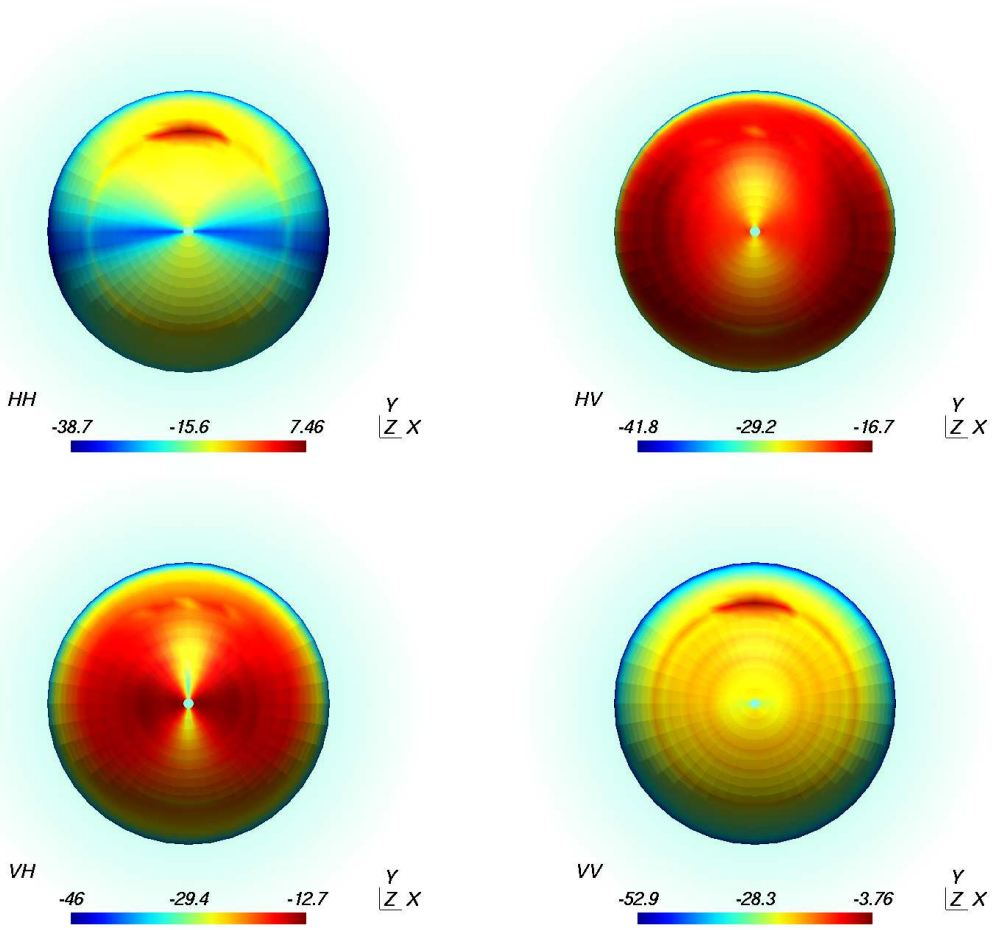

Figure 3.21: P-band (430 MHz) scattering diagram representing the bistatic scattering coefficient σ^0_{qp} for the double bounce contribution in the oriented volume case with ψ_{ins} restricted to $[0., 17.2^o]$. The standard (v,h) linear polarizations have been used as indicated above. The transmitter's location is still given by ($\theta_{\mathrm{T}} = 45^o$, $\varphi_{\mathrm{T}} = -\pi/2$) whereas the receiver's positions sweep over the whole upper hemisphere.

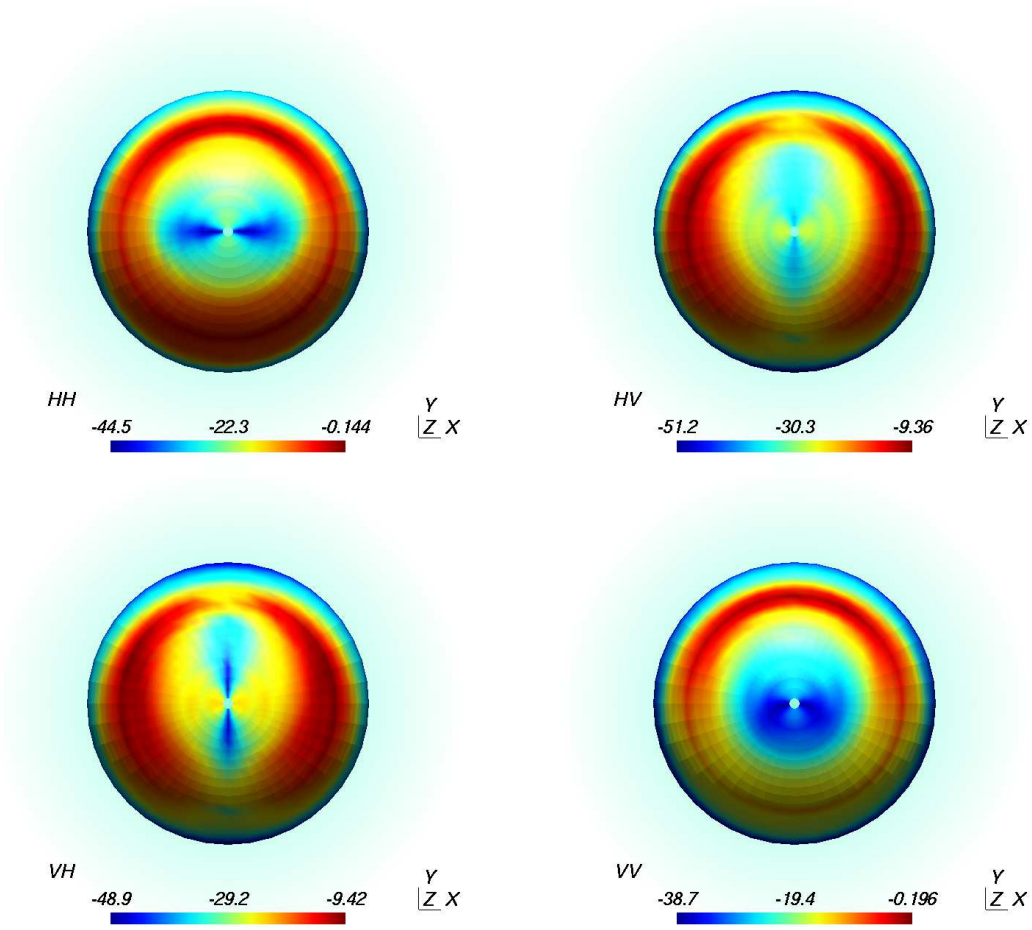

Figure 3.22: P-band (430 MHz) scattering diagram representing the bistatic scattering coefficient σ^0_{qp} for the double bounce contribution for a layer made of trunk-like scatterers (cf. table 3.1). The standard (v,h) linear polarizations have been used as indicated above. The transmitter's location is still given by ($\theta_{\mathrm{T}} = 45^o$, $\varphi_{\mathrm{T}} = -\pi/2$) whereas the receiver's positions sweep over the whole upper hemisphere.

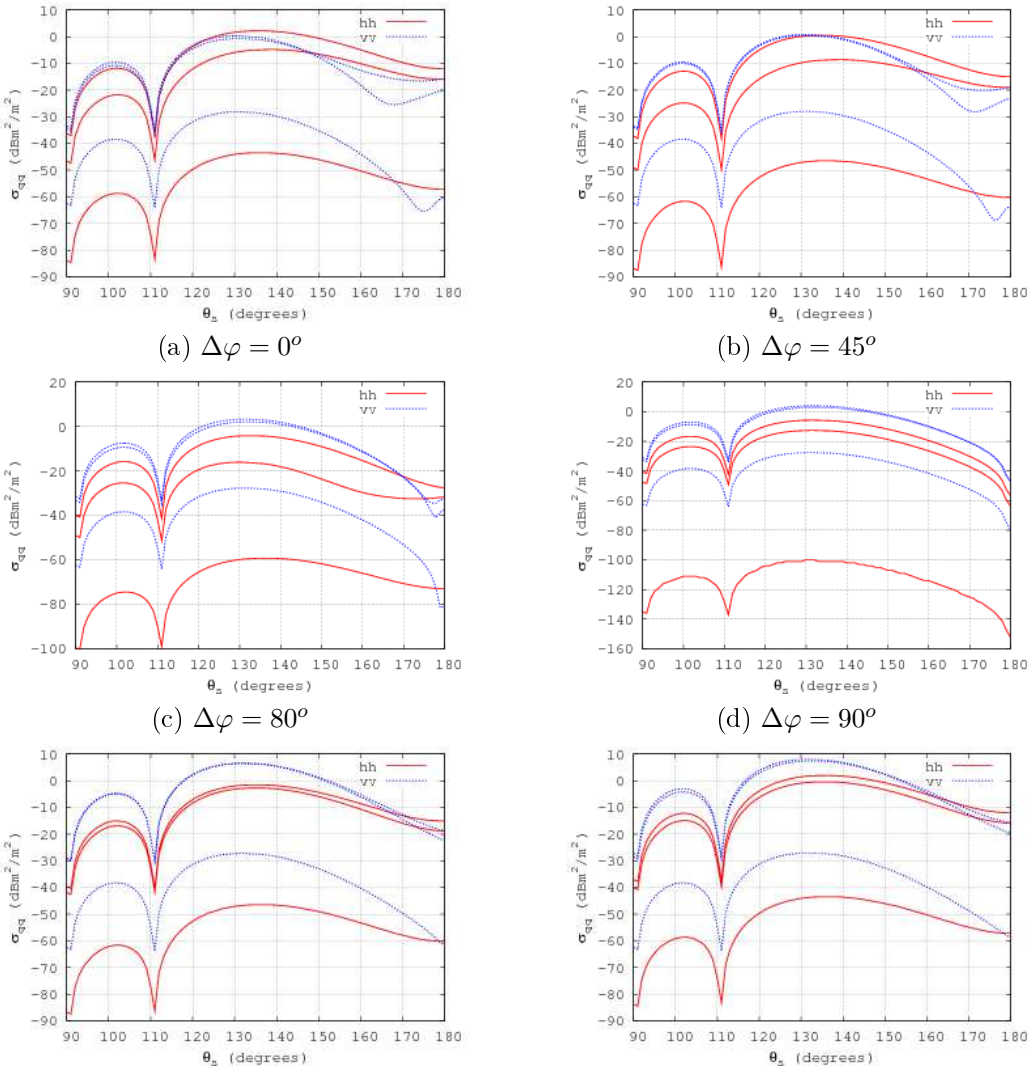

(a) $\Delta\varphi = 0^o$ (b) $\Delta\varphi = 45^o$

(c) $\Delta\varphi = 80^o$ (d) $\Delta\varphi = 90^o$

(e) $\Delta\varphi = 135^o$ (f) $\Delta\varphi = 180^o$

Figure 3.23: P-band (430 MHz) RCS (σ_{qq}) of a single vertical and 2 m heigh cylinder (all ψ angles nul) versus θ_{R} with a constant incident direction $\theta_{\mathrm{T}} =_{\mathrm{SSA}} 45^o$ and a given relative azimuth angle difference $\varphi_{\mathrm{T}} - \varphi_{\mathrm{T}}$ as indicated above for the cases (a) to (f). The sheaf of curves is obtained for 3 different radius : 0.5, 5.25 and 10 cm) going up together with the RCS amplitude. These configurations correspond to typical scattering configurations involved in the bistatic double bounce contribution.

3.4 Detection Applications in Bistatic

The electromagnetic modeling of the detection problem for camouflaged or lost targets under the vegetation cover have been presented in the second chapter. Based on the remarkable properties of bistatic radar observables set forth in this chapter (in the case of generic forest models), this section is dedicated to their potential regarding detection, that is to discriminate pixels with foreign objects among those with natural scatterers only.

As a overall principle within the context of a-priori unknown targets, detection algorithms aims at characterizing as well as possible an intrinsic attribute of the host media, in order to enhance a spatial discontinuity coming with the presence of a localized target. This rises thereby the core problem of detection within SAR images, which lies in the trade-off between sufficiently averaged data to reach this level of medium characterization and maintaining a sufficiently high resolution (the target being localized, its contribution naturally drops for coarse resolution, as opposed to distributed targets proportional to the pixel area).

As mentioned in the introduction, this problem is quite general concerning detection of coherent scatterers within SAR speckled data and approaches based on a specific SAR processing (by means of spectral sub-looks, cf. [Souyris et al., 2003; Schneider et al., 2006]) turn out to be particularly efficient, all the more as a first step before other treatments on the resulting image (mostly based on spatial statistic methods as in [El-Rouby et al., 2003; Barbaresco, 2008] but also more originally on temporal criteria in [Nashashibi and Ulaby, 2005]). As far as SAR system aspects are concerned, the detection capability, mainly in terms of expectation – goes naturally up together with additional radar measures. Among them is the Pol-InSAR acquisition (cf. chapter 5) from which the detection can be performed using the retrieved ground (or target) ratio over volume, as proposed in [Cloude et al., 2004]. The optimization of the resulting Pol-InSAR coherences may bring also a significant improvement in comparison with non interferometric ones (cf. [Colin et al., 2005]). More complex acquisitions, aiming at 3D reconstruction have shown also a straightforward great potential for detection, for instance by means of circular SAR and flashlight mode (cf. [for FOPEN using flashlight mode images along circular trajectories, 2007]).

Notwithstanding, in order to focus on the potential of bistatic polarimetry, our analysis is herein restricted to full polarimetric acquisition. In the following subsection, the typical case of a target under a homogeneous forest is considered by means of simulated images with MIPERS, as detailed at the end of chapter 2. The detection strategy will be based on the violation – due to the target presence – of the afore-demonstrated bistatic observables symmetry properties. Then, in the last subsection (3.4.2), a more specific case is assessed with the status of target detection near forest clearings, since the bistatic configuration is likely to modify the border effects.

3.4.1 Symmetry-Based Algorithms

As demonstrated in the subsection 3.1.2, the medium symmetries originates specific relations between the scattering matrix elements (equations 5.13 to 5.17) which are well synthesized within the coherency matrix T. As a result, the T matrix coefficients (t_{ij}) can be viewed as relevant classification indicators. For most of the classification applications in radar remote sensing (i.e related to environmental issues) the null coefficients t_{ij} ensued from a-priori known symmetries are rather used to assess the data noise level than as a consistent source of information. The non null terms are preferred, especially when they can be associated to the afore-mentioned scattering mechanisms. This approach is widely used in the field of monostatic radar classification (see for instance [I. Hajnsek, 2003] concerning surface parameters) and refers to target decomposition theorems (cf. [Cloude and Pottier, 1996]).

Nevertheless, as far as detection is concerned, the null (t_{ij}) coefficients are potentially great indicators as soon as the symmetry properties are violated. In order to assess their discrimination potential, simulations have been conducted with MIPERS, as described at the end of the second chapter, with the same target (truck like vehicle, located in the middle of the image) and under a typical model of temperate forest (derived from the Nezer ground truth) surrounded by a bare ground.

In view of the deterministic nature of the target – plus non isotropic and with a relatively high directivity – the generalization of the detection results is not obvious since they are really dependant on the chosen orientation attitude and on the overall radar configuration (as illustrated in chapter 2).

Two solutions have thus been envisioned, that is the analysis of the mean expectation with respect to all the possible truck orientation or the comparison between the reference standard observables (S_{qp}) corresponding to hard detection cases. With the aim at pointing out the interest of the coefficient t_{ij}, the latter solution is presented hereafter.

For that purpose, a damping factor is introduced so that the target can not be easily detected using the 4 linear polarizations scattering coefficients σ^0_{qp}, as shown in figure 3.24 – with for instance the cross-polarizations (a) and (b). In the right hand side case (c), the parameter t_{43} is displayed, corresponding to one indicator of the reflection symmetry with respect to the plane $\mathcal{P}_{\hat{\delta}}$. It can be noticed that the overall intensity level through the parcel is logically very low (-40 $\mathrm{dBm^2/m^2}$) but is greater than zero since it requires a wider multilook average to reach its theoretical value (as verified for the T matrix of the overall parcel). Nevertheless, that multilook is enough to clearly distinguish the target, as opposed to the simple use of co or cross-polarizations. This simulation has been also achieved with a forest model derived from the Nezer one, with uniformly oriented branches for the two upper layers, referred to as the C3SRVoG model. The same simulations have been achieved with oriented branches (restricted range concerning the insertion angle ψ_{ins}) as for typical temperate forest (still based on the Nezer ground truth). Likewise, the contrast is really improved by the use of the t_{43} parameter, even if this parameter is not rigorously null since both π and $\mathcal{P}_{\hat{\delta}}$ are not strictly verified.

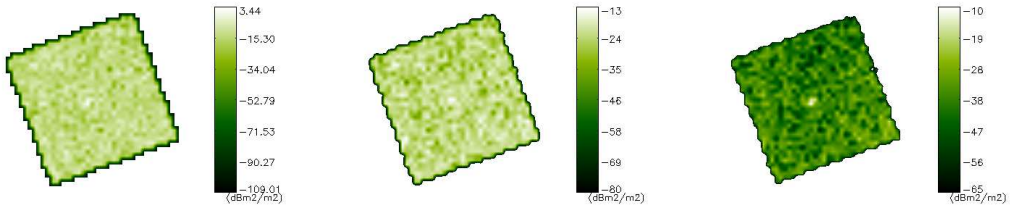

(a) HV (b) VH (c) t_{43}

Figure 3.24: Simulated images of the scattering coefficients at P-band (430 MHz) in the C3RVoG forest model case for a bistatic configuration given by the angles : $\theta_{\mathrm{T}} = 45^o, \theta_{\mathrm{R}} = 5^o, \Delta\varphi = 0$.

The other indicator within the two left bottom and right top 2*2 blocks (corresponding to the reflexion symmetry) have been also tried. Though more robust than the intensity in the standard polarization channel, t_{43} exhibit a more stable behaviour for the various target attitudes.

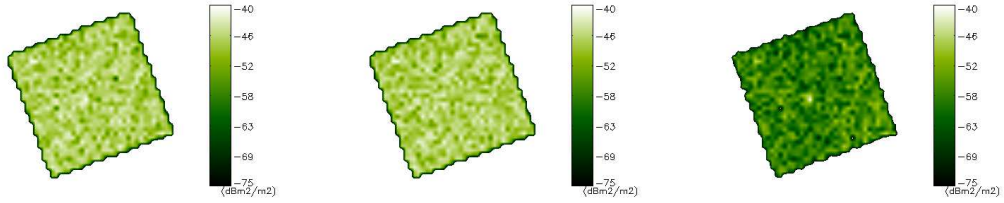

(a) HV (b) VH (c) t_{43}

Figure 3.25: Simulated images of the scattering coefficients at P-band (430 MHz) in the C3S0ψVoG forest model case for a bistatic configuration given by the angles : $\theta_{\mathrm{T}} = 45^o, \theta_{\mathrm{R}} = 5^o, \Delta\varphi = 0$.

The case of a tilted bistatic plane is now considered with for instance the configuration of a receiver within the plane $\mathcal{P}_{90}^{\perp}$, in order to maximize (with a grazing scattering angle) the effect of the titled $\mathcal{P}_{\beta}$. This configuration is indeed interesting since the sensitivity analysis of the forest scattering diagram shows that in most cases, the volume is the major contribution (as well as for steep angle) and deserve our attention with this framework since it exhibits the most complete symmetry properties. On account of the various simulated configurations for the receiver within $\mathcal{P}_{90}^{\perp}$, it has been noticed that the contrast for t_{43} goes down together with the increasing scattering angle θ_{R}, as shown in figure 3.26 case (a). This is consistent with the fact that the reflection symmetry is violated even for the volume, hence the use of the β polarization – case (b) 3.26 – which improves significantly the contrast. Nevertheless, this contrast is not as good as for the normal bistatic plane, still in view of the reflection symmetry which does not hold rigorously. This can be emphasized in the case of a more vertically oriented structure, for which the reflection symmetry violation with respect the bistatic plane is strengthened. For such configuration, the t_{43} contrast is likely to be not as good as within $\mathcal{P}_{\beta}$ but alternatively in this case, the orientation effect should be retrieved using the algorithm presented in subsection 3.2.2. Indeed, this algorithm has been performed for each pixel and the restricted range orientation angle (ψ_{ins}) corresponds consistently to a relatively constant retrieved value (as opposed for instance to case of the normal bistatic plane for which the retrieval of such angle is not relevant in view of the reflection symmetry). Besides, it can be established that it works very well for the simulated ground since its normal has been simulated constant throughout the image. Within the approximation made for the simulated ground, this algorithm evinces in addition a very efficient method for speckle filtering, naturally within the limitation of the simulated one.

Furthermore, the reciprocal symmetry – or spatially-wise the π symmetry – had been also set forth during the analysis conducted in subsection 3.2.1 in which we logically retrieved that the polarimetric scattering coefficient σ_{qp}^0 were respectively identical for the 2 reciprocal bistatic

configurations defined explicitly by the relations :

$$\begin{aligned} &\left(\theta_{\mathrm{T}}^1, \varphi_{\mathrm{T}}^1, \theta_{\mathrm{R}}{}^1, \varphi_{\mathrm{R}}^1\right) \\ &\left(\theta_{\mathrm{T}}^1, \varphi_{\mathrm{T}}^1, \theta_{\mathrm{R}}{}^1, \varphi_{\mathrm{R}}^1\right) \\ &\text{with : } \theta_{\mathrm{T}}^2 = \theta_{\mathrm{R}}^1, \\ &\qquad \varphi_{\mathrm{T}}^2 = \varphi_{\mathrm{R}}^1 - \pi \\ &\qquad \theta_{\mathrm{R}}^2 = \theta_{\mathrm{T}}^1 \\ &\qquad \varphi_{\mathrm{R}}^2 = \varphi_{\mathrm{T}}^1 - \pi \end{aligned} \tag{3.47}$$

Both configurations have been simulated and the resulting intensity corresponding to the complex difference, that is $\langle |s_{hh}^1 - s_{hh}^2| \rangle$ can be seen in (c), figure 3.28. We conclude that though improved in comparison with the typical polarization, this more complex acquisition is not more advantageous (especially regarding the required number of sub-looks) than the use of the afore-mentioned T matrix indicators which are derived from a single bistatic acquisition (naturally the comparison is limited to this reciprocal criteria).

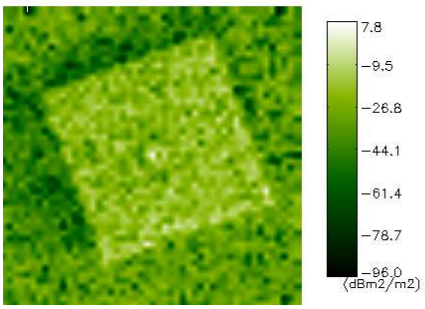

(a) t_{43}

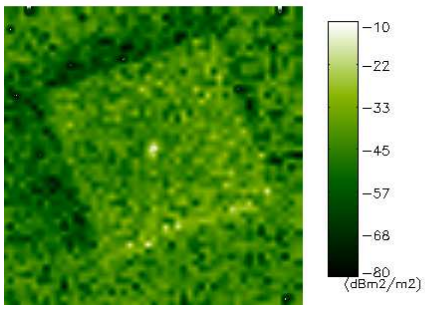

(a) t_{43}, β basis

Figure 3.26: Simulated images of the scattering coefficients at P-band (430 MHz) in the C3S0ψVoG forest model case for a bistatic configuration given by the angles : $\theta_{\mathrm{T}} = 45^o, \theta_{\mathrm{R}} = 60^o, \Delta\varphi = 90^o$.

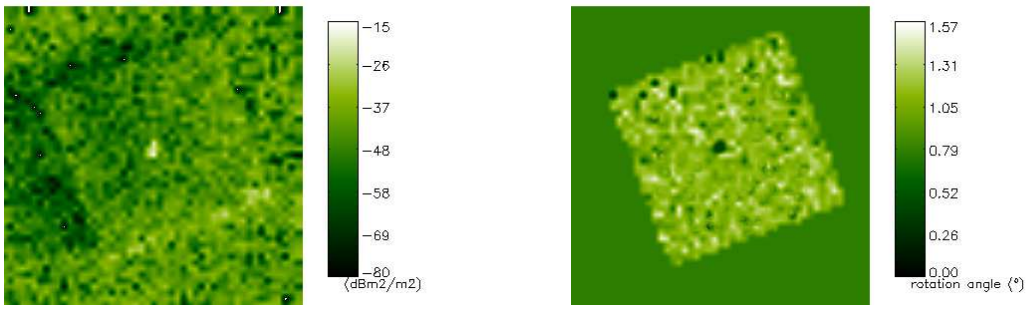

(a) t_{43} (b) optimal rotation pol

Figure 3.27: Simulated images of the scattering coefficients at P-band (430 MHz) in the case of a vertically ψ oriented forest model for a bistatic configuration given by the angles : $\theta_{\mathrm{T}} = 45^o, \theta_{\mathrm{R}} = 60^o, \Delta\varphi = 90^o$.

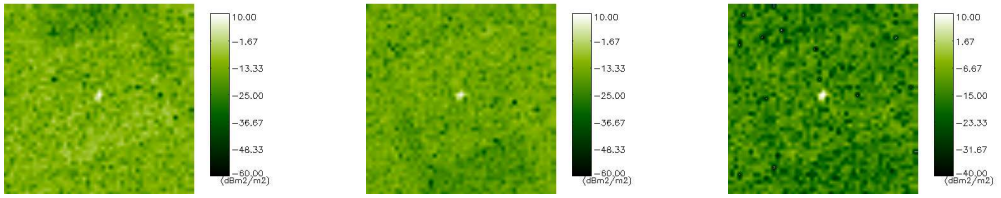

(a) (b) (c)

Figure 3.28: Simulated images of the scattering coefficients at P-band (430 MHz) in the C3SOψVoG forest model case for the reciprocal bistatic configurations in (a) and (b) that is respectively $[\theta_{\mathrm{T}} = 60^o, \theta_{\mathrm{R}} = 30^o, \varphi = 180^o]$ for the [grazing transmitter – steep receiver] and $[\theta_{\mathrm{T}} = 30^o, \theta_{\mathrm{R}} = 60^o, \varphi = 180^o]$ for its reciprocal position, assuming the π rotation symmetry property. The difference $\langle |s^1_{hh} - s^2_{hh}| \rangle$ is shown in (c).

3.4.2 Detection around Forest Clearings

Consistent with our aim at pointing out specific advantages of bistatic configurations but applicable – as far as possible – whatever the target or forest type, the suppression of the coherent enhancement pointed out beforehand is potentially worthwhile to exploit. As detailed previously (subsection 3.3.1, specific configurations are concerned, naturally the monostatic position and more generally all the ones for which the two specular ground mechanisms with respect to the transmitter or to the receiver add coherently in phase, as well illustrated in the afore-shown hemispherical scattering diagrams (e.g figures 3.21, 3.22) with a characteristic crown-shape loci.

Though dependent on the scatterers directivity, this decrease is about -3 dB, corresponding to the like polarizations drop in the case of an uniform volume from the monostatic to the quasi-monostatic configuration. As a matter of fact, this drop concerns naturally the double bounce contribution ensued from the target for which the likely high directivity effect makes hazardous the estimation of the intensity decrease. Consequently, even if the double bounce is minimized for both, it not obvious that the target over volume clutter ratio ratio μ^{C} will be strengthened for all that.

Nevertheless, even if a constant ratio is considered from a monostatic configuration to a bistatic one (away from the crown region) the image contrast – that is qualitatively the radiometric difference between the pixel entailing the target and its neighbourhood ones – turns out to be really improved in the case where the target is close to forest clearings and even more on the reinforcement side, opposite to the shadowing one. Such simulations have been indeed performed and the resulting images are displayed in 3.29 at P-band for a monostatic and site bistatic configurations, detailed within the legend. Concerning the target, the previously considered truck has been used and the vegetation cover is based on a temperate forest like Nezer. For both, the range gated acquisition have been performed in order to reproduce faithfully the layover effect at the boundary between the bare ground and the forest parcel. With such configurations parameters, it turns out that even with coarse resolution, the ratio μ^{C} is quite high whether in mono or bistatic configuration and whatever the polarization channel. Nevertheless, in the monostatic case (a), the strong reinforcement near the clearing brings an important false alarm.

Indeed, it has been shown in the second chapter that the intensity reinforcement is mainly due to the double bounce contribution (cf. also [Villard and Borderies, 2007a; Villard et al., 2007]) since it is more favoured than the volume one (it involves in the so-called quiet region a stronger attenuation coming from a longer wave propagation path within the vegetation layers). Hence our choice for the sum between the like polarization channel in order to maximize the double bounce (cf. FSA convention).

As a result, in the case where the scattering intensity for the double bounce mechanism is close to the pixel one containing the target, any bistatic configuration can significantly improve the target contrast or equivalently the false alarm rate. Though specific, such configuration is actually quite likely if mobile targets (e.g military vehicules) are considered, for which the presence of ways or sparse areas is required.

Besides, our simulations enable also to assess the possible detection of the shadows coming with the target presence. Based on geometrical considerations (cf. [Villard and Borderies, 2007b]) it turns out that the double bounce is also the most interesting scattering mechanism, being likewise the most sensitive to the attenuation effect. Nevertheless, if such approach has shown a great potential on the double bounce only contribution, the performance is severely impacted as soon as volume can not be neglected.

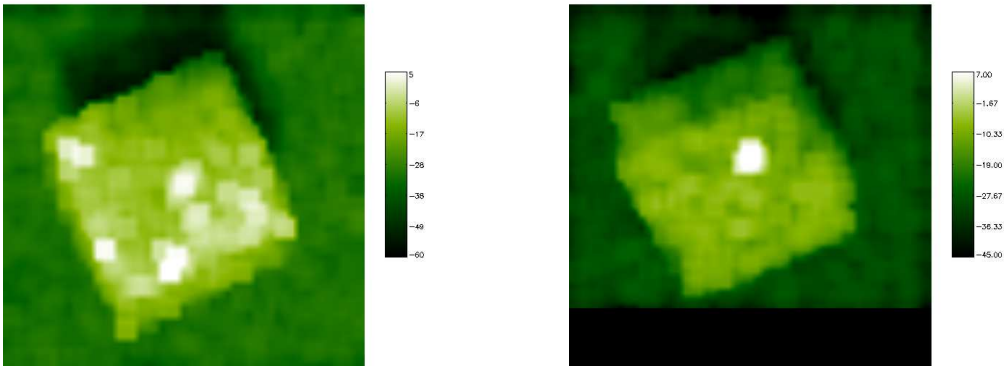

(a) $\beta = 0$ (b) $\beta = 60^o$

Figure 3.29: Simulated σ^0_{vv+hh} image at P-band (430 MHz) in a monostatic (a) and bistatic (b) configurations given by the incidence angle $\theta_{\mathrm{T}} = 60^o$ and the scattering direction $\theta_{\mathrm{R}} = 30^o$, $\Delta\varphi = 0$.

Conclusion

In this chapter, the bistatic scattering polarimetric behaviour of canonical forest models – that is the uniformly and the randomly oriented volume – have been studied, in order to set forth general properties intrinsic to the bistatic geometry. Although simple, these models evince the importance of its components attributes especially regarding the attitude angles of its scatterers. Indeed, promisingly for retrieval, the polarimetric scattering coefficients turn out to be sensitive towards the bistatic angle and the volume descriptive parameters and for most of the results analysis, considerations about the individual scattering properties were needed (i.e with the RCS study). As a great example, the difference between the cross-polarizations has been explained with respect to the scatterers mean orientation in the case of distributed targets. This study brings us to an original algorithm to retrieve the 3D Euler attitude angles of any symmetry of revolution object, by means of a hybrid fully polarimetric bistatic acquisition.

Besides, the general case of bistatic configuration has been studied that is for tilted bistatic plane. Inspired from previous work on polarization theory, the introduction of the β polarization enables to transpose this general bistatic problem to an equivalent one within the normal bistatic plane, for which the previous characterization results can be anew applied.

Furthermore, the coupling terms ensued from the volume interaction with the ground have been also analysed and specific scattering directions were emphasized which brings great applications of the bistatic configuration with the aim at maximizing a scattering mechanism.

Finally, the remarkable properties set forth with the polarimetric analysis have been used in a detection context, based on their violation caused by the target presence and more originally on the proposed algorithm concerning the retrieval angle, initially developed for coherent targets. This latter approach enables indeed to cope with bistatic situation in which the most stringent symmetry properties are not fulfilled, typically when the bistatic plane not orthogonal to the horizontal reference. For such cases, the use of the β polarization turns out to be paramount which strengthen again the great importance of full polarimetric acquisition. This approach rises in addition the question of a more thorough study of the coherency matrix coefficients (especially for the non null off diagonal terms) potentially worthwhile in a classification framework.

Bibliography

F. Barbaresco. Innovative tools for radar signal processing based on cartan's geometry of spd matrices & information geometry. In *Proceedings of the International Radar Conference*, pages 1–6. IEEE, 2008.

S.R. Cloude. Group theory and polarisation algebra. *OPTIK*, 75(1):26–36, 1986.

S.R. Cloude. *Polarimetry in Wave Scattering Applications*, volume 1. Academic Press, R. Pike & P. Sabatier edition, 2001. Chapter 1.6.2 in Scattering.

S.R. Cloude. On the status of bistatic polarimetry theory. In *Geoscience and Remote Sensing Symposium (IGARSS)*, volume 3, pages 2003–2006. IEEE International, 2005.

S.R. Cloude and E. Pottier. A review of target decomposition theorems in radar polarimetric. *IEEE Transactions on Geoscience and remote sensing*, 34(2), March 1996.

S.R. Cloude, D.G. Corr, and M.L. Williams. Target detection beneath foliage using polarimetric sar interferometry. *Waves in Random Media*, 14:393–414, 2004.

E.K. Colin, C. Titin-Schaider, and W. Tabbara. Fopen with polarimetric interferometry: Validations with experimental data at p-band. In *Proceedings of the 2nd International Workshop POLINSAR (ESA)*. ESRIN, Frascati (Italy), 2005.

E.K. Colin, C. Titin-Schnaider, and W. Tabbara. An interferometric coherence optimization method in radar polarimetry for high-resolution imagery. *IEEE Transactions on Geoscience and Remote Sensing*, 44:167–175, Jan. 2006.

Z.H. Czyz. Characteristic polarisation states for bistatic non-reciprocal coherent scattering case. In *International Conference on Antennas and Propagation (ICAP)*, volume 1, pages 253–256. IEE, 1991.

M. Davidovitz and W-M. Boerner. Extension of kennaugh's optimal polarization concept to the asymmetric scattering matrix case. *IEEE Transactions on Geoscience and Remote Sensing*, 34:569–574, April 1986.

A.E. El-Rouby, A.Y. Nashashibi, and F.T. Ulaby. Application of frequency correlation function to radar target detection. *IEEE Transactions on Geoscience and Remote Sensing*, 39:125–139, Jan. 2003.

P. Ferrazzoli and L. Guerriero. Passive microwave remote sensing of forests: a model investigation. *IEEE Transactions on Geoscience and Remote Sensing*, 34:433–443, March 1996.

POLINSAR for FOPEN using flashlight mode images along circular trajectories. H. cantalloube and e.k. colin. In *International Geoscience and Remote Sensing Symposium (IGARSS)*, pages 1139–1142. IEEE, 2007.

A.-L. Germond. *Théorie de la polarimétrie radar en bistatique*. Phd dissertation, Université de Nantes (France), Jan. 1999.

A.L. Germond, E. Pottier, and J. Saillard. Foundations of bistatic radar polarimetry theory. In *International Radar Conference (IRC)*, pages 883–837. IEE, 1997.

J.C. Hubbert. A comparison of radar, optic, and specular null polarization theories. *IEEE Transactions on Geoscience and Remote Sensing*, 32:658–671, May 1994.

H.C. Van De Hulst. *Light Scattering by Small Particules*. Courrier Dover Publications, 2 edition, 1981.

J.R. Huynen. *Phenomenological theory of radar targets*. Phd dissertation, Delft University of Technology, 1970.

S.R. Cloude I. Hajnsek, E. Pottier. Inversion of surface parameters from polarimetric sar. *IEEE Transactions on Geoscience and Remote Sensing*, 41:727–744, April 2003.

K. Iribe and M. Sato. Analysis of polarization orientation angle shifts by artificial structures. *IEEE Transactions on Geoscience and Remote Sensing*, 45:3417–3425, Nov. 2007.

A. Kostinski and W-M Boerner. On foundations of radar polarimetry. *IEEE Transactions on Antennas and Propagation*, 34:1395–1404, Dec. 1986.

P. Liang, L.E. Pierce, and M. Moghaddam. Radiative transfer model for microwave bistatic scattering from forest canopies. *IEEE Transactions on Geoscience and Remote Sensing*, 43: 2470–2483, Nov. 2005.

A. Ludwig. The definition of cross polarization. *IEEE Transactions on Antennas and Propagation*, 21:116–119, Jan. 1973.

E. Lüneburg and J.C. Hubbert. Comments on 'the specular null polarization theory' (and reply). *IEEE Transactions on Geoscience and Remote Sensing*, 35:1070–1072, July 1997.

E. Lüneburg, V. Ziegler, A. Schroth, and K. Tragl. Polarimetric covariance matrix analysis of random radar targets. In *Annual Conference of the Advisory Group for Aerospace Research and Development (AGARD)*. Ottawa (Canada), 1991.

P.M. Morse and H. Feshback. *Methods of Theoretical Physics*. McGraw-Hill Book Co, 1953. part II, pp. 1130-1131.

A.Y. Nashashibi and F.T. Ulaby. Detection of stationary foliage-obscured targets by polarimetric millimeter-wave radar. *IEEE Transactions on Geoscience and Remote Sensing*, 43:13–23, Jan 2005.

A.Y. Nashashibi and F.T. Ulaby. Mmw polarimetric radar bistatic scattering from a random surface. *IEEE Transactions on Geoscience and Remote Sensing*, 45:1743–1755, June 2007.

C. Pascal, E. Gimeno-Nieves, and J.M. Lopez-Sanchez. The equivalence between the polarisation subspace method (psm) and coherence optimisation in polarimetric radar interferometry. In *European Synthetic Aperture Radar Conference (EUSAR)*, pages 589–592, 2002.

J.E. Roy and L. Shafai. Generalization of the Ludwig-3 definition for linear copolarization and cross polarization. *IEEE Transactions on Antennas and Propagation*, 49:1006–1010, June 2001.

R. Zandoná Schneider, K.P. Papathanassiou, I. Hajnsek, and A. Moreira. Polarimetric and interferometric characterization of coherent scatterers in urban areas. *IEEE Transactions on Geoscience and Remote Sensing*, 44:971–998, April 2006.

D.L. Schuler, Jong-Sen Lee, and G. De Grandi. Measurement of topography using polarimetric sar images. *IEEE Transactions on Geoscience and Remote Sensing*, 34:1266–1277, Sep 1996.

J.C. Souyris and C. Tison. Polarimetric analysis of bistatic sar images from polar decomposition : A quaternion approach. *IEEE Transactions on Geoscience and Remote Sensing*, 45(9): 2701–2714, Sept. 2007.

J.C. Souyris, C. Henry, and F. Adragna. On the use of complex sar image spectral analysis for target detection: assessment of polarimetry. *IEEE Transactions on Geoscience and Remote Sensing*, 41:2725–2734, Dec. 2003.

L. Thirion, E. Colin, and C. Dahon. Capabilities of a forest coherent scattering model applied to radiometry, interferometry, and polarimetry at p- and l-band. *IEEE Transactions on Geoscience and Remote Sensing*, 44:849–862, April 2006.

L. Thirion-Lefevre and E. Colin-Koeniguer. First polarimetric validation and results on the bistatic scattering by a set of cylinders using a forest scattering model. In *European Conference on Synthetic Aperture Radar (EUSAR)*. Friedrichshafen (Germany), 2008.

C. Titin-Schnaider. Power optimization for polarimetric bistatic random mechanisms. *IEEE Transactions on Geoscience and Remote Sensing*, 45:3646–3660, Nov. 2007.

C. Titin-Schnaider. Polarimetric characterization of bistatic coherent mechanisms. *IEEE Transactions on Geoscience and Remote Sensing*, 46:1535–1546, May 2008.

F.T. Ulaby, R.K. Moore, and A.K. Fung. *Microwave Remote Sensing: Active and Passive*, volume I, Microwave Remote Sensing Fundamentals and Radiometry of *Advanced Book Program*. Addison-Wesley, 1981.

L. Villard and P. Borderies. Backscattering border effects for forests at C-band. *PIERS Online (Progress in Electromagnetics Research Journal)*, 3:731–735, 2007a.

L. Villard and P. Borderies. Bistatic foliage penetration modelling. In *International Geoscience and Remote Sensing Symposium (IGARSS)*, volume 4109-4112. IEEE, 2007b.

L. Villard, P. Borderies, P. Dubois Fernandez, and J.F. Nouvel. Bistatic border effects modelling in forest scattering. In *International Geoscience and Remote Sensing Symposium (IGARSS)*. IEEE, 2007.

Chapter 4

Potential Use of Bistatic Radar Intensity for Forest Biomass Retrieval

Contents

4.1 Introduction : Radar Intensity – Biomass Relationship

Beyond all-weather, day and night capabilities, microwave propagation enables to penetrate dense vegetation cover and rather, the radar response is often sensitive to the whole forest structure. Radar geometry, frequency and polarisation are paramount parameters to study that sensitivity, as testified by an extensive number of radar experiments, whether passive or active in the monostatic case and coming with theoretical electromagnetic modeling detailed in an abundant literature (cf. among others [Fung, 1994; Tsang and Kong, 2000]).

Within the scope of forest biomass monitoring, radar techniques offer thus a great potential in comparison with optical remote sensing, intrusive direct field measurements or GIS (Geographic Information System) based methods using ancillary data, as mentioned in the first chapter. The remaining challenge being however the use of this sensitivity to quantitatively estimate biomass. For that purpose, the relationship between the above ground biomass (AGB, $t.ha^{-1}$) and the radar backscattering coefficient (σ^0, dBm^2/m^2) can be set forth, as already proposed since more than a decade by [Dobson et al., 1992; Le Toan et al., 1992; Rignot et al., 1995].

In addition, radar polarimetry has also an interesting discrimination potential, for instance at P band the HH return results mainly from the trunk biomass, whereas the HV cross return is typically only sensitive to crown one and the VV results from both (cf. previous studies in [Ulaby et al., 1990; Karam et al., 1992; Beaudoin et al., 1994]). Such characteristic behaviours, exhibited thanks to electromagnetic modeling, are naturally modulated according to the forest type and radar range of frequencies.

Indeed, as far as frequency is concerned, it puts forward a physical severe limitation with the saturation problem illustrated by a constant or even decreasing backscattering level beyond

a given forest biomass, hence the P-band interest (cf. [Le Toan et al., 1992]) which enables to move further this saturation point (to about 150,200 $t.ha^{-1}$ while tropical biomass can reach 400 $t.ha^{-1}$) and still within acceptable operational constraints related to embedded system (cf. antenna size). To overcome that issue and increase the sensitivity to biomass, several studies based on electromagnetic modeling (such as [Ferrazzoli and Guerriero, 1996; Pampaloni, 2004]) as well as airborne experiments demonstrate the interest of radiometry (passive sensors) ([Macelloni et al., 2001]) especially at L-band. However, radiometers are limited by their coarse resolution, so that most of the spaceborne campaigns are carried out with higher frequency (typical resolution/frequency couple are about 5 km at 90 GHz and 25 km at 6.9 GHz, for the currently operating AMSR-E 6 bands instrument) excepted for the upcoming launch of the SMOS mission at L-band (50 km resolution), dedicated to soil moisture though.

On top of this drawback, the use of the 'σ^0-AGB' relationship as a look-up table supposes also that the various forest characteristics (from the surface to the upper crown physical properties) for a given biomass can be overlooked. Yet, ground roughness and soil water content for instance impact truly the double bounce scattering mechanism and thereby the HH return, whereas ground slopes whether local or global (at the forest stand scale) is the worst situation implying direct and specular ground scattering within the cross polarization (cf. Zyl [1993]; Luckman [1998]; Schuler et al. [1996] and section about the forward model). In addition, the crown water content may entail another bias source and likewise for orientation properties (azimuthal or more typically concerning the branch insertion angle ψ) or forest structure (cf. [Woodhouse, 2006]).

Fostered by the **BIOMASS** spaceborne mission currently under investigation at ESA (phase A in progress), the robustness of the SAR intensity based approach is currently revisited as well as improved retrieval algorithms, for the purpose of generating forest biomass map at the global scale. Based on multiple regression analysis (with polynomial decomposition) from various forest types (the Guaviare, Queensland, Maine, Landes and Remningstorp cases corresponding respectively to tropical, subtropical, temperate and sub-boreal forests), the combined use of every polarization leads to more robust inversion algorithms (cf. [Saatchi et al., 2007]) which, together with supervised approaches (as proposed by [Mattia et al., 2006] with a Bayesian formulation), improves significantly retrieval performances. Besides, the analysis conducted with the aforementioned forests and with different captors confirms the interest for the cross polarization at P-band (P-HV approach, cf. [Le Toan et al., 2005]), exhibiting a large and rather stable dynamic up to 200 $t.ha^{-1}$. Indeed, these data support the volume only dependence heuristic concerning the HV backscatter and thereby the fact that the cross-polarization is well correlated to the total biomass thanks to the allometric relationship between the biomass of branches and trunks (encompassing actually the major part of the biomass).

Furthermore, much progress can be achieved with the additional forest height information, which provides by itself a biomass estimation. Indeed, allometric considerations intrinsic to each tree specie (cf. [Brown et al., 1989; Chambers et al., 2001]) can be turned into direct analytical equations between forest biomass and height (cf. [Mette et al., 2004; Mette, 2007]). Let alone a-priori information, the Pol-InSAR acquisition and associated ad-hoc inversion algorithms (cf. [Treuhaft et al., 1996; Cloude and Papathanassiou, 2003]) has demonstrated its potential for forest height estimation. Besides, since this method is rather robust for high forest biomass (under the limit of a sufficient penetration to be sensitive to direct or specular ground contribution but also of a sufficient forest height sensitivity to biomass), the combination of both Pol-InSAR height retrieval and intensity based-methods turns out to be very promising.

As far as retrieval improvement attempts are concerned, the potential of multi-frequency acquisitions has been also studied (cf. for instance [Saatchi and Moghaddam, 2000]) and furthermore fusion with retrieved parameters from optical sensors. Although restricted to the upper

crown characteristics, many studies (based mainly on statistical multiple regression methods or neural network), demonstrate that thanks to allometric physical relations linking the whole forest structure, optical measures – such as LAI, FPAR or NDVI – can be well correlated to biomass. Indeed, the already very large amount of data analysis, as testified by the extensive number of currently operating optical captors, show the great potential of such indexes (ensued from sensors such as AVHHR, SPOT-Vegetation, MODIS, MISR, POLDER) rather than fine or medium spatial resolution data (from one to about 100 m according to pancromatic or multispectral images, e.g Ikonos, Spot-5, Quickbird satellites). Notwithstanding, this rich dataset collection rises the fusion strategy problem, with such various spectral, spatial or temporal resolutions.

Whether with a joint Pol-InSAR or multi-frequency acquisition extended possibly to the optical domain, all these approaches, though attractive, increase significantly the operational complexity and the subsequent cost in comparison with the original radiometric based approach. Besides, bistatic radars, not anymore limited by the feasibility drawback may be worthwhile to renew the radiometric based method for biomass estimation. Indeed, as testified recently by several successful campaigns, the inherent complexity of the bistatic configuration is nowadays much better handled and in view of the current large number of spaceborne radars (on top of remote sensing, navigation or telecommunication ones can be envisioned), opportunistic configurations is becoming more and more pregnant. Concerning the retrieval potential, one can intuitively set forward that the bistatic scattering coefficient may encompass the higher sensitivity of emissivity, invoking the Kirchhoff law assumption (linking the latter to the scattering diagram integral over all the bistatic directions). Previous studies ([Ferrazzoli and Guerriero, 1996; Liang et al., 2005]) paved the way to this investigation, the major conclusion confirming actually this trend. Though required, as pointed out previously, the sensitivity is yet not sufficient for all that. The purpose of the following study is thus to assess first (section 4.2) that sensitivity to biomass with the many geometric configurations offered by the bistatic space and then in section 4.3 to test the robustness of the emphasized acquisitions, in the light of the afore-mentioned drawback factors or intrinsic to bistatic ones.

4.2 Radiometric Sensitivity Assessment towards Biomass

4.2.1 Forest Growth Modeling & Resulting Scattering

To analyse the relationship between forest AGB and radar intensity, the first point at issue is about the choice of the forest description, including particularly the physical modeling of its various stages during the growing process. This choice is naturally driven by various constraints. Prominent among them is the resulting biomass, which should exhibit a sufficient range in order to analyse the subsequent radar sensitivity but also with values large enough to be consistent within the carbon issue context. Concerning the modeling of forest growth, temperate forest growth process have been found better documented, in view of their more deterministic description ensued from man exploitation. For instance, the afore-mentioned Nezer site has been already subjected to various studies, one can refer to [Champion et al., 2001; Saleh et al., 2007]) where statistical laws are proposed to geometrically describe the forest medium. Besides, one can also refer to [Fung, 1994; Ulaby et al., 1990; Beaudoin et al., 1994] for the use of such description in electromagnetic modeling and the resulting confrontations with experimental results with the AIRSAR sensor or more recently with the RAMSES one. These studies contribute to demonstrate the ability of the descriptive approach to faithfully reproduce the radar backscattering and the importance of an extensive ground truth to document the geometric and physical characteristics of the various scatterers. As a result, we base our forest description on that literature for the Nezer forest case considering however an extrapolation to higher ages (up to 75 years old) in order to deal with higher biomass levels, less realistic for temperate forests but of greatest importance to deal with the saturation issue. Indeed, we remind that our purpose is to assess the bistatic potential towards biomass retrieval in comparison with the monostatic case, so that the subsequent forest description must be viewed as a generic example rather than like a specific study of the Nezer case. The importance of the forest intrinsic characteristics is not overlooked for all that, their impact will be investigated in section 4.3) – by means of deviations concerning water content or structure in order precisely to assess the retrieval robustness in the optimal configurations set forth. Details about the simulated forest components are given in tables 4.1 and 4.2 with their geometric attributes, the trunk concentration is displayed in figure 4.1 as well as the resulting biomass in figure 4.2 according to scatterers types or layer decomposition, each time versus the forest age. The extrapolation effect can be seen in a way with a change of growth regime mainly since the trunks concentration tends to reach its asymptotic value while the size law (equations 5-7-14 in [Saleh et al., 2007]) are considered valid until the maximum ages. The branches biomass behaves as well since driven by that latter trunk concentration through allometric relations.

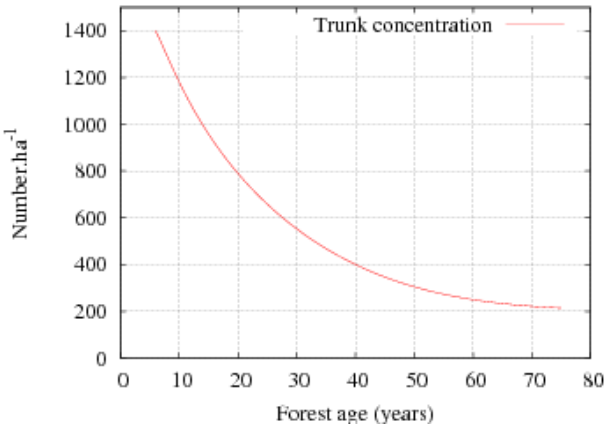

Figure 4.1: Trunk concentration versus the simulated forest growth.

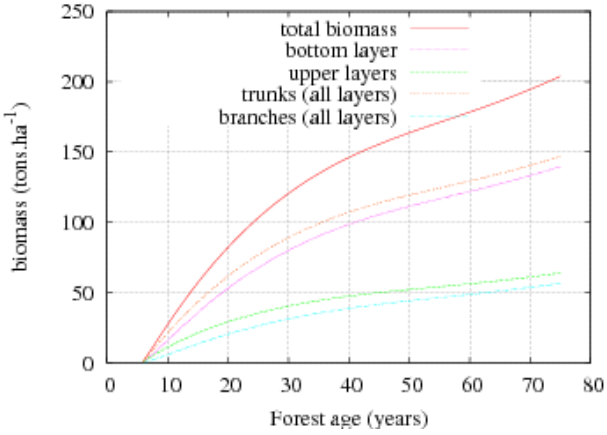

Figure 4.2: Biomass repartition versus the simulated forest growth between the various layers or on account of the scatterer type, that is herein trunks or branches.

	Layer	type	f_v	height	radius	$\psi_{min-max}$
Age 6	$L_1^\sharp$	trunks	2.21e-04	0.367	0.0224	0. – 0.6
	L_2	trunks	1.25e-04	1.436	0.017	0. – 0.6
		pr b.	6.861e-06	0.0528	0.0052	1. – 1.5708
		sc b.	7.484e-08	0.03052	0.00285	0. – 1.
		tr b.	6.502e-09	0.01761	0.00157	0. – 0.6
	L_3	trunks	2.06843e-05	1.43597	0.00685	0. – 0.6
		pr b.	5.032e-06	0.04869	0.00414	0.5 – 0.91
		S	5.060e-08	0.02808	0.00229	0. – 1.
		t	4.394e-09	0.01132	0.00125	0. – 0.6
Age 10	L_1	trunks	0.00124	2.73715	0.05736	0.0 – 0.50
	L_2	trunks	0.00054	2.69509	0.03782	0.0 – 0.5
		pr b.	0.00022	0.39346	0.01161	1. – 1.5708
		sc b.	1.78e-05	0.22724	0.00638	0.0 – 1.0
		tr b.	1.546e-06	0.13115	0.00350	0.0 – 0.6
	L_3	trunks	9.809e-05	2.69509	0.01613	0.0 – 0.5
		pr b.	0.00018	0.36255	0.00975	0.56 – 1.04
		sc b.	1.330e-05	0.20910	0.00538	0.0 – 1.0
		tr b.	1.155e-06	0.08431	0.00296	0.0 – 0.6
Age 15	L_1	trunks	0.0017575506	5.49151	0.0811278	0.0 – 0.4
	L_2	trunks	0.00062685418	3.25774	0.0484506	0.0 – 0.4
		pr b.	0.000510977	0.789405	0.0148752	1.0 – 1.5708
		sc b.	8.327e-05	0.455910	0.00817710	0.0 – 1.0
		tr b.	7.2343e-06	0.263135	0.00449655	0.0 – 0.6
	L_3	trunks	0.0001234	3.25774	0.0215011	0.0 – 0.4
		pr b.	0.0004487	0.727380	0.0129970	0.630000 – 1.17
		sc b.	6.74e-05	0.419512	0.00717240	0.0 – 1.0
		tr b.	5.8535e-06	0.169158	0.00394722	0.0 – 0.6
Age 25	L_1	trunks	0.00202	9.60275	0.108145	0.0 – 0.2
	L_2	trunks	0.000570	3.64602	0.0574660	0.0 – 0.2
		pr br.	0.000813	1.38040	0.0176431	1.0 – 1.5708
		sc br.	0.000232	0.797228	0.00969865	0.0 – 1.0
		tr br.	2.0136e-05	0.460132	0.00533325	0.0 – 0.6
	L_3	trunks	0.00012418	3.64602	0.0268084	0.0 – 0.2
		pr br.	0.00078928	1.27194	0.0162051	0.70 – 1.3
		sc br.	0.0002	0.733582	0.00894281	0.0 – 1.0
		tr br.	1.80e-05	0.295799	0.00492155	0.0 – 0.6

(♯) bottom, middle and upper layer

Table 4.1: Ground truth details about the simulated forest growth, ages from 6 to 25 years old (the sequel up to 75 yeras old is given within the next table).

	Layer	type	f_v	height	radius	$\psi_{min-max}$
Age 35	L_1	trunks	0.00196	12.5002	0.125056	0.0 – 0.2
	L_2	trunks	0.00048	3.80703	0.0620769	0.0 – 0.2
		pr br.	0.00090	1.79691	0.0190587	1.0 – 1.5708
		sc br.	0.00033	1.03778	0.0104768	0.0 – 1.0
		tr br.	2.896e-05	0.598970	0.00576118	0.0 – 0.6
	L_3	trunks	0.00011	3.80703	0.0298618	0.0 – 0.2
		pr br.	0.00093	1.65572	0.0180508	0.770000 – 1.43
		sc br.	0.00032	0.954930	0.00996135	0.0 – 1.0
		tr br.	2.753e-05	0.385052	0.00548208	0.0 – 0.6
Age 45	L_1	trunks	0.00178	14.6994	0.137510	0.0 – 0.2
	L_2	trunks	0.00040	3.90979	0.0652560	0.0 – 0.2
		pr br.	0.000875	2.11304	0.0200347	1.0 – 1.5708
		sc br.	0.000382	1.22036	0.0110134	0.0 – 1.0
		tr br.	3.3186e-05	0.704347	0.00605622	0.0 – 0.6
	L_3	trunks	9.6835e-05	3.90979	0.0320540	0.0 – 0.2
		pr br.	0.0009421	1.94702	0.0193760	0.805000 – 1.495
		sc br.	0.0003788	1.12293	0.0106927	0.0 – 1.0
		tr br.	3.2899e-05	0.452794	0.00588455	0.0 – 0.6
Age 55	L_1	trunks	0.0017	16.4591	0.147426	0.0 – 0.2
	L_2	trunks	0.00036	3.99001	0.0677522	0.0 – 0.2
		pr br.	0.00088	2.36600	0.0208011	1.0 – 1.5708
		sc br.	0.00043	1.36645	0.0114347	0.0 – 1.0
		tr br.	3.7376e-05	0.788665	0.00628788	0.0 – 0.6
	L_3	trunks	8.9676e-05	3.99001	0.0337904	0.0 – 0.2
		pr br.	0.00098	2.18010	0.0204256	0.840000 – 1.56
		sc br.	0.00044	1.25736	0.0112719	0.0 – 1.0
		tr br.	3.8197e-05	0.506999	0.00620332	0.0 – 0.6
Age 65	L_1	trunks	0.001719	17.9202	0.155691	0.0 – 0.2
	L_2	trunks	0.0003448	4.05869	0.0698448	0.0 – 0.2
		pr br.	0.00092	2.57603	0.0214436	1.0 – 1.5708
		sc br.	0.00049	1.48775	0.0117878	0.0 – 1.0
		tr br.	4.2377e-05	0.858675	0.00648209	0.0 – 0.6
	L_3	trunks	8.7785e-05	4.05869	0.0352408	0.0 – 0.2
		pr br.	0.0010	2.37362	0.0213023	0.840000 – 1.56
		sc br.	0.00051	1.36897	0.0117557	0.0 – 1.0
		tr br.	4.4325e-05	0.552005	0.00646959	0.0 – 0.6
Age 75	L_1	trunks	0.001771	19.1664	0.162790	0.0 – 0.2
	L_2	trunks	0.00034368	4.12020	0.0716658	0.0 – 0.2
		pr br.	0.00097	2.75517	0.0220027	1.0 – 1.5708
		sc br.	0.00055	1.59121	0.0120952	0.0 – 1.0
		tr br.	4.831e-05	0.918390	0.00665109	0.0 – 0.6
	L_3	trunks	8.9113e-05	4.12020	0.0364928	0.0 – 0.2
		pr br.	0.00113	2.53869	0.0220591	0.840000 – 1.56
		sc br.	0.000593	1.46418	0.0121733	0.0 – 1.0
		tr br.	5.1471e-05	0.590394	0.00669942	0.0 – 0.6

Table 4.2: In the following of 4.2, ground truth details for the simulated forest growth, from 35 to 75 years old.

Based on this forest growth description, the derived geometric and physical characteristics can be used to feed our model MIPERS described previously. The simulations are hereafter carried out according to the 'infinite' mode in order to generate a spatially homogeneous forest and according the non range or Doppler gated acquisition (as described in the section dedicated to the forward model). Indeed, rather than the image generation (of limited interest for homogenous area, excepted for speckle and texture attributes) the radiometry due to the whole forest is pointed out so that it can be done independently of the resolution cell shape. The resolution is thereby easily kept constant whatever the bistatic configuration or radar frequency. In view of both operational constrains (mainly linked to antenna sizes for embedded systems) and rather on penetration capabilities (to cope with the saturation problem), we'll assess mainly the potential of P and L band in bistatic. A resolution of four square meters is taken and the resulting radiometric coefficient is derived from the spatial average over the 25*25 pixels forming a forested extent of 1 hectare. These considerations rise thereby the radiometric and polarimetric coefficient choice, between the previously described gamma nought scattering coefficient (γ^0), the sigma nought one (σ^0) and the radar brightness (β^0).

Let alone the latter, which in our case do not present particular interest since the terrain slope simulated is deterministic and flat, σ^0 which entails the normalization by the illuminated area enables to make consistent comparisons between pixels ensued from different captors or regions along a given image swath. Indeed with the side looking radar geometry and a slant range resolution or incidence angle change, these pixels encompass a different volume of scatterers which impact proportionally the radiometric levels. Moreover, scattering events depend generally on the incidence angle, hence the use of the $gamma^0$ backscattering coefficient which takes into account both illuminated extent and scattering change with incidence, using the normalization by the wave front or the incident beam. This normalization holds rigorously only for Lambertian surface, which scattering depend only on the incoming power, whatever the observation directions (radiant intensity $I \propto \cos\theta_i$). The incoherent contribution from a rough surface can be generally considered like Lambertian as well as for a random volume. For instance, as far as forest biomass is concerned, a pregnant question concerns the validity of the correspondence between a given radiometric and biomass level whatever the forest type. When dealing with two different radar incidences on top of two different forests, it is thus more consistent to use the gamma scattering coefficient in order to emphasize the radiometric change according to forest intrinsic characteristics, rather than its dependency to radar geometry. In view of the classical dynamic of backscattering level with biomass, the starting points where the ground return dominate will be thus well corrected between various incidence angles and likewise for the HV component, as long as it matches a random volume. This property has been assessed with several dataset (cf. [Le Toan et al., 2005] and the test sites mentioned in the introduction) from different captors and supports thereby the HV polarization use. Indeed, the HH return dependence on the incidence angle is on the contrary more complicated since often driven by the trunks double bounce scattering diagram (e.g closely linked to their height).

Notwithstanding, with the aim of analysing the radar sensitivity to biomass in bistatic, the same forest (afore-described) will be considered within our simulations in the first step, so that the sigma scattering coefficient is more consistent to emphasize the impact of the bistatic geometry. For all the following bistatic configurations, the outputs of interest will thus be the polarimetric coefficients σ^0_{qp}, with the subscripts q and p standing respectively for the receiving and transmitted polarization state. In the first stage of this investigation, full polarization acquisition are simulated within the vertical and horizontal (V,H) basis, which will offer naturally the possibility to derive afterwards any other specific polarization states likely to be more judicious. Indeed, once analysed the bistatic radiometric trends within the linear basis, the use of more

specific polarization states will be discussed, especially for those concerning symmetry properties and the artefact corrections or with the aim of pointing out operational assets (quad-pol is not always worthwhile, potentially available radars of opportunity such as ALOS or GNSS systems are transmitting respectively in dual-pol or in left circular mode).

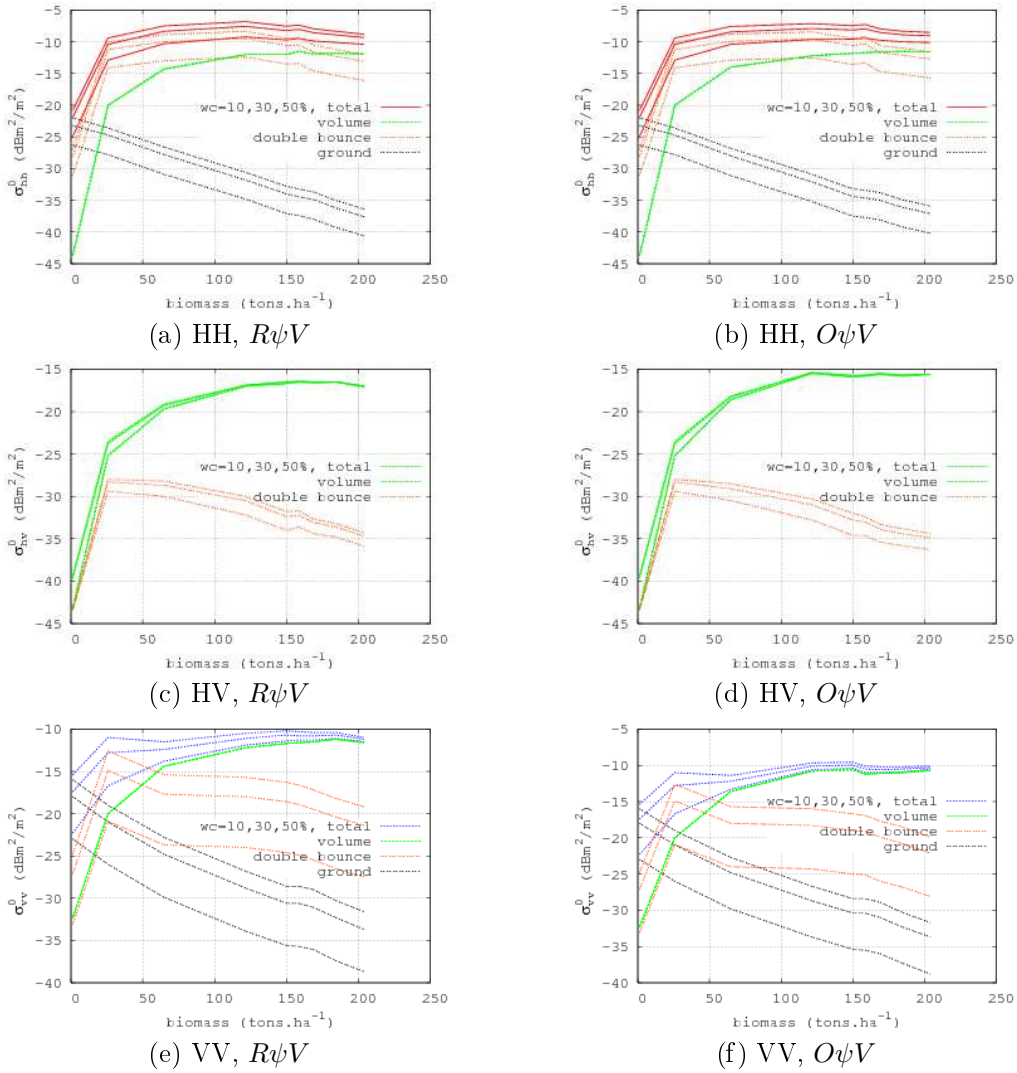

(a) HH, $R\psi V$ (b) HH, $O\psi V$

(c) HV, $R\psi V$ (d) HV, $O\psi V$

(e) VV, $R\psi V$ (f) VV, $O\psi V$

Figure 4.3: Sensitivity of the scattering mechanisms contributing to the resulting total σ^0_{qp} backscattering coefficient versus forest biomass in the monostatic configuration ($\theta_T = 45^o$). For each colored sheaf of curves, the amplitude goes up together with the soil water content parameter.

As a reference point during the following analysis and of course a particular case of bistatic configuration, the monostatic one is firstly considered. The backscattering coefficient sensitivity towards biomass is shown in figure 4.3 for uniformly oriented upper layers or oriented ones (right hand side), according to the branch insertion angle (ψ) distribution typical for the Nezer pine forest (cf. [Saleh et al., 2007]). In the following bistatic simulations, the uniformly oriented volume will be considered, to consider a primary analysis as generic as possible, after what the orientation impact will be shown as a perturbation factor in the section dedicated to the retrieval robustness (4.3). The oriented case is shown here in monostatic to get closer absolute values in comparison with experimental data from the RAMSES campaign over Nezer, or others found in the literature. These typical value are – for the mature stands – within the range of [-10,-6] dB for the HH polarization depending on the soil humidity and around -10 and -15 dB ($\pm$ 2 dB) respectively for VV and HV which both depend on branches features. On top of absolute values, these results remind the characteristic polarimetric behaviour, afore-mentioned in the introduction- for temperate forest at P band with plus now a quantitative view. The HH return is indeed truly driven by the ground coupling terms with interestingly a growing contribution from the volume, especially since the larger running distance intrinsic to the double bounce wave path through the layers is more impacted by the growing attenuation. Indeed, without this attenuation increase from the higher branches concentration, the trunks would not exhibit this decreasing trend, as confirmed by simulations with naked trunk only in figure 4.4. Also emphasized in the latter (on the left hand side) is the double bounce contribution from the branches which is in the HH polarization roughly of the same order as the volume's one (depending on the forest stage), hence an higher total backscattering coefficient in comparison with the VV channel. The orientation effect is also manifest with the difference between the volume contributions in like polarizations. Besides, the attenuation increase is well emphasized looking at the backscattering from the ground (about 15 dB higher between the youngest and oldest stage).

On account of the scattering ground model with a moderate roughness and rather no slopes, direct and specular (double bounce) ground terms can be neglected in the HV return. As a result of this canonical case, the cross polarization evinces on the one hand the largest dynamic (starting from the weak biomass return) and on the second hand absolute values independent from the soil state. The point at issue lies then essentially in the low dynamic for high biomass value, with a saturation level around 110 ton.ha^{-1} if a significant gap of 1 dB is considered. Again, in view of tropical forest case which cannot be overlooked, it constitutes a major drawback which motivates the bistatic investigation. Likewise, the saturation issue holds for the VV channel which is essentially driven by the volume contribution for the higher biomass region, whereas double bounce dominates for the young stages, hence a less interesting dynamic.

Concerning the saturation phenomenon itself, canonical studies have been performed and its threefold origin can be pointed out. First, a class of scatterers belong to the Rayleigh scattering zone and their growth get then closer to the resonance region and its associated saturation (cf. figure 4.10). Besides, for what concerns the forest growth, it can be also noticed that the just mentioned increasing trend due to larger individual elements may be compensated by a constant total volume fraction due to a decreasing concentration. For instance, this is the typical case for trunks which height increment are at the end compensated by their concentration fall, as testified by the saturation in figure 4.4 (b). On the other hand, the saturation comes from an extinction which increase versus volume fraction dominates the direct scattering one. Typically, if a random volume of surface density n_0 (number.m^{-2}) is considered at low frequencies so that the Rayleigh scattering regime holds, the scattering of each element will be proportional to k_0^2. In accordance with the Foldy's approximation, the resulting extinction coefficient defined specifically for the

power ($\sigma^{\mathcal{P}}$) will be thus proportional to $n_0 k_0$, as reminded below within the real part of the transmissivity :

$$t_{qp} = exp\big[-\frac{\sigma^{\mathcal{P}}}{2\cos\theta_i}\big] = exp\big[-\frac{2\pi n_0 h}{k_0\cos\theta_i}\langle Im\big(S_{qp}(\hat{k}_i,\hat{k}_i)\big)\rangle\big]$$

Considering futhermore a set of isotropic and identical particules, the backscattering coefficient can be analytically derived as performed in chapter 3, leading to the following expression :

$$\begin{aligned}\sigma^0 \propto & \frac{n_0}{\sigma^{\mathcal{P}}\tan\theta_i}\cdot(1-\exp(-\sigma^{\mathcal{P}}\frac{h}{\cos\theta_i})) \\ = & \frac{1}{4\pi k_0\tan\theta_i}\cdot(1-\exp(\frac{\text{-}4\pi n_0 k_0 h}{\cos\theta_i}))\end{aligned} \tag{4.1}$$

In view of the decreasing exponential term in the right hand side factor, the asymptotic behaviour of σ^0 with an increasing density leads thus to the saturation level. Naturally, the Foldy's approximation do not hold anymore beyond a certain scatterers density (typically up to 5 % of volume fraction) but it illustrates well the trade-off between scattering and extinction laws. This has been also confirmed with simulations in [Borderies et al., 2009], which pointed out the change between the volume scattering behaviour which turns into a surface one.

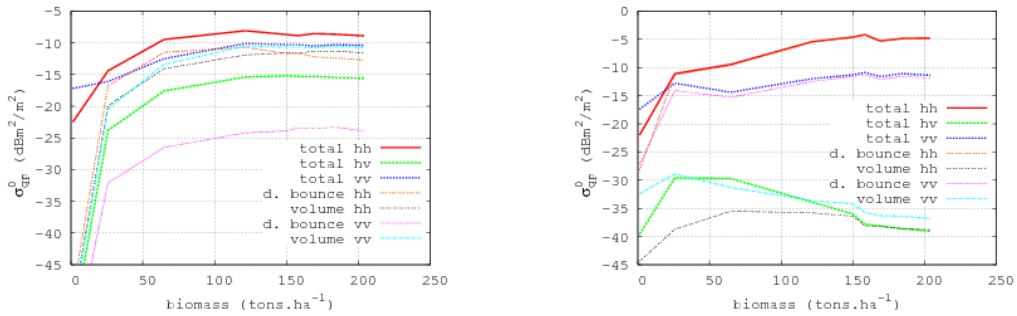

(a) branches only (b) trunks only

Figure 4.4: Contributions to the backscattering coefficient σ^0_{qp} ($\theta_T = 45^o$) in the linear polarizations, considering the two upper layers filled only with branches (a) or all the layers with naked trunks (b)

In view of these limitations, the versatility offered by the bistatic possibilities on the geometrical point of view is then worthwhile to explore, since a different scattering behaviour is likely to occur, as illustrated besides in figures 4.5 and especially for what concerns the resulting polarimetric ratios between mechanisms. For the following simulations dealing with spherical scattering diagrams, the angles are always defined according to the SSA (Specular Scattering Alignement) afore-reminded. The transmitter's position has been set to a fixed position ($\theta_{\mathrm{T}} = 45^o$, $\varphi_{\mathrm{T}} = -90^o$ whereas the receiver's position covers the quasi totality of the upper spherical space – with θ_{R} and φ_{R} ranging respectively from 0^o to about 80^o and 360^o. SAR processing constrains, naturally more or less stringent according to these configurations, are left aside at that point, since we focus first on their potential interest based on scattering considerations. The simulated forest is the 25 years old one according to the afore-mentioned ground truth (table 4.1) with however uniformly oriented branches in the upper layers with the aim of dealing with a quite generic example.

For the sake of clarity in the subsequent analysis, we remind the $\mathcal{P}_{\perp}^{\varphi X}$ notation, defined in chapter 3 as the plane orthogonal to the reference horizontal one $(\hat{x}, \hat{y})$ and which remaining freedom parameter φX is set to $\varphi_{\mathrm{R}} - \varphi_{\mathrm{T}}$ that is the relative azimuth angle between the transmitter and receiver (according to the FSA convention with X expressed in degrees). To interpret the hemispherical scattering diagram resulting from the whole forest (cf. figure 4.5), the volume, the double bounce and the ground contributions are respectively displayed in figures 4.6, 4.7, 4.8. Symmetrically-wise, in view of the receiver's position importance relatively to the transmitter, the vegetation azimuthal symmetry is retrieved in each scattering diagrams but only under the form of a reflection one with respect to the plane $\mathcal{P}_{\perp}^{\varphi 0}$. Plus, it can be noticed that in comparison with $\mathcal{P}_{\perp}^{\varphi 0}$ (the normal bistatic plane), $\mathcal{P}_{\perp}^{\varphi 90}$ turns out to be the plane which exhibits the most different and specific scattering behaviour so that the analysis of the whole bistatic space can be reasonably limited to these two planes, as proposed within the 2D slides shown afterwards.

Moreover, a crown can be also interestingly noticed which cover with a quasi constant magnitude the totality of the azimuthal angle range and for each polarization. As explained in the previous chapter and as confirmed in this specific case with figure 4.5, this behaviour is characteristic of the double bounces coherent addition between the one defined from the transmitter and the other from the receiver. These two mechanisms exhibit the same phase as long as the covered geometrical distances remain the same (or nearly the same on account of a given wavelength), hence the crown-like shape which its the loci in bistatic of the scattering enhancement. This radiometric reinforcement remains roughly constant apart from the peak in the specular direction and lower values for cross polarizations, also manifest in monostatic. Indeed, even if the vertical trunks mostly originate the double bounce, the random branches have also a significant contribution which can be seen especially in the HH polarization for the specular peak and also in the perpendicular azimuthal plane $\mathcal{P}_{\perp}^{\varphi 90}$, typically lower in the case of quasi vertical cylindric scatterers only. This effect, detailed in the previous chapter, shows the importance of the oriented structure (e.g the quasi null HH return of vertical cylinder at low frequency and within the plane $\mathcal{P}_{\perp}^{\varphi 90}$) whereas the random volume characteristic can be retrieved with the polarizations artefacts, also explained beforehand as well as its possible correction with the aim of preserving symmetric relationship. On the contrary, these reinforcements in the cross polarizations or rather the drop in the co-pol ones might evince very interesting properties with regards to radiometric sensitivity towards volume only, within the framework of biomass retrieval. Concerning the ground return, apart from the higher return when getting closer to the forward direction – typical for surfaces under a certain roughness level – the polarizations artefacts are likewise well marked in the HH return which strengthen its potential use to maximize the volume contribution.

The Lambertian afore-mentioned behaviour, as long as the forward direction is not concerned, is much more manifest once corrected the polarizations artefacts or looking directly to the SPAN (total power). Besides, by comparison between the ground and volume VV contributions, the surface behaviour from the random volume can be noticed, even with its relatively low extinction coefficients.

Furthermore, to come back to the scattering diagram of the total contribution, it can be noticed that apart from these characteristic planes where the sensitivity towards scattering angles is maximum, the intermediate points are quite stable or rather predictable. This makes an interpolation of the total diagram possible with a reasonable number of points, with the aim of performing the scattering diagram integration over the all upper space to derive the emissivity (cf. chapter one). This study, though limited to the 25 years old forest case, strengthen the interest in bistatic configurations to obtain another radiometric sensitivity to biomass. Prominent among them are the variation of site angles within the planes $\mathcal{P}_{\perp}^{\varphi 0}$ and $\mathcal{P}_{\perp}^{\varphi 90}$ which exhibit very distinct trends. The purpose of the following is thus to analyse these specific bistatic axes in order to confirm these trends versus the forest ages.

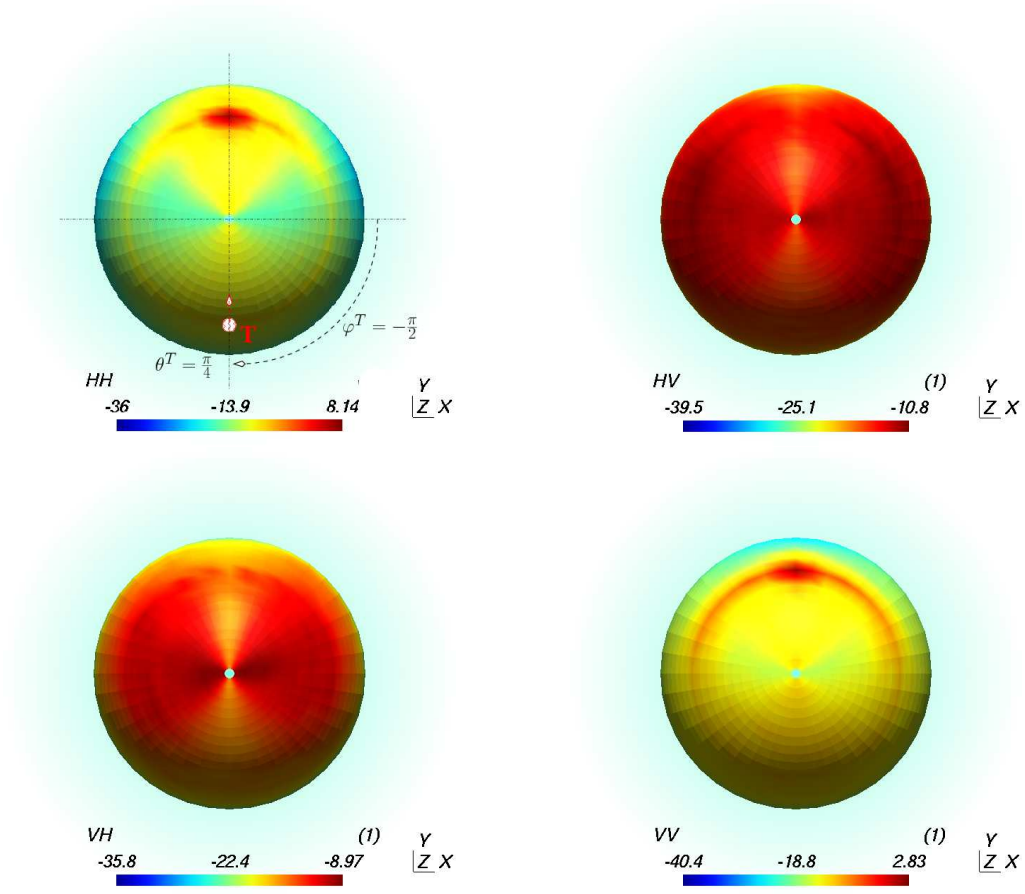

Figure 4.5: Scattering diagram representing the **total** bistatic scattering coefficient σ_{qp}^0 for all the upper hemispherical directions. The (V,H) linear polarizations are used, at P band for a transmitter position given – according to the SSA convention – by $[\theta_{\mathrm{T}} = 45^o, \varphi_{\mathrm{T}} = -90^o]_{\mathrm{SSA}}$ as drawn in (a) and implicitly considered for the following hemispherical diagrams.

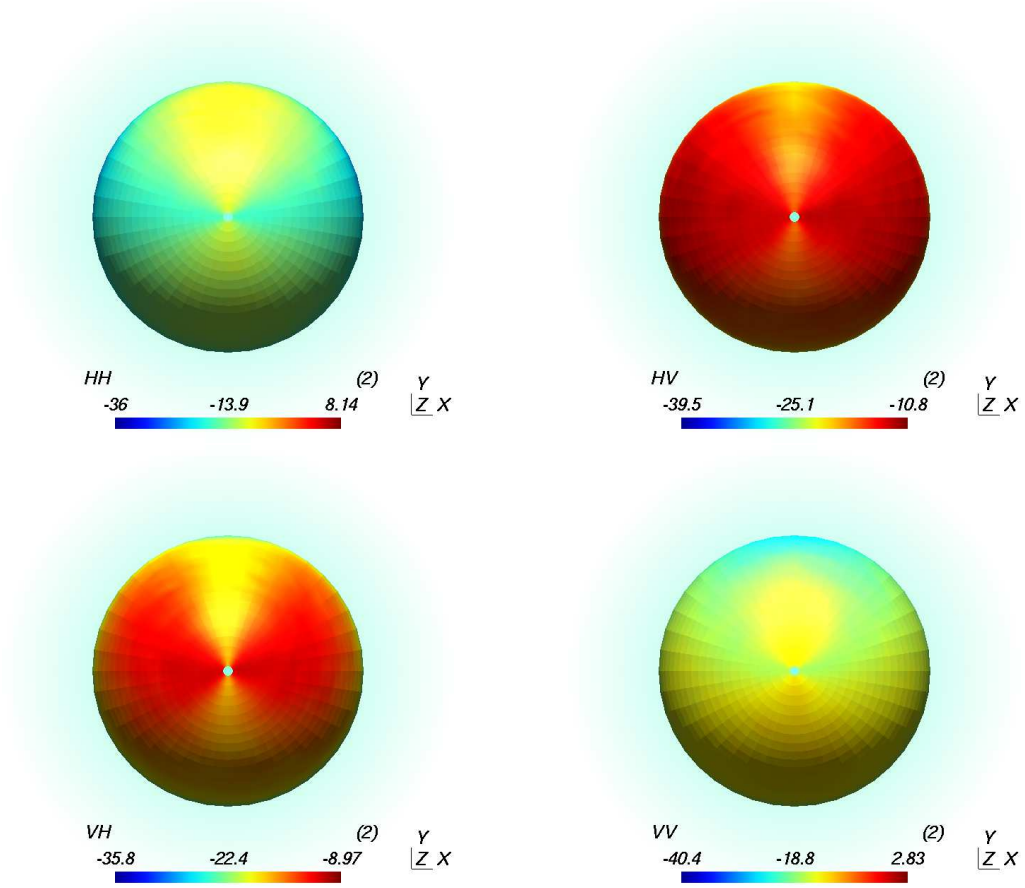

Figure 4.6: Scattering diagram representing the **volume** contribution for the bistatic scattering coefficient σ^0_{qp} for all the upper hemispherical directions. The (V,H) linear polarizations are used, at P band for an incidence angle $\theta_{\mathrm{T}} = 45^o$.

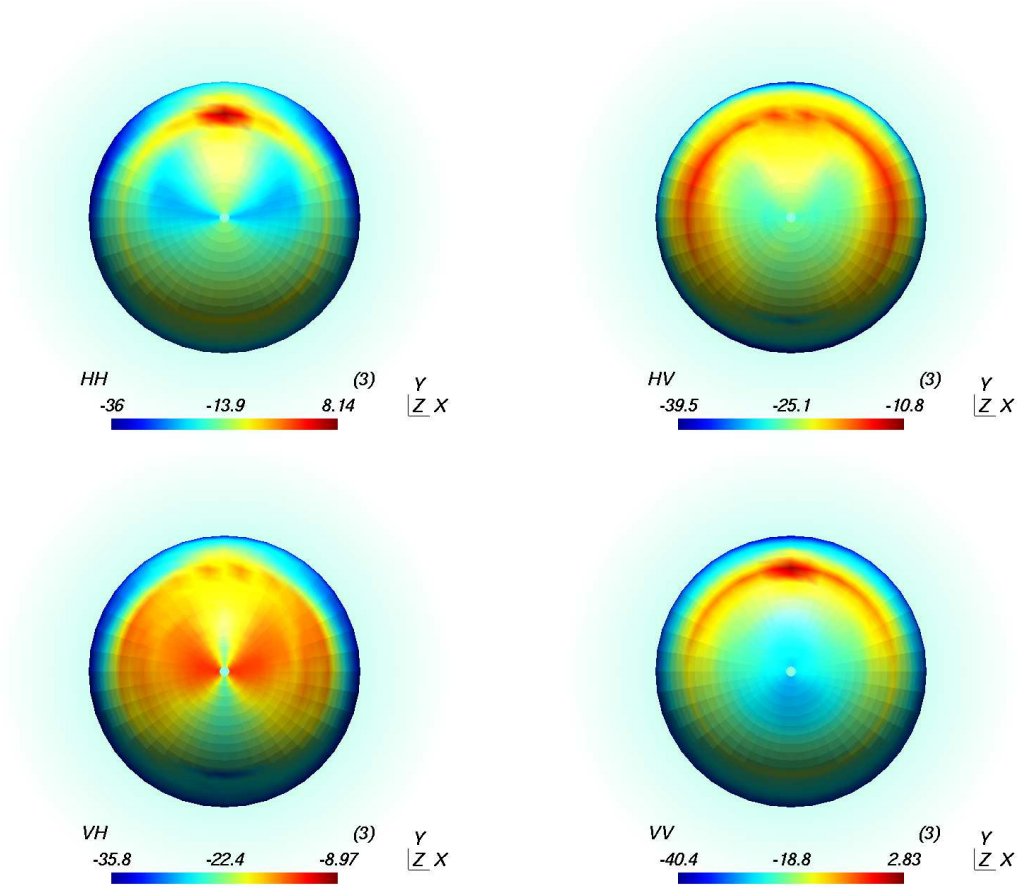

Figure 4.7: Scattering diagram representing the **double bounce** contribution for the bistatic scattering coefficient σ^0_{qp} for all the upper hemispherical directions. The (V,H) linear polarizations are used, at P band for an incidence angle $\theta_{\mathrm{T}} = 45^o$.

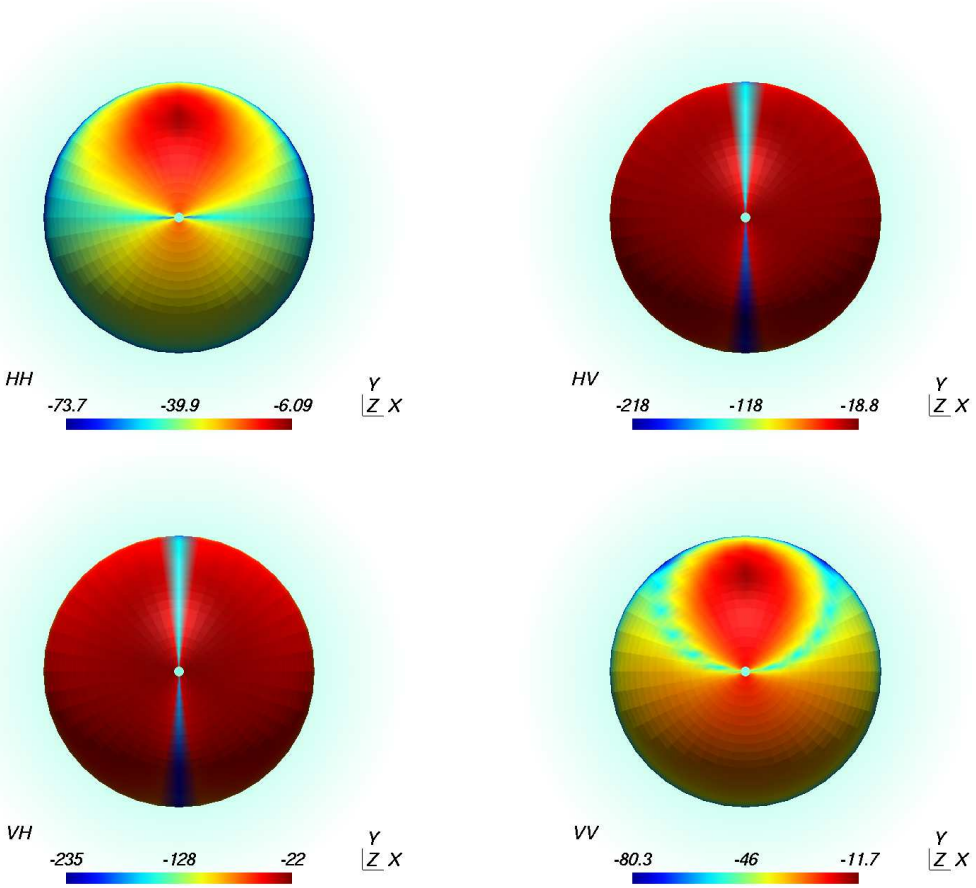

Figure 4.8: Scattering diagram representing the **ground** contribution for the bistatic scattering coefficient σ^0_{qp} for all the upper hemispherical directions. The (V,H) linear polarizations are used, at P band for an incidence angle $\theta_{\mathrm{T}} = 45^o$.

4.2.2 Simulation Results Analysis

As concluded at the end of the previous section, among all the possible bistatic configurations, two planes of bistatic site angle variations are representative of the major scattering trends. We remind that the former, called the normal bistatic plane ($\mathcal{P}_{\perp}^{\varphi 0}$), corresponds to the polarization basis vectors $(\hat{k}_i, \hat{v}_i)$ defined from an arbitrary position of transmitter. Then, the second type consists in a site angle variation within the plane ($\mathcal{P}_{\perp}^{\varphi 90}$), identical to $(\hat{k}_s, \hat{v}_s)$ when considering the local polarization basis of a receiver which relative azimuth is given by $\varphi_{\mathrm{R}} \overset{\mathrm{SSA}}{=} \varphi_{\mathrm{T}} + 90^o$.

Quasi-Monostatic Configuration

To begin with the former type of site variation, the radiometric sensitivity towards biomass is studied first in the quasi monostatic configuration. To emphasize the difference with the monostatic case, the respective various radiometric contributions to both geometry are plotted together in figure 4.9. The main point lies in the double bounce contribution decrease for the like polarizations, since the bistatic angle (about 8^o) is sufficient to leave the afore-mentioned crown. The drop magnitude is roughly 3 dB for the double bounce, likewise for HH since the volume contribution can be neglected. We remind that this decrease comes from the following summation :

$$\begin{aligned} \sigma^{0,\mathrm{sg}} \propto \langle E_s^{\mathrm{sg}}, \overset{*}{E_s^{\mathrm{sg}}} \rangle &= \langle E_s^{\mathrm{Tsg}} + E_s^{\mathrm{Rsg}}, (E_s^{\mathrm{Tsg}} + E_s^{\mathrm{Rsg}})^* \rangle \\ &= |E_s^{\mathrm{Tsg}}|^2 + |E_s^{\mathrm{Rsg}}|^2 + 2Re(\langle E_s^{\mathrm{Tsg}}, \overset{*}{E_s^{\mathrm{Rsg}}} \rangle) \end{aligned} \tag{4.2}$$

For the like polarizations, the last term in equation 4.2 is nul as long as E_s^{Tsg} and E_s^{Rsg} are not anymore correlated with the increasing bistatic angle, hence the 3 dB loss. On the contrary, for cross polarizations, since this latter correlation involves the negative product of the two modified Fresnel coefficients $(R_v \cdot R_h^*)$, the backscattering level is lower than the quasi-monostatic one, as shown by (b) in figure 4.9. This correlation is made explicit in the chapter dedicated to the bistatic Pol-InSAR from which we deduce that the magnitude of this discrepancy depends on the quantity $|R_v - R_h|^2$. Concerning the potential of the quasi monostatic configuration, it can be notice that in spite of a lower double bounce contribution, the HH dynamic is still impacted in the low biomass region whereas the VV channel is more favoured since the ground remains only on top naturally of the volume. Conversely, the HV dynamic is really spoiled by the double bounce increment, hence reservations can be formulated with respect to that configuration, despite the positive impact on the VV channel.

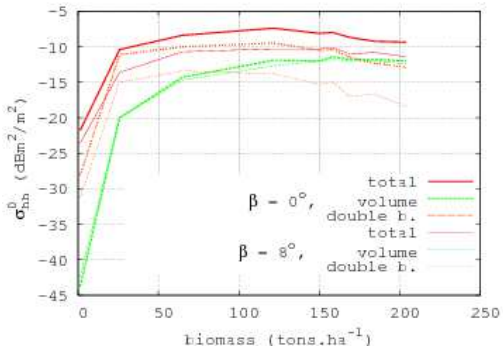

(a) HH

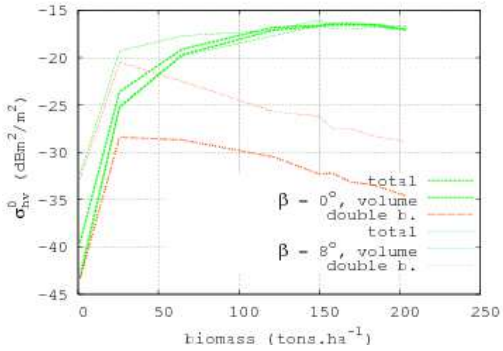

(b) HV

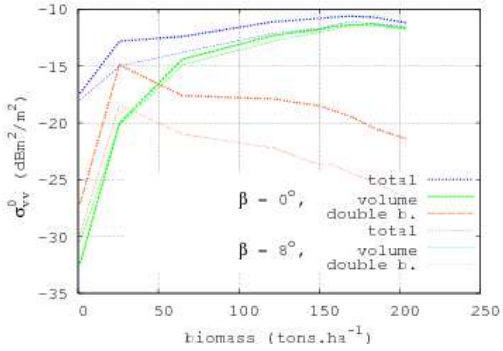

(c) VV

Figure 4.9: Comparisons between monostatic ($\theta_{\mathrm{T}} = 45^o$) and quasi-monostatic configurations ($\theta_{\mathrm{T}} = 45^o$, $\theta_{\mathrm{R}} = 53^o$)) with their respective scattering mechanisms contributing to the resulting total σ^0_{qp}.

Bistatic Angle Variation Within the Plane $\mathcal{P}_{\perp}^{\varphi 0}$

Next, simulations with higher site bistatic angles have been carried out as shown in the following four cases (figure 4.12) where β goes from -18.5^o to 67^o, in the forward region near to the specular configuration ($\beta = 90^o$). As the receiver gets closer to the forward direction, the ground contribution clearly noticeable for the young stages increases for the like polarizations. More interestingly, apart from the last configuration (d) in the forward region, the saturation point is noticeably moved further for the cross polarization channel. Indeed, these sensitivity curves exhibit an increment of about 1 dB between 120 ton.ha^{-1} – the saturation level in monostatic – to 170 ton.ha^{-1}. Though moderate, this increment is all the more attractive that it does not require any challenging bistatic configuration like the quasi specular one or other with grazing angles. For instance, from the operational point of view for what concerns aircraft embedded antennas constraints, the configuration (c) with $\beta = 45^o$ that is with an off-nadir receiver seems the easiest one.

From the physical point of view, this phenomenon is not obvious but one relevant element can be set forth. First, we can consider that a given scattering level stems mainly from the main contribution of scatterers which statistical realization matches a specular configuration. For instance, an horizontal cylinder in the forward configuration so that according to the SSA convention $\theta_i \overset{\text{SSA}}{=} \theta_s$, $\varphi_i = \varphi_s$ can be considered, as performed in figure 4.10. The saturation due to the increasing radius – limited to typical range of interest in this study – can be naturally noticed, as well as the importance of the equivalent radius on account of the refractive index ensued from different water content values (20,50,80 %) and thus different permittivities. More interestingly, it can be established that the radius corresponding to the first saturation peak depends on the specular scattering angle and goes up together. As an example for a water content of 50 %, this radius is about 4 cm in the bistatic case with $\theta_i \overset{\text{SSA}}{=} \theta_s = 60^o$ and below 3 cm in the monostatic one ($\theta_i \overset{\text{SSA}}{=} \theta_s = 0$). Besides, this behaviour is likely to be related to the effect of projected dimensions coming with the viewing angles, as testified by the greater gap between $30 - 60^o$ than $0 - 30^o$. Rather, in a more advantageously way than with the use of lower frequencies for which naturally the scattering saturation occurs for larger volume fraction, about the same extinction coefficients can be considered when comparing the bistatic case to the monostatic one (neglecting the orientation impact coming with the different viewing angles in bistatic). Consequently, although a different attenuation has to be considered (still due to the propagation directions within the forest layers), it brings about possibly different absolute σ^0 levels but the dynamic, due to the increasing scattering with biomass is not compensated by collective effects. In addition, this phenomenon is also consistent with the fact that all the bistatic angles are not similarly interesting concerning the saturation issue, as seen for instance with the previously displayed figure 4.12 which can be better emphasized if the volume contribution only is considered, as in figure 4.13. It turns out indeed that between the simulated bistatic angles, the better dynamic is obtained for $\beta = 45^o$ – referred from now on as β_{opt}^{st} to be the optimal configuration within $\mathcal{P}_{\perp}^{\varphi 0}$ – which corresponds at the level of a single cylinder to a sufficient bistatic angle to postpone the saturation zone but also small enough to avoid the magnitude drop due to the approaching Brewster angle. Again in figure 4.13, it can be noticed that the HH polarization does not exhibit the same robustness towards saturation. Likewise, on account of the single cylinder RCS in the specular configuration shown on figure 4.11, we can establish that for radius below 5 cm, the scattering behaviour towards saturation is also not really favoured in any configuration. The two azimuthal angles have been this time considered since on the contrary to the VV polarization, the specular scattering in HH is higher for $\psi_{az} = 0^o$ than for 90^o with still for both $\psi_{ins} = 90^o$.

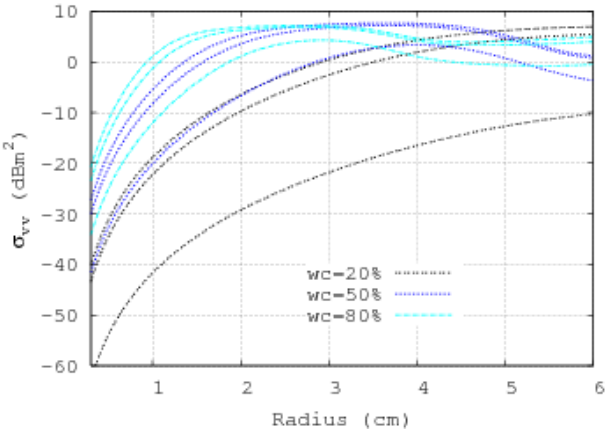

Figure 4.10: P-band σ_{vv} (RCS) of a single cylinder versus its radius in the specular configuration ($\varphi_{\mathrm{T}} = \varphi_{\mathrm{R}}$) with the scattering angles : $\theta_{\mathrm{T}} \overset{\mathrm{SSA}}{=} \theta_{\mathrm{R}} = [0., 30^o, 60^o]$ as study parameter which is going up together with the scattering level for each sheaf of same color curves, corresponding also to a given permittivity as indicated above. The cylinder is 3 m high and is horizontally placed so that its attitude orientation angles are $\psi_{az} = \pi/2, \psi_{ins} = \pi/2$.

Consistent with this assertion, the specular configuration – as a particluar case with $\theta_{\mathrm{R}} = \theta_{\mathrm{T}}$ – isn't more favorable than the monostatic with rather a less interesting dynamic in the cross polarizations with a first step below 100 ton.ha^{-1}, as shown in figure 4.14 (a). The higher ground contribution is clearly manisfest for like polarizations which spoils completely the sensitivity towards biomass, since both lower ground return caused by the higher attenuation is roughly compensated by the volume return. In a more accentuated way, the specular configuration shown on the right hand side (b) for a grazing incidence angle ($\theta_{\mathrm{T}} = 63^o$) exhibits a singular dynamic with two regimes, with an increasing trend followed by a decreasing one rather marked for like polarizations. Similarly to the first specular case (a), it results from the balance between the volume and the ground contribution which likewise plays a significant role in the resulting σ^0_{pp}. Actually, this decreasing dynamic measures the growing attenation, hence the idea to intensify this behaviour with the aim of getting only a decreasing region with as far as possible an higher dynamic amplitude.

Indeed, in view of the simulations (figure 4.15) carried out at L band the ground over volume ratio is effectively much higher so that the volume contribution increase with biomass does not perturbate the globally decreasing dynamic. This concerns of course the like polarizations only since the cross channel still just contains volume return and keeps as a result an ambiguous bell shape for biomass retrieval. Notwithstanding, both co-polarizations exhibit a very interesting sensitivity towards biomass, or more precisely towards volume attenuation. Naturally, the major drawback for a biomass retrieval based on radiometry will lie in the close dependency towards the surface state, as quantitatively (figure 4.15 (d)) assessed regarding soil humidity. Even with a relatively moderate deviation (ranging from 10 to 50% of a water content), the radiometric level is too sensitive towards humidity (roughness as well) in order to faithfully make a biomass level correspondance and all the more in the single polarization acquisition (for which the HH is clearly preferable). Nevertheless, with the combined use of both polarizations and the assumption of a electromagnetic forward model sufficiently accurate (and well documented regarding for instance the statistical roughness description) to build a faithful look-up table ($B = f(\sigma^0_{vv}, \sigma^0_{hh})$)

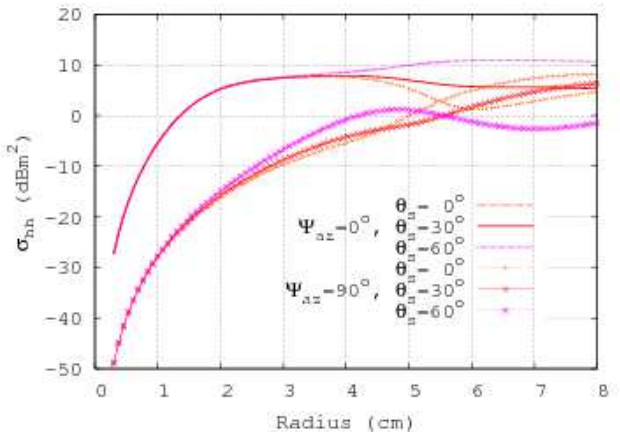

Figure 4.11: P-band σ_{hh} (RCS) of a single cylinder versus its radius in the specular configuration ($\varphi_{\mathrm{T}} \overset{\mathrm{SSA}}{=} \varphi_{\mathrm{R}}$) with the scattering angles : $\theta_{\mathrm{T}} \overset{\mathrm{SSA}}{=} \theta_{\mathrm{R}} = [0., 30^o, 60^o]$ as study parameter. The cylinder is 3 m high and is horizontally placed but in two different perpendicular position so that its attitude orientation angles are either $\psi_{az} = 0$ or $\pi/2$ and $\psi_{ins} = \pi/2$.

the retrival is conceivable and should be rather interesting regarding the saturation issue. Furthermore, within a multistatic framework, a joint monostatic plus bistatic quad pol acquisition should be also very promising not only regarding biomass retrieval but also ground characterization especially for soil moisture. Indeed, in view of their respective sensitivity, both exhibit complementary discrimination capabilities since the the monostatic HH return essentially driven by the double bounce mechanism is closely related to the surface state and adds thereby an helpful independent information to strengthen the afore-mentioned look-up table from the specular L band like polarizations. This method naturally holds as long as the saturation point is not reached, which besides constitues the first drawback of this method. Moreover, within such framework, the combined P and L band is also required since our simulations as well as experimental results found in the literature show that HH monostatic L band return does not carry only double bounce and plus, the HV dynamic is noticeably less interesting in view of its quickest convergence. Nevertheless, the study of an inversion algorithm based on multistatic and multi-frequency acquisitions would deserve another intrinsic investigation, besides preferably in the light of available experimental data, that's why this point will be kept for further prospects. In addition, the robustness of a biomass retrieval based on the L band decreasing dynamic do not depend only on surface state but also on forest attributes, as it will be shown in section 4.3.

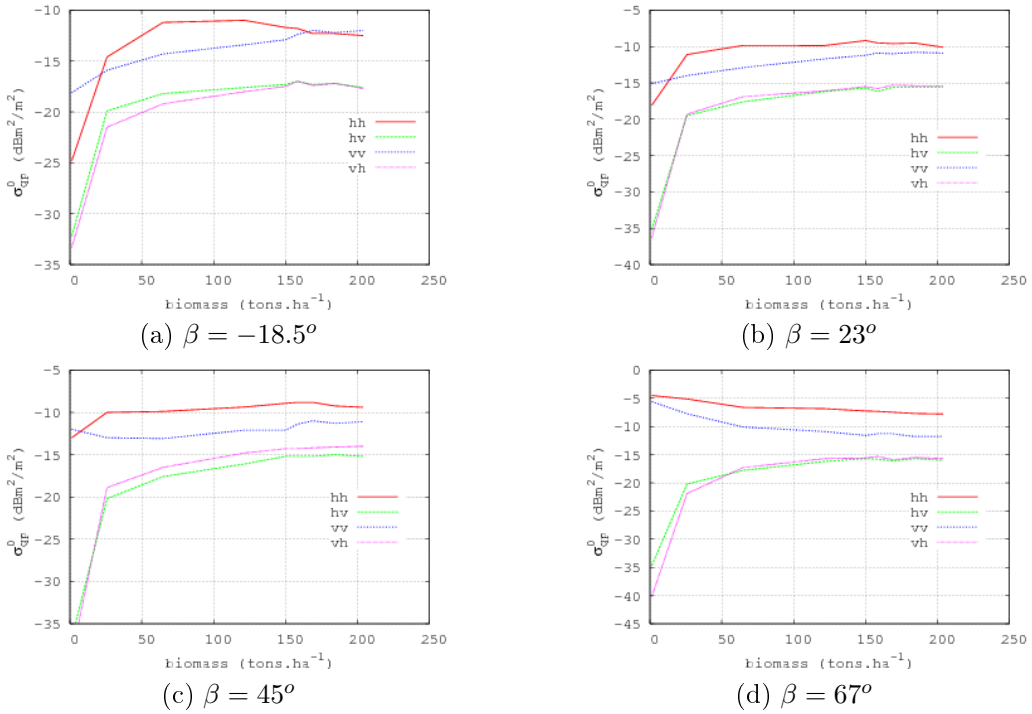

(a) $\beta = -18.5^o$ (b) $\beta = 23^o$

(c) $\beta = 45^o$ (d) $\beta = 67^o$

Figure 4.12: Sensitivity of the scattering coefficient σ^0_{qp} towards biomass for various bistatic angle β, taken with a site component only resulting from a constant incident angle $\theta_{\mathrm{T}} = 45^o$ and the following receiving ones : (a) $\theta_{\mathrm{R}} = 63.5^o$, (b) $\theta_{\mathrm{R}} = 22^o$, (c) $\theta_{\mathrm{R}} = 0^o$, (d) $\theta_{\mathrm{R}} = -22^o$

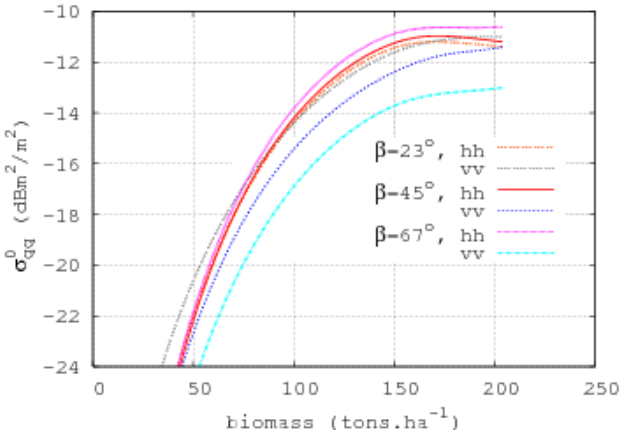

Figure 4.13: Volume contribution sensitivity for the like polarizations scattering coefficient σ^0_{pp} towards biomass for the various bistatic angle β indicated above within $\mathcal{P}^{\varphi 0}_{\perp}$, with the same incident angle $\theta_{\mathrm{T}} = 45^o$.

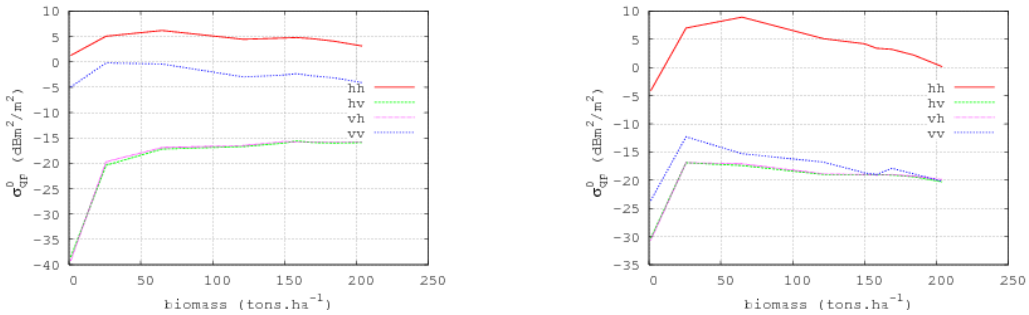

(a) $\beta = 90^o$ (b) $\beta = 127^o$

Figure 4.14: σ^0_{qp} sensitivity versus bioamss for two specular configurations at P-band, (a) $[\theta_{\mathrm{T}} = 45^o, \theta_{\mathrm{R}} = -45^o]$ and (b) $[\theta_{\mathrm{T}} = 63.5^o, \theta_{\mathrm{R}} = -63.5^o]$

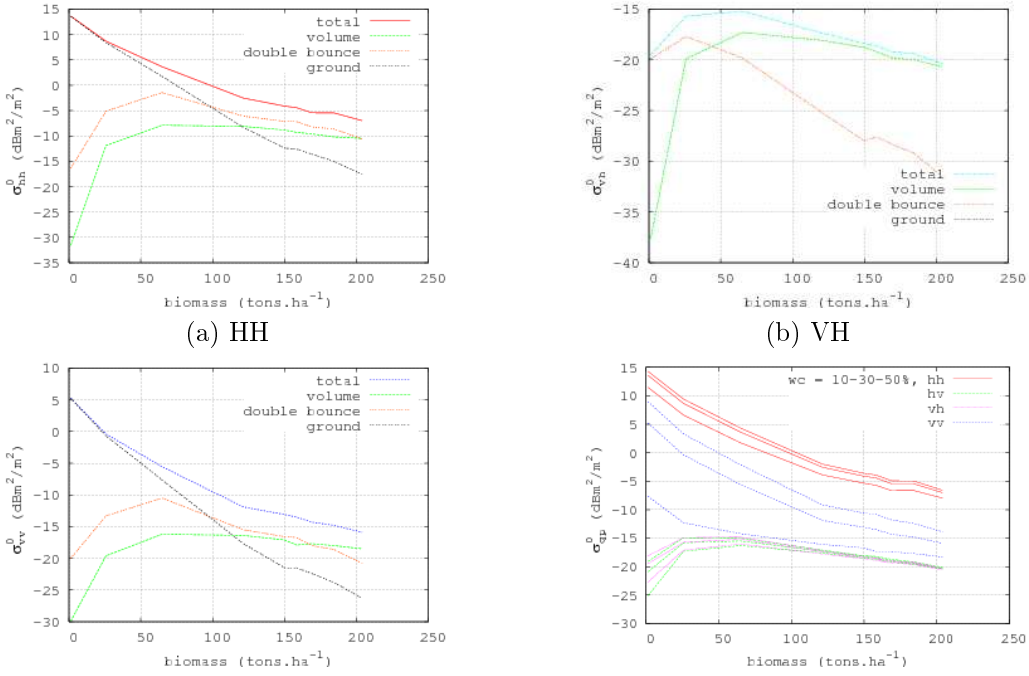

(a) HH (b) VH

(c) VV (d) soil humidity impact

Figure 4.15: Sensitivity towards biomass of the three scattering mechanisms contributing to the resulting total coefficient σ^0_{qp} at **L band** in the grazing and quasi specular bistatic configuration, $[\theta_{\mathrm{T}} = 63.5^o, \theta_{\mathrm{R}} = 63.5^o, \Delta\varphi = 180^o]_{\mathrm{SSA}}$, the soil humidity impact is shown in (d)

Bistatic Angle Variation Within the Plane $\mathcal{P}_{\perp}^{\varphi 90}$

At this point, the remaining bistatic space to study concerns the previously defined azimuthal plane $\mathcal{P}_{\perp}^{\varphi 90}$ – perpendicular to both incidence and horizontal reference ones – in which likewise the σ_{qp}^{0} sensitivity towards biomass is liable to change, depending on the scattering site angle. As emphasized at the end of section 4.2.1 with the hemispherical scattering diagrams, three regions can be distinguished with the aim of selecting the most relevant configurations : the crown region where the double bounce enhancement holds or outside which encompasses a specific part where these coupling terms seem to vanish, that is near the off-nadir position. Concerning the former configuration, the various contribution for each polarization are given in figure 4.16. Similarly to the monostatic case, the HH return is driven by double bounce as long as the growing attenuation is not too high, from which volume becomes predominant. We can notice that even for young ages, the double bounce comes mainly from the branches since the HH scattering vanishes for small vertical cylinders (relatively to frequency, cf. chapter 3). The VV return encompasses also for the young stages mainly coupling terms and likewise the trend is reversed steadily with the growing biomass with the volume domination. Nevertheless, in comparison with the monostatic case this phenomenon is much more accentuated since the volume is relatively lower, mainly because of the polarization artefact effect which transfer the scattered energy to the cross channels. The latters, whether HV or VH, exhibit on the contrary a really different sensitivity than the monostatic one since from now on, ground terms are not null anymore and spoil the dynamic and thereby prevent its use for retrieval. We remind that this cross return from the ground is due to geometrical effects on the polarization local definition (hence the marked difference between the two cross-pol, resulting directly from the common like polarizations one after rotation matrix products), as opposed to the one coming from roughness even in monostatic. It can be noticed that the volume contribution is roughly identical between both cross-pol on account of its uniform orientation and the scattering angle of 45^{o} which keeps the symmetries (cf. chapter 3). To conclude with this configuration, it turns out that every polarization channel evinces major drawbacks so that such bistatic geometry can be left aside.

In the previous configuration, the volume contribution for like polarizations has shown a potentially interesting dynamic but dominated by the coupling terms which spoiled thereby the resulting total dynamic. In view of the double bounce spherical scattering diagrams of figure 4.7, the region close to the off-nadir position looks interesting with the aim of canceling these coupling terms, though guaranteed only for the displayed age. Such configuration with a quasi off-nadir receiver is thus chosen and the resulting dynamic is given in figure 4.17 and will be referred for the sequel as β_{opt}^{az} standing for the optimal configuration within the plane $\mathcal{P}_{\perp}^{\varphi 90}$. In a quite positive way, the HH double bounce drop holds for all the forest ages apart from the youngest stages, still caused by the randomly oriented branches. The VV polarization exhibits nearly the same behaviour since both double bounce and volume contributions are also roughly identical. Indeed, on the one hand both come from the randomly oriented volume which is almost polarization independent on account of the low polarization artefacts in this bistatic region close to the incident plane $(\hat{k_i}, \hat{z})$ and on the second hand the Fresnel coefficients involved for the double bounce with respect to the receiver are barely different in view of the step incidence angle involved. The remaining discrepancy comes thus from the moderate difference between the specular V or H polarization reflection encompassed within the transmitter's double bounce mechanism. Except for the young forest region, the radiometric sensitivity of the like polarizations in this configuration is very well correlated to biomass with a saturation point noticeably moved backward (increment of 1 dB between 150 and 180 ton.ha^{-1}, better zoomed in figures 4.19 or 4.24) and all the more interesting regarding robustness that both co-pol can be

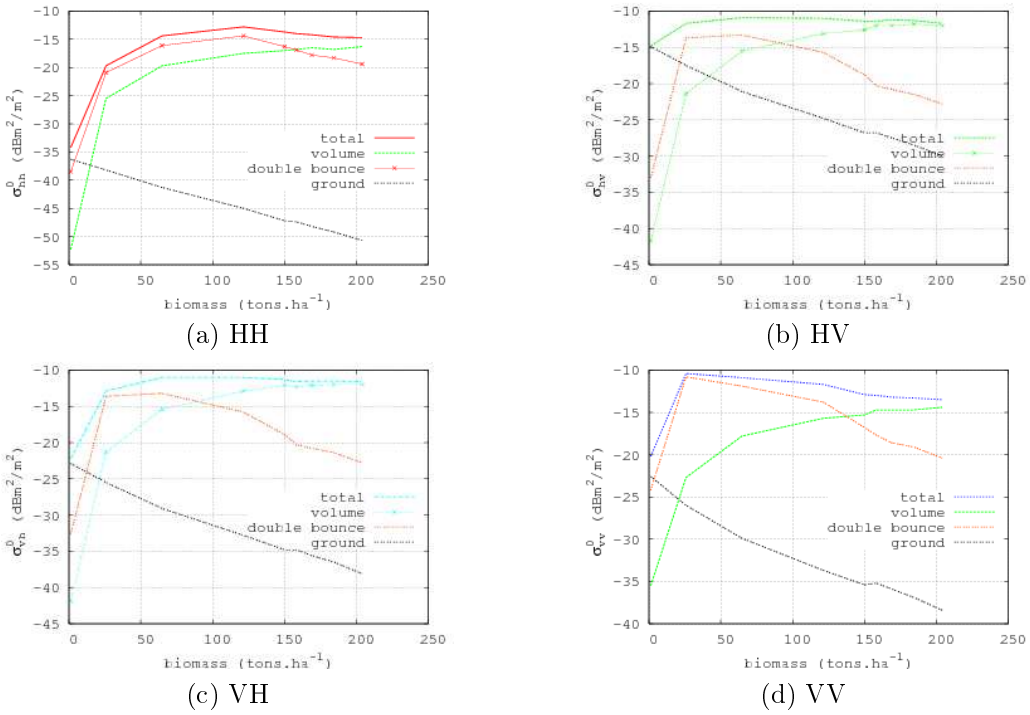

(a) HH (b) HV

(c) VH (d) VV

Figure 4.16: Scattering mechanisms contributing to the total scattering coefficient σ^0_{qp} for a bistatic configuration within the plane $\mathcal{P}_{\perp}^{\varphi 90}$ given by : $[\theta_{\mathrm{T}} = 45^o, \theta_{\mathrm{R}} = 45^o, \Delta\varphi = 90^o]_{\mathrm{SSA}}$.

used. This bistatic geometry will thus be kept for the following section, dedicated precisely to the robustness of retrieval based on the optimal configuration radiometric sensitivity. Furthermore, still with the aim of cancelling the remaining double bounce contribution in the low biomass zone, others simulations have been carried out with grazing angles in order to get close to the Brewster angle for the vertical polarization. Nevertheless, this supposes that both transmitter and receiver are in grazing positions which turns out to be also unfavourable for the volume dynamic, on top of operational issues – especially for spaceborne radars.

To conclude this research for the most promising configurations regarding sensitivity to biomass and its retrieval within the limitation of a single frequency and bistatic acquisition, their dynamic is emphasized and compared together with the monostatic case (cf. figure 4.19). Let aside the robustness criteria studied in the next section, a noticeable sensitivity gain regarding the monostatic saturation point can be pointed out for the two bistatic configurations which have just been presented (β^{st}_{opt} and β^{az}_{opt}).

Concerning the configuration β^{az}_{opt}, actually geometrically close to the site bistatic one (β^{st}_{opt}), the question of their similarity can be risen, once corrected the polarization artefact described in the previous chapter. Indeed, in view of their respective dynamic range, an obvious difference lies a kind of permutation between like and co polarizations. The artefact correction has then been achieved and the resulting dynamic is given in figure 4.18. As expected, the like polarizations retrieved higher levels than the cross ones, with the quite classical dynamic for the latter which encompass once again mainly the volume contribution. With the aim of biomass retrieval, we focus naturally on their robustness, first towards the surface state. Nevertheless, has shown with the significant deviation resulting from various soil water content (still figure 4.18), the ground

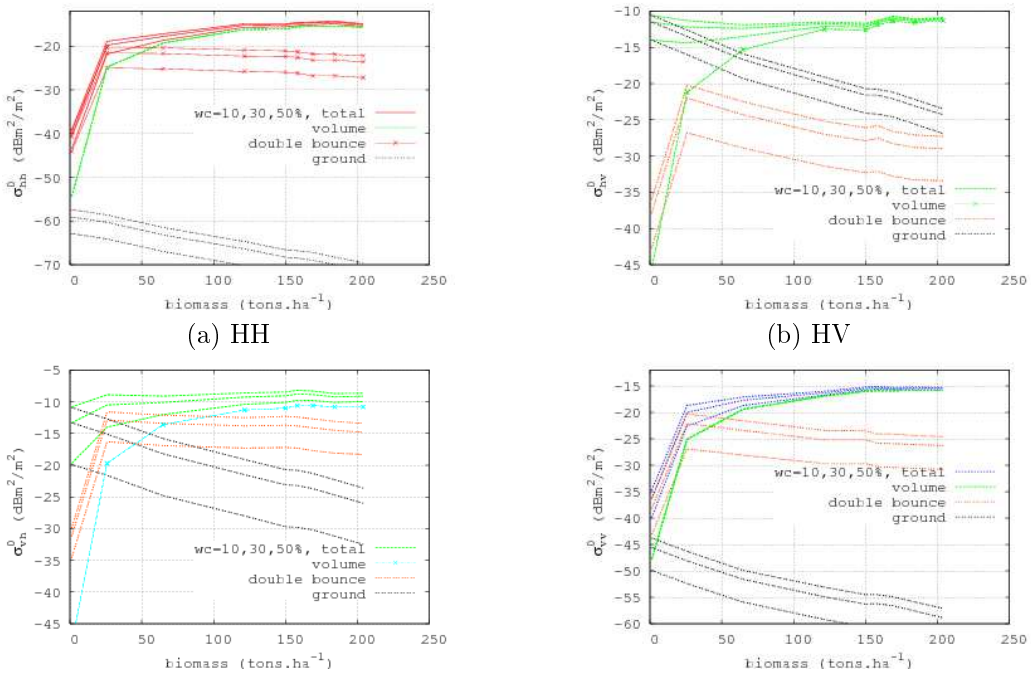

(a) HH (b) HV

(c) VH (d) VV

Figure 4.17: Scattering mechanisms contributing to the total scattering coefficient σ^0_{qp} in the bistatic configuration defined by : $[\theta_{\mathrm{T}} = 45^o, \theta_{\mathrm{R}} = 5^o, \Delta\varphi = 90^o]_{\mathrm{SSA}}$

contribution is unfortunately sufficiently important to bias the dynamic so that this polarization basis change is not relevant in this framework, though useful to retrieve some symmetry properties.

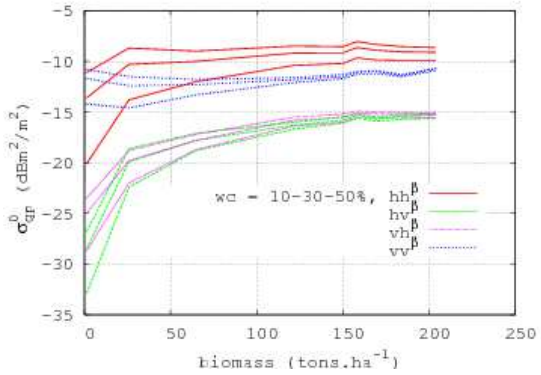

Figure 4.18: Scattering coefficient σ^0_{qp} sensitivity towards biomass within the β polarization basis for the bistatic configuration given by : $[\theta_{\mathrm{T}} = 45^o, \theta_{\mathrm{R}} = 5^o, \Delta\varphi = 90^o]_{\mathrm{SSA}}$. The deviation within each sheaf of lines goes up together with the soil water content parameter.

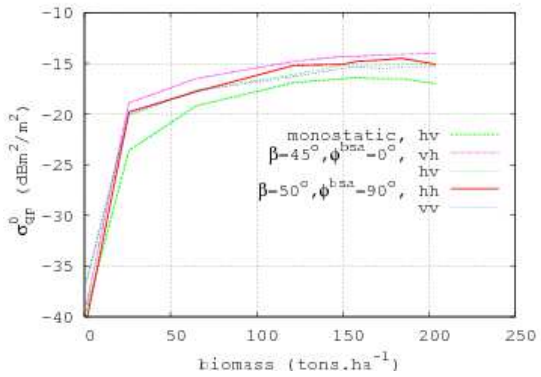

Figure 4.19: Sensitivity towards biomass of the optimal bistatic polarimetric scattering coefficients σ^0_{qp} whether in site or azimuth, respectively given by : $[\theta_{\mathrm{T}} = 45^o, \theta_{\mathrm{R}} = 0^o, \Delta\varphi = 0^o]_{\mathrm{SSA}}$, $[\theta_{\mathrm{T}} = 45^o, \theta_{\mathrm{R}} = 5^o, \Delta\varphi = 90^o]_{\mathrm{SSA}}$ and in comparison with the monostatic cross polarization.

4.3 Robustness of the Optimal Configurations

The bistatic configurations set forth at the end of the previous section has been considered optimal in view of the sensitivity criteria towards biomass. Although necessary, the other condition now at issue lies in the method reliability, that is the robustness of the biomass retrieval directly from the scattering coefficient value, whatever forest attributes liable to vary for a given biomass. On top of the surface state described by its roughness, its humidity and slope, those characteristics concern the vegetation itself with physical and structural properties. Prominent among them, branches water content, orientation and the impact of the standard deviation relative to their dimensions will be assessed. Indeed, in a general way, the return energy of a passive scatterer is – within a specific radar configuration (frequency, positions) – dependent on its intrinsic permittivity and geometry. For what concerns the radar parameters, the configurations which has been pointed out previously – that is the quasi specular one in L band and the P-band quasi off-nadir configurations within the normal bistatic plane $\mathcal{P}_{\perp}^{\varphi 0}$ or the azimuthal perpendicular one $\mathcal{P}_{\perp}^{\varphi 90}$ will be considered and each time in comparison with what holds in the monostatic case. The ground importance has been already emphasized in the previous simulations, with the soil water content as a given parameter of the sensitivity towards biomass. Its major impact for the L band dynamic has been discussed (cf. figure 4.15, § 4.2.2) with the conclusion that it requires a more thorough retrieval algorithm especially with a joint monostatic P band acquisition. For the P band optimal configuration within $\mathcal{P}_{\perp}^{\varphi 90}$, it has been also already pointed out with figures 4.17 (a) and (d) that the non negligible double bounce contribution for the young ages entails some bias risk regarding the subsequent associated biomass. Indeed, until 75 ton.ha^{-1}, this bias is about 25 ton.ha^{-1} regarding the discrepancy between the dry and wet ground (of respective water content 10 or 50 %). For the optimal configuration within the normal bistatic plane, this bias if of the same order (cf. figure 4.20) but less advantageously even for higher biomass region on account of the double bounce presence within the cross-pol, which does not vanish as for the co-polarizations in the latter azimuthal configuration.

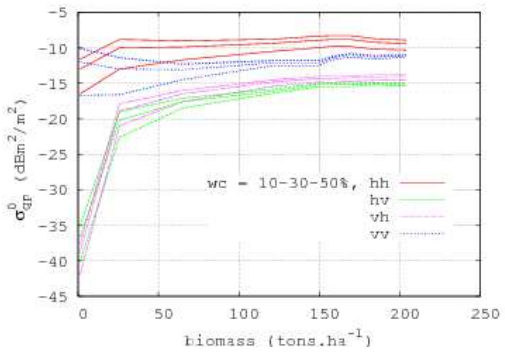

Figure 4.20: Impact of soil water content on the scattering coefficient σ^0_{qp} sensitivity towards biomass at **P band** and for the site bistatic configuration with off-nadir receiver, that is : $[\theta_{\mathrm{T}} = 45^o, \theta_{\mathrm{R}} = 0^o, \Delta\varphi = 0^o]_{\mathrm{SSA}}$. In each sheaf of curves, the amplitude is growing together with the water content.

The surface state impact has been shown only through the soil humidity since the effect of ground roughness, though different (cf. the modulation subsequent to the modified Fresnel coefficients), will exhibit similar trends as long as its contribution in the resulting σ^0 is appreciable. Likewise, ground slopes impact is not quantitatively shown since, from a theoretical point

of view, it can be shown (cf. chapter 2 about the forward model) that a titled angle within the scattering plane will simply modify the co-polar amplitude (subsequent to viewing angles change) whereas another arbitrary angle will mixed the latter to give a cross polarization term. Its magnitude, dependent on the like polarizations ones can thereby be strongly modified, especially for low biomass levels with as a result, a narrowed and biased HV dynamic. To conclude with the surface state impact from the simulations carried out within the previous assumptions, the monostatic P-HV is the most robust since the encompassed double bounce contribution is negligible whatever the forest biomass whereas it brings about a bias of roughly 25 ton.ha^{-1} for the site bistatic configuration and likewise in azimuth but only until 75 ton.ha^{-1} of biomass, all of that for typical soil water content range.

Concerning now orientation effects, simulations in the previous monostatic and bistatic optimal – or rather specific at this point – configurations have been carried out with uniformly oriented or not branches in the upper layers. We remind that this orientation concern the probability density functions (pdf) which result in favoured ranges for the branches insertion angle (ψ), according to the parameters given in tables 4.1 and 4.2. In view of the results presented in figure 4.21, the orientation effects turns out to be truly significant within the retrieval scope. Indeed, to start first with the monostatic case (a), the subsequent bias can reach 50 ton.ha^{-1}. The like polarizations of the L band specular configuration (b) are quite robust until the differential extinction between H and V become sufficiently important to modify the attenuated ground return. The HH component is however very stable until 150 ton.ha^{-1}.

Concerning now the P-band site bistatic configuration (c), both cross-pol are not similarly impacted, the VH one presents a very interesting robustness whereas the HV a resulting bias comparable to the monostatic one. As explained in chapter 3, the difference between the cross polarization is very sensitive to the branch insertion angle, the higher impact on HV rather than VH comes also from the relative position of the cylinders' direction vector projection (given by Ψ) onto the scattering plane $(\hat{k}_i, \hat{k}_s)$ relatively to the bistatic bisectrix.

The remaining bistatic configuration (d) presents the best stability, with a quasi null bias for the HH component whatever the forest biomass whereas the VV one is limited to about 25 ton.ha^{-1}.

In addition, the size standard deviation have been also considered for the geometric dimensions of every kind of scatterers (trunks and the various order branches). This parameter have been pointed out since its impact is noticeable and since it enables to introduce easily size variation, keeping in mind that within this framework the biomass must remain constant. As emphasized in figure 4.22, the subsequent bias for biomass retrieval can reach in monostatic 25 ton.ha^{-1} just before the saturation region (a). This bias is roughly the same for the two following bistatic configurations (b) and (c) with however for the latter an appreciable higher stability for the horizontal co-polarization (limited bias to 10, 15 ton.ha^{-1}).

Apart from the previous criteria based on geometric considerations (angle, size), the permittivity deviation is assessed through the vegetation water content variation, the most likely parameter liable to vary with possible significant consequences. Indeed, as mentioned in the first chapter and in the section dedicated to the vegetation description, for a given forest, water content can exhibit not only a spatial gradient (vertical from the canopy top to the trunks and even horizontal within the latter between heartwood and sapwood drier) but also temporal, whether according to diurnal or seasonal cycle (cf. [Gates, 1991]). In view of this complexity, it is almost impossible to use a priori information, hence the importance of assessing its impact on the scattering coefficient. Concerning our simulated forests, the variation given in table 4.3 has been considered based on vertical localization and scatterer type. According to the resulting impact on the radiometric levels (shown in figure 4.23), volume humidity turns out to be a strong source

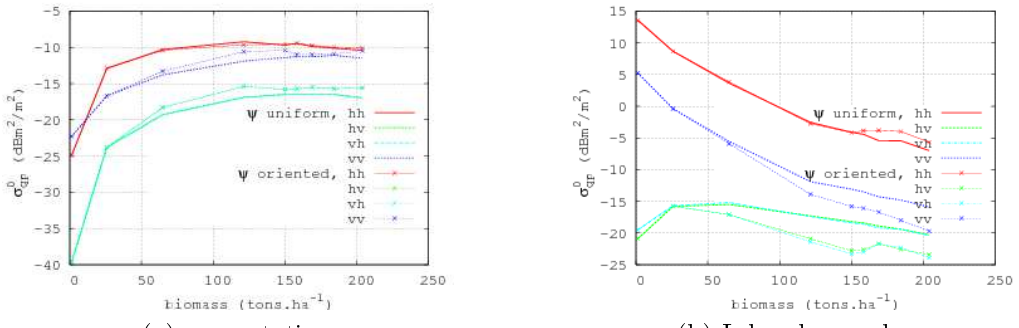

(a) monostatic (b) L band specular

(c) β^{st}_{opt} (d) β^{az}_{opt}

Figure 4.21: Orientation effect (ψ distribution) on the scattering coefficient σ^0_{qp} sensitivity to biomass for an incidence angle of $\theta_T = 45^o$ and matching the following receiver positions : (a) monostatic P-band, (b) $[\theta_R = 63.5^o, \Delta\varphi = 180^o]_{SSA}$ L-band, (c) $[\theta_R = 0^o, \Delta\varphi = 0^o]_{SSA}$ P-band, (d) $[\theta_R = 5^o, \Delta\varphi = 90^o]_{SSA}$ P-band.

of bias for biomass retrieval with accuracy errors possibly close to 50 ton.ha^{-1} and without any noticeably favoured acquisition, whether considering the cross or like polarizations respectively for the monostatic configuration (a), the site (b) or azimuth (c) bistatic ones. For the latters, the combined use of the different like polarizations have been risen, for instance with their ratio versus biomass. Nevertheless, its narrow and also ambiguous dynamic does not work rigorously, though useful – more advantageously for the azimuth bistatic configuration – but rather as a confidence indicator.

		case no 1	case no 2	case no 3
Bottom layer	trunks	20♯	30	40
Middle,upper layers	trunks	25	35	45
	primary br.	40	50	60
	secondary br.	50	60	70
	tertiary br.	50	60	70

Table 4.3: Considered cases for the various scatterers volumetric water content, given in percent (%♯).

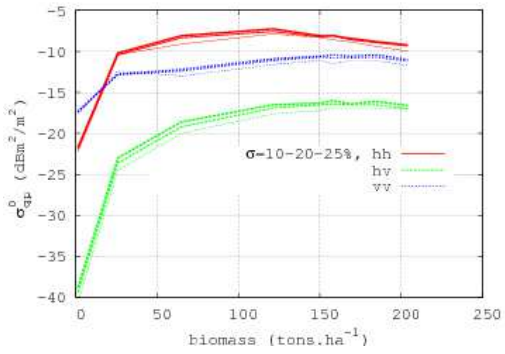

(a) $\beta = 0$

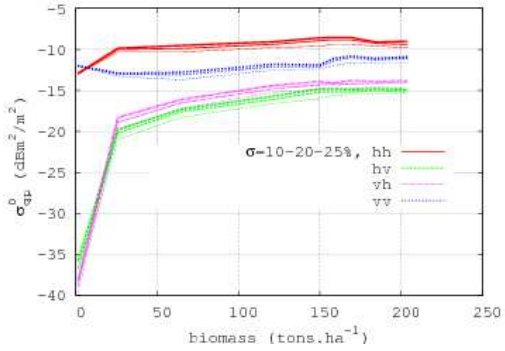

(b) β^{st}_{opt}

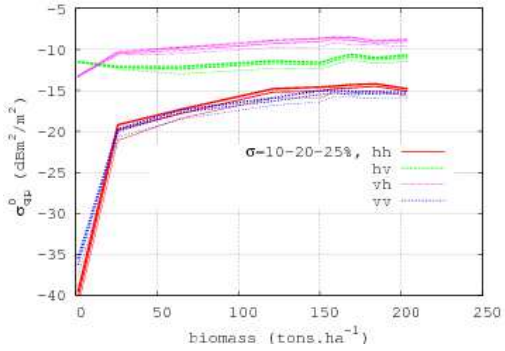

(c) β^{az}_{opt}

Figure 4.22: Size standard deviation impact on the scattering coefficient σ^0_{qp} sensitivity to biomass for an incidence angle of $\theta_{\mathrm{T}} = 45^o$ and matching the following receiver positions : (a) monostatic, (b) $[\theta_{\mathrm{R}} = 0^o, \Delta\varphi = 0^o]_{\mathrm{SSA}}$ and (c) $[\theta_{\mathrm{R}} = 5^o, \Delta\varphi = 90^o]_{\mathrm{SSA}}$. In the upper sheaf of curves, the lines thickness goes up together with the standard deviation.

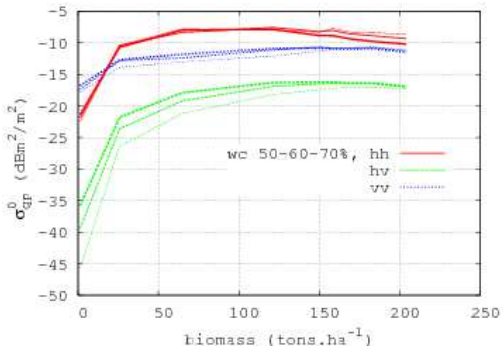

(a) monostatic

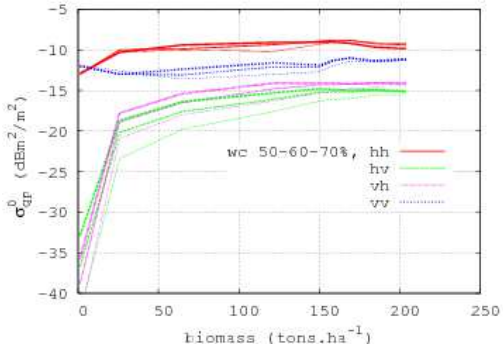

(b) β_{opt}^{st}

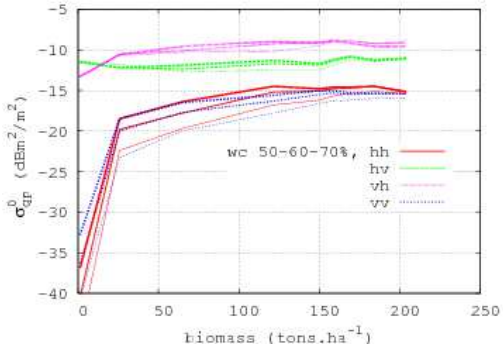

(c) β_{opt}^{az}

Figure 4.23: Volume water content effect on the polarimetric scattering coefficient σ_{qp}^0 sensitivity to biomass for an incidence angle of $\theta_{\mathrm{T}} = 45^o$ and for the following receivers' position : (a) monostatic, (b) $[\theta_{\mathrm{R}} = 0^o, \Delta\varphi = 0^o]_{\mathrm{SSA}}$, (c) $[\theta_{\mathrm{R}} = 5^o, \Delta\varphi = 90^o]_{\mathrm{SSA}}$. In the upper sheaf of curves, the lines thickness goes up together with the standard deviation.

Finally, another question rised by the bistatic configurations set forth is actually the importance of the transmitter position or more precisely the relevantness of considering similarly radiometric levels from different incident angles. Indeed, the fact that corrections could be applied to take into account the various incidences – preferably in a simple way – widen considerably the operational capabilities of the acquisition type. As a typical example, the afore-mentioned β^0 use rather than σ^0 enables to cope with the along range incidence variation within the radar swath, as long as the scatterers exhibit a Lambertian behaviour. A random volume – considering its SPAN and without attenuation – verifies this property, the point at issue concerns thus the case of oriented cylindric scatterers, which effect has been stressed a few simulations ago (figure 4.21). Besides, the deviation concerning the receiver would lead to the same conclusions invoking the reciprocity principle and the fact that both bistatic and incident angles variations have been studied. The oriented upper layers are then considered within the simulated forests and the resulting scattering is compared for various incident angles. As a matter of fact, the more consequent orientation impact for the monostatic and site bistatic configuration is also retrieved in the present simulations (figure 4.24) since for the two latters, the Lambertian assumption is less applicable in view clearly of the non constant discrepancy within each sheaf of lines, naturally for the acquisition of interests (HV in (a), HV or VH in (b)). It can be pointed out that the VH seems more stable, nevertheless it comes unfortunately from the specific branches orientation since a rather vertical one would favour the HV one. The like polarizations for the azimuth bistatic are noticeably more robust, especially the horizontal one which has shown showed already (see figure 4.21) its better stability between the oriented or the random volume.

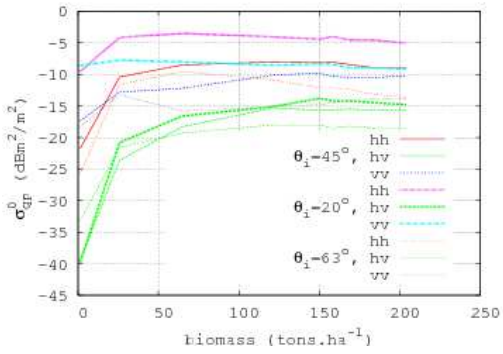

(a) monostatic

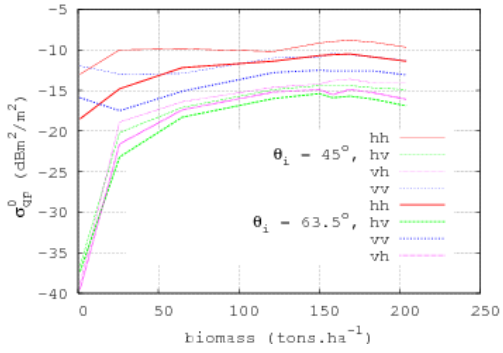

(b) β_{opt}^{st}

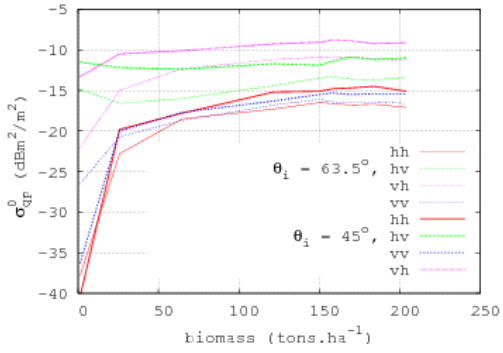

(c) β_{opt}^{az}

Figure 4.24: Transmitter incidence angle impact on the σ_{qp}^0 sensitivity towards biomass for the oriented (ψ distribution) upper layers (pine forest model). The radar configurations involved an incident angle $\theta_{\mathrm{T}} = 45^o$ and for the following receivers' position : (a) monostatic, (b) $[\theta_{\mathrm{R}} = 0^o, \Delta\varphi = 0^o]_{\mathrm{SSA}}$, (c) $[\theta_{\mathrm{R}} = 5^o, \Delta\varphi = 90^o]_{\mathrm{SSA}}$.

Conclusion

As a conclusion, it has been shown that the bistatic configuration can significantly modify the radar intensity sensitivity towards biomass, whether at P or L band. Indeed, the scattering mechanisms ratios, especially between the monostatic particular case, the forward bistatic configuration and the one within the perpendicular azimuthal plane $\mathcal{P}_{\perp}^{\varphi 90}$ exhibit a singular behaviour. Extended to these configurations as well as P or L-band frequencies, the resulting discrimination power of the scattering coefficients is considerably widened, which really plea in favor of multistatic and multi-frequency acquisitions, which cost can be advantageously limited by opportunistic bistatic configurations (particularly with hitchhiking modes). Nonetheless, the operational complexity of dealing with many data has to be realised, particularly with spatial and temporal resolution changes.

As opposed, based on a similar heuristic than the P-HV method, the respectively like or cross polarizations for the bistatic configurations within the planes $\mathcal{P}_{\perp}^{\varphi 0}$ and $\mathcal{P}_{\perp}^{\varphi 90}$ pointed out at the end (with in both a quasi off-nadir receiver) turn out to be optimal and offer a great potential for biomass retrieval, naturally within the scope of the achieved simulations. Besides, this higher sensitivity in bistatic is actually not surprising regarding the same advantage holds for forest emissivity – confirmed by previous studies based on incoherent models – and moreover on account of the specific cylinder scattering behaviour set forth in our analysis.

In addition, the originality of the present work lies in the explanation of the resulting scattering coefficient as well as in the analysis of its dynamic towards biomass, regarding robustness factors within the retrieval framework. Indeed with the set forth configurations, the major contribution of volume scattering within their respective optimal polarizations is the cornerstone of the sought dynamic which in addition postpone the saturation regime of about 50 ton.ha^{-1} in comparison with the monostatic case. Nevertheless, it has been also pointed out that for the azimuthal bistatic configuration, the whole dynamic is narrowed by the double bounce contribution which plays a non negligible role for youngest forest stages that is in the low biomass region. On the contrary, within the latter bistatic geometry and in the HH polarization, an higher stability has been established regarding the oriented structure of the forest or the scatterer size standard deviation.

As far as robustness is concerned, the major limitation lies on the volume water content impact for which the higher bias has been reached, up to 50 ton.ha^{-1} whatever the considered configurations. On that issue, the azimuth optimal one is favoured by the possible use of both like polarizations but the subsequent improvement depend on the biomass level so that ambiguities remain.

Consequently, a-priori knowledge of volume water content could significantly improve the retrieval quality, whether based on ground truth information or on multiple times series. This brings us also to promising prospects of fusion with optical data or higher microwave frequencies (e.g X band), truly complementary with its sensitiveness towards water content from the top of the canopy.

Bibliography

A. Beaudoin, T. Le Toan, S. Goze, E. Nezry, A. Lopes, E. Mougin, C.C. Hsu, H.C. Han, J.A. Kong, and R.T. Shin. Retrieval of forest biomass from sar data. *International Journal of Remote Sensing*, 15:2777–2796, 1994.

P. Borderies, L. Villard, and B. Fourestié. Sensitivity study of random volume over ground electromagnetic scattering versus volume fraction. In *International Symposium on Antennas and Propagation (ISAP)*. ECTI, KMUTMB University of Bangkok (Thailand), 2009.

S. Brown, A.J.R. Gillepsie, and A.E. Lugo. Biomass estimation methods for tropical forest with applications to forest inventory data. *Forest Science*, 223:1290–1293, 1989.

J.Q. Chambers, J. Santos, R.J. Ribeiro, and N. Higuchi. Tree damage, allometric relationships, and above-ground net primary production in central amazon forest. *Forest Ecology and Management*, 152:73–84, 2001.

I. Champion, A. Porté, D. Bert, D. Loustau, and M. Guedon. Tree architecture in remote sensing analytical models : The bray experiment. *International Journal of Remote Sensing*, 22:1827–1843, 2001.

S.R. Cloude and K.P. Papathanassiou. Three stage inversion process for polarimetric sar interferometry. *Radar Sonar and Navigation IEE Proceedings*, 39(150):125–134, 2003.

M.C. Dobson, F.T. Ulaby, T. Le Toan, A. Beaudoin, E.S. Kasishke, and N. Christensen. Dependence of radar backscatter on coniferous forest biomass. *IEEE Transactions on Geoscience and Remote Sensing*, 30:412–415, March 1992.

P. Ferrazzoli and L. Guerriero. Passive microwave remote sensing of forests: a model investigation. *IEEE Transactions on Geoscience and Remote Sensing*, 34:433–443, March 1996.

Adrian K. Fung. *Microwave Scattering and Emission Models and Their Applications*. Artech House, 1994.

D.M. Gates. Water relations of forest trees. *IEEE Transactions on Geoscience and Remote Sensing*, 29:836–842, 1991.

A.M. Karam, A.K. Fung, R.H. Lang, and N.S. Chauhan. A microwave scattering model for layered vegetation. *IEEE Transactions on Geoscience and Remote Sensing*, 4(30):767–784, 1992.

T. Le Toan, A. Beaudoin, J. Riom, and D. Guyon. Relating forest biomass to sar data. *IEEE Transactions on Geoscience and Remote Sensing*, 30:403–411, March 1992.

T. Le Toan, S. Quegan, I. Woodward, M. Lomas, N. Delbart, and G. Picard. Relating radar remote sensing of biomass to modelling of forest carbon budgets. *Climatic Change*, 67:379–402, December 2005.

P. Liang, L.E. Pierce, and M. Moghaddam. Radiative transfer model for microwave bistatic scattering from forest canopies. *IEEE Transactions on Geoscience and Remote Sensing*, 43: 2470–2483, Nov. 2005.

A.J. Luckman. Correction of sar imagery for variation in pixel scattering area caused by topography. *IEEE Transactions on Geoscience and Remote Sensing*, 36:344–350, Jan 1998.

G. Macelloni, S. Paloscia, P. Pampaloni, and R Ruisi. Airborne multi-frequency l- to ka- band radiometric measurements over forests. *IEEE Transactions on Geoscience and Remote Sensing*, 39:2507–2513, 2001.

F. Mattia, G. Satalino, L. Dente, and G. Pasquariello. Using a priori information to improve soil moisture retrieval from envisat asar ap data in semiarid regions. *IEEE Transactions on Geoscience and Remote Sensing*, 44:900–912, April 2006.

T. Mette. *Forest Biomass Estimation from Polarimetric SAR Interferometry*. Phd dissertation, Technischen Universität München — DLR (German Aerospace Center), 2007.

T. Mette, K. Papathanassiou, I. Hajnsek, H. Pretzsch, and P. Biber. Applying a common allometric equation to convert forest height from pol-insar data to forest biomass. In *Geoscience and Remote Sensing Symposium (IGARSS), Anchorage (Alaska)*, volume 20-24. IEEE, 2004.

P. Pampaloni. Microwave radiometry of forests. *Waves in Random Media*, 14:275–298, 2004.

E.J. Rignot, R. Zimmermann, and J.J. Van Zyl. Spaceborne applications of p band imaging radars for measuring forest biomass. *IEEE Transactions on Geoscience and Remote Sensing*, 33:1161–1169, Sept. 1995.

S.S. Saatchi and M. Moghaddam. Estimation of crown and stem water content and biomass of boreal forest using polarimetric sar imagery. *IEEE Transactions on Geoscience and Remote Sensing*, 38:697–709, March 2000.

S.S. Saatchi, K. Halligan, D.G. Despain, and R.L. Crabtree. Estimation of forest fuel load from radar remote sensing. *IEEE Transactions on Geoscience and Remote Sensing*, 45:1726–1740, June 2007.

K. Saleh, A. Porte, D. Guyon ans P. Ferrazzoli, and J.P. Wigneron. A forest geometric description of a maritime pine forest suitable for discrete microwave models. *Geoscience and Remote Sensing, IEEE Transactions on*, 43:2024–2035, Sept. 2007.

D.L. Schuler, Jong-Sen Lee, and G. De Grandi. Measurement of topography using polarimetric sar images. *IEEE Transactions on Geoscience and Remote Sensing*, 34:1266–1277, Sep 1996.

R.N. Treuhaft, Soren N. Madsen, Mahta Moghaddam, and Jakob J. van Zyl. Vegetation characteristics and underlying topography from interferometric radar. *Radio Science*, 31:1449–1485, November-December 1996.

L. Tsang and J.A. Kong. *Scattering of Electromagnetic Waves*, volume Theories and applications of *Remote Sensing and Digital Image Processing*. Wiley Series, 2000.

F.T. Ulaby, K. Sarabandi, K. McDonald, M. Whitt, and M.C. Dobson. Microwave canopy scattering model. *International Journal of Remote Sensing*, 11:1223–1254, 1990.

I.H. Woodhouse. Predicting backscatter-biomass and height-biomass trends using a macroecology model. *Geoscience and Remote Sensing, IEEE Transactions on*, 44:871–877, April 2006.

J.J. Van Zyl. The effect of topography on radar scattering from vegetated areas. *IEEE Transactions on Geoscience and Remote Sensing*, 31:153–160, Jan 1993.

Chapter 5

On the Potential of Bistatic Synthetic Aperture Radar Vectorial Interferometry for Forest Monitoring

Contents

To investigate the potential of bistatic Pol-InSAR (biPol-InSAR) – within the retrieval framework of Forest Model Descriptive Parameters (FMDP) – the resulting vectorial interferometric coherences from electromagnetic (em) scattering of forest models are studied under theoretical aspects. The conducted derivations bring us to an analytical operator which relate these coherences to the FMDP, whatever the bistatic angle, although restricted to the plane of incidence. Several forest models of growing complexity are considered, according to descriptive parameters such as the underlying ground surface height (topography), the volume structure characteristics – extinctions coefficients, layer heights – as well as direct and specular ground over volume scattering intensity ratios accounting thereby for the major scattering mechanisms, extended

to the bistatic geometry. Particularly emphasized are the coupling terms which come with the most innovative aspects in comparison with the standard monostatic case. The developed operator will be the cornerstone of our inversion algorithm which mathematical feasibility has to be assessed first. For that purpose, the inversion problem is examined for different scenarios of growing complexity on account of various forest descriptive models as well as radar configurations, with in addition to the bistatic specificity, the possibility of multibaseline acquisitions to cope with the increased number of unknowns. The inversion quality is assessed according to the Hadamard criteria, among which the most challenging one, namely the stability, is tackled with our simulator MIPERS, used for that purpose with multi-baselines biPol-InSAR acquisitions. The generated observables resulting from the vegetated land scattering contain the radar speckle noise characteristic of incoherent target and thereby enable us to test the algorithm stability. The electromagnetic modeling lies on a discrete description of the vegetated land approximated by means of dielectric canonical shapes over the ground. Then, an original optimal configuration regarding SAR feasibility and the inherent complexity of the forest scattering arises from this investigation where several passive off-nadir baselines and a grazing emitter are involved to quantitatively improve the FMDP retrieval.

5.1 Pol-InSAR Assets for Forest Monitoring

This study comes within the general objective of vegetated land surfaces monitoring, a fundamental stake for our future environment. The growing interest for forest state goes hand in hand with the climate change issue, since domain experts (see [IPCC, 2007]) impute the worrying last century temperature growth to anthropogenic activities. Indeed, vegetated land surfaces influence is twofold : on the one hand it acts locally on climate through its own albedo (especially for what concern precipitations, cf. [Charney et al., 1975]) and on the second hand through its sink or source role of renewable carbon (cf. [Robert and Saugier, 2003]), partly responsible for green house effect. Several studies (cf. [Cox et al., 2000],[Betts et al., 1997]) agree on the fact that as long as temperature increment does not affect forest wealth, the latter present a stabilizing capacity in absorbing more carbon. The point at issue is beyond this limit where forest behaviour is liable to turn into carbon source and thereby arming a chaotic feedback loop. Beyond this implication, forests take also on great importance for land use, being very sensitive to human activities, its intrinsic biodiversity is also fundamental for ecosystem resilience (cf. [Jactel et al., 2005]).

Aiming to estimate forest biomass using interferometry and afterwards polarimetry, InSAR (i.a [Hanssen, 2001]) then Pol-InSAR technique (see [Cloude and Papathanassiou, 1998; Treuhaft and Siquiera, 2000]) represent a real breakthrough among radar applications, especially at low frequencies bandwidth (P, L-Band) for which the received signal is sensitive to both ground and vegetation contribution. Indeed, in the case of a vegetation layer above the ground, the decorrelation introduced by the vertical distribution of scatterers (namely the volume decorrelation) is not considered as noise anymore but used as a fundamental variable containing volume intrinsic information (that is height and extinction). The remaining difficulty lies then in isolating this contribution from measurable quantities, limited to the total decorrelation (mixing volume, ground and coupling contributions). This can be done, with some additional hypothesis about the media and polarimetry, assuming that the cross polarization channel does not contain ground contribution (cf. [Cloude and Papathanassiou, 2003]) – as for the P-HV biomass estimation method (cf. [Le Toan et al., 2005]). On that subject, these hypothesis about the media

description constitute a part of the difficulty with experimental data since forests are generally more complex that the commonly supposed random volume over ground (RVoG). On top of orientation and structure effects, coupling mechanisms between volume and ground (the double bounce) turn out to be a non negligible hindrance. In monostatic, one solution to cope with the latter consists in double pass acquisition but then temporal decorrelation is liable to affect the coherences amplitude and is much more difficult to handle. A positive fact is that height estimation is quite robust to the media simplification comparatively to extinction or volume to ground ratio and several studies show that with the same a priori information, height is the most reliable single variable to retrieve biomass (cf. [Mette et al., 2004; Woodhouse, 2006; Enquist et al., 1998]). Nonetheless, improvement attempts deserve great attention and in order to cope with a more sophisticated description – involving therefore more unknowns – the observable set has naturally to be enriched. Without going as far as tomographic processing (cf. [Reigber and Moreira, 2000; Nannini et al., 2009]), even a two baselines monostatic acquisitions (cf. [Cloude and Williams, 2003]) have proven their usefulness but comes with a consequent operational cost.

Besides, it may be worthwhile to consider the bistatic configuration : on the one hand, new scattering mechanisms and the resulting new observables are liable to overcome the previous structural physical difficulties. On the other hand, the new radar geometry and its inherent larger versatility for the configuration possibilities may supply interesting operational properties especially concerning the receiving baselines length and altitude considered in a single pass acquisition.

This paper is precisely dedicated to the study of all these points, considering as a first investigation the theoretical derivation of the biPol-InSAR coherence, in the case of various forest canonical models of growing complexity and for bistatic angle defined within the plane of incidence. Following the way paved in [Treuhaft and Siquiera, 2000] and [Cloude and Papathanassiou, 2003] a specific emphasis is given on the decorrelation introduced by volume, direct and specular ground scattering mechanisms. The considered configurations concerning radar parameters as well as the various forest models – RVoG, OψVoG, COψVoG, nSCOψVoG – are presented and defined in the next section. Section 3 gives the decorrelation expression for the volume to which the ground contribution is then added. In section 4 the bistatic coupling terms are accounted for and finally section 5 tackles the structured volume case also coupled with the ground through specular terms.

Keeping in mind the quantitative retrieval purpose (detailed in sections 5.6 and 5.7), we focus herein on how the FMDP are embodied for these different cases within the biPol-InSAR coherences analytical formulae.

5.2 Considered Configurations

5.2.1 Bistatic Radar Geometry

As mentioned in the introduction, the radar configurations will be restricted to bistatic angle variation within the incidence plane in a single pass mode, fully polarimetric and with possibly several interferometric baselines corresponding to nearly the same bistatic angle. Indeed, no more than **one passive set** of antennas receiving the scattered field of a single emitting source will be studied. Nearly the same bistatic angle is thereby considered for each possible interferometric baseline. Although interesting they could be, multi-static acquisitions and its less demanding version joint monostatic plus bistatic ones are hereafter left aside. Besides, beyond the additional gain of the different final results, a mixed inversion could be limited by mis-registration problems possibly severe with large bistatic angle. The measures at our disposal will then lie on the polarimetric interferometric cross correlation corresponding to each baseline, that is for antennas 1 and 2 :

$$\Gamma(\hat{q}_1, \hat{q}_2; \hat{t}) = \langle\ \hat{p}_1 \cdot \vec{E}_{\hat{t}}(\vec{r}_1), \left(\hat{p}_2 \cdot \vec{E}_{\hat{t}}(\vec{r}_2)\right)^*\ \rangle \tag{5.1}$$

where the brackets represent a spatial average between adjacent pixels, * the complex conjugate symbol, $\hat{p}_{1,2}$ unitary receiving polarization states at antenna 1 or 2 (cf. table p7 of the frequently used symbols) and $\vec{E}_{\hat{t}}(\vec{r})$ the received field at the observation point $\vec{r}$ due to transmitting wave in polarization $\hat{t}$. The resulting coherence is then obtained by normalisation :

$$\gamma(\hat{p_1}, \hat{p_2}; \hat{t}) = \frac{\Gamma(\hat{p_1}, \hat{p_2}; \hat{t})}{\sqrt{\Gamma(\hat{p_1}, \hat{p_1}; \hat{t})} \cdot \sqrt{\Gamma(\hat{p_2}, \hat{p_2}; \hat{t})}} \tag{5.2}$$

Since the early beginning of interferometric SAR applications, the coherences sensitivity have been extensively studied. On top of the search for its best statistical estimator (cf. the optimal multilook size and the trade-off between convergence and bias, among others [Touzi et al., 1999]), several factors impact the measured coherence value γ^{msr}, as synthesized by the following multiplicative decomposition model (cf. [Hanssen, 2001; Zebker and Villasenor, 1992]) :

$$\gamma^{msr} = \gamma^{\text{syst}} \cdot \gamma^{\text{temporal}} \cdot \gamma^{\text{spatial}} \tag{5.3}$$

which emphasizes the decorrelation sources associated to system, temporal and spatial effects.As the former – including briefly Doppler centroid mismatch between the two acquisitions (cf. [Massonnet and Rabaute, 1993], processing noise due to mis-registration or interpolation (cf. [Hanssen and Bamler, 1999]) on the top of thermal one – will not impact directly the following, this term will be hereby left apart. Temporal decorrelation is due to the propagating (mainly with tropospheric and ionospheric effects) or scattering (here the forested land) media changes – coming mostly with meteorological ones – between the consecutive acquisitions (cf. [Zebker and Villasenor, 1992]) yielding for a given resolution cell to a different scattered field, especially for its proper phase, in addition to the standard interferometric phase difference. Apart from the radar wavelength essential in this physical change impact (cf. [Pipia et al., 2008; Askne et al., 1997]), other configurations parameters like the bistatic angle, are of minor importance. To get round of this decorrelation source, which is probably the most difficult to tackle, single pass acquisitions will be considered, all the more eased by the bistatic configuration that the baseline length can be possibly reduced as it will be shown, to overcome the need of separated platforms for space-borne monostatic systems (e.g interferometric cartwheel or pendulum constellations, cf. [Krieger

and Moreira, 2006]). These considerations about the baselines length bring us to the spatial decorrelation source which encompasses the volume term – due to the vertical distribution of scatterers, thereby interestingly linked to its height and discussed in the following section – and the surface term, also referred as the geometrical decorrelation. Assuming the ground slope knowledge, the latter can be corrected as long as the baseline length lies below a given critical value. The reflected signal spectrum dependence on difference between the scattered angles (cf. figure 5.1) originates the geometrical decorrelation. This difference can be expressed as follows :

$$\theta_1 - \theta_2 = d\theta_{12} = \frac{b_\perp}{r_{\mathrm{R}}} \tag{5.4}$$

with r_{R} the range towards the receiver. For the considered bistatic configurations hereafter with the same transmitter, the slight different looking angle $d\theta_{12}$ from the two passive receivers will induce a spectral shift of half the one caused in a double pass monostatic acquisition (when both down and up-going paths are concerned), reminded below (cf. [Gatelli et al., 1994]) :

$$\Delta f = -\frac{f_0}{\tan(\theta_{\mathrm{R}} - \psi_g)} \cdot d\theta_{12} = -\frac{f_0 b_\perp}{r_{\mathrm{R}} \tan(\theta_{\mathrm{R}} - \psi_g)} \tag{5.5}$$

for a signal bandwidth (B) centered on f_0 and a possible constant slope (ψ_g) as shown in figure 5.1. A maximum spectral discrepancy of $\Delta f = B$ gives thus a total correlation loss, corresponding to a baseline length beyond the critical one ($b_\perp^c$) :

$$|b_\perp^c| = \frac{B}{f_0} \cdot 2r_{\mathrm{R}} \tan(\theta_{\mathrm{R}} - \psi_g) \tag{5.6}$$

As an example, considering the ALOS PALSAR (FBS mode) signal characteristics (L-band, 28 MHz bandwidth) and an angle of 23^o, spaceborne receivers at an altitude of 700 km or airborne ones flying at 5,000 m are respectively limited by an orthogonal baseline of about 7.3 km and 100 m.

5.2.2 Forest Descriptive Models

Within the overall field of earth science, biosphere presents a singular complexity, even restricted to vegetated land surfaces as far as our study is concerned. Indeed, due to its high spatial heterogeneity and temporal variability, a consequent wide set of parameters are required to characterize forested media. However, the level of descriptive detail has naturally to be adapted on account of relevant parameters regarding on the one hand radar sensitivity – for instance all the physical attributes such as chemical composition can be simplified through a single variable with the permittivity – and on the other hand regarding their associated interest coming with the concerned applications – e.g the forest height is paramount as the most closely related single parameter to biomass.

Hence, in radar remote sensing, forested media can be characterized by canonical representation with several homogeneous layers (cf. figure 5.2), corresponding to a set of elements sufficiently close so that the mean statistics concerning their geometrical and physical attributes are relevant. As far as natural media are concerned, the azimuthal symmetry with respect to the vertical direction mostly holds and a single angle – the branch insertion angle ψ_{ins} – is sufficient to characterize their orientation, assuming also the symmetry of revolution for the various scatterers. Hence the notation **RV** or **O**ψ**V** standing for random or oriented volume, both consisting in an uniform statistical law but for the latter, the range of ψ is restricted within [ψ_{min},ψ_{max}]. The ground presence, assumed flat and characterized by its roughness and the soil

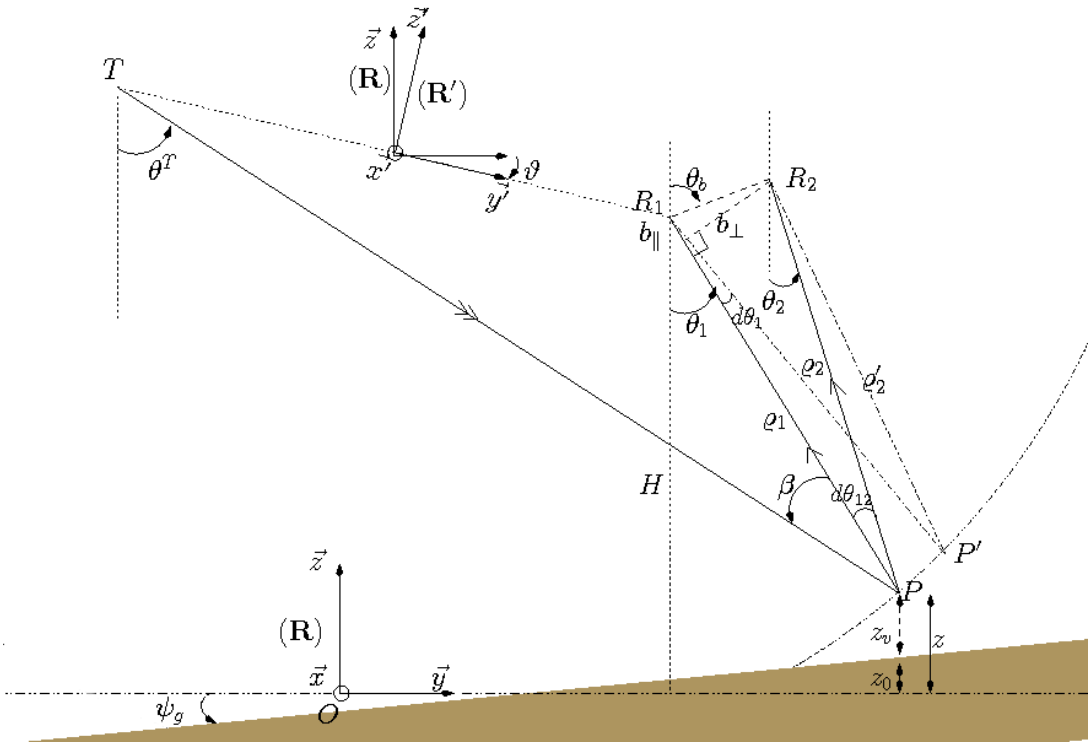

Figure 5.1: Geometry of the considered bistatic interferometric acquisition, with a single transmitter and baseline formed by the two passive receivers

water content is referred with '**oG**' (over Ground). For these models, it is also assumed that volume and ground and independent from the electromagnetic point of view, as opposed to the 'C' prefix in **COψVoG** which means that coupling terms are accounted for. Finally, the number of layers, implicitly equal to one beforehand is referred with the 'S' letter for 'Structured' with the number n indicated as in '**nSCOψVoG**'. Also introduced is the difference between the **1SR-VoG** and RVoG models since for the former, an empty space comes between the ground surface the classical filled layer, which bottom part does not match thereby the ground altitude level. Though fictive, the 1SRVoG will evince afterwards its importance in the framework of further developments in specific conditions.

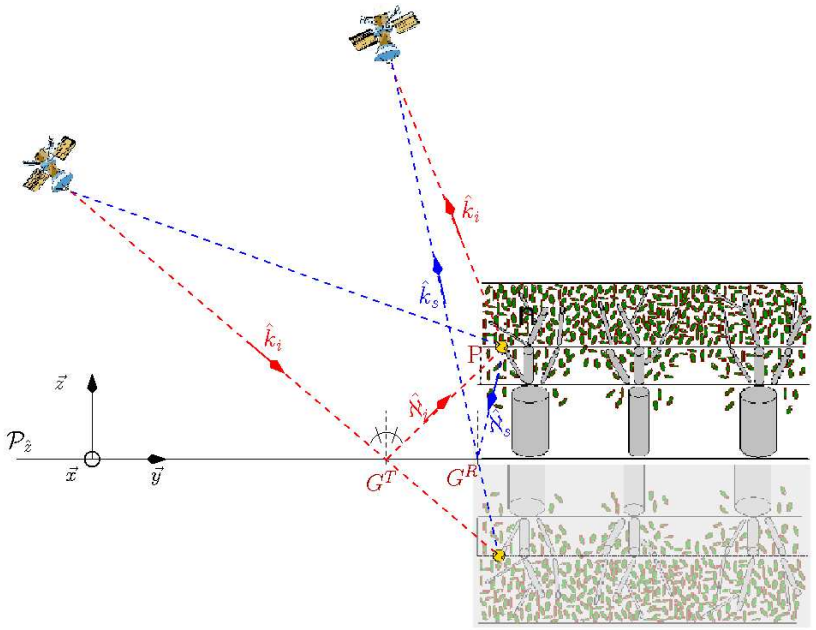

Figure 5.2: Bistatic specular ground terms with respect to the transmitter or to the receiver.

5.3 Bistatic Decorrelation for the RVoG & OψVoG Models

5.3.1 Decorrelation from Volume Scattering

In this section, most of the initial developments – concerning volume decorrelation – are conducted using results derived in [Treuhaft et al., 1996; Treuhaft and Siqueira, 2000] in order to remind fundamental concepts and rather to introduce a formalism which will ease afterwards calculations subsequent to bistatic specificities as well as more complicated forest models (mainly for those related to the double bounce mechanisms).

Volume decorrelation origin lies essentially in the fact that scatterers are vertically distributed, as opposed to ground ones. Indeed the cross correlation, for an arbitrary polarizations couple, can be estimated from the radar measures through the multi-look window (and its M pixels) performing the sum of the complex conjugate product between the fields resulting from

each pixel :

$$\widehat{\Gamma^{12}} = \sum_{l}^{M} E_l(\vec{r}_1) \cdot E_l^*(\vec{r}_2) = \sum_{l}^{M} \mathcal{V}_l e^{j\varphi_l^p} e^{j\Delta_1^2\varphi_l^{\text{geo}}} \tag{5.7}$$

where the geometric phase difference $\Delta_1^2\varphi_l^{\text{geo}}$ is emphasized for each pixel 'l' towards antennas 1 and 2. As we'll see later, assuming a large number of independant scatterers N within each resolution cell, the polar complex number $\mathcal{V}_l e^{j\varphi_l^p}$ (ensued from of the reduction of the double sum containing the N^2 contributions into the summation of N terms keeping the same proper phase between the two acquisitions) converges towards its real magnitude. For scatterers localized at a constant given height throughout the scene (typically non penetrating ground ones) or following a known slope (digital elevation model use), the flat earth correction makes as far as possible $\Delta_1^2\varphi_l^{\text{geo}}$ quasi constant from pixel to pixel. This term can then be taken out from the sum, as opposed to volume scatterers case which do not follow this Dirac behaviour and which difference between phase centers from pixel to pixel makes their cross correlation decrease. We'll see in the following quantitatively the origin of this variance but we can already infer that this drop goes with increasing volume height ($\varphi_l^{\text{geo}} \propto h$) and we can also get that it will be all the more important for low extinction coefficient since the phase centers variance will be higher. Thereby, it comes that volume decorrelation is linked to important vegetation characteristics and to our concern, is not noise at all (unlike interferometric applications only). The point now at issue is then to derive quantitatively its theoretical mean expression for a given resolution cell, that is

$$\Gamma^{12} = \langle\ \langle E(\vec{r}_1)E^*(\vec{r}_2)\rangle_{\text{med}}\rangle_{\text{ds}} \tag{5.8}$$

where brackets mean the statistical averages over propagation media and particle direct scattering distributions ('$_{\text{med}}$' and '$_{\text{ds}}$' subscripts). Indeed, on the one hand the mean incident field is considered (bulk effects on wave propagation) on each element which scattering will give, on the other hand, the received mean field once performed the average over parameters impacting (direct) scattering. In addition, if we assume a discrete, independent and linear media, the electromagnetic field results from the coherent contribution over all scatterers, giving :

$$\Gamma^{12} = \sum_{i}^{N}\sum_{j}^{N}\langle\ \langle E(\vec{r_1};i)E^*(\vec{r_2};j)\rangle_{med}\rangle_{ds} \tag{5.9}$$

with $E^*(\vec{r_2};j)$ being the field observed at $\vec{r_2}$ due to the scattering of a particle j. Considering a large number of independent scatterers N, the covariance term between scattered fields from an element s at observation points $\vec{r_a}$ and $\vec{r_b}$:

$$\langle E_s(\vec{r}_a;s)E_s^*(\vec{r_b};s)\rangle - \langle E_s(\vec{r}_a;s)\rangle\langle E_s^*(\vec{r_b};s)\rangle$$

can be neglected in comparison to

$$N \cdot (\langle E_s(\vec{r}_a;s)\rangle\langle E_s(\vec{r_b};s))$$

as demonstrated in [Treuhaft et al., 1996] so that the following approximation can be made concerning the propagation average of equation (5.9) :

$$\langle\ E(\vec{r}_1;i)E^*(\vec{r}_2;j)\rangle_{\text{med}} = \langle E(\vec{r}_1;i)\rangle_{\text{med}}\langle E^*(\vec{r}_2;j)\rangle_{\text{med}} \tag{5.10}$$

To determine $\langle E(\vec{r}_1;i)\rangle$ (the subscripts '$_{\text{med}}$' are implicit in the following and left aside), we use the first order Born approximation (cf. [Tsang and Kong, 2000]) – generalized from single particle

to bulk scattering – which states that the field at observation point $\vec{r}$ due to a given source i is the unperturbed incident one plus the scattered field resulting from the interaction with the s scatterers composing the media :

$$E(\vec{r};i) = E_{\text{inc}}(\vec{r},i) + \sum_{s}^{N} E_s(\vec{r};s) \tag{5.11}$$

which can be also expressed under a continuous summation with a given density of scatterers (volume concentration) noted $\rho(\vec{r})$. Assuming then monochromatic spherical waves, the statistic expected value over medium scatterers location and scattering amplitude probability densities yields for the mean field to :

$$\langle E(\vec{r}_j;T)\rangle = E_{\text{inc}} + \iiint \rho(r)\frac{e^{jk_0|\vec{r}_j-\vec{r}|}}{|\vec{r}_j-\vec{r}|}\cdot\langle E(\vec{r};T)\rangle\langle s^f\left(\theta_{\text{T}}^j\right)\rangle d^3r \tag{5.12}$$

with $\langle s^f\left(\theta_{\text{T}}^j\right)\rangle$ corresponding to the scattering coefficient along the forward direction, that is : $\langle s\big(\vec{r}-\vec{r}_{\text{T}};\vec{r}_j-\vec{r}\big)\rangle$. Using the stationary phase theorem (cf. appendix (A) and [Ishimaru, 1978]), equation (5.12) can be turned into :

$$\langle E(\vec{r}_j;T)\rangle = A_{\text{T}}^j|E_{\text{inc}}|\exp[jk_0|\vec{r}_j-\vec{r}_{\text{T}}| + \frac{j2\pi\rho_0\langle S\big(\vec{r}_j-\vec{r}_{\text{T}},\vec{r}_j-\vec{r}_{\text{T}}\big)\rangle l_j}{k_0\cos\theta_j^{\text{T}}} \tag{5.13}$$

where $\frac{l_j}{\cos\theta_{\text{T}}^j}$ represents the slant running distance through the media with $A_T^j = \frac{1}{|\vec{r}_j-\vec{r}_{\text{T}}|}$ as the free space propagation loss term and ρ_0 the uniform density of scatterers. As specified in the notation table (p7), when dealing with positions terms in subscripts and superscripts, it must be understood as the direction for amplitude terms (e.g in A_T^j from T to j) and the angles as well as – e.g $\theta_{\text{T}}^j = (\widehat{-\vec{z},\vec{r}_{\text{j}}\text{-}\vec{r}_{\text{T}}})$. Invoking the reciprocity property of the medium, θ_{T}^j or $\theta_j^{\text{T}} = \pi + \theta_{\text{T}}^j$ can be exchanged within the forward scattering terms (i.e the attenuation ones as detailed afterwards). Besides, it can be noticed that the azimuth angle dependency is left aside on account of the natural media azimuthal symmetry, hence the equivalent two dimensional problem involving only the site angle.

The field decomposition according to the canonical basis $(\hat{v}_{i,s},\hat{h}_{i,s})$ (intrinsic to transmitter and receiver position) is considered and the scattering matrix formalism is used – also within the spherical monochromatic wave assumption – to relate the scattered and incident fields, as reminded below :

$$\vec{E}_s(\vec{r}_1) = \begin{bmatrix} \vec{E}_s(\vec{r}_1)\cdot\hat{v}_s \\ \vec{E}_s(\vec{r}_1)\cdot\hat{h}_s \end{bmatrix} = \begin{bmatrix} S_{v_sv_i} & S_{v_sh_i} \\ S_{h_sv_i} & S_{h_sh_i} \end{bmatrix}\cdot\begin{bmatrix} \vec{E}_i(\vec{r}_1)\cdot\hat{v}_i \\ \vec{E}_i(\vec{r}_1)\cdot\hat{h}_i \end{bmatrix} \tag{5.14}$$

At this point, we can underline the fact that the downward or upward forward matrix is diagonal. Indeed, since we deal with a natural media exhibiting an azimuthal symmetry with respect to the normal of the observed scene $(\vec{z})$, the reflection symmetry property regarding the plane $(\hat{k}_{i,s},\hat{z})$ is fulfilled so that the resulting quantities $[S_{hv,vh}^f]$, averaged over positions, orientations and size probability density functions (pdf) are null. Prominent among these specific media, we remind that the random or oriented volumes (RV and OψV) can be distinguished. For the sake of simplicity, cylindrical scatterers will be hereafter considered so that their direction is fully determined by the azimuthal and insertion angles. For the random volume case, these angles are uniformly distributed according to a spherical geometry (as described in the forward model

presentation) whereas in the $0\psi V$ case, scatterers are still azimuthally oriented but the insertion angle follows a specific pdf. It is indeed a characteristic property of many tree species, usually also dependent of branches order for temperate forests (cf. among others [Saleh et al., 2007] about the Nezer forest case). The resulting forward scattering matrix keeps a diagonal form but is not anymore proportional to the identity one. For non reflection symmetric media which may happen for crops or in specific environmental and land conditions (wind or ground slope effects), non null off-diagonal elements exist, hence the use of the so-called eigen polarizations required to diagonalize the forward scattering matrix.

The generalization for each combined pair of polarization is straightforward and for a non depolarizing media, the matrix propagation operator '$[\Xi_{\mathrm{M}}^{\mathrm{N}}]$' from arbitrary points M to N turns into a vectorial one $\vec{\Xi}_{\mathrm{M}}^{\mathrm{N}}$ defined in a way that :

$$\begin{aligned}\langle \vec{E}_{\hat{t}}(N;M)\rangle &= \Xi_{\mathrm{M}}^{\mathrm{N}}(|\vec{E}(M)|\hat{t}) \\ &= \vec{\Xi}_{\mathrm{M}}^{\mathrm{N}} \odot |\vec{E}(M)|\hat{t} \\ &= A_M^N e^{jk_0|\vec{r}_{\mathrm{N}}-\vec{r}_{\mathrm{M}}|} \\ &\cdot \left[\exp\Big(j\frac{2\pi\rho_0 l_j}{k_0\cos\theta_{\mathrm{M}}^{\mathrm{N}}}\langle S_{qq}^f(\theta_M^{\mathrm{N}})\rangle \Big)\right]_{(v,h)} \odot |\vec{E}(M)|\hat{t}\end{aligned} \tag{5.15}$$

in which $\langle \vec{E}_{\hat{t}}(N;M)\rangle$ stands from the mean received field at N due to a transmitted one in the polarization state $\hat{t}$. In addition, the subscript dedicated to a given vector like $\big[x_q\big]_{v,h}$ means $[x_v, x_h]^t$ and the Hadamard product noted '$\odot$' is reminded below :

$$\begin{aligned}\vec{a}\odot\vec{b} &= diag\big(\vec{a}\cdot\vec{b}^t\big) \quad \text{(for vectors)} \\ \big[A\big]\odot\big[B\big]_{ij} &= \big[A_{ij}B_{ij}\big] \quad \text{(for matrices)}\end{aligned} \tag{5.16}$$

Relation (5.15) stands for the down-coming wave (from transmitter T to the scatterer j) and the upcoming one (from j to R) as well with the scattered field at r_j playing the incident one role. The bistatic configuration thereby intervenes with the different viewing angle embedded in the running distances through the layer $(\frac{l_j}{\cos\theta_{\mathrm{T}}^j})$ after scattering onto particle j. The received field at R can then be made explicit as follows :

$$\begin{aligned}\langle \vec{E}_{\hat{t}}(R;\vec{r}_j)\rangle &= \vec{\Xi}_j^R \odot |\vec{E}(\vec{r}_j;T)|\hat{t} \\ &= A_T^j A_j^R e^{j(k_0|\vec{r}_{\mathrm{T}}-\vec{r}_j|+|\vec{r}_{\mathrm{R}}-\vec{r}_j|)} \\ &\cdot \left[\exp\Big(j\frac{2\pi\rho_0 l_j}{k_0\cos\theta_j^{\mathrm{R}}}\langle s_{qq}^f(\theta_j^{\mathrm{R}})\rangle \Big)\right]_{(v,h)} \\ &\odot [S(\vec{r_j}-\vec{r}_{\mathrm{T}},\vec{r}_{\mathrm{R}}-\vec{r_j})] \\ &\cdot \left[\exp\Big(j\frac{2\pi\rho_0 l_j}{k_0\cos\theta_{\mathrm{T}}^j}\langle s_{qq}^f(\theta_{\mathrm{T}}^j)\rangle \Big)\right]_{(v,h)} \odot |\vec{E}(T)|\hat{t} \\ &= \vec{\Xi}_j^R \odot [S(\vec{r_j}-\vec{r}_{\mathrm{T}},\vec{r}_{\mathrm{R}}-\vec{r_j})]\cdot\vec{\Xi}_T^j \odot |\vec{E}(T)|\hat{t}\end{aligned} \tag{5.17}$$

At this point, it is also convenient to introduce the transmissivity matrix noted $[\boldsymbol{t}_{\mathrm{T}}^{\mathrm{R}}(j)]$ for the scatterer j with the associated wave paths from T to R and defined by :

$$[\boldsymbol{t}_{\mathrm{T}}^{\mathrm{R}}(j)] = \vec{\Xi}_j^R\cdot\big(\vec{\Xi}_T^j\big)^t$$

Hence, equation (5.17) can be also rewritten as :

$$\langle \vec{E}_{\hat{t}}(R;\vec{r}_j)\rangle = diag\Big([S(\vec{r}_j-\vec{r}_{\mathrm{T}},\vec{r}_{\mathrm{R}}-\vec{r}_j)]\cdot[\boldsymbol{t}_{\mathrm{T}}^{\mathrm{R}}(j)]^t]\Big)\odot|\vec{E}(T)|\hat{t} \tag{5.18}$$

Until now the monochromatic wave assumption has been made with actually the pulsation w as parameter : $\vec{E}(R;\vec{r}_j) = \vec{E^w}(R;\vec{r}_j)$. To be more consistent with SAR measures, a full bandwidth incident field can be considered which matches mostly to a chirp signal, hereafter centered around w_0 and with C(w) standing as its Fourier transform. Assuming a stationary bistatic configuration (i.e time invariant regarding geometric variables except for the along track abscissa, see the site parallel configuration displayed in figure 5.1), SAR processing consists in the correlation between the received field and a known wave form, that is the emitted one for processing along the range direction or the one deduced from the Doppler history of the samples during the azimuth acquisition. To be more explicit, for range compression :

$$\langle \vec{E}(R;\vec{r}_j)\rangle = \int_{-\infty}^{+\infty}[\int_{-\infty}^{+\infty}\langle\vec{E}^w(R;\vec{r}_j)\rangle C(w)e^{-jwt}dw]\cdot \mathrm{ref}(\tau-t)dt \tag{5.19}$$

where τ stands for the shift in order that the temporal reference function 'ref' matches to the resolution cell centered in $\vec{r}_0$. As mentioned later, this parameter can be strongly affected by the bistatic configuration (cf. specular one). With : $W_r(\tau)e^{-jw_0\tau} = \int_{-\infty}^{+\infty}[\int_{-\infty}^{+\infty}C(w)e^{-jwt}dw]\cdot ref(\tau-t)dt$ as the resolution range function (a *sinc* with the chirp assumption), the full bandwidth received signal is then :

$$\begin{aligned}
\langle \vec{E}_{\hat{t}}(R;\vec{r}_j)\rangle &= W_r\big(|\vec{r}_{\mathrm{R}}-\vec{r}_0|+|\vec{r}_{\mathrm{T}}-\vec{r}_0|-(|\vec{r}_{\mathrm{R}}-\vec{r}_j|+|\vec{r}_j-\vec{r}_{\mathrm{T}}| \\
&\quad +\Delta_{\mathrm{refractivity}})\big)\cdot diag\Big([S(\vec{r}_j-\vec{r}_{\mathrm{T}},\vec{r}_{\mathrm{R}}-\vec{r}_j)]\cdot[\boldsymbol{t}_{\mathrm{T}}^{\mathrm{R}}(j)]^t]\Big)\odot|\vec{E}(T)|\hat{t} \\
&= W_r\Big(|\vec{r}_{\mathrm{R}}-\vec{r}_0|+|\vec{r}_{\mathrm{T}}-\vec{r}_0|-\big(|\vec{r}_{\mathrm{R}}-\vec{r}_j|+|\vec{r}_j-\vec{r}_{\mathrm{T}}| \\
&\qquad +\frac{2\pi\rho_0 l_j}{k_0}\Re e\big(\frac{\langle[s^f(\theta_j^{\mathrm{R}})]_q\rangle}{\cos\theta_j^{\mathrm{R}}}+\frac{\langle[s^f(\theta_{\mathrm{T}}^T)]_p\rangle}{\cos\theta_j^{\mathrm{R}}}\big)\big)\Big)_{v,h} \\
&\cdot A_T^j A_j^R e^{j(k_0|\vec{r}_{\mathrm{T}}-\vec{r}_j|+|\vec{r}_{\mathrm{R}}-\vec{r}_j|)}\cdot diag\Big([S(\vec{r}_j-\vec{r}_{\mathrm{T}},\vec{r}_{\mathrm{R}}-\vec{r}_j)] \\
&\cdot\Big[\exp\big[\frac{j2\pi\rho_0 l_j}{k_0}\Re e\big(\frac{\langle[S^f(\theta_{\mathrm{R}}^j)]_q\rangle}{\cos\theta_j^{\mathrm{R}}}+\frac{\langle[S^f(\theta_{\mathrm{T}}^j)]_p\rangle}{\cos\theta_{\mathrm{T}}^j}\big)\big] \\
&\cdot\exp\big[-\frac{2\pi\rho_0 l_j}{k_0}\Im m\big(\frac{\langle[S^f(\theta_j^{\mathrm{R}})]_q\rangle}{\cos\theta_j^{\mathrm{R}}}+\frac{\langle[S^f(\theta_{\mathrm{T}}^j)]_p\rangle}{\cos\theta_{\mathrm{T}}^j}\big)\big]\Big]_{\mathrm{v,h}}^t\Big)\odot\vec{E}(T)|\hat{t}
\end{aligned} \tag{5.20}$$

Regarding equation (5.20), refractivity and extinction coefficients can be emphasized respectively from $[S^f]$ real and imaginary parts (noted '$\Re e(.)$' and '$\Im m(.)$') since related to phase delay and loss factor. Indeed :

$$[S^f] = \begin{bmatrix} s_v^f & 0 \\ 0 & s_h^f \end{bmatrix} = \frac{k_0}{2\pi\rho_0}\begin{bmatrix} k_0\chi_v + j\frac{\sigma_v}{2} & 0 \\ 0 & k_0\chi_h + j\frac{\sigma_h}{2} \end{bmatrix} \tag{5.21}$$

Within these notations, it can be stressed that the subsequent definitions for $\sigma_{v,h}$ concern the power extinction coefficient which are twice the field ones. In addition, the superscript notation $\sigma^{\mathrm{T,R}}$ stands for $\sigma(\theta_{\mathrm{T}})$ or $\sigma(\theta_{\mathrm{R}})$ since for a possible oriented volume the extinction coefficients are function of the incident or scattered site angles (likewise we noted $\chi^{\mathrm{T,R}}$).

As a result, equation (5.20) turns into :

$$\begin{aligned}\langle \vec{E}_{\hat{t}}(R;\vec{r_j})\rangle = A_T^j A_j^R \cdot W_r \Big(& |\vec{r}_R - \vec{r}_0| + |\vec{r}_T - \vec{r}_0| - \big(|\vec{r_R} - \vec{r_j}| + |\vec{r_j} - \vec{r_T}| \\ & + k_0 l_j \big(\frac{\chi_q^{\mathrm{R}}}{\cos\theta_j^{\mathrm{R}}} + \frac{\chi_p^{\mathrm{T}}}{\cos\theta_{\mathrm{T}}^j}\big)\big)\Big)_{v,h} \\ & \cdot diag\Big([S(\vec{r_j} - \vec{r}_{\mathrm{T}}, \vec{r}_{\mathrm{R}} - \vec{r_j})] \\ & \cdot \Big[\exp\big[jk_0 l_j \big(\frac{\chi_q^{\mathrm{R}}}{\cos\theta_j^{\mathrm{R}}} + \frac{\chi_p^{\mathrm{T}}}{\cos\theta_{\mathrm{T}}^j} + |\vec{r}_{\mathrm{T}} - \vec{r_j}| + |\vec{r}_{\mathrm{R}} - \vec{r_j}|\big)\big] \\ & \exp\big[-\frac{l_j}{2}\varpi_{qp}(\theta_{\mathrm{T}}^j, \theta_j^{\mathrm{R}})\big]\Big]_{v,h}^{t}\Big) \odot |\vec{E}(T)|\hat{t}\end{aligned} \tag{5.22}$$

in which the following quantity have been also introduced :

$$\varpi_{qp}(\theta_{\mathrm{T}}^j, \theta_j^{\mathrm{R}}) = \frac{\sigma_q^{\mathrm{R}}}{\cos\theta_{\mathrm{R}}} + \frac{\sigma_p^{\mathrm{T}}}{\cos\theta_{\mathrm{T}}} \tag{5.23}$$

Furthermore, using equation (5.10), $\langle E(\vec{r}_1;i)E^*(\vec{r}_2;j)\rangle_{\mathrm{med}}$ can now be made more explicit and extended to an arbitrary combination of polarization. For the sake of simplicity, the same polarization state will be assumed at the receiving antennas, also restricted either to $\hat{v}$ or $\hat{h}$. The following notation for the cross correlation can thus be used :

$$\begin{aligned}\Gamma_{qp} &= \Gamma(\hat{q},\hat{q};\hat{p}) \\ &= \langle\, \langle \hat{q}\cdot\vec{E}_{\hat{p}}(\vec{r}_1), \hat{q}\cdot\vec{E}^*_{\hat{p}}(\vec{r}_2)\rangle_{\mathrm{med}}\rangle_{\mathrm{ds}} \\ &(q,p) \in [v,h]\end{aligned} \tag{5.24}$$

On account of equation (5.22) the average over direct scattering properties yields then to the following Pol-InSAR cross correlation (for volume scattering) :

$$\begin{aligned}\Gamma_{qp} = \sum_i^N \sum_j^N \int_{S^i}\int_{S^i}\int_{r_i}\int_{r_j} & \langle E(\vec{r}_1,i)\rangle_{med}\langle E^*(\vec{r}_2,j)\rangle_{med} \\ & \mathcal{P}(S_{qp}^i = s^i)\mathcal{P}(S_{qp}^j = s^j)\mathcal{P}(r=r_i)\mathcal{P}(r=r_j)dS^i dS^j dr_i dr_j\end{aligned} \tag{5.25}$$

where P(X=x) stands for the probability for X to takes on value x. In line with the independence hypothesis between scattering events i and j, only the terms i=j remain in the previous sum, leading to :

$$\begin{aligned}\Gamma_{qp} = \rho_0 \iiint A^R A^T)^2 \qquad & W^2_{\vec{r}_{\mathrm{R}1,2}} W^2_{\varphi^{\mathrm{R}}_{1,2}} \langle |s_{qp}(\vec{r} - \vec{r}_{\mathrm{T}}, \vec{r}_{\mathrm{R}} - \vec{r})|^2\rangle_{ds} \\ & e^{jk_0(|\vec{r}_1 - \vec{r}_2|)} \exp\big[\text{-}\big(h_v - (z - z_0^v)\big)\varpi_{qp}(\theta_{\mathrm{R}}, \theta_{\mathrm{T}})\big] d^3r\end{aligned} \tag{5.26}$$

where the azimuth resolution W_{φ^R} has been introduced and assumed identical for the two acquisitions forming the baseline, as well as for the range resolution function in which the polarimetric dependency (through the refractivity) term is neglected. Indeed, regarding the very small difference between scattering angles towards the antennas forming the baseline and the moderate refractivity values, the pixel misregistration can be neglected. With the average over direct scattering statistics, the individual discrete distance to the top of the volume layer (l_j) turns into '$h_v - (z - z_0^v)$', z_0^v being the height for the bottom part of the volume layer which height (or

thickness) is noted h_v. The integration in (5.26) is performed over the whole resolution cell, with respect to spherical coordinates with origin at the receiver antenna. In order to clarify the integration over the vertical coordinate ($\cos\theta = -\frac{z}{r}$), spherical coordinates are modified as follows :

$$d^3r = dr\, rd\theta\, r\sin\theta d\varphi = rdrdzd\varphi \tag{5.27}$$

In addition, the first order Taylor development around r_0, φ_0, z_0 makes explicit $r_1 - r_2$:

$$\begin{aligned} r_1 - r_2 = (r_1 - r_2)|_{r=r_0,\varphi=\varphi_0,z=z_0} + \frac{\partial(r_1 - r_2)}{\partial r}(r - r_0) \\ + \frac{\partial(r_1 - r_2)}{\partial \varphi}(\varphi - \varphi_0) + \frac{\partial(r_1 - r_2)}{\partial z}(z - z_0) \end{aligned} \tag{5.28}$$

so that the cross correlation turns into :

$$\begin{aligned} \Gamma_{qp} = A_R A_T\big)^2 \langle |S_{qp}(\vec{r}_0 - \vec{r}_{\mathrm{T}}, \vec{r}_{\mathrm{R}} - \vec{r}_0)|^2 \rangle_{ds} \\ \exp\big[-\varpi_{qp}(\theta_{\mathrm{R}}, \theta_{\mathrm{T}}) \cdot h_v \big] \\ e^{j\Phi_0(r_0,z_0)} \int W^2_{\varphi^{\mathrm{R}}}(\varphi^{\mathrm{R}} - \varphi^{\mathrm{R}}_0) d\varphi \int_{-\infty}^{+\infty} W^2_r r_0 e^{j\alpha_r r} dr \\ \int_{z_0}^{z_0^v + h_v} e^{j\alpha_z z} e^{\varpi_{qp}(\theta_{\mathrm{R}},\theta_{\mathrm{T}})\cdot(z - z_0)} dz \end{aligned} \tag{5.29}$$

with (cf. appendix B for explicit expressions)

$$\Phi_0(r_0, z_0) = k_0(r_1 - r_2)\big|_{r=r_0,\varphi=\varphi_0,z=z_0} - \alpha_r r_0 - \alpha_z z_0$$

which takes into account – through the last two terms – the flat earth component and the along range reference height variability ($z_0(y)$, cf. figure 5.1). Assuming a sufficient small scattering discrepancy between baseline antennas $\langle E(R_1)E^*(R_1)\rangle \simeq \langle E(R_2)E^*(R_2)\rangle$ the volume decorrelation is then deduced normalizing the previous cross correlation by the ones corresponding to the 0 m baseline case ($\alpha_z = 0$ or $h_a = \infty$) :

$$\begin{aligned} \gamma^{\mathrm{vlm}}_{\mathrm{qp}} &= e^{j\Phi_0^{(\mathrm{v})}} \frac{\int_0^{h_v} e^{j\alpha_z z} \exp[\varpi_{qp} \cdot z] dz}{\int_0^{h_v} \exp[\varpi_{qp} \cdot z] dz} \\ &= e^{j\Phi_0^{(\mathrm{v})}} \frac{\varpi_{qp}}{j\alpha_z + \varpi_{qp}} \frac{\exp[(j\alpha_z + \varpi_{qp})h_v] - 1}{e^{\varpi_{qp} h_v} - 1} \end{aligned} \tag{5.30}$$

in which :

$$\Phi_0^{(v)} = \Phi_0 + \alpha_z z_0^v$$

as well as the integration limits are ensued from the variable change : $z - z_0^v \curvearrowright z$. It can be also noticed that in equation (5.29) the last integration in has is limits reduced to the filled part, that is from z_0^v to $z_0^v + h_v$.

In comparison with the monostatic case, the volume decorrelation in bistatic is thus modified with the attenuation term (the real exponential within the previous integral) and through the interferometric sensitivity, closely dependent to the bistatic geometry as derived in the appendix B.

The extension to vectorial – ensued from an abritrary combination of polarization states – interferometric coherences can then be derived using expression (5.31). Indeed, better than using the resulting fields at receiving antenna (made of the two terms resulting from the receiving

polarization basis), the incident polarization state knowledge and choice enables to derive the full [S] matrix defined previously providing thereby the following set of coherences :

$$\gamma^{12}_{qpmn} = \frac{\langle s^1_{\mathrm{qp}} \cdot {s^2_{\mathrm{mn}}}^* \rangle}{\langle |s^1_{\mathrm{qp}}|^2 \rangle \langle |s^2_{\mathrm{mn}}|^2 \rangle} \tag{5.31}$$

For the purpose of localizing vertically a specific scattering behaviour (providing the phase center of specific scatterers or scattering mechanism) other polarization state combination may be used (for instance γ_{hhvv}, entailing the v and h polarization decorrelation combined to the interferometric one, which phase center would be attracted towards scatterers exhibiting a linear polarization ratio). However interesting it could be, apart from illustrative examples in section 5.5 (figures 5.3 and 5.4), the same polarization states will be considered at the end of each interferometric couple.

5.3.2 Decorrelation from Volume plus Direct Ground Contributions

Though useful the previous expression may be, especially to evaluate the correlation loss in the framework of interferometric applications, a parameter inversion would suppose the bottom volume height knowledge and a polarization state for which the correlation is not sensitive to the ground echo. In order to derive the {volume+direct ground} correlation and as mentioned previously, a Dirac behaviour will be assumed for soil scattering in the sense that scattering events are localized on the ground (unlike volume ones vertically distributed). Wave ground penetration or undergrowth effects are then neglected which will partly constrain the scope of possible latter on inversion scenario. Going back over expressions (5.25,5.26), in which ground scatterers can now be considered among the i indices, another fundamental hypothesis is the two mechanisms independence so that the cross product will still be limited to the sum over i=j considering volume and ground contributions separately. Therefore, with cross correlation terms involving volume or ground scatterers null, the superposition property can be emphasized :

$$\langle E_1^{(\mathrm{tot})} E_2^{(\mathrm{tot})^*} \rangle = \langle E_1^{(\mathrm{v})} E_2^{(\mathrm{v})^*} \rangle + \langle E_1^{(\mathrm{dg})} E_2^{(\mathrm{dg})^*} \rangle \tag{5.32}$$

Introducing the scalar quantity :

$$\mu^{(\mathrm{dg})} = \frac{\langle E_1^{(\mathrm{dg})} E_1^{(\mathrm{dg})^*} \rangle}{\langle E_1^{(\mathrm{v})} E_1^{(\mathrm{v})^*} \rangle} \simeq \frac{\langle E_2^{(\mathrm{dg})} E_2^{(\mathrm{dg})^*} \rangle}{\langle E_2^{(\mathrm{v})} E_2^{(\mathrm{v})^*} \rangle} \tag{5.33}$$

leads then to :

$$\begin{aligned} \langle E_1^{(\mathrm{tot})} E_2^{(\mathrm{tot})^*} \rangle &= \langle E_1^{(\mathrm{v})} E_1^{(\mathrm{v})^*} \rangle \gamma^{(\mathrm{v})} + \mu \langle E_1^{(\mathrm{v})} E_1^{(\mathrm{v})^*} \rangle \cdot \gamma^{(\mathrm{dg})} \\ &= \langle E_1^{(\mathrm{v})} E_1^{(\mathrm{v})^*} \rangle (\gamma^{(\mathrm{v})} + \mu \cdot \gamma^{(\mathrm{dg})}) \end{aligned} \tag{5.34}$$

Likewise with the zero baseline correlations at each receiving ends R_1, R_2 :

$$\langle E_1^{(\mathrm{tot})} E_1^{(\mathrm{tot})^*} \rangle = \langle E_1^{(\mathrm{v})} E_1^{(\mathrm{v})^*} \rangle (1 + \mu) \tag{5.35}$$

providing the following normalization :

$$\gamma^{(\mathrm{tot})} = \frac{\gamma^{(\mathrm{v})} + \mu \gamma^{(\mathrm{dg})}}{1 + \mu} \tag{5.36}$$

In addition, the Dirac behaviour initial hypothesis for the ground scattering leads to :

$$\begin{aligned} \gamma^{(\mathrm{dg})} &= \langle E_1^{(\mathrm{dg})^*} E_2^{(\mathrm{dg})^*} \rangle \\ &\propto e^{j\Phi_0} \int_{z_0}^{z_0+h} e^{j\alpha_z (z-z_0)} \exp[\varpi_{qp}(z-z_0)] \delta(z-z_0) dz \\ &= e^{j\Phi_0} \cdot \Big(e^{j\alpha_z (z-z_0)} \exp[\varpi_{qp}(z-z_0)](z-z_0) \Big) \Big|_{z=z_0} \\ &= e^{j\Phi_0} \end{aligned} \tag{5.37}$$

Finally, considering the polarimetric scattering ratios μ_{qpmn} the vectorial extension (cf. 5.31) noted $\gamma_{qpmn}^{(\mathrm{tot})}$ is straightforward :

$$\begin{aligned} \gamma_{\mathrm{qpmn}}^{(\mathrm{tot})} &= e^{j\Phi_0} \cdot \frac{\gamma_{\mathrm{qpmn}}^{(\mathrm{v})} e^{j(\Phi_0^{(\mathrm{v})} - \Phi_0)} + \mu}{1 + \mu} \\ &= \gamma_{\mathrm{qpmn}}^{(\mathrm{v})} + \frac{\mu_{\mathrm{qpmn}}}{1 + \mu_{\mathrm{qpmn}}} \big(e^{j\Phi_0} - \gamma_{\mathrm{qpmn}}^{(\mathrm{v})} \big) \end{aligned} \tag{5.38}$$

Considering a given complex volume and ground decorrelation, this relation expresses the fact that the total coherence loci follows a straight line between the latter coherence points while varying the scattering ratio. As shown by [Cloude and Papathanassiou, 2003], this can be interestingly used as an inversion method and has been successfully applied since then with experimental data, naturally as long as the RVoG model assumptions hold.

5.4 Bistatic Decorrelation for the CRVoG Model

A similar approach will be used to take into account coupling effects between volume and ground, namely the double bounces with respect to transmitter and receiver also called herein specular ground contributions since these mechanisms involve such reflection onto the ground. As will be seen, the wave path involved within the double bounce mechanism is determined by scattering ground points entailing a specular reflection which localization depends on both transmitter and receiver positions. Consequently, for an arbitrary scatterer (positioned at $\vec{r}$) two different paths are taken into account, as opposed to the monostatic configuration. To derive the resulting scattered field, the ground is hereafter assumed rough with a zero average slope. The Kirchhoff approximation – assuming that the horizontal dimensions of surface roughness are larger than the wavelength – for the total tangential fields throughout the surface is combined to the far field zone one. This yields to the Stratton-Chu integral for the received field at $\vec{r}$ after ground interaction at $\vec{r}_{sg}$ from T (for the sake of clarity, only the transmitter double bounce will be considered first as well as a non lossy media) :

$$\vec{E}_{\hat{p}}(\vec{r};\vec{r}_{sg};T) = \iiint \left(f_{qp}\hat{q} + f_{pp}\hat{p}\right)\mathcal{P}(z) \exp(-j(\hat{k}_s - \hat{k}_i)\cdot\vec{r'})dx'dy'dz \tag{5.39}$$

where the coordinate superscripts ($'$) stands for local surface coordinates and f_{qp} the Kirchhoff coefficients (see [Fung, 1994]) and with $\mathcal{P}(z)$ the pdf of the surface function $z = \xi(x,y)$. The latter enables us to turn the local coordinates x', y' running throughout the surface, into global ones :

$$d\Sigma = dx'dy' = \sqrt{1 + \frac{\partial\xi}{\partial x} + \frac{\partial\xi}{\partial y}}dxdy = \mathcal{J}dxdy$$

The Kirchhoff coefficients are reminded f_{qp} with q,p respectively for receiving and emitting polarization :

$$f_{qp} = [(\hat{q}\times\hat{k}_s)\cdot(\hat{n}\times\vec{E}_p^t) + \eta\hat{q}\cdot(\hat{n}\times\vec{H}_p^t)] \tag{5.40}$$

with $\hat{n} = (-\frac{\partial\xi}{\partial x}\hat{x} - \frac{\partial\xi}{\partial y}\hat{y} + 1)\cdot\mathcal{J}^{-1}$. Within the scalar approximation which states that for small surface height standard deviation σ_h (i.e $k_0(\cos\theta_i + \cos\theta_s)\sigma_h < 4$)), the polarizations change due to slope terms in local coordinate vectors can be neglected, these coefficients become :

$$\begin{aligned} f_{pp} &\simeq \frac{\pm R_{//,\perp}}{\cos\theta_i + \cos\theta_s}[\sin\theta_i + \sin\theta_s - (1+\cos\theta_i\cos\theta_s)\sin(\varphi_s - \varphi_i)],\ p = v,h \\ f_{qp} &\simeq 2\frac{(R_{//} - R_\perp)}{2}\sin(\varphi_s - \varphi_i), \quad p \neq q = v,h \end{aligned} \tag{5.41}$$

leading for (5.39) to an Helmotz type integral, though formulated in the vectorial case. Also involved in equation (5.41) the Fresnel coefficients scattering problem (interface vegetation -

air) :

$$\begin{bmatrix} \mathcal{R}_{//} = \mathcal{R}_v \\ \\ \mathcal{R}_{\perp} = \mathcal{R}_h \end{bmatrix} = \begin{bmatrix} \frac{n_2\cos\theta_i - n_1\cos\theta_t}{n_2\cos\theta_i + n_1\cos\theta_t} \\ \\ \frac{n_1\cos\theta_i - n_2\cos\theta_t}{n_1\cos\theta_i + n_2\cos\theta_t} \end{bmatrix} = \begin{bmatrix} \frac{\varepsilon_r\cos\theta_i - \sqrt{\varepsilon_r - \sin^2\theta_i}}{\varepsilon_r\cos\theta_i + \sqrt{\varepsilon_r - \sin^2\theta_i}} \\ \frac{\cos\theta_i - \sqrt{\varepsilon_r - \sin^2\theta_i}}{\cos\theta_i - \sqrt{\varepsilon_r + \sin^2\theta_i}} \end{bmatrix} \tag{5.42}$$

As derived in [Beckmann and Spizzichino, 1963; Ulaby et al., 1981], integration of (5.39) can then be performed using the stationary phase method with respect to the phase function :

$$g(x,y) = (\hat{k}_s - \hat{k}_i)\cdot\vec{r} = q_x x + q_y y + q_z\xi(x,y)$$

This leads to retain only the major contributions minimizing the previous phase term which turn out to be the points (x_s, y_s) verifying :

$$\frac{\partial\xi}{\partial x}|_{x_s,y_s} = -\frac{q_x}{q_z}, \quad \frac{\partial\xi}{\partial y}|_{x_s,y_s} = -\frac{q_y}{q_z}$$

and thereby the points where specular reflections hold – the local tangent to the surface being normal to the vector '$\hat{k}_s - \hat{k}_i$'. As a result :

$$\begin{aligned} \vec{E}_{\hat{p}}(\vec{r};\vec{r}_{sg};T) \propto \left(f_{qp}\hat{q} + f_{pp}\hat{p}\right)\big|_{\frac{\partial z}{\partial x} = -\frac{q_x}{q_z}, \frac{\partial z}{\partial y} = -\frac{q_y}{q_z}} \\ \int \mathcal{P}(z)e^{jq_z z(x,y)}dz \end{aligned} \tag{5.43}$$

simplifying meanwhile the Kirchhoff coefficients f_{qp} (with $\theta_s = \theta_i, \phi_s = \phi_i$). Then, considering for the surface height variation the following Gaussian distribution of standard deviation σ_h :

$$\mathcal{P}(z) = \frac{1}{\sqrt{2\pi}\sigma_h}\exp[\frac{-z^2}{2\sigma_h^2}]$$

the remaining integral in (5.43) can be recognized as the characteristic function of a normal distribution. Therefore, having in mind the derivation properties of the Fourier transform ($\mathcal{F}(w) \propto e^{-\frac{w^2}{2}}$), it yields to :

$$\begin{aligned} \int \mathcal{P}(z)e^{jq_z z(x,y)}dz &= \frac{1}{\sqrt{2\pi}}\int \exp[\frac{-z^2}{2}]dz \ \cdot \ e^{-\frac{q_z^2\sigma_h}{2}} \\ &= exp[-\frac{(2k_0\cos\theta_i\sigma_h)^2}{2}] \end{aligned} \tag{5.44}$$

making clear the link between the optical roughness and the loss factor (which expressed the vertical surface roughness effect on the wave phase). Finally, these derivations brings us to the modified Fresnel coefficients :

$$\left[\mathcal{R}_p^m\right]_{v,h} = e^{-(\sqrt{2}k_0\cos\theta_i\sigma_h)^2}\cdot\begin{bmatrix} \mathcal{R}_v \\ \mathcal{R}_h \end{bmatrix} \tag{5.45}$$

As mentioned previously, the specular ground interaction do not introduce any depolarization effects within the scalar approximation. Therefore, the Hadamard product can be applied to express the receiving field onto a scatterer j at $\vec{r}_j$, using also the equivalent transmitter $T_{\aleph}$ (the

mirror point of T with respect to the ground, cf. appendix C) to involve easily the specular ground point :

$$\begin{aligned}\langle \vec{E}_{\hat{p}}(\vec{r_j};\vec{r}_{sg};)\rangle &= \langle \vec{E}_{\hat{p}}(\vec{r_j};\vec{r}_{sg};T_{\aleph})\rangle \\ &= [\mathcal{R}_p^m(\theta_{sg})]_{v,h} \odot \vec{\Xi}^j_{T_{\aleph}} \\ &= \frac{e^{j(k_0|\vec{r}_{\mathrm{T}}-\vec{r}_{sg}|+|\vec{r}_j-\vec{r}_{sg}|)}}{|\vec{r}_{\mathrm{T}}-\vec{r}_{sg}|+|\vec{r}_j-\vec{r}_{sg}|}\cdot[\mathcal{R}_p^m(\theta_{sg})]_{v,h} \\ &\odot \big[\exp\big(\, j\frac{2\pi\rho_0(h_v+z_j)}{k_0\cos\theta^j_{\mathrm{T}}}\langle s^f_{qq}(\theta^j_{\mathrm{T}})\rangle\,\big)\big]_{v,h}\odot|\vec{E}(T)|\hat{p}\end{aligned} \tag{5.46}$$

for which a single layer which bottom part matches the reference ground surface is firstly assumed, so that z_j corresponds to the vertical distance from z_0 to j. The interaction with the scatterer j can be expressed as in equation (5.17), leading then to the received field at R for the arbitrary emitting polarization state $\hat{p}$:

$$\langle \vec{E}_{\hat{p}}(\vec{r_j};\vec{r}_{sg};T)\rangle = [\mathcal{R}_p^m(\theta_{sg})]_{v,h}\odot\vec{\Xi}^R_j\cdot[S_{\mathrm{ds}}]_{v,h}\cdot\vec{\Xi}^j_T\odot|\vec{E}(T)|\hat{p} \tag{5.47}$$

At this point, the various explicit forms of the product : $\vec{\Xi}^R_j\cdot\big(\vec{\Xi}^j_{T^{\aleph}}\big)^t$ can be emphasized. Indeed :

$$\begin{aligned}\vec{\Xi}^R_j\cdot\big(\vec{\Xi}^j_{T^{\aleph}}\big)^t \propto &\Big[\exp\big(\, j\frac{2\pi\rho_0(h_v-z_j)}{k_0\cos\theta^R_j}\langle s^f_{qq}(\theta^R_j)\rangle\,\big)\Big]_{v,h} \\ &\cdot\Big[\exp\big(\, j\frac{2\pi\rho_0(h_v+z_j)}{k_0\cos\theta^j_T}\langle s^f_{qq}(\theta^j_T)\rangle\,\big)\Big]^t_{v,h}\end{aligned} \tag{5.48}$$

so that for co-polarization channels in the monostatic or specular bistatic configuration, this product do not depend anymore on the scatterer height since :

$$\Im m\big(\langle s^f_{qq}(\theta^{\mathrm{R}}_j)\rangle\big)\frac{(h_v-z)}{\cos\theta^{\mathrm{R}}_j}+\Im m\big(\langle s^f_{qq}(\theta^j_{\mathrm{T}})\rangle\big)\frac{(h_v+z)}{\cos\theta^j_{\mathrm{T}}}\propto\frac{2\sigma_q h_v}{\cos\theta_i}$$

Furthermore, the resulting cross correlation between these contributions at the ends of the baseline can be expressed as shown in subsection 5.3.1, in the shape of an integration over the volume ($\mathcal{V}_{\mathrm{sg}}$) entailing the specular ground scattering events :

$$\begin{aligned}\Gamma^{(\mathrm{Tsg})}_{qp} &= \langle\hat{q}_1\cdot E^{(Tsg)}_{\hat{p}},\big(\hat{q}_2\cdot E^{(Tsg)}_{\hat{p}}\big)^*\rangle \\ &= \iiint\limits_{V_{\mathrm{sg}}} W_r\Big(|\vec{r}_{\mathrm{R}}-\vec{r}_0|+|\vec{r}_{T_{\aleph}}-\vec{r}_0|- \\ &\big(|\vec{r}_{\mathrm{R}}-\vec{r}|+|\vec{r}-\vec{r}_{T_{\aleph}}|+\frac{k_0(h_v\text{-}z)\;\chi_{\mathrm{q}}}{\cos\theta_{\mathrm{R}}}+\frac{k_0(h_v+z)\;\chi_{\mathrm{p}}}{\cos\theta_{\mathrm{T}}}\big)\Big)\cdot W^2_{\varphi^R_{1,2}} \\ &\big(A_R A_{T_{\aleph}}\big)^2\rho_0|\mathcal{R}^m_p|^2|\langle\hat{q}\cdot[S\big(\theta_{T_{\aleph}},\theta_{\mathrm{R}}\big)]\cdot\hat{p}\rangle|^2\cdot\exp\big[-\big(\frac{\sigma^{\mathrm{R}}_q}{\cos\theta_{\mathrm{R}}}+\frac{\sigma^{\mathrm{T}}_p}{\cos\theta_{\mathrm{T}}}\big)h_v\big] \\ &\cdot exp\big[\varpi^{\mathrm{Tsg}}_{qp}z\big]\cdot e^{jk_0(|\vec{r}_1-\vec{r}_2|)}d^3r\end{aligned} \tag{5.49}$$

where the following parameter has been introduced :

$$\varpi^{\mathrm{Tsg}}_{qp} = \;+\;\frac{\sigma_q(\theta_{\mathrm{R}})}{\cos\theta_{\mathrm{R}}}\;\text{-}\;\frac{\sigma_p(\theta_{\mathrm{T}})}{\cos\theta_{\mathrm{T}}} \tag{5.50}$$

Likewise, the resulting field for the specular ground interaction with respect to the receiver can be derived using as the specular point onto the ground the intersection between the ground plane and the line supported by the vector $\vec{r}_{R_\aleph} - \vec{r}_j$, $R_\aleph$ being the mirror image of R. Similarly, to make explicit the cross correlation expression suiting the receiver specular ground term, the following quantity is introduced :

$$\varpi_{qp}^{\mathrm{R\,sg}} = - \frac{\sigma_q(\theta_{\mathrm{R}})}{\cos\theta_{\mathrm{R}}} + \frac{\sigma_p(\theta_{\mathrm{T}})}{\cos\theta_{\mathrm{T}}} \tag{5.51}$$

To perform the remaining integration formulated in equation 5.49, the point now at issue lies in the coupling terms localization due to their specific path and range delay. To this end, an important relation is demonstrated in appendix C which states that for both coupling mechanisms, an equivalent point on the ground can be found involving the same running distance and a single scattering interaction. This equivalent ground point is actually the cornerstone to perform the previous integral using the parallelepipedic shape (cf. figure C.1) of the integration domain. Indeed, for both specular ground mechanisms, the parallax variation $(r_1 - r_2)$ due to an elementary displacement $dM = dx + dy + dz$ is equivalent to the one from the matching specular ground point (cf. figure C.1, appendix C). This comes with another specificity with the following proportional link between the coordinates variables :

$$dy = -\tan\widehat{\iota}\, dz$$

which expressed the fact that an elementary vertical variation dz of a volume scatterer matches the displacement $dy = -\tan\widehat{\iota}\, dz$ onto the ground. Since the concerned integration volume is not spherical anymore (as for the volume one, cf. subsection 5.3.1), rectangular (x,y,z) coordinates will be considered. Using also a Taylor expansion, the distance variation $(r_1 - r_2)$ can be written under the form :

$$\begin{aligned}(r_1 - r_2) - (r_1 - r_2)\Big|_{x=x_0,y=y_0,z=z_0} &= +\frac{1}{k}\cdot\big[\kappa_x(x-x_0) \\ &+ \kappa_y(y-y_0) - \kappa_z(z-z_0)\big] \\ &= \frac{1}{k}\cdot\big[\frac{\partial(r_1-r_2)}{\partial x}(x-x_0) + \frac{\partial(r_1-r_2)}{\partial y}(y-y_0) \\ &- \frac{\partial(r_1-r_2)}{\partial y\tan\widehat{\iota}}(z-z_0)\big]\end{aligned} \tag{5.52}$$

where $\kappa_x, \kappa_y, \kappa_z\big(= -\tan\widehat{\iota}\,\kappa_y\big)$ are made explicit in appendix B (equation (B.19) and more precisely with the opposite angles $\widehat{\iota}_{\mathrm{R}}$ and $\widehat{\iota}_{\mathrm{T}}$, stressed respectively for the transmitter and the receiver specular ground terms. When omitted to ease the notations, the variable $\widehat{\iota}$ suits either to $\widehat{\iota}_{\mathrm{R}}$ or $\widehat{\iota}_{\mathrm{T}}$ according naturally to the concerned mechanism.

Similarly, the following notations matching the cross correlation between the double bounce contributions are used for these cousins terms :

$$\begin{aligned}\langle\, \hat{q}_1\cdot E_{\hat{p}}^{(T,Rsg)}, \big(\hat{q}_2\cdot E_{\hat{p}}^{(T,Rsg)}\big)^*\rangle &= \langle E_1^{(T,Rsg)}\cdot E_2^{(T,Rsg)*}\rangle_{qp} \\ &= e^{j\Phi_0^{T,Rsg}}\big(A_{R,T_\aleph}A_{R_\aleph,T}\big)^2|\mathcal{R}_{(p,q)}^m|^2 \\ &\cdot|\langle\hat{q}\cdot[S\big(\theta_{\mathrm{T}_\aleph},\theta_{\mathrm{R}}\big)]\hat{p}\rangle|^2\rho_0\int W_x^2(x-x_0)e^{i\kappa_x x}dx \\ &\cdot\int\limits_{(S_{\mathcal{P}})} W_y^2(y-y_0)e^{j\kappa_y y}e^{j\kappa_z z}L_{qp}^{T,Rsg}(y,z)dydz\end{aligned} \tag{5.53}$$

where '(T,Rsg)' means either Tsg or Rsg and with $L_{qp}^{T,Rsg}$ encompassing the attenuation term, by identification with respect to expression (5.49). Then, with u and v being the parametric variables of the explicit surface $\vec{f}_{\mathcal{P}}(u,v)$:

$$\begin{aligned}\vec{f}_{\mathcal{P}}(u,v) &= \vec{r}_0 + u\hat{y} + v\hat{\mathfrak{p}},\\ &[u,v] \in (\mathcal{D}) \equiv [y_0, y_0 + \Delta_{res}y] \times [z_0, z_0 + h_v]\\ &(\Delta_{res}y \text{ being the ground range resolution})\\ &\hat{\mathfrak{p}} = -\sin\hat{\imath}\ \hat{\mathbf{y}} + \cos\hat{\imath}\ \hat{\mathbf{z}}\end{aligned} \tag{5.54}$$

the normal vector to the integration surface $(S_{\mathcal{P}})$ is therefore :

$$\vec{n}_{\mathcal{P}} = \|\frac{\partial\vec{f}}{\partial u} \wedge \frac{\partial\vec{f}}{\partial v}\| = \cos\hat{\imath}$$

leading to :

$$\begin{aligned}\langle E_1^{(T,Rsg)} \cdot E_2^{(T,Rsg)*}\rangle_{qp} &= e^{j\Phi_0^{(T,Rsg)}}\big(A_{R,T_{\aleph}}A_{R_{\aleph},T}\big)^2\\ &\cdot |\mathcal{R}^m_{(p,q)}|^2\langle S_{qp}\big(\theta_{\mathrm{T},\mathrm{R}_{\aleph}},\theta_{\mathrm{R}}\big)\rangle|^2\rho_0\int W_x^2(x-x_0)e^{j\kappa_x x}dx\\ &\cdot \int_{(\mathcal{D})} W_u^2(u-u_0)e^{j\kappa_y(u-v\sin\hat{\imath})}e^{j\kappa_z v\cos\hat{\imath}}L_{qp}^{T,Rsg}(y,z)\|\vec{n}_{\mathcal{P}}\|\ du\ dv\\ &= e^{j\Phi_0^{T,Rsg}}\big(A_{R,T_{\aleph}}A_{R_{\aleph},T}\big)^2|\mathcal{R}^m_{(p,q)}|^2\\ &|\langle S_{qp}\big(\theta_{\mathrm{T},\mathrm{R}_{\aleph}},\theta_{\mathrm{R}}\big)\rangle|^2\rho_0\int W_x^2(x-x_0)e^{i\kappa_x x}dx\\ &\cdot \int_{y_0}^{y_0+\Delta_y^{res}} W_u^2(u-u_0)e^{j\kappa_y u}\ du\\ &\cdot \int_{z_0}^{z_0+\frac{h_v}{\cos\hat{\imath}}} e^{j(-\kappa_y\sin\hat{\imath}+\kappa_z\cos\hat{\imath})v}L_{qp}^{T,Rsg}(v\cos\hat{\imath})\ \cos\hat{\imath}dv\end{aligned} \tag{5.55}$$

Finally, the normalization of the considered individual cross correlations is achieved as in equation (5.30) so that in the canonical basis (v,h) :

$$\gamma_{qp}^{(T,Rsg)} = e^{j\Phi_0^{(\mathrm{T},\mathrm{Rsg})}}\frac{\int_0^{\frac{h}{\cos\hat{\imath}}} e^{j\kappa_v v}\exp\big[\varpi_{qp}^{\mathrm{T},\mathrm{Rsg}}\cdot v\cos\widehat{\imath}\big]dv}{\int_0^{\frac{h}{\cos\hat{\imath}}}\exp\big[\varpi_{qp}^{\mathrm{T},\mathrm{Rsg}}\cdot v\cos\widehat{\imath}\big]dv} \tag{5.56}$$

with κ_v defined by :

$$\kappa_v = \ -\ \kappa_y\sin\hat{\imath} + \kappa_z\cos\hat{\imath} \tag{5.57}$$

As formulated at the end of appendix B, it can be noted that the identity $\kappa_v = \kappa_{z_{\hat{\imath}}}$ also holds $(\kappa_y = \kappa_{y_{\hat{\imath}=0}}, \kappa_z = \kappa_{z_{\hat{\imath}=0}})$ which confirms the radar configuration equivalence with an incidence $\theta - \hat{\imath}$. From the factors $\varpi_{qp}^{\mathrm{T},\mathrm{Rsg}}$ given above in equation (5.51), the particular effect of differential extinction coefficients and bistatic can be pointed out. Indeed, in the random volume case :

$$\varpi_{qp}^{\mathrm{Tsg}} = \sigma(\frac{1}{\cos\theta_{\mathrm{T}}} - \frac{1}{\cos\theta_{\mathrm{R}}}) = -\varpi_{qp}^{\mathrm{Rsg}}$$

so that these coefficients are null in monostatic and the matching individual specular ground coherences are therefore polarimetric invariant with a magnitude minimized by the 'sinc' shape (equivalently to the volume decorrelation with no attenuation), as made explicit in equation 5.58. Furthermore, another singularity of the monostatic configuration lies also in the correlation between both specular ground mechanisms. Indeed, as opposed to the bistatic case, the integration volume as well as the scattering return involved are similar in monostatic so that the correlations $\langle E_1^{(Tsg)} \cdot E_2^{(Tsg)*} \rangle_{qp}$ or $\langle E_1^{(Rsg)} \cdot E_2^{(Rsg)*} \rangle_{qp}$ are not null and the following equalities hold for like polarizations terms :

$$\begin{aligned}
\langle E_1^{(Tsg)}, E_2^{(Rsg)} \rangle_{pp}^{\beta=0} &= \langle E_1^{(Rsg)}, E_2^{(Rsg)} \rangle_{pp}^{\beta=0} = \Gamma_{pp}^{(\mathrm{Rsg})}(\beta = 0) \\
&= e^{j\Phi_0^{(\mathrm{sg})}} \int_0^{h_v} e^{-j\kappa_z z}\, dz \\
&= e^{j\Phi_0^{(\mathrm{sg})}} h_v e^{-j\frac{\kappa_z h_v}{2}} sinc(\frac{\kappa_z h_v}{2}) \\
\langle E_1^{(Rsg)}, E_2^{(Tsg)} \rangle_{pp}^{\beta=0} &= \langle E_2^{(Tsg)}, E_2^{(Tsg)} \rangle_{pp}^{\beta=0} = \Gamma_{pp}^{(\mathrm{Tsg})}(\beta = 0) \\
&= e^{j\Phi_0^{(\mathrm{sg})}} h_v e^{j\frac{\kappa_z h_v}{2}} sinc(\frac{\kappa_z h_v}{2})
\end{aligned} \tag{5.58}$$

whereas for cross polarizations, two specificities – coming from the importance of interaction order (time effect on propagation) – occur : on the first hand, the product between Fresnel coefficients $(R_v \cdot R_h)$ and on the second hand the following ones :

$$\begin{aligned}
&\langle s_{qp}(\hat{\aleph}_i, \hat{k}_s) \rangle \cdot \langle s_{qp}^*(\hat{k}_i, \hat{\aleph}_s) \rangle \\
\text{and } &\langle s_{qp}(\hat{k}_i, \hat{\aleph}_s) \rangle \cdot \langle s_{qp}^*(\hat{\aleph}_i, \hat{k}_s) \rangle
\end{aligned} \tag{5.59}$$

respectively for the (Tsg) and (Rsg) mechanisms with $\hat{\aleph}_i$ and $\hat{\aleph}_s$ as the wave vectors involved in the scattering interaction with the volume scatterer, as depicted in figure 5.2. The former amounts to a phase shift (around π) while the two latter are liable to bring also a drop of the modulus correlation and can be studied further. Indeed, invoking the reciprocity theorem for passive media, the following identity : $S(\hat{k}_1, \hat{k}_2) = S^t(-\hat{k}_2, -\hat{k}_1)$ holds – within sensor coordinates (cf. [Cloude, 2001]) – so that with respect to the wave ones (namely the FSA -Forward Scattering Alignment- convention) it becomes :

$$s_{qp}(\hat{k}_1, \hat{k}_2) \underset{p \neq q}{=} -s_{pq}(-\hat{k}_2, -\hat{k}_1)$$

As a result, in the specific monostatic case, with $\hat{k}_i = -\hat{k}_i$ and $\hat{\aleph}_i = -\hat{\aleph}_s$, the following equalities matching both specular mechanisms hold :

$$\begin{aligned}
s_{qp}(\hat{\aleph}_i, \hat{k}_s) &\underset{\substack{p \neq q \\ \beta=0}}{=} -s_{pq}(\hat{k}_i, \hat{\aleph}_s) \\
s_{qp}(\hat{k}_i, \hat{\aleph}_s) &\underset{\substack{p \neq q \\ \beta=0}}{=} -s_{pq}(\hat{\aleph}_i, \hat{k}_s)
\end{aligned} \tag{5.60}$$

so that it leads to the following expressions for of the cross polarization monostatic individual

coherences :

$$\begin{aligned}\langle E_1^{(\mathrm{Tsg})},\ E_2^{(\mathrm{Rsg})}\rangle_{qp} &\underset{\beta=0}{\propto} \mathcal{R}_p^m \mathcal{R}_q^{m*} \cdot {}_{(\text{-})}\langle s_{qp}(\hat{k}_i, \hat{\aleph}_s)\rangle \langle s_{pq}^*(\hat{k}_i, \hat{\aleph}_s)\rangle \\ &\quad \cdot e^{j\Phi_0^{(\mathrm{sg})}} e^{j\frac{-\kappa_z h_v}{2}} h_v sinc(\frac{\kappa_z h_v}{2}) \\ \langle E_1^{(\mathrm{Rsg})},\ E_2^{(\mathrm{Tsg})}\rangle_{qp} &\underset{\beta=0}{\propto} \mathcal{R}_q^m \mathcal{R}_p^{m*} \cdot {}_{(\text{-})}\langle s_{qp}(\hat{\aleph}_i, \hat{k}_s)\rangle \langle s_{pq}^*(\hat{\aleph}_i, -\hat{k}_s)\rangle \\ &\quad \cdot e^{j\Phi_0^{(\mathrm{sg})}} e^{j\frac{\kappa_z h_v}{2}} h_v sinc(\frac{\kappa_z h_v}{2})\end{aligned} \tag{5.61}$$

Still within the FSA convention, the polarimetric coherence term ($\propto \langle S_{qp} S_{pq}^*\rangle$) has a phase histogram centered on π so that the terms in equation (5.61) clarify the fact that the phases of monostatic coherences for the cross polarizations are π shifted from the like ones, as confirmed by the simulated results shown in figures 5.3 and 5.4, cases (a) to (d). Theses simulations have been carried out in the CRVoG and COψ VoG cases (we remind that 'C' stands from coupled and thereby the specular interaction between volume and ground) from which several points can be stressed, beyond the radar or the ground truth detailed description given in subsection 5.6.3.To start with the most manifest fact, a severe decorrelation can be caused by the just mentioned polarimetric coherences term encompassed in the mixed individual coherences $\langle E_1^{(Tsg)} \cdot E_2^{(Rsg)*}\rangle_{qp}$ or $\langle E_1^{(Rsg)} \cdot E_2^{(Tsg)*}\rangle_{qp}$ Indeed, this quantity – intrinsic to the bistatic configuration – is really sensitive to the geometrical parameters. Naturally, as long as ground slopes or roughness are moderated, these cross polarization terms are generally negligible (from the radiometric point of view) in comparison with the direct volume ones, so that this individual decorrelation does not impact noticeably the total one. In addition, it can also be noticed that in the C0ψVoG, the difference between co and cross polarization is not appreciable whether concerning their magnitude or their phase, in spite the theoretical difference on account of equation (5.51). The differential extinction of about 0.05 dB.m^{-1} caused by the preferable branches orientation angles (ψ) is not significant enough to enhance the coherence magnitude in comparison with the like polarizations. Indeed, for the latter, the 'sinc' variation entailed in their coherence modulus brings a non negligible decorrelation with as a consequence, a sum between both individual transmitter and receiver double bounce coherences which certainly results in a null phase, like the ground reference point but with a modulus lower than one. Within an inversion strategy scope, this term can significantly spoil the results since it comes with an equivalent modified ground point, which constitutes a major drawback when used as a reference height point (as for the look-up table and straight line method, cf. [Cloude and Papathanassiou, 2003]). Likewise in bistatic for the like polarizations, the specular ground mechanisms are also affected by volume type decorrelation with on the contrary an enhanced difference between both and polarimetric dependence due to the higher differential attenuation brought by the different down and upwards wave paths. Indeed, in view of the simulated coherences in figures 5.3 and 5.4 respectively for the CRVoG or the COψVoG models, the coherence loci difference is noticeable. In the CRVoG case, the difference concerns mainly the phase between $\gamma_{qp}^{(\mathrm{Tsg})}$ and $\gamma_{qp}^{(\mathrm{Rsg})}$ whatever the polarization, whereas in the oriented one, the discrepancy is appreciable between each channel combination and differently for the two type of double bounces, even with a non grazing incidence angle ($\theta_{\mathrm{T}} = 45^o$) as opposite to the CRVoG case. Indeed, these differences come naturally directly from the extinction coefficients enhanced by the propagation length within the media ($l_j / \cos\theta_{\mathrm{R,T}}$), playing thereby a more or mess significant role within the exponential attenuation function (cf. the expression of ϖ_{qp} in 5.51). Besides, these simulations confirm also in bistatic the absence of correlation, justified previously, between both specular ground mechanisms – see (g) and (h).

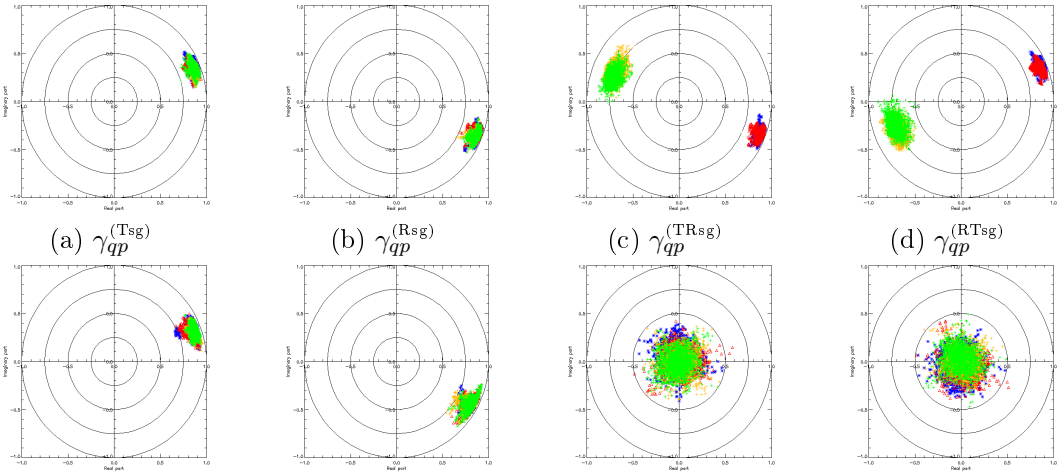

(a) $\gamma_{qp}^{(\mathrm{Tsg})}$ (b) $\gamma_{qp}^{(\mathrm{Rsg})}$ (c) $\gamma_{qp}^{(\mathrm{TRsg})}$ (d) $\gamma_{qp}^{(\mathrm{RTsg})}$

(e) $\gamma_{qp}^{(\mathrm{Tsg})}$ (f) $\gamma_{qp}^{(\mathrm{Rsg})}$ (g) $\gamma_{qp}^{(\mathrm{TRsg})}$ (h) $\gamma_{qp}^{(\mathrm{RTsg})}$

Figure 5.3: Loci on the complex unit circle of simulated Pol-InSAR coherences for the specular ground mechanism resulting from a CRVoG model. The monostatic configuration correspond to case (a) to (d), with a typical incidence $\theta^{\mathrm{T}} = 45^o$, $b_\perp = 20m$, $h_a = 47m$, $\kappa_z = 120m^{-1}$ whereas (e) to (h) are bistatic, characterized by a grazing transmitter $\theta^{\mathrm{T}} = 70^o$ and an off-nadir receiver with $b_\perp = 10.5m$, $h_a = 58m$, $\kappa_v = 124m$. In this figure – and permanently in this study – the red, blue, green and gold colour loci match respectively the HH, VV, HV and VH like and cross polarizations.

As opposed, this additional decorrelation entailed by coupling terms do not concern the double pass or ping pong mode (cf.[Rosen et al., 2000]) since in such case $\kappa_z = 0$. This is actually an intrinsic bistatic effect – in the sense that even a quasi-monostatic configuration is concerned – which on the one hand comes with a more complicated retrieval algorithm but on the other hand, opens some further retrieval prospects, as it will be shown in the following sections.

In view of these individual contributions, the total (volume + direct ground + specular ground) cross product can then be derived as in section 5.3.2 with from now on the additional coupling contributions considered likewise independent from the volume and direct ground terms :

$$\begin{aligned}\langle E_1 E_2^* \rangle = \langle E_1^{(v)} \cdot E_2^{(v)*} \rangle + \langle E_1^{(dg)} \cdot E_2^{(dg)*} \rangle + \\ \langle E_1^{(Tsg)} \cdot E_2^{(Tsg)*} \rangle + \langle E_1^{(Rsg)} \cdot E_2^{(Rsg)*} \rangle + \\ \langle E_1^{(Tsg)} \cdot E_2^{(Rsg)*} \rangle + \langle E_1^{(Rsg)} \cdot E_2^{(Tsg)*} \rangle\end{aligned} \tag{5.62}$$

To emphasize the relative importance of these various contributions, the following ratios are introduced :

$$\begin{aligned}\mu^{(\mathrm{dg})} &= \frac{\langle E_1^{(\mathrm{dg})} E_1^{(\mathrm{dg})*} \rangle}{\langle E_1^{(\mathrm{v})} E_1^{(\mathrm{v})*} \rangle} \\ \mu^{(\mathrm{Tsg})} &= \frac{\langle E_1^{(\mathrm{Tsg})} E_1^{(\mathrm{Tsg})*} \rangle}{\langle E_1^{(\mathrm{v})} E_1^{(\mathrm{v})*} \rangle} \\ \mu^{(\mathrm{Rsg})} &= \frac{\langle E_1^{(\mathrm{Rsg})} E_1^{(\mathrm{Rsg})*} \rangle}{\langle E_1^{(\mathrm{v})} E_1^{(\mathrm{v})*} \rangle}\end{aligned} \tag{5.63}$$

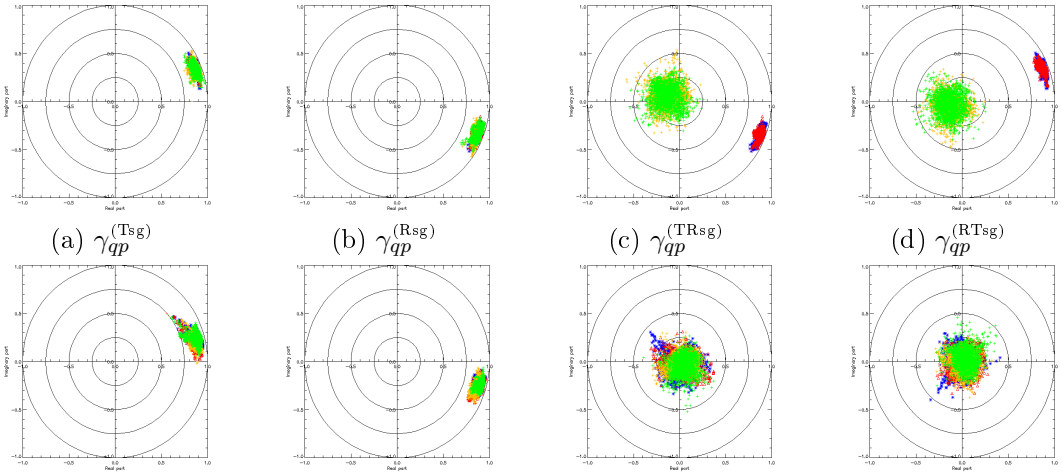

(a) $\gamma_{qp}^{(\mathrm{Tsg})}$ (b) $\gamma_{qp}^{(\mathrm{Rsg})}$ (c) $\gamma_{qp}^{(\mathrm{TRsg})}$ (d) $\gamma_{qp}^{(\mathrm{RTsg})}$

(e) $\gamma_{qp}^{(\mathrm{Tsg})}$ (f) $\gamma_{qp}^{(\mathrm{Rsg})}$ (g) $\gamma_{qp}^{(\mathrm{TRsg})}$ (h) $\gamma_{qp}^{(\mathrm{RTsg})}$

Figure 5.4: Simulated Pol-InSAR coherences for the specular ground mechanisms resulting from a COψVoG model. A similar monostatic configuration than in figure 5.3 is considered from cases (a) to (d) as well as for the bistatic ones (e) to (h) apart from the incidence angle $\theta^{\mathrm{T}} = 45^{o}$ not anymore grazing, so that $h_a = 37.5m$, $\kappa_v = 180m^{-1}$.

so that proceeding as in section 5.3.2, the resulting total biPol-InSAR coherences can then be expressed as :

$$\begin{aligned}\gamma_{qp}^{(\mathrm{tot})} = e^{j\Phi_0}\Big[e^{j(\Phi_0^V-\Phi_0)}\gamma_{qp}^{(\mathrm{v})} + \mu_{qp}^{\mathrm{dg}}\cdot\gamma_{qp}^{(\mathrm{dG})} + (1+\delta_\beta\delta_{q-p})\mu_{qp}^{(\mathrm{Tsg})}\cdot\gamma_{qp}^{(\mathrm{Tsg})} \\ + (1+\delta_\beta\delta_{q-p})\mu_{qp}^{(\mathrm{Rsg})}\cdot\gamma_{qp}^{(\mathrm{Rsg})} + \delta_\beta(1-\delta_{q-p})\mu_{qp}^{(\mathrm{TRsg})}\cdot(\gamma_{qp}^{(\mathrm{TRsg})}+\gamma_{qp}^{(\mathrm{RTsg})})\Big] \\ \cdot\Big[1+\mu_{qp}^{(\mathrm{dG})} + (1+\delta_\beta\delta_{q-p})(\mu_{qp}^{(\mathrm{Tsg})}+\mu_{qp}^{(\mathrm{Rsg})}) + 2\delta_\beta(1-\delta_{q-p})\mu_{qp}^{(\mathrm{TRsg})}\Big]^{-1} \\ \Big(p\subset(v,h), q\subset(v,h), p\neq q\Big)\end{aligned} \tag{5.64}$$

with the Kronecker symbol : $\begin{cases}\delta_\beta = \delta_0(\beta)\\ \delta_{p-q} = \delta_0(p-q)\end{cases}$ that is equal to one only in monostatic ($\beta = 0$) or for co-polarized terms. At first sight from expression 5.64, one can already set forth that the total correlation will follow the shape of the functional :

$$\frac{c_0 + \mu_1 c_1 + \mu_2 c_2 + ...}{1 + \mu_1 + \mu_2 + ...}$$

in the same way as for the monostatic RVoG case (cf. [Krieger et al., 2005]) excepted that several individual correlations (i.e per mechanism) are brought into play, involving also additional parameters mainly through the attenuation terms ($\frac{\sigma_{\mathrm{qp}}^{\mathrm{T,R}}}{\cos\theta_{\mathrm{T,R}}}$) as well as through the interferometric sensitivity (with α_z, κ_z). As far as the FMDP inversion is concerned, the total correlation dependence on these parameters will be particularly interesting and will be treated in section 5.6.1.

5.5 Decorrelation for the nSCOψVoG Model

Until now, a homogeneous volume layer above the ground have been assumed. As a matter of fact, most forests and especially temperate ones rather than their very dense tropical counterparts exhibit – a least according to the ground truth – a layered structure which is very likely to impact the radar measurements, as shown by some vertical scattering profile retrieval (see for instance [Nannini et al., 2009; Tebaldini, 2010]). Besides, vertical structures and its inherent strong volume-ground interaction has arisen the standard RVoG model improvement with specular ground terms (as in [Treuhaft and Siquiera, 2000]). In this general framework of forest characterization, the vertical structure estimation is naturally of greatest importance, whether for improved biomass estimation, species discrimination, biodiversity studies or for FOPEN applications. Theoretically-wise, invoking independence and linearity properties, the superposition principle holds and the previous analytical expressions are still valid and come with an additional relation concerning the vertical direction. In a general way and whatever the scattering mechanisms, the corresponding coherences can be expressed by :

$$\begin{aligned} &\langle E_1, E_2^* \rangle^{(\mathrm{v}),(\mathrm{dg}),(\mathrm{T,Rsg})} \\ &\propto \int_V \rho(z) \langle S(z) \rangle^2(z) L[\sigma(z), z] e^{j\kappa_z z}\, dz \end{aligned} \tag{5.65}$$

Since this formulation entails much more unknowns, additional measurements and reformulated inversion schemes are needed in order to get out of the retrieval process. Let alone radar tomography – based on wide spectral processing and focusing methods to synthesize the vertical resolution but at the cost of about fifteen baselines (cf. [Reigber and Moreira, 2000; Fornaro et al., 2003; Guillaso and Reigber, 2005]) – two approaches can be emphasized. Both are still based on the analytical decorrelation heuristic studied so far but they differ from the formulation of the attenuation, either as a continuous or discrete function. In the first place, expression (5.68) can be viewed as a Fourier transform which inverse can be performed by means of a sufficient number of experimental correlations, meaning also a quite important number of baselines (about 10 according to [R Treuhaft, 2006]). Less stringent in terms of baseline number is Polarization Coherence Tomography (PCT). Developed in ([Cloude, 2006]), it lies in the decomposition of the attenuation functions according to Fourrier-Legendre series. Their dependence to the vertical direction z can thus be expressed as follows :

$$f(z) = \sum_n a_n \mathcal{P}_n, \quad a_n = \frac{2n+1}{2} \int_{-1}^{1} f(z) \mathcal{P}_n dz \tag{5.66}$$

a_n and $\mathcal{P}_n$ being respectively the Legendre coefficients and polynomials. Limiting the series expansion (typically to third order), the inversion can be performed using the Pol-InSAR coherence matching to the volume only decorrelation (by means for instance of polarimetric phase optimization). Thereby, this process may only involve a one-baseline monostatic acquisition but providing heights information, that is the topographic and volume ones as the boundary limits to complete the Legendre polynomial definitions. To this end, classical Pol-InSAR retrieval algorithm may be performed (cf. [Cloude and Papathanassiou, 2008]) but optical-radar fusion approach have also been demonstrated by means of LIDAR or Laser techniques as in [Praks et al., 2008]. Concerning this matter, hyperspectral data may be also combined to the attenuation function inversion, as proposed in [Treuhaft et al., 2002].

In the second place but within the scope of keeping the entire input vector retrieval formulated so far and only from radar observables, a natural solution is to consider the extinction coefficients

as discrete distributions :

$$\begin{aligned} \sigma(z) &= \sum_{k}^{N} \sigma_k \delta_{h_k}(z - z_0 - h_{k-1}), \\ \text{with } &\begin{cases} \delta_h(z) = 1, \ z \in D = [0, h] \\ \delta_h(z) = 0, \ z \notin D \end{cases} \end{aligned} \tag{5.67}$$

considering N layers k of height h_k. Likewise, this step distribution holds for density and direct scattering return as well. Consistent with the forest homogeneous layer description and going back to expression 5.65, the following generalization is straightforward :

$$\begin{aligned} \langle E_1, E_2^* \rangle^{(\mathrm{v}),(\mathrm{dg}),(\mathrm{T,Rsg})} \propto \sum_{k}^{N} \int_{h_{k-1}}^{h_k} & \rho_k(z) \langle S_k(z) \rangle^2 \\ & L(\sigma_k(z), z) e^{j\kappa_z z} \, dz \end{aligned} \tag{5.68}$$

This formulation applies to individual decorrelation and can also be extended to the total one as in paragraph 5.3.2 with a specific concern to define the scattering ratios and the associated normalizations. Indeed, several definitions are possible between the different volume decorrelation terms and to this respect, the latter will entail after integration different attenuation and scattering coefficient ratios. To be explicit through an example handled afterwards, let's consider the case of two layers which bottom part are located respectively at h_0 (the topographic height, matching also the coordinate z_0 used in section 5.3 for the single layer case) and h_1, with also $h_2 - h_1 = h_v$. The first layer (bottom one) mean scattering coefficients will be neglected regarding the second ones (top layer herein) whether for direct volume or specular ground returns (s). Furthermore, for the sake of clarity, the transmitter specular ground and the polarimetric dependence are dropped. However, the first layer entails non null extinction coefficients. Consequently, the total cross correlation and the associated scattering ratios can be derived as follows :

$$\begin{aligned} \langle E_1, E_2^* \rangle^{(\mathrm{tot})} = e^{j\alpha_z h_0} A_r^2 W_r^2 W_{az}^2 \cdot \Big(& \\ & \int_0^{h_1 - h_0 + h_v} \delta(z) \langle S^{(\mathrm{dg})} \rangle^2 L^{\mathrm{dg}}[\sigma_{1,2}^{\mathrm{T,R}}(z), z] e^{j\kappa_z z} \, dz \\ & + \int_0^{h_1 - h_0} \rho_1 \langle S_1^{(ds)} \rangle^2 L^{\mathrm{v}}(\sigma_1^{\mathrm{T,R}}, z) e^{j\alpha_z z} \, dz \\ & + \int_{h_1 - h_0}^{h_1 - h_0 + h_v} \rho_2 \langle S_2^{(ds)} \rangle^2 L^{\mathrm{v}}(\sigma_2^{\mathrm{T,R}}, z) e^{j\alpha_z z} \, dz \\ & + \int_0^{\frac{h_1 - h_0}{\cos \widehat{\imath}}} \rho_1 \langle \mathcal{R}^m \rangle^2 \langle S_1^{(\mathrm{Rsg})} \rangle^2 L^{\mathrm{Rsg}}(\sigma_1^{\mathrm{T,R}}, z) e^{-j\kappa_v v \cos \widehat{\imath}} \, dv \\ & + \int_{\frac{h_1 - h_0}{cos \widehat{\imath}}}^{\frac{h_1 - h_0 + h_v}{\cos \widehat{\imath}}} \rho_2 \langle \mathcal{R}^m \rangle^2 \langle S_2^{(Rsg)} \rangle^2 L^{\mathrm{Rsg}}(\sigma_2^{\mathrm{T,R}}, z) e^{-j\kappa_v v \cos \widehat{\imath}} \, dv \Big) \end{aligned} \tag{5.69}$$

where the far field propagation factor (A_r) variations between each mechanism have been ne-

glected. This expression entails also attenuation functions $L^{(v,dg,Rsg)}$ reminded hereafter :

$$\begin{aligned} L^{\mathrm{v}}[\sigma^{\mathrm{T,R}}(z),z] &= L^{\mathrm{dg}}[\sigma^{\mathrm{T,R}}(z),z] \\ &= \exp[\,-\,(\frac{\sigma^{\mathrm{R}}}{\cos\theta_{\mathrm{R}}}+\frac{\sigma^{\mathrm{T}}}{\cos\theta_{\mathrm{T}}})\cdot(h_t+h_v-z)] \\ L^{\mathrm{Rsg}}[\sigma^{\mathrm{T,R}}(z),z] &= \exp[\,-\,\big(\frac{\sigma^{\mathrm{R}}}{\cos\theta_{\mathrm{R}}}(h_t+h_v+z) \\ &\quad +\frac{\sigma^{\mathrm{T}}}{\cos\theta_{\mathrm{T}}}(h_t+h_v-z)\big)] \end{aligned} \tag{5.70}$$

in which the first layer height is noted and defined by $h_t = h_2 - h_1$ (since it mostly matches the trunk layer). Then, with $l_k|_{k=1,2...n}$ referring to the corresponding layer, the calculations can be pursued with the introduction of the correlation matching the second layer volume only em fields contribution :

$$\begin{aligned} \langle E_1, E_1^*\rangle^{(\mathrm{v},l_2)} &= A_r^2 W_r^2 W_{az}^2 \rho_2 \langle S_2\rangle^2 \cdot \Big(\int_{h_1-h_0}^{h_1-h_0+h_v} L^{\mathrm{v}}(\sigma_2,z)\ dz \Big) \\ &= A_r^2 W_r^2 W_{az}^2 \rho_2 \langle S_2\rangle^2 \cdot \Big(\int_{0}^{h_v} L^{\mathrm{v}}(\sigma_2,z+h_1)\ dz \Big) \end{aligned} \tag{5.71}$$

so that equation (5.69) becomes :

$$\begin{aligned} \langle E_1,E_2^*\rangle^{(\mathrm{tot})} = \langle E_1, E_1^*\rangle^{(\mathrm{v},l_2)} \cdot \Big(& \\ e^{j\alpha_z h_0} & \frac{\rho_{\mathrm{dg}}\langle S^{(dg)}\rangle^2 L^{\mathrm{dg}}(\sigma_{1,2},0.)}{\rho_2\langle S_2^{(v)}\rangle^2 \int_0^{h_v} L^{\mathrm{v}}(\sigma_2,z+h_1)\ dz} \\ + e^{j\alpha_z h_0} & \frac{\rho_1\langle S_1^{(v)}\rangle^2 \int_0^{h_1-h_0} L^{\mathrm{v}}(\sigma_1,z)e^{j\alpha_z z}\ dz}{\rho_2\langle S_2^{(v)}\rangle^2 \int_0^{h_v} L^{\mathrm{v}}(\sigma_2,z+h_1)\ dz} \\ + e^{j\alpha_z h_1} & \Gamma^{(\mathrm{v},L_2)} \\ + e^{j\alpha_z h_0} & \frac{\rho_1\langle \mathcal{R}^m\rangle^2\langle S_1^{(Rsg)}\rangle^2 \int_0^{\frac{h_1-h_0}{\cos\widehat{\imath}}} L^{\mathrm{Rsg}}(\sigma_1,z)e^{-j\kappa_v v\cos\widehat{\imath}}\ dv}{\rho_2\langle S_2^{(v)}\rangle^2 \int_0^{h_v} L^{\mathrm{v}}(\sigma_2,z+h_1)\ dz} \\ + e^{j(\alpha_z h_0+\kappa_v h_t)} & \frac{\langle \mathcal{R}^m\rangle^2\langle S_2^{(Rsg)}\rangle^2 \int_0^{\frac{h_v}{\cos\widehat{\imath}}} L^{\mathrm{Rsg}}(\sigma_2,z+h_1)e^{-j\kappa_v(v+h_1)}\cos\widehat{\imath}\ dv}{\rho_2\langle S_2^{(v)}\rangle^2 \int_0^{h_v} L^{\mathrm{v}}(\sigma_2,z+h_1)\ dz} \Big) \end{aligned} \tag{5.72}$$

and that the assumptions :

$$\langle S_1^{(\mathrm{v})}\rangle \ll \langle S_2^{(\mathrm{v})}\rangle \text{ and } \langle S_1^{(\mathrm{Rsg})}\rangle \ll \langle S_2^{(\mathrm{v})}\rangle$$

lead to :

$$\langle E_1,E_2^*\rangle^{(\mathrm{tot})} = \langle E_1, E_1^*\rangle^{(\mathrm{v}),l_2} \cdot \Big(e^{j\alpha_z h_1}\Gamma^{(\mathrm{v},L_2)} + e^{j\alpha_z h_0}\mu^{(\mathrm{dg})} + e^{j(\alpha_z h_0+\kappa_v h_t)}\Gamma^{((\mathrm{Rsg}),l_2)} \Big)$$

$$with: \begin{cases} \mu^{(\mathrm{dg})} = \dfrac{\rho_{\mathrm{dg}}\langle S^{(\mathrm{dg})}\rangle^2}{\rho_2\langle S_2^{(\mathrm{v})}\rangle^2} \cdot \dfrac{\exp[\,-\,\big(\frac{\sigma_2^{\mathrm{R}}h_v+\sigma_1^{\mathrm{R}}h_t}{\cos\theta_{\mathrm{R}}}+\frac{\sigma_2^{\mathrm{T}}h_v+\sigma_1^{\mathrm{T}}h_t}{\cos\theta_{\mathrm{T}}}\big)]}{\exp(\,-\,\varpi_2 h_v)\ \int_0^{h_v} e^{\varpi_2 z}\ dz} \\ \\ \mu^{(\mathrm{Rsg})} = \dfrac{\langle \mathcal{R}^m\rangle\langle S_2^{(\mathrm{Rsg})}\rangle^2}{\langle S_2^{(\mathrm{v})}\rangle^2} \cdot \dfrac{\exp[\,-\,\big(\frac{\sigma_2^{\mathrm{R}}h_v+2\sigma_1^{\mathrm{R}}h_t}{\cos\theta_{\mathrm{R}}}+\frac{\sigma_2^{\mathrm{T}}h_v}{\cos\theta_{\mathrm{T}}}\big)]\cdot\int_0^{\frac{h_v}{\cos\widehat{\imath}}} e^{\varpi_2^{\mathrm{Rsg}}v}\ \cos\widehat{\imath}\,dv}{\exp(\,-\,\varpi_2 h_v)\cdot\int_0^{h_v} e^{\varpi_2 z}\ dz} \end{cases} \tag{5.73}$$

The derivations can be carried on and lead to more explicit scattering ratios :

$$\begin{cases} \mu^{(\mathrm{dg})} = \dfrac{\rho_{\mathrm{dg}}\langle S^{(dg)}\rangle^2\ \varpi_2\ e^{-\varpi_1 h_t}}{\rho_2\langle S_2^{(\mathrm{v})}\rangle^2\ \left(e^{-\varpi_2 h_v}-1\right)} \\ \\ \mu^{(\mathrm{Rsg})} = \dfrac{\langle \mathcal{R}^m\rangle\langle S_2^{(\mathrm{Rsg})}\rangle^2\ \varpi_2^{\mathrm{v}}\ \cos\hat{\imath}\ \exp[\,-\,\frac{2\sigma_1^{\mathrm{R}} h_t}{\cos\theta_{\mathrm{R}}}]\ \left(e^{-\varpi_2^{\mathrm{Rsg}} h_v/\cos\hat{\imath}}-1\right)}{\langle S_2^{(\mathrm{v})}\rangle^2\ \varpi_2^{\mathrm{Rsg}}\left(e^{-\varpi_2 h_v}-1\right)} \end{cases} \tag{5.74}$$

Through this two layers specific example, it is thus interesting to emphasize the structure effect to see how that the attenuation information is encompassed within the scattering ratios. Indeed, both come quite predictably with an additional attenuation term regarding the first layer (i.e height plus extinction coefficient) so that in the framework of a quantitative inversion, this forest model simply adds – to the unknown vector – the second layer bottom height as if this layer were empty and again, the remaining information or dependence is contained through the scattering ratios. Though hazardous the retrieval of these parameters may be, these expressions are very interesting in the sense that encompassed are the first layer extinction coefficients, corresponding mostly to the trunk one which carries in many cases the biomass major part. Rather, the Fresnel coefficients within the double bounce term and conjugated to the direct ground ones could rise the ambiguity between soil humidity and roughness. This will be discussed afterwards in the light of a specific bistatic configuration which may ease that formulation. Furthermore, alternatively to a quantitative inversion, these relations could have a great potential in the framework of images interpretation or classification, using an estimation of these new variables for all the image pixels.

Besides, the polarimetric extension does not present any difficulties using the corresponding extinction coefficients for incident, scattering, layer one and two paths within the different ϖ_{qp} terms given in equations 5.51,5.23.

Towards the retrieval approach

On account of the derivations conducted in the previous sections, the theoretical formulae for the biPol-InSAR coherences, expressing the decorrelation generated by the vegetation cover through direct volume, direct ground and specular ground contributions, have been extended in the bistatic configuration, with the restriction nevertheless to the plane of incidence for this first investigation. In addition to more realistic canonical forest descriptions, the most innovative aspects of this investigation in comparison with the standard monostatic case concern the ambiguity height formula and the derivations about the coupling terms. Indeed, the double bounce with respect to the transmitter or to the receiver can be distinguished in bistatic, on account of different scattering intensities and different interferometric behaviour (actually as in monostatic single-pass mode) for which an elegant relation has been emphasized with an equivalent ground point.

Coming with the overall model improvement, the additional forest model descriptive parameters rise besides the question of the quantitative inversion feasibility. This brings us to introduce the following next sections, especially dedicated to the retrieval approach and to the potential of specific bistatic geometries which may reduce the unknown number thanks to intrinsic scattering properties. As further theoretical developments concerning this study, the generalization to tilted bistatic planes (non normal to the horizontal reference plane) – coming with more complex but simply geometrical effects – is currently under development, particularly for coupling terms.

Introduction to the Inversion Problem

As reminded in the chapter introduction (5.1), worldwide forest monitoring is nowadays truly paramount, on account of the general importance of vegetated land surfaces concerning whether environmental issues – especially with the climate change stakes – or overall anthropogenic activities (land use applications). Within that context, radar remote sensing evinces considerable assets, particularly with the relatively young polarimetric and interferometric SAR acquisition (Pol-InSAR), as testified by the extensive number of studies and campaigns conducted so far (among others [Treuhaft and Siquiera, 2000; Cloude and Papathanassiou, 2003]). Also aforementioned, research is nonetheless still ongoing in order to cope with some limitations, such as the robustness of the retrieval approach. Among promising prospects, the bistatic configuration can be considered and the theoretical analysis of the resulting possible measures – that is the biPol-InSAR coherences – has been precisely the topic of the previous sections 5.3, 5.4 and 5.5.

On top of the extension to the bistatic radar geometry, the previous part accounted also for more realistic forest canonical models (derived from the RV – random volume – to the nSCOψVoG) in order to ensure the existence condition in the subsequent inversion algorithm. Nevertheless, these additional Forest Model Descriptive Parameters (FMDP) bring us to a more complicated retrieval problem, the latter parameters corresponding naturally to further unknowns. The point herein at issue is thus how to perform the inversion, based on the constructed analytical operator which makes the link between the FMDP and the coherences, whether synthetic or experimental.

As a first investigation and since such experimental data at suitable frequencies (i.e L or P-band) haven't been performed yet – to the author's best knowledge – the following inversion scenarios will be achieved with synthetic coherences ensued from MIPERS – Multistatic Interferometric Polarimetric Electromagnetic model for Remote Sensing –, an ad-hoc simulator with multi-baselines biPol-InSAR capabilities. This approach illustrates well the fundamental asset of forward electromagnetic models able to carry out such simulations, as faithfully as possible, with respect to reference points where experimental comparisons are possible.

Concerning the status of bistatic SAR experiments, it can be pointed out that much progress has been recently achieved, though limited to demonstrative campaigns. Indeed, fostered by noticeable advances on time oscillators – the cornerstone of the synchronisation issues (cf. [Nies et al., 2007; Younis et al., 2006]) – and by the nowadays consequent number of potentially usable opportunistic signals, very encouraging projects and rather campaigns can be pointed out, see for instance [D'Errico and Fasano, 2008; Sanz-Marcos et al., 2007] and [Dubois-Fernandez et al., 2006; Walterscheid et al., 2006; Rodriguez-Cassola et al., 2010], the two latter involving hybrid monostatic plus bistatic acquisition with spaceborne (TerraSAR-X) and airborne (PAMIR, F-SAR) radars.

Apart from the origin of the used coherences (whether synthetic or experimental) and the analytical operator expression, the formulation of the inversion problem is of course paramount and in a general way, can be characterized from the mathematical point of view by the Hadamard requirements. The overall inversion procedure will be thus detailed in the second section, starting with the optimization problem formulation and the use of MIPERS simulated data before tackling an application case with the inversion of coherences ensued from a single baseline acquisition, coming thereby with limitations concerning the number of FMDP. Section 3 is precisely dedicated to the various possible bistatic acquisitions which may ease the inversion problem for more sophisticated forest models, thanks to an observation vector enriched with multibaseline coherences and with possible simplifications brought by the scattering behaviour intrinsic to specific bistatic geometries.

5.6 Inversion Method & Algorithm

The analytical formulas based on theoretical derivations and detailed in sections 5.3 to 5.5, made explicit the link between the biPol-InSAR coherences and the FMDP of interest. The point herein at issue is the retrieval feasibility of these unknown parameters, for which a non linear optimization method is chosen, as detailed in the following subsection 5.6.1 and applied in 5.6.3 and in section 5.7 with simulated coherences from MIPERS. An overview of this model is besides presented at paragraph 5.6.2.

The simulations will be naturally restricted to cases for which the afore-mentioned theoretical operator holds, which brings us to remind that the bistatic configurations will be considered within the plane of incidence. Besides, for the purpose of investigating the bistatic intrinsic potential, we remind that this study is also restricted to possible multibaseline acquisitions corresponding to nearly the same bistatic angle. Multistatic configurations or hybrid ones (monostatic plus bistatic acquisitions) are thus left aside for this first investigation.

5.6.1 The Non Linear Optimization Problem

Formulation & Cost Function Choice

The simulated Pol-InSAR complex coherences noted '$\mathfrak{J}_{qp}$' and the theoretical ones '$\gamma_{qp}(X)$' corresponding to a given test vector X are now at our disposal. The inversion procedure will thus consists in fitting both kind of coherences resulting from the solution vector X_s, encompassing the FMDP of interest. Its size depends naturally on the chosen inverse scheme (between the RVoG and its derivatives). In the absence of a rigorous vector solution, its best estimate $\check{X}_s$ will be defined as the one minimizing the functional $\mathcal{F}$ defined as the following cost function :

$$\begin{aligned}\mathcal{F}(X) = \sum_{(q,p)\in[v,h]} &\Big[\quad \Re e\big(\mathfrak{J}_{qp}\big) - \Re e\big(\gamma_{qp}(X)\big) \quad \Big]^2 \\ &+ \Big[\quad \Im m\big(\mathfrak{J}_{qp}\big) - \Im m\big(\gamma_{qp}(X)\big) \quad \Big]^2,\ X \in (\mathcal{C})\end{aligned} \tag{5.75}$$

with '$\Re e(.)$" and '$\Im m(.)$' as the real and imaginary parts and and $(\mathcal{C})$ as the set of constraints on the test vector X. To assess the residuals errors between synthetic and analytical coherences, the Euclidean quadratic distance have been chosen resulting in a classical non-linear least square minimization of a real functional. Due to the non-linearity nature of the problem and the complex equivalent statistical distribution, an optimal norm is difficult to exhibit and the estimated vector with the L2 one is likely to be biased.

Besides, a deeper statistical analysis may plea in favour of distances such as the Bhattacharya or the Mahalanobis one, introducing a weighted sum of the residuals. The weighted coefficients are derived from the residuals intrinsic distribution properties (for instance their variance or higher order moments) and leads to an extended Chi-square cost function. These formulations are known as the generalized least square (GLS) method as opposed to the ordinary one (OLS) which has been a posteriori considered satisfactory enough within the scope of this first investigation. The optimization task can thus be formulated as follows :

$$\Big\{ \min_{g_i(\boldsymbol{X})\leq 0,\ 1\leq i\leq N} \mathcal{F}(\boldsymbol{X}) \Big\} \tag{5.76}$$

that is as a non-linear minimization problem with a number N of inequality constraints (from which equality ones can be derived if needed). This constraints set will be naturally all the more

important that the considered forest model is simple.
For instance, the associated set for the RVoG model is :

$$\left\{ \begin{array}{c} -h_0 \leq 0,\, h_0 \leq 50. \\ \pm h_1 \leq 0 \\ -h_v \leq 0,\, h_v \leq 50. \\ \pm(\sigma_v^i + \sigma_h^i) \leq 0 \\ \pm(\sigma_v^s + \sigma_h^s) \leq 0 \\ \pm(\sigma_v^s + \sigma_v^i) \leq 0 \\ -\mu_{qq} \leq 0,\, \mu_{qq} \leq 10. \\ \pm\mu_{qp}^{\mathrm{dg}} \leq 0, q \neq p \\ \pm\mu_{qp}^{\mathrm{T,Rdg}} \leq 0, q \neq p \end{array} \right\} \text{ with } [q,p] \text{ running over } [v,h] \tag{5.77}$$

Due to the non-linearity of the problem, usual gradient methods (conjugate, biconjugate) can't be employed and therefore we head for Newton ones under the local quadratic convergence assumption. Rather, the Quasi-Newton approach will be performed with an approximation of the Hessian matrix. Indeed, in spite of the analytical formulation for γ_{qp}, the gradient has been provided as well but in view of the consequent derivations (the gradient vector is already a nineteenth vector element), the second order approximation has been admitted. Besides, in order to deal with the inequality constraints (possibly non-linear), the augmented Lagrangian formulation is employed :

$$\mathcal{L} = \mathcal{F}(\boldsymbol{X}) + \nu^t \boldsymbol{g}(\boldsymbol{X}) \tag{5.78}$$

($\boldsymbol{\nu}$) being the Lagrangian multiplier vectors) leading to the quadratic programming (QP) sub-problem :

$$\Big\{ \min_{(\nabla \boldsymbol{g})^t \cdot s + \boldsymbol{g} \leq 0} \mathcal{Q}\ , \quad \mathcal{Q}(\boldsymbol{s}) = (\nabla \mathcal{F})^t \cdot \boldsymbol{s} + \frac{1}{2} \boldsymbol{s}^t \cdot (\nabla^2 \mathcal{L}) \cdot \boldsymbol{s} \ \Big\} \tag{5.79}$$

Its solution $\mathbf{s}$ provides the search direction along which the optimal displacement length (ω) is derived from the one dimensional minimization of a merit function (usually the augmented Lagrangian). That step length gives the updated test vector :

$$\boldsymbol{x}' = \boldsymbol{x} + \omega \boldsymbol{s}$$

The quasi-Newton Hessian matrix approximation is then in its turn updated performing the BFGS (Broyden-Fletcher-Goldfarb-Shanno) method (cf. Dennis and Schnabel [1983]) and the process is sequentially repeated (hence the SQP designation) as long as the convergence criteria is reached and the necessary Kuhn-Tucker conditions are fulfilled. For further details, one can refer among an abundant literature to Powell [1983].
As a result, this formulation is very versatile, not only with regards to the forest model considered (by setting the different constraints) but also concerning the measures at our disposal. One can imagine compact polarimetric (CP) coherences possibly from different configurations, monostatic plus bistatic or multistatic (cf. GNSS-R future acquisitions). For instance, a case of interest afterwards will be the fully polarimetric coherences set from one bistatic angle and with several baselines. The N-baselines extension is straightforward according to the following formulation :

$$\begin{aligned} \mathcal{F}(X) = \sum_{1 \leq i \leq N} \sum_{(q,p) \in [v,h]} & \Big[\quad \Re e\big(\beth_{qp}^{Bi}\big) - \Re e\big(\gamma_{qp}^{Bi}(X)\big) \quad \Big]^2 \\ & + \Big[\quad \Im m\big(\beth_{qp}^{Bi}\big) - \Im m\big(\gamma_{qp}^{Bi}(X)\big) \quad \Big]^2,\ X \in (\mathcal{C}) \end{aligned} \tag{5.80}$$

The price paid for this generalization is certainly an inversion process less intuitive to handle in comparison with other approaches. Indeed, still for the RVoG case – in monostatic (cf. [Cloude and Papathanassiou, 2003] as well as in bistatic besides (cf. section 5.3.2) – the considered absence of depolarization from the ground return puts the different polarimetric coherences along a straight line which distances from the ground reference point are governed by the corresponding scattering ratios. Though nice and convenient it is, this becomes obsolete as soon as it is impossible to exhibit a specific polarimetric combination filtering the volume only decorrelation or in other words, as soon as there remains for each polarization a scattering ratio dependence not only with respect to a possibly depolarizing ground but also to the specular one (cf. $\mu^{\mathrm{dg}}, \mu^{\mathrm{T,Rsg}}$) – excepted naturally when both have the same phase center and can be pieced together. Besides, independently of the ground surface nature or orientation, it can be reminded that depolarization terms are liable to be important for bistatic configuration with an azimuthal component, though not considered afterwards.

Cost Function Sensitivity

Prominent within the inversion scope, the cost function sensitivity towards the input vector (that is the FMDP) will be addressed hereafter. For that purpose, the volume and total decorrelation functions can be studied beforehand. Indeed, as embedded within expression (5.75), their sensitivity as well as the one of their partial derivatives will be paramount for the global cost function behaviour. In view of the multivariate formulation, this study will be naturally restricted to sliced decompositions and does not aim to be complete but rather gives the general trends to understand the afterwards main inversion issues.

First, it can be noticed that the analytical formula for the volume coherence does not present deep changes with the bistatic configuration in the sense of the mathematical function kind. Indeed, we remind that in view of formula (30) in part I, the changes coming with the bistatic angle concern the ambiguity height and the attenuation terms related to the wave optical paths. The resulting volume coherence sensitivity versus the volume height and the extinction coefficient – assumed in this case height independent – will thus keep the same shape as in monostatic. This is reminded in figure 5.5, giving also the chosen parameters among which the range of variation for height (to be considered regarding the ambiguity value) and extinction. Also well illustrated in this figure is the surface behaviour (with no correlation loss) for higher attenuation.

Likewise, the specific coherences for the specular ground polarimetric mechanisms will exhibit the same variation shape, considering naturally their respective ambiguity height and attenuation term (cf. $\varpi_{qp}^{(\mathrm{v}),(\mathrm{T,Rsg})}$). Thus, the total coherence behaviour can be assessed. Indeed, as expressed in formula (62-part I), it results from the sum of volume, direct and specular ground coherences weighted by their respective scattering ratio. In view of its multivariate form, a complete representation of the coherence versus the input vector elements is difficult to handle. However, the dependence towards several scattering ratios can be emphasized as a bistatic specificity. For instance, the total coherence variation towards ground and receiver specular ground scattering ratios can be considered for a CRVoG model in a site bistatic configuration (defined by $\theta_{\mathrm{T}} = 60^o, \theta_{\mathrm{R}} = 0.$). The amplitude and phase, running between $\gamma^{(\mathrm{v})}, \gamma^{(\mathrm{Rsg})}, \gamma^{(\mathrm{dg})}$, are represented respectively in figures 5.8 and 5.9, which detail also the various input parameters. We remind also that physically, the scattering ratios variations can be obtained through the different polarization combination, let alone naturally the considered forest descriptive parameters. In this example, the general shape (weighted average) is not surprising and the two dimensional slices (keeping constant one scattering ratio) exhibit a behaviour already studied in the literature (cf. [Cloude

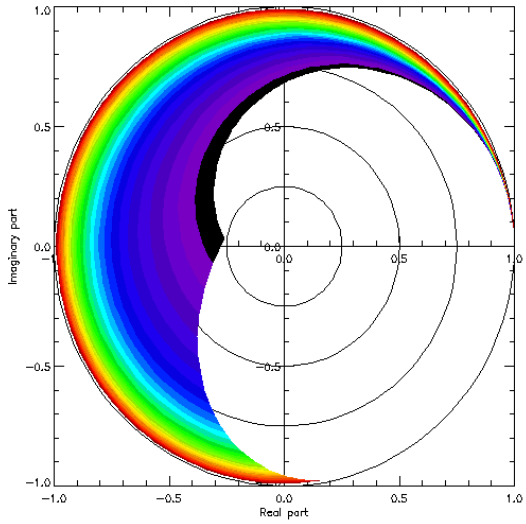

Figure 5.5: Complex volume coherence versus height ($0 <$ h < 50 m, $h_a = 60m$) and extinction coefficient σ, color represented step by step and linearly from 0 in black to 0.255 m^{-1} (2.2 $dB.m^{-1}$) in red

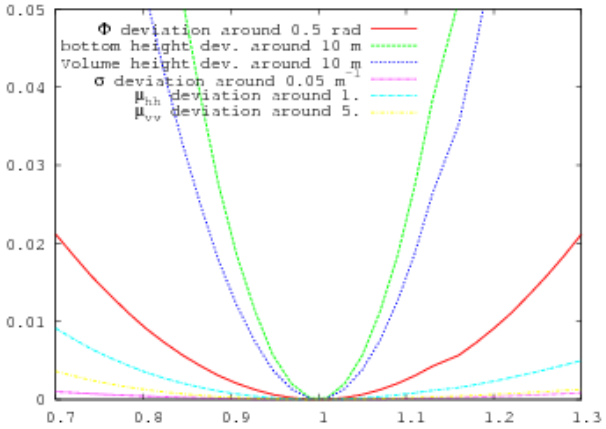

Figure 5.6: Cost function **F** versus input vector components, related to a 1SRVoG model

et al., 2004; Krieger et al., 2005]) but it shows rather the interest of maximizing the difference between the involved coherences. Indeed, within the inversion scope, the resulting sensitivity towards scattering ratios will be strengthened as well as the discrimination power. Alternatively, a configuration where both specular ground ratios are of same magnitude and opposite in phase (we remind that their phases have necessarily an opposite sign) will result in a coherence very close to the ground one and consequently, in weak discrimination chance. The bistatic configuration, providing the opportunity to have very different scattering ratios is thereby truly promising, as it will be shown further (cf. section 5.7. Besides, there is not need to mention that it may also cope with the case of a poor direct ground contribution, often encountered but replaced, more or less easily by double bounce (cf. single pass and transmitter case). In addition, the total coherence sensitivity towards input variables can naturally be assessed regarding its derivatives. Though

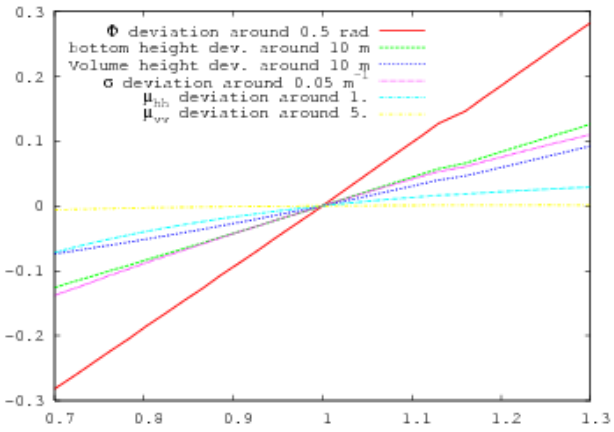

Figure 5.7: Cost function partial derivatives ($\frac{\partial \mathbf{F}}{\partial x_i}$) versus input vector components, related to a 1SRVoG model

cumbersome, the analytical gradient expression can be obtained easily. Again, the multivariate formulation makes an exhaustive representation awkward. Nonetheless, some specific points can be underlined considering for instance an RVoG model in mono and bistatic configuration. In figures 5.10, 5.11 are represented the modulus and phase of the total coherence partial derivatives, considering a given input vector as a 'medium point' from which deviations are applied on each variable (with a multiplicative factor), keeping the others constant. The chosen numerical values are given within the figure legend. The bistatic configuration has mainly an impact regarding the modulus of the extinction partial derivative, which comes actually from the multiplicative factor $1/\cos\theta_{\mathrm{T}}$. Otherwise, a similar sensitivity can be established, as expected since both involve different parameters but with the same function structure concerning variables. The quasi constant phase and decreasing modulus can be interpreted as a elementary shift of constant direction and dropping magnitude, as established within figure 5.5 for $\gamma^{(\mathrm{vlm})}$. On the contrary, the elementary shift due to an height variation has a linear trend in magnitude but with a varying direction to follow the characteristic curved shape also seen in figure 5.5. These behaviours are naturally weighted by the scattering ratio. The variation regarding the latter is also characteristic, the magnitude variation is of course related to the shape shown in figure 5.8 but rather, the constant phase expressed the well known RVoG model behaviour along the μ straight line (emphasized by [Cloude and Papathanassiou, 2003]).

In view of the behaviour of the encompassed expressions, the cost function sensitivity can be illustrated through the example of a S(Structured)RVoG forest model in a bistatic configuration within the incidence plane with $\theta_{\mathrm{T}} = 70^o$ and $\theta_{\mathrm{R}} = 50^o$. As in figures 5.10 and 5.11, the deviation on a single input vector component is considered, keeping the other variables as constant parameters and centered on the chosen medium point.

Criteria to Assess the Inversion Quality

Next to the study of the cost function sensitivity, the point now at issue lies in the nature of that inverse problem, which can be classically analysed through the Hadamard formulation, namely with the existence, the uniqueness and the stability conditions.

The first Hadamard criteria is reminded to determine whether the image of the input domain

under the function $\mathcal{F}$ includes the measures subset or not. Through this requirement, the match between the analytical formulation and Monte-Carlo's one carried with MIPERS can be assessed, which thereby validates partly both approaches. To this end, the simulated coherence loci for various forest models have been compared to the analytical complex values and will be presented in the next paragraph (§ 5.6.3).

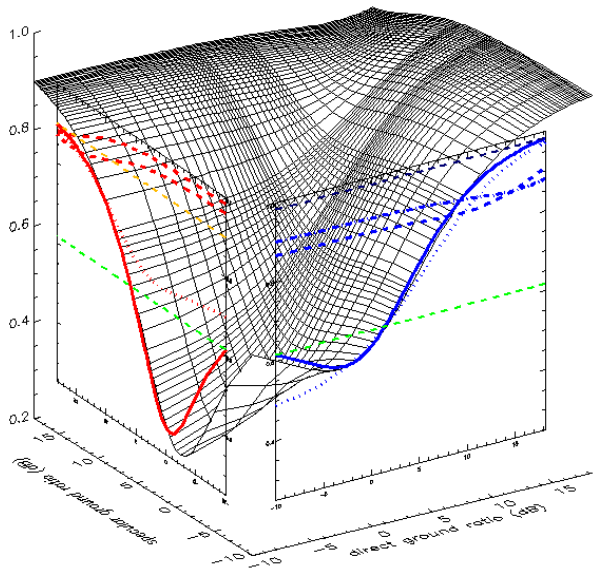

Figure 5.8: Total coherence modulus versus $\mu^{(\mathrm{dg})}$ and $\mu^{(\mathrm{Rsg})}$ for an arbitrary polarization with the following input parameters describing a CRVoG model : $\alpha_z = 0.1, \Phi_0 = 0., h_v = 25m, \sigma = 0.03m^{-1}, \kappa_v = 0.05, \mu^{(\mathrm{Tsg})} = 0.$, the resulting partial coherences : $\gamma^{(\mathrm{v})} = 0.81e^{j1.7}, \gamma^{(\mathrm{Rsg})} = 0.92e^{-j0.77}, \gamma^{(\mathrm{dg})} = 1.$

Likewise, since uniqueness is mathematically quite tricky to demonstrate using the analytical formulation, that condition will be considered violated as soon as the inversion algorithm will exhibit distinct solution vectors. For that matter, a given set of complex coherences resulting from the analytical formula is chosen and the inversion algorithm is performed sequentially within the same constraints but initialized from various candidate vector and the different final solutions reaching about the same level of accuracy are compared.

Third, considering a given complex coherences set, the stability condition concerns the difference between its respective solution vector and the one of the same output altered with a slight deviation. Mathematically-wise, the problem will be unstable or ill-conditioned if the inverse of $\mathcal{F}$ is not continue on the subset $\mathbf{Im}(\mathcal{F})$ that is if the following statement holds :

$$\exists\, \varepsilon,\ \exists\, \boldsymbol{\gamma},\ \boldsymbol{\gamma} + \boldsymbol{\alpha\delta\gamma} \quad / \quad \|\mathcal{F}^{-1}(\boldsymbol{\gamma} + \boldsymbol{\alpha\delta\gamma}) - \mathcal{F}^{-1}(\boldsymbol{\gamma})\| > \varepsilon \tag{5.81}$$

Consequently, this question is of major importance since the difference between the analytical and the Monte-Carlo coherences lies essentially in the speckle introduced by the radar modeling through MIPERS.

As illustrated with the following simulated forest cases, the robustness to that noise which test these three necessary conditions will be the cornerstone of the inversion feasibility, making the problem well or illy posed.

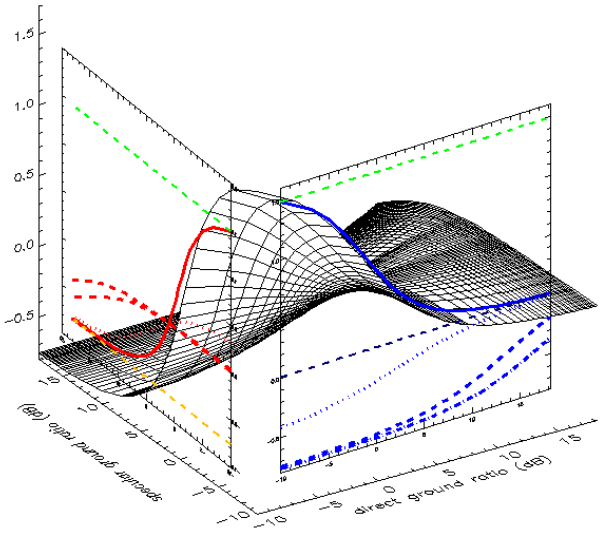

Figure 5.9: Total coherence modulus versus $\mu^{(\mathrm{dg})}$ and $\mu^{(\mathrm{Rsg})}$ with the aforementioned input parameters describing the CRVoG model leading to the following partial coherences : $\gamma^{(\mathrm{v})} = 0.8e^{j1.7}, \gamma^{(\mathrm{Rsg})} = 0.92e^{-j0.77}, \gamma^{(\mathrm{dg})} = 1$.

5.6.2 Modeling the Inverse Problem, MIPERS Synthetic Data Use

For the purpose of modeling as faithfully as possible the bistatic vectorial and interferometric SAR coherences, two kinds of requirements need to be fulfilled by the model outputs : electromagnetic and system ones which overall presentation with MIPERS has been given in chapter 2. Since MIPERS has various modes, the main features used in this chapter will be briefly reminded in the following. As far as interferometry will be concerned, the phase preserving characteristic is fundamental. Theoretically wise, the same assumptions than in section 5.3 have been used, which lies mainly in the scattering individual events independence and in the distorted wave Born approximation (DWBA) which, as reminded previously, leads to the Foldy-Lax formulation. Extinction coefficients are computed according to the forward scattering theorem, performing the integration over every kind of scatterers and their respective statistical pdf concerning size dimensions and geometrical orientation (see section 2.1.1). In order to reproduce a faithful vertical extinction profile, several layers can be defined which gather elements exhibiting similar geometrical characteristics and makes the average more representative. According to these statistical laws, the different scatterers are generated following a discrete approach. The latter are derived from canonical shapes (cylinders or ellipsoids) characterized by their analytical scattering matrix which thereby eases the generation of fully polarimetric and bistatic observables. Besides, the most significant mechanisms are taken into account, that is the direct contribution from the volume, the direct one from the ground and coupling terms formulated previously, namely the double bounce with respect to the transmitter and the receiver. For each of them, it can be reminded that a specific wave path is involved, naturally in close relationship with the bistatic geometry. The running distance through the different layers is derived from a ray tracing process involving a chain list process for the sake of computing time efficiency.

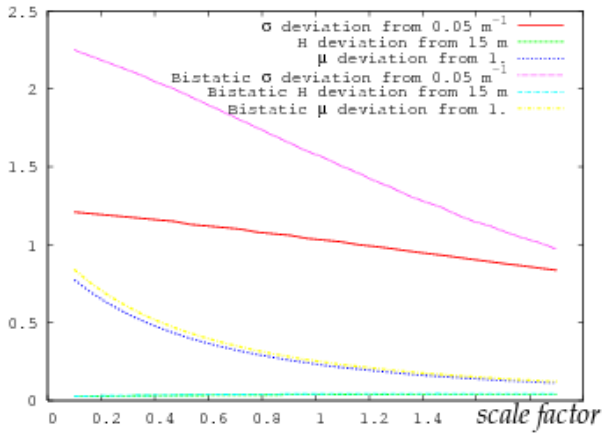

Figure 5.10: Modulus of the total coherence partial derivatives related to the RVoG variables : $\Phi_0, h_v, \sigma, \mu_{vv}$ and μ_{hh}. Deviations are considered for each of these variables from the medium input vector defined by the values indicated above and with a linear/scale factor ranging from about 10 % to twice each value. Mono and bistatic angles are respectively $\theta_{\mathrm{T}} = 50^o, 70^o, \theta_{\mathrm{R}} = 50^o, 50^o$).

Since extinction calculation has been performed for each layer, the resulting attenuation on each scatterer and for each mechanism is then straightforward. The contribution of each scatterer with its associated mechanisms can thus be obtained and all the ones matching to a given pixel are then coherently added.

The last consideration rises the problem of the pixel definition which lead us to the SAR processing effects to be simulated. In sections 5.3 and 5.4, the volume integration importance has been emphasized, especially concerning the interferometric phase sensitivity and the resulting ambiguity height. This is all the more fundamental for structured and also coupled media. Indeed, the former introduces a reference phase shift intrinsic to the volume phase sensitivity and the specular terms their own ambiguity height. It is therefore essential to record the contributions according to their corresponding propagation delay. For that, the range gate number associated to a given time t_c is derived from the floor of $\frac{t_c - t_{ref}}{\Delta t}$, with t_{ref} and Δt respectively as the radar time origin and resolution. Likewise, a Doppler gate process is performed for the SAR long time direction, that is the commonly named azimuth direction either in monostatic or in bistatic with parallel tracks. Since the scope of this study has been limited to the latter configurations, the Doppler acquisition is of lesser importance and do not introduce significant pixel distortions. In addition, the question of the double bounce SAR compression (still for the previously treated bistatic configurations) has been addressed in appendix D and it has been shown that in spite of its multi-interaction nature, the defocusing effect is less important than for volume contribution and can be neglected under the same conditions. Besides, excluding also forward configurations close to the specular for which the range resolution is severely damaged and where distance ambiguities are likely to occur, other issues such as SNR, antenna pattern, range or azimuth ambiguities effects can be put aside in this framework. As well and still about modeling considerations, the frequency range validity, linked to the approximations inherent to the individual scatterers involved for classical forested area, goes from about 100 MHz to the C-band.

In the following applications, our choice has been directed to the L-band. Indeed, for Pol-

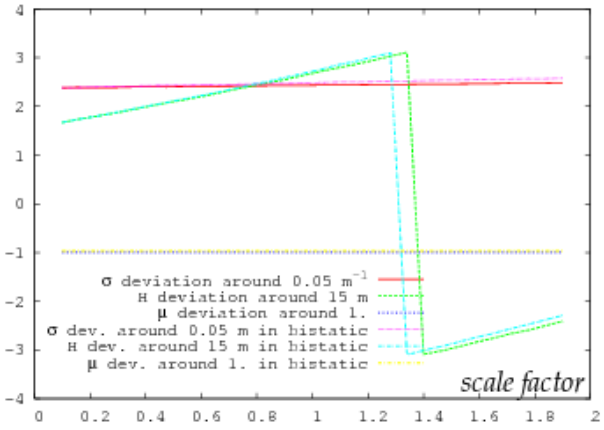

Figure 5.11: Phase of the total coherence partial derivatives related to the RVoG variables. Deviations are considered for each of these variables from the medium input vector aforementioned in figure 5.10 with a linear/scale factor ranging from about 10 % to twice each value. Mono and bistatic angles are respectively $\theta_{\mathrm{T}} = 50^o, 70^o, \theta_{\mathrm{R}} = 50^o, 50^o$)

InSAR applications aiming at ground and volume characterization, the scattering contribution must be significant for both so that the L-band and its penetration capability has been chosen (besides, a specific sensitivity study concerning bistatic scattering ratios will be conducted afterwards). For another thing, higher frequency radar are not only easier usually to handle for embedded systems but also they enable shorter baselines length for an equivalent interferometric sensitivity, which is of major importance for single pass and possibly multi-baselines configuration. The latter permit also to put aside the temporal decorrelation issue, usually the drawback of higher frequency systems. Plus, this choice is also strengthened by higher resolution capability (liable to be damaged by the bistatic aspect), a better immunity to ionospheric Faraday rotation (e.g in comparison with P-band).

Concerning forest modeling, the versatility of our simulator makes possible various scenarios and more precisely, the considered cases – of growing complexity – will go from the RVoG to the C2SObtVoG that is a structured forest made of 2 layers (2S), coupled (C) with specular ground mechanisms and oriented (O) according to the branch insertion angle (ψ, keeping the azimuthal symmetry) over a possible depolarizing ground (DG). The resulting range gated radiometric images are illustrated herein with figure 5.12 to show the envisioned scene, with the forest stand surrounded by a bare ground. The latter's presence is justified by the range gated process and programming reasons, since it requires a references points without layover. Otherwise, the stand is homogeneous, hence the limited display to the VV polarization since in such cases images representation is not the most relevant. Nevertheless, it emphasizes the ground over volume change between these particular monostatic and bistatic configurations, the resolution impact – arbitrarily chosen but sufficiently coarse to neglect the co-registration problem – on speckle and image texture and finally the actually moderate range gated effect, characterized by the slightly spherical pixel shape. The ground truth details of the considered forest are given in table 5.2.

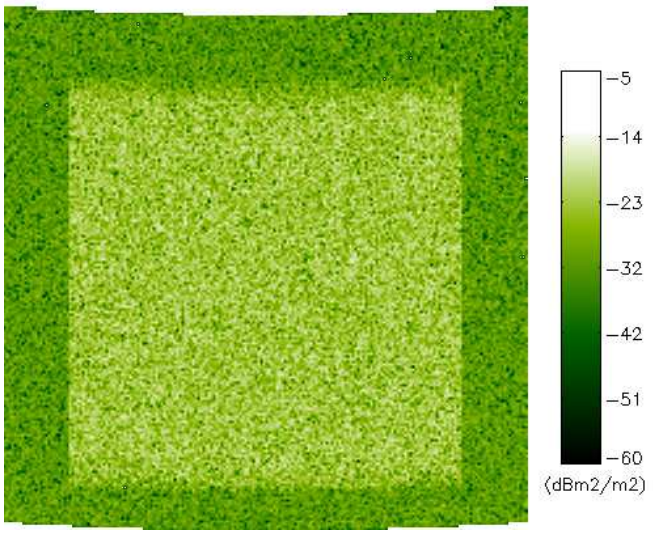

(a) $\sigma^0_{vv}(\beta = 0)$

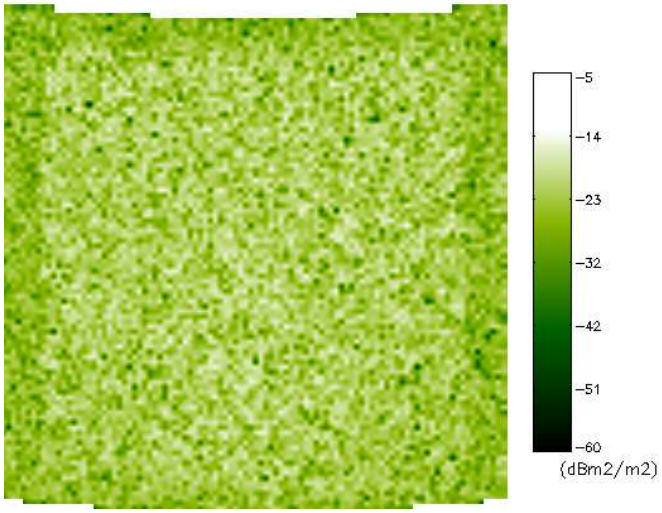

(b) $\sigma^0_{vv}(\beta = 70^o)$

Figure 5.12: VV radiometric images of the scattering coefficient $\sigma^0_{vv}(dBm^2/m^2)$ for range gated acquisitions in monostatic (a) and bistatic configurations (b) respectively with a 2*2 m^2 and 6*6 m^2 resolution.

5.6.3 Applications : Inversion of Single Baseline Data

The purpose of the following subsection is twofold: on the one hand, it illustrates and makes more explicit the inversion method with cases of growing difficulty, on the other hand the retrieval feasibility of various forest models is assessed, in view of simulated Pol-InSAR coherences by MIPERS considering first single baseline acquisitions. The measure space provides then up to four complex coherences ensued from the vertical and horizontal polarizations. As a result, the descriptive parameters required for each forest model will be also first limited to eight ones so that the inversion status of the RVoG, OψVoG, RVoDG and 1SOψVoG forest models can be considered, as formulated within the table 5.1.
The RVoDG model stands for the Random Volume over a Depolarizing Ground, encompassing thereby additional scattering ratios for the cross polarizations which physically might come from ground local or general slopes. The $1SO\psi VoG$ means a structured general volume with one filled layer which bottom height do not correspond to the topographic one, requiring thereby an additional height or phase parameter (Φ_0^v). We insist on the fact that the layer number indicates the ones participating to scattering and attenuation, so that in $1SO\psi VoG$ the case, an empty layer is considered between the ground and the volume layer. The comparison between the available measures and the number of unknowns rises first the solution uniqueness problem for which however MIPERS simulations are not required. As mentioned in the previous paragraph, a given set of forest descriptive parameters is chosen, then the inversion algorithm is performed with the complex coherences derived from the analytical relations, that is without simulated radar speckle. The inversion is performed iteratively (typically a thousand times), with different initial guess parameters, for the purpose of exhibiting several solution vectors, considered as such whenever the cost function is minimized with the same accuracy than with the true solution, determined by machine precision. As mentioned previously, the uniqueness condition is then considered fulfilled if the various solutions do not present relevant differences. In this case, we can note of course that it does not constitute a mathematical proof, but a reliable indication within the scope of our study.

To start with the simplest case, the RVoG model is considered, requiring 5 descriptive parameters for 6 measures resulting for the complex coherences, in monostatic as well as for bistatic configurations (in the plane of incidence). Indeed, within the model's hypothesis, the linear cross polarizations come entirely from the volume which scattering behaviour (and the resulting extinction), is identical for both cases, thanks to the uniform insertion and azimuthal orientation angle properties. The uniqueness condition being fulfilled in view of the aforementioned criteria, the existence one is checked by comparison between simulated Pol-InSAR coherences and those ensued from the analytical formula. To this end, the scattering of a random volume over a bare ground is considered, without coupling terms and made with one layer fifteen meters high layer filled with cylindrical scatterers. The various geometrical characteristics are given in table 5.2.

Concerning the radar parameters, we remind the L band choice and a resolution of 6 meters for both range and azimuth direction. Indeed, on the one hand this quite low value is consistent with the range resolution loss when the bistatic angle goes towards the forward direction (cf. appendix D) and on the second hand, decorrelation from pixel misregistration inherent to the interferometric parallax is minimized. A scene of six hundred meters square is then simulated and the resulting coherences loci are displayed on the complex unit circles in figure 5.13 for a 45^o transmitting incidence angle and a grazing one at 70^o. Each time, the tilted baseline angle is 45^o, its length is given in the corresponding figure legend as well as transmitting and receiving angles. The cloud coherence colours are blue, red, green and yellow respectively for the VV, HH, HV and VH. Also indicated with the same colour convention are the complex

	configurations	phases,heights	extinctions	$\mu^{(\mathrm{dg})}$	$\mu^{(\mathrm{Tsg})}$	$\mu^{(\mathrm{Rsg})}$	
RVoG	$\forall\ (\beta, \theta_{\mathrm{R}})$	Φ_0^{g}, h_v	σ	$\mu_{pp}^{(\mathrm{dg})}$ (♯)	∘	∘	$\hookrightarrow 5^{\diamondsuit}$
OψVoG	$\forall\ (\beta, \theta_{\mathrm{R}})$	Φ_0^{g}, h_v	$\sigma_{v,h}^{\theta_{\mathrm{T,R}}}$	$\mu_{pp}^{(\mathrm{dg})}$	∘	∘	$\hookrightarrow 8$
	$\beta = 0$		$\sigma_{v,h}^{\theta_{\mathrm{T}}}$	$\mu_{pp}^{(\mathrm{dg})}$	∘	∘	$\hookrightarrow 6$
	$\forall\ \beta, \theta_{\mathrm{R}} = 0$		$\sigma_{v,h}^{\theta_{\mathrm{T}}, \theta_{\mathrm{R}}}$	∘	∘	∘	$\hookrightarrow 7$
RVoDG	$\forall\ (\beta, \theta_{\mathrm{R}})$	Φ_0^{g}, h_v	σ	μ_{qp}	∘	∘	$\hookrightarrow 7$
	$\beta = 0$			$\mu_{vv,hh,hv}$	∘	∘	$\hookrightarrow 6$
1SOψVoG	$\forall\ (\beta, \theta_{\mathrm{R}})$	$\Phi_0^{\mathrm{g}}, \Phi_0^{\mathrm{v}}, h_v$	$\sigma_{v,h}^{\theta_{\mathrm{T,R}}}$	$\mu_{pp}^{(\mathrm{dg})}$	∘	∘	$\hookrightarrow 7$
	$\beta = 0$		$\sigma_{v,h}^{\theta_{\mathrm{T}}}$	$\mu_{pp}^{(\mathrm{dg})}$	∘	∘	$\hookrightarrow 6$
	$\forall\ \beta, \theta_{\mathrm{R}} = 0$		$\sigma_{v,h}^{\theta_{\mathrm{T}}, \theta_{\mathrm{R}}}$	∘	∘	∘	$\hookrightarrow 7$
CRVoG	$\forall\ (\beta, \theta_{\mathrm{R}})$	$\Phi_0^{\mathrm{g}} = \Phi_0^{\mathrm{v}}, h_v$	σ	$\mu_{pp}^{(\mathrm{dg})}$	$\mu_{qp}^{(\mathrm{Tsg})}$	$\mu_{qp}^{(\mathrm{Rsg})}$	$\hookrightarrow 13$
	$\beta = 0$				$\mu_{vv,hh,hv}^{(\mathrm{T,Rsg})}$	$\varphi(\mathbf{R}_v \mathbf{R}_h^*)^{\clubsuit}$	$\hookrightarrow 9$
C2SOψVoG	$\forall\ \beta, \theta_{\mathrm{R}} = 0$	$\Phi_0^{\mathrm{g}}, \Phi_0^{\mathrm{v}}, h_v$	$\sigma_{v,h}^{\theta_{\mathrm{T}}, \theta_{\mathrm{R}}}$	$\mu_{pp}^{(\mathrm{dg})}$	$\mu_{qp}^{(\mathrm{Tsg})}$	$\mu_{qp}^{(\mathrm{Rsg})}$	$\hookrightarrow 16$
	$\beta = 0$		$\sigma_{v,h}^{\theta_{\mathrm{T}}}$		$\mu_{vv,hh,hv}^{(\mathrm{T,Rsg})}$	$\varphi(\mathbf{R}_v \mathbf{R}_h^*)$	$\hookrightarrow 11$

(♯) q,p standing for v or h polarizations
(♣) φ standing for the phase operator
($\diamondsuit$) unknown number

Table 5.1: Descriptive parameters associated to the various forest scattering models, depending not only on forest intrinsic attributes but also on the radar configuration. Hence a different unknown number indicated on the right hand side of the table between monostatic or bistatic configuration. For the latter, the particular off-nadir receiver case is also pointed out. The associated measurements – considered with the specific inversion algorithm – result from the complex coherences, typically $[\gamma_{qp}^{b_i}]$ where b_i entails the multi-baselines acquisition possibility in order to cope with the more complicated models.

coherences derived analytically, shown with straight arrows from the origin. Considering the respective mean loci values, the existence condition is fulfilled, which validates especially the interferometric sensitivity in bistatic through the implemented ambiguity height formula. The coherences variance rises then the last Hadamard criteria, that is stability, assessed in view of the continuity of the retrieved results. The inversion is performed pixel by pixel, considering the non linear optimization constraints intrinsic to the RVoG hypothesis, that is :

$$\Phi_0^g = \Phi_0^v,\ \sigma_v = \sigma_h,\ \mu^{\mathrm{T,Rsg}} = 0.$$

whereas the typical range values of the remaining 'free' parameters have been given in subsection 5.6.3. The retrieved descriptive parameters are then averaged over the scene pixels. We can note that the opposite approach, which would perform the inversion on the mean coherences over all the scene pixels, is less consistent with the statistics average derived previously since it do not include the ambiguity height or angle variations for large areas. As illustrated with the two cases in figure 5.13, the accuracy of the inversion results turns out to be closely dependent on the cloud coherences separation, as given in table 5.3.

Indeed, as for the look-up table method (cf [Cloude and Papathanassiou, 2003]), the discrimination power is naturally better when cross and full polarization are distant, that is within this model when direct ground VV and HH scattering ratios are sufficiently important. Also consistent with the sensitivity analysis of the inversion operator, the extinction coefficient is the worst

parameter with for instance in the weak polarimetric dependence case a bias of 30 % whereas topographic and volume retrieved height are both less than 10 %, 20 % and 10 % respectively for the scattering ratios μ_{vv} and μ_{hh}. We remind that the scattering ratios depend on both isolated direct ground contribution and layer attenuation – cf. relation (72) in part I, with h_t=0. – which however is the same for the vv and hh polarizations in the RVoG case. As illustrated in this figure, the forward bistatic configuration with non very grazing incidence angle present therefore the advantage of maximizing the direct ground contribution. This property will be further on discussed for various surface state when dealing with forest models including coupling effects. Indeed, the comparison will be thereby more consistent with the monostatic case for which double bounce is always dominant – as far as L band or lower frequencies are concerned.

Nevertheless, the inversion is performed in monostatic, for the validation purpose and rather to assess the orientation effect. We remind that throughout this study, the possible orientation will be restricted to the elevation component, keeping always the azimuthal symmetry, as for standard vegetated area with the branch insertion angle (ψ_b) description. Scattering from an oriented volume is then simulated, giving a preferential horizontal direction to the scatterers with ψ ranging from about 70^o to 90^o. Apart from the scatterers elevation orientation angles, the same layer composition is considered in all the subsequent simulations, as well as radar frequency, resolution and scene dimensions. The simulated complex coherence loci are shown in figure 5.14, displaying also the radar configuration. The main impact concerns the scattering ratios in view of the resulting differential extinction (of about 20 % larger for horizontal polarization and at 45^o) and their dependence to the layer attenuation, as mentioned previously. Concerning the inversion, the $O\psi VoG$ model introduces one additional unknown and whereas uniqueness and existence conditions are satisfied, the estimated extinction coefficients exhibit the largest relative bias of about 30 %, with however the correct differential value.

Furthermore, as summarized in table 5.1, the oriented volume requires three more parameters for an arbitrary bistatic site angle, hence the off nadir receiving position. Indeed, on the top of the operational attractive configuration (cf. antennas handling among other interests), it enables to save one unknown since $\sigma_v(\theta_{\rm R}) = \sigma_h(\theta_{\rm R})$ by azimuthal symmetry property. Notwithstanding, even with only seven parameters for the four different complex coherences (since $\gamma_{vh} \neq \gamma_{hv}$), the uniqueness is this time not fulfilled. It is indeed possible to exhibit various combination of extinction coefficients yielding to the same level of accuracy than with the great ones, as shown with figure 5.15 showing the normalized biased for the estimated parameter mean and variance values. Likewise, the uniqueness condition for the 1SRVoG and the RVoDG models has been studied and reveals also ambiguities, as evinced in figure 5.16. The latter involve respectively one additional unknown for the additional bottom volume layer height and one or two supplementary scattering ratios ($\mu_{qp}^{\rm dg}$) in the monostatic or bistatic case (cf. table 5.1). Whereas depolarizing

	f_v	height	radius	$\psi^{\rm R,O\psi V}\updownarrow_{\rm (min,max)}$
Trunk layer	$2.2*10^{-3}$	9.9	0.1	0.,0.10
Upper layer	$2.5*10^{-5}$	0.3	0.01	0., $\frac{\pi}{2}\updownarrow\frac{2\pi}{5}$, $\frac{\pi}{2}$
	$1.0*10^{-4}$	0.4	0.02	
	$2.0*10^{-4}$	0.5	0.03	
	$3.0*10^{-4}$	0.6	0.04	
	$7.0*10^{-4}$	0.7	0.05	

Table 5.2: Geometrical details (dimensions in meter) for the various simulated forest models

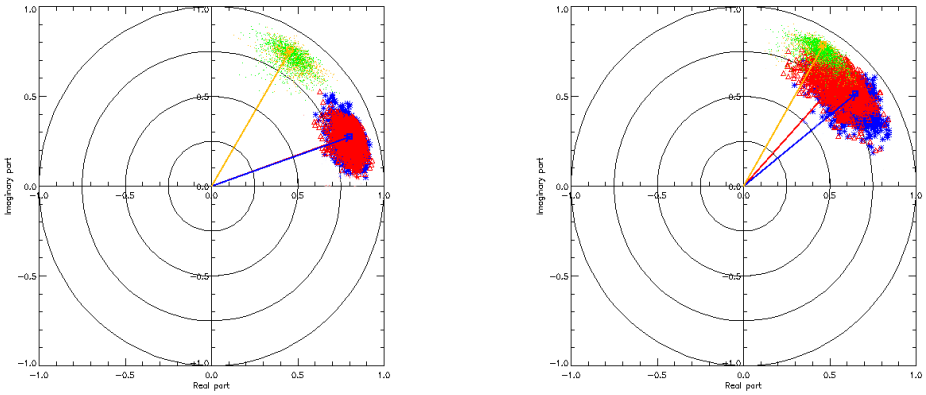

(a) $\theta^{\mathrm{T}} = 45^o$ (b) $\theta^{\mathrm{T}} = 70^o$

Figure 5.13: Loci on the complex unit circle of Pol-InSAR coherences resulting from a simulated RVoG model in two bistatic configurations with an off-nadir receiver and different incident angle as indicated above in (a) and (b), with respectively $b_\perp = 7$ and 10.5 m, $h_a = 53$ and 58 m.

ground constitutes a severe limitation since the coherences loci are likely to be overlapped, the structure effect is less stringent. Indeed, even if the height of the bottom part of the volume layer presents large discrepancy, the resulting height after summation – giving the top of the vegetation layer – is much better estimated (both individual heights are ambiguous). Concerning the various tested cases for the RVoDG model, we can note that the bistatic configuration with an additional different cross polarization coherence offer a lower risk of coherence loci superposition, hence non biased mean values for the scattering ratios, as illustrated with case (b) in figure 5.16.

Also important to consider are the forest models with coupling terms between volume and ground, entailing the double bounce terms. To take into account rigorously their impact, supplementary scattering ratios must be included which would involve more unknowns than the measures ensued from the monostatic or bistatic single baseline acquisition, that's why the RVoDG and SOψVoG models have been treated before. Notwithstanding, in view of these limitations, the question of the inversion algorithm tolerance can be risen, keeping the RVoG constraints as a priori hypothesis to perform the retrieval from CRVoG simulated coherences. The resulting estimated parameters can thus be viewed as effective ones. As a well-known example, we can

	$\hat{\Phi}_0^g$	$\hat{h}$	$\hat{\sigma}$	$\hat{\mu}_{vv}^{(\mathrm{dg})}$	$\hat{\mu}_{hh}^{(\mathrm{dg})}$
$\theta_{\mathrm{T}} = 45^o, \beta = 45^o$	$0.02\vert_{\text{4e-2}}$	$14.9\vert_{0.7}$	$0.022\vert_{\text{1e-3}}$	$1.7\vert_{0.3}$	$1.8\vert_{0.35}$
$[\Phi_0, h, \sigma, \mu_{hh}, \mu_{vv}] = [0.,15.,3\text{e-}2,1.5,1.6]$					
$\theta_{\mathrm{T}} = 70^o, \beta = 70^o$	$0.04\vert_{\text{4e-2}}$	$15.7\vert_{1.}$	$0.016\vert_{\text{5e-3}}$	$0.35\vert_{0.15}$	$0.7\vert_{0.2}$
$[\Phi_0, h, \sigma, \mu_{hh}, \mu_{vv}] = [0.,15.,3\text{e-}2,0.27,0.55]$					

Table 5.3: Accuracy and precision of the retrieved parameters for the RVoG model in bistatic expressed with the notation $\{\text{mean value}\}\vert_{\{\text{standard deviation}\}}$. The target vector is given below the concerned cases.

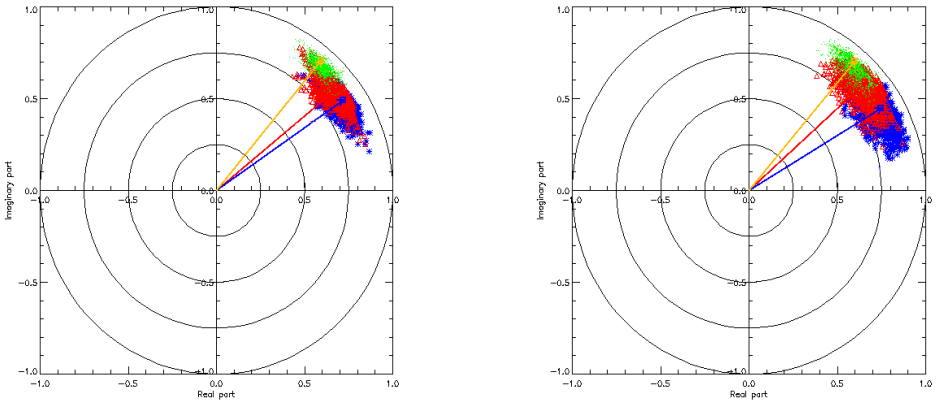

(a) RVoG (b) 0ψVoG

Figure 5.14: Loci of monostatic Pol-InSAR coherences ($\theta^{\mathrm{T}} = 45^o$, $b_\perp = 20.$ m, $h_a = 64.5$ m) resulting from the simulated RVoG (a) and OψVoG models.

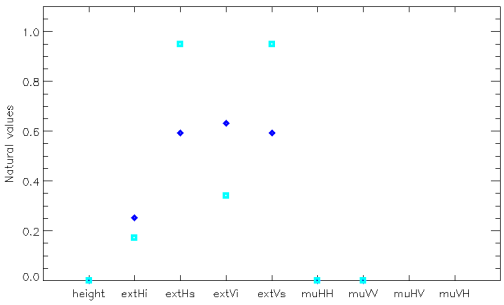

Figure 5.15: Non uniqueness of the $0\psi VoG$ in bistatic, even with the off-nadir receiving position

refer to the monostatic acquisitions either in 'ping pong' or double pass mode, for which the double bounce can be mixed up with the direct ground since it encompasses neither intrinsic decorrelation nor interferometric phase shift (cf. § 5.4). The ambiguity between the two types of scattering ratios can not be risen but more prominent are the non affected topographic and volume heights estimation. Besides, as seen before with the simulation involving the bistatic forward configuration (cf. figure 5.13 and $\theta_{\mathrm{T}} = 45^o$), the double bounce terms may be neglectible in comparison with the resulting highest direct ground return, making the RVoG model consistent. The inversion has thus been carried out in this configuration, based this time on simulated measures with volume-ground coupled scatterers. Though lower than direct ground contributions, we can see in view of the inversion results than the double bounce scattering ratios are sufficiently important to bring about a significant height bias. Indeed, as illustrated with the coherence loci in figure 5.17 the additional decorrelation introduced by the double bounce turns the effective ground reference into a lowest point, modifying thereby the topographic height estimation as well as the volume one. This effect is also typical in the monostatic case, with the same type of biased equivalent ground point, mixing direct and specular ground terms, as explained in § 5.3.2 with figures 5.3 and 5.4. Another set of soil parameters might be of course more favourable but it emphasizes the non robustness of the retrieval, which thus can not be performed whether in

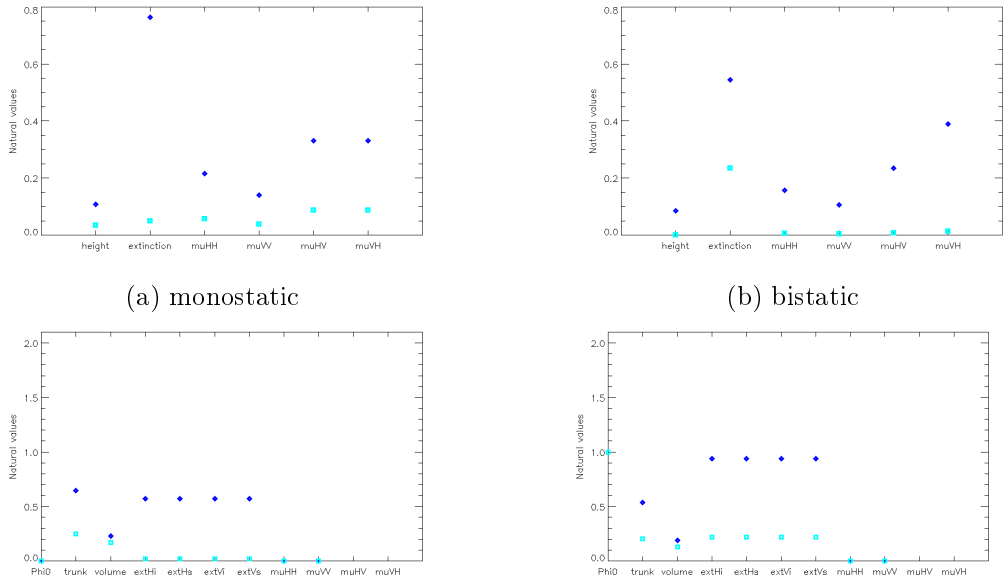

(a) monostatic (b) bistatic

(c) monostatic (d) bistatic

Figure 5.16: Illustration of the non uniqueness of the RVoDG (a,b) and 1SRVoG (c,d) problem whether in monostatic or in bistatic

this bistatic configuration or in the monostatic one.

Although interesting to explicit our inversion algorithm and for the sake of validation between the analytical and the MIPERS approach, coupling effects are lacking in the previous cases to deal more faithfully and generally with forest scattering. Indeed, as shown with the previous inversion attempt, the latter can not be simply mixed up with direct ground contributions and must be included more rigorously, that is with respect to their respective theoretical expression derived previously.

5.7 Specific Asset and Potential of the Bistatic Configuration

In view of conclusions drawn in the last paragraph, either more stringent constraints – robust enough to be generalized to the various possible forest cases – or richer measure sets (or both) are needed to cope with more realistic forest models. Hence the aim to investigate various acquisitions, offered by the geometrical versatility of bistatic configurations. Indeed, beyond the operational well known assets, the physical interest of bistatic observables remain so far. In this section, keeping the same bistatic angle, the gain ensued from supplementary baselines will be emphasized, before the study of forest scattering versus the bistatic elevation angle and within the scope of exhibiting general properties liable to ease the inversion formulation. As mentioned in the general introduction, we remind that multistatic or a joint monostatic plus bistatic acquisition could be naturally envisioned to enlarge the measures set. They are however not considered hereafter since significant co-registration problems would deserve their own parallel study. Besides such configurations present the disadvantage of coming with additional unknowns through scattering ratios for each different bistatic angle. As far as forest description improvements are concerned, the previously approached CRVoG model and the 2SCRVoG one will be

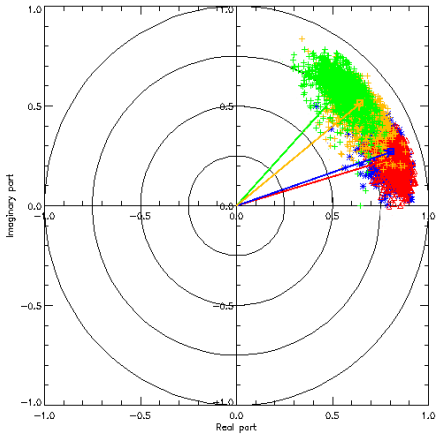

Figure 5.17: Loci of the Pol-InSAR coherences resulting from a simulated CRVoG model in bistatic with $\theta^{\mathrm{T}} = 45^o$ and an off-nadir receiver, $b_\perp = 7.$ m, $h_a = 53.$ m. The straight line bias brings by the coupling terms decorrelation is cleary manifest with the co-polarizations loci.

studied (along with their derivatives in the case of specific branch orientation, cf. C2SOψVoG). Both are indeed paramount to simulate faithfully scattering in L band from tropical forests or more organized temperate ones exhibiting in general at least two distinct layers with the tree crown and trunks.

5.7.1 Benefits of Several Baselines

As mentioned in section 5.5, the multibaseline acquisition has been already assessed under several perspectives in monostatic, whether for tomography or rather within this framework to obtain additional Pol-InSAR measures (as in [Cloude and Williams, 2003; R Treuhaft, 2006]). Yet, in view of the baseline length increase with altitude, a monostatic single pass acquisition at L band is necessarily restricted to airborne flight altitude (coming with several disadvantages, such as flight track precision). An hybrid spaceborne transmitter, airborne receiving baselines constitutes thereby a specific advantage of bistatic system (all the more interesting in the hitchhiker mode), again within this single pass acquisition scope.

The previously considered forest models (cf. § 5.6.3 can be then re-examined, according likewise to the Hadarmard criteria. The significant improvement concerns the height or phase estimation which satisfy now the uniqueness criteria whereas extinction coefficients ambiguities can not be risen, even with three baselines (cf. cases (a) and (b) in figure 5.18). In addition, the CRVoG model, coming with eight more unknowns (cf. table 5.1) exhibits an unique solution with three baselines, also acceptable with two. The existence condition is also satisfied as illustrated in figure 5.19 which validates the theoretical derivations for the double bounce coherences. Concerning the stability one, the inversion performed with simulated data shows that in this configuration the problem is still illy posed and scattering ratios can not be retrieved. Notwithstanding, the height estimation is quite robust with a quasi non biased mean value, as shown in figure 5.20 and we notice that more stringent constraints (by comparison to the typical ones given in section 5.6) for specular ground terms improve significantly their subsequent estimation.

Despite this progress in comparison with the single baseline acquisition, we see with the

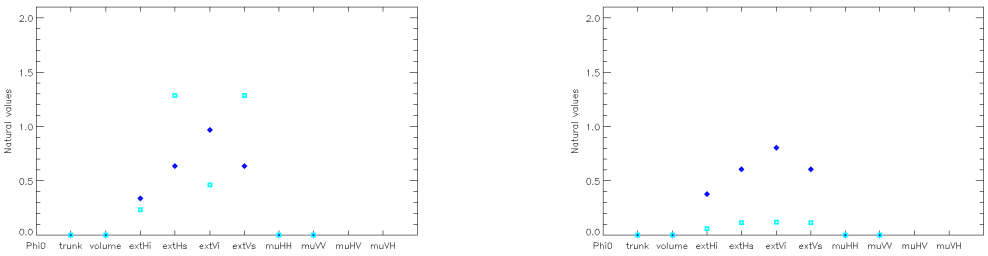

(a) 2 baselines (b) 3 baselines

Figure 5.18: Illustration of the non uniqueness of the 1SOψVoG problem with either 2 or 3 baselines, respectively in (a) and (b)

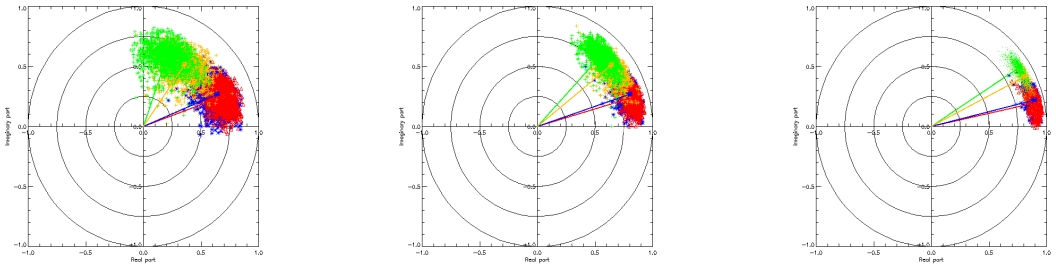

(a) b= 15 m (b) b= 10 m (c) b= 7 m

Figure 5.19: Complex Pol-InSAR coherences loci with their respective baseline, simulated according to CRVoG model in bistatic with $\theta^{\mathrm{T}} = 70^{o}$ and an off-nadir receiver

last example that further considerations are needed before tackling the 2SCRVoG, hence the upcoming study of scattering contributions versus the site bistatic angle.

5.7.2 Remarkable properties of the GT-OR configuration

The underlying idea now at issue is about the possibilities offered by the site bistatic geometry and the resulting forest scattering behaviour, for the purpose of finding optimal configurations which might add constraints on the descriptive models (CRVoG, 2CSR,OψVoG) and this regardless of soil nature (keeping in mind the close dependency of scattering ratios to soil roughness and humidity). Naturally, the sought constraints are about specular ground scattering ratios, which number reaches eight for an arbitrary bistatic configuration. As seen with the examples aforetreated, the inversion quality and feasibility is closely linked to the number of freedom degrees and to the coherence loci separation, coming from the polarimetric dependency. Hence, keeping in mind the specular ground reflectivity (according to the modified Fresnel coefficients, reminded in figure 5.42), the interest of the high sensitivity towards specular angle appears in order to maximize the polarimetric scattering ratios difference. Indeed, as detailed in the appendix C, the double bounce with respect to the transmitter or to the receiver involves two distinct specular angles onto the ground. For instance, with an off-nadir receiver and a grazing transmitter (GT-OR configuration), the left and the Brewster side regions on the reflectivity curves (figure 5.42) will be respectively involved. Simulations have thus been carried out to assess the global impact

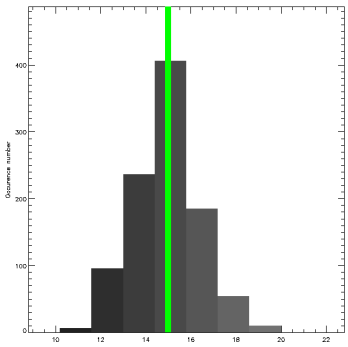

Figure 5.20: Retrived height histogram

of that property, considering in the first place the CRVoG model.

Case of the CRVoG model :

In order to emphasize the specular ground contribution in comparison with the direct one, a quite smooth and wet surface is first considered. The resulting plots versus the bistatic angle are given in figures 5.21 and 5.22 respectively for $\theta_{\mathrm{T}} = 40^o$ and 70^o as incident angles. These results confirm the ground specular reflectivity impact and the more favourable situation with the grazing transmitter which exhibit larger difference between the two types of double bounce, as sought within the inversion scope. ground or less humid Since this difference relies on the Fresnel modified coefficients which keep the same shape whatever the soil state, the emphasized advantage of the grazing transmitter can be considered as optimal in general, with an amplitude determined by the soil humidity (cf. the near Brewster region, figure 5.42) and the ground roughness. Indeed, it can be stressed that this magnitude involves not only the height standard deviation profile (h_{rms}) but also the specular angle (hence the optical roughness designation, cf. § 5.4). That impact can be seen with plots in figures 5.23, 5.24, 5.25 simulated with an higher roughness, exhibiting stronger difference between the 45^o and 70^o incident angles, again more favourable for the latter. This configuration reveals also that for every polarization, the receiver specular ground scattering ratios could be neglected, providing interesting a-priori information concerning the algorithm constraints. Nevertheless, it can not be generalized since the smooth case (figure 5.21) has shown on the contrary significant ratios higher than the transmitter ones whatever the polarization. Consequently, in order to establish independent constraints, additional simulations have been achieved with this time a dry soil (wc = 10 %).

In view of these four cases between low and high roughness and humidity values, we conclude that null constraints can only be applied to the transmitter specular ground terms. The uniqueness and existence conditions being fulfilled, the inversion algorithm of CRVoG simulated coherences has been performed and these additional constrains turn out to be of greatest importance. Indeed, in comparison with the unconstrained situation (CRVoG case in § 5.7.1, figure 5.19), we found that topographic and volume height are still the more accurately estimated parameters but this time, the six remaining scattering ratios are not ambiguous and can be retrieved with an accuracy of about 10 %. Extinction coefficient present still the worst accuracy (about 30%) and precision.

Concerning the scattering ratios precision (i.e the standard deviation of the solution vectors), we notice also that we could afford a significant improvement by means of supplementary

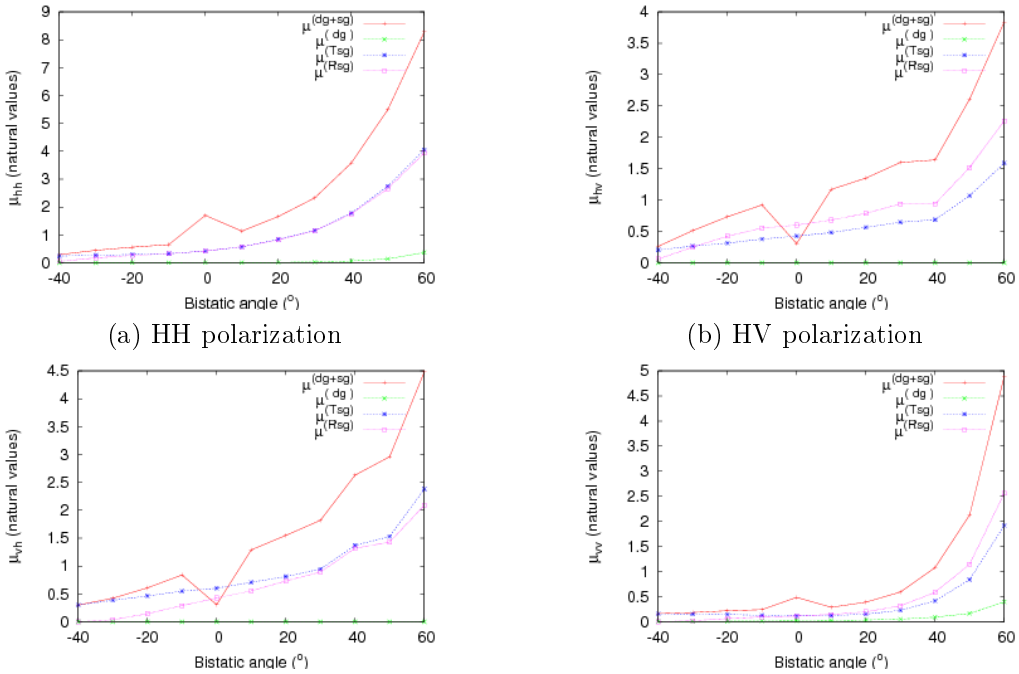

(a) HH polarization (b) HV polarization

(c) VH polarization (d) VV polarization

Figure 5.21: Scattering ratios versus bistatic angle, CRVoG, $h_{rms} = 0.5$ cm, wc = 50 %, $\theta^{\mathrm{T}} = 40^o$

constraints. Indeed, two a-priori cases can be considered, a rough one where receiver specular ground scattering ratios can be neglected, whatever the roughness and the smooth one, with no direct ground ones. Within this likelihood approach, the obtained final precision determines which hypothesis is true, providing the matching solution vector. This method has been used especially for the worst case with low roughness and soil water content, that is when there is a quasi null direct ground contribution and the smallest difference between specular ground terms. The inversion difficulty can be shown again by the poor polarimetric separation between coherence loci (cf. figure 5.28, 5.29), illustrating also the paramount importance of several baselines. Besides, a more grazing incidence (i.e $\simeq 80^o$) has been envisioned, as displayed in figure 5.26. Though interesting to increase again the difference between double bounce mechanisms with respect to the receiver or transmitter, this configuration is exposed to the risk of volume only scattering, beyond the operational difficulty of such grazing angle. Indeed, in the rough and dry cases, scattering ratios relied previously on direct ground ones which suffer with the involved angle from a too high attenuation (still figure 5.26).

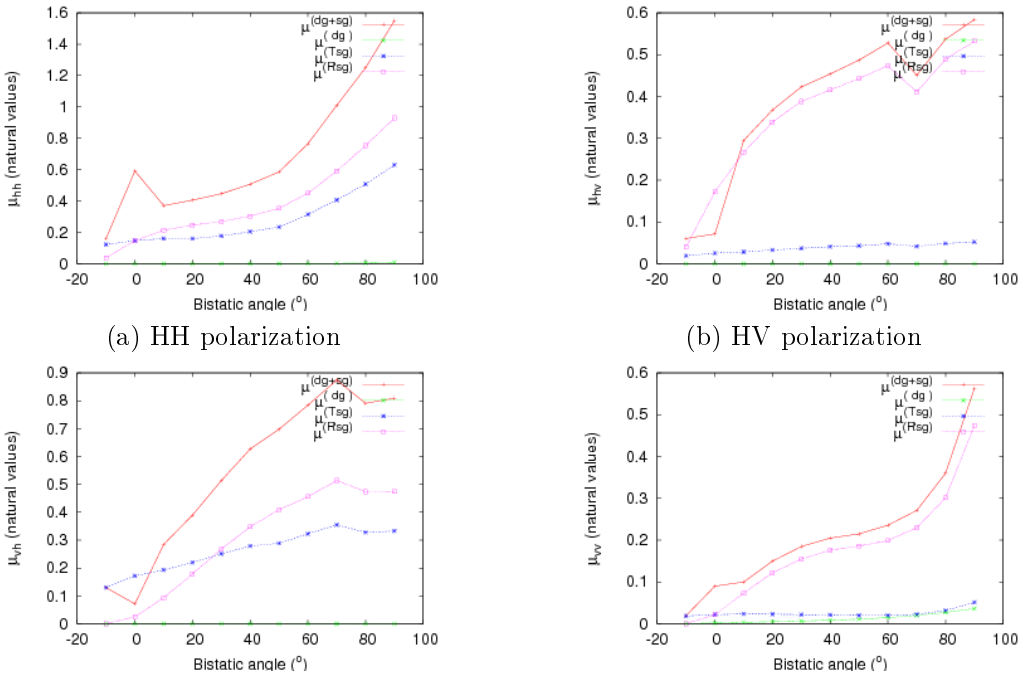

(a) HH polarization (b) HV polarization

(c) VH polarization (d) VV polarization

Figure 5.22: Scattering ratios versus bistatic angle, CRVoG, $h_{rms} = 0.5$ cm, wc = 50 %, $\theta^{\mathrm{T}} = 70^{o}$

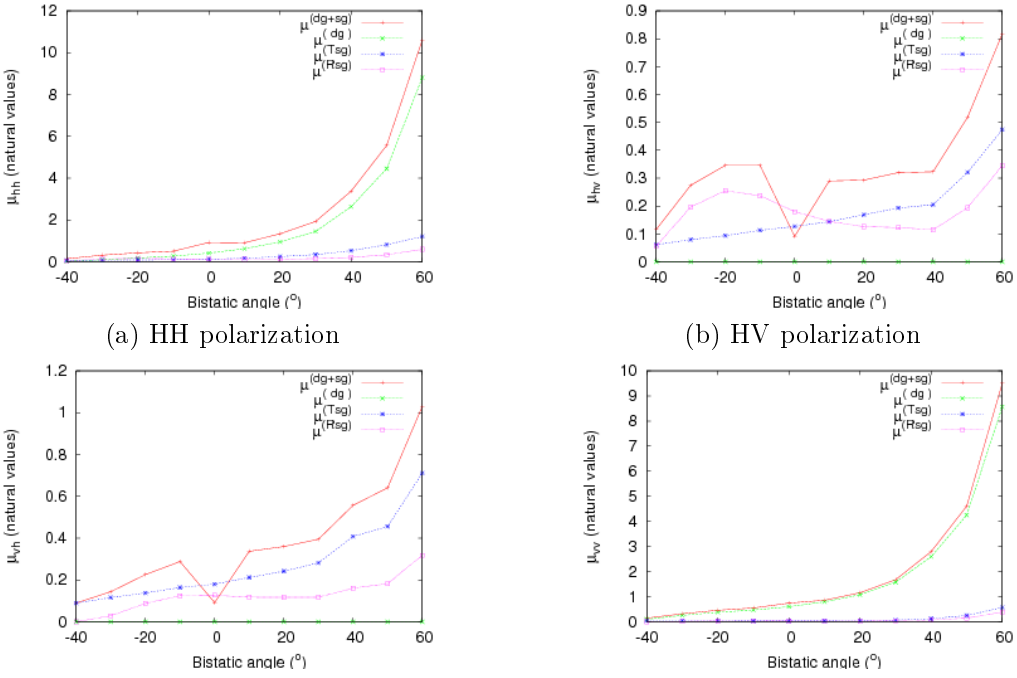

(a) HH polarization

(b) HV polarization

(c) VH polarization

(d) VV polarization

Figure 5.23: Scattering ratios versus bistatic angle, CRVoG, $h_{rms} = 3.5$ cm, wc = 50 %, $\theta^{\mathrm{T}} = 40^o$

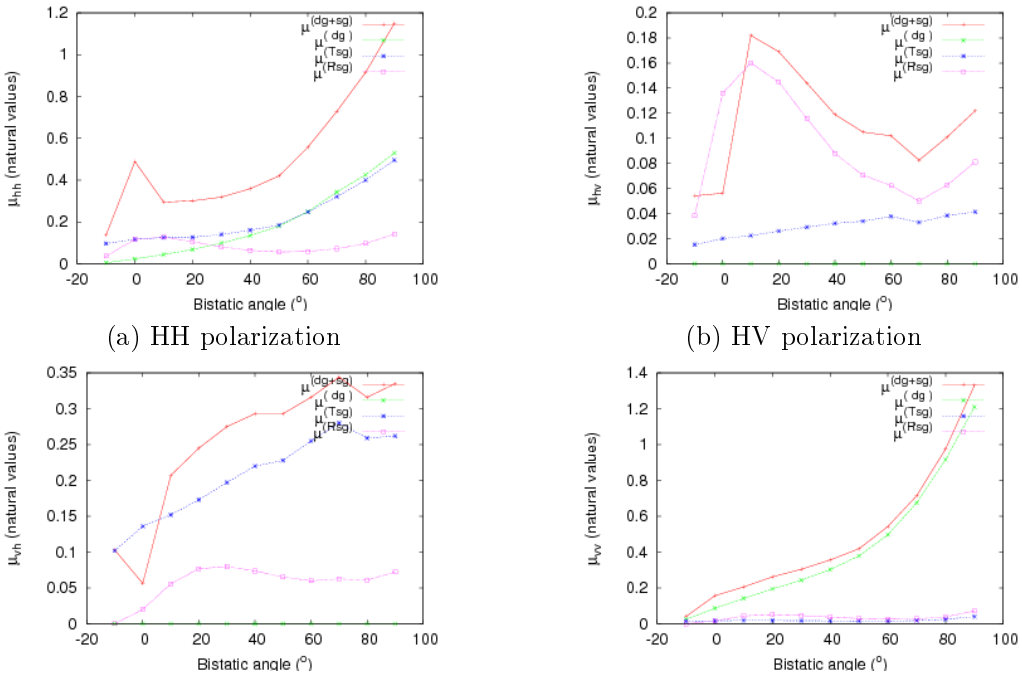

(a) HH polarization

(b) HV polarization

(c) VH polarization

(d) VV polarization

Figure 5.24: Scattering ratios versus bistatic angle, CRVoG, $h_{rms} = 3.5$ cm, wc = 50 %, $\theta^{\mathrm{T}} = 70^{o}$

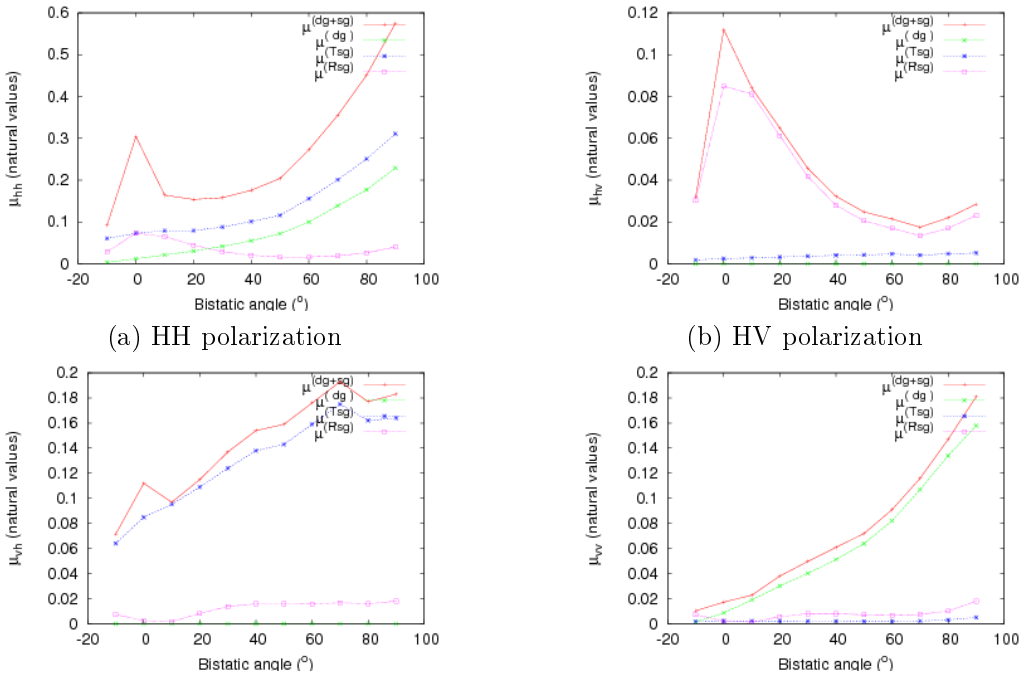

(a) HH polarization (b) HV polarization

(c) VH polarization (d) VV polarization

Figure 5.25: Scattering ratios versus bistatic angle, CRVoG, $h_{rms} = 3.5$ cm, wc = 10 %, $\theta^{\mathrm{T}} = 70^{o}$

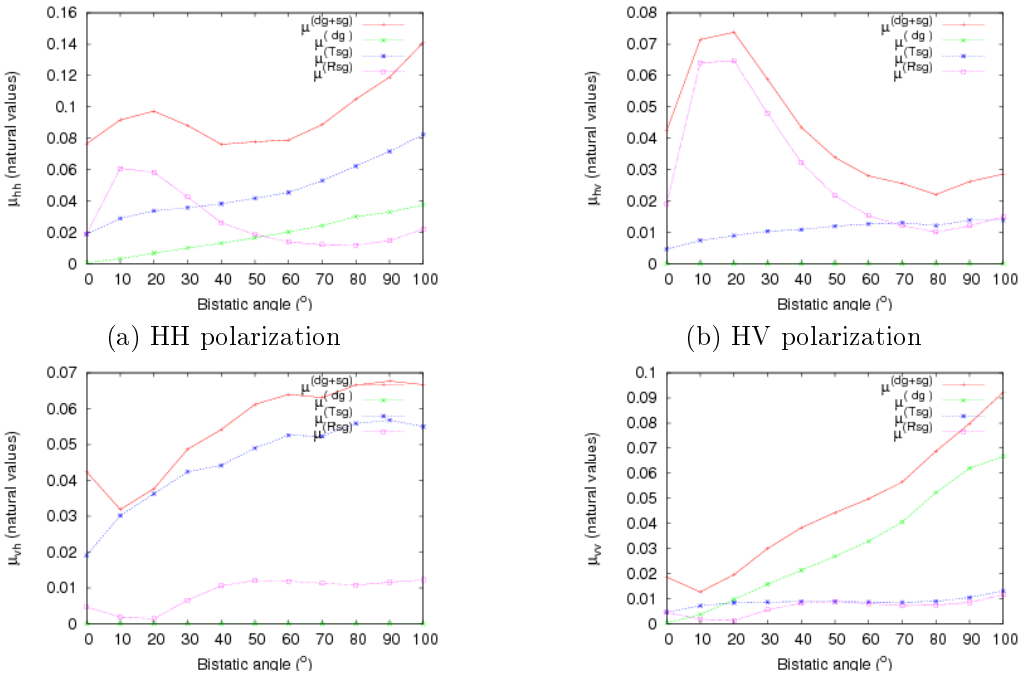

(a) HH polarization

(b) HV polarization

(c) VH polarization

(d) VV polarization

Figure 5.26: Scattering ratios versus bistatic angle, CRVoG, $h_{rms} = 3.5$ cm, wc = 10 %, $\theta^{\mathrm{T}} = 80^{o}$

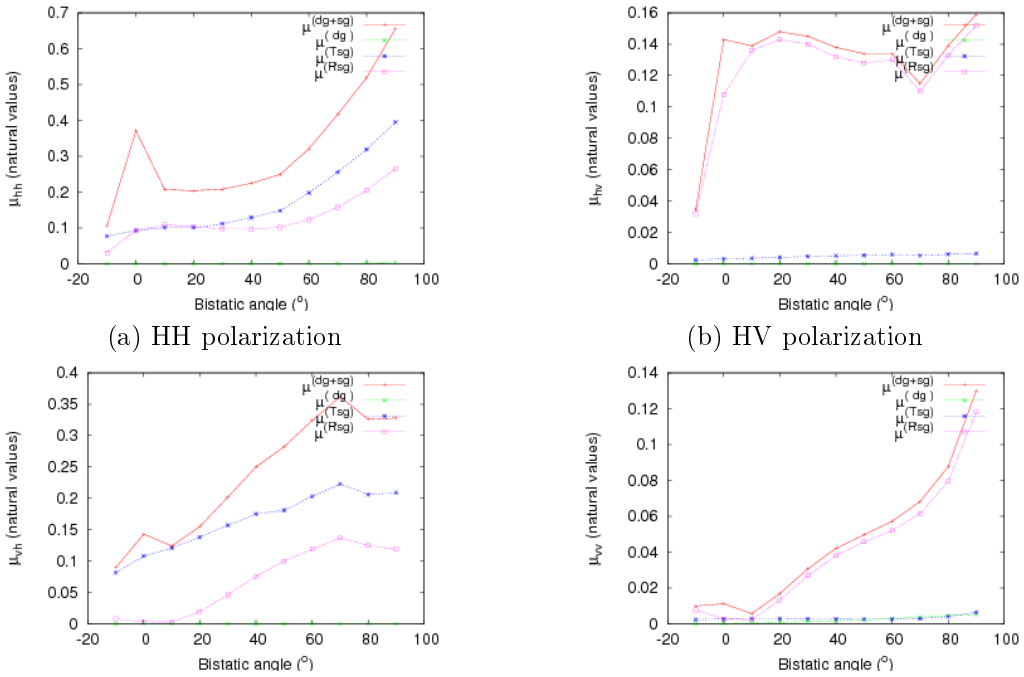

(a) HH polarization (b) HV polarization

(c) VH polarization (d) VV polarization

Figure 5.27: Scattering ratios versus bistatic angle, CRVoG, $h_{rms} = 0.5$ cm, wc = 10 %, $\theta^{\mathrm{T}} = 70^{o}$

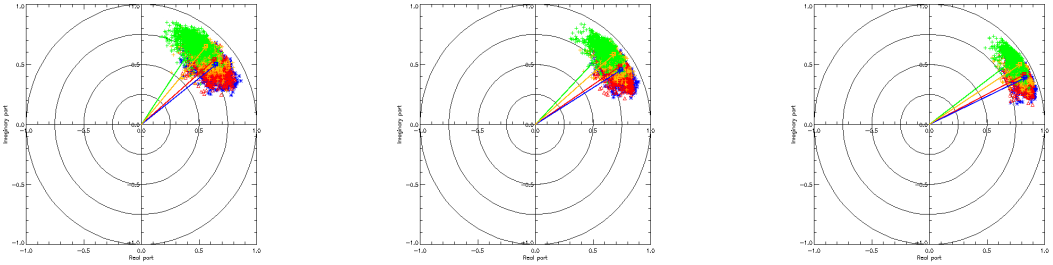

(a) b= 15 m (b) b= 12.5 m (c) b= 10 m

Figure 5.28: Complex Pol-InSAR coherences loci with their respective baseline, simulated according to CRVoG model in bistatic with $\theta^{\mathrm{T}} = 70^{o}$ and an off-nadir receiver, ground roughness $h_{rms} = 3.5$ cm and soil humidity wc = 50 %

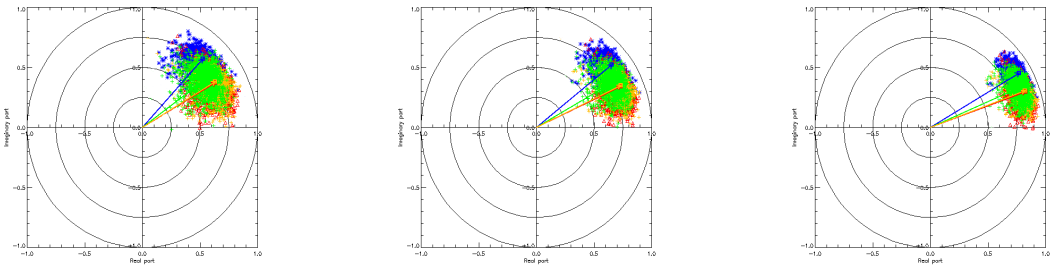

(a) b= 15 m (b) b= 12.5 m (c) b= 10 m

Figure 5.29: Complex Pol-InSAR coherences loci with their respective baseline, simulated according to CRVoG model in bistatic with $\theta^{\mathrm{T}} = 70^o$ and an off-nadir receiver, ground roughness $h_{rms} = 0.5$ cm and soil humidity wc = 50 %

Case of the C2SRVoG model :

The case of interest from now on, namely the 2SCRVoG model, rises the problem of the structured forest model with two layers, as opposed to the previously tackled 1SRVoG one which considered simply a volume layer bottom distinct from the topographic ground. As detailed in section 5.5, the number of unknowns really increases, considering the intrinsic scattering properties of the two layers (extinctions, scattering ratios...). Again, the study of bistatic scattering according to the various site angle may be worthwhile. Indeed, in view of the simulations presented from figures 5.30 to 5.33 one can notice that the scattering ensued from the first layer (bottom one) can be neglected everywhere excepted in the region close to the monostatic configuration where the respective curves are not overlapped anymore. Naturally, this holds with the assumption of a bottom layer made of trunks vertically oriented, which involved the main specular scattering lobe onto the trunks for monostatic double bounce, hence the significant impact for full polarization terms. In bistatic, the inversion can thus be performed using the C1SRVoG parameters, keeping in mind however within a quantitative approach that the analytical expressions for specular ground ratios encompass the trunk layer effect through the attenuation factor (cf. the role of h_t and $\sigma_{v,h}^{\theta^{\mathrm{T,R}}}$ in equation 5.74, subsection 5.4). These simulations have been achieved for two incidence angles (40^o and 70^o), both cases confirm the fact that the first trunk layer impact only the monostatic configuration. For the latter, as long as double bounce cross polarization is negligible, height estimation will be not affected unlike the scattering ratios expression. However, as often shown with experimental data, this contribution coming from roughness and local slopes (introducing cross polarization terms for the ground specular reflectivity) may be a severe source of height bias. Besides, a smooth and wet ground case have been chosen in the previously mentioned simulations, in order to test the trunk layer impact in the 'worst case'.

Furthermore, these simulations for various incident angles and soil states (figures 5.31, 5.33 and 5.34) have been carried out in order to set forth independent constraints concerning specular ground scattering ratios as detailed through the CRVoG study and likewise the 70^o grazing incident angle have been retained as the optimal one. In comparison with the CRVoG case, the difference between transmitter and receiver scattering ratios is all the more important that the formers, involving a grazing double bounce path through the trunk layer are much more affected than the off-nadir path, since extinction coefficients are this time closely linked to the incident angle (cf. figure 5.44 giving also the comparison between $\sigma_v(\theta_{\mathrm{T}})$ and $\sigma_v(\theta_{\mathrm{R}})$).

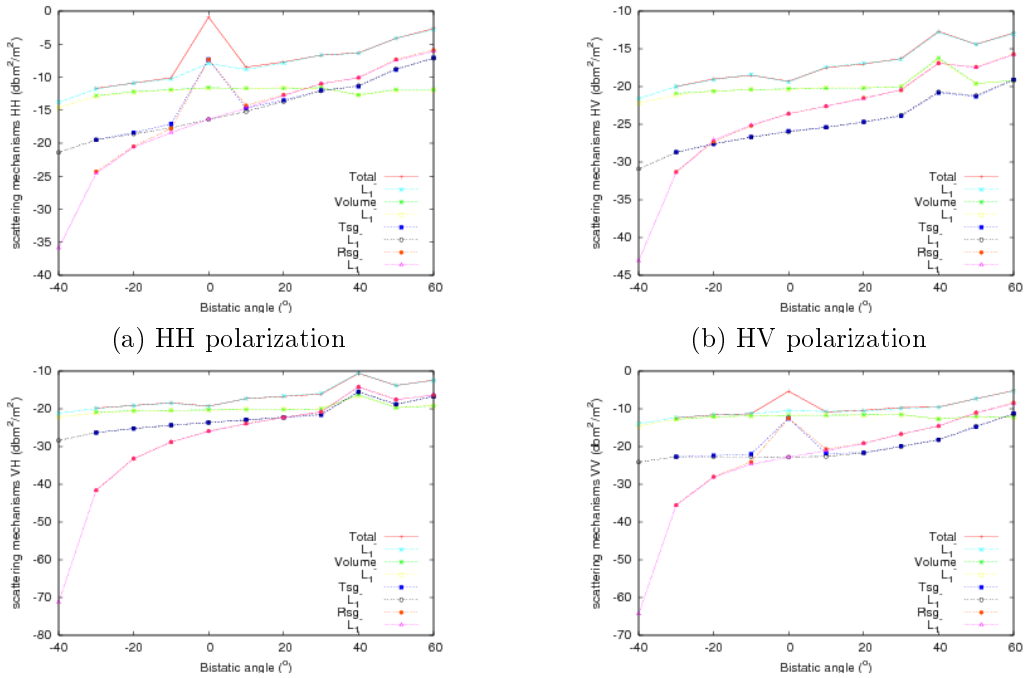

(a) HH polarization

(b) HV polarization

(c) VH polarization

(d) VV polarization

Figure 5.30: Scattering mechanisms comparison between the C2SRVoG with a typical trunk layer or with an empty one (noted above L_1^-) by layer number one giving the same attenuation, $h_{rms} = 0.5$ cm, $\theta^{\mathrm{T}} = 40^o$

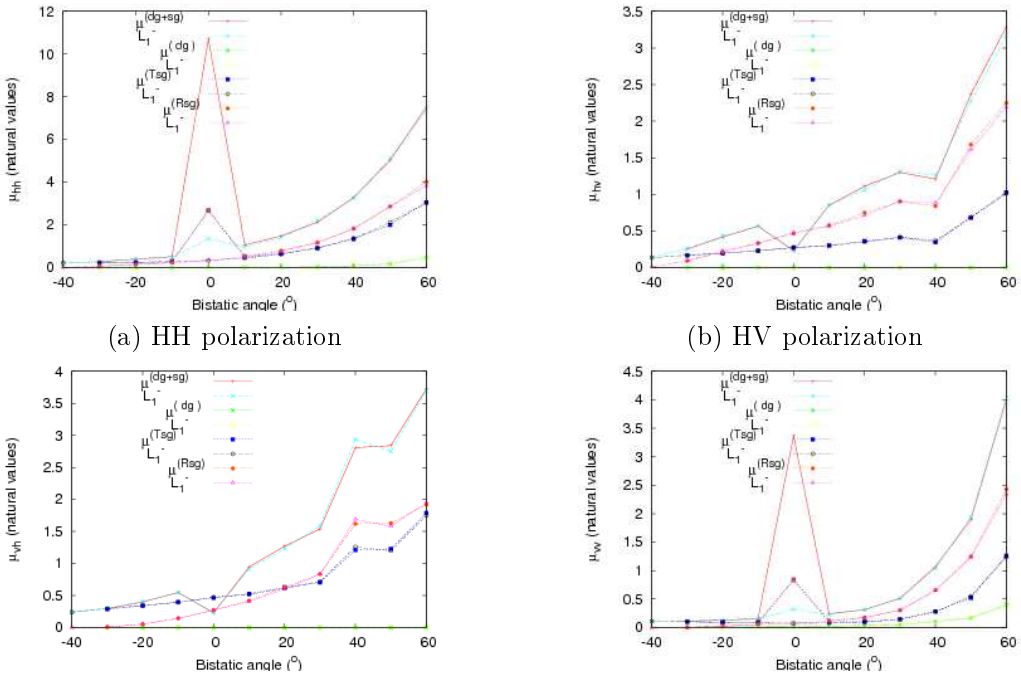

(a) HH polarization

(b) HV polarization

(c) VH polarization

(d) VV polarization

Figure 5.31: Scattering ratios comparison between the C2SRVoG with a typical trunk layer or with an empty one giving the same attenuation, $h_{rms} = 0.5$ cm, $\theta^{\mathrm{T}} = 40^o$

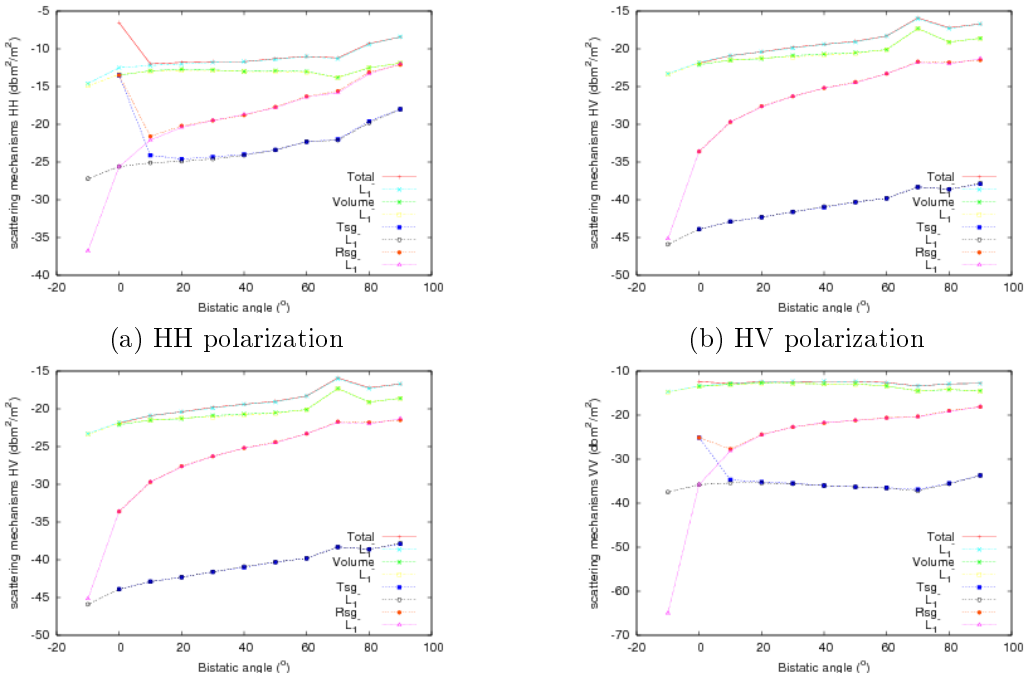

(a) HH polarization

(b) HV polarization

(c) VH polarization

(d) VV polarization

Figure 5.32: Scattering mechanisms comparison between the C2SRVoG with a typical trunk layer or with an empty one giving the same attenuation, $h_{rms} = 0.5$ cm, $\theta^{\mathrm{T}} = 70^o$

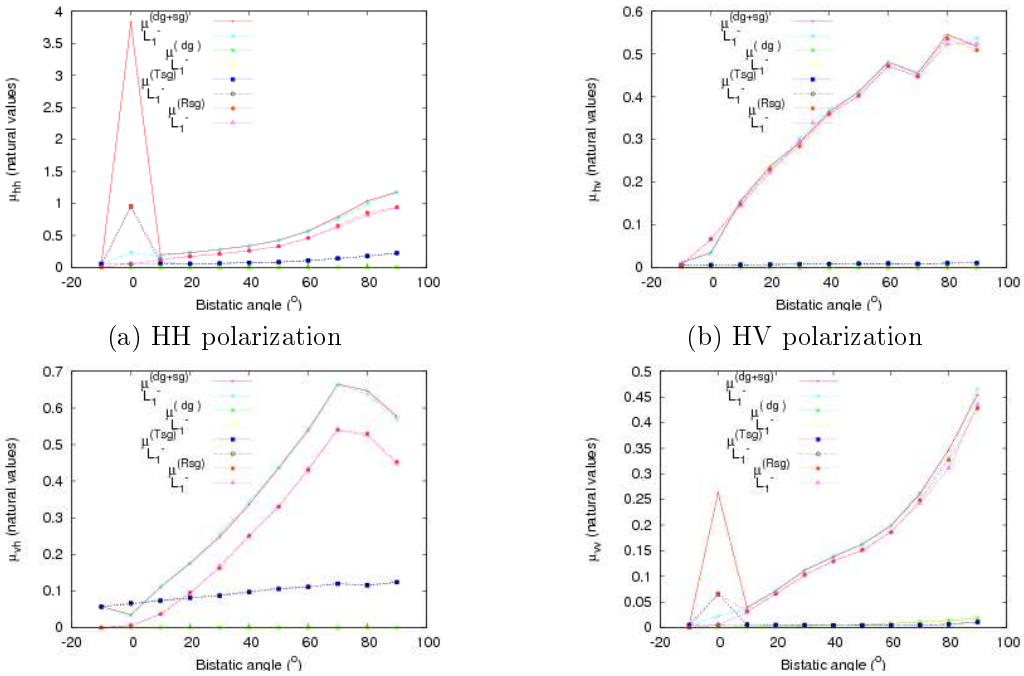

(a) HH polarization (b) HV polarization

(c) VH polarization (d) VV polarization

Figure 5.33: Scattering ratios comparison between the C2SRVoG with a typical trunk layer or with an empty one giving the same attenuation, $h_{rms} = 0.5$ cm, $\theta^{\mathrm{T}} = 70^{o}$

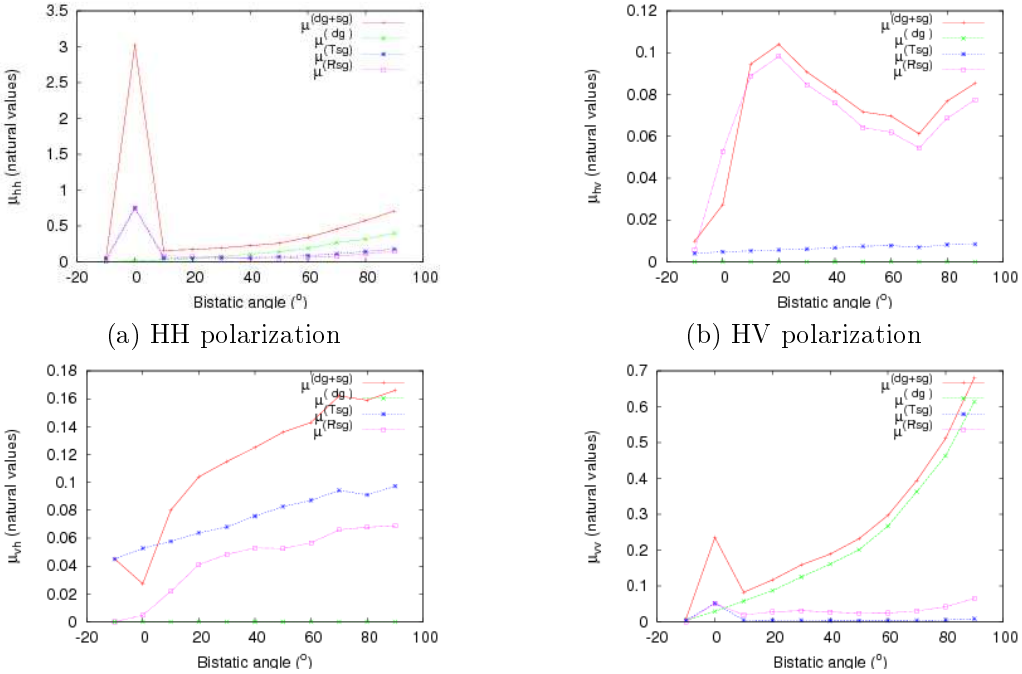

(a) HH polarization

(b) HV polarization

(c) VH polarization

(d) VV polarization

Figure 5.34: Scattering ratios versus bistatic angle, C2SRVoG, $h_{rms} = 3.5$ cm, soil wc = 50 %, $\theta^{\mathrm{T}} = 70^{o}$

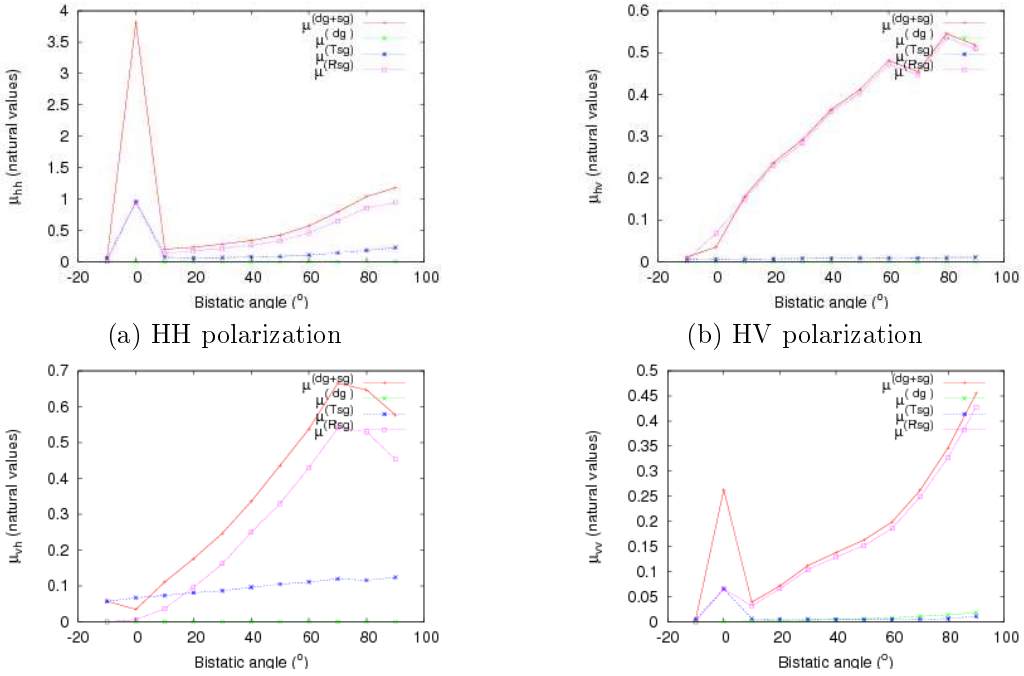

(a) HH polarization

(b) HV polarization

(c) VH polarization

(d) VV polarization

Figure 5.35: Scattering ratios versus bistatic angle, C2SRVoG, $h_{rms} = 0.5$ cm, $\theta^{\mathrm{T}} = 70^o$

Our inversion algorithm have thus been applied to these various cases. Again, we point out the importance of the constraints level and similarly to the CRVoG model, transmitter specular ground scattering ratios can be neglected in VV and HV polarizations whatever the soil nature. Concerning the retrieval performance, trunk layer and crown heights are ambiguous, as it already takes place for the 1SRoG case but likewise their sum is non biased, giving a good estimated value for the top of the vegetation (cf. figure 5.38). The coherences loci shown in figure 5.36 match the smooth and wet soil case, in order to give a higher importance to specular ground ratios, more challenging to retrieve than direct ones which are prominent for the rough case (cf. figure 5.34). The importance of the several baselines is also emphasized, to ensure the coherence loci separation, conditioning the discrimination capacity. For that purpose, the chosen baseline values must be sufficiently different, yet too high value (within naturally the ambiguity height requirement) may not be favourable, especially when the phases of volume and receiver specular ground only coherences are opposite and make the resulting one tumble (cf. the 20 m case in figure 5.37). Not surprisingly, extinction coefficients retrieval is not better in this configuration and present still an accuracy of about 30 %, but with the correct order between the highest and lowest ones in the C2SOψVoG case. Rather, setting the afore-mentioned constraints, the scattering ratios can be retrieved with about 10 % of accuracy (cf. figure 5.39), so that *the quantitative inversion may be reasonably pursued towards soil characteristics or first layer extinction coefficient.* Indeed, as far as applications are concerned, the retrieved scattering ratios were up to now considered like classification indicators, since it contains ratios between scattering matrix terms with respect to volume and double bounce mechanisms (cf. formula 5.74, subsection 5.4), as well as also the ambiguity between roughness and humidity. Notwithstanding, the considerable advantage of the GT-OR configuration is that the involved angles approaches the ideal situation with ($\theta_{\mathrm{T}} = \frac{\pi}{2}$, $\theta_{\mathrm{R}} = 0.$) for which the previously mentioned scattering ratios are theoretically equal to one, invoking scattering symmetry for a random volume. Since our configuration is barely different from this geometry, these equalities do not hold exactly but are quite close, as testified by the displayed scattering ratios. Indeed, this attests that specular ground scattering ratios with respect to the receiver depend only on the Fresnel coefficient in the nadir direction, that is also independently of vertical or horizontal polarizations. As a result, assuming a better estimation of the trunk layer and an a-priori extinction coefficient for the trunk layer in the nadir direction (quasi constant for a wide set of trunk types, as shown in figure 5.44, unlike the grazing direction much more sensitive), it is straightforward to deduce the nadir Fresnel coefficient (i.e $e^{-(\sqrt{2}kh_{rms})^2} \cdot \frac{\varepsilon_r - \sqrt{\varepsilon_r}}{\varepsilon_r + \sqrt{\varepsilon_r}}$. Furthermore, in order to solve the remaining ambiguity between roughness and humidity, the direct ground scattering ratios can be used, providing the polarization ratio which, together with the Fresnel nadir coefficient brings us to the solution, making use of a look-up table method illustrated with figure 5.45. This relies naturally on the scattering model validity (for instance the IEM one) and on the previous a-priori assumption, nevertheless it illustrates the great potential of such configuration with a major improvement in the quantitative inversion.

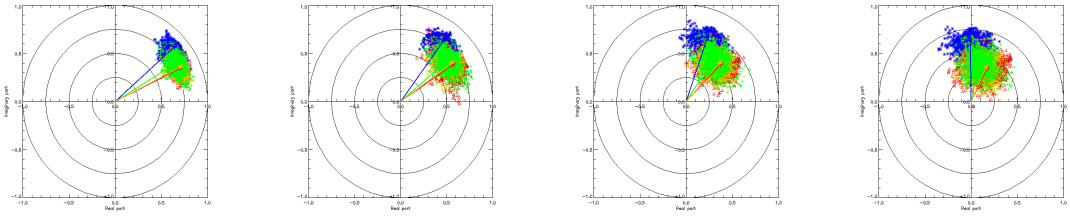

(a) b= 8 m (b) b= 10 m (c) b= 12.5 m (d) b= 15 m

Figure 5.36: Loci of the Pol-InSAR coherences resulting from the simulated C2SRVoG model with a rough and wet ground ($h_{rms} = 0.5cm$, $wc = 50\%$). Four different baselines – indicated above – are considered for the radar geometry involving a grazing transmitter $\theta^{\mathrm{T}} = 70^o$ and an off-nadir receiver

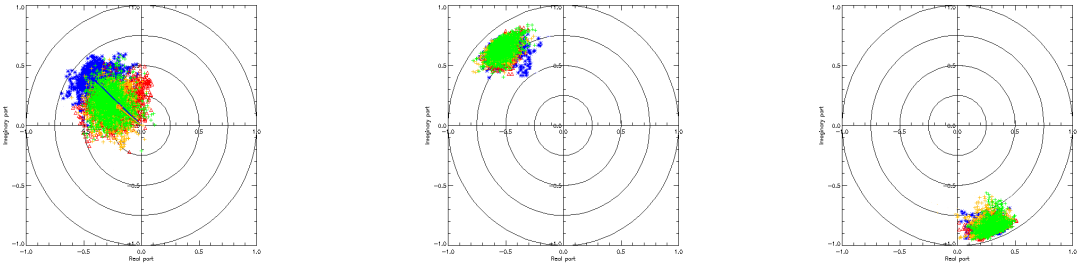

(a) total contribution (b) volume only (c) Rsg only

Figure 5.37: Loci of the Pol-InSAR coherences resulting from the simulated C2SRVoG model, $h_{rms} = 0.5cm$, $wc = 50\%$, b = 20 m, grazing transmitter : $\theta^{\mathrm{T}} = 70^o$ and off-nadir receiver

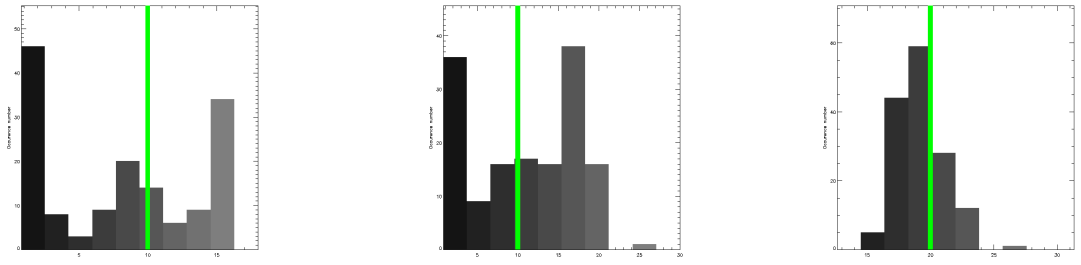

(a) trunk layer height (b) volume layer height (c) total height

Figure 5.38: Complex Pol-InSAR coherences loci, C2SRVoG, $h_{rms} = 0.5cm$, $wc = 50\%$, b = 20 m, grazing transmitter : $\theta^{\mathrm{T}} = 70^o$ and off-nadir receiver

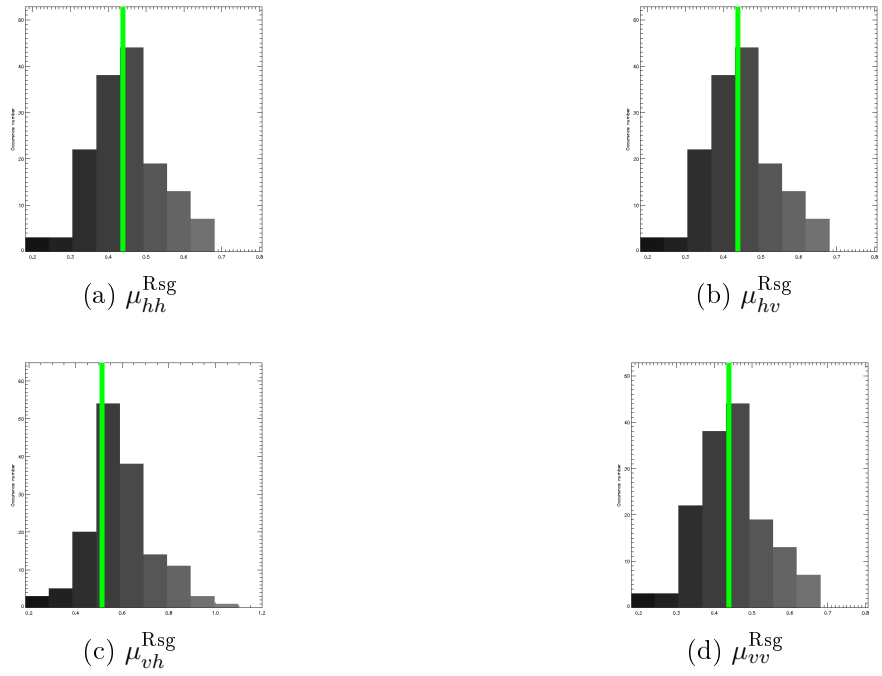

(a) μ_{hh}^{Rsg} (b) μ_{hv}^{Rsg}

(c) μ_{vh}^{Rsg} (d) μ_{vv}^{Rsg}

Figure 5.39: Retrieval results for the receiver specular ground scattering ratios, C2SRVoG model, 3 baselines, grazing transmitter : $\theta^{\mathrm{T}} = 70^o$ and off-nadir receiver

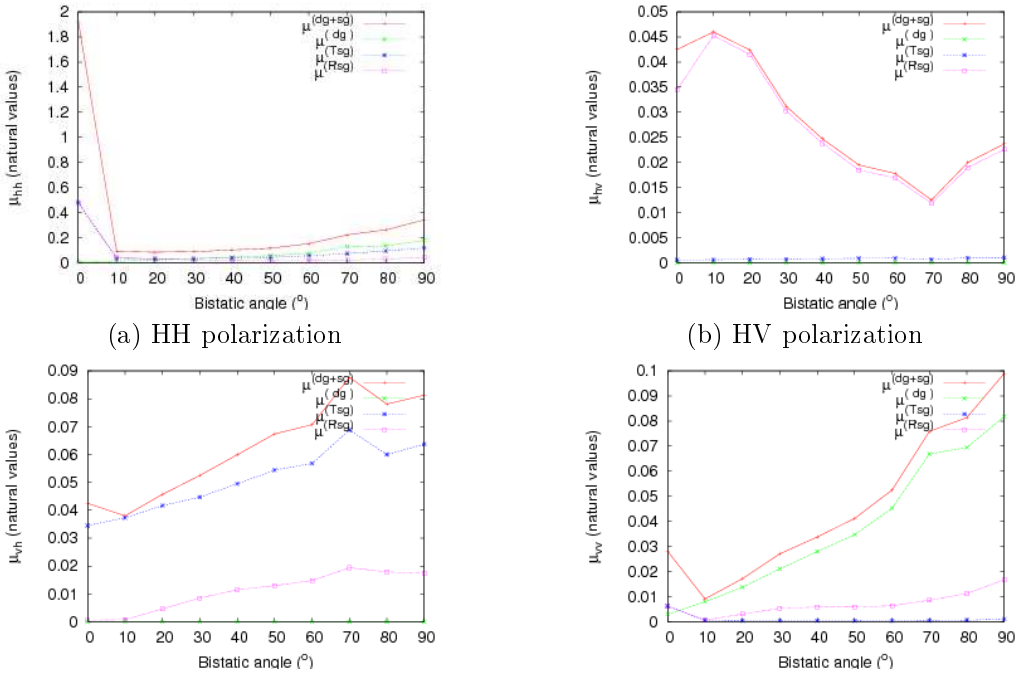

(a) HH polarization

(b) HV polarization

(c) VH polarization

(d) VV polarization

Figure 5.40: Scattering ratios versus bistatic angle, C2SRVoG, h_{rms} = 3.5 cm, wc = 10 % $\theta^{\mathrm{T}} = 70^{o}$

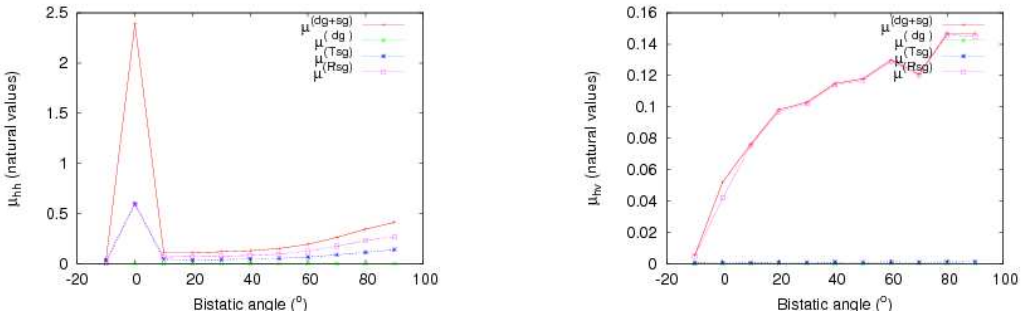

(a) HH polarization (b) HV polarization

(c) VH polarization (d) VV polarization

Figure 5.41: Scattering ratios versus bistatic angle, C2SRVoG, h_{rms} = 0.5 cm, wc = 10 % $\theta^{\mathrm{T}} = 70^{o}$

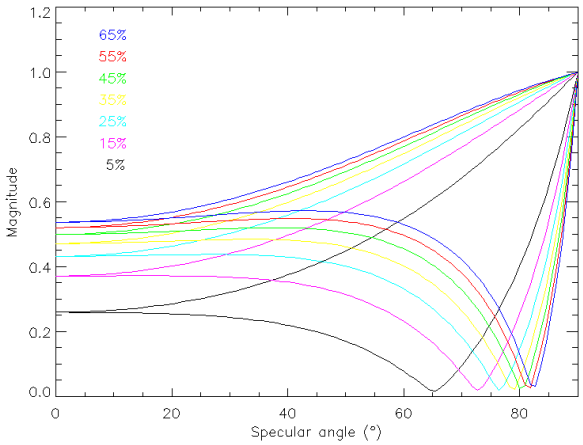

Figure 5.42: Ground reflectivity according to the modified Fresnel coefficient and versus specular angle with soil water content as parameter producing the colored sheaf of lines (constant roughness $h_{rms} = 2cm$

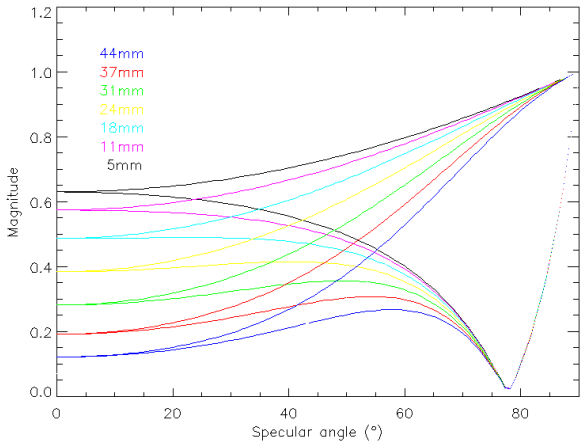

Figure 5.43: Ground reflectivity according to the modified Fresnel coefficient and versus specular angle with roughness (height standard deviation h_{rms}) as parameter producing the colored sheaf of lines, constant water content (wc = 30 %)

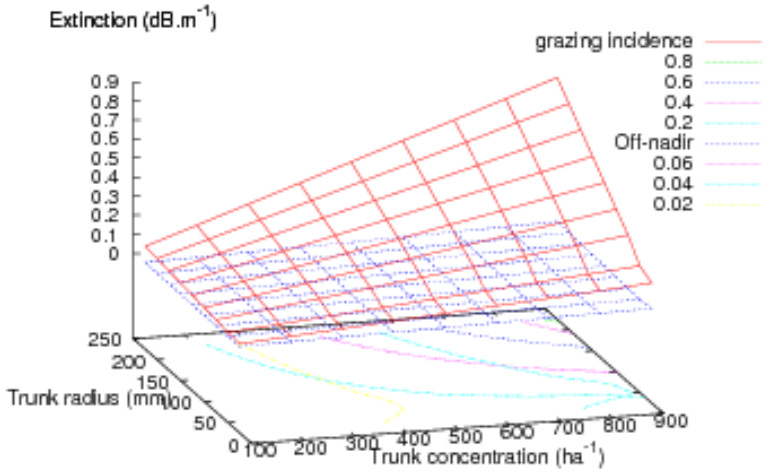

Figure 5.44: Extinction coefficient (vertical polarization) of a trunk layer, varying with trunk concentration and radius

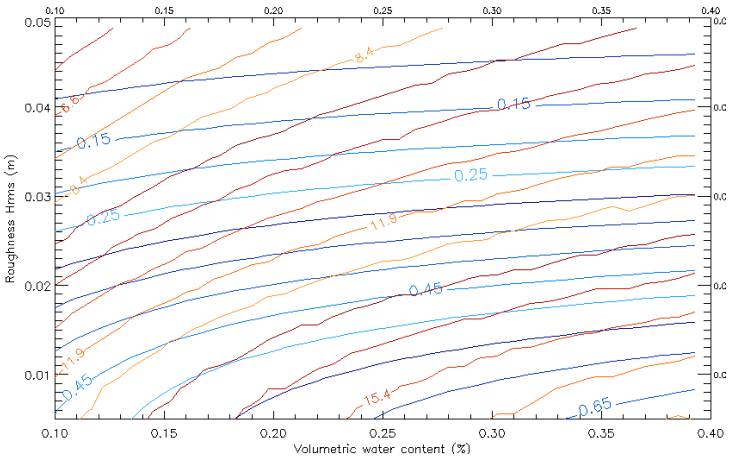

Figure 5.45: Contour line for the scattering coefficient difference vv-hh (dBm^2/m^2) as well as for the modified Fresnel coefficient, versus soil water content and ground roughness

5.8 Conclusion

In view of the presented results, the following conclusions can be drawn about the potential of bistatic Pol-InSAR to improve the forest descriptive parameters inversion and overcome the current monostatic drawbacks and limitations :

As the cornerstone of our inversion approach, the biPol-InSAR coherence theoretical formula, derived in sections 5.3 to 5.5 provides the link between measures (synthetic or experimental) and the FMDP, with possibly multibaseline acquisition corresponding to a given bistatic angle, within the incident plane. Whereas the overall formulation keeps the same structure as for the monostatic configuration, the interferometric phase sensitivity as well as specular ground terms exhibit paramount changes with the bistatic angle as formulated with their respective theoretical development. This additional complexity, conjugated to a more complete and realistic forest description with the CRVoG and C2SRVoG models, lead us to carry out a non linear optimization method for the quantitative inversion purpose. The inverse problem nature, conditioning naturally the retrieval feasibility, is assessed by means of simulated data generated by our ad-hoc model **MIPERS**. Whereas the study of the existence condition brings satisfying validation points between the analytical coherence derivations and the Monte-Carlo simulations, the uniqueness and stability ones turn out to be severe limitations. Hence comes the bistatic assets demonstrated through the proposal of a specific configuration, involving a grazing transmitter and an off-nadir passive receiver with three baselines.

Indeed, the interest of such configuration is twofold : whereas the three baselines acquisition enrich the measure vector, scattering properties with such bistatic angle enable to neglect either the transmitter or the receiver specular ground contributions or enable to maximize their difference, which simplifies thereby the unknown vector. Besides, on the contrary to the monostatic case, the scattering resulting from the possible first trunk layer can be neglected – in comparison with the upper volume's one – and thereby within the analytical decorrelation formula. With regards to the CRVoG, C2SRVoG or C2SOψVoG forest models, which constitute relevant and often encountered cases (respectively tropical and temperate forest), this combination brings paramount advantages concerning the inversion feasibility and robustness. Indeed, the total height can be retrieved with about 5 % accuracy, even for the structured two layered model with however a non negligible bias (around 30 %) between the trunk and the volume layer heights. The extinction coefficients turned out to be the most difficult to retrieve, with an accuracy and precision of about 30 %, ensued from the poor cost function sensitivity to these variables. The scattering ratios regarding direct ground can be retrieved with about 10 % accuracy as well as specular ground ones as long as either transmitter or receiver double bounce contributions can be neglected. This constitutes an important step and improvement, since it offers the possibility to follow the ground roughness and humidity, which range variation has been considered to ensure the inversion robustness for various possible soil nature. The quantitative inversion of the latter has been initiated but would need additional observables. Let alone the soil parameters retrieval, the main improvement lies in the more robust forest height estimation, in the sense of the quite wide range of humidity and roughness tested values. This comes from the employed forest description and the matching theoretical formulation which can cope rigorously with coupled effects, providing an alternative solution in case of weak direct ground scattering. Indeed, the contributions of the two latter remain the paramount condition to retrieve both topographic and volume heights and for the purpose of maximizing both, the receiver's off-nadir position is optimal in view of the wave path attenuation and on the top of suppressing also one extinction coefficient unknown.

Besides, concerning operational considerations, such configuration enables an L-band single

pass acquisition with an hybrid spaceborne transmitter - airborne receiver. On top of avoiding any temporal and ionospheric decorrelation disturbance, it offers the very interesting advantage of the hitchhiker opportunity configuration, with the widely used and mastered L band at the moment. Such configuration benefits also from the well known discretion of receiving only systems, since the presented direct and rather specular ground retrieved terms offer additional detection indicators, on the top of the likely topographic and layer's heights misestimation.

As further prospects, the retrieval formulation which has been put forward presents also the great advantage to be easily extended to various polarization combination (e.g compact polarization) and bistatic angles, which open the way to investigate the potential of multistatic Pol-InSAR, such as for instance those possibly derived from opportunistic GNSS-R acquisitions with airborne or ground based receiving station. Furthermore, concerning the inversion formulation itself, the statistical properties at the origin of complex coherences clouds distribution remain not exploited. Indeed, as suggested beforehand about the cost function, other distances than quadratic could be used, especially those derived from weighted or generalized least square methods which could profit from the coherences' variance information. Likewise, the radiometric levels are not used either, although their use would require another formulation, combining for instance the presented inversion to trial and errors iterative approach, based on forward models. Such progress, whether concerning the inversion algorithm itself – which could besides be of great interest even in monostatic – or concerning additional measures with multistatic passive acquisitions could enable to cope with the retrieval of additional layer heights and extinction coefficients, in order to obtain finer vegetation profile, as well as the quantitative inversion of soil humidity and roughness through the presented scattering ratios formulas. Finally, within the scope of testing the presented results with experimental data, the planning of airborne campaigns by means of ONERA and DLR facilities have been assessed and theoretical analysis, widened to other frequencies (P or C-band) and azimuthal bistatic angles is naturally worthwhile in this framework.

Bibliography

J.I.H. Askne, P.B.G Dammert, L.M.H. Ulander, and G. Smith. C-band repeat-pass interferometric sar observations of the forest. *IEEE Transactions on Geoscience and Remote Sensing*, 35:25–35, Jan. 1997.

P. Beckmann and A. Spizzichino. *The Scattering of Electromagnetic Waves From Rough Surfaces*. Pergamon, 1963.

R.A. Betts, P. M. Cox, S.E. Lee, and F.I. Woodward. Contrasting physiological and structural vegetation feedbacks in climate change simulations. *Nature*, 387:796–799, 1997.

J. Charney, P. H. Stone, and W.J. Quirk. Drought in sahara - biogeophysical feedback mechanism. *Science*, 187(4175):434–435, February 1975.

S.R. Cloude. *Polarimetry in Wave Scattering Applications*, volume 1. Academic Press, R. Pike & P. Sabatier edition, 2001. Chapter 1.6.2 in Scattering.

S.R. Cloude. Polarization coherence tomography. *Radio Science*, 41,RS4017, August 2006.

S.R. Cloude and K.P. Papathanassiou. Polarimetric sar interferometry. *IEEE Transactions on Geoscience and Remote Sensing*, 36:1551–1565, Sept 1998.

S.R. Cloude and K.P. Papathanassiou. Three stage inversion process for polarimetric sar interferometry. *Radar Sonar and Navigation IEE Proceedings*, 39(150):125–134, 2003.

S.R. Cloude and K.P. Papathanassiou. Forest vertical structure estimation using coherence tomography. In *International Geoscience and Remote Sensing Symposium (IGARSS)*, volume 5, pages 275–278. IEEE, 2008.

S.R. Cloude and M.L. Williams. A coherent em scattering model for dual baseline pol-insar. In *Geoscience and Remote Sensing Symposium (IGARSS)*, volume 3, pages 1423–1425. IEEE International, 2003.

S.R. Cloude, D.G. Corr, and M.L. Williams. Target detection beneath foliage using polarimetric sar interferometry. *Waves in Random Media*, 14:393–414, 2004.

P. M. Cox, R. A. Betts, C. D. Jones, S. A. Spall, and I. J. Totterdell. Acceleration of global warming due to carbon-cycle feedbacks in a coupled climate model. *Nature*, 409:184–187, 2000.

J.E.Jr. Dennis and R.B. Schnabel. *Numerical Methods for Unconstrained Optimization and Nonlinear Equations*. Prentice-Hall, 1983.

M. D'Errico and G. Fasano. Design of interferometric and bistatic mission phases of cosmo/skymed constellation. *Acta Astronautica*, 62 (2-3):97–111, 2008.

P. Dubois-Fernandez, H. Cantalloube, B. Vaizan, G. Krieger, R. Horn, M. Wendler, and V. Giroux. Onera-dlr bistatic sar campaign: planning, data acquistiton, and first analysis of bistatic scattering behaviour of natural and urban targets. *Radar, Sonar and Navigation, IEE Proceedings*, 153:214 – 223, June 2006.

B. J. Enquist, J. H. Brown, and G. B. West. Allometric scaling of plant energetics and population density. *Nature*, 395:163–165, 1998.

G. Fornaro, F. Serafino, and F. Soldovieri. Three-dimensional focusing with multipass sar data. *IEEE Transactions on Geoscience and Remote Sensing*, 41:507–517, March 2003.

Adrian K. Fung. *Microwave Scattering and Emission Models and Their Applications*. Artech House, 1994.

F. Gatelli, A.M. Guamieri, F. Parizzi, P. Pascali, C. Prati, and F. Rocca. The wavenumber shift in sar interferometry. *IEEE Transactions on Geoscience and Remote Sensing*, 32:855–865, Jul 1994.

S. Guillaso and A. Reigber. Scatterer characterisation using polarimetric sar tomography. In *International Geoscience and Remote Sensing Symposium (IGARSS)*, volume 4, pages 2685 – 2688. IEEE, 2005.

R. Hanssen and R. Bamler. Evaluation of interpolation kernels for sar interferometry. *IEEE Transactions on Geoscience and Remote Sensing*, 37:318–321, Jan 1999.

Ramon F. Hanssen. *Radar Interferometry: Data Interpretation and Error Analysis*, volume 2 of *Remote Sensing and Digital Image Processing*. Springer, 2001.

IPCC. *Climate Change 2007: Synthesis Report. Contribution of Working Groups I, II and III to the Fourth Assessment Report of the Intergovernmental Panel on Climate Change [Core Writing Team, Pachauri, R.K and Reisinger, A. (eds.)]*. Academic Press, November 2007.

A. Ishimaru. *Wave propagation and scattering in random media*, volume 1. Academic Press, 1978.

H. Jactel, E. Brockerhoff, and P. Duelli. A test of the biodiversity-stability theory: Meta-analysis of tree species diversity effects on insect pest infestations, and re-examination of responsible factors. *Forest Diversity and Function: Temperate and Boreal Systems*, 176:235–262, 2005.

G. Krieger and A. Moreira. Spaceborne bi- and multistatic sar : potential and challenge. In *Radar, Sonar and Navigation, Proceedings*, volume 153, pages 184–198, 2006.

G. Krieger, K. Papathanassiou, S. Cloude, A. Moreira, H. Fiedler, and M. Völker. Spaceborne polarimetric sar interferometry: Performance analysis and mission concepts. In *Proceedings of 2nd POLInSAR Workshop*. ESA, 2005.

T. Le Toan, S. Quegan, I. Woodward, M. Lomas, N. Delbart, and G. Picard. Relating radar remote sensing of biomass to modelling of forest carbon budgets. *Climatic Change*, 67:379–402, December 2005.

D. Massonnet and T. Rabaute. Radar interferometry: limits and potential. *IEEE Transactions on Geoscience and Remote Sensing*, 31:455–464, 1993.

T. Mette, K. Papathanassiou, I. Hajnsek, H. Pretzsch, and P. Biber. Applying a common allometric equation to convert forest height from pol-insar data to forest biomass. In *Geoscience and Remote Sensing Symposium (IGARSS), Anchorage (Alaska)*, volume 20-24. IEEE, 2004.

M. Nannini, R. Scheiber, and A. Moreira. Estimation of the minimum number of tracks for sar tomography. *IEEE Transactions on Geoscience and Remote Sensing*, 47:531–543, Feb. 2009.

H. Nies, O. Loffeld, and K. Natroshvili. Analysis and focusing of bistatic airborne sar data. *IEEE Transactions on Geoscience and Remote Sensing*, 45:3342–3349, Nov. 2007.

L. Pipia, X. Fabregas, A. Aguasca, and C. Lopez-Martinez. Atmospheric artifact compensation in ground-based dinsar applications. *Geoscience and Remote Sensing Letters, IEEE*, 5:88–92, Jan 2008.

M.J.D. Powell. *Variable metric methods in constrained optimization Mathematical Programming: The State of the Art.* Springer-Verlag, ed. a. bachem, m. Grötschel and b. korte edition, 1983.

J. Praks, F. Kugler, J. Hyyppa, K. Papathanassiou, and M. Hallikainen. Sar coherence tomography for boreal forest with aid of laser measurements. In *International Geoscience and Remote Sensing Symposium (IGARSS)*. IEEE, 2008.

JR dos Santos R Treuhaft, B Chapman. Estimating tropical-forest density profiles from multibaseline interferometric sar. In *European Conference on Synthetic Aperture Radar (EUSAR)*. VDE, Dresden, 2006.

A. Reigber and A. Moreira. First demonstration of airborne sar tomography using multibaseline l-band data. *IEEE Transactions on Geoscience and Remote Sensing*, 38:2142–2152, Sept. 2000.

M. Robert and B. Saugier. Contribution of terrestrial ecosystems to carbon sequestration. *Comptes Rendus - Geoscience*, 335 (6-7):577–595, 2003.

M. Rodriguez-Cassola, S.V. Baumgartner, G. Krieger, and A. Moreira. Bistatic terraSAR-x/f-SAR spaceborne/airborne sar experiment : Description, data processing and results. *IEEE Transactions on Geoscience and Remote Sensing*, 48(2):781–794, Feb. 2010.

P.A. Rosen, S. Hensley, I.R. Joughin, F.K. Li, S.N. Madsen, E. Rodriguez, and R.M. Goldstein. Synthetic aperture radar interferometry. *Proceedings of the IEEE*, 88:333–382, March 2000.

K. Saleh, A. Porte, D. Guyon ans P. Ferrazzoli, and J.P. Wigneron. A forest geometric description of a maritime pine forest suitable for discrete microwave models. *Geoscience and Remote Sensing, IEEE Transactions on*, 43:2024–2035, Sept. 2007.

J. Sanz-Marcos, P. Lopez-Dekker, J.J. Mallorqui, A. Aguasca, and P. Pratts. Sabrina: A sar bistatic receiver for interferometric applications. *Geoscience and Remote Sensing Letters, IEEE*, 4:307–311, April 2007.

S. Tebaldini. Single and multipolarimetric sar tomography of forested areas: A parametric approach. *IEEE Transactions on Geoscience and Remote Sensing*, PP(99):1 –13, 2010.

R. Touzi, A. Lopés, J. Bruniquel, and P.W. Vachon. Coherence estimation of sar imagery. *IEEE Transactions on Geoscience and Remote Sensing*, 37:135–149, 1999.

R.N. Treuhaft and P. R. Siquiera. Vertical structure of vegetated land surfaces from interferometricand polarimetric radar. *Radio Science*, 35(1):141–177, 2000.

R.N. Treuhaft, Soren N. Madsen, Mahta Moghaddam, and Jakob J. van Zyl. Vegetation characteristics and underlying topography from interferometric radar. *Radio Science*, 31:1449–1485, November-December 1996.

R.N. Treuhaft, G.P. Asner, B.E. Law, and S.V. Tuyl. Forest leaf area density profiles from the quantitative fusion of radar and hyperspectral data. *Journal Of Geophysical Research*, 107, 2002.

L. Tsang and J.A. Kong. *Scattering of Electromagnetic Waves*, volume Theories and applications of *Remote Sensing and Digital Image Processing*. Wiley Series, 2000.

F.T. Ulaby, R.K. Moore, and A.K. Fung. *Microwave Remote Sensing: Active and Passive*, volume I, Radar Remote Sensing and Surface Scattering and Emission Theory of *Advanced Book Program*. Addison-Wesley, 1981.

I. Walterscheid, J.H.G. Ender, and O. Loffeld. Bistatic image processing for a hybrid sar experiment between terrasar-x and pamir. In *Geoscience and Remote Sensing Symposium (IGARSS)*, pages 1934–1937. IEEE International Conference, 2006.

I.H. Woodhouse. Predicting backscatter-biomass and height-biomass trends using a macroecology model. *Geoscience and Remote Sensing, IEEE Transactions on*, 44:871–877, April 2006.

M. Younis, R. Metzig, and G. Krieger. Performance prediction of a phase synchronization link for bistatic sar. *Geoscience and Remote Sensing Letters, IEEE*, 3:429–433, July 2006.

H.A. Zebker and J. Villasenor. Decorrelation in interferometric radar echoes. *IEEE Transactions on Geoscience and Remote Sensing*, 30:950–959, Sept 1992.

Conclusion

As a general conclusion, the main advantages of the bistatic configuration for forest remote sensing turn out to be intrinsic to specific geometries, for which the sensitivity of SAR observables to forest characteristics is enhanced.

Based on electromagnetic simulations from the developed model MIPERS the specific advantages of these configurations have been set forth regarding the resulting improvement of two fundamental retrieval approaches in monostatic (respectively detailed in chapters 4 & 5). On the first hand, the retrieval based on the sensitivity of SAR intensities to biomass has been improved using two types of geometries – specular and transverse – which enable to outperform the monostatic range of retrieved biomass, limited by the saturation phenomenon and marginal sensitivities. On the second hand, the capability of bistatic multi-baseline vectorial interferometry to retrieve quantitatively forest model descriptive parameters has been also demonstrated in comparison to the monostatic configuration and likewise for with a specific bistatic geometry : this innovative acquisition is formed by a grazing transmitter and an off-nadir receiver. The employed quantitative inversion of the forest model descriptive parameters is based on a preliminary theoretical formulation of the analytical operator specific to the bistatic Pol-InSAR coherences. On top of improving the robustness of the forest height estimation, the main achievement lies in the inversion of scattering ratios related to the coupling terms, made possible by an carefully crafted relationship involving an equivalent fictive point on the ground.

For both approaches, the ad-hoc forward model MIPERS precisely developed in order to simulate bistatic Pol-InSAR observables has shown its great interest. Indeed, this model has been used to analyse the bistatic scattering behaviour of the various observables, permitting thereby to point out the specific configurations which make the inversion algorithm – mostly illy-posed – feasible. Concerning the scattering analysis, remarkable properties intrinsic to the bistatic configurations has been stressed in the third chapter, converging likewise to more favourable configurations for retrieval. In addition, the study of the consequences of the medium symmetries on the observables brings us to original results concerning the characterization of disoriented coherent target and its presence through a random media like vegetation, in the detection framework. Such approaches truly plea in favour of fully polarimetric acquisition, even more for tilted bistatic plane configurations for which the introduction of the β polarization has revealed its greatest importance.

Moreover, the possibly stringent operational constraints coming with SAR processing in bistatic have been carefully taken into account for the previously optimal configurations, set forth regarding criteria for the inversion feasibility. Overall, we restrict the investigated configurations to a single bistatic angle in order to give generic conclusions concerning the intrinsic potential of bistatic geometry. Indeed, as presented in the first chapter, even if experimental bistatic data are not yet widely available, it seems that most of the operational hindrances which have limited for a long time the use of many promising bistatic concepts can be currently overcome, as testified by the increasing number of bistatic campaign projects.

This consideration brings us to stress the fact that our conclusions have been drawn on account of simulated results. Though extensively validated from theoretical considerations as well as monostatic data, our great interest for the following investigations is naturally directed towards the analysis of experimental data corresponding to the proposed configurations. As far as further prospects are concerned, on top of the improvements concerning the retrieval methods – already pointed out in the previous intermediate conclusions – our overall approach contributes to pave the way for a general inversion scheme combining the forward model to the afore-mentioned retrieval algorithms. As a matter of fact, such method has been up to now implicitly followed but the nowadays computing performance makes possible the incorporation of the forward model within a feedback loop, directed by the specific retrieval methods in order to use the whole set of

combination between the experimental measures at our disposal. Besides, such approach gives a great importance to the forward model validity, its feasibility will be naturally limited by the capacity of the simulations to ensure the inverse problem existence condition, which thereby truly plea in favour of further improvements concerning the challenging aspects in electromagnetism for forest scattering.

Appendix A

Stationary Phase Method & First Order Propagation Operator

In subsection 5.3.1, with the aim of making explicit the propagation operator, the calculation of an integral of the following shape has been arisen :

$$\begin{aligned} \mathcal{I} &= \int_{\Re^n} g(r) e^{j\Phi(r)} dr \\ &= \int_{\Re^n} g(x_1, \cdots, x_n) e^{j\Phi(x_1,\cdots,x_n)} dr \end{aligned} \tag{A.1}$$

As demonstrated in [Ishimaru, 1978], if the phase function exhibits a stationary phase point $M^s(x_1^s, \cdots, x_n^s)$ satisfying :

$$\frac{\partial \Phi}{\partial x_1}\Big)_{M^s} = \cdots = \frac{\partial \Phi}{\partial x_n}\Big)_{M^s} = 0$$

then such integral can be approximated by :

$$\mathcal{I} = g(x_1^s, \cdots, x_n^s) \frac{(j2\pi)^{n/2}}{\sqrt{\Delta}} e^{j\Phi(x_1^s,\cdots,x_n^s)} \tag{A.2}$$

where the Hessian Δ is the determinant of the following second derivatives matrix :

$$\begin{bmatrix} \Phi_{11} & \cdots & \Phi 1n \\ \vdots & & \\ \Phi_{n1} & \cdots & \Phi nn \end{bmatrix}, \quad \Phi_{ij} = \frac{\partial^2 \Phi}{\partial x_i \partial x_j \Phi}$$

Considering the propagation operator (cf. section 5.3.1) from the transmitter T — hereby at the coordinates system origin defined in figure A.1 — to a scatterer j at (x_j, y_x, z_j), the following case holds :

$$\begin{aligned} \Phi &= k(r + \rho) \\ g(\vec{r}, \vec{r}_j) &= \langle f(\vec{r} - \vec{r}_T; \vec{r}_j - \vec{r}) \rangle \end{aligned} \tag{A.3}$$

with $r^2 = x^2 + y^2 + z^2$, $\rho^2 = (x_j - x)^2 + (y_j - y)^2 + (z_j - z)^2$.
The first partial derivatives are thus :

$$\begin{aligned} \frac{\partial \Phi}{\partial x} &= k\big(\frac{x}{r} - \frac{x_j - x}{\rho}\big) \\ \frac{\partial \Phi}{\partial y} &= k\big(\frac{y}{r} - \frac{y_j - y}{\rho}\big) \end{aligned} \tag{A.4}$$

A stationary point (x_s, ys) should then satisfy :

$$\frac{x_s}{x_j} = \frac{y_s}{y_j} = \frac{r_s}{r_s + \rho_s} \tag{A.5}$$

This relation is verified by several points which can be determined from geometrical considerations : as an example, within the region bounded by the conditions $z \leq 0$ and $y \geq 0$, the point S' can be constructed as in figure A.1 with the angles relation $\pi - \beta_{\mathrm{S}'} = \beta_j$. Indeed, relation A.5 can be checked using the Thales' theorem considering the triangle of vertices T, j and $j^{\aleph}$ (defined as the mirror image of j with respect to the plane z=0) and the parallel lines to the vertical directions ($\vec{z}$) passing by S' and j.

Likewise, another point S" can be emphasized within the region $z \geq z_j$ and $y \geq 0$ and more interestingly the point S as far as the volume integration of interest concerns only the $z_{\mathrm{T}} - h \leq z \leq z_{\mathrm{T}}$) one. Thus S will be used as the stationary phase point, hence the focus on the forward direction in view of its position belonging to the line passing by T and j. Besides, the Hessian calculation does not present any difficulties and can be expressed according to the coordinates of S as follows :

$$\sqrt{\Delta} = k\frac{(r_s + \rho_s)^2 + (x_s + y_s)^2}{r_s \rho_s} \tag{A.6}$$

The formula A.2 with n=2 and $0 < z < z_j$ yields thus to :

$$\mathcal{I} = \langle f(\vec{r}_s - \vec{r}_T; \vec{r}_j - \vec{r}_s)\rangle \frac{j2\pi}{z_j} e^{ik(r_s + \rho_s)} \tag{A.7}$$

The propagation operator in its scalar form can then be made explicit like :

$$\begin{aligned}
\Xi_T^j &= E_0 \frac{e^{jk|\vec{r}_j - \vec{r}_T|}}{|\vec{r}_j - \vec{r}_T|} + \iiint \rho(r) \frac{e^{jk(|\vec{r}_j - \vec{r}| + |\vec{r}_j - \vec{r}_T|)}}{|\vec{r}_j - \vec{r}| \cdot |\vec{r}_j - \vec{r}_T|} \langle f(\vec{r} - \vec{r}_T; \vec{r}_j - \vec{r})\rangle d^3 r \\
&= E_0 \frac{e^{jkr_j}}{r_j} + \int_{z_T - h}^{z_j} E_0 \langle S_f(\vec{r}_j)\rangle \frac{j2\pi}{z_j} e^{ikr_j} dz \\
&= E_0 \frac{e^{jkr_j}}{r_j} (1 + \langle S_f(\vec{r}_j)\rangle j2\pi \frac{r_j}{z_j} l_j) \\
&\quad \text{(with } l_j = z_j - (z_{\mathrm{T}} - h) \text{the vertical distance} \\
&\quad \text{from the scatterer j to the top of the volume layer)} \\
&= E_0 \frac{e^{jkr_j}}{r_j} (1 + \langle S_f(\vec{r}_j)\rangle \frac{j2\pi l_j}{\cos\theta_T}) \\
&= \frac{E_0}{r_j} \exp[jkr_j + j\frac{2\pi l_j}{\cos\theta_T} \langle S_f(\vec{r}_j)\rangle] \\
&= \frac{E_0}{r_j} \exp\left[j\big(kr_j + \frac{2\pi l_j}{\cos\theta_T} \langle S_f(\vec{r}_j)\rangle\big)\right]
\end{aligned} \tag{A.8}$$

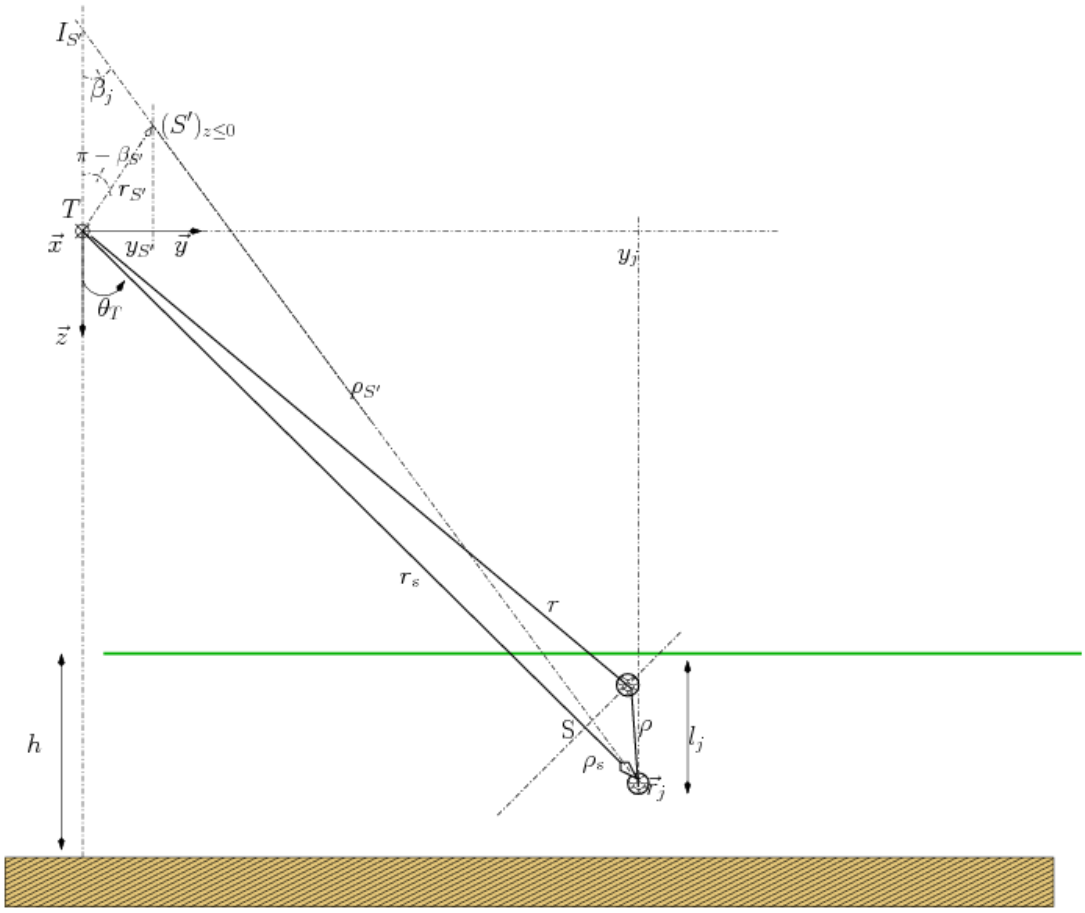

Figure A.1: Stationary phase points

Appendix B

Interferometric Sensitivity, Distance Ambiguities Derivation

In section 5.3.1, the derivation of interferometric cross correlation introduced the derivatives of the range difference from a elementary volume element towards the antennas forming the baseline ($b = \|\overrightarrow{R_1R_2}\|$). Their analytical expressions, closely linked to the geometrical parameters of the configuration, are the purpose of the following derivations. Considering a given point P, the distance difference between the paths towards the receiving antennas at R_1 and R_2 (cf. figure B.1) can be approximated as follows :

$$\begin{aligned} r_1 - r_2 &= -\frac{\overrightarrow{PR_1} \cdot \overrightarrow{R_1R_2}}{\|\overrightarrow{PR_1}\|} \\ &= -b\big(\sin\theta_1 \sin\varphi_1 \sin\theta_b + \cos\theta_1 \cos\theta_b\big) \end{aligned} \tag{B.1}$$

assuming a Taylor development for $\|\overrightarrow{PR_1}\| >> b$. The angles used above are defined by the link between spherical coordinates from the origin R_1 and Cartesian ones so that :

$$\begin{aligned} \cos\theta_1 &= \frac{H-z}{r_1} \\ \sin\theta_1 \sin\varphi_1 &= \frac{y}{r_1} \\ \sin\theta_1 \cos\varphi_1 &= \frac{x}{r_1} \end{aligned} \tag{B.2}$$

and θ_b (R_2 being restricted to the plane of yOz for the sake of simplicity) with :

$$\overrightarrow{R_1R_2} = -\sin\theta_b \hat{y} + \cos\theta_b \hat{z}$$

The differentiation from equation (B.1) leads to :

$$\begin{aligned} \partial(r_1 - r_2) &= b\big(\cos\theta_1 \sin\varphi_1 \sin\theta_b - \sin\theta_1 \cos\theta_b\big)\partial\theta_1 \\ \partial(r_1 - r_2) &= b\big(\sin\theta_1 \cos\varphi_1 \sin\theta_b\big)\partial\varphi_1 \end{aligned} \tag{B.3}$$

Keeping z and φ constant, the first equality in B.2 gives :

$$\partial r = r \tan\theta \partial\theta$$

hence :

$$\begin{aligned}\frac{\partial(r_1-r_2)}{\partial r}|_{z,\varphi} &= \frac{b\big(\sin\theta_1\cos\theta_b-\cos\theta_1\sin\varphi\sin\theta_b\big)}{r\tan\theta_1}\\ \frac{\partial(r_1-r_2)}{\partial\varphi}|_{\varrho_1,z} &= b\sin\theta_1\sin\theta_b\cos\varphi_1\end{aligned} \tag{B.4}$$

This brings us actually to consider the restriction for P to belong to the iso-range bistatic ellipsoid (noted $\mathcal{E}$ as the set of all the points located at a similar distance towards the transmitter or the receiver) in order to consider a point within a given resolution cell. This originates the core of the difference with the monostatic and in this case, the hereby notation is used :

$$\varrho_{1,2} = r_{1,2}|_{P\in\mathcal{E}} \tag{B.5}$$

In view of the approximation employed in equation (B.1) and the resulting independence on the distance r, it can be noted that the introduced parallax for P restricted to a spherical iso-range domain or to an ellipsoid one (cf. the variation from P to P' shown in figure B.1) can be assumed equal :

$$\varrho_1-\varrho_2 \simeq r_1-r_2$$

The difference in bistatic comes with the relationship between $\partial\theta$ and ∂z which can be derived from the ellipsoid equation, that is for $P\in\mathcal{E}$:

$$R_1P = \varrho(\theta_1,\varphi_1) = \frac{a_{\mathcal{E}}(1-\epsilon)}{1+\epsilon sin\varphi'\sin(\theta_1-\vartheta)} \tag{B.6}$$

with a and ϵ respectively the semimajor axis and the eccentricity while $\theta_1-\vartheta$ matches the complementary angle of the true anomaly, ϑ being defined as the rotation along $\hat{x}$ to come from the local coordinate system $\mathbf{R}'$ to the reference one $\mathbf{R}$ Equations B.2 and B.6 can then be combined as follows :

$$\begin{aligned}\cos\theta_1 &= \frac{H-z}{\varrho(\theta_1,\varphi_1)}\\ &= \frac{H-z}{a_{\mathcal{E}}(1-\epsilon)}\big[1+\epsilon(\cos\vartheta\sin\varphi_1\sin\theta_1-\sin\vartheta\cos\theta)\big]\\ \text{so that :}\quad -\frac{\sin\theta_1\partial\theta_1}{\cos\theta_1} &= -\frac{\partial z}{H-z}+\frac{\epsilon\big[\cos\vartheta\sin\varphi_1\cos\theta_1\partial\theta_1+\sin\vartheta\sin\theta_1 d\theta_1\big]}{1+\epsilon(\cos\vartheta\sin\varphi_1\sin\theta_1-\sin\vartheta\cos\theta)\big]}\\ \text{and finally :}\ \partial\theta_1 &= \frac{\partial z}{H-z}\cdot\Big[\tan\theta_1+\frac{\epsilon\big[\cos\vartheta\sin\varphi_1\cos\theta_1+\sin\vartheta\sin\theta_1\big]}{1+\epsilon\big[\cos\vartheta\sin\varphi_1\sin\theta_1-\sin\vartheta\cos\theta_1\big]}\Big]^{-1}\end{aligned} \tag{B.7}$$

Therefore, it can be deduced with equations (B.1) and B.5 :

$$\begin{aligned}\frac{\partial(\varrho_1-\varrho_2)}{\partial z} &= \frac{\partial(\varrho_1-\varrho_2)}{\partial\theta}\cdot\frac{\partial\theta}{\partial z}\\ &= \frac{b\big(\sin\theta_1\cos\theta_b-\cos\theta_1\sin\varphi_1\sin\theta_b\big)}{\varrho\cos\theta_1}\\ &\qquad\Big[\tan\theta_1+\frac{\epsilon\big(\cos\vartheta\sin\varphi_1\cos\theta_1+\sin\vartheta\sin\theta_1\big)}{1+\epsilon\big(\cos\vartheta\sin\varphi_1\sin\theta_1-\sin\vartheta\cos\theta_1\big)}\Big]^{-1}\end{aligned} \tag{B.8}$$

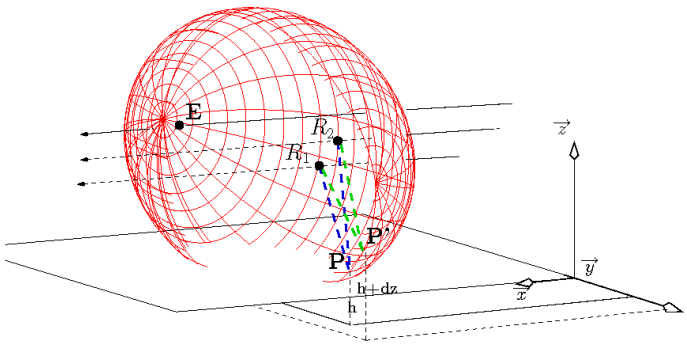

Figure B.1: Geometry of the envisioned bistatic interferometric acquisition and resulting iso-range ellipsoid defining the points P and P' loci to derive the subsequent ambiguity height.

At this point, the ambiguity height noted h_a can be introduced by the relation :

$$\frac{\partial(\varrho_1 - \varrho_2)}{\partial z}_{|_{\varrho_1,\varphi_1}} = \frac{\lambda}{h_a}$$

which illustrates the fact that an height increment of $\Delta z = h_a$ of P $\in \mathcal{E}$ leads to a parallax $d\theta_1$ (cf. figure 5.1) large enough to wrap the interferometric phase with a 2π shift :

$$\Delta\phi(P, P') = k\Delta\varrho(P, P') = k\frac{\lambda}{h_a}\Delta z$$

hence the following formula for the bistatic ambiguity height :

$$\boxed{h_a = \frac{\lambda\varrho\cos\theta_1}{\big(\sin\theta_1\cos\theta_b - \cos\theta_1\sin\varphi_1\sin\theta_b\big)} \cdot \Big[\tan\theta_1 + \frac{\epsilon\big(\cos\vartheta\sin\varphi_1\cos\theta_1 + \sin\vartheta\sin\theta_1\big)}{1 + \epsilon\big(\cos\vartheta\sin\varphi_1\sin\theta_1 - \sin\vartheta\cos\theta_1\big)}\Big]} \tag{B.9}$$

While the second term within the brackets indicated above matches the additional factor which takes into account the bistatic specificity with the ellipsoid parameters (ϵ, ϑ), the first one is consistent with the classical monostatic formula. Indeed $\epsilon = 0$ and a non depointing system (without squint i.e $\varphi_1 = 0$) gives :

$$\begin{aligned} h_a &= \frac{\lambda a_{\mathcal{E}}\cos\theta_1}{b\sin(\theta_1 - \theta_b)} \cdot \tan\theta_1 \\ &= \frac{\lambda r_1\sin\theta_1}{b\sin(\theta_1 - \theta_b)} \end{aligned} \tag{B.10}$$

This expression is particularly important since it constitutes the link between the height information and the estimation of the measured phase — and its associated accuracy. Its choice is thus paramount to design interferometric systems : in a general way it lies in the trade-off between a value small enough to bring a good phase sensitivity and large enough to limit phase

unwrapping. With the aim of forest height estimation, it is relevant to use the range 50 to 120 meters for the ambiguity height. In view of its expression (formula B.9) and its dependency towards system parameters, the question is thus how stringent is this relation to reach this range, which mainly leads to the choice between single platforms or separated ones (e.g in the case of too large baselines to be carried on the same mast). If the impact of the aforementioned monostatic term within equation (B.9) is well-known (determined by the wavelength, range, incidence and orthogonal baseline values), the bistatic additional term deserves herein our attention and is the purpose of the following numerical analysis.

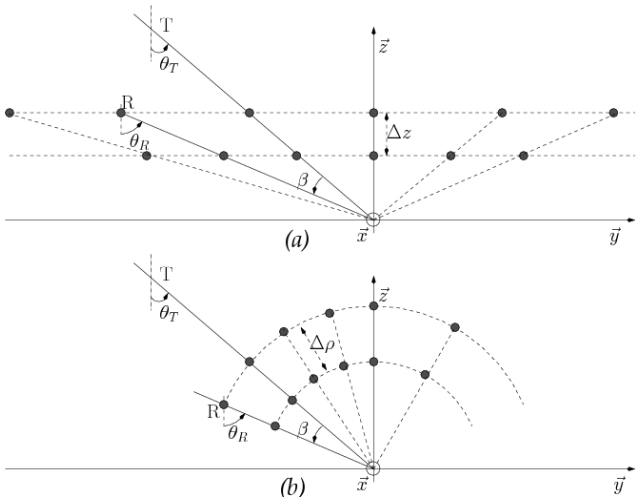

Figure B.2: Sketches representing the variation of the receiving platform (R, carrying the baseline) with the black points illustrating the different positions for a given transmitter position (T). As shown above, the receiver's height or range towards the scene are kept constant as a parameter while varying β respectively for the upper (a) and below (b) cases.

As shown in figure B.2, two kinds of position variation of the receiving platform — carrying the baseline — are considered with a given localization of the transmitter. For both, these simulations come thereby with the corresponding ambiguity height variation versus the bistatic angle, as shown in figures B.3 and B.4. In order to assess and emphasize the importance of the bistatic term, also plotted (dot lines) are the ambiguity height matching the monostatic equivalent configurations. For such comparisons, the latter are defined considering only the receiving platform which plays also the role of the transmitter, as in a classical single-pass configuration. Although the null bistatic angle case does not match the monostatic configuration (the ranges towards the scene r_{T} and r_{R} being different), the ambiguity height is actually the same (cf. the line intersection $\beta = 0^o$ in both figures). Indeed, it can be stressed that for a given scattering and bistatic angles (θ_{R} and β), the ambiguity height is invariant to the range r_{T}, as long as the range cell dimensions are small in comparison with the distances towards T and R (i.e $PP' \ll r_{\mathrm{T,R}}$). This property comes from the fact that the tangent to the ellipsoid is given by the normal to the bisectrix $\hat{\beta}$ — as reminded in figure D.2 — and is particularly important from the operational point of view. Indeed, it offers the possibility of a mixed spaceborne-airborne acquisition keeping about the same baseline length for the airborne receiving platform, that is sufficiently small to be carried by the same aircraft.

As a result, the bistatic additional term impact goes up with the difference between the ellipsoid tangent and the equivalent monostatic one. As shown in both figures B.3 and B.4,

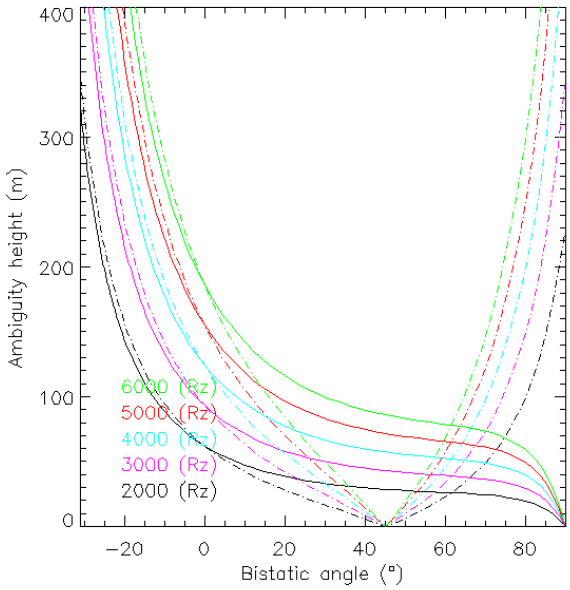

Figure B.3: Interferometric ambiguity height sensitivity versus bistatic angle, with a constant baseline angle ($\theta_b = -60^o$, b = 10 m, implying a changing orthogonal baseline $b_\perp$). Each colour is associated to a given receiver altitude (R_z) for both bistatic and equivalent monostatic configurations plotted respectively with plain and dot lines. The equivalent monostatic configuration is defined from the receiver, which in this case plays also the transmitter role from R_1. The transmitter is set in a medium Earth orbit by T $\left(., -3.10^5, 3.10^5\right)$, hence $\theta_{\mathrm{R}} = 45^o$ for $\beta = 0$ in the monostatic case.

this matches naturally the increasing bistatic angle value $|\beta|$, weighted though by the first term in B.9 (before the brackets) which contains the ratio between the vertical projection of $\vec{r}_{\mathrm{R}}$ (i.e the receiver height R_z) over the orthogonal baseline.

These two latter quantities have been kept constant respectively in figures B.3 and B.4 for a varying bistatic angle, as shown more explicitly within the sketches (a) and (b) depicted in B.2. In addition, the range r_{R} or its vertical projection $R_z = r_{\mathrm{R}} \cos\theta_{\mathrm{R}}$ has been chosen as a parameter of the study respectively in (a) and (b). It originates the displayed sheaf of lines which values goes up together with the receiver's range which is consistent with the multiplicative range factor ϱ in B.9.

For both cases, two bistatic angles matching to null values for the ambiguity heights can be noticed. These angles do correspond actually to the monostatic off-nadir position and the specular bistatic one for which the normal vector to the spherical or ellipsoid iso-ranges is also perpendicular to the ground, resulting likewise in resolution singularities and in cases where imaging processing is not tractable (sounder or specular configurations). The range resolution being infinite for this theoretical case, it simply traduces the fact that two points of identical height can be ambiguous, since they can arbitrarily move along a horizontal line. Mathematically, $\theta_{\mathrm{R}} = 0$ directly gives $h_a = 0$ for the monostatic off-nadir case while in the specular bistatic one ($\theta_{\mathrm{R}} = -\theta_{\mathrm{T}}$), we can consider the case of $r_{\mathrm{R}} = r_{\mathrm{T}}$ without loss of generality in view of the r_{T}

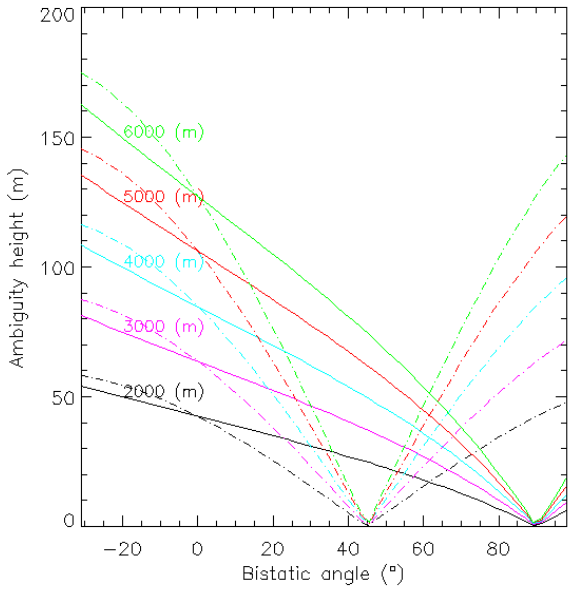

Figure B.4: Interferometric ambiguity height sensitivity versus bistatic angle with a varying baseline angle (θ_b) to keep the orthogonal baseline constant ($b_\perp = 10m = b$), so that ($\theta_b = -90^o$ for $\theta_{\mathrm{R}} = 0.$). Each colour is associated to a given receiver range (r_{R}) for both bistatic and equivalent monostatic configurations plotted respectively with plain and dot lines, as in figure B.3. Likewise, the transmitter is set in a medium Earth orbit by T $\left(., -3.10^5, 3.10^5\right)$, hence $\theta_{\mathrm{R}} = 45^o$ for $\beta = 0$ in the monostatic case.

invariance aforementioned. Hence $\vartheta = 0$ and it suits the specific case where :

$$\tan\theta_{\mathrm{R}} = -\frac{\epsilon a_{\mathcal{E}}}{b_{\mathcal{E}}} \text{and } \varrho = \frac{b_{\mathcal{E}}}{\varrho(\theta_{\mathrm{R}}, \varphi_{\mathrm{R}} = \pi/2)}$$

with $b_{\mathcal{E}}$ the semiminor axis. Besides, the following relations can be reminded for an arbitrary ellipsoid :

$$\frac{b_{\mathcal{E}}^2}{\epsilon a_{\mathcal{E}}} = \frac{b_{\mathcal{E}}^2}{c_{\mathcal{E}}} = \frac{p_{\mathcal{E}}}{\epsilon} = \frac{a_{\mathcal{E}}(1-\epsilon)}{\epsilon}$$

Considering then the term within the brackets in equation (B.9), it gives finally :

$$\begin{aligned} &\tan\theta_{\mathrm{R}} + \frac{\epsilon\cos\theta_{\mathrm{R}}}{1+\epsilon\sin\theta_{\mathrm{R}}} \\ &= \tan\theta_{\mathrm{R}} + \frac{\epsilon}{p_{\mathcal{E}}}\varrho(\theta_{\mathrm{R}}, \varphi_{\mathrm{R}} = \pi/2)\cos\theta_{\mathrm{R}} \\ &= -\frac{a_{\mathcal{E}}\epsilon}{b_{\mathcal{E}}} + \frac{\epsilon}{p_{\mathcal{E}}} b_{\mathcal{E}} \\ &= 0 \end{aligned} \tag{B.11}$$

hence the null value for the ambiguity height in the specular bistatic configuration.

In opposition to these zero values, the case of an infinite ambiguity height can be also encountered, brought by a null orthogonal baseline ($b_\perp = 0$). In addition to the fact that the range

increment is higher for (a) since it matches a vertical projection projection one ($R_z + \Delta_z$), such singularity is actually at the origin of the difference between the plots in figures B.3 and B.4. Indeed, in the case (b), the $b_\perp$ is kept constant so that the singularity or its surrounding region can not appear, hence the smoother variation than in the case former case (a). Qualitatively, this infinite value traduces the fact that when both antennas are along the line of sight, all the points within the resolution cell will have the same interferometric phase whatever their height, which naturally results from the far region assumption (cf. formula B.1).

To synthesize the formulae required in section for direct scattering mechanisms (from the volume or the ground), it has been demonstrated that :

$$\begin{aligned}
\frac{\partial(\varrho_1 - \varrho_2)}{\partial \varrho}|_{z,\varphi} &= \frac{b\big(\sin\theta_1\cos\theta_b - \cos\theta\sin\varphi\sin\theta_b\big)}{\varrho\tan\theta} \\
\frac{\partial(\varrho_1 - \varrho_2)}{\partial z}|_{\varrho,\varphi} &= \frac{b\big(\sin\theta\cos\theta_b - \cos\theta\sin\varphi\sin\theta_b\big)}{\varrho\cos\theta} \\
&\quad \cdot \Big[\tan\theta + \frac{\epsilon\big[\cos\vartheta\sin\varphi\cos\theta + \sin\vartheta\sin\theta\big]}{1+\epsilon\big[\cos\vartheta\sin\varphi\sin\theta - \sin\vartheta\cos\theta\big]}\Big]^{-1} \\
&= \lambda/h_a \\
\frac{\partial(\varrho_1 - \varrho_2)}{\partial \varphi}|_{\varrho,z} &= b\sin\theta\sin\theta_b\cos\varphi
\end{aligned} \tag{B.12}$$

(in which the subscripts '$_1$' have been dropped since $\theta_2(=\theta_1 + d\theta_1)$ is not involved).

The point now at issue consists in the derivation of the above expressions in the case of the coupling mechanisms, as formulated in section 5.3.2, the bistatic specificity lies herein in the volume integration which matches a tilted parallelepiped (cf. figure B.5. The new coordinate system $\mathbf{R}_{\widehat{\imath}}$ can thus be considered, deduced from the reference one after a rotation of $\widehat{\imath}$ around $\hat{x}$. As a result, it transposes the problem with a straight parallelepiped simply viewed under another incidence angle. For the sake of simplicity, we remind that the envisioned bistatic configuration have been restricted to the incidence plane concerning the localization of the volume integration (originated by the equivalent ground point for the specular ground mechanisms), so that a non depointing angle $\varphi = \pi/2$ will be herein likewise assumed. In this framework and considering the spherical coordinate system within $\mathbf{R}_{\hat{\imath}}$ and the origin at R_1, the following relations can be derived :

$$\tan(\theta_1 - \widehat{\imath}) = \tfrac{y_{\hat{\imath}}}{H\cos\widehat{\imath} - z_{\hat{\imath}}} \tag{B.13}$$

$$\Rightarrow \begin{cases} \frac{d\theta}{\cos^2(\theta_1-\hat{\imath})\tan(\theta_1-\hat{\imath})}|_{x_{\hat{\imath}},z_{\hat{\imath}}} & = \frac{dy_{\hat{\imath}}}{r\sin(\theta-\hat{\imath})} \\ \frac{d\theta}{\cos^2(\theta_1-\hat{\imath})\tan(\theta_1-\hat{\imath})}|_{y_{\hat{\imath}},z_{\hat{\imath}}} & = -\frac{dz_{\hat{\imath}}}{H\cos\hat{\imath} - z_{\hat{\imath}}} \end{cases} \tag{B.14}$$

$$\tan\varphi = \tfrac{y_{\hat{\imath}}}{x_{\hat{\imath}}} \tag{B.15}$$

$$\Rightarrow \tfrac{d\varphi}{\cos^2(\varphi)\tan(\varphi)}|_{y_{\hat{\imath}},z_{\hat{\imath}}} = -\frac{dx_{\hat{\imath}}}{r\sin\theta\cos\varphi} \tag{B.16}$$

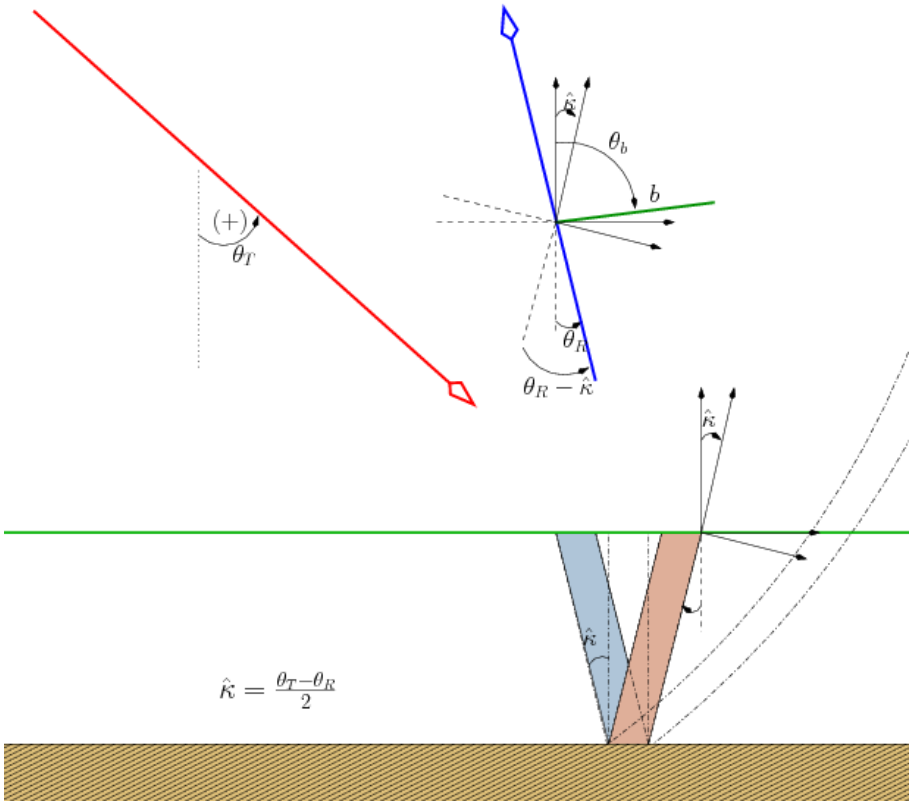

Figure B.5: Domains of integration corresponding to the specular ground mechanisms with respect to the transmitter and to the receiver, respectively indicated by the red and blue tilted ($\pm\,\widehat{\iota}$ parallelepipeds).

so that :

$$\begin{aligned} d\theta &= \frac{\cos(\theta_1 - \hat{\iota})}{r} dy_{\hat{\iota}} \\ d\theta &= \frac{\sin(\theta_1 - \hat{\iota})}{r} dz_{\hat{\iota}} \\ d\varphi &= -\frac{sin\varphi}{r\sin(\theta - \hat{\iota})} dx_{\hat{\iota}} \end{aligned} \tag{B.17}$$

Then, reminding the previous relations which still holds with $(\theta - \hat{\iota})$ and $(\theta_B - \hat{\iota})$ instead of respectively θ and θ_B :

$$\begin{aligned} \frac{\partial(r_1 - r_2)}{d\theta} &= b\sin(\theta - \theta_b) \\ \frac{\partial(r_1 - r_2)}{d\varphi} &= b\sin(\theta - \hat{\iota})\sin(\theta_B - \hat{\iota})\cos\varphi \end{aligned} \tag{B.18}$$

the following expressions can be finally be obtained :

$$\begin{aligned}
\frac{\partial(r_1 - r_2)}{dx_{\hat{\imath}}}|_{y_{\hat{\imath}},z_{\hat{\imath}}} &= \kappa_{x_{\hat{\imath}}}/k = \frac{b}{r}\sin\varphi\sin(\theta_b - \hat{\imath})\cos\varphi_1 = 0 \\
\frac{\partial(r_1 - r_2)}{dy_{\hat{\imath}}}|_{x_{\hat{\imath}},z_{\hat{\imath}}} &= \kappa_{y_{\hat{\imath}}}/k = \frac{b}{r}\sin(\theta - \theta_b)\cos(\theta - \hat{\imath}) \\
\frac{\partial(r_1 - r_2)}{dz_{\hat{\imath}}}|_{x_{\hat{\imath}},y_{\hat{\imath}}} &= \kappa_{z_{\hat{\imath}}}/k = \frac{b}{r}\sin(\theta - \theta_b)\sin(\theta - \hat{\imath})
\end{aligned} \tag{B.19}$$

Appendix C

Double Bounce Localization in Bistatic

Considering a given scatterer, the importance of localizing its double bounce return has been arisen especially to define the associated correlation integration volume (and the embodied interferometric phase sensitivity) as well as the SAR processing issue. Behind the localization term, we seek to attribute a resolution cell to this specular ground return. To clarify the geometrical parameters, the envisioned configuration is shown in figure C.1 for the case of the double bounce with respect to the transmitter, firstly tackled as a coplanar problem. Within this plane, an arbitrary point (P) of height h above the ground is chosen, in addition to the transmitter (T) and receiver (R) positions. As mentioned in section 5.3.2 within the geometrical optics approximation, the transmitter specular ground point is determined by the intersection of lines respectively supported by the tangent vector to the ground and vector $T_{\aleph}\vec{P}$, $T_{\aleph}$ being the orthogonal symmetric point of T with respect to the tangent line to the ground. At this point, we consider an arbitray point lying on the ground (E) which position is defined by the angle noted 'ι' initiated from P. With the path initiated from T to R passing by E, the angles $\theta_{\mathrm{T}} - \iota = (\widehat{\overrightarrow{\mathrm{PG_T}}, \overrightarrow{\mathrm{PE}}})$ and $\theta_R + \iota = (\widehat{\overrightarrow{\mathrm{ER}}, \overrightarrow{\mathrm{EP}}})$ can be emphasized. Assuming that both transmitter and receiver are far enough from P in order to consider the equiphase planes, the distances $[E_1, T]$ and $[G_{\mathrm{T}}, T]$ are roughly equal as well as $[P, R]$ and $[E_3, R]$. Besides, whatever ι, $[E_2, G_{\mathrm{T}}] = [E, E_1]$ since by construction of specular point G_{T}, the triangle of base $[G_{\mathrm{T}}, E]$ is isosceles and E_2 is positioned so that (E_1E_2) // $(G_{\mathrm{T}}E)$. Likewise with trapezoid ($\mathrm{EPE_{3}E_{2}}$) whose shape depends on varying point E, $EE_3 = E_2R$ if and only if triangle of base EP is also isosceles. Thereby, the sufficient and necessary condition concerning the localization of point E to make the path $T \to E \to R$ equals to $T \to G_{\mathrm{T}} \to P \to R$ lies in :

$$\widehat{a} = \widehat{b} \qquad \left(\text{i.e} \quad \widehat{\iota} + \theta_{\mathrm{R}} = \theta_{\mathrm{T}} - \widehat{\iota} \right)$$

hence the double bounce projection onto the ground giving by the angle :

$$\boxed{\widehat{\iota} = \frac{\theta_{\mathrm{T}} - \theta_{\mathrm{R}}}{2}} \tag{C.1}$$

Concerning now the double bounce with respect to the receiver, the reciprocity of the configuration can be invoked : if T and R are inverted, we come back to the transmitter double bounce, the equivalent path is once more given by point E and its associated angle $\widehat{\iota} = \frac{\theta_{\mathrm{T}} - \theta_{\mathrm{R}}}{2}$. Reversing the situation by reciprocity do correspond to the same path and thereby yields to the opposite angle $\widehat{\iota} = \frac{\theta_{\mathrm{R}} - \theta_{\mathrm{T}}}{2}$. In comparison with the common monostatic case where $\widehat{\iota}$ is null and both double bounce are projected onto the ground, we conclude that depending on the upper angle

between θ_{T} and θ_{R}, double bounce equivalent points are either projected forward or backward. Besides, as detailed in section 5.3.2 about the integration volume involved for the specular ground coherence theoretical derivation, all the points bringing a double bounce contribution within a resolution cell are those belonging to the tilted parallelepipeds along $\pm\,\widehat{\iota}$.

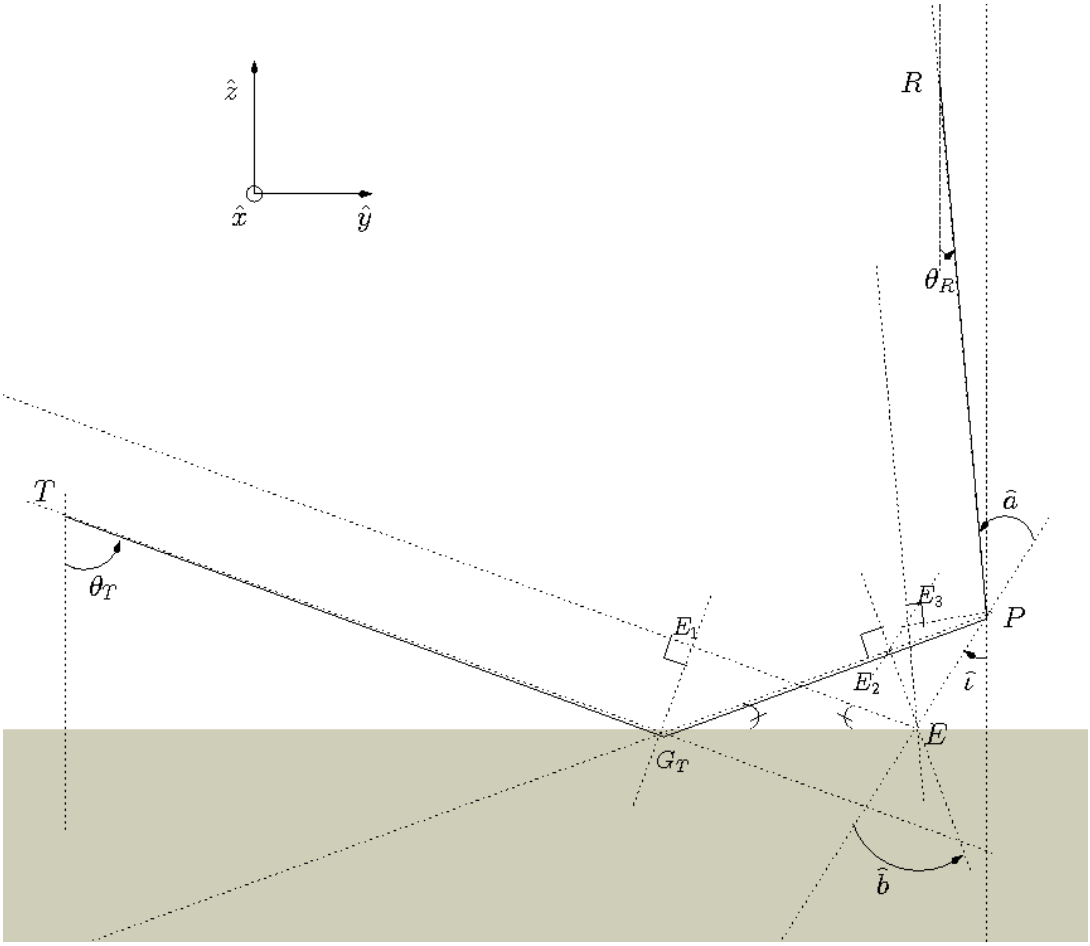

Figure C.1: Equivalent ground point localization for the double bounce with respect to the transmitter

Appendix D

Bistatic SAR Processing Impacts on Double Bounce Mechanism

The point at issue hereafter is to wonder if the double bounce contribution will be faithfully reproduced by a classical (but bistatic) SAR processing. By classical, we mean that a stationary (that is translationally invariant) configuration is considered involving thereby a linear chirp as target point spectrum. No doubt that more sophisticated SAR processing methods could be invocated but it would be beyond that study, specifically focused on verifying that double bounce, as a multipass contribution, is not spoiled by algorithms made according to simple interaction target point. Mostly, the question is not arisen in monostatic since the double bounce behaves as a single ground point which position does not vary during the azimuth acquisition (long time axis). Whenever it is not the case, two fundamental points can be questioned, namely the target point spectrum as well as the range migration. Both involve the propagation phase derivative for an arbitrary target point P. In the case of permanent parallel tracks during the long time acquisition, for instance along direction $\vec{x}$ (cf. figure D.2 with $\vec{v}_{\mathrm{T,R}} = v_{\mathrm{T,R}}\vec{x}$), the phase's derivative can be expressed in the following form :

$$\begin{aligned} f(t) &= 2\pi \frac{\varphi(t)}{dt} \\ \text{with } \varphi(t) &= k_0 \cdot \big(r_{\mathrm{T}} + r_{\mathrm{R}}\big) \\ &= k_0 \cdot \Big(\sqrt{r_{\mathrm{T}}^0)^2 + x_{\mathrm{T}})^2} + \sqrt{r_{\mathrm{R}}^0)^2 + x_{\mathrm{R}})^2} \Big) \end{aligned} \tag{D.1}$$

with the superscript '^{0}' suiting the zero Doppler position as the reference one (cf. figure D.1). As commonly assumed for SAR configuration in the absence of significant squint angle, the approximation $x_{\mathrm{T,R}} \ll r^0_{\mathrm{T,R}}$ yields to :

$$\begin{aligned} \varphi(t) &= k_0 \cdot \Big(r^0_{\mathrm{T}}\big[1 + \frac{1}{2}\frac{x_{\mathrm{T}}^2}{r_{\mathrm{T}}^0)^2}\big] + r^0_{\mathrm{R}}\big[1 + \frac{1}{2}\frac{x_{\mathrm{R}}^2}{r_{\mathrm{R}}^0)^2}\big] \Big) \\ &= \frac{k_0}{2}\Big(\frac{v_{\mathrm{T}}^2}{r^0_{\mathrm{T}}} + \frac{v_{\mathrm{R}}^2}{r^0_{\mathrm{R}}}\Big)t^2 + const. \end{aligned} \tag{D.2}$$

which leads to an hyperbole shape for the range only compressed signal since within the stationary hypothesis, the term $k_0(r_{\mathrm{R}_0} + r_{\mathrm{T}_0})$ used above is time invariant (as confirmed with the following simulations illustrated in figure D.1). The resulting spectrum is thus driven by a linear chirp, in the same way as in monostatic.

The previous point has been implicitly considered on the ground from which a volume one can then be defined : $[x_P, y_P, z_P = h]$. With the layover effect, this point will be recorded in a resolution cell of abscissa given by : $G_{\mathrm{V}}\ [x_P, y_P - h \cdot \tan^{-1} \frac{\theta_T + \theta_R}{2}, z_0]$. This comes from the fact that whatever P of height z_P and far from the antennas, the resolution cell along the range direction can be approximated by the tangent to the iso-ranges. Using the property about the tangent to an ellipse which states that its normal bisects the angle $(\widehat{\vec{\mathrm{PT}}, \vec{\mathrm{PR}}})$ defined towards the focus T and R (cf. figure D.2), that tangent line is tilted according to the angle $\frac{\theta_{\mathrm{T}} + \theta_{\mathrm{R}}}{2}$.

Similarly, as shown previously in appendix C, a volume scatterer P will initiate specular ground mechanisms which will be — again along the range axis — projected onto the ground at positions :

$$G_{\mathrm{T}} \begin{bmatrix} x_{\mathrm{P}} \\ y_{\mathrm{P}} - h \cdot \tan \frac{\theta_{\mathrm{T}} - \theta_{\mathrm{R}}}{2} \\ z_0 \end{bmatrix}, G_{\mathrm{R}} \begin{bmatrix} x_{\mathrm{P}} \\ y_{\mathrm{P}} + h \cdot \tan \frac{\theta_{\mathrm{T}} - \theta_{\mathrm{R}}}{2} \\ z_0 \end{bmatrix}$$

respectively for transmitter and receiver. Since the localization of these points $(G_{\mathrm{V}}, G_{\mathrm{T}}, G_{\mathrm{R}})$ depends on the viewing angles which vary slightly during the along track axis, their behaviour will be rigorously different from a standard point lying on the ground (G), as classically considered to derive for instance formula D.2.

This difference concerning both Doppler phase history and range migration can be quantified through the variation of the matching distance (or phase) one during the along track acquisition. With $\varphi^+(x)$ being the algebraic additional phase term in comparison with (G), we have :

$$\varphi^+ = k_0 h \cos \widehat{a}$$

with $\widehat{a}$ being equal either to $\frac{\theta_{\mathrm{T}} - \theta_{\mathrm{R}}}{2}$, $\widehat{\imath}$ or - $\widehat{\imath}$ respectively in the case of volume direct scattering or double bounce mechanisms associated to the transmitter or the receiver. Keeping a constant scatterer height (h = z_P), the differentiation of the above expression leads to :

$$\frac{\partial \varphi^+}{\partial \widehat{a}} = -k_0 h \sin \widehat{a} \tag{D.3}$$

which traduces — through $\widehat{a}$ — the sensitivity towards the radar elevation angles.

Besides, the sensitivity of these radar elevation angles towards the along-track displacement can be assessed as follows :

$$\begin{aligned} z_{\mathrm{T}} \tan \theta_{\mathrm{T}} + z_{\mathrm{R}} \tan \theta_{\mathrm{R}} &= \|\vec{r}_{\mathrm{T}} - (\vec{r}_{\mathrm{T}} \cdot \vec{z})\vec{z}\| + \|\vec{r}_{\mathrm{R}} - (\vec{r}_{\mathrm{R}} \cdot \vec{z})\vec{z}\| \\ \text{hence with : } \vec{p}_{\mathrm{T,R}} &= \vec{r}_{\mathrm{T,R}} - (\vec{r}_{\mathrm{T,R}} \cdot \vec{z})\vec{z} \\ p_{\mathrm{T,R}} &\simeq p^0_{\mathrm{T,R}} + \frac{x_{\mathrm{T,R}}}{2y^0_{\mathrm{T,R}}} \\ \text{and assuming } x = x_{\mathrm{T}} &= x_{\mathrm{R}}, \\ \text{it brings : } \frac{\partial \theta_{\mathrm{T}}}{\partial x} + \frac{\partial \theta_{\mathrm{R}}}{\partial x} &= \Big(\frac{\cos^2 \theta_{\mathrm{T}}}{z_{\mathrm{T}} y^0_{\mathrm{T}}} + \frac{\cos^2 \theta_{\mathrm{R}}}{z_{\mathrm{R}} y^0_{\mathrm{R}}}\Big) x \end{aligned} \tag{D.4}$$

Combined to D.3, D.4 gives the following variation along x for the additional phase term :

$$\begin{aligned} \frac{\partial \theta_{\mathrm{T}}}{\partial x} &= -k_0 h \sin \widehat{a} \cdot \Big(\frac{\cos^2 \theta_{\mathrm{T}}}{z_{\mathrm{T}} y^0_{\mathrm{T}}} + \frac{\cos^2 \theta_{\mathrm{R}}}{z_{\mathrm{R}} y^0_{\mathrm{R}}}\Big) x \\ &\text{(volume direct interaction)} \\ \frac{\partial \theta_{\mathrm{T}}}{\partial x} &= \pm k_0 h \sin \widehat{a} \cdot \Big(\frac{\cos^2 \theta_{\mathrm{T}}}{z_{\mathrm{T}} y^0_{\mathrm{T}}} - \frac{\cos^2 \theta_{\mathrm{R}}}{z_{\mathrm{R}} y^0_{\mathrm{R}}}\Big) x \\ &\text{(specular ground interaction)} \end{aligned} \tag{D.5}$$

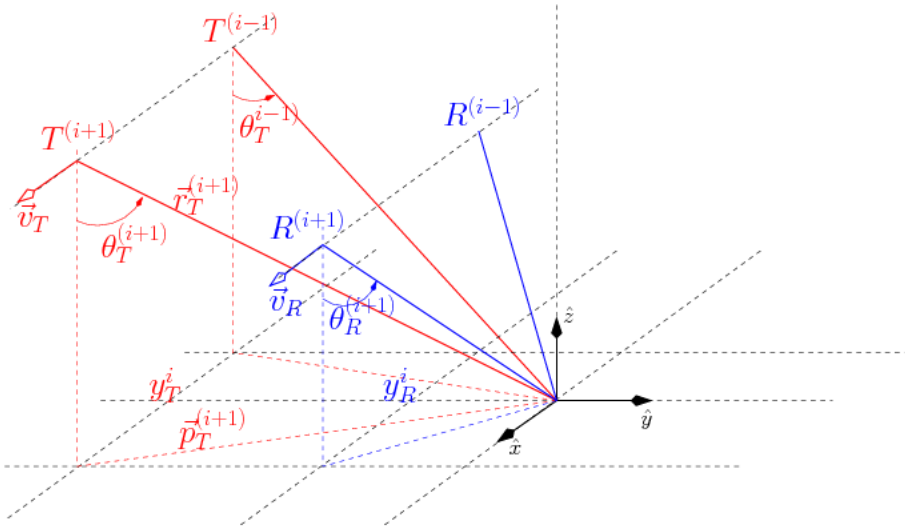

Figure D.1: Along-track acquisitions originating the SAR processing for bistatic configurations limited to the plane of incidence, i.e parallel tracks and same velocities between the transmitter and receiver.

Consequently, with x $\ll z_{\mathrm{T,R}}$ (zero or small squinted radar), $\frac{\partial \theta_{\mathrm{T}} \pm \theta_{\mathrm{R}}}{\partial x}$ can be neglected as well as $\frac{\partial \varphi^{+}}{\partial x}$ which justifies the fact that specular ground or volume mechanism spectrum can be approximated by the equivalent ground point one.

Simulations have then be carried out using a coherent summation process. Concerning the along range compression, a bandwidth of 318.7 MHz has been resulting in a ground resolution Δ_{rng} of roughly one meter (cf. [Krieger and Moreira, 2006; Villard et al., 2008]) :

$$\Delta_{rng} = \frac{c/B}{\|\vec{grad} f\|} = \frac{c/B}{\sin\theta_{\mathrm{T}} + \sin\theta_{\mathrm{R}}}$$

Considering an observation time $t_{obs} = N/_{\mathrm{PRF}}$ and for the sake of simplicity similar velocities $v = v_{\mathrm{T}} = v_{\mathrm{R}}$, the chirp bandwidth generated by the synthetic aperture can be formulated from equations (D.1) and (D.2) as follows :

$$\begin{aligned} B_{az} &= \frac{1}{2\pi} \cdot f(t_{obs}/2) = \frac{1}{2\pi} \frac{kv^2}{r_{eq}} \frac{t_{obs}}{2} \\ &= \frac{kNv^2}{\pi \cdot \mathrm{PRF}} r_{\mathrm{eq}}^{-1} \qquad \text{(D.6)} \\ &\qquad \text{with } r_{\mathrm{eq}} = \frac{2 r_{\mathrm{T}} r_{\mathrm{R}}}{r_{\mathrm{T}} + r_{\mathrm{R}}} \end{aligned}$$

providing an azimuth resolution ($\frac{v}{B}$) of about 5.5 meters with the previously indicated parameters.

The resulting processed images are shown in (a) and (b) on figure D.1 respectively for the single along range compression and for both range and azimuth one, where also envisioned are two coherent and isotropic scatterers with their direct and double bounce returns. It can be noticed that both kind of mechanisms exhibit nearly the same range variation, resulting in slightly the same Doppler phase history as well as range migration, which confirms the validity of the aforementioned approximations.

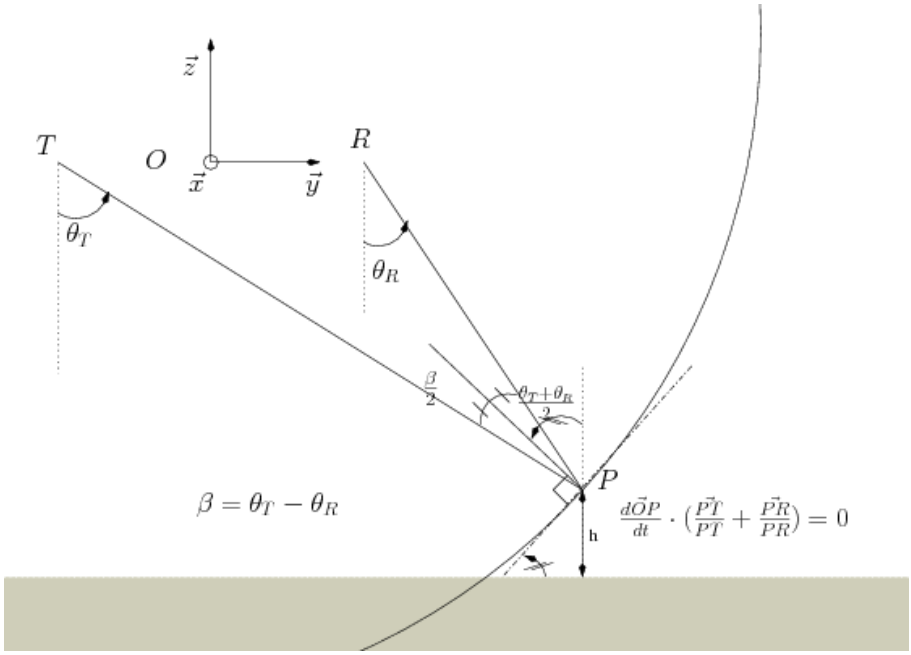

Figure D.2: Layover projection approximated by the tangent to the bistatic ellipsoid

Unlike other multiple interactions exhibiting a different spectrum due to an intrinsic phase history, it turns out that double bounce can be still considered after SAR processing without any additional distortion in comparison with simple interaction. This lies mainly on the fact that both double bounces regarding transmitter or receiver have an equivalent ground point (cf. appendix C) which lies approximately in the same plane which is never forward or backward projected further than the volume equivalent one (projected by layover effect).

Bibliography

A. Ishimaru. *Wave propagation and scattering in random media*, volume 2. Academic Press, 1978.

G. Krieger and A. Moreira. Spaceborne bi- and multistatic sar : potential and challenge. In *Radar, Sonar and Navigation, Proceedings*, volume 153, pages 184–198, 2006.

L. Villard, I. Hajnsek, P. Borderies, and K. Papathanassiou. Pol-insar simulations in forest bistatic scattering. In *7th European Conference on Synthetic Aperture Radar (Friedrichshafen)*. VDE Verlag, 2008.

Glossary

This glossary includes the frequently used acronyms, mathematical symbols and notations can be found in page 7.

A

AGB: Above Ground Biomass 11

B

BGMTI: Bistatic Ground Moving Target Indicator 31
biPol-InSAR: Bistatic Pol-InSAR v
BRDF: Bidirectional Reflectance Distribution Function 26
BSA: Backward Scattering Alignment 98

C

C: Covariance matrix 99
CRVoG: Coupled Random Volume over Ground 189

D

D2M: Delay Doppler Map 32
DBF: Digital Beam Forming 31
DBH: Diameter at Breast Height 15
DBWA: Distorted Born Wave Approximation 50
DLR: Deustche Zentrum für Luft und Raumfahrt i
DOA: Direction Of Arrival 22

E

EEA: European Environment Agency 2
EREA: European Research Establishments in Aeronautics i
ESA: European Space Agency 2

F

FAO: Forest and Agriculture Organization . 10
FDTD: Finite-Difference Time Domain 57
FMDP: Forest Model Descriptive Parameters 187
FOPEN: Foliage Penetration 86
FSA: Forward Scattering Alignment 98

G

GEOSS: Global Earth Observation System of System 2
GIS: Geographic Information System 11
GMES: Global Monitoring for the Environment and Security 2
GNSS-R: Global Navigation Satellite Systems - Reflectometry 30
GO: Geometrical Optics 45

H

H,A,α: Entropy; Anisotropy; α angle 105

I

IEM, AIEM: [Advanced] Integral Equation Method 46
IPCC: Intergovernmental Panel on Climate Change 2

K

K: Kennaugh matrix 99
KA: Kirchhoff Approximation 45

L

LA[IP]: Leaf Area [Index, Density] 15
LIDAR: LIght Detection And Ranging 21
LoS: Line of Sight 120

M

M: Muller matrix 99
MIPERS: Multistatic Interferometric and Polarimetric model for Remote Sensing v

N

ND[IVW]I: Normalized Difference [Infrared, Vegetation, Water] Index 19
nSCOψVoG: n (layers) Structured Coupled ψ-Oriented Volume over Ground 189

O

P

R

S

T

U

V

W

Index

In alphabetical order, the following entries cover the main keywords and concepts of the thesis.

Appendix E

Résumé détaillé (version française)

"Modélisation directe et inverse des observables radar à synthèse d'ouverture en configuration bistatique. Applications en télédétection des milieux forestiers."

Contents

Introduction

L'observation des forêts est fondamentale dans de nombreuses disciplines, en premier lieu pour celles liées aux problématiques environnementales, que ce soit à l'échelle mondiale (enjeux climatique et problématique carbone) ou locale (état des écosystèmes) mais aussi pour celles liées aux activités anthropiques (sylviculture, détection relevant d'application militaire ou d'assistance). Dans ce contexte, les techniques de télédétection sont devenues incontournables, offrant des capacités uniques en terme de couverture planétaire, de résolution spatiale et temporelle et de façon non intrusive. Parmi elles, le succès du radar à synthèse d'ouverture (SAR) réside principalement dans sa capacité à imager des zones de grande échelle de façon robuste vis à vis des conditions de propagation atmosphérique. Cette capacité de pénétration des ondes radar est aussi primordiale pour caractériser la structure de milieux naturels comme les couverts forestiers. Supportés par de nombreuses campagnes aéroportées ou spatioportées témoignant de l'âge d'or du SAR, divers modes ont été mis en oeuvre répondant à des applications spécifiques comme l'acquisition **Pol-In**SAR permettant d'attribuer aux mécanismes de diffraction discriminés par la **Pol**arimétrie une hauteur via l'information **In**terférométrique, permettant par exemple de retrouver des paramètres descriptifs d'intérêts pour l'étude des forêts. La configuration bistatique – communément définie par une distance de séparation entre émetteur et récepteur significative par rapport à l'une des distances avec la scène observée – s'inscrit dans ce cadre de recherche d'améliorations. Revisité à plusieurs reprises dans l'histoire du radar, le bistatique ne constitue pas un concept nouveau en soit mais peut s'avérer potentiellement intéressant pour des applications spécifiques, en particulier celles où la physique des observables, fondamentale pour les perspectives d'inversion, a été peu abordée. Actuellement, plusieurs campagnes aéroportées dont celle associant en 2003 les senseurs RAMSES (ONERA) et E-SAR (DLR) ou projets spaciaux (e.g TanDEM-X, BISSAT) attestent d'une certaine résurgence pour le bistatique dont l'origine réside principalement dans les avancées technologiques sur la synchronisation, motivée de surcroît par une multitude de signaux d'opportunité exploitable, tels que les signaux de télécommunication numérique (GSM, DVB) ou de radio navigation (GPS, Galliléo). Cette thèse s'inscrit dans l'objectif principal de déterminer le potentiel du bistatisme quant à la capacité des nouvelles observables (BiPol-InSAR) à faciliter l'inversion des paramètres descriptifs des forêts. La modélisation du problème direct (diffraction du milieu en bistatique) constitue un appui fondamental pour évaluer la sensibilité des observables ainsi que la qualité des critères d'inversion.

Au vu des interogations sous-jacentes à cette thématique, les lignes directrices de la thèse sont organisées selon les cinq chapitres suivants :

- Au travers du **premier chapitre**, nous nous proposons de mettre en avant les spécificités des forêts en tant que milieu naturel

d'intérêt ainsi que les spécificités du radar comme moyen pour la télédétection. En premier lieu, nous abordons les enjeux liés à la surveillance des forêts ainsi que leur possible caractérisation, au regard de grandeurs quantitatives d'intérêts pour ces mêmes enjeux. Dans un second temps, les particularités du radar sont présentés parmi les autres techniques de télédétection, dans les domaines micro-ondes passif ou optique, de façcon qualitative ainsi qu'au travers des différentes mesures résultantes de ces approches.

- Fondamental pour ce type d'investigation en amont de futures campagnes expérimentales, le simulateur MIPERS – Multistatic Interferometric and Polarimetric model for Remote Sensing –, développé afin de nous permettre de générer des observables Pol-InSAR en configuration multistatique, est décrit dans le **deuxième chapitre**. Si la formulation du modèle cohérent et discret est tout à fait classique pour la modélisation de la diffraction par les forêts, les aspects plus originaux dans MIPERS sont mis en avant, via notamment l'introduction de classes de diffuseurs non canoniques, les différentes possibilités de génération de scènes comprenant entre autre une modélisation multi-zone permettant de traiter les effets de lisières dans le cas de forêts finies ainsi que d'inclure des éléments exogènes de type cibles artificielles. En outre, la question de la simulation d'images bistatique SAR, prenant en compte les principales contraintes de faisabilité est aussi présenté via un algorithme de recalge des données distance/Doppler. Ces différentes capacités seront illustrées aux travers d'applications, à titre de validation (comparaisons dans le cas monostatique) ou d'analyse démonstrative.

- Le **troisième chapitre** est dédié à une analyse générique du comportement en bistatique de milieux simples – de type volume à une couche homogène de diffuseurs possiblement orientés – mais typiquement rencontrés au sein de cas plus complexes dans les chapitres ultérieures. Au préalable à cette analyse, une synthèse des différentes observables radar est présentée, mettant en évidence les plus pertinentes pour les cibles distribuées en bistatique. Les questions relatives à l'impact des définitions choisies, spécifiquement pour la polarisation en bistatique, sont abordées afin de distinguer les effets physiques (propre au milieu) des effets géométriques, possiblement très important dans le cas de configurations bistatiques hors du plan d'incidence. Les liens entre les coefficients de la matrice de diffraction – via la construction des termes de covariance, mais aussi via l'interprétation de leur différence (les polarisations croisés étant possiblement différentes) –

ainsi que leur sensibilité en bistatique pour des milieux canoniques (montrant de fortes propriétés de symétrie) constituent une étape phénoménologique fondamentale dans l'analyse. Cette caractérisation peut en outre permettre de discriminer de façon efficace des diffuseurs plus particuliers, comme abordé en fin de chapitre par des applications de détection.

- Le **quatrième chapitre** propose l'étude de l'apport du bistatique pour l'estimation de la biomasse des forêts à partir des coefficients d'intensité polarimétriques. Cette approche, basée dans l'idéal sur une relation de bijection entre l'intensité et la valeure de biomasse a été appliquée avec succès en monostatique (méthode P-HV) mais s'avère limitée par sa robustesse envers différents type de forêts, dont celles à forte biomasse non envisageable en raison du phénomène de saturation. Motivés par des études préliminaires ayant montré l'intérêt du bistatique sur ce dernier point, nous proposons ici de revisiter ces perspectives, via l'approche de modélisation cohérente (MIPERS) afin de plus d'expliquer l'origine de ce domaine de sensibilité élargie ainsi que d'évaluer l'incertitude de l'estimation, résultant de l'influence des autres paramètres caractéristiques de la forêt, pour un même niveau de biomasse.

- Devenue incontournable pour une caractérisation quantitative des modèles de forêts, le potentiel des cohérences Pol-InSAR constitue une réelle rupture mais est encore sujet à de multiples recherches, dans le but d'améliorer la robustesse des algorithmes d'inversion associés. Parmies elles, l'extension à la configuration bistatique est traitée dans ce dernier et **cinquième chapitre**. Cette étude soulève tout d'abord le choix du type d'acquisition interferométrique (position de la ligne de base) puis de la formulation théorique de la décorrélation due à la végétation, pivot de la méthode inverse, via la dépendence aux paramètres descriptifs du modèle de forêt. Nous essayerons aussi d'enrichir ces paramètres dans le but de prendre en compte des modèles canoniques plus réalistes, en adéquation naturellement avec les possibilités d'inversion, possiblement facilitées par des configurations bistatiques spécifiques. Les différents scénarios d'inversion seront conduits au moyen de cohérences simulées, à l'issue desquels nous tenterons de dégager les géométries bistatiques optimales, en se limitant à un seul angle bistatique dans le plan d'incidence avec possiblement plusieurs lignes de base.

Chapter 1

Télédétection RADAR des forêts

Avec environ 3,9 milliard d'hectares à l'échelle du globe, les forêts représente une part prépondérante dans la caractérisation de la biosphère et dont la surveillance est d'autant plus pertinente que leur évolution est tangible. En effet, conjointement à leur sensibilité aux activités anthropiques (agriculture, sylviculture), l'implication des milieux forestiers est fondamentale pour les cycles de l'eau (précipitations, cycle de désertification cf. [Charney et al., 1975]) et du carbone. Pour ce dernier, bien que plus modeste que l'océan en quantité accumulée, sa capacité de stockage en terme de flux – sans compter les 2 Gt par an rejetées par la déforestation – est équivalente (2 $Gt.an^{-1}$, s'avérant de fait fondamental pour la régulation climatique face aux émissions anthropiques de l'ordre de 5.4 Gt par an (cf. rapport [IPCC, 2007]).

Forte des possibilités micro-onde de pénétration à travers le couvert (et de propagation en général), en plus d'atouts opérationnels (auto-indépendence de la source émetrice, capacité d'imageur, résolution spatiale et temporelle, couverture) le SAR représente un moyen de télédétection unique, en comparaison aux techniques radar (radiomètres passifs, scattéromètres) ou optique (domaine réflectif ou infrarouge).

Néanmoins, l'exploitation de la sensibilité des mesures SAR aux variables d'intérêts de terrain n'est pas évidente, et constitue de multiples axes de recherche et d'améliorations des algorithmes existants. Parmi elles, la configuration bistatique – communément définie par une distance de séparation entre émetteur et récepteur significative par rapport à celle à la cible (cf. figure 1.1) – peut-être envisagée au travers de son potentiel physique pour faciliter cette caractérisation, propos même de cette thèse, parallèlement à ses avantages opérationnels le plus souvent traités au cours de ses différentes revisites (cf. [David, 1969; Willis and Griffiths, 2007]. En effet, mis en oeuvre peu de temps après les débuts du radar, ses avantages découlant directement de la géométrie bistatique ont été mis en avant, notamment pour des applications militaires de détéction/localisation – les mesures de temps de propagation et de direction d'arrivée au niveau du récepteur fournissant la

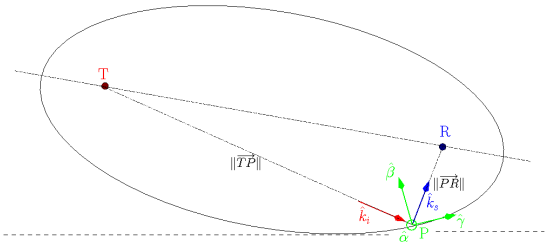

Figure 1.1: Géométrie bistatique générale et ellipsoïde caractéristique des iso-distances, lieu des points situé à la même distance du transmetteur T et du récepteur R.

position sur l'ellipsoïde des iso-distances, cf. figure 1.1 – dont les fameuses exploitations de type 'barrière électromagnétique' (cf. [David, 1969; Cherniakov et al., 2008]) et de défense anti-balistiques. Dans ce contexte, son intérêt pour la détection de cibles furtives est aussi bien connu (cf. [Cherniakov et al., 2008]), les conditions de minimisation de leur SER en monostatique n'étant en général plus valables en bistatique (cf. méthode cohérente des points brillants). Néanmoins, face à la simplicité du monostatique, d'autant plus manifeste avec le duplexeur et les l'utimisation de formes d'ondes (nécessitant une très bonne synchronisation) introduits après la seconde guerre mondiale, le radar bistatique a été depuis lors complétement marginalisé.

La période actuelle atteste d'une résurgence manifeste pour les configurations bistatiques, des progrès technologiques significatifs ayant été accomplies concernant la synchronisation ainsi que la localisation (par GPS), comme en témoigne plusieurs campagnes hybrides (i.e acquisition conjointe mono et bistatique), aéroportées (cf. [Dubois-Fernandez et al., 2006]), spatioportées (projet BISSAT cf. [D'Errico and Moccia, 2003; D'Errico and Fasano, 2008]) ou mixte spatioportées-aéroportées (avec TerraSAR-X cf. [Walterscheid et al., 2006; Rodriguez-Cassola et al., 2010]).

En outre, au vu de la multiplicité et de la diversité des signaux potentiellement exploitables, la mise en place de configurations d'opportunités – avantage singulier rendu possible par la maîtrise du bistatique – devient tout à faite prégnante. Parmi elles, il est possible de distinguer les configurations profitant d'un radar monostatique ('hitchhiker' mode), de signaux de radiocommunications (radio, TV, DVB-[STH]) ou encore de façon très prometteur pour la télédétection de radionavigation (GNSS-R, cf. [Zavorotny and Voronovich, 2000; Martin-Neira et al., 2001]).

Ainsi, ces avancées opérationnelles pour la mise en oeuvre du bistatique rend tout à fait prégnante la question de son potentiel physique pour la caractérisation des scènes et d'autre part, illustre bien – en tant qu'une des possibles voies d'amélioration du monostatique – toute la capacité du radar en télédétection. De plus, véritablement complémentaire aux autres approches issues du radar passif ou de l'optique, les perpectives de fusion apparaissent très prometteuses et par ailleurs, au vu des similarités avancées se montrent manifestement facilitées par la configuration bistatique.

Chapter 2

Modélisation du problème direct

Comme décrit au premier chapitre, la forêt est un milieu complexe de par sa nature inhomogène. Néanmoins, au regard de la sensibilité micro-ondes, sa description par un ensemble d'élements diélectriques de formes géométriques canoniques (ellipsoïdes, cylindres) est pertinente, conduisant à une formulation discrète. Cette dernière est aussi bien appropriée dans la mesure les fractions volumiques des diffuseurs sont relativement modérées (typiquement inférieures à 5 %), rendant possible l'utilisation de l'approximation de Born étendue (DWBA – Distorted Wave Born Approximation). Pour la propagation du champ, son application conduit à l'approximation de Foldy-Lax aussi appelée EFA (Effective Field Approximation), étant dérivé du 'Forward Scattering Theorem', lui-même résultant de l'utilisation du théorème de la phase stationaire (les calculs associés sont plus explicitement détaillés au dernier chapitre, se aussi référant à [Ishimaru, 1978]). De plus, étant donnée la symétrie azimuthale (symétrie de réflexion quelque soit le plan d"incidence) présentée par la forêt (généralement vérifiée par tous les milieux naturels) la loi de propagation du champ au travers du milieu se simplifie (cf. [Tsang and Kong, 2000]) et peut de mettre sous la forme :

$$\frac{d\langle E_q\rangle}{dr} = j\big(k - \frac{\sigma_q}{2}\big)\langle E_q\rangle, \qquad q \in [v,h] \tag{2.1}$$

de laquelle les matrices de transmittivité peuvent facilement s'exprimer au moyen de la longueur de propagation au travers du des l différents couches et de leur coefficient d'extinction (σ_q^l) :

$$[t(\vec{r})] = \begin{bmatrix} \prod_l e^{-\sigma_h^l(\theta)d_l/2} & 0 \\ 0 & \prod_l e^{-\sigma_v^l(\theta)d_l/2} \end{bmatrix} \tag{2.2}$$

Similairement, le champ diffracté reçu résulte de l'application du DWBA en considérant cependant, non pas la valeur moyénnée mais la somme cohérente des contributions des diffuseurs mis en jeu. La phase de l'onde est alors préservée (par opposition aux modèles incohérents, typiquement basés sur la résolution de l'équation de transfert radiatif), attribut essentiel pour les simulations interférométriques. Les contributions directes et de doubles rebonds (couplage volume-sol) sont considérées et respectivement rappelées ci-dessous :

$$\begin{aligned} \mathbf{E}_s(\vec{r}_{\mathrm{R}};\vec{r}_{\mathrm{T}}) = \Big(\sum_p e^{-j\varphi_p^{\mathrm{ds}}}[t_p(\hat{k}_s)]\cdot\big[S_p(\hat{k}_i,\hat{k}_s)\big] \\ \cdot[t_p(\hat{k}_i)]\Big)\cdot\mathbf{E}_i(\hat{k}_i) \end{aligned} \tag{2.3}$$

$$
\begin{aligned}
\mathbf{E}_s^{T,RsG}(\vec{r}_{\mathrm{R}}) &= \left[\mathcal{S}^{\mathrm{T,RsG}}(\hat{k}_i,\hat{k}_s)\right]\cdot\mathbf{E}_i(\vec{r}_{\mathrm{T}}) \\
\left[\mathcal{S}^{\mathrm{TsG}}(\hat{k}_i,\hat{k}_s)\right] &= \sum_p [t_p(\vec{r}_{\mathrm{R}}-\vec{r}_{\mathrm{P}})]\cdot\left[S_p(\hat{\aleph}_i^p,\hat{k}_s^p)\right] \\
&\qquad\cdot[t_p(\vec{r}_{\mathrm{P}}-\vec{r}_{\mathrm{GT}})]\cdot[\mathcal{R}(\theta_i^p)]\cdot[t_p(\vec{r}_{\mathrm{GT}}-\vec{r}_{\mathrm{T}})] \qquad (2.4)\\
\left[\mathcal{S}^{\mathrm{RsG}}(\hat{k}_i,\hat{k}_s)\right] &= \sum_p [t_p(\vec{r}_{\mathrm{R}}-\vec{r}_{\mathrm{GR}})]\cdot[\mathcal{R}(\theta_s^p)]\cdot[t_p(\vec{r}_{\mathrm{GR}}-\vec{r}_{\mathrm{P}})] \\
&\qquad\cdot\left[S_p(\hat{k}_i^p,\hat{\aleph}_s^p,)\right]\cdot[t_p(\vec{r}_{\mathrm{P}}-\vec{r}_{\mathrm{T}})]
\end{aligned}
$$

Concernant les matrices de diffraction des diffuseurs, les expressions analytiques dérivées des approximations de Rayleigh-Gans sont supposées pour les ellipsoïdes, tandis que le rayonnement de courants équivalents correspondants au cas de longueur infinie est utilisé pour les cylindres (formulation par intégrale de surface, cf. [Tsang et al., 1985]). Les modèles de constantes diélectriques issus de loi de mélange (entre composante de végétation, d'eau libre et liée) et tirés de sont employées, mettant en évidence l'importance fondamentale de la teneur en eau. A partir de ces formes canoniques, diverses améliorations peuvent être envisagées telles que le cylindre multi-couches diélectriques (typiquement rencontré pour les troncs composés de cf. [Franchois et al., 1998]), les rugosités de surface (cf. [Lin and Sarabandi, 1995]) ou courbes à section évolutives. Bien que possiblement très significantes, ces améliorations posent aussi le problème de l'acquisition de données de vérité terrain suffisemment complètes. De ce fait, notre attention s'est portée spécifiquement sur les formes courbes, très souvent rencontrées et plus facilement prises en compte par les mesures de terrain.

Concernant le sol, sa modélisation par une surface diélectrique (cf. [Peplinski et al., 1995] pour le modèle de permittivité fonction de la fréquence et de la teneur en eau) et rugueuse (profil statistique exponentiel généralement plus approprié que gaussien) est utilisé pour calculé le champ diffracté via la méthode d'équation intégrale – IEM (cf. [Fung, 1994]). Similairement à la végétation, des modèles analytiques plus sophistiqués ont été proposées dans la littérature (cf. [Elfouhaily and Guérin, 2004] et parmi les plus avancés l'AIEM), une hybridation par méthode numérique (e.g FDTD) pouvant être plus facilement envisagée que pour les diffuseurs de par leur mode de génération différent, introduisant le paragraphe suivant.

Outre la possible utilisation de cylindres courbes, l'originalité de MIPERS réside dans sa polyvalence au niveau de la génération de scènes dont les hétérogénéités spatiales peuvent être prises en compte via par description en zone multiples, dans lesquelles différentes couches homogènes (caractérisées par leur coefficient d'extinction) sont disposées verticalement. Pour chaque couche, différents modes de génération sont envisageables suivant les éléments de vérité terrain déterminant les statistiques de taille et d'orientation des diffuseurs mais de façon indépendendante ou suivant des modèles de

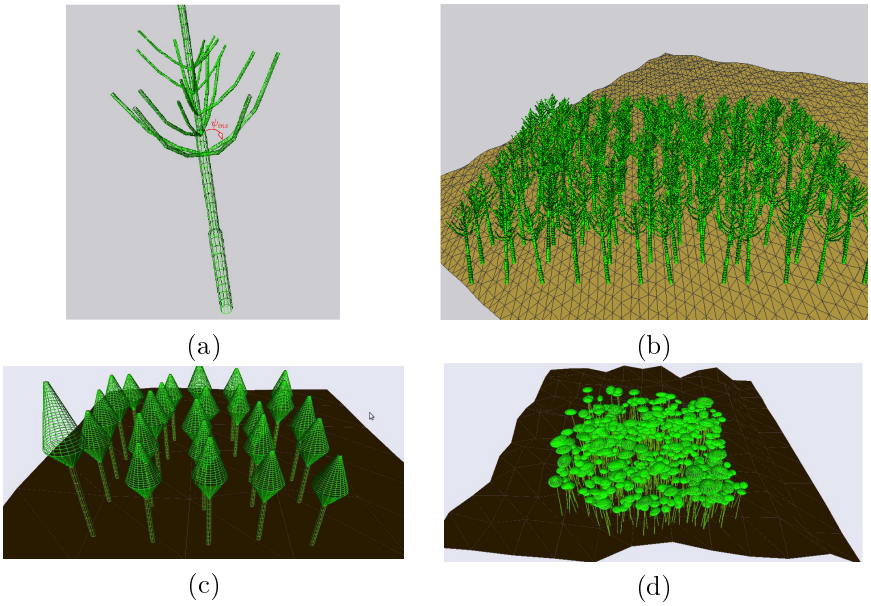

Figure 2.1: (a) illustration du mode génération lié (modèle d'architecture d'arbre) présentant aussi l'angle d'insertion noté ψ_{ins} (défini dans le repère parent). Exemples de forêts générées suivant un modèle d'architecture complet (b) ou suivant les modèles troncs plus houpiers coniques (c) ou ellipsoïdes (d).

croissance, qu'ils concernent l'arbre dans son ensemble ou bien une branche seule (classe de diffuseurs courbes à section évolutive). Parmi ces lois, un soin particulier est accordé aux distributions concernant l'angle d'insertion, défini à la figure 2.1 et dont l'impact sur la radiométrie est important. Pour le sol, une fois sa normale définie (constante sur la zone considérée), une subdivision en multi-facettes à orientation possiblement variable par rapport à la pente globle permet aussi d'attribuer une phase propre aléatoire, permettant de modéliser l'effet de speckle.

Le mode multi-zone nous a permis d'analyser les effets de lisière (d'autant plus manifestes dans les images SAR de bonnes résolutions ($\leq$ 2 m) et de montrer, outre les effets de distortions (layover, shadowing) l'importance du mécanisme de double rebond à l'origine des renforcements d'intensités observés du côté du layover (cf. [Villard and Borderies, 2007a]).

De plus, cette facilité nous a aussi permis de prendre en compte des zones internes au couvert, afin notamment modéliser la présence de cibles artificielles. Ces dernières peuvent être alors considérées comme un diffuseur classique avec champ incident résultant de l'hypothèse DWBA associé à notre méthode de tracé de rayon par listes chainées (cf. [Villard and Borderies, 2007b]), la contribution de la cible étant issue d'une hybridation par méthode

numérique (FDTD, cf. [Berenger, 1994]). Cet aspect a été exploité dans une analyse des capacités de détection en bistatique d'un véhicule (camion militaire) sous une forêt de type tempérée, montrant l'importance de l'acquisition de toutes les polarisations.

Par ailleurs, le modèle a été validé suivant des tests théoriques fondamentaux, notamment polarimétriques (cf. [Villard et al., 2007] ainsi que chapitre 3) et par comparaison des niveaux radiométriques avec les résultats expérimentaux monostatiques issus d'ERS (bande C), des campagnes sur les forêts d'Ebergsberg (E-SAR en bande L) et de Nezer (RAMSES en bande P), cette dernière présentant l'intérêt de comparaisons à différents âges et biomasses.

Chapter 3

Propriétés remarquables de la diffusion en bistatique

En amont des chapitres quatre et cinq dediés à des approches inverses de paramètres caractéristiques des forêts, ce chapitre propose de façon prémiminaire l'analyse des propriétés de diffraction de milieux simples – volumes à une seule couche – mais caractérisées par les observables polarimétriques suivant toutes les géométries bistatiques. Ces géométries soulèvent d'abord la question des mesures associées, notamment via les différentes conventions liées aux bases de polarisations, dont celle propre au FSA – Forward Scattering Algignement – rappelée à la figure 3.1.

Dans ce cadre académique (la théorie de polarisation constituant un riche sujet d'algèbre), la généralisation des différentes définitions, propriétés et intérêts des observables dérivées des vecteurs Jones ou de Stokes ainsi que des matrices de cohérence, covariance, de Muller ou de Kennaugh sont synthétisés, essentiellement à partir de travaux antérieurs tirés de [Davidovitz and Boerner, 1986; Czyz, 1991; Germond, 1999])

A la différence de [Titin-Schnaider, 2007, 2008], notre approche ne visant pas à une optimisation des polarisations sur tous les degrés de libertés offerts par les bases de polarisation (paramètres de l'ellipse), nous nous focalisarons plus particulièrement sur les termes de la matrice S (de Sinclair). Les relations fondamentales liant ces termes et fonction des symétries caractéristiques du milieu — temporelle via la réciprocité et spatiales suivant différents plans de réflection — sont mises en évidence en s'inspirant des travaux réalisés dans cf. [Nashashibi and Ulaby, 2007].

Limité dans un premier temps à des configurations dans le plan d'incidence, l'évolution des coefficients s_{qp} en fonction de l'angle bistatique montrent de façon intéréssante pour la descrimination toute l'importance de la nature des

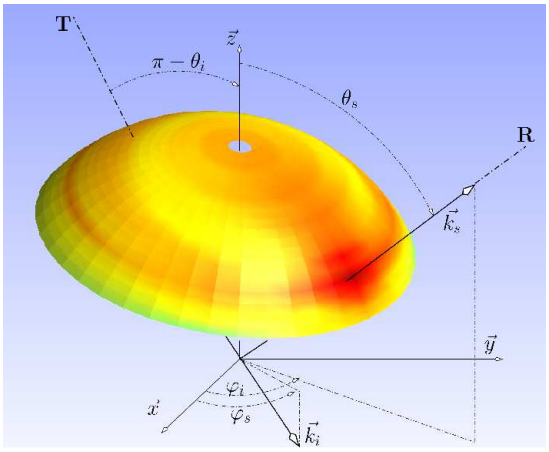

Figure 3.1: Définition des bases de polarisations en convention FSA avec leurs angles associés, utilisés ultérieurement pour les diagrames de diffraction hémisphériques.

diffuseurs (via leur diagramme individuel de diffraction) ainsi que de leur orientation (suivant les bornes limitant les variations de l'angle d'insertion ψ_{ins}) notamment via la relation mise en évidence avec l'écart entre les termes de polarisation croisés, différence clairement manifeste avec la matrice S monostatique anti-symmétrique (cas réciproque en FSA).

Cette caractérisation a par ailleurs été étudié dans le cas de cibles cohérentes en mettant en oeuvre un algorithme d'inversion des angles d'attitudes d'une cible à symétrie de révolution à partir des matrices S résultant d'une configuration hybride monostatique et bistatique, en cherchant à diagonaliser la première et à rendre anti-symétrique la seconde.

Ces différentes propriétés sont alors analysées dans le cas d'une géométrie bistatique générale, leur transposition n'étant manifestement pas possible pour les cas de plans bistatiques inclinés (plan non normal au plan horizontal de référence $\mathcal{P}_{\hat{z}}$). Nous montrons alors que ces effets sont essentiellement liés à la géométrie des définitions des bases de polarisations. Initié récemment dans [Nashashibi and Ulaby, 2007], l'introduction d'une nouvelle base permet de corriger significativement ces artefacts de polarisation, permettant alors de trouver une configuration équivalente dans le plan bistatique normal – ou plan d'incidence $\widehat{(\hat{k}_i, \hat{z})}$).

Notre étude s'intéresse alors aux termes de couplage, mettant en évidence l'importance de la modélisation cohérente pour leur prise en compte, conduisant aussi à la généralisation du phénomène de backscattering enhancement en bistatique. Similairement au volume, l'importance des effets de diagramme des diffuseurs individuels (spécifiquement pour les cylindres orientés verticalement) est aussi clairement manifeste, étant de façon générale d'une grande importance pour la capacité de la géométrie bistatique à filtrer les mécanismes de diffraction.

A titre d'applications les plus directes, une utilisation des propriétés de symétrie mises en évidence pour la discrimination de cibles artificielles – ou plus exactement ne vérifiant pas ces symétries – est proposée. Nous montrons en effet via les coefficients la matrice de cohérence, permettant de bien synthétiser ces relations caractéristiques, que le contraste radiométrique est significativement amélioré par rapport à l'utimisation simple des coefficients σ^0_{qp}.

Enfin, dans le cas spécifique de la détection au voisinage de lisière, nous montrons – comme précédement au moyen de l'exemple du camion sous une forêt de type tempérée détaillée au chapitre 1 – que la configuration bistatique, en supprimant les effets de renforcements (côté du layover) permet de réduire clairement le taux de fausse alarme.

Chapter 4

Utilisation de l'intensité en bistatique pour l'estimation de biomasse

Plus que sa mise en évidence – déjà entreprise dans plusieurs études antérieurs (cf. [Ulaby et al., 1990; Karam et al., 1992; Dobson et al., 1992; Toan et al., 1992]) – l'exploitation de la sensibilité micro-onde à la biomasse des forêts est une question d'actualité, particulièrement prégnante dans le cadre de la quantification des stocks de carbone renouvelable à l'échelle mondiale. Motivées par plusieurs missions spatiales en préparation, dont BIOMASS conduite par l'ESA, diverses approches ont été proposées, le plus souvent basé sur des régressions multivariées sur les mesures radiométriques, que ce soit dans le domaine radar passif, actif (utilisation des coefficients de rétrodiffusion σ^0_{qp}) ou optique (via les indices dérivés des réflectances), les perspectives de fusion étant encore au stade de prospective (hormis avec la technologie LIDAR, cf. mission NASA DESDnyl). Forte de son efficacité et de sa simplicité (une seule fréquence, polarisation et performances opérationnelles uniques dérivées du SAR en termes de couverture, de résolution spatiale et temporelle) la méthode P-HV est basé idéalement sur la relation de bijection en bande P entre le coefficient de rétrodiffusion σ^0_{hv} et la valeur de biomasse (cf. figure 4.1). Même si son application à divers types de forêts s'est révélé très encourageante (cf. [Toan et al., 2004]), les perspectives d'améliorations de la méthode concernent le problème de la saturation (atteinte pour des biomasses de l'ordre de 150 $t.ha^{-1}$) ainsi que sa robustesse vis à vis de paramètres perturbateurs résultant de la sensibilité possible au sol — défaut principal des polarisations pleines σ^0_{hh} ou σ^0_{vv} — ou à d'autres caractéristiques du volume (e.g teneur en eau, orientation et dimensions des diffuseurs). Dans cet objectif, l'utilisation de l'interférométrie (cf. chapitre 5) ou plusieurs fréquences (cf. [Saatchi et al., 2007]) peut être envisagée, tout comme la configuration bistatique qui permettrait de con-

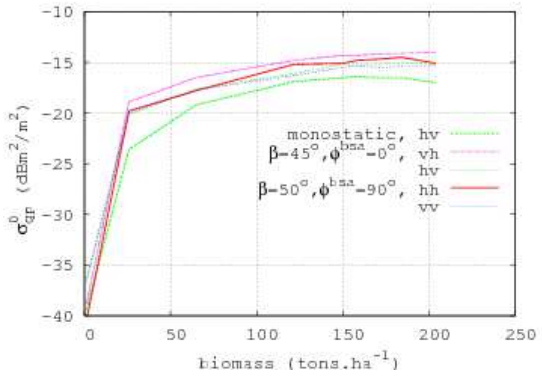

Figure 4.1: Sensibilité des intensités en fonction de la biomasse pour les configurations bistatiques optimales déterminées par $[\theta_{\mathrm{T}} = 45^o, \theta_{\mathrm{R}} = 0^o, \Delta\varphi = 0^o]_{\mathrm{SSA}}$, $[\theta_{\mathrm{T}} = 45^o, \theta_{\mathrm{R}} = 5^o, \Delta\varphi = 90^o]_{\mathrm{SSA}}$ en comparaison avec le monostatique ($[\theta_{\mathrm{T}} = 45^o$).

server la même efficacité que pour la méthode P-HV monostatique.

Afin de d'essayer transposer cette approche en bistatique, un modèle de croissance de forêt a été choisi, basé sur les charactéristiques de la forêt de Nezer avec toutefois des adaptations de façon à rendre l'étude aussi générique que possible. Au vu des critères précédents concernant la saturation et la robustesse, l'analyse des simulations effectuées avec MIPERS pour diverses configurations bistatiques a abouti à deux types de configurations optimales, présentées à la figure 4.1. Leur intérêt principal réside dans un domaine de sensibilité exploitable élargi (de l'ordre 30 $t.ha^{-1}$), que nous avons expliqué par le comportement individuel des diffuseurs favorisé bistatique pour une robustesse équivalente, s'avérant le plus mis en défaut par la teneur en eau du volume.

Chapter 5

Potentiel de l'interférométrie vectorielle en bistatique

Ce chapitre est dédié à l'intérêt d'une utilisation de cohérences polarimétriques et interféromètriques en bistatique (biPol-InSAR). En monostatique, leur potentiel pour l'inversion quantitative de paramètres descriptifs du modèle RVoG (Random Volume Over Ground, i.e modèle canonique constitué d'un volume à une couche de diffuseur uniformément orienté au dessus d'un sol non dépolarisant) – de fait particulièrement bien adapté pour la caractérisation des milieux forestiers – constitue une véritable avancée et rupture par rapport aux autres techniques. Le pivot de l'inversion réside dans l'expression analytique de la cohérence interférométrique fonction de la hauteur et de l'extinction du volume, comme l'ont démontré les auteurs dans [Treuhaft et al., 1996]. La polarimétrie permet alors de discrimer le volume du sol, permettant ainsi de retrouver la hauteur topographique et donc la hauteur de forêt sans mesures additionnelles, avec naturellement des applications très riches notamment pour l'estimation de la biomasse, la hauteur étant le paramètre unique le plus correlé (cf. [Mette et al., 2004]). Deux approches principales ont alors été mise en place, graphique et par table de référence (cf. [Cloude and Papathanassiou, 1998, 2003]) ou paramétrique (cf. [Treuhaft and Siquiera, 2000]), moins élégante mais offrant potentiellement une plus grande robustesse et la capacité de traiter les termes de couplage sous réserve de cohérences supplémentaires (plusieurs baselines). Ces deux aspects, robustesse – nécessitant un modèle à-priori de forêt suffisamment complet – et nombre suffisant d'observables constituent les deux principales limitations. Parmi divers axes de recherche, des acquisitions multi-baselines (approche paramétrique précédente ou approche PCT – Polarization Coherence Tomography [Cloude, 2006] – à différencier de la tomographie SAR) ont été entrepris, auquels nous proposons la configuration bistatique.

Au vu de certaines difficultés rencontrées en monostatique pour la qualité des interférogrammes, nous nous limitons dans le cadre de cette première investigation au cas d'acquisitions bistatiques dans le plan d'incidence, rendant possible des vols simples rectilignes et parallèles. Toujours dans un souci de performances opérationelles et d'étude du potentiel intrinsèque au bistatique, les acquisition multi-baselines considérées correspondent au même angle bistatique (cf. figure 5.1) et peuvent être réalisées en mode single-pass bande-L (antennes communément embarquées, lignes de bases inférieures à 20 m) afin aussi d'éviter les problèmes de coregistration, de ligne de base critique (b^c) et de décorrélation temporelle.

Nous démontrons alors que la cohérence biPol-InSAR peuvent se mettre

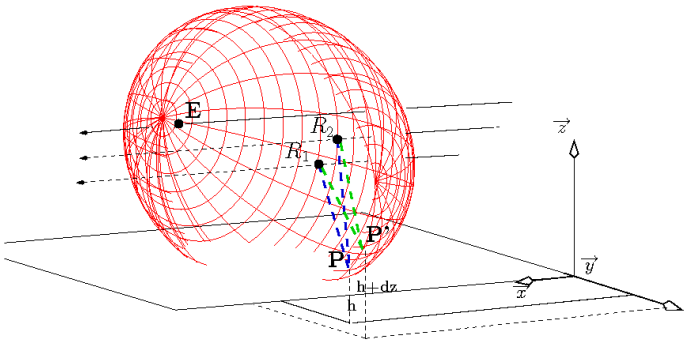

Figure 5.1: Acquisition BiPol-InSAR single-pass, émetteur E et baseline formée par les antennes passives R_1, R_2.

sous la forme suivante :

$$\begin{aligned}\gamma_{qp}^{(\mathrm{tot})} = e^{j\Phi_0}\Big[e^{j(\Phi_0^V-\Phi_0)}\gamma_{qp}^{(\mathrm{v})} + \mu_{qp}^{\mathrm{dg}}\cdot\gamma_{qp}^{(\mathrm{dG})} + (1+\delta_\beta\delta_{q-p})\mu_{qp}^{(\mathrm{Tsg})}\cdot\gamma_{qp}^{(\mathrm{Tsg})} \\ + (1+\delta_\beta\delta_{q-p})\mu_{qp}^{(\mathrm{Rsg})}\cdot\gamma_{qp}^{(\mathrm{Rsg})} + \delta_\beta(1-\delta_{q-p})\mu_{qp}^{(\mathrm{TRsg})}\cdot(\gamma_{qp}^{(\mathrm{TRsg})}+\gamma_{qp}^{(\mathrm{RTsg})})\Big] \\ \cdot\Big[1+\mu_{qp}^{(\mathrm{dG})} + (1+\delta_\beta\delta_{q-p})(\mu_{qp}^{(\mathrm{Tsg})}+\mu_{qp}^{(\mathrm{Rsg})}) + 2\delta_\beta(1-\delta_{q-p})\mu_{qp}^{(\mathrm{TRsg})}\Big]^{-1} \\ \Big(p\subset(v,h), q\subset(v,h), p\neq q\Big)\end{aligned} \tag{5.1}$$

exprimant en fait une relation de barycentre de coefficients de pondérations les rapports d'énergie relatifs aux mécanismes du sol direct et spéculaires sur celui de volume, respectivement notés $\mu_{qp}^{\mathrm{dg}}, \mu_{qp}^{(\mathrm{Tsg})}$ et $\mu_{qp}^{(\mathrm{Rsg})}$.

Les changements fondamentaux se trouvent tout d'abord dans l'extention en géométrie bistatique de la hauteur d'ambiguité, impliqué via le terme α_z dans la décorrélation due au volume il suit :

$$\gamma_{\mathrm{qp}}^{\mathrm{vlm}} = e^{j\Phi_0^{(\mathrm{v})}}\frac{\int_0^h e^{i\alpha_z z}\exp[\varpi_{qp}^{\mathrm{v}}\cdot z]}{|\int_0^h \exp[\varpi_{qp}^{\mathrm{v}}\cdot z]} \qquad p,q\subset[v,h] \tag{5.2}$$

$$\text{with}: \ \varpi_{qp}^{\mathrm{v}} = \frac{\sigma_q(\theta_{\mathrm{R}})}{\cos\theta_{\mathrm{R}}} + \frac{\sigma_p(\theta_{\mathrm{T}})}{\cos\theta_{\mathrm{T}}} \tag{5.3}$$

De façon intéréssante pour l'inversion à venir, les termes de couplage peuvent aussi être explicités en fonction des paramètres caractéristiques du

volume (comme ci-dessus 5.3), par l'intermédiaire d'une solution originale de point équivalent au sol (cf. appendix 5) nous permettant de déterminer le volume d'intégration ainsi que leur sensibililté interférométrique (terme κ_v).

Dans un second temps, l'extension a un volume structuré est aussi proposé, permettant de traiter les cas de forêt décrites par plusieurs couches.

La complexification de la description du modèle de forêt soulève alors le problème de la faisabilité de l'inversion, comme le résume la formulation suivante entre vecteur de mesures et des paramètres d'intérêts :

$$\begin{bmatrix} \gamma_{qp}^{b_1,b_2,b_3} \end{bmatrix} \underset{\substack{p \in [v,h] \\ q \in [v,h]}}{=} M_{b_1,b_2,b_3}^{qp} \cdot \begin{bmatrix} \phi_0^{g,v} \\ h_v \\ \sigma_q^{\theta_i,\theta_s}, \sigma_p^{\theta_i,\theta_s} \\ \\ \mu_{qp}^{(dg),(Tsg),(Rsg)} \end{bmatrix}$$

avec la phase topographique ϕ_0^g, la hauteur du volume ϕ_0^v, h_v, les coefficients d'extinctions ($\sigma_{v,h}^{i,s}$) ainsi que les rapports d'énergie ($\mu_{qp}^{(dg),(T,Rsg)}$).

Ce problème inverse est évaluée au moyen des critères d'Hadamard, d'unicité, d'existence et de stabilité, les deux derniers points étant étudiés via le modèle direct MIPERS. Nous montrons alors que l'acquisition à plusieurs lignes de bases (limitée cependant à 3) permet d'améliorer significativement le pouvoir de discrimination des cohérences.

Notre analyse met alors en évidence tout l'intérêt du comportement bistatique des mécanismes de diffraction — certains termes de couplage pouvant être négligés — afin de traiter des modèles de forêt plus conformes aux données de terrain, avec le CRVoG (modèle RVoG comprenant les terms couplage) et 2CSRVoG (modèle couplé à deux couches). Le cas des volumes orientés est aussi traité (COψVoG,2CSOψVoG) mettant en avant les difficultés d'une estimation précise des coefficients d'extinctions (notre fonction de coût lui étant faiblement sensible).

Il apparaît alors que l'amélioration principale concerne la robustesse de l'estimation des hauteurs topographique et du volume total (somme des hauteurs des couches individuelles) ainsi que dans l'inversion de nouveau paramètres liés à la nature du sol, permettant d'envisager de multiples applications.

Bibliography

J.P Berenger. A perfectly matched layer for the absorption of electromagnetics waves. *Journal of computational physics*, 114:185–200, 1994.

J. Charney, P. H. Stone, and W.J. Quirk. Drought in sahara - biogeophysical feedback mechanism. *Science*, 187(4175):434–435, February 1975.

M. Cherniakov, Antonio Moccia, Alberto Moreira, Gerhard Krieger, and Marco D'Errico. *Bistatic Radars : Emerging Technology*. John Wiley & Sons., 2008.

S.R. Cloude. Polarization coherence tomography. *Radio Science*, 41,RS4017, August 2006.

S.R. Cloude and K.P. Papathanassiou. Three stage inversion process for polarimetric sar interferometry. *Radar Sonar and Navigation IEE Proceedings*, 39(150):125–134, 2003.

S.R. Cloude and K.P. Papathanassiou. Polarimetric sar interferometry. *IEEE Transactions on Geoscience and Remote Sensing*, 36:1551–1565, Sept 1998.

Z.H. Czyz. Characteristic polarisation states for bistatic non-reciprocal coherent scattering case. In *International Conference on Antennas and Propagation (ICAP)*, volume 1, pages 253–256. IEE, 1991.

P. David. *Le Radar*, volume 381. PUF, coll. Que sais-je ?, editions des presses universitaires de france edition, 1969.

M. Davidovitz and W-M. Boerner. Extension of kennaugh's optimal polarization concept to the asymmetric scattering matrix case. *IEEE Transactions on Geoscience and Remote Sensing*, 34:569–574, April 1986.

M. D'Errico and G. Fasano. Design of interferometric and bistatic mission phases of cosmo/skymed constellation. *Acta Astronautica*, 62 (2-3):97–111, 2008.

M. D'Errico and A. Moccia. Attitude and antenna pointing design of bistatic radar formations. *IEEE Transactions on Geoscience and Remote Sensing*, 39:949–960, July 2003.

M.C. Dobson, F.T. Ulaby, T. Le Toan, A. Beaudoin, E.S. Kasishke, and N. Christensen. Dependence of radar backscatter on coniferous forest biomass. *IEEE Transactions on Geoscience and Remote Sensing*, 30:412–415, March 1992.

P. Dubois-Fernandez, H. Cantalloube, B. Vaizan, G. Krieger, R. Horn, M. Wendler, and V. Giroux. Onera-dlr bistatic sar campaign: planning, data acquistiton, and first analysis of bistatic scattering behaviour of natural and urban targets. *Radar, Sonar and Navigation, IEE Proceedings*, 153:214 – 223, June 2006.

T. Elfouhaily and C-A. Guérin. A critical survey of approximate scattering wave theories from random rough surfaces. *journal Waves in Random and Complex Media*, 14:R1–R40, Oct. 2004.

A. Franchois, Y. Pineiro, and R.H. Lang. Microwave permittivity measurements of two conifers. *IEEE Transactions on Geoscience and Remote Sensing*, 36:1384–1395, Sept. 1998.

Adrian K. Fung. *Microwave Scattering and Emission Models and Their Applications*. Artech House, 1994.

A.-L. Germond. *Théorie de la polarimétrie radar en bistatique*. Phd dissertation, Université de Nantes (France), Jan. 1999.

IPCC. *Climate Change 2007: Synthesis Report. Contribution of Working Groups I, II and III to the Fourth Assessment Report of the Intergovernmental Panel on Climate Change [Core Writing Team, Pachauri, R.K and Reisinger, A. (eds.)]*. Academic Press, November 2007.

A. Ishimaru. *Wave propagation and scattering in random media*, volume 2. Academic Press, 1978.

A.M. Karam, A.K. Fung, R.H. Lang, and N.S. Chauhan. A microwave scattering model for layered vegetation. *IEEE Transactions on Geoscience and Remote Sensing*, 4(30):767–784, 1992.

Yi-Cheng Lin and K. Sarabandi. Electromagnetic scattering model for a tree trunk above a tilted ground plane. *IEEE Transactions on Geoscience and Remote Sensing*, 33:1063–1070, July 1995.

M. Martin-Neira, M. Caparrini, and J. Font-Rosselo. The paris concept: An experimental demonstration of sea surface altimetry using gps reflected signals. *IEEE Transactions on Geoscience and Remote Sensing*, 39:142–150, 2001.

T. Mette, K. Papathanassiou, I. Hajnsek, H. Pretzsch, and P. Biber. Applying a common allometric equation to convert forest height from pol-insar data to forest biomass. In *Geoscience and Remote Sensing Symposium (IGARSS), Anchorage (Alaska)*, volume 20-24. IEEE, 2004.

A.Y. Nashashibi and F.T. Ulaby. Mmw polarimetric radar bistatic scattering from a random surface. *IEEE Transactions on Geoscience and Remote Sensing*, 45:1743–1755, June 2007.

N.R. Peplinski, F.T. Uaby, and M.C. Dobson. Dielectric properties of soils in the 0.3-1.3-ghz range. *IEEE Transactions on Geoscience and Remote Sensing*, 33:803–807, May 1995.

M. Rodriguez-Cassola, S.V. Baumgartner, G. Krieger, and A. Moreira. Bistatic terrasar-x/f-sar spaceborne/airborne sar experiment : Description, data processing and results. *IEEE Transactions on Geoscience and Remote Sensing*, 48(2):781–794, Feb. 2010.

S.S. Saatchi, K. Halligan, D.G. Despain, and R.L. Crabtree. Estimation of forest fuel load from radar remote sensing. *IEEE Transactions on Geoscience and Remote Sensing*, 45:1726–1740, June 2007.

C. Titin-Schnaider. Power optimization for polarimetric bistatic random mechanisms. *IEEE Transactions on Geoscience and Remote Sensing*, 45: 3646–3660, Nov. 2007.

C. Titin-Schnaider. Polarimetric characterization of bistatic coherent mechanisms. *IEEE Transactions on Geoscience and Remote Sensing*, 46:1535–1546, May 2008.

T. Le Toan, A. Beaudoin, J. Riom, and D. Guyon. Relating forest biomass to sar data. *IEEE Transactions on Geoscience and Remote Sensing*, 30: 403–411, March 1992.

T. Le Toan, S. Quegan, I. Woodward, M. Lomas, N. Delbart, and G. Picard. Relating radar remote sensing of biomass to modelling of forest carbon budgets. *Climatic Change*, 67:379–402, December 2004.

R.N. Treuhaft and P. R. Siquiera. Vertical structure of vegetated land surfaces from interferometricand polarimetric radar. *Radio Science*, 35(1): 141–177, 2000.

R.N. Treuhaft, Soren N. Madsen, Mahta Moghaddam, and Jakob J. van Zyl. Vegetation characteristics and underlying topography from interferometric radar. *Radio Science*, 31:1449–1485, November-December 1996.

L. Tsang and J.A. Kong. *Scattering of Electromagnetic Waves*, volume Advanced Topics. Wiley Series, 2000.

L. Tsang, J.A. Kong, and R. Shin. *Theory of Microwave remote sensing*. Wiley Interscience, 1985.

F.T. Ulaby, K. Sarabandi, K. McDonald, M. Whitt, and M.C. Dobson. Microwave canopy scattering model. *International Journal of Remote Sensing*, 11:1223–1254, 1990.

L. Villard and P. Borderies. Backscattering border effects for forests at C-band. *PIERS Online (Progress in Electromagnetics Research Journal)*, 3: 731–735, 2007a.

L. Villard and P. Borderies. Bistatic foliage penetration modelling. In *International Geoscience and Remote Sensing Symposium (IGARSS)*, volume 4109-4112. IEEE, 2007b.

L. Villard, I. Hajnsek, and P. Borderies. Bistatic forest scattering modeling. In *ODAS symposium*. ONERA-DLR, Göttingen (Germany), 2007.

I. Walterscheid, J.H.G. Ender, and O. Loffeld. Bistatic image processing for a hybrid sar experiment between terrasar-x and pamir. In *Geoscience and Remote Sensing Symposium (IGARSS)*, pages 1934–1937. IEEE International Conference, 2006.

Nicholas J. Willis and Hugh D. Griffiths. *Advances in Bistatic Radar*. SciTech Publishing, 2007.

V.U. Zavorotny and A.G. Voronovich. Scattering of gps signals from the ocean with wind remote sensing application. *IEEE Transactions on Geoscience and Remote Sensing*, Mar 2000.

Conclusion

Au terme de cette étude, le modèle développé – MIPERS – a montré toute son importance au travers de l'investigation de nouvelles configurations bistatiques, dans le cadre de la télédétection des milieux forestiers. En effet, si le bistatique – revisité à maintes reprises et principalement mis en avant pour des considérations opérationnelles – ne constitue pas un concept nouveau en soit, l'originalité des travaux présentés réside avant tout dans la physique des observables en bistatique et dans leur potentiel pour faciliter et améliorer la charactérisation des forêts. Plus spécifiquement, ce potentiel a été principalement mis en avant au travers de l'extension en bistatique des deux approches principales en télédétection radar monostatique des forêts à savoir l'approche P-HV ainsi que l'utilisation des cohérences Pol-InSAR, respectivement abordées au chapitres 4 et 5.

L'intérêt du bistatique pour la première réside essentiellement dans une sensibilité étendue à des valeurs de biomasse plus élevées, pour lesquelles la phase de saturation – phénomène physique incontournable de la méthode – est déjà atteinte en monostatique. Bien que mise évidence antérieurement, notre approche se distingue par l'utilisation de modèle cohérent et surtout par une explication de cette propriété bistatique via les contributions individuelles des diffuseurs. Par ailleurs, différents critères de robustesse ont été évalués, parmi lesquelles les charactéristiques du sol ainsi que la teneur en eau de la végétation se sont avérées fondamentales pour l'incertitude sur la biomasse estimée et nous a conduit à deux configurations bistatiques optimales.

Enrichie par l'acquisition interférométrique, l'utilisation de la polarimétrie via les cohérences Pol-InSAR en bistatique s'est aussi avérée très prometteuse, en proposant une inversion quantitative de paramètres descriptifs d'intérêts pour la forêt. En s'inspirant de l'inversion en monostatique du cas canonique du RVoG, un opérateur analytique liant les paramètres descriptifs du milieu forestier aux cohérences Pol-InSAR a été mis en place, permettant de prendre des modèles de forêts plus complexes (2SCOψVoG). Pour ce faire, une analyse fine des termes de couplage a été proposée, conduisant à une solution élégante de diffuseur équivalent sur le sol. Pivot dans la fonction de coût introduite, cet opérateur munit des cohérences simulées par MIPERS nous a permis par une approche d'optimisation non linéaire d'évaluer la faisabilité du problème inverse pour de multiple configurations. L'intérêt du bistatique est alors mise en évidence par une géométrie particulière (GT-OR), impliquant un émetteur en incidence rasante avec un récepteur au nadir, munit de trois lignes de bases interférométriques. La robustesse de la hauteur retrouvée est alors très significativement améliorée et l'estimation des rapports d'énergie entre termes de volume et de couplage s'avère très prometteuse concernant la charactérisation du sol ou pour des applications de détection.

Préalablement à ces deux approches, une étude générique des propriétés polarimétriques en bistatique a été conduite, en s'intéressant aux termes

de la matrice de diffraction et à ses observables dérivées pour des milieux canoniques. Cette étude a permis de mettre en évidence des artefacts de polarisation dues aux géométries bistatiques hors du plan d'incidence. La correction de ces artéfacts – via l'introduction d'une base adaptée de polarisation – nous a permis d'élargir les comportements charactéristiques de cas canoniques (volume d'une seule couche aléatoire ou orienté) expliqués dans le cas du bistatisme dans le plan d'incidence, pour les contributions directes et issues du double rebond. De plus, l'analyse polarimétrique nous a permis d'établir un lien entre orientation des diffuseurs et la différence entre les termes croisés de la matrice S, avec notamment pour application un algorithme original d'estimation des angles d'Euler pour les diffuseurs cohérents à symétrie de révolution au moyen d'une acquisition hybride, monostatique plus bistatique. Des applications prometteuses pour retrouver les angles de pente (du problème 3D) de surfaces naturelles peuvent être de fait envisagées. En outre, l'étude approfondie des conséquences des symétries du milieu sur les observables bistatiques, bien synthétisés en utilisant la matrice de cohérence (T), a débouché sur un algorithme efficace de détection de cibles artificielles, ne vérifiant pas les propriétés de symétrie des milieux naturels.

Par ailleurs, les différentes configurations optimales proposées ont aussi pris en compte les critères fondamentaux de faisabilité opérationnels, particulièrement importants concernant l'imagerie SAR bistatique, comme nous l'avons montré au deuxième chapitre via l'algorithme de recalage des données de l'espace distance-Doppler à l'espace cartésien. Hormis l'acquisition hybride permettant de charactériser les angles d'attitude des cibles cohérentes, nous nous sommes aussi limités à des configurations bistatiques simples (un émetteur et un seul angle bistatique) afin de mettre en évidence le potentiel intrinsèque de ces configurations. Néanmoins, comme nous l'avons souligné dans le premier chapitre, les systèmes d'opportunités répartis (multistatique) représente un avantage indéniable dérivé de la maitrîse de la configuration bistatique et constituent à ce titre des perspectives de travaux très prometteuses notamment à partir des applications mise en avant dans cette thèse. A titre de futurs axes de recherche, le premier chapitre a aussi souligné des plus grandes similarités de la configuration bistatique avec les domaine micro-onde passif ou optique, facilitant certainement les perspectives de fusion optique radar (bistatique), via notamment la position de réception souvent optimale au nadir.

Conjointement à ces perspectives de campagnes, notre démarche a montré l'importance de la modélisation directe, en particulier pour la formulation du problème inverse. Etant donné les performances du modèle (temps de calcul, adéquation aux données expérimentales), une méthode globale de type assimilation (basée sur la réactualisation de paramètres tests en fonction de l'écart entre données simulées et mesurées) pourrait être envisagée, en enrichissant par exemple les mesures in-situ de mesures de proximité RADAR.

Modélisation directe et inverse des observables radar à synthèse d'ouverture en configuration bistatique. Applications à la télédétection des milieux forestiers

Le radar à synthèse d'ouverture (RSO) constitue un instrument unique en télédétection des forêts, fort des propriétés physiques micro-ondes en sus d'atouts opérationnels. Néanmoins, l'utilisation de la sensibilité des mesures SAR aux variables d'intérêts in-situ n'est pas triviale et constitue de multiples axes de recherche dont l'étude de la configuration bistatique. Le succès de récentes acquisitions aéroportées (e.g campagne conjointe ONERA-DLR) ou hybrides témoigne d'une certaine résurgence pour la géométrie bistatique, principalement mis en avant pour des considérations opérationnelles. La question du potentiel physique des observables bistatiques reste cependant peu traitée. La thèse s'inscrit dans cet objectif, via l'étude de configurations bistatiques optimales pour améliorer l'inversion de paramètres in-situ d'intérêts, tout en considérant leur faisabilité. Dans ce cadre, la modélisation électromagnétique est fondamentale, illustrée ici par le développement du simulateur ad-hoc MIPERS dont les originalités par rapport aux modèles existants ont démontré toute leur importance pour analyser ces nouvelles observables. Des extensions novatrices des algorithmes de référence en monostatique basées sur l'intensité et l'interférométrie vectorielle – pour une estimation directe de la biomasse ou via l'inversion de paramètres descriptifs de modèles de forêts – sont alors proposées, à l'issue de formulations théoriques supportées par les résultats de simulations. Outre de futures campagnes expérimentales bistatiques, sont aussi mises en avant les perspectives innovantes de configurations multistatiques.

Mots clés : Modélisation électromagnétique directe et inverse – Pol-InSAR bistatique – Télédétection des forêts

Forward and Inverse Modeling for Synthetic Aperture Radar Observables in the Bistatic Configuration. Applications in Forest Remote Sensing

Synthetic aperture radar (SAR) turns out to be particularly powerful in forest remote sensing, benefiting from micro-waves properties jointly to operational assets. Nevertheless, the interpretation of SAR measurements regarding in-situ parameters is not straightforward and originates many fields of research, such as the bistatic configuration. The success of recent airborne campaigns (e.g joint ONERA-DLR acquisition) or hybrid ones illustrates certain resurgence for bistatic, mostly fostered by system and strategic advantages. Yet, the physical potential of bistatic observables remains poorly known, particularly for forest monitoring. Initiated by that question, the thesis aims at investigating optimal bistatic configurations in order to ease and improve the retrieval problem, keeping in mind the operational feasibility. For such topic, electromagnetic modeling is of the greatest importance, as shown with the development of the simulator MIPERS which assets regarding existing models evince all their relevance for the understanding of the new observables. Based on theoretical and phenomenological results supported by our simulations, innovative extensions of monostatic reference algorithms based on the backscatter or on vectorial interferometry have been set forth, in order to estimate the biomass directly or through forest model descriptive parameters. On top of experimental bistatic campaigns, also set forward are promising prospects on multistatic acquisitions.

Keywords : Forward and Inverse Electromagnetic Modeling – Bistatic Pol-InSAR – Forest Remote Sensing